Cancer Cell

Volume 22
Number 2

August 14, 2012

www.cellpress.com

ASXL1 Mutations and Loss of H3K27me3

Genomic Analysis Drives Tailored Therapy in Poor Risk Childhood Leukemia

Christine J. Harrison[1,*]
[1]Northern Institute for Cancer Research, Newcastle University, Newcastle upon Tyne NE2 4HH, UK
*Correspondence: christine.harrison@newcastle.ac.uk
http://dx.doi.org/10.1016/j.ccr.2012.07.012

Ph-like acute lymphoblastic leukemia (ALL) is a novel subgroup of high-risk childhood ALL. In this issue of *Cancer Cell*, Roberts et al. describe the identification of genetic alterations that lead to activated kinase and cytokine receptor signaling in Ph-like ALL and demonstrate that this aberrant signaling can be inhibited effectively.

The improving survival rate for children with acute lymphoblastic leukemia (ALL) is one of the greatest success stories of cancer treatment. However, a small proportion of patients will relapse; relapsed disease has a poor response to current therapy, resulting in reduced survival. Thus, to ensure optimum treatment, it is essential that patients at high-risk of relapse are identified at the time of diagnosis.

The prognostic relevance of specific chromosomal abnormalities in B-lineage ALL has been known for some time. To date, this information remains an important factor in risk stratification of these patients for treatment (Moorman et al., 2010). In particular, patients with the translocation, t(9;22)(q34;q11.2), resulting in the *BCR-ABL1* fusion, known as Philadelphia chromosome (Ph)-positive ALL, with rearrangements of the *MLL* gene, or with hypodiploidy (<40 chromosomes) are stratified as high-risk and treated on intensive therapy. More recently, using fluorescence in situ hybridization and genomic approaches, novel genetic aberrations have been identified, including those leading to dysregulated expression of CRLF2 or those targeting genes involved in transcriptional regulation of lymphoid development (Mullighan et al., 2007, 2009a; Russell et al., 2009). It was noted that alterations of one of these genes, *IZKF1*, was strongly associated not only with the poor-risk Ph-positive ALL but also with poor-risk among Ph-negative ALL. Many of these Ph-negative cases show a gene expression profile similar to that of the Ph-positive ALL and share the same high-risk of relapse and poor outcome. These cases of ALL were defined as *BCR-ABL1*-like or Ph-like (Den Boer et al., 2009; Mullighan et al., 2009b) and account for ~10% of childhood B-ALL. A pattern of genetic aberrations was beginning to emerge among these Ph-like ALL to facilitate their identification in the many study groups for which gene expression profiling is not available. In addition to the high incidence of *IKZF1* deletions, another genomic pointer of Ph-like ALL so far identified is dysregulated CRLF2 expression. This abnormality is present in ~50% of Ph-like cases, of which ~50% also harbor Janus kinase (*JAK*) mutations. However, in the remaining cases, the genetic alterations were unknown.

In the paper by Roberts and colleagues in this issue of *Cancer Cell* (Roberts et al., 2012), the authors provide a comprehensive genomic definition of Ph-like ALL with genetic alterations of a range of kinase and cytokine receptors. Initially, transcriptome and whole genome sequencing approaches were used to interrogate the genomes of 15 Ph-like cases. The altered genes discovered from this analysis included previously reported, albeit rarely, and novel fusions and mutations: for example *ABL1*, including the *NUP214-ABL1* fusion that had been previously shown to be amplified in T-ALL, *EPOR*, *JAK2*, *PDGFRβ, EBF1, FLT3, IL7R*, and *SH2B3.* Largely, these genes facilitate leukemic transformation by inducing constitutive kinase activation and signaling through the Ras and JAK/STAT5 pathways. All 15 cases showed at least one of these abnormalities (Figures 1A and 1B), indicating that more extensive screening would be required to determine a more accurate incidence as well as the distribution of these alterations. A range of techniques was then applied to screen an extended high-risk cohort from the Children's Oncology Group. The same types of aberrations were identified, and their estimated incidence is shown in Figure 1C.

Although a range of aberrations were identified in Ph-like ALL, the activation of ABL1 and/or JAK/STAT signaling pathways was the common mechanism for transformation. An exciting observation was that the transformation induced by these alterations was attenuated by tyrosine kinase inhibitors (TKI). The basal level of substrate phosphorylation as determined by phosphoflow cytometry was reduced by several TKI in two primary patient samples harboring the *NUP214-ABL1* fusion and by a JAK2 inhibitor in two *JAK2* rearranged samples. In addition, the therapeutic efficacy of the JAK2 inhibitor, ruxolitinib, was demonstrated in a xenograft model of a *JAK2* rearranged primary ALL sample. Another xenograft model of a human B-ALL harboring both an *IL7R* activating mutation and deletion of *SH2B3* responded to ruxolitinib. Also of interest was that a *NUP214-ABL1* ALL xenograft model responded to the ABL1 inhibitor, dasatinib, confirming that cells expressing *NUP214-ABL1* are sensitive to TKI within both T- and B-lineage ALL.

TKI treatment in addition to chemotherapy has led to dramatic improvements in outcome for Ph-positive ALL patients (Schultz et al., 2009). Patients with *PDGFRβ* rearrangements show complete hematological and molecular response to imatinib (Apperley et al., 2002). It had been shown previously that B-ALL cells harboring *CRLF2* rearrangements have enhanced signaling through oncogenic pathways that can be targeted with JAK or P13K inhibitors (Tasian et al., 2012). The Roberts et al. (2012) study now shows

that Ph-like leukemic cells are sensitive to currently available TKI. Thus, taken together, these observations indicate that screening at diagnosis to identify those Ph-like patients who may benefit from the addition of TKI to their current treatment regimen would be a feasible proposition.

At present, gene expression profiling, next generation sequencing, as well as the range of complex molecular techniques required to reliably identify the specific genetic alterations described in the Roberts et al. (2012) paper are not routinely available in most diagnostic laboratories and will no doubt preclude widespread screening for these cases in the near future. However, with the rising implementation of flow cytometry in the diagnostic arena and the increased application of phosphoflow cytometry worldwide, it may be possible to integrate flow cytometric phosphosignaling analysis for activated kinase pathways in conjunction with flow cytometric detection of CRLF2 overexpression as a diagnostic test to identify Ph-like cases.

Alternatively, by making use of the distinctive gene expression profile of Ph-like ALL, it may become possible to design customized targeted low density gene expression arrays suitable for routine diagnostic use. Such arrays would serve as the initial screen for Ph-like ALL, followed by testing for the specific alterations in kinase and cytokine receptors. These patients could then be considered for treatment combining chemotherapy with appropriate TKI, thus improving the outcome for another group of high-risk childhood ALL patients.

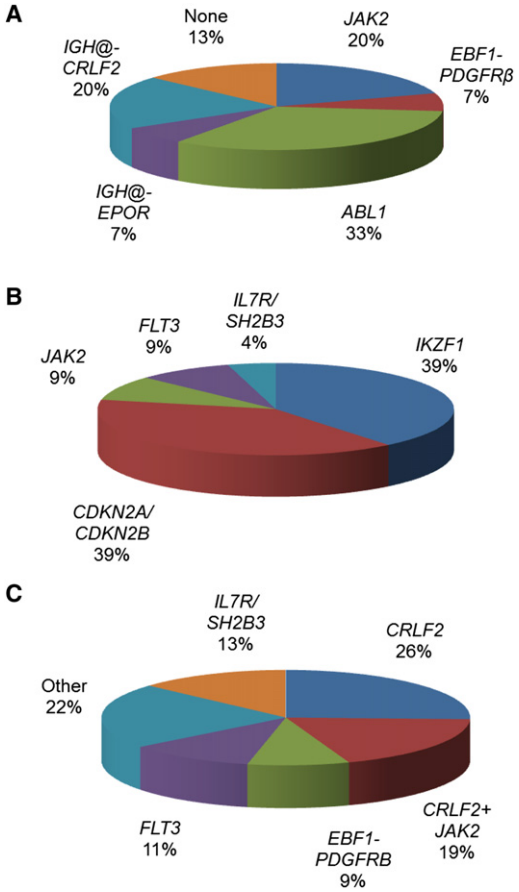

Figure 1. Distribution of Rearrangements, Mutations, and Deletions Affecting Kinase and Cytokine Signaling

(A and B) Distribution of rearrangements (A), mutations, and deletions (B) among the 15 discovery Ph-like ALL patients described in Roberts et al. (2012). The rearrangements of *ABL1* include two cases of *NUP214-ABL1*. The *IKZF1* category includes deletions and mutations; two mutations occurred along with deletions. The *CDKN2A/CDKN2B* category includes deletions only. The remaining aberrations are mutations. The distribution is an estimate as some patients harbored more than one of these aberrations.

(C) Estimated distribution of aberrations among Ph-like ALL calculated from Children's Oncology Group high-risk cohorts. In these high-risk cohorts 15%–20% of patients were classified as Ph-like according to their gene expression signature. In total, ~50% of cases had CRLF2 high expression, of which ~30% have *JAK2* mutations. The "Other" category includes an estimated incidence of *ABL1*, *JAK2*, *PDGFRβ*, and other kinase rearrangements and sequence mutations.

REFERENCES

Apperley, J.F., Gardembas, M., Melo, J.V., Russell-Jones, R., Bain, B.J., Baxter, E.J., Chase, A., Chessells, J.M., Colombat, M., Dearden, C.E., et al. (2002). N. Engl. J. Med. *347*, 481–487.

Den Boer, M.L., van Slegtenhorst, M., De Menezes, R.X., Cheok, M.H., Buijs-Gladdines, J.G., Peters, S.T., Van Zutven, L.J., Beverloo, H.B., Van der Spek, P.J., Escherich, G., et al. (2009). Lancet Oncol. *10*, 125–134.

Moorman, A.V., Ensor, H.M., Richards, S.M., Chilton, L., Schwab, C., Kinsey, S.E., Vora, A., Mitchell, C.D., and Harrison, C.J. (2010). Lancet Oncol. *11*, 429–438.

Mullighan, C.G., Goorha, S., Radtke, I., Miller, C.B., Coustan-Smith, E., Dalton, J.D., Girtman, K., Mathew, S., Ma, J., Pounds, S.B., et al. (2007). Nature *446*, 758–764.

Mullighan, C.G., Collins-Underwood, J.R., Phillips, L.A., Loudin, M.G., Liu, W., Zhang, J., Ma, J., Coustan-Smith, E., Harvey, R.C., Willman, C.L., et al. (2009a). Nat. Genet. *41*, 1243–1246.

Mullighan, C.G., Su, X., Zhang, J., Radtke, I., Phillips, L.A., Miller, C.B., Ma, J., Liu, W., Cheng, C., Schulman, B.A., et al; Children's Oncology Group. (2009b). N. Engl. J. Med. *360*, 470–480.

Roberts, K.G., Morin, R.D., Zhang, J., Hirst, M., Zhao, Y., Su, X., Chen, S.-C., Payne-Turner, D., Churchman, M.L., Harvey, R.C., et al. (2012). Cancer Cell *22*, this issue, 153–166.

Russell, L.J., Capasso, M., Vater, I., Akasaka, T., Bernard, O.A., Calasanz, M.J., Chandrasekaran, T., Chapiro, E., Gesk, S., Griffiths, M., et al. (2009). Blood *114*, 2688–2698.

Schultz, K.R., Bowman, W.P., Aledo, A., Slayton, W.B., Sather, H., Devidas, M., Wang, C., Davies, S.M., Gaynon, P.S., Trigg, M., et al. (2009). J. Clin. Oncol. *27*, 5175–5181.

Tasian, S.K., Doral, M.Y., Borowitz, M.J., Wood, B.L., Chen, I.M., Harvey, R.C., Gastier-Foster, J.M., Willman, C.L., Hunger, S.P., Mullighan, C.G., and Loh, M.L. (2012). Blood *120*, 833–842.

Burkitt Lymphoma: Much More than MYC

David Dominguez-Sola[1] and Riccardo Dalla-Favera[1,*]
[1]Institute for Cancer Genetics, Columbia University, New York, NY 10032, USA
*Correspondence: rd10@columbia.edu
http://dx.doi.org/10.1016/j.ccr.2012.07.018

Chromosomal translocations causing deregulated c-MYC expression are detectable in most Burkitt lymphoma cases. However, little is known about the additional lesions necessary for lymphomagenesis. Now, two independent studies, one of which was performed by Sander et al. in this issue of *Cancer Cell*, identify constitutive PI3K signaling and CyclinD3 mutations as cooperating lesions in both mice and humans. The results have directly actionable therapeutic implications.

Burkitt lymphoma (BL) arises from the malignant transformation of germinal center (GC) B cells and displays heterogeneous epidemiological features (Magrath, 2012). Although BL can occur sporadically in any population (sporadic BL [sBL]), it is endemic in several equatorial regions typically in Africa (endemic BL [eBL]) and can also develop at significant frequency in HIV-infected individuals (hivBL) (Magrath, 2012). The etiology of BL is associated with Epstein-Barr virus (EBV) infection, and in the case of eBL, with malaria, although the pathogenic significance of these associations is still unclear. For instance, EBV infection of tumor cells is detectable in all eBL but is detectable in only 30% of sBL and hivBL cases. Moreover, most EBV transforming genes are not expressed in the tumor cells (Magrath, 2012). Intensive chemotherapeutic regimens can cure the majority of BL cases but cannot be used in developing countries due to their toxicity and limited availability.

BL has garnered intense attention because of its unusual epidemiological distribution, which suggests complex biological interactions with the host and the environment (Magrath, 2012). Furthermore, it represents a landmark in tumor biology research, being among the first tumors for which a genetic alteration of clear pathogenic significance was discovered (Dalla-Favera et al., 1982; Taub et al., 1982). In fact, chromosomal translocations that involve the c-MYC (MYC) proto-oncogene and the immunoglobulin loci and lead to deregulated MYC expression are detectable in virtually all BL cases. Substantial evidence indicates that MYC deregulation elicits a range of cancer-causing effects that include aberrant cell proliferation, metabolic reprogramming, and genomic instability.

As for most cancer types, BL is likely to develop through multiple genetic alterations. Numerous studies have established that MYC deregulation is not sufficient for malignant transformation but that additional lesions are required. Yet, except for inactivation of p53, which is detectable at variable frequencies in the different BL subtypes (Gaidano et al., 1991), little is known about the cooperating lesions that lead to BL development. Now, however, two independent studies (Sander et al., 2012 [in this issue of *Cancer Cell*]; Schmitz et al., 2012), remarkably complementary in their findings in mice and humans, provide fundamental insights into the pathogenesis of BL with important and directly actionable therapeutic implications.

In this issue of *Cancer Cell*, researchers in the laboratory of Klaus Rajewsky, in collaboration with long-standing BL experts in Europe, have identified novel genetic lesions that cooperate with MYC deregulation in generating BL in the mouse (Sander et al., 2012). Based on their previous work implicating the PI3K pathway in the survival of mature B cells (Srinivasan et al., 2009), Sander et al. (2012) engineered mice expressing deregulated MYC and constitutively-active PI3K specifically in GC B cells, the putative BL cell of origin. These mice develop lymphoid malignancies strikingly similar to human BL, indicating that PI3K signaling can cooperate with MYC in the development of BL. Compared with previous attempts to model human BL in mice, the present one stands out for its faithful recapitulation of BL in terms of the activating pathways commonly deregulated in this lymphoma, the site of activation of these lesions (GC), and the resulting tumor phenotype, which displays all the characteristics of human BL in terms of histology, cell surface markers, expression of key transcription factors, and immunological history (Sander et al., 2012). Furthermore, co-activation of MYC-PI3K often selects for stabilizing mutations in cyclin D3, a key regulator of cell cycle progression in GC B cells (Peled et al., 2010). Importantly, similar mutations are reported in a small survey of human BL, further confirming this mouse model as an accurate phenocopy of human BL.

While the synergy between PI3K signaling and MYC deregulation was suspected based on normal B cell biology (Kumar et al., 2006) and confirmed by the phenotype of the new BL mouse model, it remained unclear whether and how the PI3K pathway contributes to human BL. However, an independent team led by Louis Staudt has now resolved this issue and determined the essential regulatory pathways that cooperate with MYC in BL pathogenesis (Schmitz et al., 2012). By comprehensive high-throughput RNA sequencing, they identified a cadre of somatic coding mutations in a large panel of BL cases and then examined which of the mutated genes/pathways was required to maintain the BL phenotype. Remarkably, they found that 70% of sBL display constitutive activation of PI3K signaling caused by mutations that either deregulate the activity of the transcription factor TCF3 (E2A) or inactivate its negative regulator ID3. The E2A/PI3K association in BL is especially intriguing in light of recent reports that this "module" has essential functions in B cell fate and GC biology (Kwon et al., 2008; Lin et al., 2010).

Furthermore, as observed in the mouse model above, a sizable fraction of human BLs carried somatic mutations that increase the stability of the E2A direct target cyclin D3, probably driving cell cycle progression. Pharmacological or genetic inactivation of either PI3K signaling or cyclin D3 function is toxic to BL cells, indicating that these lesions are required for tumor cell viability (Schmitz et al., 2012). Overall, these results demonstrate that the synergy between deregulated MYC, PI3K and cyclin D3 experimentally observed in mice is a naturally occurring pathway of BL lymphomagenesis in humans.

These new results raise a number of intriguing questions and opportunities. The transcriptome analysis of human BL samples clearly indicate that a substantial number of additional, recurrent, genetic lesions of potential functional significance are present in the coding genome of human BL (Schmitz et al., 2012). No doubt, additional analyses will be necessary to ascertain which of these are more relevant and/or required for full transformation. Given its remarkable mechanistic similarity to human BL, the new mouse model (Sander et al., 2012) should facilitate a systematic evaluation of these lesions in BL development. In addition, the initial analysis of human BL suggests that the eBL subtype may carry at least partially distinct lesions from sBL and hivBL (e.g., a much lower frequency of cyclin D3 mutation). Although this observation is still preliminary due to the limited number of eBL cases examined, it would be consistent with the distinctive features of eBL, including different chromosomal breakpoints and a much higher frequency of EBV infection of tumor cells. As such, eBL may arise from pathogenic pathways that are partially distinct from those driving sBL and hivBL. Finally, both the mouse and human tumors conclusively show that BL is a genetically distinct entity from other aggressive B cell lymphomas, especially diffuse large B cell lymphoma. These findings may therefore help in their differential diagnosis in cases in which the histologic pattern is not clearly discriminating.

Despite more than three decades of research, no effective drugs have yet been developed to counter the oncogenic consequences of MYC deregulation. Thus, a particularly welcome outcome of the new studies is their identification of feasible targets for BL therapy. Indeed, several approved drugs are already available to either inactivate PI3K signaling or cyclin D3 function, and preliminary results show that some of these are active against BL. If validated in appropriate clinical trials, these drugs would be far less toxic than currently available chemotherapeutic regimens for BL. If confirmed, these therapeutic developments could improve the already high rate of cure of sBL. But more importantly, they could change the still ominous clinical history of eBL and hivBL in developing countries. The availability of a faithful preclinical model of the disease, clearly identified targets, and continuously emerging new drugs suggest that important changes in the diagnostic, prognostic, and therapeutic management of BL may appear in the textbooks in the not so distant future.

REFERENCES

Dalla-Favera, R., Bregni, M., Erikson, J., Patterson, D., Gallo, R.C., and Croce, C.M. (1982). Proc. Natl. Acad. Sci. USA *79*, 7824–7827.

Gaidano, G., Ballerini, P., Gong, J.Z., Inghirami, G., Neri, A., Newcomb, E.W., Magrath, I.T., Knowles, D.M., and Dalla-Favera, R. (1991). Proc. Natl. Acad. Sci. USA *88*, 5413–5417.

Kumar, A., Marqués, M., and Carrera, A.C. (2006). Mol. Cell. Biol. *26*, 9116–9125.

Kwon, K., Hutter, C., Sun, Q., Bilic, I., Cobaleda, C., Malin, S., and Busslinger, M. (2008). Immunity *28*, 751–762.

Lin, Y.C., Jhunjhunwala, S., Benner, C., Heinz, S., Welinder, E., Mansson, R., Sigvardsson, M., Hagman, J., Espinoza, C.A., Dutkowski, J., et al. (2010). Nat. Immunol. *11*, 635–643.

Magrath, I. (2012). Br. J. Haematol. *156*, 744–756.

Peled, J.U., Yu, J.J., Venkatesh, J., Bi, E., Ding, B.B., Krupski-Downs, M., Shaknovich, R., Sicinski, P., Diamond, B., Scharff, M.D., and Ye, B.H. (2010). Cell Res. *20*, 631–646.

Sander, S., Calado, D.P., Srinivasan, L., Köchert, K., Zhang, B., Rosolowski, M., Rodig, S.J., Holzmann, K., Siebert, R., Bullinger, L., et al. (2012). Cancer Cell *22*, this issue, 167–179.

Schmitz, R., Young, R.M., Ceribelli, M., Jhavar, S., Xiao, W., Zhang, M., Wright, G.W., Shaffer, A.L., Hodson, D.J., Buras, E., et al. (2012). Nature. Published online August 12, 2012. http://dx.doi.org/10.1038/nature11378.

Srinivasan, L., Sasaki, Y., Calado, D.P., Zhang, B., Paik, J.H., DePinho, R.A., Kutok, J.L., Kearney, J.F., Otipoby, K.L., and Rajewsky, K. (2009). Cell *139*, 573–586.

Taub, R., Kirsch, I., Morton, C., Lenoir, G., Swan, D., Tronick, S., Aaronson, S., and Leder, P. (1982). Proc. Natl. Acad. Sci. USA *79*, 7837–7841.

A New Role for PHD in Chemotherapy

Rui-hua Xu[1] and Peng Huang[2,*]
[1]Department of Medical Oncology and State Key Laboratory of Oncology in South China, Sun Yat-sen University Cancer Center, Guangzhou 510275, China
[2]Department of Molecular Pathology, The University of Texas MD Anderson Cancer Center, Houston, TX 77030, USA
*Correspondence: phuang@mdanderson.org
http://dx.doi.org/10.1016/j.ccr.2012.07.013

Enhancing therapeutic activity against cancer cells and minimizing toxic effects on normal cells are critical elements in chemotherapy. In this issue of *Cancer Cell*, Leite de Oliveira and colleagues reveal a previously unrecognized role of a prolyl hydroxylase domain in promoting drug delivery to tumors and reducing toxicity in normal organs.

Chemotherapy using cytotoxic agents, such as doxorubicin and cisplatin, to damage cancer cells and inhibit tumor growth remains a major therapeutic modality in cancer treatment. The low selectivity of cytotoxic agents in killing cancer cells over normal cells has been a major challenge and significantly limits the application of these drugs for cancer treatment. This problem is further compounded by the fact that tumors usually have blood vessels that seem to be leaky and tend to cause high interstitial fluid pressure. This abnormal vasculature limits drug delivery to cancer cells and, therefore, reduces the effectiveness of systemic chemotherapy (Carmeliet and Jain, 2011; Heldin et al., 2004). In most cases, the administration of higher drug doses to increase drug concentrations in tumor tissues is not a practical option due to the risk of severe side effects. Although local administration by injecting cytotoxic agents into the tumor or the main blood vessels feeding the tumor may enhance anticancer activity and reduce systemic toxicity, such approaches may only be applied to a small subset of tumors at certain anatomic locations. Clearly, new therapeutic approaches, including novel strategies to normalize the aberrant tumor vessels and developing tumor-specific agents, are needed to improve cancer treatment outcome.

Recent studies suggest that targeting the prolyl hydroxylase domain-containing protein 2 (PHD2) may lead to normalization of blood vessels in tumors (Mazzone et al., 2009) and prevent oxygen-induced microvascular obliteration in the retina (Duan et al., 2011) through HIF-dependent mechanisms. Prolyl hydroxylases are a family of enzymes that catalyze the hydroxylation of proline residues in a variety of proteins and affect multiple biological functions including collagen formation, oxygen sensing, RNA transcription, and NF-κB signaling (Gorres and Raines, 2010). Among the prolyl hydroxylases, PHD2 seems to play a major role in oxygen sensing and blood vessel formation and significantly affects cancer oxygenation and metastasis. It was recently shown that heterozygous deletion of *Phd2* in mice caused an increased expression of HIF-1α and HIF-2α in endothelial cells, leading to the transition of endothelial tip cells to a more quiescent stage and normalization of the endothelial lining of tumor vasculatures (Mazzone et al., 2009). The profound effect of PHD2 on the structure of tumor blood vessel provides the intriguing possibility of targeting this molecule to normalize blood flow in tumor tissues and to increase drug delivery to cancer cells.

In this issue of *Cancer Cell*, Leite de Oliveira et al. (2012) report that reduced PHD2 expression by heterozygous gene deletion could significantly enhance the therapeutic activity of doxorubicin and cisplatin in mice and substantially reduce the toxic side effects of the drugs in normal organs, such as the heart and kidneys. These striking effects seem to be mediated by two separate mechanisms, both linked to the activation of hypoxia inducible factors (Figure 1). First, the decrease in PHD2 activity caused a significant increase in HIF-1α and HIF-2α protein levels in endothelial cells, leading to a normalization of the endothelial lining of blood vessels within tumor tissues. This, in turn, improved blood circulation and reduced interstitial fluid pressure in the tumor, resulting in an increase in the delivery of anticancer agents to the tumor. The authors suggest that this mechanism was mainly mediated through the oxygen-sensing function of PDH2 via HIF-2. In contrast, the blood circulation in normal organs seemed not to be affected by heterozygous deletion of *Phd2*, and there was no increase in drug concentrations in the normal tissues. Importantly, *Phd2* deficiency in normal cells led to HIF-mediated upregulation of several key antioxidant enzymes, including superoxide dismutases, catalase, and glutathione peroxidase-1, which enhanced the antioxidant capacity of normal cells and increased their ability to tolerate the production of reactive oxygen species (ROS) induced by anticancer drugs. The authors showed that the protection of normal organs by *Phd2* heterozygous deletion was likely due to activation of the ROS-sensing mechanism of HIF-1 and HIF-2, which upregulate the expression of antioxidant enzymes.

The significant in vivo antitumor activity of doxorubicin and cisplatin observed in $Phd2^{+/-}$ mice suggests that targeting PDH2 is a potentially promising strategy to improve the overall therapeutic outcome for cancer patients and that the local drug concentrations in tumor tissues may play a major role in determining in vivo drug response. However, other mechanisms, in addition to increased local drug concentrations, could contribute to the striking inhibition of tumor growth by doxorubicin and cisplatin in $Phd2^{+/-}$ mice. For instance, *Phd2* deletion might, through the activation of HIF-1 and HIF-2, affect the energy metabolism and redox regulation in tumor stroma and, thus, potentially impair stromal support for the tumor cells.

Indeed, recent studies suggest that the tumor-stromal cell interaction plays a major role in affecting the ROS status in cancer cells and their drug sensitivity (Zhang et al., 2012; Nakasone et al., 2012). Thus, testing the potential role of PHD2 in modulating tumor-stroma interaction would be an interesting area of future investigation.

It is important to note that the normalization of tumor blood vasculature in *Phd2*$^{+/-}$ mice seem to be mediated, at least in part, by the HIF-driven upregulation of VEGFR1 and VE-cadherin (Mazzone et al., 2009). Thus, suppression of the VEGF pathway might potentially have an opposite and perhaps unfavorable effect. Indeed, inhibition of angiogenesis by blocking VEGF using the humanized monoclonal antibody bevacizumab has been shown to cause a decrease in the delivery of anticancer drugs to the tumor tissues (Van der Veldt et al., 2012). These observations together suggest that caution should be exercised in considering combination of VEGF blocking drugs and traditional chemotherapeutic agents. The proper timing of drug administration would be important in avoiding potential antagonist effect.

The two major consequences of *Phd2* deletion, namely normalization of tumor vasculature and enhancement of antioxidant and detoxification capacity in normal organs, suggest that pharmacological inhibition of PHD2 may be an effective strategy to increase the therapeutic activity and reduce the toxic side-effect of traditional chemotherapeutic agents. However, systemic administration of PHD2 inhibitors might potentially cause an increase in HIF-1 and HIF-2 in cancer cells and, in turn, upregulation of detoxification enzymes and drug resistance. However, the observation by Leite de Oliveira et al. (2012) that silencing of *Phd2* in tumor cells did not significantly alter their expression of antioxidant enzymes and drug response seem to ease this potential concern, although the mechanisms responsible for the major difference between normal cells and cancer cells in their response to PHD2 abrogation remain largely unclear. This is obviously an important area for future study. Furthermore, since there are multiple prolyl hydroxylases that affect many important biological functions, development of specific inhibitors of PHD2 is important for successful pharmacological targeting. In summary, the study by Leite de Oliveira et al. (2012) suggests that PHD2 is a promising therapeutic target and warrants further in vitro and in vivo studies in terms of mechanisms and clinical applications.

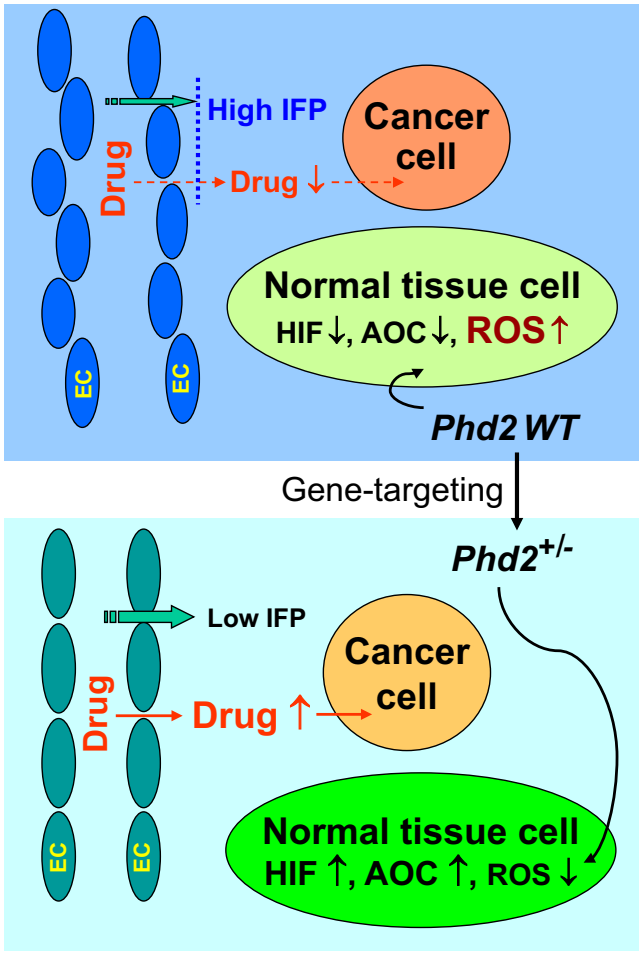

Figure 1. PHD2 Deficiency Increases the Therapeutic Activity of Anticancer Agents and Decreases Side-Toxicity

In mice with wild-type *Phd2*, the blood vessels in tumor tissue have abnormal endothelial lining, are leaky, and often cause high interstitial fluid pressure (IFP), leading to a decrease in drug distribution to cancer cells (upper panel). Heterozygous deletion of *Phd2* promotes normalization of the tumor vasculature and enhances drug delivery to cancer cells (lower panel). A decrease in PHD2 activity also leads to elevated HIF-1α and HIF-2α, resulting in an upregulation of antioxidant enzymes in normal tissue cells, thus, enhancing their antioxidant capacity to detoxify ROS induced by anticancer agents.

PHD2, prolyl hydroxylase domain-2; HIF, hypoxia inducible factor; WT, wild-type; AOC, antioxidant capacity; ROS, reactive oxygen species; EC, endothelial cells; IFP, interstitial fluid pressure.

REFERENCES

Carmeliet, P., and Jain, R.K. (2011). Nat. Rev. Drug Discov. *10*, 417–427.

Duan, L.J., Takeda, K., and Fong, G.H. (2011). Am. J. Pathol. *178*, 1881–1890.

Gorres, K.L., and Raines, R.T. (2010). Crit. Rev. Biochem. Mol. Biol. *45*, 106–124.

Heldin, C.H., Rubin, K., Pietras, K., and Ostman, A. (2004). Nat. Rev. Cancer *4*, 806–813.

Leite de Oliveira, R., Deschoemaeker, S., Henze, A.-T., Debackere, K., Finisguerra, V., Takeda, Y., Roncal, C., Detorri, D., Tack, E., Jönsson, Y., et al. (2012). Cancer Cell *22*, this issue, 263–277.

Mazzone, M., Dettori, D., Leite de Oliveira, R., Loges, S., Schmidt, T., Jonckx, B., Tian, Y.M., Lanahan, A.A., Pollard, P., Ruiz de Almodovar, C., et al. (2009). Cell *136*, 839–851.

Nakasone, E.S., Askautrud, H.A., Kees, T., Park, J.H., Plaks, V., Ewald, A.J., Fein, M., Rasch, M.G., Tan, Y.X., Qiu, J., et al. (2012). Cancer Cell *21*, 488–503.

Van der Veldt, A.A., Lubberink, M., Bahce, I., Walraven, M., de Boer, M.P., Greuter, H.N., Hendrikse, N.H., Eriksson, J., Windhorst, A.D., Postmus, P.E., et al. (2012). Cancer Cell *21*, 82–91.

Zhang, W., Trachootham, D., Liu, J., Chen, G., Pelicano, H., Garcia-Prieto, C., Lu, W., Burger, J.A., Croce, C.M., Plunkett, W., et al. (2012). Nat. Cell Biol. *14*, 276–286.

Cancer Cell
Review

Emerging Role of Semaphorins as Major Regulatory Signals and Potential Therapeutic Targets in Cancer

Luca Tamagnone[1,2,*]
[1]IRCC - Institute for Cancer Research at Candiolo, 10060 Candiolo, Italy
[2]University of Torino Medical School, 10060 Candiolo, Italy
*Correspondence: luca.tamagnone@ircc.it
http://dx.doi.org/10.1016/j.ccr.2012.06.031

Semaphorins are mainly known as guidance signals in development, acting through receptors called Plexins. However, their role in cancer is rapidly emerging in the regulation of tumor angiogenesis, tumor growth, cancer cell invasiveness, and metastatic spreading. Intriguingly, activated plexins can transactivate receptor tyrosine kinases, such as MET, VEGFR2, FGFR2, and ERBB2, and lead to distinctive effects in a cell-context-dependent manner. Moreover, certain semaphorins concomitantly target endothelial and cancer cells, and can achieve remarkable inhibition of angiogenesis and tumor growth, associated with anti-metastatic activity. Altogether, these data validate the identification of semaphorin signals as promising therapeutic targets in cancer.

Introduction

Semaphorins

There are around 20 semaphorin genes in vertebrates that can be subdivided into multiple subclasses based on common structural features (Kolodkin et al., 1993; Semaphorin Nomenclature Committee, 1999). Members of subclass 3 are secreted, while the others are membrane-bound and, under certain circumstances, can be shed upon cleavage. All semaphorins have in common a *sema* domain, characterized by a seven-blade beta propeller structure, which contains sites for semaphorin dimerization and receptor binding (Liu et al., 2010; Nogi et al., 2010; Janssen et al., 2010).

Semaphorin Receptors

Main receptors for semaphorins are the plexins, a family comprising nine members in vertebrates (reviewed by Tamagnone and Comoglio, 2000). The extracellular domain of plexins also includes a *sema* domain that is putatively involved in ligand binding. A subset of the secreted semaphorins cannot interact with plexins alone, but require the presence of obligate coreceptor molecules called neuropilins (Nrp1/Nrp2) (Tamagnone et al., 1999; Takahashi et al., 1999), providing additional binding sites for ligands (see Figure 1) (for general reviews, see Kruger et al., 2005; Zhou et al., 2008; Neufeld and Kessler, 2008). Notably, neuropilins are also well-known coreceptors for vascular endothelial growth factors (VEGFs).

Semaphorin Signaling

Plexins are responsible for most known intracellular pathways triggered by semaphorins, while the short cytoplasmic tail of neuropilins is apparently devoid of signaling functions. The intracellular domain of plexins is largely conserved in the family and carries an unconventional split domain with GTPase-activating protein (GAP) activity for R-Ras, M-Ras, and Rap (Oinuma et al., 2004; Wang et al., 2012). Moreover, the cytoplasmic domain of different plexins was found to associate with other putative effector proteins, such as p190RhoGAP, PDZ-RhoGEFs, MICALs, FARP2 (reviewed by Zhou et al., 2008), and 14.3.3 proteins (Yang and Terman, 2012). Typical outcomes of plexin activation are inhibition of integrin-mediated cell-substrate adhesion and cytoskeletal remodeling. In experimental models, this leads to retraction of pseudopodia, and eventually to cell rounding, or to the typical "collapse" of axonal growth cone processes. In physiology, these mechanisms are thought to mediate semaphorin-dependent guidance of axonal extension and directional cell migration (Tran et al., 2007). Notably, semaphorin and plexin mouse knock-out models display defects in axon guidance, cardiovascular development (sometimes lethal), bone homeostasis, and immune response.

Additional Interactors and Signaling Pathways

Certain semaphorins were found to interact with additional molecules on the cell surface beyond their plexin receptors (see Figure 1), thereby mediating alternative signaling pathways in specific cellular settings. For instance, in lymphocytes, Semaphorin4D (Sema4D) can bind CD72 (Kumanogoh et al., 2000), and Sema4A the membrane receptor Tim-2 (Kumanogoh et al., 2002). Sema7A can engage integrin-beta1 through an RGD motif included in its amino acid sequence and trigger Focal Adhesion Kinase-dependent pathway (Pasterkamp et al., 2003). Moreover, other signaling receptors have been found in association with plexins and neuropilins on the cell surface; these include the adhesion molecule L1-CAM (Castellani et al., 2002) and the receptor tyrosine kinases (RTKs) OTK/PTK7, MET, RON, VEGFR2, and ERBB2 (reviewed by Franco and Tamagnone, 2008). In particular, it was shown that semaphorins can transactivate plexin-associated RTKs and promote cell growth and invasion, as opposed to the usual pathways leading to inhibition of migration. Thus, semaphorins can trigger multiple signaling cascades and often distinctive functions in a cell-context-dependent manner.

Semaphorins Are Versatile and Multifaceted Regulatory Signals in the Tumor Context

Accumulating evidence indicates that semaphorin signals can play a major role in the tumor context, beyond their established role in development (reviewed by Capparuccia and Tamagnone,

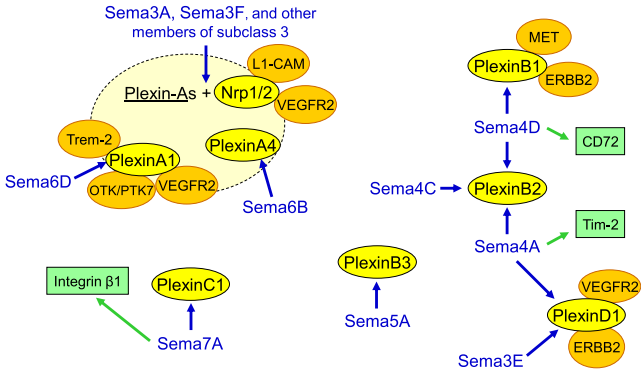

Figure 1. Schematic Representation of Main Semaphorin-Plexin Interactions

Plexins and plexin-associated molecules are indicated in ovals, while other putative semaphorin receptors are shown in green boxes.

2009). Cancer cells typically express both semaphorins and their receptors, and experimental data show that these signals can either promote, or inhibit, tumor cell migration, growth, and survival. Thereby, semaphorin functions in the tumor context may be partly due to a direct ("autocrine" or paracrine) regulation of cancer cells; a few specific examples will be discussed in this review. Notably, the expression of semaphorins and their receptors in tumors has been found up- or downregulated compared to normal tissues. The molecular mechanisms responsible for this regulation are largely unknown, but certain transcription factors and miRNAs have been implicated (e.g., Clarhaut et al., 2009; Coma et al., 2011; Urbich et al., 2012). On the other hand, mutations or other alterations of semaphorin or semaphorin receptor genes are rarely seen in human tumors (Balakrishnan et al., 2009), with the exception of PlexinB1 mutations reported in prostate cancer (Wong et al., 2007).

In addition to cancer cells, semaphorins and their receptors are expressed in normal cells of the tumor microenvironment. In particular, several semaphorins have been found to regulate endothelial cell function, either as inhibitors or promoters of angiogenesis (reviewed by Neufeld et al., 2012), and a number of them were recently shown to control tumor vasculature (diffusely discussed below). Certain semaphorins are furthermore importantly involved in the regulation of immune response (for a review see Takamatsu and Kumanogoh, 2012). For instance, Sema4D signaling was found to promote B lymphocyte activation, while Sema4A and Sema6D were implicated in T lymphocytes function. In one study, Sema3A promoted the cytokine storm induced by inflammatory signals (Wen et al., 2010), whereas others reported that Sema3A signaling inhibits T-cell function (Catalano et al., 2006; Lepelletier et al., 2006; Yamamoto et al., 2008). A recent report indicated that Sema4A is a chemoattractant for monocyte-macrophages (Meda et al., 2012); in addition, both Sema4A and Sema7A were found to induce monocytes to release pro-inflammatory and pro-angiogenic molecules (Meda et al., 2012; Holmes et al., 2002; Suzuki et al., 2007). Thus, specific semaphorins could have a role in controlling the recruitment of leucocytes into the tumor microenvironment, and their immuno-modulatory activity could have an impact on tumor progression; however, these potential functions have not been carefully investigated as yet.

A further semaphorin function potentially relevant to cancer is linked to their emerging role in bone homeostasis. In fact, signaling cascades triggered by Sema6D/PlexinA1, Sema4D/PlexinB1, and Sema3A/Nrp1 have been shown to play a crucial role in the regulation of osteoclast and osteoblast differentiation and the balance between osteolysis and osteodeposition (Takegahara et al., 2006; Negishi-Koga et al., 2011; Hayashi et al., 2012). As tumor cells can release all of the above signals within the tumor microenvironment, this could be relevant with respect to the development of bone metastatic sites.

Due to their versatile activity and wide receptor distribution in different cell types, semaphorin signals could mediate an intense cross-talk between cancer cells and the microenvironment, and play multiple concomitant functions potentially relevant to tumor progression. This complex scenario has been investigated for few family members by experiments in vivo, in mouse models. This review will mainly focus on recent studies that highlighted certain semaphorin signaling pathways as major modifiers of cancer progression and potential therapeutic targets relevant in translational perspective.

Semaphorins Are Potent Regulators of Tumor Angiogenesis In Vivo

Growing tumors can release strong and diverse pro-angiogenic stimuli and usually they become dependent on angiogenesis for growth and survival; this explains why anti-VEGF drugs, for example, can dramatically induce tumor shrinkage. However, refractoriness to drugs blocking individual pro-angiogenic factors may eventually arise due to the increased production of alternative signals sustaining tumor vessel development (Carmeliet and Jain, 2011). A further worrying aspect of VEGF-targeted drugs is the reported risk of inducing tumor invasion and metastatic spreading. Although the mechanisms underlying this process are still controversial, this seems to involve hypoxia-driven induction of tumor invasiveness (Semenza, 2012), and it is presently addressed by combined treatment with drugs directly targeting cancer cells.

Multiple semaphorins have been associated with the regulation of tumor vasculature, including Sema3A, Sema3E, Sema3F, and Sema3G (as inhibitory signals); Sema4D (as pro-angiogenic factor); and others (reviewed by Neufeld et al., 2012). These semaphorins may be released by cancer cells, as well as by stromal cells in the tumor microenvironment. Furthermore, endothelial cells themselves produce semaphorins controlling angiogenesis in autocrine manner. Importantly, the expression of certain semaphorins (and receptors) seems to be regulated in response to tissue hypoxia, including upon the "angiogenic switch" of growing tumors, as part of a balanced set of antagonistic signals controlling the development of new vessels (Coma et al., 2011; Moriya et al., 2010; Sun et al., 2009; Maione et al., 2009). However, this physiologic function of semaphorins seems to be distorted in cancer progression. For instance, the levels of anti-angiogenic factors Sema3A and Sema3F are often downregulated in advanced tumors (Maione et al., 2009; Bielenberg et al., 2004), while the pro-angiogenic Sema4D is typically increased (Basile et al., 2006). It was furthermore reported that Sema4D levels are induced by VEGF and inflammatory cytokines (Smith et al., 2011). Notably, in addition to being produced by cancer cells, Sema4D may be released into the tumor

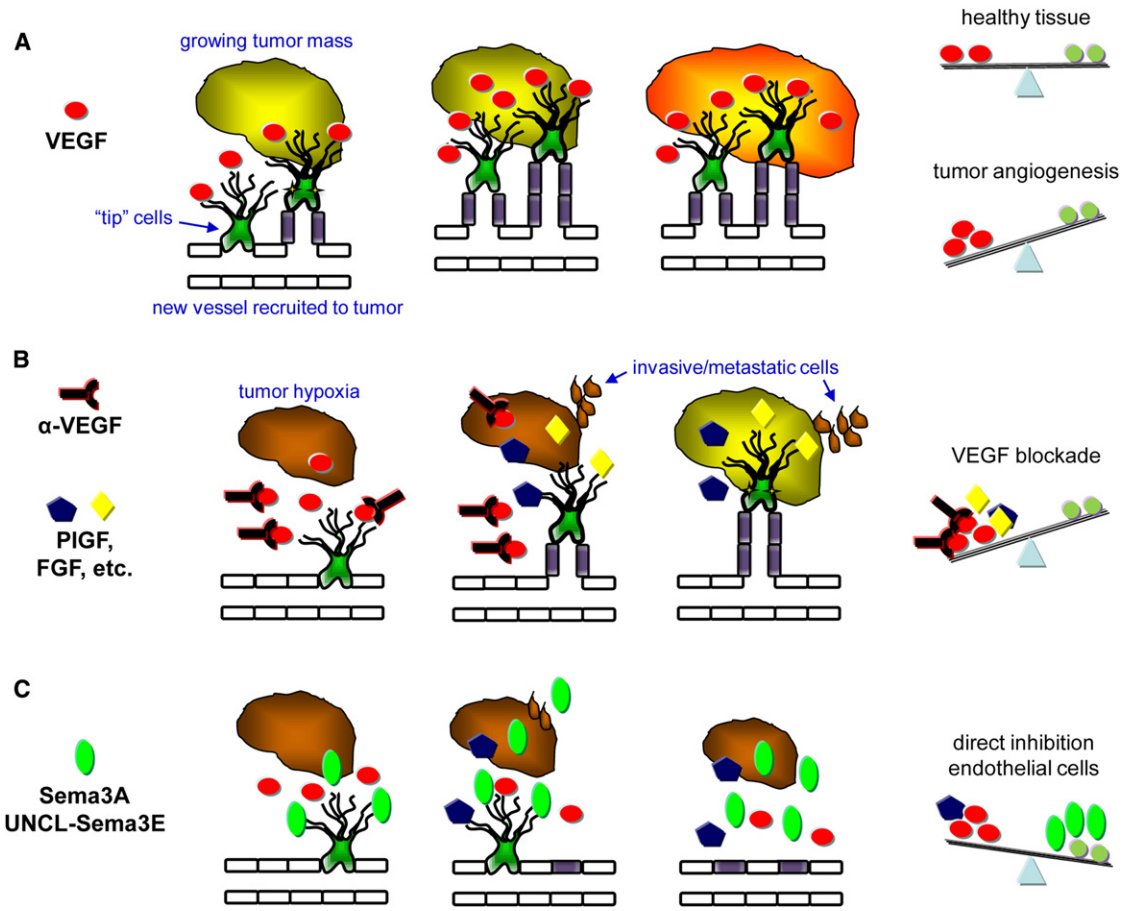

Figure 2. Semaphorins: A Novel Type of Anti-Angiogenic Factors Inhibiting Cancer Progression
(A) Unlike in normal tissues, the balanced activity of antagonistic signals controlling new vessel development is often distorted in tumors, which are characterized by predominance of pro-angiogenic signals (including VEGF, Sema4D, and others).
(B) Upon treatment with drugs blocking pro-angiogenic factors, tumors undergo hypoxia and shrinkage; but eventually they may become resistant by exploiting alternative pro-angiogenic signals. Moreover, tumor hypoxia may induce cancer cell invasiveness and metastatic spreading.
(C) Anti-angiogenic molecules directly targeting endothelial cells (such as Sema3A or Uncl-Sema3E) may be able to overcome these problems. Moreover, by directly inhibiting tumor cell invasiveness (with Sema3A, Uncl-Sema3E, but also anti-PlexinB1 antibodies), the metastatic spreading associated with tumor hypoxia could be prevented.

microenvironment by inflammatory cells, tumor-associated macrophages (Sierra et al., 2008) and, potentially, platelets (Zhu et al., 2007). Although genetic deletion in mice demonstrated that Sema4D is not required for developmental angiogenesis, experiments in vivo indicated that this semaphorin has a strong pro-angiogenic activity in tumor models (Sierra et al., 2008). While Sema4D loss or functional blockade in the microenviroment inhibited tumor growth and progression, this effect does not seem to rely exclusively on the main Sema4D-receptor PlexinB1, potentially implicating the alternative homolog PlexinB2 (Fazzari et al., 2007). Notably, Sema4D can control cancer cells in addition to tumor vasculature (discussed below), sustaining invasion and metastasis.

As an alternative to blocking the activity of pro-angiogenic factors, the direct targeting of endothelial cells by treatment with inhibitory semaphorins was assayed in preclinical tumor models in mice (see Figure 2). Sema3F was in fact the first semaphorin shown to have an anti-angiogenic activity in tumor models in mice (Bielenberg et al., 2004; Kessler et al., 2004). Sema3F binds to the coreceptor molecule Neuropilin-2 (Nrp2), which—in addition to interacting with plexins—is typically found in endothelial and lympho-endothelial cells in association with VEGFR2 and VEGFR3 (Kärpänen et al., 2006; Caunt et al., 2008). Intriguingly, derivatives of neural crest cells, including melanoma, also express Nrp2; and the forced overexpression of Sema3F in melanoma cells transplanted in mice blocked tumor angiogenesis, tumor growth, and metastatic spreading (Bielenberg et al., 2004). These data demonstrated that Sema3F is capable of inhibiting tumor angiogenesis and lympho-angiogenesis in vivo, and suggested that it may regulate a subset of cancer cells via Nrp2. Later studies have reported Nrp2 overexpression in human tumors (e.g., Dallas et al., 2008) and linked it with cancer progression; however, the implicated signaling pathways have not been clearly elucidated and they might reflect semaphorin-independent functions.

Recent reports highlighted other semaphorin molecules that potently inhibit tumor angiogenesis in vivo, independent of VEGF blockade, and concomitantly control invasive/metastatic

progression. Sema3A was actually the first semaphorin found to inhibit endothelial cells (Miao et al., 1999). This was initially associated with the fact that Sema3A coreceptor Neuropilin-1 (Nrp1) also binds VEGF and mediates its pro-angiogenic activity. It was later shown that Sema3A- and VEGF-binding sites on Nrp1 are largely independent (Appleton et al., 2007); moreover, the antagonistic activity of these signals in endothelial cells seems to implicate distinct signaling pathways, rather than binding competition to Nrp1. Sema3A-receptor complexes are thought to include plexins of A-subfamily, beyond Nrp1, especially PlexinA4 and/or PlexinA1. Notably, a recent report (discussed below) suggests that these plexins may play a role in the regulation of both endothelial and cancer cells (Kigel et al., 2011). Sema3A was found to inhibit integrin-mediated adhesion to the extracellular matrix, which is crucially required for endothelial cell migration and survival (Serini et al., 2003; Casazza et al., 2011). Upon delivery in different preclinical tumor models in mice, Sema3A displayed a strong anti-angiogenic effect associated with inhibition of cancer cell motility and metastatic spreading in different tumor models (Maione et al., 2009, 2012; Casazza et al., 2011; Chakraborty et al., 2012). According to one study, the treatment with Sema3A can achieve "normalization" of the tumor vasculature in spontaneous tumor models in mice, possibly by pruning aberrant tumor vessels (Maione et al., 2009). In another study, the sustained treatment with Sema3A resulted in extensive vessel disruption and hypoxia in transplanted tumors (Casazza et al., 2011), suggesting that vessel normalization may be obtained in a specific therapeutic window. Moreover, Sema3A directly inhibited cancer cell invasiveness dependent on Nrp1 expression (Casazza et al., 2011). Importantly, Nrp1 levels are typically higher in tumors compared to respective normal tissues, and Nrp1 expression seems to confer a selective advantage in tumor progression (reviewed by (Rizzolio and Tamagnone, 2011), which may implicate fewer risks of developing resistance to Sema3A-mediated inhibition. Of note, combined treatment with Sema3A could prevent the metastatic spreading induced by VEGF-blocking drugs in a spontaneous tumor model in mice (Maione et al., 2012).

Another secreted semaphorin found to inhibit tumor angiogenesis is Sema3E. The role of Sema3E in developmental angiogenesis is well established, even if multiple signaling cascades have been implicated (reviewed by Tamagnone and Mazzone, 2011). Importantly, Sema3E signaling in endothelial cells does not require neuropilins, but rather depends on the specific receptor PlexinD1 (Gu et al., 2005). PlexinD1 is expressed at high levels in developing vessels, especially in the endothelial "tip" cells that lead vascular sprouts. In the adult, PlexinD1 expression is mainly found in sites of neo-angiogenesis, including tissues recovering from ischemic insults, and growing tumors (Roodink et al., 2005; Moriya et al., 2010; Fukushima et al., 2011). Intriguingly, Sema3E-PlexinD1 signaling was found to trigger VEGFR2 activation in certain neurons (Bellon et al., 2010). Instead, PlexinD1 activation in endothelial cells inhibits their migration and restricts sprouting angiogenesis, antagonizing pro-angiogenic signals; in fact, during development, Sema3E is strictly localized in order to define permissive and non-permissive areas for vascularization (Gu et al., 2005). Recent studies implicated ARF6 activation by PlexinD1 in the negative regulation of integrin function mediated by Sema3E in endothelial cells (Sakurai et al., 2010, 2011). Notably, forced Sema3E overexpression in experimental tumor models resulted in a dramatic anti-angiogenic effect, associated with strong suppression of tumor growth (Casazza et al., 2010).

Sema3E Is a Dual-Activity Factor Independently Controlling Endothelial and Cancer Cells

Importantly, in addition to inhibiting endothelial cells, Sema3E was found to control the behavior of cancer cells through an independent signaling cascade. In fact, this secreted semaphorin is proteolytically converted into a fragment, known as p61-Sema3E, which plays a distinctive autocrine function in cancer cells by driving invasion and metastasis without significantly impinging tumor growth (Casazza et al., 2010). This activity is strictly dependent on the transactivation of the oncogenic tyrosine kinase ERBB2, associated with PlexinD1, in response to p61-Sema3E stimulation. By expression profiling analysis, it was found that higher Sema3E expression in primary tumors (colorectal and melanoma) correlates with increased metastatic progression (Casazza et al., 2010). Notably, another group reported that Sema3E-PlexinD1 signaling induces epithelial-to-mesenchymal transition in ovarian endometrioid cancer cells (Tseng et al., 2011).

In a recent study, it was shown that a mutated non-processable version of Sema3E (Uncl-Sema3E) is unable to elicit ERBB2 transactivation and pro-metastatic signaling in cancer cells (Casazza et al., 2012). Yet, Uncl-Sema3E remains fully competent for binding PlexinD1 and triggering its inhibitory activity in endothelial cells, which leads to decreased angiogenesis and tumor growth in mice. Moreover, the same molecule "competed out" the autocrine signaling of endogenous p61-Sema3E in cancer cells and blocked their invasive and metastatic behavior (Casazza et al., 2012). Uncl-Sema3E was effective in multiple tumor models in mice, including spontaneous RipTag2 pancreatic tumors, and transplanted LLC tumors nonresponsive to VEGF blockade. This is consistent with the idea that these semaphorins exert a direct anti-angiogenic activity on endothelial cells, rather than interfering with pro-angiogenic signals (Figure 2). Moreover, a concomitant direct inhibitory effect of Uncl-Sema3E in cancer cells was implicated to prevent hypoxia-driven invasion and metastasis. Together with the examples discussed in the previous section, these data highlight the relevance of anti-angiogenic semaphorins that can directly target endothelial cells and potently suppress tumor growth in mouse models without promoting cancer invasiveness, and even concomitantly reducing metastatic spreading. An open question concerns the possibility of developing functional antibodies or small molecules, alternative to the large recombinant semaphorin proteins tested so far in mouse models, in order to trigger plexin-mediated inhibitory signals or block signaling pathways elicited by endogenous semaphorins.

PlexinB1 Plays Tumor-Type-Specific Functions in Cancer Progression

PlexinB1 is another family member coupled with RTKs on the cell surface, in particular with MET (Giordano et al., 2002) and ERBB2 (Swiercz et al., 2004). These interactions have a major role in Sema4D-PlexinB1 signaling, as they can mediate distinctive and sometimes divergent pathways in a cell-context-dependent manner, for instance leading to opposite regulation of RhoA

activity (Swiercz et al., 2008). This possibly explains the controversial literature related to the functional role of PlexinB1 in human tumors. In fact, in addition to its pro-angiogenic activity in endothelial cells, a number of studies reported pro-invasive functions of Sema4D-PlexinB1 signaling in a variety of cancer cell types (Giordano et al., 2002; Swiercz et al., 2008; Sierra et al., 2008; Binmadi et al., 2012; Ye et al., 2010; Qiang et al., 2011). Moreover PlexinB1 is overexpressed and frequently mutated in prostatic cancer, and some of these genetic changes were associated with a "switch" of receptor signaling accompanied by increased invasiveness and metastasis (Wong et al., 2007). On the other hand, in melanoma, oncogenic signaling by mutated constitutively active BRAF was found instead to suppress PlexinB1 expression (Argast et al., 2009); furthermore, experimental evidence indicated a tumor suppressor function of overexpressed PlexinB1 in melanoma cells (Argast et al., 2009; Stevens et al., 2010). One group recently addressed this issue in vivo by breeding an ERBB2-driven mouse breast carcinoma model in a PlexinB1 null background (Worzfeld et al., 2012). It emerged that PlexinB1 expression in vivo is not required for tumor growth or tumor angiogenesis, consistent with previous data, but it has a major role in promoting metastatic spreading. The specific role of Sema4D was not elucidated in this study; however, in vitro experiments suggested that PlexinB1 expression in cancer cells is required to mediate RhoA/RhoC activation elicited by overexpressed and constitutively active ERBB2 kinase (Worzfeld et al., 2012). Notably, low levels of PlexinB1 in ERBB2-overexpressing human breast tumors significantly correlated with better patient prognosis. Moreover, interfering with PlexinB1 was proposed as complementary therapeutic approach to block invasion and metastasis of ERBB2-positive tumors. Beyond the analysis of gene-deficient mouse models and RNAi approaches in vitro, this conclusion was based on the application of PlexinB1-blocking antibodies to cultured cells (Worzfeld et al., 2012). In fact, the use of interfering antibodies in vivo to manipulate Sema4D/PlexinB1 function in tumors has not been tested as yet. Interestingly, in a previous study, co-expression of PlexinB1 and MET tyrosine kinase in human breast and ovarian cancers was similarly found to correlate with metastatic progression (Valente et al., 2009). On the other hand, another group reported opposite prognostic significance of PlexinB1 expression in a subset of patients with estrogen receptor-positive breast cancer, indicating better survival in PlexinB1-expressing tumors and poor prognosis upon PlexinB1 loss (Rody et al., 2009). Thus, depending on the tumor type, PlexinB1 expression may be considered as a negative or a positive prognostic factor. Emerging data seem to suggest a similar scenario of tumor context-dependence for the homologous receptor PlexinB3, interacting with Sema5A (Artigiani et al., 2004). For instance, it was reported that an increased expression of Sema5A and PlexinB3 significantly correlates with invasion and metastasis in human gastric and pancreatic tumors (Pan et al., 2009; Sadanandam et al., 2010). On the other hand, another group found that Sema5A-PlexinB3 signaling inhibits the migration of human glioma cells and leads to inactivation of the pro-invasive protein fascin (Li et al., 2012). Further studies are required to elucidate whether this reflects the involvement of distinct receptor complexes and alternative signaling pathways, as seen for PlexinB1.

PlexinA4 Is Involved in Multiple Semaphorin Receptor Complexes, Responsible for Different Functions in Cancer and Endothelial Cells

In a recent study, PlexinA4 was reported to associate with RTKs VEGFR2 and FGFR2, and thereby promote signaling pathways leading to increased viability of endothelial and tumor cells (Kigel et al., 2011). Similar effects were observed upon overexpression of PlexinA4-ligand Sema6B, potentially suggesting that elevated Sema6B and/or PlexinA4 levels in tumors may correlate with progression. Intriguingly, it was proposed that PlexinA4-RTK receptor complexes may be functionally alternative to PlexinA4-PlexinA1 heterodimers responsible for Sema3A anti-angiogenic signals (Kigel et al., 2011). Thereby PlexinA4 might mediate opposite biological functions depending on the implicated semaphorin ligand and plexin-associated signal transducers. Based on these data, it could be envisaged that cancer treatment with Sema3A (or related molecules) could lead not only to direct inhibition of tumor cell migration and angiogenesis, but also prevent stimulatory signaling cascades by titrating out the bivalent receptor component PlexinA4.

Conclusions

In summary, inhibitory semaphorins that restrict cell migration and angiogenesis during development are often downregulated in advanced tumors, and proved to be effective tumor suppressor molecules in preclinical mouse models. Other semaphorins and plexins, such as Sema4D, PlexinB1, Sema3E and PlexinD1, are frequently upregulated in tumors as they support cancer progression and metastatic spreading. They have been proposed as prognostic predictors and recombinant molecular tools capable of blocking these pathways and effectively reducing tumor angiogenesis and metastatic spreading in preclinical trials in mice. Because the network of semaphorin signals is rather complex and cell-context-dependent, further studies may help to establish the relevance of individual family members as prognostic predictors and therapeutic targets for specific tumor types in humans. Moreover, biotechnological studies will aid in the development of improved molecular tools interfering with plexin activation and applicable for use in clinical trials.

ACKNOWLEDGMENTS

Many thanks to Silvia Giordano, Flavia Di Renzo, and Emily H. Crowley for critically reading the manuscript. The research activity in the author's lab is supported by the Italian Association for Cancer Research (AIRC; IG-11598), the International Association for Cancer Research (AICR-UK, Grant no. 11-0274), and the Italian Ministry for Research (PRIN Grant).

REFERENCES

Appleton, B.A., Wu, P., Maloney, J., Yin, J., Liang, W.C., Stawicki, S., Mortara, K., Bowman, K.K., Elliott, J.M., Desmarais, W., et al. (2007). Structural studies of neuropilin/antibody complexes provide insights into semaphorin and VEGF binding. EMBO J. *26*, 4902–4912.

Argast, G.M., Croy, C.H., Couts, K.L., Zhang, Z., Litman, E., Chan, D.C., and Ahn, N.G. (2009). Plexin B1 is repressed by oncogenic B-Raf signaling and functions as a tumor suppressor in melanoma cells. Oncogene *28*, 2697–2709.

Artigiani, S., Conrotto, P., Fazzari, P., Gilestro, G.F., Barberis, D., Giordano, S., Comoglio, P.M., and Tamagnone, L. (2004). Plexin-B3 is a functional receptor for semaphorin 5A. EMBO Rep. *5*, 710–714.

Balakrishnan, A., Penachioni, J.Y., Lamba, S., Bleeker, F.E., Zanon, C., Rodolfo, M., Vallacchi, V., Scarpa, A., Felicioni, L., Buck, M., et al. (2009). Molecular profiling of the "plexinome" in melanoma and pancreatic cancer. Hum. Mutat. *30*, 1167–1174.

Basile, J.R., Castilho, R.M., Williams, V.P., and Gutkind, J.S. (2006). Semaphorin 4D provides a link between axon guidance processes and tumor-induced angiogenesis. Proc. Natl. Acad. Sci. USA *103*, 9017–9022.

Bellon, A., Luchino, J., Haigh, K., Rougon, G., Haigh, J., Chauvet, S., and Mann, F. (2010). VEGFR2 (KDR/Flk1) signaling mediates axon growth in response to semaphorin 3E in the developing brain. Neuron *66*, 205–219.

Bielenberg, D.R., Hida, Y., Shimizu, A., Kaipainen, A., Kreuter, M., Kim, C.C., and Klagsbrun, M. (2004). Semaphorin 3F, a chemorepulsant for endothelial cells, induces a poorly vascularized, encapsulated, nonmetastatic tumor phenotype. J. Clin. Invest. *114*, 1260–1271.

Binmadi, N.O., Yang, Y.H., Zhou, H., Proia, P., Lin, Y.L., De Paula, A.M., Guimarães, A.L., Poswar, F.O., Sundararajan, D., and Basile, J.R. (2012). Plexin-B1 and semaphorin 4D cooperate to promote perineural invasion in a RhoA/ROK-dependent manner. Am. J. Pathol. *180*, 1232–1242.

Capparuccia, L., and Tamagnone, L. (2009). Semaphorin signaling in cancer cells and in cells of the tumor microenvironment—two sides of a coin. J. Cell Sci. *122*, 1723–1736.

Carmeliet, P., and Jain, R.K. (2011). Molecular mechanisms and clinical applications of angiogenesis. Nature *473*, 298–307.

Casazza, A., Finisguerra, V., Capparuccia, L., Camperi, A., Swiercz, J.M., Rizzolio, S., Rolny, C., Christensen, C., Bertotti, A., Sarotto, I., et al. (2010). Sema3E-Plexin D1 signaling drives human cancer cell invasiveness and metastatic spreading in mice. J. Clin. Invest. *120*, 2684–2698.

Casazza, A., Fu, X., Johansson, I., Capparuccia, L., Andersson, F., Giustacchini, A., Squadrito, M.L., Venneri, M.A., Mazzone, M., Larsson, E., Carmeliet, P., De, P.M., Naldini, L., Tamagnone, L., and Rolny, C. (2011). Systemic and targeted delivery of semaphorin 3a inhibits tumor angiogenesis and progression in mouse tumor models. Arterioscler Thromb Vasc Biol. *31*, 741–749.

Casazza, A., Kigel, B., Maione, F., Capparuccia, L., Kessler, O., Giraudo, E., Mazzone, M., Neufeld, G., and Tamagnone, L. (2012). Tumour growth inhibition and anti-metastatic activity of a mutated furin-resistant Semaphorin 3E isoform. EMBO Mol Med *4*, 234–250.

Castellani, V., De Angelis, E., Kenwrick, S., and Rougon, G. (2002). Cis and trans interactions of L1 with neuropilin-1 control axonal responses to semaphorin 3A. EMBO J. *21*, 6348–6357.

Catalano, A., Caprari, P., Moretti, S., Faronato, M., Tamagnone, L., and Procopio, A. (2006). Semaphorin-3A is expressed by tumor cells and alters T-cell signal transduction and function. Blood *107*, 3321–3329.

Caunt, M., Mak, J., Liang, W.C., Stawicki, S., Pan, Q., Tong, R.K., Kowalski, J., Ho, C., Reslan, H.B., Ross, J., et al. (2008). Blocking neuropilin-2 function inhibits tumor cell metastasis. Cancer Cell *13*, 331–342.

Chakraborty, G., Kumar, S., Mishra, R., Patil, T.V., and Kundu, G.C. (2012). Semaphorin 3A suppresses tumor growth and metastasis in mice melanoma model. PLoS ONE *7*, e33633.

Clarhaut, J., Gemmill, R.M., Potiron, V.A., Ait-Si-Ali, S., Imbert, J., Drabkin, H.A., and Roche, J. (2009). ZEB-1, a repressor of the semaphorin 3F tumor suppressor gene in lung cancer cells. Neoplasia *11*, 157–166.

Coma, S., Shimizu, A., and Klagsbrun, M. (2011). Hypoxia induces tumor and endothelial cell migration in a semaphorin 3F- and VEGF-dependent manner via transcriptional repression of their common receptor neuropilin 2. Cell Adhes. Migr. *5*, 266–275.

Dallas, N.A., Gray, M.J., Xia, L., Fan, F., van Buren, G., 2nd, Gaur, P., Samuel, S., Lim, S.J., Arumugam, T., Ramachandran, V., et al. (2008). Neuropilin-2-mediated tumor growth and angiogenesis in pancreatic adenocarcinoma. Clin. Cancer Res. *14*, 8052–8060.

Fazzari, P., Penachioni, J., Gianola, S., Rossi, F., Eickholt, B.J., Maina, F., Alexopoulou, L., Sottile, A., Comoglio, P.M., Flavell, R.A., and Tamagnone, L. (2007). Plexin-B1 plays a redundant role during mouse development and in tumour angiogenesis. BMC Dev. Biol. *7*, 55.

Franco, M., and Tamagnone, L. (2008). Tyrosine phosphorylation in semaphorin signalling: shifting into overdrive. EMBO Rep. *9*, 865–871.

Fukushima, Y., Okada, M., Kataoka, H., Hirashima, M., Yoshida, Y., Mann, F., Gomi, F., Nishida, K., Nishikawa, S., and Uemura, A. (2011). Sema3E-PlexinD1 signaling selectively suppresses disoriented angiogenesis in ischemic retinopathy in mice. J. Clin. Invest. *121*, 1974–1985.

Giordano, S., Corso, S., Conrotto, P., Artigiani, S., Gilestro, G., Barberis, D., Tamagnone, L., and Comoglio, P.M. (2002). The semaphorin 4D receptor controls invasive growth by coupling with Met. Nat. Cell Biol. *4*, 720–724.

Gu, C., Yoshida, Y., Livet, J., Reimert, D.V., Mann, F., Merte, J., Henderson, C.E., Jessell, T.M., Kolodkin, A.L., and Ginty, D.D. (2005). Semaphorin 3E and plexin-D1 control vascular pattern independently of neuropilins. Science *307*, 265–268.

Hayashi, M., Nakashima, T., Taniguchi, M., Kodama, T., Kumanogoh, A., and Takayanagi, H. (2012). Osteoprotection by semaphorin 3A. Nature *485*, 69–74.

Holmes, S., Downs, A.M., Fosberry, A., Hayes, P.D., Michalovich, D., Murdoch, P., Moores, K., Fox, J., Deen, K., Pettman, G., et al. (2002). Sema7A is a potent monocyte stimulator. Scand. J. Immunol. *56*, 270–275.

Janssen, B.J., Robinson, R.A., Pérez-Brangulí, F., Bell, C.H., Mitchell, K.J., Siebold, C., and Jones, E.Y. (2010). Structural basis of semaphorin-plexin signalling. Nature *467*, 1118–1122.

Kärpänen, T., Heckman, C.A., Keskitalo, S., Jeltsch, M., Ollila, H., Neufeld, G., Tamagnone, L., and Alitalo, K. (2006). Functional interaction of VEGF-C and VEGF-D with neuropilin receptors. FASEB J. *20*, 1462–1472.

Kessler, O., Shraga-Heled, N., Lange, T., Gutmann-Raviv, N., Sabo, E., Baruch, L., Machluf, M., and Neufeld, G. (2004). Semaphorin-3F is an inhibitor of tumor angiogenesis. Cancer Res. *64*, 1008–1015.

Kigel, B., Rabinowicz, N., Varshavsky, A., Kessler, O., and Neufeld, G. (2011). Plexin-A4 promotes tumor progression and tumor angiogenesis by enhancement of VEGF and bFGF signaling. Blood *118*, 4285–4296.

Kolodkin, A.L., Matthes, D.J., and Goodman, C.S. (1993). The semaphorin genes encode a family of transmembrane and secreted growth cone guidance molecules. Cell *75*, 1389–1399.

Kruger, R.P., Aurandt, J., and Guan, K.L. (2005). Semaphorins command cells to move. Nat. Rev. Mol. Cell Biol. *6*, 789–800.

Kumanogoh, A., Watanabe, C., Lee, I., Wang, X., Shi, W., Araki, H., Hirata, H., Iwahori, K., Uchida, J., Yasui, T., et al. (2000). Identification of CD72 as a lymphocyte receptor for the class IV semaphorin CD100: a novel mechanism for regulating B cell signaling. Immunity *13*, 621–631.

Kumanogoh, A., Marukawa, S., Suzuki, K., Takegahara, N., Watanabe, C., Ch'ng, E., Ishida, I., Fujimura, H., Sakoda, S., Yoshida, K., and Kikutani, H. (2002). Class IV semaphorin Sema4A enhances T-cell activation and interacts with Tim-2. Nature *419*, 629–633.

Lepelletier, Y., Moura, I.C., Hadj-Slimane, R., Renand, A., Fiorentino, S., Baude, C., Shirvan, A., Barzilai, A., and Hermine, O. (2006). Immunosuppressive role of semaphorin-3A on T cell proliferation is mediated by inhibition of actin cytoskeleton reorganization. Eur. J. Immunol. *36*, 1782–1793.

Li, X., Law, J.W., and Lee, A.Y. (2012). Semaphorin 5A and plexin-B3 regulate human glioma cell motility and morphology through Rac1 and the actin cytoskeleton. Oncogene *31*, 595–610.

Liu, H., Juo, Z.S., Shim, A.H., Focia, P.J., Chen, X., Garcia, K.C., and He, X. (2010). Structural basis of semaphorin-plexin recognition and viral mimicry from Sema7A and A39R complexes with PlexinC1. Cell *142*, 749–761.

Maione, F., Molla, F., Meda, C., Latini, R., Zentilin, L., Giacca, M., Seano, G., Serini, G., Bussolino, F., and Giraudo, E. (2009). Semaphorin 3A is an endogenous angiogenesis inhibitor that blocks tumor growth and normalizes tumor vasculature in transgenic mouse models. J. Clin. Invest. *119*, 3356–3372.

Maione, F., Capano, S., Regano, D., Zentilin, L., Giacca, M., Casanovas, O., Bussolino, F., Serini, G., and Giraudo, E. (2012). Semaphorin 3A overcomes cancer hypoxia and metastatic dissemination induced by antiangiogenic treatment in mice. J. Clin. Invest. *122*, 1832–1848.

Meda, C., Molla, F., De Pizzol, M., Regano, D., Maione, F., Capano, S., Locati, M., Mantovani, A., Latini, R., Bussolino, F., and Giraudo, E. (2012). Semaphorin 4A exerts a proangiogenic effect by enhancing vascular endothelial growth factor-A expression in macrophages. J. Immunol. *188*, 4081–4092.

Miao, H.Q., Soker, S., Feiner, L., Alonso, J.L., Raper, J.A., and Klagsbrun, M. (1999). Neuropilin-1 mediates collapsin-1/semaphorin III inhibition of endothelial cell motility: functional competition of collapsin-1 and vascular endothelial growth factor-165. J. Cell Biol. *146*, 233–242.

Moriya, J., Minamino, T., Tateno, K., Okada, S., Uemura, A., Shimizu, I., Yokoyama, M., Nojima, A., Okada, M., Koga, H., and Komuro, I. (2010). Inhibition of semaphorin as a novel strategy for therapeutic angiogenesis. Circ. Res. *106*, 391–398.

Negishi-Koga, T., Shinohara, M., Komatsu, N., Bito, H., Kodama, T., Friedel, R.H., and Takayanagi, H. (2011). Suppression of bone formation by osteoclastic expression of semaphorin 4D. Nat. Med. *17*, 1473–1480.

Neufeld, G., and Kessler, O. (2008). The semaphorins: versatile regulators of tumour progression and tumour angiogenesis. Nat. Rev. Cancer *8*, 632–645.

Neufeld, G., Sabag, A.D., Rabinovicz, N., and Kessler, O. (2012). Semaphorins in angiogenesis and tumor progression. Cold Spring Harb Perspect Med. *2*, a006718.

Nogi, T., Yasui, N., Mihara, E., Matsunaga, Y., Noda, M., Yamashita, N., Toyofuku, T., Uchiyama, S., Goshima, Y., Kumanogoh, A., and Takagi, J. (2010). Structural basis for semaphorin signalling through the plexin receptor. Nature *467*, 1123–1127.

Oinuma, I., Ishikawa, Y., Katoh, H., and Negishi, M. (2004). The Semaphorin 4D receptor Plexin-B1 is a GTPase activating protein for R-Ras. Science *305*, 862–865.

Pan, G.Q., Ren, H.Z., Zhang, S.F., Wang, X.M., and Wen, J.F. (2009). Expression of semaphorin 5A and its receptor plexin B3 contributes to invasion and metastasis of gastric carcinoma. World J. Gastroenterol. *15*, 2800–2804.

Pasterkamp, R.J., Peschon, J.J., Spriggs, M.K., and Kolodkin, A.L. (2003). Semaphorin 7A promotes axon outgrowth through integrins and MAPKs. Nature *424*, 398–405.

Qiang, R., Wang, F., Shi, L.Y., Liu, M., Chen, S., Wan, H.Y., Li, Y.X., Li, X., Gao, S.Y., Sun, B.C., and Tang, H. (2011). Plexin-B1 is a target of miR-214 in cervical cancer and promotes the growth and invasion of HeLa cells. Int. J. Biochem. Cell Biol. *43*, 632–641.

Rizzolio, S., and Tamagnone, L. (2011). Multifaceted role of neuropilins in cancer. Curr. Med. Chem. *18*, 3563–3575.

Rody, A., Karn, T., Ruckhäberle, E., Hanker, L., Metzler, D., Müller, V., Solbach, C., Ahr, A., Gätje, R., Holtrich, U., and Kaufmann, M. (2009). Loss of Plexin B1 is highly prognostic in low proliferating ER positive breast cancers—results of a large scale microarray analysis. Eur. J. Cancer *45*, 405–413.

Roodink, I., Raats, J., van der Zwaag, B., Verrijp, K., Kusters, B., van Bokhoven, H., Linkels, M., de Waal, R.M., and Leenders, W.P. (2005). Plexin D1 expression is induced on tumor vasculature and tumor cells: a novel target for diagnosis and therapy? Cancer Res. *65*, 8317–8323.

Sadanandam, A., Varney, M.L., Singh, S., Ashour, A.E., Moniaux, N., Deb, S., Lele, S.M., Batra, S.K., and Singh, R.K. (2010). High gene expression of semaphorin 5A in pancreatic cancer is associated with tumor growth, invasion and metastasis. Int. J. Cancer *127*, 1373–1383.

Sakurai, A., Gavard, J., Annas-Linhares, Y., Basile, J.R., Amornphimoltham, P., Palmby, T.R., Yagi, H., Zhang, F., Randazzo, P.A., Li, X., et al. (2010). Semaphorin 3E initiates antiangiogenic signaling through plexin D1 by regulating Arf6 and R-Ras. Mol. Cell. Biol. *30*, 3086–3098.

Sakurai, A., Jian, X., Lee, C.J., Manavski, Y., Chavakis, E., Donaldson, J., Randazzo, P.A., and Gutkind, J.S. (2011). Phosphatidylinositol-4-phosphate 5-kinase and GEP100/Brag2 protein mediate antiangiogenic signaling by semaphorin 3E-plexin-D1 through Arf6 protein. J. Biol. Chem. *286*, 34335–34345.

Semaphorin Nomenclature Committee. (1999). Unified nomenclature for the semaphorins/collapsins. Cell *97*, 551–552.

Semenza, G.L. (2012). Hypoxia-inducible factors: mediators of cancer progression and targets for cancer therapy. Trends Pharmacol. Sci. *33*, 207–214.

Serini, G., Valdembri, D., Zanivan, S., Morterra, G., Burkhardt, C., Caccavari, F., Zammataro, L., Primo, L., Tamagnone, L., Logan, M., et al. (2003). Class 3 semaphorins control vascular morphogenesis by inhibiting integrin function. Nature *424*, 391–397.

Sierra, J.R., Corso, S., Caione, L., Cepero, V., Conrotto, P., Cignetti, A., Piacibello, W., Kumanogoh, A., Kikutani, H., Comoglio, P.M., et al. (2008). Tumor angiogenesis and progression are enhanced by Sema4D produced by tumor-associated macrophages. J. Exp. Med. *205*, 1673–1685.

Smith, E.P., Shanks, K., Lipsky, M.M., DeTolla, L.J., Keegan, A.D., and Chapoval, S.P. (2011). Expression of neuroimmune semaphorins 4A and 4D and their receptors in the lung is enhanced by allergen and vascular endothelial growth factor. BMC Immunol. *12*, 30.

Stevens, L., McClelland, L., Fricke, A., Williamson, M., Kuo, I., and Scott, G. (2010). Plexin B1 suppresses c-Met in melanoma: a role for plexin B1 as a tumor-suppressor protein through regulation of c-Met. J. Invest. Dermatol. *130*, 1636–1645.

Sun, Q., Zhou, H., Binmadi, N.O., and Basile, J.R. (2009). Hypoxia-inducible factor-1-mediated regulation of semaphorin 4D affects tumor growth and vascularity. J. Biol. Chem. *284*, 32066–32074.

Suzuki, K., Okuno, T., Yamamoto, M., Pasterkamp, R.J., Takegahara, N., Takamatsu, H., Kitao, T., Takagi, J., Rennert, P.D., Kolodkin, A.L., et al. (2007). Semaphorin 7A initiates T-cell-mediated inflammatory responses through alpha1beta1 integrin. Nature *446*, 680–684.

Swiercz, J.M., Kuner, R., and Offermanns, S. (2004). Plexin-B1/RhoGEF-mediated RhoA activation involves the receptor tyrosine kinase ErbB-2. J. Cell Biol. *165*, 869–880.

Swiercz, J.M., Worzfeld, T., and Offermanns, S. (2008). ErbB-2 and met reciprocally regulate cellular signaling via plexin-B1. J. Biol. Chem. *283*, 1893–1901.

Takahashi, T., Fournier, A., Nakamura, F., Wang, L.H., Murakami, Y., Kalb, R.G., Fujisawa, H., and Strittmatter, S.M. (1999). Plexin-neuropilin-1 complexes form functional semaphorin-3A receptors. Cell *99*, 59–69.

Takamatsu, H., and Kumanogoh, A. (2012). Diverse roles for semaphorin-plexin signaling in the immune system. Trends Immunol. *33*, 127–135.

Takegahara, N., Takamatsu, H., Toyofuku, T., Tsujimura, T., Okuno, T., Yukawa, K., Mizui, M., Yamamoto, M., Prasad, D.V., Suzuki, K., et al. (2006). Plexin-A1 and its interaction with DAP12 in immune responses and bone homeostasis. Nat. Cell Biol. *8*, 615–622.

Tamagnone, L., and Comoglio, P.M. (2000). Signalling by semaphorin receptors: cell guidance and beyond. Trends Cell Biol. *10*, 377–383.

Tamagnone, L., and Mazzone, M. (2011). Semaphorin signals on the road of endothelial tip cells. Dev. Cell *21*, 189–190.

Tamagnone, L., Artigiani, S., Chen, H., He, Z., Ming, G.I., Song, H., Chedotal, A., Winberg, M.L., Goodman, C.S., Poo, M., et al. (1999). Plexins are a large family of receptors for transmembrane, secreted, and GPI-anchored semaphorins in vertebrates. Cell *99*, 71–80.

Tran, T.S., Kolodkin, A.L., and Bharadwaj, R. (2007). Semaphorin regulation of cellular morphology. Annu. Rev. Cell Dev. Biol. *23*, 263–292.

Tseng, C.H., Murray, K.D., Jou, M.F., Hsu, S.M., Cheng, H.J., and Huang, P.H. (2011). Sema3E/plexin-D1 mediated epithelial-to-mesenchymal transition in ovarian endometrioid cancer. PLoS ONE *6*, e19396.

Urbich, C., Kaluza, D., Frömel, T., Knau, A., Bennewitz, K., Boon, R.A., Bonauer, A., Doebele, C., Boeckel, J.N., Hergenreider, E., et al. (2012). MicroRNA-27a/b controls endothelial cell repulsion and angiogenesis by targeting semaphorin 6A. Blood *119*, 1607–1616.

Valente, G., Nicotra, G., Arrondini, M., Castino, R., Capparuccia, L., Prat, M., Kerim, S., Tamagnone, L., and Isidoro, C. (2009). Co-expression of plexin-B1 and Met in human breast and ovary tumours enhances the risk of progression. Cell. Oncol. *31*, 423–436.

Wang, Y., He, H., Srivastava, N., Vikarunnessa, S., Chen, Y.B., Jiang, J., Cowan, C.W., and Zhang, X. (2012). Plexins are GTPase-activating proteins for Rap and are activated by induced dimerization. Sci. Signal. *5*, ra6.

Wen, H., Lei, Y., Eun, S.Y., and Ting, J.P. (2010). Plexin-A4-semaphorin 3A signaling is required for Toll-like receptor- and sepsis-induced cytokine storm. J. Exp. Med. *207*, 2943–2957.

Wong, O.G., Nitkunan, T., Oinuma, I., Zhou, C., Blanc, V., Brown, R.S., Bott, S.R., Nariculam, J., Box, G., Munson, P., et al. (2007). Plexin-B1 mutations in prostate cancer. Proc. Natl. Acad. Sci. USA *104*, 19040–19045.

Worzfeld, T., Swiercz, J.M., Looso, M., Straub, B.K., Sivaraj, K.K., and Offermanns, S. (2012). ErbB-2 signals through Plexin-B1 to promote breast cancer metastasis. J. Clin. Invest. *122*, 1296–1305.

Yamamoto, M., Suzuki, K., Okuno, T., Ogata, T., Takegahara, N., Takamatsu, H., Mizui, M., Taniguchi, M., Chédotal, A., Suto, F., et al. (2008). Plexin-A4 negatively regulates T lymphocyte responses. Int. Immunol. *20*, 413–420.

Yang, T., and Terman, J.R. (2012). 14-3-3ε couples protein kinase A to semaphorin signaling and silences plexin RasGAP-mediated axonal repulsion. Neuron *74*, 108–121.

Ye, S., Hao, X., Zhou, T., Wu, M., Wei, J., Wang, Y., Zhou, L., Jiang, X., Ji, L., Chen, Y., et al. (2010). Plexin-B1 silencing inhibits ovarian cancer cell migration and invasion. BMC Cancer *10*, 611.

Zhou, Y., Gunput, R.A., and Pasterkamp, R.J. (2008). Semaphorin signaling: progress made and promises ahead. Trends Biochem. Sci. *33*, 161–170.

Zhu, L., Bergmeier, W., Wu, J., Jiang, H., Stalker, T.J., Cieslak, M., Fan, R., Boumsell, L., Kumanogoh, A., Kikutani, H., et al. (2007). Regulated surface expression and shedding support a dual role for semaphorin 4D in platelet responses to vascular injury. Proc. Natl. Acad. Sci. USA *104*, 1621–1626.

Cancer Cell
Article

Genetic Alterations Activating Kinase and Cytokine Receptor Signaling in High-Risk Acute Lymphoblastic Leukemia

Kathryn G. Roberts,[1,23] Ryan D. Morin,[6,23] Jinghui Zhang,[2] Martin Hirst,[6] Yongjun Zhao,[6] Xiaoping Su,[1] Shann-Ching Chen,[1] Debbie Payne-Turner,[1] Michelle L. Churchman,[1] Richard C. Harvey,[7] Xiang Chen,[2] Corynn Kasap,[8] Chunhua Yan,[10] Jared Becksfort,[3] Richard P. Finney,[10] David T. Teachey,[14] Shannon L. Maude,[14] Kane Tse,[6] Richard Moore,[6] Steven Jones,[6] Karen Mungall,[6] Inanc Birol,[6] Michael N. Edmonson,[11] Ying Hu,[11] Kenneth E. Buetow,[11] I-Ming Chen,[7] William L. Carroll,[15] Lei Wei,[1] Jing Ma,[1] Maria Kleppe,[16] Ross L. Levine,[16] Guillermo Garcia-Manero,[17] Eric Larsen,[18] Neil P. Shah,[8] Meenakshi Devidas,[19] Gregory Reaman,[20] Malcolm Smith,[12] Steven W. Paugh,[5] William E. Evans,[5] Stephan A. Grupp,[14] Sima Jeha,[4] Ching-Hon Pui,[4] Daniela S. Gerhard,[13] James R. Downing,[1] Cheryl L. Willman,[7] Mignon Loh,[9] Stephen P. Hunger,[21,*] Marco A. Marra,[6,22,*] and Charles G. Mullighan[1,*]

[1]Department of Pathology
[2]Department of Computational Biology and Bioinformatics
[3]Department of Information Sciences
[4]Department of Oncology
[5]Department of Pharmaceutical Sciences
St. Jude Children's Research Hospital, Memphis, TN 38105, USA
[6]Genome Sciences Centre, BC Cancer Agency, Vancouver, BC V5Z 1L3, Canada
[7]University of New Mexico Cancer Research and Treatment Center, Albuquerque, NM 87131, USA
[8]School of Medicine
[9]Department of Pediatrics
University of California, San Francisco, San Francisco, CA 94143, USA
[10]Center for Bioinformatics and Information Technology
[11]Laboratory of Population Genetics
[12]Cancer Therapy Evaluation Program, National Cancer Institute
[13]Office of Cancer Genomics, National Cancer Institute
National Institutes of Health, Bethesda, MD 20892, USA
[14]Division of Oncology, The Children's Hospital of Philadelphia, Philadelphia, PA 19104, USA
[15]New York University Cancer Institute, New York, NY 10016, USA
[16]Human Oncology and Pathogenesis Program, Memorial Sloan Kettering Cancer Center, New York, NY 10065, USA
[17]Department of Leukemia, M.D. Anderson Cancer Center, University of Texas, Houston, TX 77030, USA
[18]Maine Children's Cancer Program, Scarborough, ME 04074, USA
[19]Epidemiology and Health Policy Research, University of Florida, Gainesville, FL 32601, USA
[20]Children's National Medical Center, Washington, DC 20010, USA
[21]University of Colorado School of Medicine and The Children's Hospital Colorado, Aurora, CO 80045, USA
[22]Department of Medical Genetics, University of British Columbia, Vancouver, BC VSZ 1L3, Canada
[23]These authors contributed equally to this work
*Correspondence: stephen.hunger@childrenscolorado.org (S.P.H.), mmarra@bcgsc.ca (M.A.M.), charles.mullighan@stjude.org (C.G.M.)
http://dx.doi.org/10.1016/j.ccr.2012.06.005

SUMMARY

Genomic profiling has identified a subtype of high-risk B-progenitor acute lymphoblastic leukemia (B-ALL) with alteration of *IKZF1*, a gene expression profile similar to *BCR-ABL1*-positive ALL and poor outcome (Ph-like ALL). The genetic alterations that activate kinase signaling in Ph-like ALL are poorly understood. We performed transcriptome and whole genome sequencing on 15 cases of Ph-like ALL and identified

Significance

Ph-like ALL patients comprise up to 15% of childhood ALL, exhibit a high risk of relapse and have a poor outcome. Using next-generation sequencing, we have shown that genetic alterations activating kinase or cytokine receptor signaling are a hallmark of this subtype and that a number of these lesions are sensitive to tyrosine kinase inhibitors (TKIs). Thus, our findings support screening at diagnosis to identify Ph-like ALL patients that may benefit from the addition of TKI treatment to current chemotherapeutic regimens. Furthermore, this study illustrates how genomic analysis can be used to drive tailored therapy for cancer patients.

rearrangements involving *ABL1*, *JAK2*, *PDGFRB*, *CRLF2*, and *EPOR*, activating mutations of *IL7R* and *FLT3*, and deletion of *SH2B3*, which encodes the JAK2-negative regulator LNK. Importantly, several of these alterations induce transformation that is attenuated with tyrosine kinase inhibitors, suggesting the treatment outcome of these patients may be improved with targeted therapy.

INTRODUCTION

Acute lymphoblastic leukemia (ALL) is the most common pediatric malignancy, and relapsed B-lineage ALL remains a leading cause of cancer death in young people (Pui et al., 2008). B-progenitor acute lymphoblastic leukemia (B-ALL) is characterized by recurring chromosomal abnormalities, including aneuploidy, chromosomal rearrangements (e.g., *ETV6-RUNX1*, *BCR-ABL1*, and *TCF3-PBX1*), and rearrangements of *MLL* and *CRLF2* (Pui et al., 2008; Mullighan et al., 2009a; Russell et al., 2009a; Harvey et al., 2010a; Yoda et al., 2010). However, leukemic cells from many patients with relapsed B-ALL lack known chromosomal alterations. Therefore, identifying the full repertoire of genetic lesions in high-risk ALL is essential to improve the treatment outcome of this disease.

Genome-wide analyses have identified genetic alterations targeting transcriptional regulators of lymphoid development (*PAX5*, *EBF1*, and *IKZF1*) in over 60% of B-ALL patients (Kuiper et al., 2007; Mullighan et al., 2007, 2009b). *IZKF1* alteration is a hallmark of Philadelphia chromosome (Ph^+) ALL with *BCR-ABL1* fusion (Mullighan et al., 2008; Iacobucci et al., 2009) and is also associated with poor outcome in both *BCR-ABL1*-positive and *BCR-ABL1*-negative ALL (Den Boer et al., 2009; Martinelli et al., 2009; Mullighan et al., 2009b). Notably, *IKZF1*-mutated, *BCR-ABL1*-negative cases commonly exhibit a gene expression profile similar to *BCR-ABL1*-positive ALL, and these cases are referred to as "Ph-like ALL" (Den Boer et al., 2009; Mullighan et al., 2009b). Ph-like ALL comprises up to 15% of pediatric B-ALL, and these patients have a higher risk of relapse compared to other *BCR-ABL1*-negative patients, with 5-year event-free survival rates of 63% and 86%, respectively (our unpublished data). Approximately 50% of Ph-like patients harbor rearrangements of *CRLF2* (*CRLF2*r) (Harvey et al., 2010a), with concomitant Janus kinase (*JAK*) mutations detected in approximately 50% of *CRLF2*r cases (Mullighan et al., 2009a; Russell et al., 2009a; Harvey et al., 2010a; Yoda et al., 2010). However, the genetic alterations responsible for activated kinase signaling in the remaining Ph-like cases are unknown. To identify the genetic basis of this subtype, we performed transcriptome and whole genome sequencing on tumor and matched normal material from 15 patients with Ph-like ALL.

RESULTS

Chromosomal Rearrangements in Ph-like ALL

To identify genetic alterations in Ph-like ALL, we performed paired-end messenger RNA sequencing (mRNA-seq) on 15 B-ALL cases that were identified as Ph-like using prediction analysis of microarrays (PAM; Table 1; Table S1 available online) (Tibshirani et al., 2002) and Recognition of Outliers by Sampling Ends (ROSE) (Harvey et al., 2010b). Importantly, the gene expression profile of Ph-like ALL determined by *limma* (Linear Models for Microarray Analysis; Table S2) (Smyth, 2004) exhibited highly significant enrichment for the previously described signature of high-risk, *IKZF1*-deleted ALL (Mullighan et al., 2009b) (data not shown). Whole genome sequencing (WGS) of tumor DNA was also performed for two cases lacking kinase-activating rearrangements on analysis of mRNA-seq data. We used multiple complementary analysis pipelines, including deFuse (McPherson et al., 2011), Mosaik (Marth, 2010), CREST (Wang et al., 2011), CONSERTING (Zhang et al., 2012), and Trans-ABySS (Robertson et al., 2010) to identify rearrangements, structural variations, and sequence mutations. Putative somatic sequence variants were identified by comparing tumor data to WGS data of matched normal DNA and were validated using orthogonal sequencing methods. Overviews of methodology and findings are provided in Figure 1 and Figure S1.

Strikingly, we identified alteration of genes encoding cytokine receptors and regulators of kinase signaling in all 15 cases studied (Table 1). Putative rearrangements were validated by reverse transcription followed by polymerase chain reaction (RT-PCR) and Sanger sequencing (Figure 2), with an average of 1.9 rearrangements identified per case (range 0–5; Table S3 and Figure S2). The rearrangements included two cases with *NUP214-ABL1*, one case with insertion of the erythropoietin receptor gene (*EPOR*) into the immunoglobulin heavy chain locus (*IGH@-EPOR*), and one case each with the in-frame fusions *EBF1-PDGFRB*, *BCR-JAK2*, *STRN3-JAK2*, *PAX5-JAK2*, *ETV6-ABL1*, *RANBP2-ABL1*, and *RCSD1-ABL1.* These rearrangements were either cryptic on cytogenetic analysis or the fusion partners could not be identified on examination of karyotypic data alone (Table 1). In each case multiple paired-end reads mapped to the partner genes, and split reads mapping across the fusion were identified (Figure 3A and Figure S3A). Additional putative fusion transcripts were identified for each case (Figure S2 and Table S3); however, these commonly showed a low level of read support, did not encode an open-reading frame (SEM*A6A-FEM1C*, *OAZ1-KLF2*, and *ZNF292-SYNCRIP*), or involved intronic fusion break points (*DOCK8-CBWD2* and *TSHZ2-SLC35A1*), suggesting they do not contribute to leukemogenesis. We also identified an inversion involving *PAX5* and the adjacent gene *ZCCHC7*, resulting in a reciprocal fusion that disrupts the open reading frame of *PAX5* (Figure S2H). Deletions, translocations, and sequence mutations of *PAX5* are detected in approximately 30% of B-ALL patients (Mullighan et al., 2007), and this inversion represents another mechanism for *PAX5* inactivation.

CRLF2 is overexpressed in up to 7% of B-ALL, including over 50% of ALL cases in children with Down syndrome, and occurs via multiple mechanisms involving either a cryptic translocation that juxtaposes *CRLF2* to the regulatory elements of the immunoglobulin heavy chain locus (*IGH@-CRLF2*) (Mullighan et al., 2009a; Russell et al., 2009a) or an interstitial deletion of the pseudoautosomal region one (PAR1) centromeric to *CRLF2* resulting in the *P2RY8-CRLF2* rearrangement (Mullighan et al., 2009a). Less frequently, the point mutation affecting codon

Table 1. Chromosomal Rearrangements Detected in High-Risk B-Lineage ALL

Sample ID	Cohort	Rearrangement	Sex	Age (Years)	WCC × 10^9/l	Key Lesions	Karyotype
PAKTAL	P9906	*STRN3-JAK2*[a]	Female	12.2	478	*IKZF1* deletion and p.Leu117fs mutation	N/A
PAKKCA	P9906	*EBF1-PDGFRB*[a]	Male	11.7	236.4	*IKZF1* (IK6); *EBF1* deletion; *PAX5* inversion[a]; *CDKN2A/CDKN2B* deletion	46,XY,del(6)(q13q23),del(9)(p22)[20]
PAKVKK	P9906	*NUP214-ABL1*[a]	Male	14.4	220.7	*IKZF1* p.Ser402fs mutation; *PAX5* deletion; *CDKN2A/CDKN2B* deletion	N/A
PALIBN	P9906	*IGH@-EPOR*[a]	Male	14.3	29.9	*IKZF1* e1-5 deletion; *CDKN2A/CDKN2B* deletion	N/A
PAKYEP	P9906	*BCR-JAK2*[a]	Male	2.7	958.8	*IKZF1* (IK6); *EBF1* deletion; *PAX5* deletion and p.Gly24Arg mutation; *CDKN2A/CDKN2B* deletion	47,XY,+2,del(2)(p23),t(3;22;9)(p12;q11.2;p24) [10]/46,XY[2]
PAMDRM	P9906	*IGH@-CRLF2*[b]	Male	7.9	351.3	*JAK2* p.Ile682_Arg683insGlyPro[a]; *IKZF1* deletion e1-e6; *EBF1* deletion; *PAX5* p.Val319fs; *CDKN2A/CDKN2B* deletion	46,XY[20]
PAKKXB	P9906	*IGH@-CRLF2*[b]	Female	14.5	92.7	*IKZF1* (IK6); *CDKN2A/CDKN2B* deletion; *FLT3* p.Asn609ins23aa[c]	46,XX[21]
PALETF	P9906	None	Female	7.6	105.7	*EBF1* deletion; *FLT3* p.Leu604ins23aa[a]	47,XX,+10[3]/46,XX,+10,−21[7]/46,XX[8]
PAKHZT	P9906	*IGH@-CRLF2*[b]	Male	13.9	307	JAK2 p.Arg867Gln; *CDKN2A/CDKN2B* deletion	N/A
PALJDL	P9906	None	Male	3.2	156	*PAX5* deletion; *CDKN2A/CDKN2B* deletion; *IL7R* p.L242_L243insFPGVC mutation[d]; *SH2B3* e1–2 deletion[d]	N/A
PANNGL	AALL0232	*PAX5-JAK2*[a]	Female	12.9	15.8	*IKZF1* deletion	47,XX,r(7)(p12q31),+9[14]/46,XX[6]
PANSFD	AALL0232	*ETV6-ABL1*[a]	Male	5.4	83	*IKZF1* (IK6); *PAX5* deletion; *CDKN2A/CDKN2B* deletion	46,XY,ins(12;9)(p13;q34q34)[20]
PANEHF	AALL0232	*RCSD1-ABL1*[a]	Male	15.7	47.8	N/A	N/A
SJBALL085	Total XV	*NUP214-ABL1*[a]	Male	16.3	135.6	*IKZF1* (IK6) and p.Ala79fs mutation[a]	46,XY
SJBALL010	Total XVI	*RANBP2-ABL1*[a]	Male	15	121	*PAX5* deletion[a]	46,XY,t(2;9)(q21;q34)[14]/46, XY[6]

Chromosomal rearrangements affecting kinase and cytokine receptor signaling identified by mRNA-seq in 15 Ph-like cases. Genetic lesions disrupting B cell development (*IKZF1*, *EBF1*, and *PAX5*) and *JAK2*-activating mutations are also shown. IK6 refers to the deletion of *IKZF1* exons 4–7 (coding exons 3–6), which results in the expression of a dominant negative IKZF1 isoform that lacks the N-terminal DNA-binding zinc fingers. All cases were of B-precursor immunophenotype and did not exhibit expression of T-lineage markers. Frame shifts (fs) are designated using the short nomenclature as outlined by the Human Genome Variation Society. aa, amino acid; e, exon; ITD, internal tandem duplication; N/A, not available; WCC, white cell count (× 10^9/l).

[a]Identified by RNA-seq analysis.

[b]Previously known (Harvey et al., 2010a).

[c]Previously known (Zhang et al., 2011).

[d]Identified by whole genome sequencing. See Tables S1, S2, S3, S4, S5, S6, S7, S8, and S9.

232 (p.Phe232Cys) has also been identified (Yoda et al., 2010; Chapiro et al., 2010). Mutations activating *JAK* are present in approximately 50% of *CRLF2*r cases (Mullighan et al., 2009a; Russell et al., 2009a; Harvey et al., 2010a; Hertzberg et al., 2010; Yoda et al., 2010); however, the nature of kinase-activating mutations in *CRLF2*r cases lacking *JAK* mutations is unknown. Three cases in the discovery cohort were known to have the *IGH@-CRLF2* translocation, and one of these harbored a known JAK2 mutation (p.Arg867Gln) (Mullighan et al., 2009c). Two additional *CRLF2*r cases lacking known *JAK* mutations were sequenced, one of which harbored a FLT3 internal tandem duplication (ITD; p.Asn609ins23aa) (Zhang et al., 2011), and the other harbored a complex JAK2 mutation (p.Ile682_Arg683insGlyPro in case PAMDRM) that was not identified by previous Sanger sequencing (Mullighan et al., 2009c). No additional kinase-activating lesions were identified in the *CRLF2*r cases. A full listing of somatic single nucleotide variants (SNVs) and insertions/deletions identified by mRNA-seq are provided in Table S4.

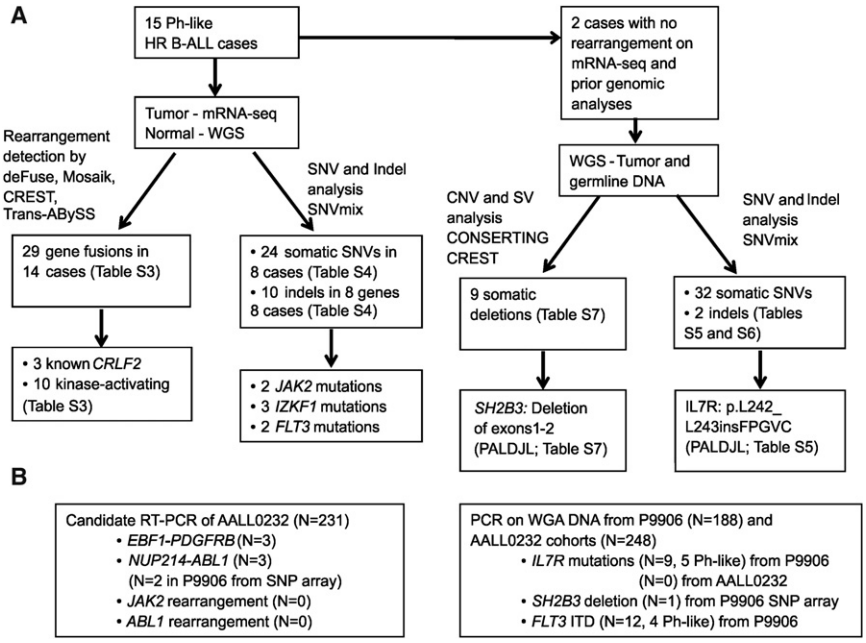

Figure 1. Flow Chart of Methodology

(A) Fifteen Ph-like high-risk (HR) ALL cases were subjected to mRNA-seq, with matched normal DNA subjected to whole genome sequencing (WGS). Two cases also had WGS of tumor DNA.

(B) For recurrence testing of *ABL1*, *JAK2*, and *PDGFRB* fusions, cases with available RNA from AALL0232 were screened by RT-PCR. The two *NUP214-ABL1* cases identified in P9906 showed gain of 9q34 between *NUP214* and *ABL1* on SNP array analysis, and the presence of *NUP214-ABL1* was confirmed by RT-PCR. Whole genome amplified (WGA) leukemic DNA was used for recurrence of *IL7R* and *SH2B3* mutations. *FLT3* mutations were reported previously (Zhang et al., 2011).

See also Figure S1.

Case PAKKCA harbored the previously unknown *EBF1-PDGFRB* fusion that was present in the predominant leukemic clone, as confirmed by fluorescence in situ hybridization (FISH) (Figure S3). mRNA-seq coverage analysis for this case showed a sharp increase in read depth at intron 10 of *PDGFRB* that corresponds to the genomic break point (Figure 3B). Both genes are located on chromosome 5q, and analysis of DNA copy number data revealed a deletion between the two break points (Figure 3C). Genomic PCR identified the break point 0.5 kb downstream of *EBF1* exon 15 and 2.3 kb upstream of *PDGFRB* exon 11 in the index case (Figure 3D). Several copy number alterations and rearrangements in B-ALL arise from aberrant recombination-activating gene (RAG) activity (Mullighan et al., 2007, 2009a); however, analysis of the sequences adjacent to the genomic break points of *EBF1* and *PDGFRB* showed no evidence of RAG-mediated activity in this case.

The *NUP214-ABL1* rearrangement has not previously been reported in B-ALL but is present in 5% of T-lineage ALL and commonly accompanies episomal amplification of 9q34 (Graux et al., 2004). Notably, both *NUP214-ABL1* cases had pre-B-ALL immunophenotype with no expression of T-lineage markers, and in contrast to T-ALL, did not show high-level episomal amplification by FISH analysis (data not shown). Instead, we observed gain of only one copy of DNA between the two partner genes at 9q34 (Figure S2I). The *ABL1* break points correspond to those observed in *NUP214-ABL1* T-ALL (De Braekeleer et al., 2011) and Ph^+ chronic myeloid leukemia or B-ALL (Melo, 1996), which retain the SH2, SH3, and kinase domains of ABL1.

Case PAKYEP harbored the *BCR-JAK2* fusion, which has previously been identified in myeloid leukemia (Griesinger et al., 2005; Cirmena et al., 2008) but not in B-ALL. Visualization of mRNA-seq split-reads using Bambino (Edmonson et al., 2011) identified two *BCR-JAK2* fusion transcripts in this case involving exon 1 of *BCR* fused to either exon 15 or 17 of *JAK2*, both of which were validated by RT-PCR and sequencing (Figure S4A). Using Bambino, we also mapped the genomic break point at intron 1 of *BCR*, located within the minor break point cluster region, to intron 14 of *JAK2* (Figure S4B). Notably, all *JAK2* fusions identified in this study are in-frame and disrupt the pseudokinase domain of JAK2, which is thought to relieve autoinhibition of the kinase domain, thus resulting in a constitutively active fusion protein.

The *IGH@-EPOR* rearrangement arising from a reciprocal t(14;19)(q32;p13) translocation has been documented in B cell precursor ALL (Russell et al., 2009b). However, FISH for the t(14;19) rearrangement in case PALIBN was negative. Detailed analysis of mRNA-seq data and genomic mapping demonstrated that the rearrangement involved a 7.5 kb insertion of *EPOR* into the immunoglobulin heavy chain locus downstream of the IgH enhancer domain with similar cytogenetic break points as the previously identified translocation, thus identifying another mechanism of *IGH@-EPOR* rearrangement (Figure 4).

Sequence Mutations and Deletions in Ph-like ALL

WGS of tumor and normal DNA was performed on two Ph-like cases for which a kinase-activating rearrangement was not identified by mRNA-seq. Case PALJDL harbored two alterations predicted to activate tyrosine kinase signaling, the first being an in-frame insertion in the transmembrane domain of the interleukin 7 receptor, IL7R (p.Leu242_Leu243insFPGVC; Figure 5A). Using the mRNA-seq mutant allele read counts, we estimated the *IL7R* mutation to be expressed in approximately 93.4% of cells in the sample sequenced. Similar activating mutations in *IL7R* have recently been described in pediatric B and T-lineage ALL (Shochat et al., 2011; Zenatti et al., 2011; Zhang et al., 2012). Interestingly, case PALJDL also harbored a focal homozygous deletion removing the first two exons of *SH2B3* that was not evident by SNP array analysis, with a concomitant absence of *SH2B3* expression by mRNA-seq analysis (Figures 5B and 5C). By comparing the coverage in the region of homozygous deletion (1.15×) to that of the undeleted region downstream on the same chromosome (30.86×), we estimate this deletion to be in at least 96% of cells in the sample sequenced. *SH2B3* encodes the protein LNK, which is a negative regulator of

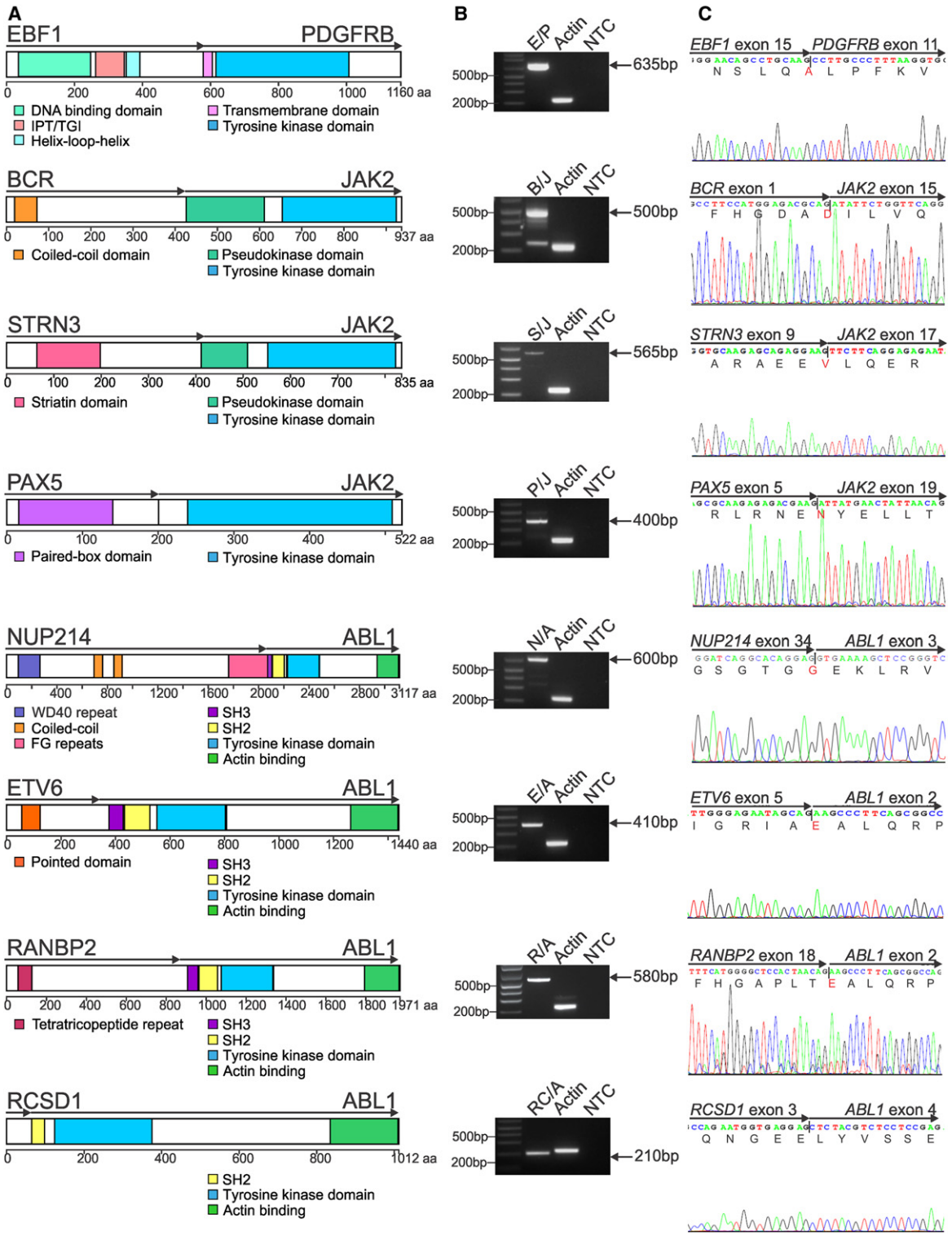

Figure 2. Rearrangements in Ph-like ALL

(A) Predicted domain structure of the in-frame fusions EBF1-PDGFRB (E/P), BCR-JAK2 (B/J), STRN3-JAK2 (S/J), PAX5-JAK2 (P/J), NUP214-ABL1 (N/A), ETV6-ABL1 (E/A), RANBP2-ABL1 (R/A), and RCSD1-ABL1 (RC/A) identified by mRNA-seq in eight Ph-like ALL cases. Confirmation of predicted fusions by RT-PCR (B) and Sanger sequencing (C). The two bands for *BCR-JAK2* correspond to two different fusion break points within *JAK2* (exon 15 and 17), both of which were confirmed by Sanger sequencing. IPT/TIG, immunoglobulin-like fold, plexins, transcription factors/transcription factor immunoglobulin; FG, phenylalanine and glycine; SH, Src homology domain.

See also Figure S2.

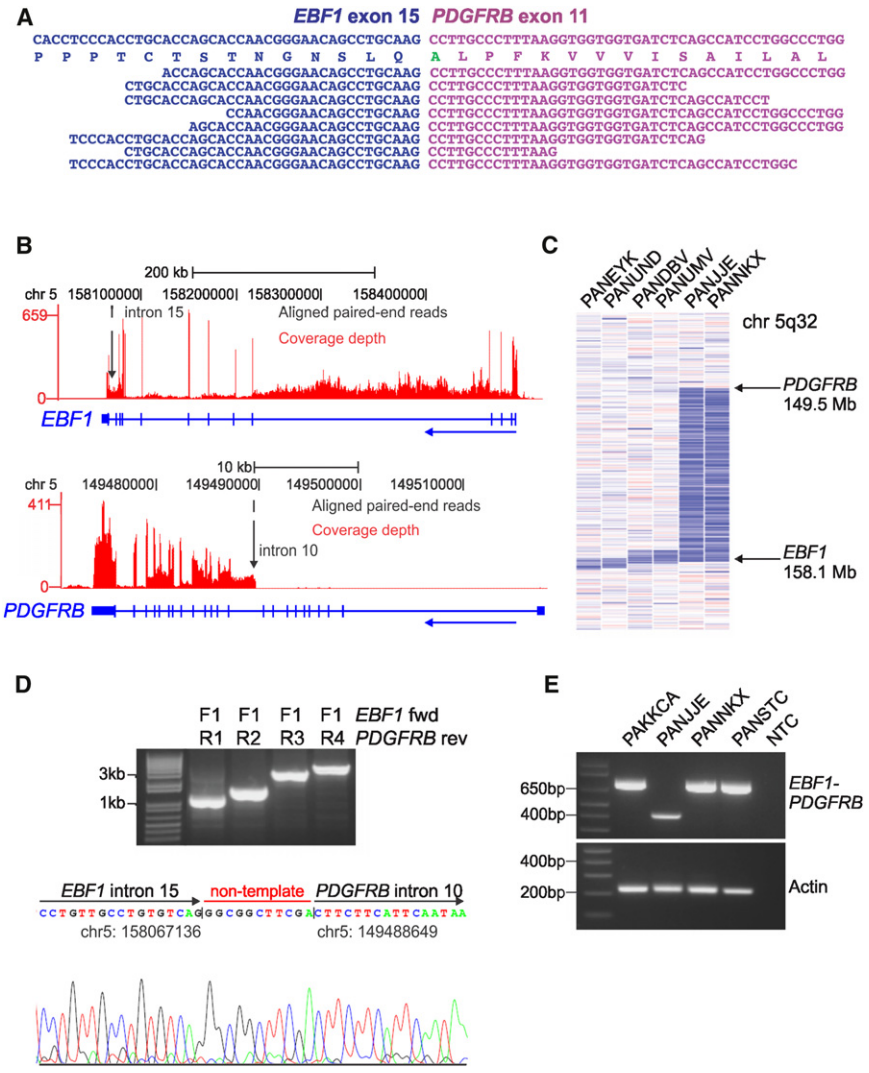

Figure 3. mRNA-seq Data, Recurrence Screening, and Genomic Mapping of the *EBF1-PDGFRB* Fusion

(A) Split reads mapping across the *EBF1-PDGFRB* fusion point for case PAKKCA. Amino acid substitution from wild-type PDGFRB (Ser > Ala) is highlighted in green.

(B) Coverage depth for all mRNA-seq reads at the *EBF1* and *PDGFRB* locus in case PAKKCA, showing expression across the *EBF1* locus and increased expression of *PDGFRB* at intron 10 (arrowed). The vertical height of the red bar indicates the number of reads covering the site.

(C) SNP 6.0 microarray $\log_2$ ratio DNA copy number heatmap showing deletion (blue) between *EBF1* and *PDGFRB* for two *EBF1-PDGFRB* cases (PANJJE and PANNKX) and four non-rearranged cases with focal *EBF1* deletions (left).

(D) Genomic mapping of the *EBF1-PDGFRB* rearrangement break point by PCR (top) and sequencing (bottom), showing juxtaposition of *EBF1* intron 15 (chr5:158067136) to *PDGFRB* intron 10 (chr5:149488649), with the addition of nontemplate nucleotides between the break points.

(E) RT-PCR confirmation of *EBF1-PDGFRB* fusion in four high-risk B-ALL cases with exon 14 (bottom band) or exon 15 (top band) of *EBF1* fused to exon 11 of *PDGFRB*.

See also Figure S3.

JAK2 signaling (Tong et al., 2005), and inactivating mutations within exon 2 have been identified in JAK2 p.Val617Phe-negative myeloproliferative neoplasms (MPN) (Oh et al., 2010; Pardanani et al., 2010) and early T cell precursor ALL (Zhang et al., 2012).

Case PALETF was found to harbor an in-frame ITD within the FLT3 juxtamembrane domain (p.Leu604ins23aa; Table S4). FLT3 ITDs and increased expression of wild-type FLT3 are also present in high-risk acute myeloid and lymphoblastic leukemia (Schnittger et al., 2002; Armstrong et al., 2003; Paietta et al., 2004; Zhang et al., 2012). Similar to *PDGFRB* and *JAK2* rearrangements, *FLT3* mutations facilitate leukemic transformation by inducing constitutive kinase activation and signaling through the Ras and JAK/STAT5 pathways (Mizuki et al., 2000). Additional SNVs and structural variations identified by WGS of PALJDL and PALETF are provided in Tables S5, S6 and, S7 and Figure S5.

Recurrence of Genetic Alterations in Ph-like B-ALL

We next performed recurrence screening of extended cohorts of high-risk B-ALL to determine the frequency of these genetic alterations (Figure 1). RT-PCR for the *EBF1-PDGFRB*, *BCR-JAK2*, *STRN3-JAK2*, *PAX5-JAK2*, *NUP214-ABL1*, *ETV6-ABL1*, *RANBP2-ABL1*, and *RCSD1-ABL1* fusions was performed for 231 cases from a separate consecutively recruited cohort of high-risk B-progenitor ALL obtained from the Children's Oncology Group (COG) AALL0232 study. Screening for these fusions in the COG P9906 discovery cohort was not possible because of a lack of RNA for many cases. We investigated the presence of *IL7R* and *SH2B3* variants in both the P9906 and AALL0232 cohorts by Sanger sequencing of tumor DNA and SNP array analysis of tumor and matched nontumor DNA. *CRLF2* rearrangements, *JAK* mutations and amplification between *NUP214* and *ABL1* were examined in both P9906 and AALL0232 cohorts by SNP array analysis, genomic PCR and sequencing, and FISH for cases with 9q34 amplification. We also performed RT-PCR for the fusions and genomic sequencing for *IL7R* in other hematopoietic malignancies, including 23 MPN cases lacking *JAK2* or *MPL* mutations, 25 chronic myelomonocytic leukemia (CMML) cases and 44 childhood acute myeloid leukemia (AML) cases, including 34 that lacked recurring chromosomal rearrangements.

Forty of 231 cases (14%) of the AALL0232 cohort were identified as Ph-like (Table S8). Twenty-five cases (8.8%) had high *CRLF2* expression, 19 of which were Ph-like and 6 non-Ph-like. *JAK* mutations were present in ten cases with high *CRLF2* expression, all of which were Ph-like (Table S9). The *EBF1-PDGFRB* fusion was detected in three additional Ph-like patients (8% of Ph-like ALL), in which exon 15 (n = 2) or exon 14 (n = 1) of

EBF1 was fused to exon 11 of *PDGFRB* (Figure 3E). Each of the *EBF1-PDGFRB* cases showed an increase in *PDGFRB* expression by gene expression profiling and two of these patients (PANJJE and PANNKX) had an interstitial deletion between the partner gene break points (Figure 3C).

No additional cases with the *ABL1* or *JAK2* rearrangements identified in the discovery cohort were observed in the AALL0232 cohort. Analysis of SNP array data identified two cases in P9906 (PAMBWU and PALFBA, one Ph-like) with a single copy gain of DNA between *NUP214* and *ABL1* (Figure 2I). The presence of the *NUP214-ABL1* rearrangement was confirmed by RT-PCR and Sanger sequencing (Figure 2J), indicating that this fusion is also recurrent in B-ALL. No *ABL1*, *JAK2*, or *PDGFRB* rearrangements were identified in the MPN, CMML, and AML cohorts and have not been detected in other childhood B-ALL subtypes studied by WGS and mRNA-seq (Downing et al., 2012), indicating these genetic lesions are highly enriched in the Ph-like subtype.

Mutations within the transmembrane domain of *IL7R* were found in eight additional cases from P9906, five of which were Ph-like (12.5% of Ph-like ALL) (Figure 5A). An additional Ph-like case from the AALL0232 cohort (PANKMB) had a focal homozygous deletion removing exons 1–2 of *SH2B3* that was identified using the higher resolution SNP 6.0 microarray, and subsequently confirmed by PCR (data not shown). Interestingly, this case harbors a *P2RY8-CRLF2* rearrangement but lacks a *JAK* mutation, suggesting that removal of JAK2 regulation by LNK augments JAK signaling in this case. No additional somatic *SH2B3* mutations or deletions were identified in this study. Sanger sequencing of *FLT3* in the P9906 cohort reported mutations in 12 cases, 4 of which were Ph-like (Table S9) (Zhang et al., 2011).

Rearrangements Are Transforming and Sensitive to Tyrosine Kinase Inhibitors

Recent phosphoflow cytometry studies have shown that B-ALL leukemic cells harboring *CRLF2* rearrangements (with or without concomitant *JAK* mutations) have enhanced signaling through oncogenic pathways that can be targeted with JAK or PI3K inhibitors (Tasian et al., 2012). To determine if the genetic alterations we identified in Ph-like ALL activate kinase signaling and respond to TKIs, we performed flow cytometric phosphosignaling analysis on four primary leukemic samples (two cases with the *NUP214-ABL1* fusion, one case with the *BCR-JAK2* fusion, and one case with the *STRN3-JAK2* fusion). All cases demonstrated activation of downstream signaling pathways, with phosphorylation of the ABL1 substrate CRKL in the *NUP214-ABL1* cases and tyrosine phosphorylation in the cases with *BCR-JAK2* and *STRN3-JAK2* fusions (Figure 6). Importantly, this basal level of phosphorylation was reduced with imatinib, dasatinib, and XL228 in samples harboring the *ABL1* fusion, and the JAK2 inhibitor, XL019, in the *JAK2*-rearranged samples (Figure 6). Notably, XL019 had no effect on CRKL phosphorylation in *ABL1*-positive cases; however, we did observe slight inhibition of tyrosine phosphorylation with dasatinib in the *JAK2*-cases. Five non-Ph-like B-ALL cases were also assessed by phosphoflow and showed minimal activation of signaling pathways compared to Ph-like ALL, with no response to ABL1 or JAK2 inhibitors (Figure S6).

To evaluate the transforming potential of the *EBF1-PDGFRB* fusion, we assessed the ability of murine Ba/F3 and *Arf*$^{-/-}$ pre-B cells (Williams et al., 2006) expressing EBF1-PDGFRB to proliferate in the absence of exogenous cytokines. EBF1-PDGFRB expression (Figure 7A) conferred growth factor independence and resulted in significantly faster proliferation compared to Ba/F3 cells expressing the most common PDGFRB rearrangement, ETV6-PDGFRB (Figures 7B and 7C). Importantly, cytokine-independent proliferation was inhibited by imatinib (Figures 7B and 7C) and the multikinase inhibitors dasatinib and dovitinib (Figure S7A). Accordingly, imatinib treatment reduced phosphorylation of the PDGFRB receptor, with no change in total PDGFRB expression (Figure S7B). Several oncogenic pathways were constitutively activated by EBF1-PDGFRB in pre-B cells, demonstrated by elevated levels of pSTAT5, pAKT, and pERK1/2. Notably, this signaling was also inhibited with dasatinib (Figures 7B, 7C, and S7C). In addition, we also have evidence of a patient with *EBF1-PDGFRB*$^{+}$ B-ALL refractory to induction chemotherapy entering remission with the addition of imatinib (data not shown).

We next investigated the therapeutic efficacy of the JAK2 inhibitor, ruxolitinib, in a xenograft model of *BCR-JAK2*-rearranged ALL (case PAKYEP). In this model cryopreserved *BCR-JAK2*$^{+}$ cells were injected into NOD.Cg-*Prkdc*^{scid} *Il2rg*^{tm1Wjl}/Szj (NSG) mice, and continuous infusion of ruxolitinib or vehicle was commenced once engraftment exceeded 5% of peripheral blood leukocytes (determined by measuring human CD19^{+}/45^{+} cells). The presence of the fusion in xenografted cells was confirmed by RT-PCR (data not shown). We observed a striking decrease in leukemic burden after 4 weeks of ruxolitinib treatment compared to vehicle-treated controls, as measured by reduced peripheral blood ($p < 0.001$; Figure 7D) and spleen blast counts (data not shown). Furthermore, a xenograft model of *NUP214-ABL1* ALL responded to dasatinib up to 8 weeks of treatment (Figure 7D), confirming that cells expressing *NUP214-ABL1* are sensitive to TKIs (Quintás-Cardama et al., 2008; Deenik et al., 2009). In addition, ruxolitinib significantly decreased peripheral blood and spleen blast counts in a xenograft model of case PALJDL, which harbors both an *IL7R* activating mutation and a somatic *SH2B3* (LNK) deletion (data not shown). Together, these data indicate that *EBF1-PDGFRB*, *BCR-JAK2*, and *NUP214-ABL1* fusions and sequence mutations in *IL7R*/*SH2B3* are transforming, and represent excellent candidates for therapy with currently available TKIs.

DISCUSSION

Ph-like ALL represents approximately 10% of childhood B-ALL and 15% of high-risk B-ALL and is three to four times more common than Ph^{+} ALL. Among a large cohort of patients with high-risk B-ALL treated on COG AALL0232, the Ph-like phenotype is associated with older age (12.4 versus 9.5 years, $p < 0.0001$) and significantly inferior 5-year event-free survival compared to non-Ph-like patients (our unpublished data). Using next-generation sequencing, we have shown that rearrangements and sequence mutations activating tyrosine kinase and cytokine receptor signaling are a hallmark of Ph-like ALL. Moreover, each of the cases studied harbored genomic lesions affecting lymphoid transcription factors (most commonly

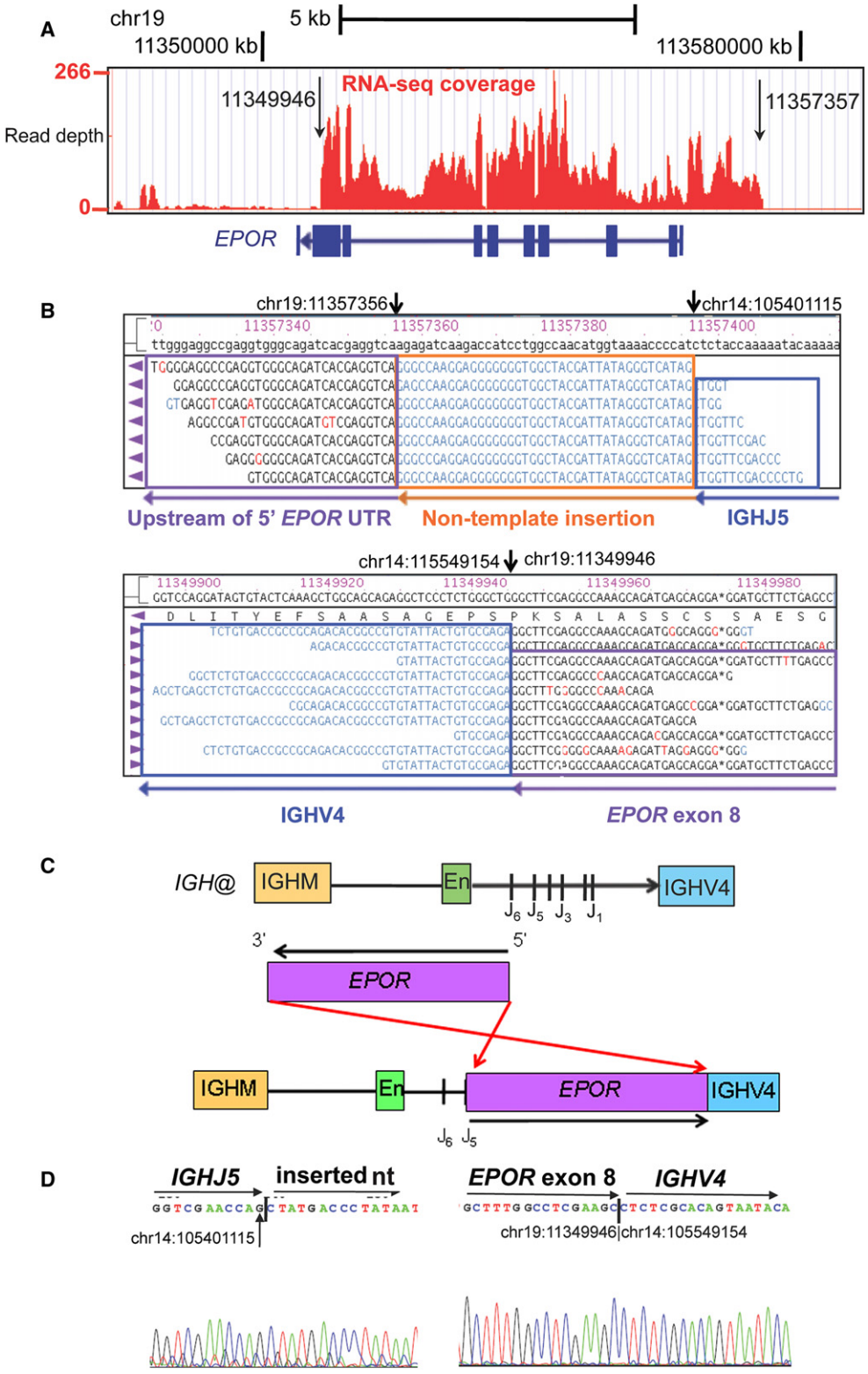

Figure 4. Schematic of the *IGH@-EPOR* Rearrangement

(A) Plot of read depth obtained from mRNA-seq data showing increased read depth across the *EPOR* locus. The arrows correspond to the genomic break points identified by genomic PCR and sequencing.

(B) Bambino viewer of mRNA-seq reads showing *IGHJ5* with 40 bp of inserted sequence joined to ~1.3 kb upstream of *EPOR* 5′ untranslated region (UTR) on chromosome 19. Bottom view shows split reads spanning exon 8 of *EPOR* adjacent to *IGHV4*.

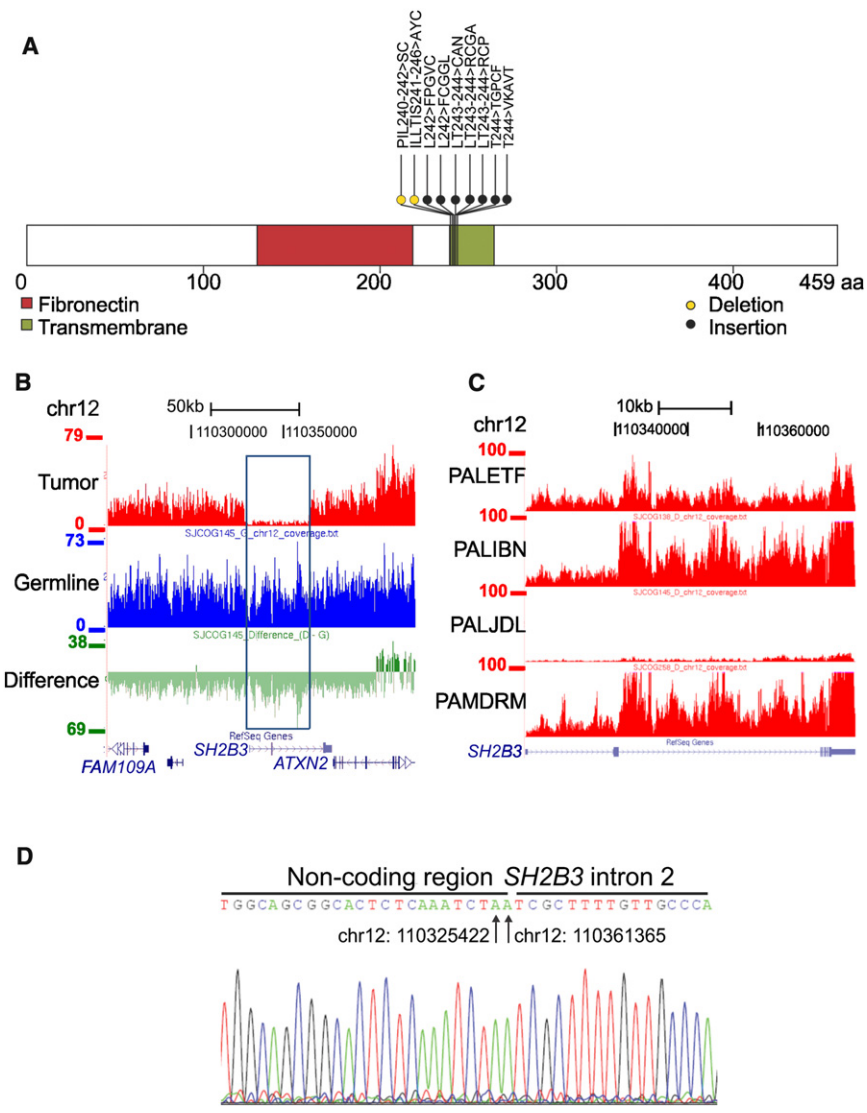

Figure 5. *IL7R*-Activating Mutations and *SH2B3* Deletion

(A) Protein domain structure of IL7R with location of sequence mutations identified in the transmembrane domain of nine B-ALL cases.

(B) Copy number variant analysis of PALDJL comparing tumor and matched nontumor DNA at the *SH2B3* locus.

(C) Transcript read depth data from mRNA-seq analysis comparing three cases with normal expression of *SH2B3* to PALJDL. The vertical height of the red bar indicates the number of reads covering the site.

(D) Sanger sequencing confirming the deletion from chr12:110325422 (first arrow) to chr12:110361365 (second arrow).

See also Figure S5.

deletions and/or mutations of *IKZF1*), suggesting that perturbation of these two pathways cooperate to induce B-lineage ALL and drive the Ph-like gene expression profile.

Chromosomal rearrangements resulting in activated tyrosine kinase signaling are recognized as driver lesions in a number of hematopoietic malignancies, the prototype being *BCR-ABL1* in CML (Melo, 1996) and Ph$^+$ B-ALL (De Braekeleer et al., 2011). Here, we report five fusions that, to our knowledge, have not been reported in B-ALL (*EBF1-PDGFRB*, *NUP214-ABL1*, *BCR-JAK2*, *STRN3-JAK2*, and *RANBP2-ABL1*) and several that have been reported in very few patients, including *IGH@-EPOR* (Russell et al., 2009b), *PAX5-JAK2* (Nebral et al., 2009), *ETV6-ABL1*, and *RCSD1-ABL1* (De Braekeleer et al., 2011).

Rearrangements involving the PDGFRB receptor are present at low frequency in Ph-negative myeloid neoplasms (Golub et al., 1994; Cross and Reiter, 2008). The identification of a *PDGFRB* fusion is of clinical importance, as patients with chronic myeloproliferative disease and activating *PDGFRB* rearrangements show complete hematologic and molecular responses to imatinib treatment (Apperley et al., 2002). For *EBF1-PDGFRB*, the coding region of EBF1 is juxtaposed to the C-terminal region of PDGFRB, preserving the transmembrane and kinase domains. It is predicted that the EBF1 helix-loop-helix domain mediates homodimerization (Hagman et al., 1995) and facilitates constitutive activation of PDGFRB as is observed with *ETV6-PDGFRB* (Carroll et al., 1996). Furthermore, EBF1 is a transcription factor that plays a major role in regulating B cell differentiation (Hagman and Lukin, 2006), and deletions that abolish normal EBF1 function have been reported in B-lineage ALL (Mullighan et al., 2007). The fusion of EBF1 to PDGFRB is also likely to impair the normal function of EBF1 and represents a mechanism resulting in PDGFRB overexpression.

We also identified *RANBP2* as a fusion partner for *ABL1*. RANBP2 (or NUP358) localizes to the cytoplasmic side of the nuclear pore complex via interaction with NUP88 and forms a subcomplex with NUP214 (Bernad et al., 2004). The structural features of RANBP2 retained in the fusion protein include the leucine zipper, which is predicted to mediate homodimerization of *RANBP2-ABL1*, as observed with *RANBP2-ALK* in atypical

(C) *IGH@* contains an IGHM domain, enhancer (En), J domains (J1–J6) and the downstream *IGHV4* gene segment. The *EPOR* locus is inverted so the 5′ end is adjacent to the J5 domain and the 3′ end is within the *IGHV4* gene segment.

(D) Sanger sequencing confirming the rearrangement at *IGHJ5* (chr14:105401115) to nontemplate sequence (left) and exon 8 of *EPOR* (chr19:11349946) to *IGHV4* (chr14:105549154).

See also Figure S4.

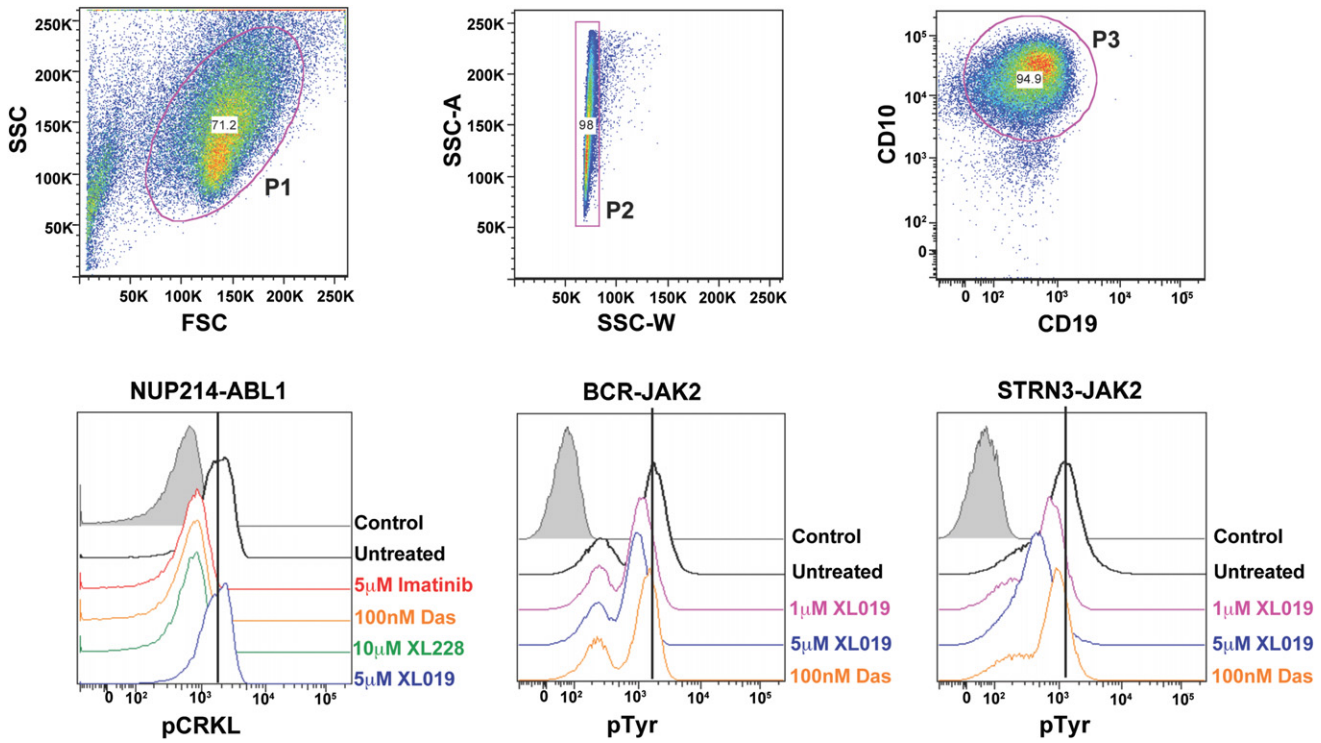

Figure 6. Phosphosignaling Analysis of Primary Leukemic Blasts Harboring *NUP214-ABL1*, *BCR-JAK2*, and *STRN3-JAK2* Rearrangements
Cells were untreated or treated with indicated tyrosine kinase inhibitors for 1 hr, and levels of phosphorylated CRKL or tyrosine were assessed by phosphoflow cytometric analysis. Viable (P1) and single cells (P2) were gated by expression of CD10 and CD19 (P3). Das, dasatinib. Control is secondary antibody alone. See also Figure S6.

myeloproliferative leukemia (Röttgers et al., 2010). Furthermore, localization of NUP214-ABL1 to the nuclear pore complex and interaction with additional nuclear pore proteins is required for ABL1 kinase activity of this fusion protein (De Keersmaecker et al., 2008). Thus, we hypothesize that RANBP2-ABL1 may be activated in a similar manner.

Although a diverse range of kinase lesions are present in Ph-like ALL, activation of ABL1 and/or JAK/STAT signaling pathways is a common mechanism for transformation. The dramatic improvement in outcome observed in Ph^+ B-ALL patients treated with chemotherapy and imatinib (Schultz et al., 2009) and our demonstration that Ph-like leukemic cells are sensitive to currently available TKIs provide a strong rationale to test chemotherapy plus TKI treatment in Ph-like ALL patients. At present, next-generation sequencing is not widely available in diagnostic laboratories. However, our results indicate that flow cytometric phosphosignaling analysis can identify Ph-like cases with activation of kinase pathways, and in conjunction with flow-cytometric detection of CRLF2 overexpression (Mullighan et al., 2009a), may be implemented as a routine diagnostic test. In addition, the gene expression profile of Ph-like ALL can be used to design targeted low-density gene expression arrays suitable for diagnostic use. Although the majority of Ph-like patients do not harbor known recurring chromosomal rearrangements, initial screening may be performed on all ALL cases. Patients identified as Ph-like can then undergo additional testing for known genetic lesions associated with this subtype and be directed to treatment that combines chemotherapy with ABL1, PDGFRB, or JAK inhibitors. It is important to note that rare non-Ph-like patients that harbor kinase alterations (e.g., *NUP214-ABL1*) may also benefit from the addition of TKI therapy.

In summary, this study illustrates how the use of genomic analysis can identify rationale therapeutic targets that drive tailored treatment and provides a model that can be applied to a wide range of cancer subtypes to benefit patients with high-risk disease.

EXPERIMENTAL PROCEDURES

Patients and Samples

Ten Ph-like ALL cases from the COG P9906 high-risk B-ALL study (Bowman et al., 2011), three cases enrolled on the high-risk COG AALL0232 study (http://ClinicalTrials.gov Identifier NCT00075725), and two cases treated on the St. Jude Children's Research Hospital Total XV (Pui et al., 2009) and Total XVI protocols (http://ClinicalTrials.gov Identifiers NCT00137111 and NCT00549848, respectively) were selected for mRNA-seq based on a similar gene expression profile to *BCR-ABL1* ALL, as determined by ROSE clustering (Harvey et al., 2010b), PAM (Tibshirani et al., 2002), and the availability of suitable genomic material. All samples were obtained with patient or parent/guardian provided informed consent under protocols approved by the Institutional Review Board at each COG institution and St. Jude Children's Research Hospital. Details on case selection and recurrence are outlined in the Supplemental Experimental Procedures.

mRNA-seq and Whole Genome Sequencing

mRNA-seq was performed using a method similar to that previously described (Morin et al., 2010). For WGS, Illumina paired-end whole genome shotgun libraries were prepared from 1 μg of genomic DNA as described (Shah et al., 2009). Sequencing was performed on the Illumina Genome Analyzer GAIIx

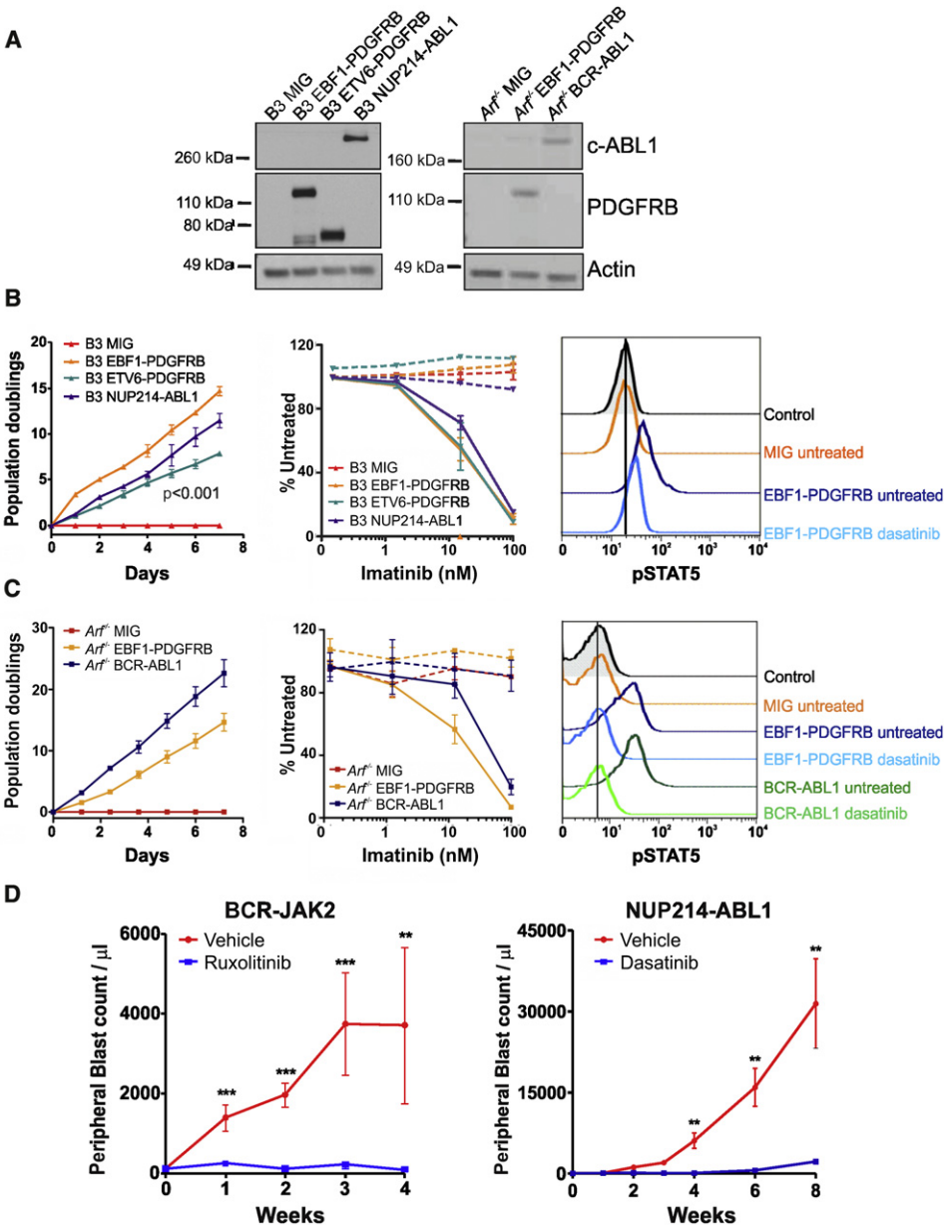

Figure 7. Kinase-Activating Fusions Induce Growth Factor-Independence and Show Response to Tyrosine Kinase Inhibitors

(A) Immunoblot of c-ABL1 and PDGFRB in Ba/F3 (B3) and $Arf^{-/-}$ pre-B cells expressing empty vector (MIG), EBF1-PDGFRB, ETV6-PDGFRB, or NUP214-ABL1.

(B and C) Transduced Ba/F3 (B) or $Arf^{-/-}$ pre-B cells (C) were grown in the absence of cytokine and cell number was recorded as indicated (left). Ba/F3 or $Arf^{-/-}$ pre-B cells were grown in increasing concentrations of imatinib (middle). No cytokine (solid line) or cytokine (dotted line). Error bars represent mean ± SD of three independent experiments. Cells were untreated or treated with dasatinib for 1 hr, and levels of phosphorylated STAT5 were assessed by phosphoflow cytometric analysis (right).

(D) Xenograft model of *BCR-JAK2* and *NUP214-ABL1*. Mice were randomized to receive vehicle (40% dimethyl acetamide, 60% propylene glycol; n = 5), ruxolitinib (30 mg/kg/day; n = 7) or dasatinib (20 mg/kg/day; n = 5). Error bars represent mean ± SEM. **p < 0.001; ***p < 0.0001.

See also Figure S7.

or HiSeq 2000 platforms. Methods for library preparation, sequencing and detection of rearrangements, DNA copy number alterations, and sequence variations are provided in the Supplemental Experimental Procedures.

RT-PCR, Genomic Mapping, and Sequencing

Putative rearrangements identified by mRNA-seq were validated by RT-PCR and Sanger sequencing. Leukemic cell RNA was reverse-transcribed using Superscript III (Life Technologies, Carlsbad, CA, USA) and fusion products amplified with Phusion HF polymerase (New England Biolabs, Ipswich, MA, USA). Genomic mapping of the *EBF1-PDGFRB* and *BCR-JAK2* rearrangement break points was performed using whole genome amplified (Qiagen, Hilden, Germany) leukemic cell DNA.

Retroviral Constructs, Infection, and Cell Proliferation Assays

The full-length *EBF1-PDGFRB* fusion was amplified from leukemic cell cDNA, cloned into pGEM-T-Easy (Promega), and then subcloned into the

MSCV-IRES-GFP retroviral vector. Retroviral supernatants containing MSCV-*EBF1-PDGFRB*-IRES-GFP, MSCV-*ETV6-PDGFRB*-IRES-GFP (Carroll et al., 1996), MSCV-*NUP214-ABL1*-IRES-GFP (De Keersmaecker et al., 2008), or MSCV-*BCR-ABL1*-IRES-GFP (p185) (Williams et al., 2006) were produced using the ecotropic Phoenix packaging cell line and used to infect murine hematopoietic progenitor Ba/F3 or primary $Arf^{-/-}$ pre-B cells (Williams et al., 2006). To evaluate factor-independent growth, cells were washed three times, seeded in triplicate without cytokine, and the cell number was recorded daily using a Vicell cell counter (Beckman Coulter, Fullerton, CA, USA). Proliferation rates of each cell line were compared using a linear mixed-effect model with order-1 autoregressive covariance structure for longitudinal data in the SAS package (SAS Inc, Cary, NC, USA). Drug sensitivity was assessed using the CellTiter-Blue Cell Viability Assay (Promega. Madison, WI, USA) in accordance with the manufacturer's instructions, and IC_{50} was determined using nonlinear regression (GraphPad Prism, La Jolla, CA). Each experiment was performed three times.

Phosphoflow Analysis and Immunoblotting

To assess signaling within leukemic samples and cell lines, intracellular phosphoflow cytometric analysis were performed as previously described (Kotecha et al., 2008). Briefly, cryopreserved patient samples were thawed, or cells in culture were harvested at 1×10^6 cells per tube and treated with the TKIs imatinib (Novartis, Basel, Switzerland), dasatinib (Bristol Myers Squibb, New York, NY, USA), XL228, or XL019 (Exelixis, South San Francisco, CA, USA) for 1 hr. Cells were fixed, permeabilized, and stained with either anti-phospho-tyrosine-4G10 (Upstate, now EMD Millipore Corporation, Billerica, MA, USA), anti-pAKT (S573), anti-pCRKL (Y207), anti-pERK1/2 (T202/Y204), or anti-pSTAT5 (Y694; Cell Signaling Technology, Danvers, MA, USA) and then Alexa Fluor 647 conjugated anti-rabbit or Pacific Blue conjugated anti-mouse IgG secondary antibodies (Life Technologies, Carlsbad, CA, USA). Cellular fluorescence data were collected on an LSR II flow cytometer (BD Biosciences, Franklin Lakes, NJ, USA) using DIVA software (BD Biosciences) and analyzed with FlowJo (Tree Star, Ashland, OR, USA). For immunoblotting, cells were lysed in RIPA buffer, subjected to SDS-PAGE, and probed with anti-phospho-tyrosine-4G10 (Upstate [now EMD Millipore Corporation]), anti-c-ABL, anti-PDGFRB, and anti-Actin (Santa Cruz Biotechnology, Santa Cruz, CA, USA).

Xenograft Models

Xenograft models of case PAKYEP (*BCR-JAK2*) and PAKVKK (*NUP214-ABL1*) were established as previously described with modifications (Teachey et al., 2006). Primary leukemia cells from bone marrow were intravenously injected into the tail vein of NSG mice (10^7 cells/mouse). Following engraftment (>5% human $CD19^+/45^+$ blasts in peripheral blood), *BCR-JAK2* mice were randomized to receive ruxolitinib (30 mg/kg/day; Incyte, Wilmington, DE, USA) or vehicle (40% dimethyl acetamide, 60% propylene glycol) by continuous subcutaneous infusion using implanted mini-osmotic pumps (Alzet). For *NUP214-ABL1* mice, dasatinib (20 mg/kg; Bristol Myers Squibb) or vehicle (10% citric acid in 80 mM sodium citrate) was given 5 days a week by oral gavage. Disease burden was assessed weekly by flow cytometric determination of human $CD19^+/45^+$ blast count in peripheral blood, using CountBright beads (Invitrogen, Carlsbad, CA, USA). Deaths within 72 hr of pump placement were considered secondary to anesthesia or surgery, and these mice were censored at the time of death. All experiments were conducted on protocols approved by the Institutional Animal Care and Use Committee and Institutional Review Board of The Children's Hospital of Philadelphia.

ACCESSION NUMBERS

The sequence data and SNP microarray data have been deposited in the database of genotypes and phenotypes (dbGAP, http://www.ncbi.nlm.nih.gov/gap) database under the accession number phs000218.v1.p1. The gene expression data for COG P9906 has been deposited at the National Center for Biotechnology Information (NCBI) Gene Expression Omnibus (GEO), accession GSE11877. The gene expression data without metadata for COG AALL0232 is deposited at the National Cancer Institute caArray site (https://array.nci.nih.gov/caarray/project/EXP-578). The NCBI Genbank database accession number for the *EBF1-PDGFRB* sequence reported in this paper is JN003579.

SUPPLEMENTAL INFORMATION

Supplemental information includes seven figures, nine tables, Supplemental Experimental Procedures, and Supplemental References and can be found with this article online at http://dx.doi.org/10.1016/j.ccr.2012.06.005.

ACKNOWLEDGMENTS

We thank M. Tomasson and J. Cools for providing the MSCV-*ETV6-PDGFRB*-IRES-GFP and MSCV-*NUP214-ABL1*-IRES-GFP constructs, respectively; D. Pei and C. Cheng for statistical analyses of cell line proliferation data; Garry Nolan for providing the Phoenix cell line (http://www.stanford.edu/group/nolan/retroviral_systems/phx.html); Beckman Coulter Genomics for Sanger Sequencing; and the Flow Cytometry Core Facility, Tissue Resources Core Facility, and Clinical Application of Core Technology (Affymetrix) Laboratory of the Hartwell Center for Bioinformatics and Biotechnology of St. Jude Children's Research Hospital. The correlative biology studies described in this manuscript were funded by grants from the National Institutes of Health (NIH) and philanthropic funds of the Children's Oncology Group and not a commercial entity. The sequencing was part-funded with Federal funds from the NCI and NIH under Contract No. N01-C0-12400 as part of the Therapeutically Applicable Research to Generate Effective Treatments initiative. This work was supported by funds provided as a supplement to the Children's Oncology Group Chair's award (CA098543, G.R.); grants to the COG, including U10 CA98543 (COG Chair's grant), U10 CA98413 (COG Statistical Center), and U24 CA114766 (COG Specimen Banking); a National Cancer Institute Strategic Partnering to Evaluate Cancer Signatures Program award CA114762 (W.L.C., I-M.C., R.C.H., and C.L.W.); NIH Cancer Center Core Grant CA21765 (J.R.D., C.G.M., W.E.E., C.-H.P., and S.J.); St. Jude Children's Research Hospital - Washington University Pediatric Cancer Genome Project; a Stand Up To Cancer Innovative Research Grant (C.G.M.); and the American Lebanese Syrian Associated Charities of St. Jude Children's Research Hospital. K.G.R. is supported by a National Health and Medical Research Council (Australia) Overseas Training Fellowship and a Haematology Society of Australia and New Zealand Novartis New Investigator Scholarship. R.D.M. is a Vanier Scholar (CIHR) and holds a MSFHR senior graduate studentship. M.A.M. is a UBC Canada Research Chair in Genome Science and a Michael Smith Senior Research Scholar. S.P.H. is the Ergen Family Chair in Pediatric Cancer. C.G.M. is a Pew Scholar in the Biomedical Sciences and a St. Baldrick's Scholar. S.P.H. is a member of the Bristol Myers Squibb pediatric dasatinib advisory board.

Received: April 12, 2012
Revised: May 21, 2012
Accepted: June 11, 2012
Published: August 13, 2012

REFERENCES

Apperley, J.F., Gardembas, M., Melo, J.V., Russell-Jones, R., Bain, B.J., Baxter, E.J., Chase, A., Chessells, J.M., Colombat, M., Dearden, C.E., et al. (2002). Response to imatinib mesylate in patients with chronic myeloproliferative diseases with rearrangements of the platelet-derived growth factor receptor beta. N. Engl. J. Med. *347*, 481–487.

Armstrong, S.A., Kung, A.L., Mabon, M.E., Silverman, L.B., Stam, R.W., Den Boer, M.L., Pieters, R., Kersey, J.H., Sallan, S.E., Fletcher, J.A., et al. (2003). Inhibition of FLT3 in MLL. Validation of a therapeutic target identified by gene expression based classification. Cancer Cell *3*, 173–183.

Bernad, R., van der Velde, H., Fornerod, M., and Pickersgill, H. (2004). Nup358/RanBP2 attaches to the nuclear pore complex via association with Nup88 and Nup214/CAN and plays a supporting role in CRM1-mediated nuclear protein export. Mol. Cell. Biol. *24*, 2373–2384.

Bowman, W.P., Larsen, E.L., Devidas, M., Linda, S.B., Blach, L., Carroll, A.J., Carroll, W.L., Pullen, D.J., Shuster, J., Willman, C.L., et al. (2011). Augmented

therapy improves outcome for pediatric high risk acute lymphocytic leukemia: results of Children's Oncology Group trial P9906. Pediatr. Blood Cancer *57*, 569–577.

Carroll, M., Tomasson, M.H., Barker, G.F., Golub, T.R., and Gilliland, D.G. (1996). The TEL/platelet-derived growth factor beta receptor (PDGF beta R) fusion in chronic myelomonocytic leukemia is a transforming protein that self-associates and activates PDGF beta R kinase-dependent signaling pathways. Proc. Natl. Acad. Sci. USA *93*, 14845–14850.

Chapiro, E., Russell, L., Lainey, E., Kaltenbach, S., Ragu, C., Della-Valle, V., Hanssens, K., Macintyre, E.A., Radford-Weiss, I., Delabesse, E., et al. (2010). Activating mutation in the TSLPR gene in B-cell precursor lymphoblastic leukemia. Leukemia *24*, 642–645.

Cirmena, G., Aliano, S., Fugazza, G., Bruzzone, R., Garuti, A., Bocciardi, R., Bacigalupo, A., Ravazzolo, R., Ballestrero, A., and Sessarego, M. (2008). A BCR-JAK2 fusion gene as the result of a t(9;22)(p24;q11) in a patient with acute myeloid leukemia. Cancer Genet. Cytogenet. *183*, 105–108.

Cross, N.C., and Reiter, A. (2008). Fibroblast growth factor receptor and platelet-derived growth factor receptor abnormalities in eosinophilic myeloproliferative disorders. Acta Haematol. *119*, 199–206.

De Braekeleer, E., Douet-Guilbert, N., Rowe, D., Bown, N., Morel, F., Berthou, C., Férec, C., and De Braekeleer, M. (2011). ABL1 fusion genes in hematological malignancies: a review. Eur. J. Haematol. *86*, 361–371.

De Keersmaecker, K., Rocnik, J.L., Bernad, R., Lee, B.H., Leeman, D., Gielen, O., Verachtert, H., Folens, C., Munck, S., Marynen, P., et al. (2008). Kinase activation and transformation by NUP214-ABL1 is dependent on the context of the nuclear pore. Mol. Cell *31*, 134–142.

Deenik, W., Beverloo, H.B., van der Poel-van de Luytgaarde, S.C., Wattel, M.M., van Esser, J.W., Valk, P.J., and Cornelissen, J.J. (2009). Rapid complete cytogenetic remission after upfront dasatinib monotherapy in a patient with a NUP214-ABL1-positive T-cell acute lymphoblastic leukemia. Leukemia *23*, 627–629.

Den Boer, M.L., van Slegtenhorst, M., De Menezes, R.X., Cheok, M.H., Buijs-Gladdines, J.G., Peters, S.T., Van Zutven, L.J., Beverloo, H.B., Van der Spek, P.J., Escherich, G., et al. (2009). A subtype of childhood acute lymphoblastic leukaemia with poor treatment outcome: a genome-wide classification study. Lancet Oncol. *10*, 125–134.

Downing, J.R., Wilson, R.K., Zhang, J., Mardis, E.R., Pui, C.H., Ding, L., Ley, T.J., and Evans, W.E. (2012). The pediatric cancer genome project. Nat. Genet. *44*, 619–622.

Edmonson, M.N., Zhang, J., Yan, C., Finney, R.P., Meerzaman, D.M., and Buetow, K.H. (2011). Bambino: a variant detector and alignment viewer for next-generation sequencing data in the SAM/BAM format. Bioinformatics *27*, 865–866.

Golub, T.R., Barker, G.F., Lovett, M., and Gilliland, D.G. (1994). Fusion of PDGF receptor beta to a novel ets-like gene, tel, in chronic myelomonocytic leukemia with t(5;12) chromosomal translocation. Cell *77*, 307–316.

Graux, C., Cools, J., Melotte, C., Quentmeier, H., Ferrando, A., Levine, R., Vermeesch, J.R., Stul, M., Dutta, B., Boeckx, N., et al. (2004). Fusion of NUP214 to ABL1 on amplified episomes in T-cell acute lymphoblastic leukemia. Nat. Genet. *36*, 1084–1089.

Griesinger, F., Hennig, H., Hillmer, F., Podleschny, M., Steffens, R., Pies, A., Wörmann, B., Haase, D., and Bohlander, S.K. (2005). A BCR-JAK2 fusion gene as the result of a t(9;22)(p24;q11.2) translocation in a patient with a clinically typical chronic myeloid leukemia. Genes Chromosomes Cancer *44*, 329–333.

Hagman, J., and Lukin, K. (2006). Transcription factors drive B cell development. Curr. Opin. Immunol. *18*, 127–134.

Hagman, J., Gutch, M.J., Lin, H., and Grosschedl, R. (1995). EBF contains a novel zinc coordination motif and multiple dimerization and transcriptional activation domains. EMBO J. *14*, 2907–2916.

Harvey, R.C., Mullighan, C.G., Chen, I.M., Wharton, W., Mikhail, F.M., Carroll, A.J., Kang, H., Liu, W., Dobbin, K.K., Smith, M.A., et al. (2010a). Rearrangement of CRLF2 is associated with mutation of JAK kinases, alteration of IKZF1, Hispanic/Latino ethnicity, and a poor outcome in pediatric B-progenitor acute lymphoblastic leukemia. Blood *115*, 5312–5321.

Harvey, R.C., Mullighan, C.G., Wang, X., Dobbin, K.K., Davidson, G.S., Bedrick, E.J., Chen, I.M., Atlas, S.R., Kang, H., Ar, K., et al. (2010b). Identification of novel cluster groups in pediatric high-risk B-precursor acute lymphoblastic leukemia with gene expression profiling: correlation with genome-wide DNA copy number alterations, clinical characteristics, and outcome. Blood *116*, 4874–4884.

Hertzberg, L., Vendramini, E., Ganmore, I., Cazzaniga, G., Schmitz, M., Chalker, J., Shiloh, R., Iacobucci, I., Shochat, C., Zeligson, S., et al. (2010). Down syndrome acute lymphoblastic leukemia, a highly heterogeneous disease in which aberrant expression of CRLF2 is associated with mutated JAK2: a report from the International BFM Study Group. Blood *115*, 1006–1017.

Iacobucci, I., Storlazzi, C.T., Cilloni, D., Lonetti, A., Ottaviani, E., Soverini, S., Astolfi, A., Chiaretti, S., Vitale, A., Messa, F., et al. (2009). Identification and molecular characterization of recurrent genomic deletions on 7p12 in the IKZF1 gene in a large cohort of BCR-ABL1-positive acute lymphoblastic leukemia patients: on behalf of Gruppo Italiano Malattie Ematologiche dell'Adulto Acute Leukemia Working Party (GIMEMA AL WP). Blood *114*, 2159–2167.

Kotecha, N., Flores, N.J., Irish, J.M., Simonds, E.F., Sakai, D.S., Archambeault, S., Diaz-Flores, E., Coram, M., Shannon, K.M., Nolan, G.P., and Loh, M.L. (2008). Single-cell profiling identifies aberrant STAT5 activation in myeloid malignancies with specific clinical and biologic correlates. Cancer Cell *14*, 335–343.

Kuiper, R.P., Schoenmakers, E.F., van Reijmersdal, S.V., Hehir-Kwa, J.Y., van Kessel, A.G., van Leeuwen, F.N., and Hoogerbrugge, P.M. (2007). High-resolution genomic profiling of childhood ALL reveals novel recurrent genetic lesions affecting pathways involved in lymphocyte differentiation and cell cycle progression. Leukemia *21*, 1258–1266.

Marth, G. (2010) MOSAIK assembler. Available from http://bioinformatics.bc.edu/marthlab/Mosaik.

Martinelli, G., Iacobucci, I., Storlazzi, C.T., Vignetti, M., Paoloni, F., Cilloni, D., Soverini, S., Vitale, A., Chiaretti, S., Cimino, G., et al. (2009). IKZF1 (Ikaros) deletions in BCR-ABL1-positive acute lymphoblastic leukemia are associated with short disease-free survival and high rate of cumulative incidence of relapse: a GIMEMA AL WP report. J. Clin. Oncol. *27*, 5202–5207.

McPherson, A., Hormozdiari, F., Zayed, A., Giuliany, R., Ha, G., Sun, M.G., Griffith, M., Heravi Moussavi, A., Senz, J., Melnyk, N., et al. (2011). deFuse: an algorithm for gene fusion discovery in tumor RNA-Seq data. PLoS Comput. Biol. *7*, e1001138.

Melo, J.V. (1996). The diversity of BCR-ABL fusion proteins and their relationship to leukemia phenotype. Blood *88*, 2375–2384.

Mizuki, M., Fenski, R., Halfter, H., Matsumura, I., Schmidt, R., Müller, C., Grüning, W., Kratz-Albers, K., Serve, S., Steur, C., et al. (2000). Flt3 mutations from patients with acute myeloid leukemia induce transformation of 32D cells mediated by the Ras and STAT5 pathways. Blood *96*, 3907–3914.

Morin, R.D., Johnson, N.A., Severson, T.M., Mungall, A.J., An, J., Goya, R., Paul, J.E., Boyle, M., Woolcock, B.W., Kuchenbauer, F., et al. (2010). Somatic mutations altering EZH2 (Tyr641) in follicular and diffuse large B-cell lymphomas of germinal-center origin. Nat. Genet. *42*, 181–185.

Mullighan, C.G., Goorha, S., Radtke, I., Miller, C.B., Coustan-Smith, E., Dalton, J.D., Girtman, K., Mathew, S., Ma, J., Pounds, S.B., et al. (2007). Genome-wide analysis of genetic alterations in acute lymphoblastic leukaemia. Nature *446*, 758–764.

Mullighan, C.G., Miller, C.B., Radtke, I., Phillips, L.A., Dalton, J., Ma, J., White, D., Hughes, T.P., Le Beau, M.M., Pui, C.H., et al. (2008). BCR-ABL1 lymphoblastic leukaemia is characterized by the deletion of Ikaros. Nature *453*, 110–114.

Mullighan, C.G., Collins-Underwood, J.R., Phillips, L.A., Loudin, M.G., Liu, W., Zhang, J., Ma, J., Coustan-Smith, E., Harvey, R.C., Willman, C.L., et al. (2009a). Rearrangement of CRLF2 in B-progenitor- and Down syndrome-associated acute lymphoblastic leukemia. Nat. Genet. *41*, 1243–1246.

Mullighan, C.G., Su, X., Zhang, J., Radtke, I., Phillips, L.A., Miller, C.B., Ma, J., Liu, W., Cheng, C., Schulman, B.A., et al; Children's Oncology Group. (2009b). Deletion of IKZF1 and prognosis in acute lymphoblastic leukemia. N. Engl. J. Med. *360*, 470–480.

Mullighan, C.G., Zhang, J., Harvey, R.C., Collins-Underwood, J.R., Schulman, B.A., Phillips, L.A., Tasian, S.K., Loh, M.L., Su, X., Liu, W., et al. (2009c). JAK mutations in high-risk childhood acute lymphoblastic leukemia. Proc. Natl. Acad. Sci. USA *106*, 9414–9418.

Nebral, K., Denk, D., Attarbaschi, A., König, M., Mann, G., Haas, O.A., and Strehl, S. (2009). Incidence and diversity of PAX5 fusion genes in childhood acute lymphoblastic leukemia. Leukemia *23*, 134–143.

Oh, S.T., Simonds, E.F., Jones, C., Hale, M.B., Goltsev, Y., Gibbs, K.D., Jr., Merker, J.D., Zehnder, J.L., Nolan, G.P., and Gotlib, J. (2010). Novel mutations in the inhibitory adaptor protein LNK drive JAK-STAT signaling in patients with myeloproliferative neoplasms. Blood *116*, 988–992.

Paietta, E., Ferrando, A.A., Neuberg, D., Bennett, J.M., Racevskis, J., Lazarus, H., Dewald, G., Rowe, J.M., Wiernik, P.H., Tallman, M.S., and Look, A.T. (2004). Activating FLT3 mutations in CD117/KIT(+) T-cell acute lymphoblastic leukemias. Blood *104*, 558–560.

Pardanani, A., Lasho, T., Finke, C., Oh, S.T., Gotlib, J., and Tefferi, A. (2010). LNK mutation studies in blast-phase myeloproliferative neoplasms, and in chronic-phase disease with TET2, IDH, JAK2 or MPL mutations. Leukemia *24*, 1713–1718.

Pui, C.H., Robison, L.L., and Look, A.T. (2008). Acute lymphoblastic leukaemia. Lancet *371*, 1030–1043.

Pui, C.H., Campana, D., Pei, D., Bowman, W.P., Sandlund, J.T., Kaste, S.C., Ribeiro, R.C., Rubnitz, J.E., Raimondi, S.C., Onciu, M., et al. (2009). Treating childhood acute lymphoblastic leukemia without cranial irradiation. N. Engl. J. Med. *360*, 2730–2741.

Quintás-Cardama, A., Tong, W., Manshouri, T., Vega, F., Lennon, P.A., Cools, J., Gilliland, D.G., Lee, F., Cortes, J., Kantarjian, H., and Garcia-Manero, G. (2008). Activity of tyrosine kinase inhibitors against human NUP214-ABL1-positive T cell malignancies. Leukemia *22*, 1117–1124.

Robertson, G., Schein, J., Chiu, R., Corbett, R., Field, M., Jackman, S.D., Mungall, K., Lee, S., Okada, H.M., Qian, J.Q., et al. (2010). De novo assembly and analysis of RNA-seq data. Nat. Methods *7*, 909–912.

Röttgers, S., Gombert, M., Teigler-Schlegel, A., Busch, K., Gamerdinger, U., Slany, R., Harbott, J., and Borkhardt, A. (2010). ALK fusion genes in children with atypical myeloproliferative leukemia. Leukemia *24*, 1197–1200.

Russell, L.J., Capasso, M., Vater, I., Akasaka, T., Bernard, O.A., Calasanz, M.J., Chandrasekaran, T., Chapiro, E., Gesk, S., Griffiths, M., et al. (2009a). Deregulated expression of cytokine receptor gene, CRLF2, is involved in lymphoid transformation in B-cell precursor acute lymphoblastic leukemia. Blood *114*, 2688–2698.

Russell, L.J., De Castro, D.G., Griffiths, M., Telford, N., Bernard, O., Panzer-Grümayer, R., Heidenreich, O., Moorman, A.V., and Harrison, C.J. (2009b). A novel translocation, t(14;19)(q32;p13), involving IGH@ and the cytokine receptor for erythropoietin. Leukemia *23*, 614–617.

Schnittger, S., Schoch, C., Dugas, M., Kern, W., Staib, P., Wuchter, C., Löffler, H., Sauerland, C.M., Serve, H., Büchner, T., et al. (2002). Analysis of FLT3 length mutations in 1003 patients with acute myeloid leukemia: correlation to cytogenetics, FAB subtype, and prognosis in the AMLCG study and usefulness as a marker for the detection of minimal residual disease. Blood *100*, 59–66.

Schultz, K.R., Bowman, W.P., Aledo, A., Slayton, W.B., Sather, H., Devidas, M., Wang, C., Davies, S.M., Gaynon, P.S., Trigg, M., et al. (2009). Improved early event-free survival with imatinib in Philadelphia chromosome-positive acute lymphoblastic leukemia: a children's oncology group study. J. Clin. Oncol. *27*, 5175–5181.

Shah, S.P., Morin, R.D., Khattra, J., Prentice, L., Pugh, T., Burleigh, A., Delaney, A., Gelmon, K., Guliany, R., Senz, J., et al. (2009). Mutational evolution in a lobular breast tumour profiled at single nucleotide resolution. Nature *461*, 809–813.

Shochat, C., Tal, N., Bandapalli, O.R., Palmi, C., Ganmore, I., te Kronnie, G., Cario, G., Cazzaniga, G., Kulozik, A.E., Stanulla, M., et al. (2011). Gain-of-function mutations in interleukin-7 receptor-α (IL7R) in childhood acute lymphoblastic leukemias. J. Exp. Med. *208*, 901–908.

Smyth, G.K. (2004). Linear models and empirical bayes methods for assessing differential expression in microarray experiments. Stat. Appl. Genet. Mol. Biol., *2004*, 3:Article3.

Tasian, S.K., Doral, M.Y., Borowitz, M.J., Wood, B.L., Chen, I.-M., Harvey, R.C., Gastier-Foster, J.M., Willman, C.L., Hunger, S.P., Mullighan, C.G., and Loh, M.L. (2012). Aberrant STAT5 and PI3K/mTOR pathway signaling occurs in human CRLF2-rearranged B-precursor acute lymphoblastic leukemia. Blood. 10.1182/blood-2011-12-389932.

Teachey, D.T., Obzut, D.A., Cooperman, J., Fang, J., Carroll, M., Choi, J.K., Houghton, P.J., Brown, V.I., and Grupp, S.A. (2006). The mTOR inhibitor CCI-779 induces apoptosis and inhibits growth in preclinical models of primary adult human ALL. Blood *107*, 1149–1155.

Tibshirani, R., Hastie, T., Narasimhan, B., and Chu, G. (2002). Diagnosis of multiple cancer types by shrunken centroids of gene expression. Proc. Natl. Acad. Sci. USA *99*, 6567–6572.

Tong, W., Zhang, J., and Lodish, H.F. (2005). Lnk inhibits erythropoiesis and Epo-dependent JAK2 activation and downstream signaling pathways. Blood *105*, 4604–4612.

Wang, J., Mullighan, C.G., Easton, J., Roberts, S., Heatley, S.L., Ma, J., Rusch, M.C., Chen, K., Harris, C.C., Ding, L., et al. (2011). CREST maps somatic structural variation in cancer genomes with base-pair resolution. Nat. Methods *8*, 652–654.

Williams, R.T., Roussel, M.F., and Sherr, C.J. (2006). Arf gene loss enhances oncogenicity and limits imatinib response in mouse models of Bcr-Abl-induced acute lymphoblastic leukemia. Proc. Natl. Acad. Sci. USA *103*, 6688–6693.

Yoda, A., Yoda, Y., Chiaretti, S., Bar-Natan, M., Mani, K., Rodig, S.J., West, N., Xiao, Y., Brown, J.R., Mitsiades, C., et al. (2010). Functional screening identifies CRLF2 in precursor B-cell acute lymphoblastic leukemia. Proc. Natl. Acad. Sci. USA *107*, 252–257.

Zenatti, P.P., Ribeiro, D., Li, W., Zuurbier, L., Silva, M.C., Paganin, M., Tritapoe, J., Hixon, J.A., Silveira, A.B., Cardoso, B.A., et al. (2011). Oncogenic IL7R gain-of-function mutations in childhood T-cell acute lymphoblastic leukemia. Nat. Genet. *43*, 932–939.

Zhang, J., Mullighan, C.G., Harvey, R.C., Wu, G., Chen, X., Edmonson, M., Buetow, K.H., Carroll, W.L., Chen, I.M., Devidas, M., et al. (2011). Key pathways are frequently mutated in high-risk childhood acute lymphoblastic leukemia: a report from the Children's Oncology Group. Blood *118*, 3080–3087.

Zhang, J., Ding, L., Holmfeldt, L., Wu, G., Heatley, S.L., Payne-Turner, D., Easton, J., Chen, X., Wang, J., Rusch, M., et al. (2012). The genetic basis of early T-cell precursor acute lymphoblastic leukaemia. Nature *481*, 157–163.

Cancer Cell
Article

Synergy between PI3K Signaling and MYC in Burkitt Lymphomagenesis

Sandrine Sander,[1,2] Dinis P. Calado,[1,2] Lakshmi Srinivasan,[1] Karl Köchert,[2] Baochun Zhang,[1] Maciej Rosolowski,[3] Scott J. Rodig,[4] Karlheinz Holzmann,[5] Stephan Stilgenbauer,[6] Reiner Siebert,[7] Lars Bullinger,[6] and Klaus Rajewsky[1,2,*]
[1]Program of Cellular and Molecular Medicine, Children's Hospital, and Immune Disease Institute, Harvard Medical School, Boston, MA 02115, USA
[2]Max Delbrück Center for Molecular Medicine, Berlin-Buch 13092, Germany
[3]Institute for Medical Informatics, Statistics and Epidemiology, University of Leipzig, Leipzig 04107, Germany
[4]Department of Pathology, Brigham and Women's Hospital, Boston, MA 02115, USA
[5]Microarray Core Facility, University of Ulm, Ulm 89081, Germany
[6]Department of Internal Medicine III, University Hospital of Ulm, Ulm 89081, Germany
[7]Institute of Human Genetics, University Hospital Schleswig-Holstein Campus Kiel/Christian-Albrechts University Kiel, Kiel 24105, Germany
*Correspondence: klaus.rajewsky@mdc-berlin.de
http://dx.doi.org/10.1016/j.ccr.2012.06.012

SUMMARY

In Burkitt lymphoma (BL), a germinal center B-cell-derived tumor, the pro-apoptotic properties of c-MYC must be counterbalanced. Predicting that survival signals would be delivered by phosphoinositide-3-kinase (PI3K), a major survival determinant in mature B cells, we indeed found that combining constitutive c-MYC expression and PI3K activity in germinal center B cells of the mouse led to BL-like tumors, which fully phenocopy human BL with regard to histology, surface and other markers, and gene expression profile. The tumors also accumulate tertiary mutational events, some of which are recurrent in the human disease. These results and our finding of recurrent PI3K pathway activation in human BL indicate that deregulated c-MYC and PI3K activity cooperate in BL pathogenesis.

INTRODUCTION

While c-MYC (MYC) deregulation is a hallmark of BL (Jaffe and Pittaluga, 2011), an aggressive germinal center (GC)-derived B cell lymphoma characterized by *immunoglobulin* (*IG*)-*MYC* translocations, cooperating transforming events in BL are still poorly understood, despite the existence of MYC-induced murine lymphoma models (Adams and Cory, 1985; Kovalchuk et al., 2000; Park et al., 2005). MYC expression promotes malignancies by inhibiting cell differentiation and inducing proliferation, but also makes the cells prone to apoptosis. Since unlike other lymphoma entities BL typically do not exhibit constitutive activity of the pro-survival factor NF-κB (Dave et al., 2006; Klapproth et al., 2009), we considered a possible involvement of the PI3K pathway when we had identified PI3K signaling as the B cell receptor (BCR)-mediated survival signal in mature B cells (Srinivasan et al., 2009): MYC deregulation in BL is due to translocation of the *MYC* gene into one of the immunoglobulin loci of the cell, but exclusively non-productively rearranged immunoglobulin loci are affected, indicating that the cells are selected for BCR expression (Küppers et al., 1999). There is also evidence for a role of BCR signaling in MYC-driven lymphomagenesis from a transgenic mouse model in which the B cells express a BCR with specificity for a concomitantly expressed transgenic protein antigen (Refaeli et al., 2008). Although the polyclonal B cell proliferation seen in this model was in clear contrast to human BL and it remained unclear from which B cell differentiation stage it originated, we felt encouraged by the available evidence to try to better model BL pathogenesis.

RESULTS

Impact of MYC Overexpression and Constitutive PI3K Activation on the GC Reaction

To determine the impact of MYC expression and PI3K pathway activation on GC B cells and lymphomagenesis, we generated

Significance

We describe a mouse model of a human lymphoma through targeting expression of an oncogene known to be involved in tumor pathogenesis together with the activation of a suspected pathogenic signaling pathway into the presumed cell of origin. The resulting tumors faithfully model their human counterparts and accumulate additional genetic alterations, with clear perspectives for an assessment of their clinical relevance. Our data establish a framework of Burkitt lymphoma pathogenesis by identifying PI3K pathway activation as a key element for the malignant transformation of c-MYC-expressing germinal center B cells and highlight this pathway as a potential therapeutic target.

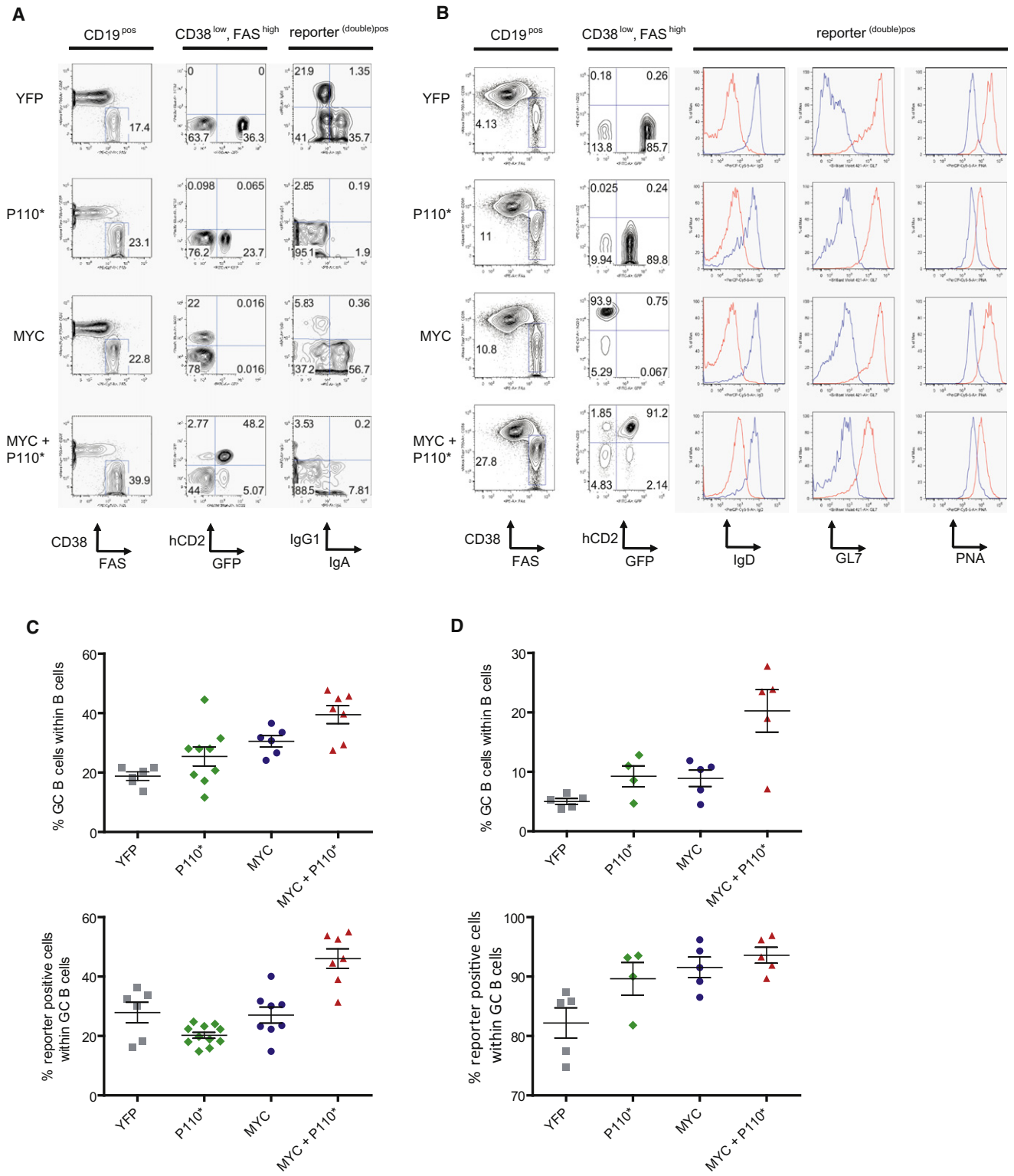

Figure 1. MYC and P110* Co-Expression Results in Increased GC B Cell Formation

(A) Representative FACS analysis of PP isolated from *Cγ1-cre, R26Stop^{FL}eYFP* (YFP); *Cγ1-cre, R26Stop^{FL}P110**(P110*); *Cγ1-cre, R26Stop^{FL}MYC* (MYC) and *Cγ1-cre, R26Stop^{FL}MYC, R26Stop^{FL}P110** (MYC+P110*) animals. The sequential gating strategy is shown on top of each column.

(B) Representative FACS analysis in *Rag2cg^{KO}* animals reconstituted with BM of the various genotypes and immunized with SRBC 10 days before analysis. The gating was performed according to (A). The histograms show expression of classical GC B cell markers in reporter (double) positive cells (red) and non-GC B cells (blue).

mice expressing MYC and a constitutively active form of PI3K, here referred to as P110* (Srinivasan et al., 2009), specifically in B cells undergoing the GC reaction (*Cγ1-cre,R26Stop^{FL}MYC,R26Stop^{FL}P110**; Figure S1 available online). Ten days after sheep red blood cell (SRBC) immunization, Peyer's patches (PP) and spleens of transgenic mice were analyzed for reporter positive cells and their expression of GC B cell markers (Figures 1A and 1B). Transgenic expression of MYC and P110* was compatible with the formation of GCs. An increased proportion of GC B cells (CD38^{low}, FAS^{high}) in the PP and the spleen of MYC and P110* co-expressing animals was detectable, accompanied by an increased proportion of reporter double-positive cells in comparison to the controls (Figures 1C and 1D). In addition to CD38 and FAS expression, MYC and P110* co-expressing GC B cells expressed less surface IgD than non-GC cells, at levels comparable to the controls (Figure 1B). The GC markers GL7 and PNA were also detectable on these cells although at lower levels than on GC B cells derived from *Cγ1-cre,R26Stop^{FL}eYFP* animals (Figure 1B). Class switch recombination (CSR) was impaired in MYC and P110* co-expressing cells (Figure 1A), presumably because of PI3K activation (Omori et al., 2006).

MYC and P110* Cooperate in Tumorigenesis

In order to obtain meaningful numbers of experimental animals in a timely fashion, bone marrow (BM) of individual triple transgenic animals (*Cγ1-cre,R26Stop^{FL}MYC,R26Stop^{FL}P110**) and the corresponding controls was transferred to *Rag2cg^{KO}* animals (Figure 2A). These animals lack a lymphatic system due to deficiency of the recombinase Rag2 and the cytokine receptor common subunit gamma (DiSanto et al., 1995; Shinkai et al., 1992). After BM transfer, the recipient mice generate lymphocytes that are genotypically identical to the donor BM cells. Blood analyses performed before and after a single boost of GC formation by SRBC demonstrated a steady increase of the percentage of lymphocytes co-expressing MYC and P110* over time, more so than in the case of lymphocytes expressing either transgene alone (Figure 2B). This correlated with lymphoma development and a reduced life span of the animals reconstituted with triple transgenic BM (median survival 227 days) (Figure 2C). In reconstituted animals expressing either MYC or P110* alone, tumor development was not detected within the period of observation.

Macroscopically the animals reconstituted with triple transgenic BM displayed large tumors originating from the PP of the small intestine (12/21 tumors) or other lymphoid organs (spleen, lymph nodes) and infiltrating the liver and other nonlymphoid organs (e.g., kidney, lung) at an advanced stage (Figure 2D; Table S1). Histologic analysis revealed a characteristic BL morphology defined by the monotonous infiltration with medium-sized cells carrying uniform nuclei, prominent basophilic nucleoli, and frequent mitotic figures (Figure 2E). Like in human BL, the tumors displayed the typical "starry sky" pattern due to invading tissue macrophages that clear apoptotic tumor cells. In accordance with the diagnostic criteria of human BL, Ki67 staining demonstrated a proliferative index of nearly 100% in the tumors (Figure 2F).

The analysis of immunoglobulin heavy chain (*IgH*) gene rearrangements by Southern blot in the tumors and affected organs showed that the tumors were monoclonal (Figure 2G). The finding of distinct, unique *VDJ* rearrangements in B cell tumors of different recipient animals transferred with BM from a single donor argues against a transfer of tumor cells from the donor (Figure 2G). In three tumors derived from different recipient animals reconstituted with the same donor BM sequencing of the rearranged *IgH* variable (V) region genes confirmed unique *VDJ* rearrangements in the tumors (data not shown).

MYC and P110* Co-Expressing Tumors Originate from GC B Cells

In accordance with our intention to generate a GC-derived MYC and PI3K induced tumor model, the tumor cells expressed both transgenes (GFP^{pos}, hCD2^{pos}) as well as mature GC B cell markers (B220^{pos}, CD19^{pos}, AA4.1^{low}, CD38^{low}, FAS^{high}, CD138^{neg}, CD23^{neg}, CD43^{neg}, CD5^{neg}; Figure 3A; Figure S2A). Similar to human BL, the tumors arose from non-switched GC B cells expressing surface IgM (Figure 3A). In addition, immunohistochemical analyses revealed expression of the GC B cell markers BCL6 and GL7 in the mouse tumors (Figures 3B and 3C) while PNA binding was not detectable in the tumors (Figure S2B). The latter might reflect its impaired binding on GC B cells upon P110* expression (see Figure 1B). The lack of IRF4/MUM1 expression, denoting B cell maturation toward plasma cells during late GC B cell differentiation, might indicate that the tumors arise from B cells at an early phase of the GC reaction (Figure 3D).

The finding of extensive ongoing somatic hypermutation (SHM) in the rearranged *IgH-V* region genes of the tumor cells (mean mutation frequency 508×10^{-4}) confirmed the GC cell origin of the tumors (Figures 4A and 4B; Figure S3A). In agreement with this observation the tumors expressed cytidine deaminase AID at comparable transcript levels as GC and in vitro stimulated B cells (Figure 4C).

The GC cell origin of the B cell tumors was also evident from gene expression profiling (GEP) data of purified MYC and P110* co-expressing tumor cells which we compared with published GEP data sets of various B cell subpopulations and mouse lymphoma models. Our tumors expressed a prominent GC B cell signature (Figures 4D and S3B), which was less pronounced in murine lymphomas resulting from transgenic expression of the GC B cell-specific transcriptional repressor BCL6 either alone or in combination with MYC (Green et al., 2011).

The Mouse Tumors Resemble Human BL

GC markers are typically associated with human BL, but are shared by a major subgroup of diffuse large cell B cell lymphomas (Alizadeh et al., 2000). We therefore performed a supervised comparison of global gene expression patterns

(C) Mean percentage (±SEM) of GC B cells (CD38^{low}, FAS^{high}) and reporter (double) positive cells within PP of mice analyzed according to (A). At least six animals per genotype were analyzed.
(D) Mean percentage (±SEM) of GC B cells (CD38^{low}, FAS^{high}) and reporter (double) positive cells within spleens of mice analyzed according to (B). At least 4 BM reconstituted animals per genotype were analyzed.
See also Figure S1.

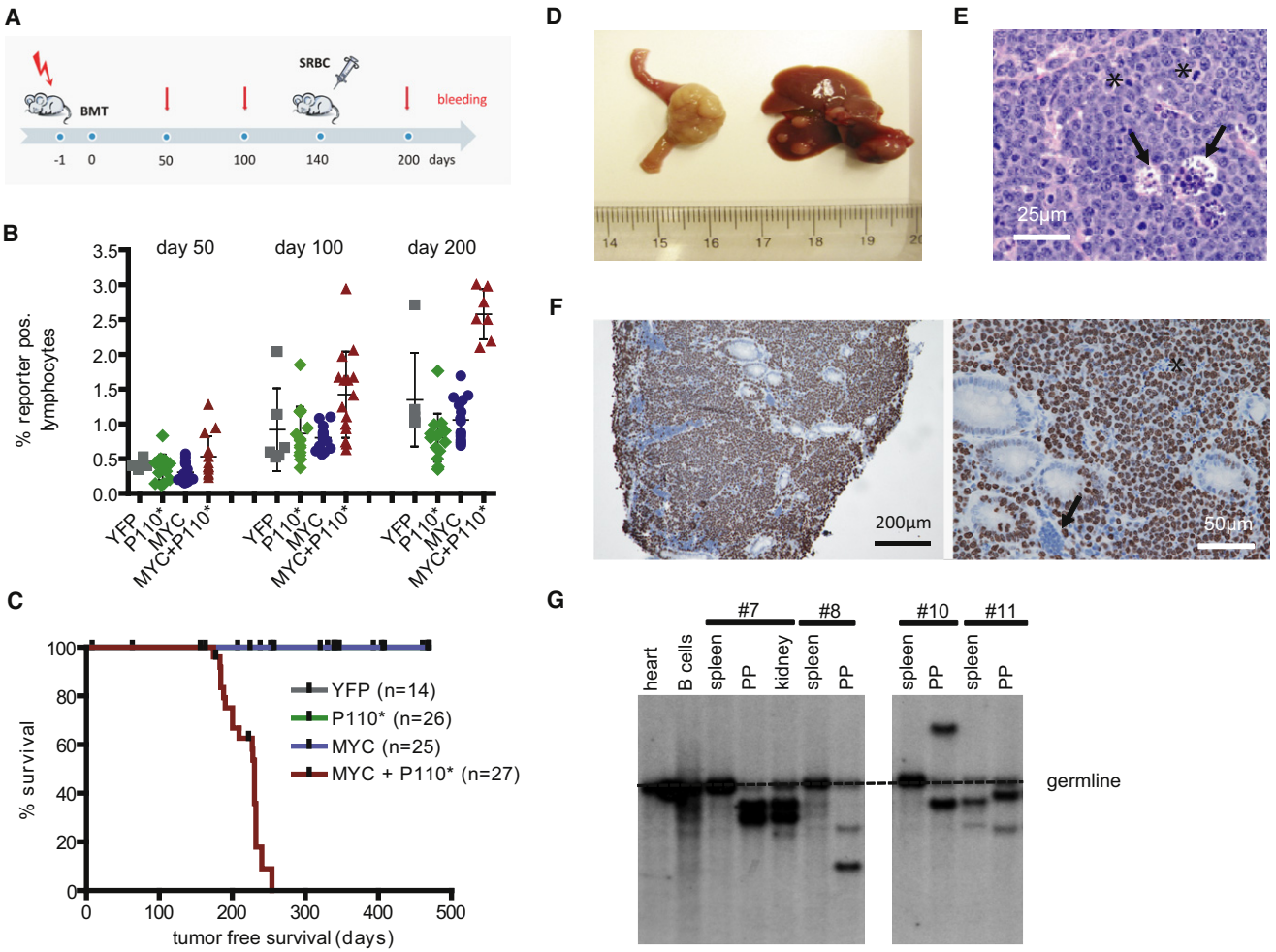

Figure 2. MYC and PI3K Pathway Activation Cooperate in Tumorigenesis

(A) Experimental protocol. Sublethally irradiated (day −1) *Rag2cg*^{KO} mice were reconstituted with donor BM (from *Cγ1-cre, R26Stop*^{FL}*eYFP; Cγ1-cre, R26Stop*^{FL}*P110*; Cγ1-cre, R26Stop*^{FL}*MYC;* or *Cγ1-cre, R26Stop*^{FL}*MYC, R26Stop*^{FL}*P110** animals) on day 0. Per genotype three individual BM donors were used. Transgene expression was enforced by a single SRBC immunization at day 140. Blood analyses were performed at days 50, 100, and 200 after BM transfer.

(B) Blood analysis of *Rag2cg*^{KO} animals reconstituted with BM of the indicated genotypes. FACS analyses were performed at days 50, 100, and 200 after BM transfer. Mean percentage (±SEM) of reporter (double) positive lymphocytes is shown.

(C) Tumor-free survival of reconstituted *Rag2cg*^{KO} animals. The total number of BM recipients is shown in parentheses. The ticks indicate non-tumor-related deaths.

(D) 12/21 tumors originated from the PP in the small intestine of MYC and P110* co-expressing animals (left). In 17/21 animals tumors disseminated to the liver (right).

(E) Representative HE staining in tumor no. 7. The asterisks mark mitotic figures within dividing cells. The arrowheads point to histiocytes clearing apoptotic cells. In total seven tumors were analyzed.

(F) Representative immunohistochemical staining for Ki67 in tumor no. 7. Interspersed nonmalignant (arrowhead) and dead cells (asterisk) are Ki67 negative. In total seven tumors were analyzed.

(G) Southern blot analysis for *IgH* gene rearrangements in PP derived tumors and potentially infiltrated organs using a JH4 probe. Monoclonal B cell expansion was seen in the PP, but not in the spleens of diseased animals (with exception of animal no. 11 showing expansion of an additional B cell clone in the spleen). See also Table S1.

established from MYC and P110* co-expressing tumors and BCL6 driven lymphomas, a mouse model recapitulating the pathogenesis of human DLBCL (Cattoretti et al., 2005), and identified a total of 2407 genes that were differentially expressed between these tumor entities (Figure 5A). We then looked among those genes for two sets of BL signature genes that had been identified in the human as differentially expressed between BL and DLBCL (Dave et al., 2006; Hummel et al., 2006). Comparing the expression of these BL signature genes between the two mouse lymphoma models, a clear positive association was detected between the MYC and P110* co-expressing mouse tumors and human BL (Figure 5B).

To further distinguish our BL-like tumors from DLBCL we determined BL-typical proteins by immunohistochemistry, western blot, and immunofluorescence (Figures 5C–5E). Typically, human BL show elevated MYC levels due to translocations

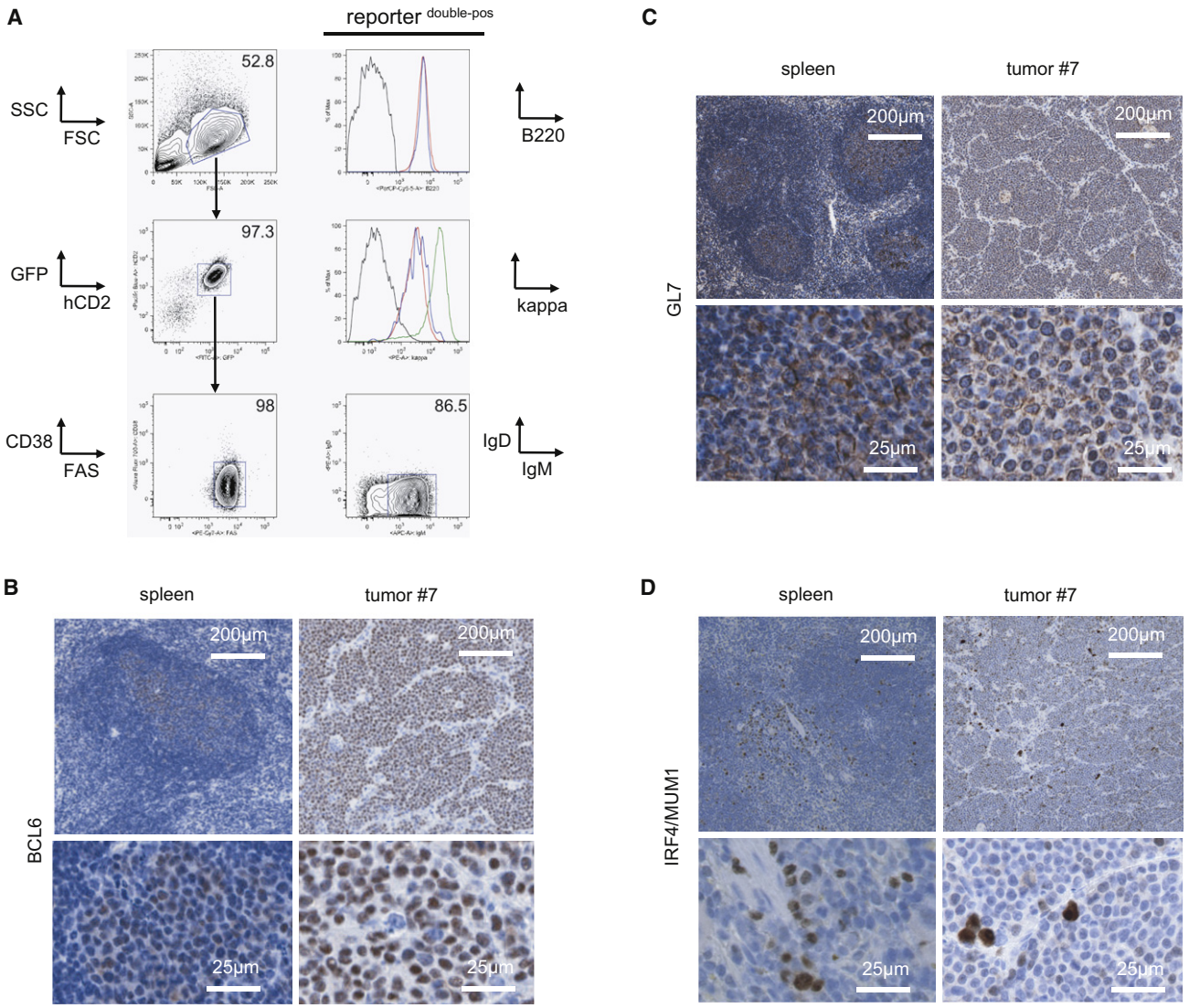

Figure 3. Lymphomas Arising upon MYC and PI3K Activation Express GC B-Cell-Specific Markers

(A) Representative FACS analysis of GC B cell markers (B220, CD38, FAS, sIgD) and sIgM expression on tumor cells (defined as GFP^{pos} and $hCD2^{pos}$ cells). The sequential gating strategy is indicated by arrows. Upper histogram: B220 expression on tumor cells (red) and normal splenic B cells (blue) in comparison to non-B cells (black). Lower histogram: Kappa light chain expression on tumor cells (red) and normal GC B cells (blue) in comparison to non-B cells (black) and normal follicular B cells (green).

(B–D) Representative immunohistochemical stainings for BCL6 (B), GL7 (C) and IRF4/MUM1 (D) in tumor no. 7 and control spleen (derived from a *Cγ1-cre, R26Stop^{FL}eYFP* animal 10 days after SRBC immunization). Per staining seven tumors were analyzed.

See also Figure S2.

and mutations of the *MYC* gene. Similarly, *MYC* transgene expression in our tumor model resulted in abundant MYC protein as it is seen in primary BL samples and BL cell lines (Figures 5C and 5D). Besides MYC expression, histologic features and the high proliferation rate (Ki67 >95%), human BL cells as well as the mouse tumor cells are positive for BCL6 (Figure 3B) and lack BCL2 expression (Figure 5E).

The MYC and P110* induced tumors did not only express BL characteristic markers and exhibit a GEP signature resembling that of human BL, but also displayed genomic aberrations reminiscent of aberrations previously reported in human BL (Mitelman et al., 2012). Overall SNP array analysis revealed a simple karyotype of the mouse tumors: beside the B cell specific rearrangements of the Ig loci the tumors displayed 1.8 aberrations per case (Figure 6A). The most frequent (4/6 tumors) DNA copy number alteration was a gain of chromosome 6, which comprises genomic regions gained in human BL such as 7q21.1qter and 12p13 (Figure 6B) (Boerma et al., 2009; Scholtysik et al., 2012). Exome sequencing of five murine MYC and P110* co-expressing lymphomas and the respective germline DNA revealed additional candidate oncogenic events (Table S2). In total, we observed on average 103 missense

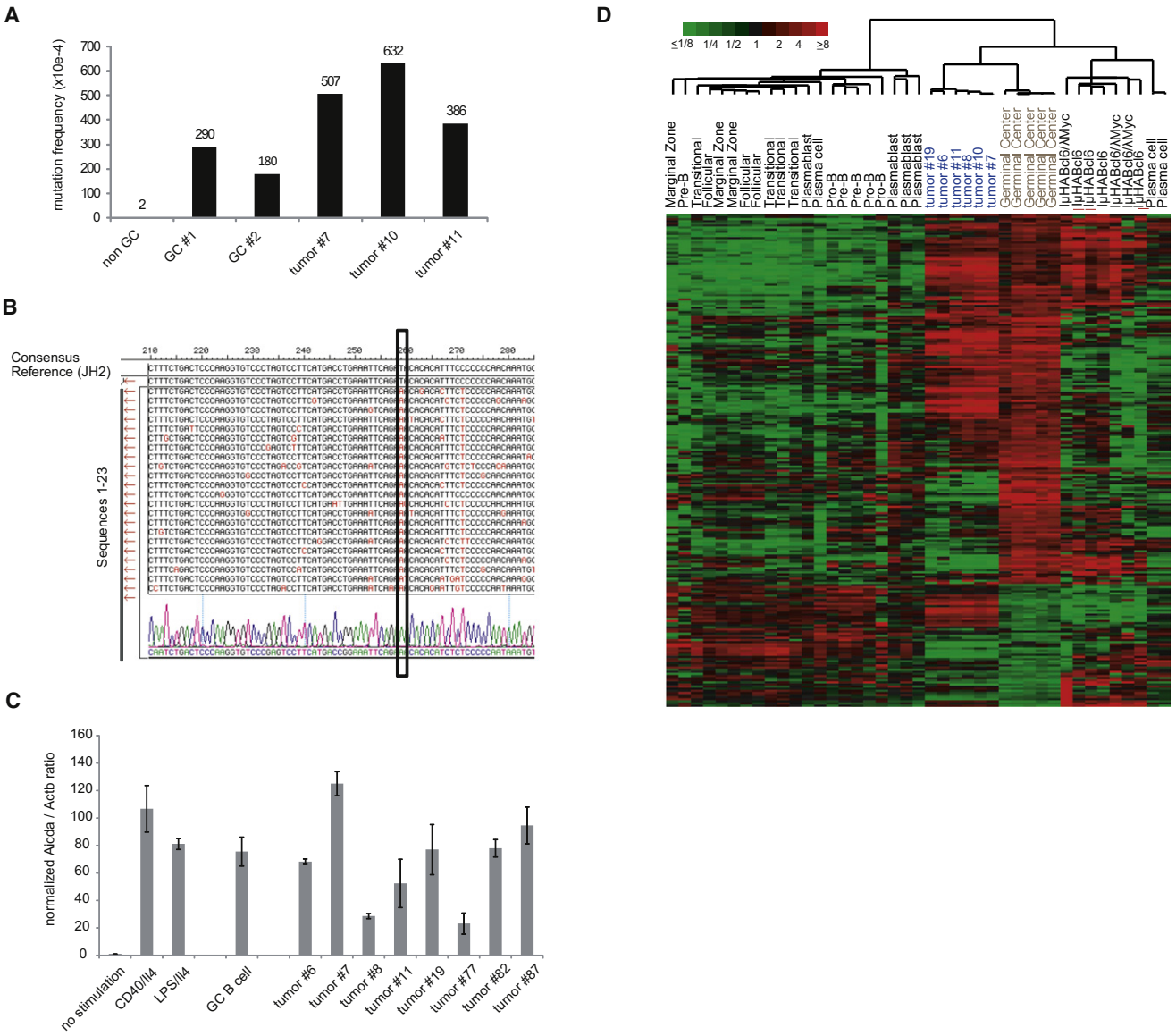

Figure 4. MYC and P110* Co-Expressing Tumors Show Ongoing SHM and Express GC B-Cell-Specific Genes

(A) Mutation frequency in rearranged *IgH-V* region genes of non-GC B cells, GC B cells, and MYC+P110* co-expressing tumors (n = 3).

(B) SHM analysis in tumor no. 7. The rearranged *IgH-V* region genes of individual tumor cells were aligned to the JH2 reference sequence (n = 23). Mutations are labeled in red. The box marks a mutation shared by all sequences of this particular tumor.

(C) *Aicda* expression in stimulated B cells, GC B cells and MYC+P110* co-expressing tumors (n = 8) was analyzed by qRT-PCR. The ratio *Aicda*/*Actb* in non-stimulated cells was arbitrary defined as 1 and the values of the other samples were normalized to it. The mean expression from triplicate measurements (±SEM) was used for the calculations.

(D) Hierarchical cluster analysis based on relative transcript levels of 233 genes comprised in a GC B cell signature (Green et al., 2011) in normal B cell populations, MYC and P110* co-expressing tumor samples (n = 6) as well as other mouse lymphomas (*IμHABcl6* (n = 4) and *IμHABcl6*/*λMyc* (n = 3); mean-centered $\log_2$ gene expression ratios are depicted by color scale). The meta-analysis was based on GEP data from Green et al. (GEO26408) and own experiments (GEO35219). Additional information is provided in the Supplemental Experimental Procedures.

See also Figure S3.

and/or nonsense mutations per murine BL tumor (Figure 6C). Although AID expression was clearly detectable in the tumor cells at the mRNA level, the mutations rarely coincided with classical AID hotspots (WRCY or the inverse RGYW; Figure S4).

Some of these additional mutations have recently also been identified in a parallel analysis of a large collection of human BL in the laboratory of L. Staudt (Schmitz et al., 2012). An example is the heterozygous mutation of cyclin D3 (*Ccnd3*) at codon 283 (A1129G) encoding a threonine residue which regulates cyclin D3 stability through phosphorylation (Figure 6D; Casanovas et al., 2004). An essential role of cyclin D3 in the control of GC B cell proliferation was recently reported (Cato et al., 2011; Peled et al., 2010).

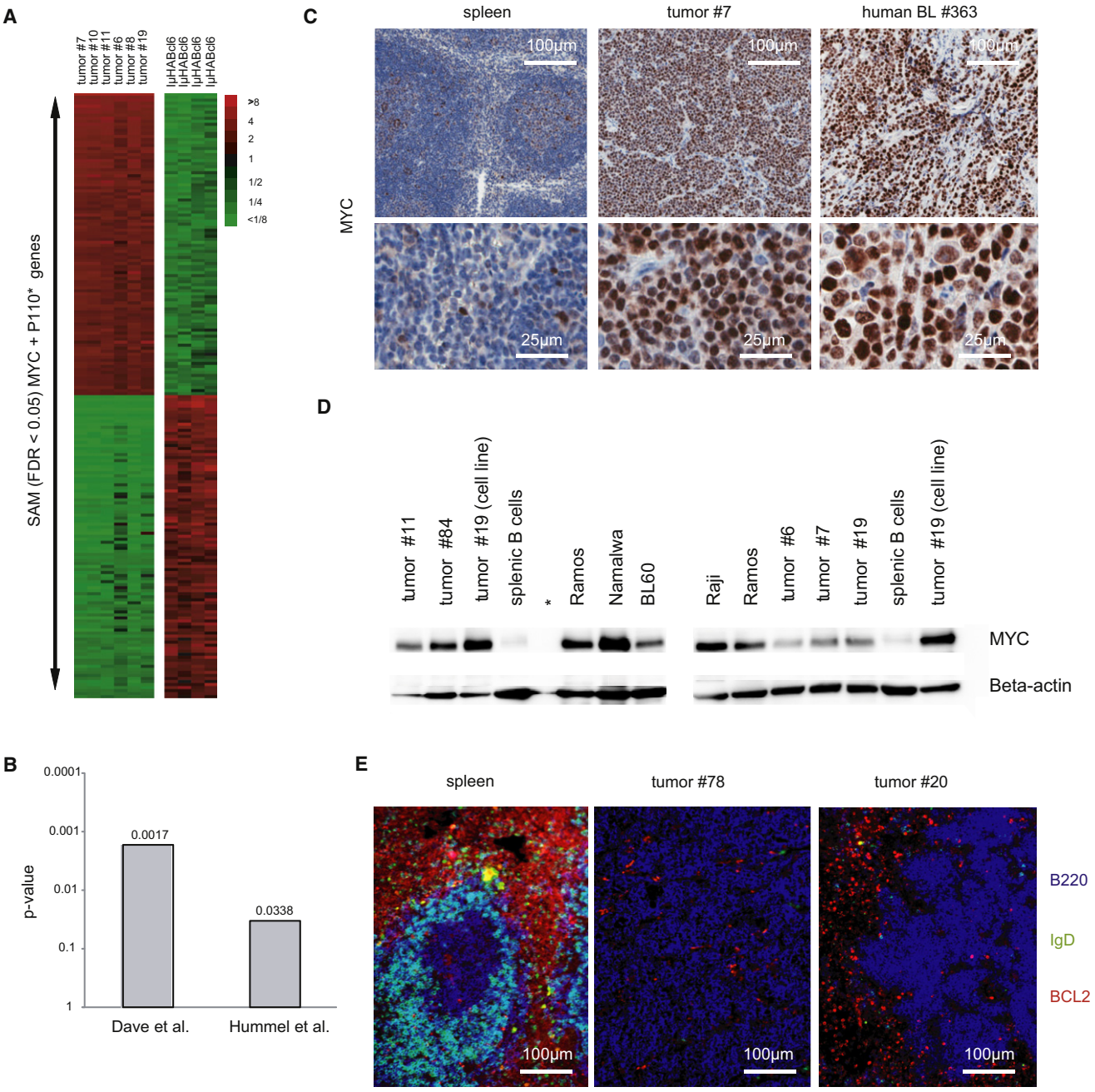

Figure 5. MYC and P110* Co-Expressing Tumors Resemble Human BL

(A) Heat map showing relative transcript levels of the top 100 up- and downregulated genes distinguishing MYC and P110* co-expressing tumors (n = 6) from *IμHABcl6* induced lymphomas (n = 4) as determined by SAM analysis (FDR < 0.05).

(B) p-values for the positive association of two human BL signatures (Dave et al., 2006; Hummel et al., 2006) with the MYC + P110* tumor signature as defined by SAM analysis.

(C) Representative immunohistochemical staining for MYC in tumor no. 7, primary human BL no. 363 and control spleen (derived from a *Cγ1-cre, R26Stop^{FL}eYFP* animal 10 days after SRBC immunization). In total seven mouse tumors and nine primary human BL were analyzed.

(D) Western blot analysis for MYC expression in five primary mouse tumors (tumor nos. 6, 7, 11, 19, and 84), one cell line derived from mouse tumor no. 19 (tumor no. 19 [cell line]), four human BL cell lines (BL60, Namalwa, Raji, Ramos), and splenic B cells. Beta-actin served as loading control. *Empty lane.

(E) Representative immunofluorescence analysis for BCL2 (red), B220 (blue), and IgD (green) in two tumors (tumor no. 78 and tumor no. 20) and control spleen (derived from a C57BL/6 animal 10 days after SRBC immunization).

To determine the incidence of *Ccnd3* mutations in a larger tumor cohort we sequenced the 3′ end of the gene in 10 additional MYC and P110* co-expressing mouse tumors and identified two additional *Ccnd3* mutations: a non-synonymous mutation at codon 239 (T997G) and a frameshift caused by a single base pair insertion (1087insC).

A

SNP analysis	IGH: del(12qF1)	additional aberrations
tumor #6	+	+6, del(11qA3.2)
tumor #7	+	+6, del(15qF3), del(11qA3.2)
tumor #8	+	+6, del(13qA2)
tumor #10	+	+6
tumor #11	+	+1, +7, del(11qA3.2)
tumor #19	+	-

B

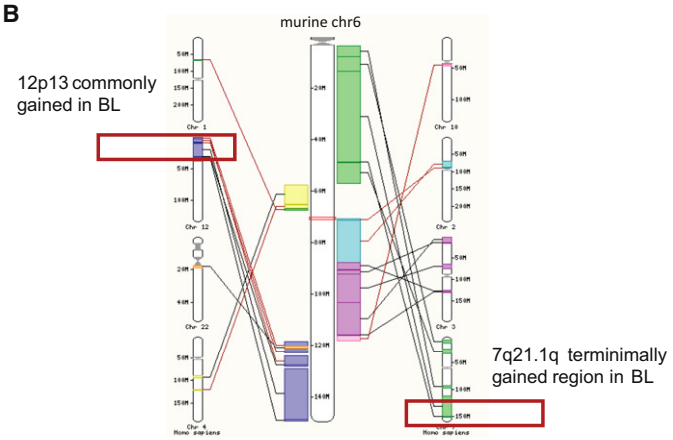

C

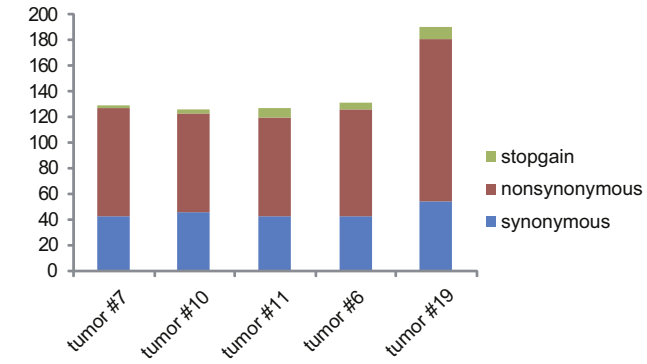

D

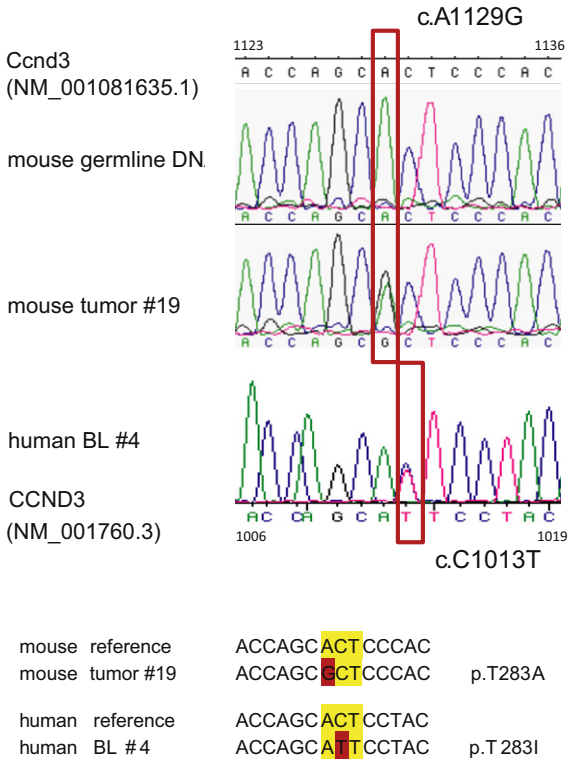

E

BL ID	gene	cDNA	protein	mutation type
BL #18	CCND3	942_943delTC	-	frameshift
BL #20	CCND3	954_963insCAGCCCAGCG	-	frameshift
BL #15	CCND3	970insC	-	frameshift
BL #2	CCND3	971delC	-	frameshift
BL #21	CCND3	991C>T	p.Q276X	nonsense
BL #10	CCND3	991C>T	p.Q276X	nonsense
BL #4	CCND3	1013C>T	p.T283I	missense

CCND3: cDNA reference: NM_001760.3, protein reference: NP_001751.1

Figure 6. Lymphomas Originating from MYC and P110* Co-Expressing GC B Cells Display Genetic Aberrations Commonly Found in Human BL

(A) Summary of genomic aberrations detected by SNP microarray analysis in 6 MYC and P110* co-expressing tumors.

(B) Schematic view of mouse chromosome 6 and its syntenic regions in human (based on Ensembl genome browser 65). Syntenic regions that have been described as gained in human BL (Boerma et al., 2009; Scholtysik et al., 2012) are marked in red.

(C) Number and classification of somatically acquired mutations based on exome sequencing in MYC and P110* co-expressing tumors (n = 5).

(D) Sanger sequencing of the *Ccnd3* mutation (A1129G) in mouse tumor no. 19 and the corresponding germline DNA (upper and middle panel). In human BL no. 4 the *CCND3* mutation (C1013T) affects the same codon as detected in the mouse tumor (lower panel).

(E) Summary of *CCND3* mutations detected by Sanger Sequencing in 29 primary BL samples. Positions that are also affected in the mouse tumors are marked in red.

See also Figure S4 and Table S2.

We also confirmed that cyclin D3 is recurrently mutated in human BL. Sequencing a 346-bp amplicon comprising part of *CCND3* exon 5 in 29 primary BL samples, we found mutations in seven of the cases (Figure 6E). Strikingly, the mutation at codon 283 (C1013T) and the frameshift mutations at positions 970 and 971 (970insC, 971 delC) affected the very same conserved codons mutated in the mouse tumors (Figures 6D and 6E).

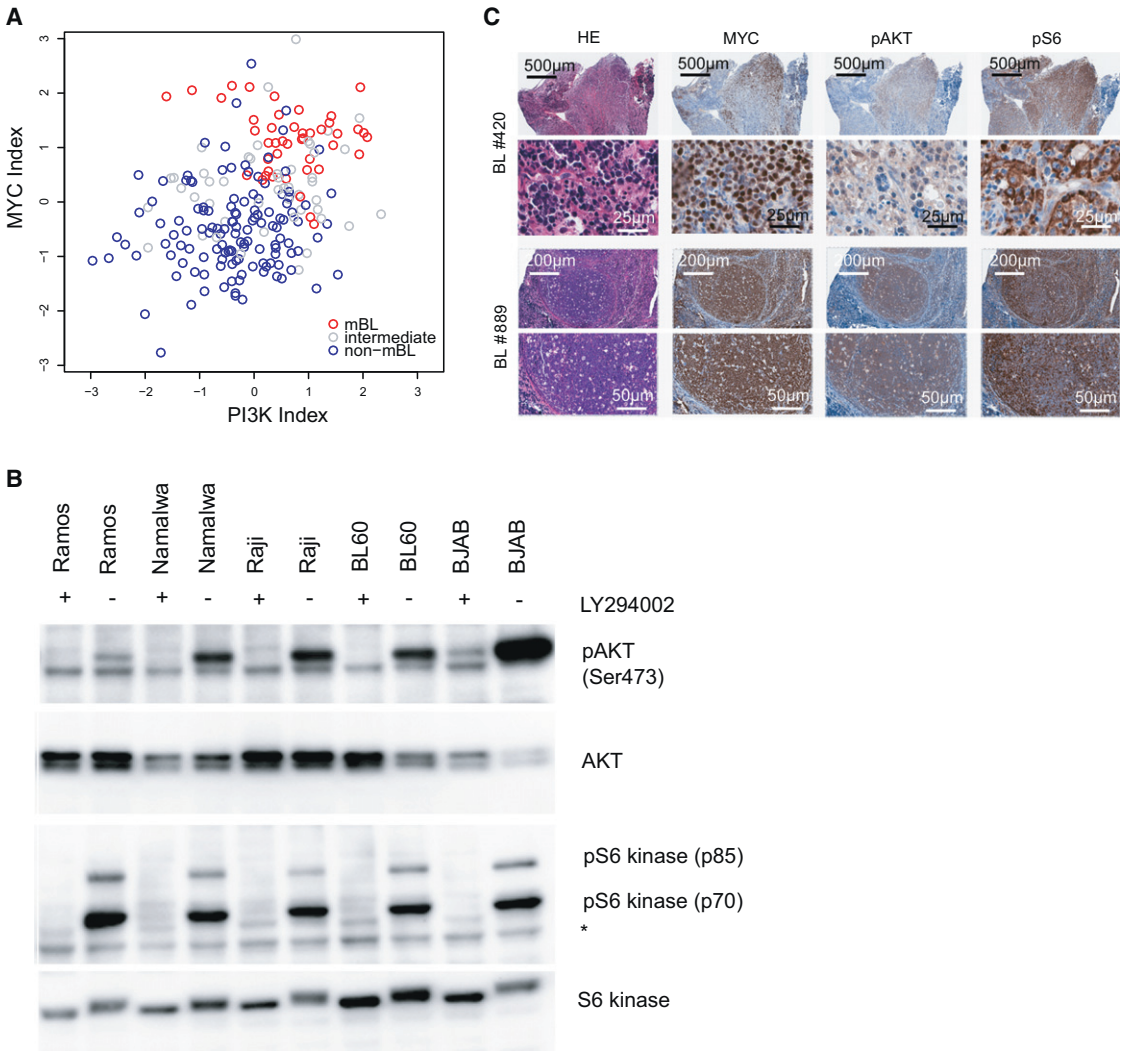

Figure 7. PI3K Pathway Activation in Human BL

(A) Scatter plot of the PI3K pathway activity (Gustafson et al., 2010) index against the MYC activation index (Bild et al., 2006) in human BL (GEO accession number GSE35219) (Hummel et al., 2006). Samples classified as molecular BL (mBL), intermediate, and non-mBL in the original study are shown as red, gray, and blue dots, respectively.

(B) Western blot analysis for Phospho-AKT (Ser473), AKT, phospho-S6 kinase (Thr389), and S6 kinase expression in five human BL cell lines (BJAB, BL60, Namalwa, Raji, Ramos). Cells were either treated with LY-294002 (+) or DMSO (–) 1 hr before protein extraction. *unspecific band.

(C) Representative immunohistochemical staining for MYC, phospho-AKT (Ser473), phospho-S6 (Ser235/236) in two primary human BL (human BL nos. 420 and 889). In total nine human BL were analyzed.

PI3K Pathway Activation in Human BL

The present mouse model predicts PI3K pathway activation in human BL. To directly address this issue, we performed a bioinformatic analysis of GEP data of primary BL in comparison to other human lymphoma entities (Hummel et al., 2006), which revealed accompanying MYC activation ($p < 2.2^{-16}$) and PI3K pathway activation ($p = 2.3^{-8}$) in human BL (Figure 7A). In addition, western blot analysis indicated activation of the PI3K pathway as determined by phosphorylation of AKT at serine 473 and p70S6 kinase at threonine 389 in 5 human BL cell lines (Figure 7B). Phosphorylation of both kinases was reversible upon treatment with the PI3K inhibitor LY-294002 (Figure 7B). Finally, immunohistochemistry of nine primary human BL revealed phosphorylation of AKT and S6 in six of nine analyzed patients (Figure 7C), suggesting PI3K pathway inhibition as a therapeutic option in human BL.

DISCUSSION

The present work describes the construction of a clinically relevant mouse model of a life-threatening human tumor by targeting constitutive expression of an oncogene known to be involved in tumor pathogenesis together with the activation of a suspected pathogenic signaling pathway specifically into the presumed cell of origin. The resulting tumors faithfully phenocopy their human counterparts, including strikingly similar gene expression

profiles, expression of BL-typical markers like BCL6 and MYC at the protein level and tertiary transforming events, as discussed further below. The similarities between human BL and the mouse tumors also include histologic peculiarities like starry sky appearance, high proliferative activity with homogeneous Ki67 staining, and the conspicuous absence of the pro-survival protein BCL2, whose expression is observed in many other classes of B cell lymphomas. Like in human BL, the tumors predominantly originated from the PP (which are enriched in the ileocecal region in human where BL frequently arises), exhibit ongoing somatic hypermutation, and their monoclonality indicates a multistep pathogenesis with MYC and PI3K activation as initiating events. Consistent with the latter notion and underlining the relevance of the mouse model for the human disease we find PI3K pathway activation in human BL lines and a major fraction of primary Burkitt tumors.

While MYC deregulation is an established hallmark of human BL and was the basis of previous mouse models (Adams and Cory, 1985; Kovalchuk et al., 2000; Park et al., 2005), PI3K signaling had not been recognized as a critical element of BL pathogenesis. Although PI3K signaling can support MYC activity by blocking its degradation (Kumar et al., 2006) and inducing the degradation of the MYC antagonist MAD1 (Zhu et al., 2008), and MYC-mediated miR17-92 induction can increase PI3K signaling by targeting *PTEN* (Mu et al., 2009; Olive et al., 2009), combined MYC and PI3K pathway activation does not necessarily lead to malignant transformation of the targeted cells (Radziszewska et al., 2009).

Our initial motivation to study PI3K pathway activation in concert with MYC deregulation in GC B cells came from our previous identification of PI3K signaling as the "tonic" survival signal in B cells downstream of the BCR, for whose expression normal B cells as well as BL cells are known to be positively selected (Küppers et al., 1999; Srinivasan et al., 2009). Indeed, the present results indicate significant PI3K pathway activation in human BL, contrasting with the absence in these tumors of survival signals through the NF-κB pathway (Dave et al., 2006). Consistent with these data, recurrent mutations promoting PI3K signaling have recently been identified in human BL (Schmitz et al., 2012). The efficiency of MYC-PI3K cooperation in promoting the transformation of GC B cells to give rise to BL-like tumors in the mouse model indicates that these two factors indeed play a functional role in BL pathogenesis.

The induction of PI3K activation by the *P110** transgene represents a limitation of the present mouse model in that the tumors arising in the mice cannot be expected to be selected for mutations promoting PI3K signaling. A similar argument can be made for mutations of tumor suppressor genes like *TP53* or *CDKN2A* (recurrently mutated in human BL) (Bhatia et al., 1992; Sánchez-Beato et al., 2001), whose inactivation is considered to be an early event in tumorigenesis (Barrett et al., 1999) and may thus be upstream of the mutations deliberately introduced into the mouse model. The situation is different, however, for the tertiary mutations that are required for lymphomagenesis in the mice in addition to deregulated MYC and PI3K activity. Strikingly, these mutations include several genetic alterations that are recurrently seen in human BL. Thus, apart from shared copy number gains, the gene encoding cyclin D3, a critical cell cycle regulator in GC B cells, was mutated in both human BL and the mouse tumors. In both cases a point mutation affected a conserved codon critical for cyclin D3 stability, and frameshift mutations were found in the 3′ region of the gene. This further validates the mutant mice as a preclinical BL model, assigns functional significance to the mutations shared between the mouse and human tumors, and opens the way to in vivo analyses of their clinical relevance.

Taken together, we show that targeting MYC expression together with PI3K pathway activation into mouse GC B cells generates a faithful mouse model of human BL. The mouse tumors accumulate tertiary mutations at least some of which are recapitulated in the human disease; others may reflect genetic or epigenetic alterations that have not yet been uncovered in BL. The significance of the tertiary mutations for tumor progression can be assessed in the mouse model in functional terms, with clear perspectives for new therapeutic approaches. Already at this point the PI3K pathway has emerged as a promising therapeutic target in BL.

EXPERIMENTAL PROCEDURES

Mice, Immunization, and Tumor Cohorts

Cγ1-cre; R26Stop^{FL}P110;* and *R26Stop^{FL}eYFP* alleles have been described (Calado et al., 2010; Casola et al., 2006; Srinivasan et al., 2009). The *R26Stop^{FL}MYC* allele was generated following a strategy previously developed (Sasaki et al., 2006). Briefly, the ROSA26 allele was targeted with a construct containing human *c-MYC* cDNA preceded by a loxP flanked STOP cassette and marked by a signaling deficient truncated version of *hCD2* under the control of an internal ribosomal entry site (IRES) downstream of the inserted cDNA. Transgene transcription is controlled by the CAG promoter. A detailed description of the mice will be given elsewhere (D.P.C., unpublished data).

Rag2cg^{KO} animals were bred in our mouse colony or purchased from Taconic. 1×10^6 viable total BM cells were intravenously injected into sublethally irradiated (600 rad) 9- to 11-week-old *Rag2cg^{KO}* animals. For each genotype BM of three different donor animals was individually transferred to at least five (or three in the case of *Cγ1-cre*, *R26Stop^{FL}eYFP* BM) recipients. At day 140 after BM transfer, mice were immunized once by i.v. injection of 1×10^9 sheep red blood cells (SRBCs; Cedarlane). Mouse cohorts were monitored twice a week for tumor development and euthanized if signs of tumor development were seen. All animal care and procedures were approved by the Institutional Animal Care and Use Committee (IACUC 03341) of Harvard University and the Immune Disease Institute as well as the governmental review board (Landesamt für Gesundheit und Soziales Berlin, LaGeSo G0273/11).

Flow Cytometry and Cell Sorting

Single-cell suspensions were stained with PNA (Vector Laboratories) and the following monoclonal antibodies from BD Biosciences, Biolegends or eBioscience: αCD19(ID3), αB220(RA3-6B2), αCD95(Jo2), αCD138(281-2), αCD38(90), αhCD2(TS1/8), αCD93(AA4.1), αIgM(FAB), αIgD(11-26c.2a), αIgG1(A85-1), αIgA(mA-6E1), αIgkappa(187.1), αCD23(B3B4), αCD43(S7), αCD5(53-7.3), αGL7(GL7). Topro3 or PI (Invitrogen) was used to exclude dead cells. Samples were acquired on a FACSCantoII (BD Biosciences), and analyzed using FlowJo software (Tree star). Viable (Topro3^{neg}) GFP and hCD2 co-expressing tumor cells and GC B cells (CD19^{pos}, CD38^{low}, FAS^{high}, YFP^{pos}) of *Cγ1-cre, R26Stop^{FL}eYFP* animals were sorted on a FACSAriaII (BD Biosciences) and used for RNA and DNA preparation.

Real-Time RT-PCR

Total RNA from sorted cells was extracted using the AllPrep DNA/RNA Kit (QIAGEN) and cDNA was synthesized using the Thermoscript RT-PCR system (Invitrogen). For qRT-PCR, we used Power SYBR Green, followed by analysis with the StepOnePlus system (Applied Biosystems). Samples were assayed in triplicate and messenger abundance was normalized to that of *Actb*.

Analysis of Tumor Clonality by Southern Blot

EcoRI digested genomic DNA from tumor bearing mice and normal splenic B cells (C57BL/6 animal) was probed with a J_H probe spanning the J_{H4} exon and part of the downstream intronic sequence.

Histology and Immunohistochemistry

Tissues were fixed with 10% formalin (Sigma) and paraffin embedded sections were stained with H&E (Sigma), Ki67 (SP6; Vector Laboratories), PNA (Vector Laboratories), αGL7 (eBioscience), αMYC (N-terminal, Epitomics), αBCL6 (D65C10; Cell signaling), αpAKT (Ser473; D9E; Cell signaling), αpS6 (Ser235/236; D57.2.2E; Cell signaling), and αIRF4 (MUM1; Santa Cruz).

Immunofluorescence

Tissues were frozen in OCT (Sakura Finetek) in liquid nitrogen and staining was performed as described previously (Srinivasan et al., 2009) using B220-APC, IgD-FITC, and BCL2-PE (BD Biosciences) antibodies.

In Vitro Cell Culture of Splenic B Cells

Splenic B cells of C57BL/6 mice were purified by CD43 depletion (Miltenyi). Cells were cultured in the presence of 1 μg/ml of αCD40 (HM40-3, eBioscience) or 20 μg/ml of LPS (Sigma) and 25 ng/ml of IL-4 (R&D Systems) for 3 days. RNA was isolated using the RNeasy kit (QIAGEN) and cDNA was synthesized using the Thermoscript RT-PCR system (Invitrogen).

IgH Somatic Mutation Analysis

Genomic DNA was prepared from sorted tumor cells or GC B cells of *Cγ1-cre, R26Stop^{FL}eYFP* animals. *IgH-V* gene rearrangements were PCR amplified using the Expand High fidelity PCR system (Roche) combined with forward primers V_HA, V_HE, or V_HG (Ehlich et al., 1994) and a reverse primer in the J_H4 intron (5′-CTCCACCAGACCTCTCTAGACAGC-3′). Fragments were cloned, sequenced, and blasted against the NCBI database (http://www.ncbi.nlm.nih.gov/igblast/). Germline polymorphisms were excluded by blasting against the database of sequences generated in our laboratory.

Gene Expression Profiling and Data Analysis

GEP was performed on tumor samples and purified GC B cells and non-GC B cells from immunized *Cγ1-cre, R26Stop^{FL}eYFP* animals using Affymetrix GeneChip Mouse Genome 430 2.0 Arrays according to the manufacturer's recommendations (Affymetrix). The complete microarray data are available at the Gene Expression Omnibus (http://www.ncbi.nlm.nih.gov/projects/geo; accession number GSE35219). Further information is provided in Supplemental Experimental Procedures.

Pathway Activation Indices

The method to compute pathway activation indices is an extension of our previously published strategy (Läuter et al., 2009). Based on gene expression, we generated 50 clusters of highly correlated genes in the data set of Hummel et al. (GSE4475) (Hummel et al., 2006). We then mapped these clusters to interventional data sets from experiments in which either MYC (GSE3151) (Bild et al., 2006) or PI3K (GSE12815) (Gustafson et al., 2010) were activated. In all data sets, we summarized the clusters to 50 metagenes. To obtain an index of the relative activity of a pathway in a tumor sample, we computed the sum of the values of the 50 metagenes in this sample weighted by the correlations of the metagenes with the activation of this pathway in the corresponding interventional data set. We used preprocessed data as available at the Gene Expression Omnibus. Further information is provided in Supplemental Experimental Procedures.

SNP Microarray Analysis

For genomic profiling we used Affymetrix Mouse Diversity Genotyping Arrays according to the manufacturer's recommendations (Affymetrix). After generation of the raw data (CEL-files) using Command_Console software (Affymetrix) paired analysis of tumor and respective germline DNA samples was performed. Using R version 2.12.1 (http://www.r-project.org/), data were normalized using the aroma.affymetrix R package (Bengtsson et al., 2008) in combination with the R package DNAcopy (Olshen et al., 2004) for segmentation and detection of copy number aberrations. The complete SNP array data are available at the Gene Expression Omnibus (accession number GSE35219).

Exome Sequencing

Nonamplified genomic DNA (1μg) from sorted murine tumor cells and matched germline tissue (mouse tail) were used for exome sequencing using Illumina technology. Further information is provided in Supplemental Experimental Procedures.

Human BL Cell Lines

Human BL cell lines were cultured in RPMI medium 1640 with 10% fetal calf serum, 1% penicillin/streptomycin, 1% L-glutamine, 1% nonessential amino acids, and 0.1% beta-mercaptoethanol. For detection of PI3K pathway activation cell lines were treated with either 25 μM LY-294002 (Sigma) or DMSO for 1 hr.

Patient Samples

Primary BL samples [9 peripheral blood/BM (B cell acute lymphoblastic leukemia, B-ALL), 27 lymph node (BL), 1 jaw (BL), and 1 parotid gland (BL) specimens; all cases were translocation t(8;14) positive] were provided by the Department of Pathology, Brigham and Women's Hospital (n = 9), and the Department of Internal Medicine III, University Hospital of Ulm (n = 29) with patient informed consent and institutional review board approval from all participating centers. One case represents endemic BL (1/38) whereas the others belong to the sporadic/HIV-associated subgroup (37/38). Sanger Sequencing was performed with genomic DNA obtained from frozen lymphoid tissue blocks (n = 20) and mononuclear cells isolated from the peripheral blood or BM (n = 9).

Cyclin D3 Mutation Analysis in Primary Human BL and Mouse Tumors

Genomic DNA of primary human BL samples (n = 29) was prepared using the QIAGEN DNeasy blood and tissue kit (QIAGEN). A 346bp amplicon within exon 5 of human *CCND3* was PCR amplified (forward primer: 5′-GAAGCTGCACTC AGGGAGAG; reverse primer: 5′-AGCTTGACTAGCCACCGAAA) and sequenced (Sanger Sequencing). The 3′ end of *Ccnd3* was amplified in genomic DNA of MYC and P110* co-expressing mouse tumors (n = 15) using 5′-CACCTGCTTGCTGTCAGTGCTGTGAG as forward primer and 5′- GCATGG ATTGTTCTAGAGGCAGGGA as reverse primer.

Western Blot Analysis

RIPA extracts were fractionated on 10% sodium dodecyl sulfate polyacrylamide gels, electroblotted to polyvinylidene difluoride membranes and reacted with α-MYC (N-terminal, Epitomics), α-pAKT (Ser473) (D9E), α-AKT (5G3), α-pS6 kinase (Thr389) (108D2), α-S6 kinase (Cat #9202) (Cell Signaling), and α-beta-actin (Cat #A5316, Sigma) antibodies. Immunoreactivity was determined using the enhanced chemiluminescence method (Pierce Chemical).

Statistical Analysis

Data were analyzed using unpaired two-tailed Student's t test and Fisher's exact test, a p value $\leq$ 0.05 was considered significant. Survival curves were compared using the Logrank test. Data in text and figures are represented as mean ± SEM (standard error of the mean).

ACCESSION NUMBERS

The Gene Expression Omnibus accession number for the microarray data is GSE35219. The exome sequencing data are available at the Sequence Read Archive (SRA055727).

SUPPLEMENTAL INFORMATION

Supplemental Information includes four figures, two tables, Supplemental Experimental Procedures, and Supplemental References and can be found with this article online at http://dx.doi.org/10.1016/j.ccr.2012.06.012.

ACKNOWLEDGMENTS

We thank J. Xia, C. Grosse, J. Grundy, X. Chen, D. Ghitza, C. Unitt, and M. Bamberg for technical assistance; M. Ottaviano for administrative

assistance; T. Yasuda for contribution of reagents; E. Derudder and J. Seagal for assistance with irradiation; S. Koralov for help with SHM analyses; D. Bolgehn and T. Sommermann for technical support; and present and former Rajewsky lab members for critical comments and suggestions. We are grateful to L. Staudt and R. Schmitz for sharing unpublished results and primer sequences. This work was supported by grants from the National Institutes of Health to K.R. (P01 CA92625; R37 AI054636), the Leukemia & Lymphoma Society (Leukemia & Lymphoma Society SCOR) and the European Research Council (ERC advanced Grant ERC-AG-LS6) to K.R.; Leukemia & Lymphoma Society fellowships to S. Sander, B.Z., and D.P.C., and a Heisenberg scholarship by the Deutsche Forschungsgemeinschaft to L.B.

S. Sander, D.P.C., L.B., and K.R. designed research; S. Sander, D.P.C., L.S., B.Z., S.R.. and K.H. performed experiments; S. Sander, D.P.C., S.R., K.H., L.B., and K.R. analyzed data; S.R., S. Stilgenbauer, and R.S. provided primary human BL samples and human tumor data; K.K. and M.R. performed statistical analyses. S. Sander, L.B., and K.R. wrote the manuscript with contributions from all authors.

Received: February 11, 2012
Revised: May 26, 2012
Accepted: June 18, 2012
Published: August 13, 2012

REFERENCES

Adams, J.M., and Cory, S. (1985). Myc oncogene activation in B and T lymphoid tumours. Proc. R. Soc. Lond. B Biol. Sci. *226*, 59–72.

Alizadeh, A.A., Eisen, M.B., Davis, R.E., Ma, C., Lossos, I.S., Rosenwald, A., Boldrick, J.C., Sabet, H., Tran, T., Yu, X., et al. (2000). Distinct types of diffuse large B-cell lymphoma identified by gene expression profiling. Nature *403*, 503–511.

Barrett, M.T., Sanchez, C.A., Prevo, L.J., Wong, D.J., Galipeau, P.C., Paulson, T.G., Rabinovitch, P.S., and Reid, B.J. (1999). Evolution of neoplastic cell lineages in Barrett oesophagus. Nat. Genet. *22*, 106–109.

Bengtsson, H., Irizarry, R., Carvalho, B., and Speed, T.P. (2008). Estimation and assessment of raw copy numbers at the single locus level. Bioinformatics *24*, 759–767.

Bhatia, K.G., Gutiérrez, M.I., Huppi, K., Siwarski, D., and Magrath, I.T. (1992). The pattern of p53 mutations in Burkitt's lymphoma differs from that of solid tumors. Cancer Res. *52*, 4273–4276.

Bild, A.H., Yao, G., Chang, J.T., Wang, Q., Potti, A., Chasse, D., Joshi, M.B., Harpole, D., Lancaster, J.M., Berchuck, A., et al. (2006). Oncogenic pathway signatures in human cancers as a guide to targeted therapies. Nature *439*, 353–357.

Boerma, E.G., Siebert, R., Kluin, P.M., and Baudis, M. (2009). Translocations involving 8q24 in Burkitt lymphoma and other malignant lymphomas: a historical review of cytogenetics in the light of todays knowledge. Leukemia *23*, 225–234.

Calado, D.P., Zhang, B., Srinivasan, L., Sasaki, Y., Seagal, J., Unitt, C., Rodig, S., Kutok, J., Tarakhovsky, A., Schmidt-Supprian, M., and Rajewsky, K. (2010). Constitutive canonical NF-κB activation cooperates with disruption of BLIMP1 in the pathogenesis of activated B cell-like diffuse large cell lymphoma. Cancer Cell *18*, 580–589.

Casanovas, O., Jaumot, M., Paules, A.B., Agell, N., and Bachs, O. (2004). P38SAPK2 phosphorylates cyclin D3 at Thr-283 and targets it for proteasomal degradation. Oncogene *23*, 7537–7544.

Casola, S., Cattoretti, G., Uyttersprot, N., Koralov, S.B., Seagal, J., Hao, Z., Waisman, A., Egert, A., Ghitza, D., and Rajewsky, K. (2006). Tracking germinal center B cells expressing germ-line immunoglobulin gamma1 transcripts by conditional gene targeting. Proc. Natl. Acad. Sci. USA *103*, 7396–7401.

Cato, M.H., Chintalapati, S.K., Yau, I.W., Omori, S.A., and Rickert, R.C. (2011). Cyclin D3 is selectively required for proliferative expansion of germinal center B cells. Mol. Cell. Biol. *31*, 127–137.

Cattoretti, G., Pasqualucci, L., Ballon, G., Tam, W., Nandula, S.V., Shen, Q., Mo, T., Murty, V.V., and Dalla-Favera, R. (2005). Deregulated BCL6 expression recapitulates the pathogenesis of human diffuse large B cell lymphomas in mice. Cancer Cell *7*, 445–455.

Dave, S.S., Fu, K., Wright, G.W., Lam, L.T., Kluin, P., Boerma, E.J., Greiner, T.C., Weisenburger, D.D., Rosenwald, A., Ott, G., et al; Lymphoma/Leukemia Molecular Profiling Project. (2006). Molecular diagnosis of Burkitt's lymphoma. N. Engl. J. Med. *354*, 2431–2442.

DiSanto, J.P., Müller, W., Guy-Grand, D., Fischer, A., and Rajewsky, K. (1995). Lymphoid development in mice with a targeted deletion of the interleukin 2 receptor gamma chain. Proc. Natl. Acad. Sci. USA *92*, 377–381.

Ehlich, A., Martin, V., Müller, W., and Rajewsky, K. (1994). Analysis of the B-cell progenitor compartment at the level of single cells. Curr. Biol. *4*, 573–583.

Green, M.R., Monti, S., Dalla-Favera, R., Pasqualucci, L., Walsh, N.C., Schmidt-Supprian, M., Kutok, J.L., Rodig, S.J., Neuberg, D.S., Rajewsky, K., et al. (2011). Signatures of murine B-cell development implicate Yy1 as a regulator of the germinal center-specific program. Proc. Natl. Acad. Sci. USA *108*, 2873–2878.

Gustafson, A.M., Soldi, R., Anderlind, C., Scholand, M.B., Qian, J., Zhang, X., Cooper, K., Walker, D., McWilliams, A., Liu, G., et al. (2010). Airway PI3K pathway activation is an early and reversible event in lung cancer development. Sci. Transl. Med. *2*, 26ra25.

Hummel, M., Bentink, S., Berger, H., Klapper, W., Wessendorf, S., Barth, T.F., Bernd, H.W., Cogliatti, S.B., Dierlamm, J., Feller, A.C., et al; Molecular Mechanisms in Malignant Lymphomas Network Project of the Deutsche Krebshilfe. (2006). A biologic definition of Burkitt's lymphoma from transcriptional and genomic profiling. N. Engl. J. Med. *354*, 2419–2430.

Jaffe, E.S., and Pittaluga, S. (2011). Aggressive B-cell lymphomas: a review of new and old entities in the WHO classification. Hematology (Am. Soc. Hematol. Educ. Program) *2011*, 506–514.

Klapproth, K., Sander, S., Marinkovic, D., Baumann, B., and Wirth, T. (2009). The IKK2/NF-kappaB pathway suppresses MYC-induced lymphomagenesis. Blood *114*, 2448–2458.

Kovalchuk, A.L., Qi, C.F., Torrey, T.A., Taddesse-Heath, L., Feigenbaum, L., Park, S.S., Gerbitz, A., Klobeck, G., Hoertnagel, K., Polack, A., et al. (2000). Burkitt lymphoma in the mouse. J. Exp. Med. *192*, 1183–1190.

Kumar, A., Marqués, M., and Carrera, A.C. (2006). Phosphoinositide 3-kinase activation in late G1 is required for c-Myc stabilization and S phase entry. Mol. Cell. Biol. *26*, 9116–9125.

Küppers, R., Klein, U., Hansmann, M.L., and Rajewsky, K. (1999). Cellular origin of human B-cell lymphomas. N. Engl. J. Med. *341*, 1520–1529.

Läuter, J., Horn, F., Rosołowski, M., and Glimm, E. (2009). High-dimensional data analysis: selection of variables, data compression and graphics—application to gene expression. Biom. J. *51*, 235–251.

Mitelman, F., Johansson, B., and Mertens, F.E. (2012). Mitelman Database of Chromosome Aberrations and Gene Fusions in Cancer. http://cgapncinihgov/Chromosomes/Mitelman.

Mu, P., Han, Y.C., Betel, D., Yao, E., Squatrito, M., Ogrodowski, P., de Stanchina, E., D'Andrea, A., Sander, C., and Ventura, A. (2009). Genetic dissection of the miR-17~92 cluster of microRNAs in Myc-induced B-cell lymphomas. Genes Dev. *23*, 2806–2811.

Olive, V., Bennett, M.J., Walker, J.C., Ma, C., Jiang, I., Cordon-Cardo, C., Li, Q.J., Lowe, S.W., Hannon, G.J., and He, L. (2009). miR-19 is a key oncogenic component of mir-17-92. Genes Dev. *23*, 2839–2849.

Olshen, A.B., Venkatraman, E.S., Lucito, R., and Wigler, M. (2004). Circular binary segmentation for the analysis of array-based DNA copy number data. Biostatistics *5*, 557–572.

Omori, S.A., Cato, M.H., Anzelon-Mills, A., Puri, K.D., Shapiro-Shelef, M., Calame, K., and Rickert, R.C. (2006). Regulation of class-switch recombination and plasma cell differentiation by phosphatidylinositol 3-kinase signaling. Immunity *25*, 545–557.

Park, S.S., Kim, J.S., Tessarollo, L., Owens, J.D., Peng, L., Han, S.S., Tae Chung, S., Torrey, T.A., Cheung, W.C., Polakiewicz, R.D., et al. (2005). Insertion of c-Myc into Igh induces B-cell and plasma-cell neoplasms in mice. Cancer Res. *65*, 1306–1315.

Peled, J.U., Yu, J.J., Venkatesh, J., Bi, E., Ding, B.B., Krupski-Downs, M., Shaknovich, R., Sicinski, P., Diamond, B., Scharff, M.D., and Ye, B.H. (2010). Requirement for cyclin D3 in germinal center formation and function. Cell Res. *20*, 631–646.

Radziszewska, A., Choi, D., Nguyen, K.T., Schroer, S.A., Tajmir, P., Wang, L., Suzuki, A., Mak, T.W., Evan, G.I., and Woo, M. (2009). PTEN deletion and concomitant c-Myc activation do not lead to tumor formation in pancreatic beta cells. J. Biol. Chem. *284*, 2917–2922.

Refaeli, Y., Young, R.M., Turner, B.C., Duda, J., Field, K.A., and Bishop, J.M. (2008). The B cell antigen receptor and overexpression of MYC can cooperate in the genesis of B cell lymphomas. PLoS Biol. *6*, e152.

Sánchez-Beato, M., Sáez, A.I., Navas, I.C., Algara, P., Sol Mateo, M., Villuendas, R., Camacho, F., Sánchez-Aguilera, A., Sánchez, E., and Piris, M.A. (2001). Overall survival in aggressive B-cell lymphomas is dependent on the accumulation of alterations in p53, p16, and p27. Am. J. Pathol. *159*, 205–213.

Sasaki, Y., Derudder, E., Hobeika, E., Pelanda, R., Reth, M., Rajewsky, K., and Schmidt-Supprian, M. (2006). Canonical NF-kappaB activity, dispensable for B cell development, replaces BAFF-receptor signals and promotes B cell proliferation upon activation. Immunity *24*, 729–739.

Schmitz, R., Young, R.M., Ceribelli, M., Jhavar, S., Xiao, W., Zhang, M., Wright, G., Schaffer, A.L., Hodson, D.J., Buras, E., et al. (2012). Burkitt lymphoma pathogenesis and therapeutic targets from structural and functional genomics. Nature. http://dx.doi.org/10.1038/nature11378.

Scholtysik, R., Nagel, I., Kreuz, M., Vater, I., Giefing, M., Schwaenen, C., Wessendorf, S., Trümper, L., Loeffler, M., Siebert, R., and Küppers, R. (2012). Recurrent deletions of the TNFSF7 and TNFSF9 genes in 19p13.3 in diffuse large B-cell and Burkitt lymphomas. Int. J. Cancer *131*, E830–E835.

Shinkai, Y., Rathbun, G., Lam, K.P., Oltz, E.M., Stewart, V., Mendelsohn, M., Charron, J., Datta, M., Young, F., Stall, A.M., et al. (1992). RAG-2-deficient mice lack mature lymphocytes owing to inability to initiate V(D)J rearrangement. Cell *68*, 855–867.

Srinivasan, L., Sasaki, Y., Calado, D.P., Zhang, B., Paik, J.H., DePinho, R.A., Kutok, J.L., Kearney, J.F., Otipoby, K.L., and Rajewsky, K. (2009). PI3 kinase signals BCR-dependent mature B cell survival. Cell *139*, 573–586.

Zhu, J., Blenis, J., and Yuan, J. (2008). Activation of PI3K/Akt and MAPK pathways regulates Myc-mediated transcription by phosphorylating and promoting the degradation of Mad1. Proc. Natl. Acad. Sci. USA *105*, 6584–6589.

Cancer Cell
Article

ASXL1 Mutations Promote Myeloid Transformation through Loss of PRC2-Mediated Gene Repression

Omar Abdel-Wahab,[1,12] Mazhar Adli,[2,12] Lindsay M. LaFave,[1,3,12] Jie Gao,[5] Todd Hricik,[1] Alan H. Shih,[1] Suveg Pandey,[1] Jay P. Patel,[1] Young Rock Chung,[1] Richard Koche,[2] Fabiana Perna,[4] Xinyang Zhao,[6] Jordan E. Taylor,[7] Christopher Y. Park,[1] Martin Carroll,[8] Ari Melnick,[9] Stephen D. Nimer,[11] Jacob D. Jaffe,[7] Iannis Aifantis,[4] Bradley E. Bernstein,[2,*] and Ross L. Levine[1,10,*]

[1]Human Oncology and Pathogenesis Program and Leukemia Service, Memorial Sloan-Kettering Cancer Center, 1275 York Avenue, Box 20, New York, NY 10065, USA
[2]Howard Hughes Medical Institute, Broad Institute of Harvard and MIT, Department of Pathology, Massachusetts General Hospital, and Harvard Medical School, MGH-Simches Research Building, CPZN 8400,185 Cambridge Street, Boston, MA 02114, USA
[3]Gerstner Sloan Kettering School of Biomedical Sciences
[4]Molecular Pharmacology and Chemistry Program
Memorial Sloan-Kettering Cancer Center, New York, NY 10065, USA
[5]Howard Hughes Medical Institute and Department of Pathology, New York University School of Medicine, New York, NY 10016, USA
[6]Department of Biochemistry and Molecular Genetics, University of Alabama, Birmingham, AL 35233, USA
[7]Broad Institute of Harvard and MIT, Cambridge, MA 02142, USA
[8]Division of Hematology and Oncology, University of Pennsylvania, Philadelphia, PA 19104, USA
[9]Division of Hematology/Oncology
[10]Biochemistry and Molecular Biology Program
Weill Cornell Medical College, New York, NY 10065, USA
[11]Sylvester Comprehensive Cancer Center, University of Miami, Miami, FL 33136, USA
[12]These authors contributed equally to this work
*Correspondence: bernstein.bradley@mgh.harvard.edu (B.E.B.), leviner@mskcc.org (R.L.L.)
http://dx.doi.org/10.1016/j.ccr.2012.06.032

SUMMARY

Recurrent somatic *ASXL1* mutations occur in patients with myelodysplastic syndrome, myeloproliferative neoplasms, and acute myeloid leukemia, and are associated with adverse outcome. Despite the genetic and clinical data implicating *ASXL1* mutations in myeloid malignancies, the mechanisms of transformation by *ASXL1* mutations are not understood. Here, we identify that *ASXL1* mutations result in loss of polycomb repressive complex 2 (PRC2)-mediated histone H3 lysine 27 (H3K27) tri-methylation. Through integration of microarray data with genome-wide histone modification ChIP-Seq data, we identify targets of ASXL1 repression, including the posterior *HOXA* cluster that is known to contribute to myeloid transformation. We demonstrate that ASXL1 associates with the PRC2, and that loss of ASXL1 in vivo collaborates with *NRASG12D* to promote myeloid leukemogenesis.

INTRODUCTION

Recent genome-wide and candidate-gene discovery efforts have identified a series of novel somatic genetic alterations in patients with myeloid malignancies with relevance to pathogenesis, prognostication, and/or therapy. Notably, these include mutations in genes with known or putative roles in the epigenetic regulation of gene transcription. One such example is the mutations in the gene *Addition of sex combs-like 1* (*ASXL1*), which is mutated in ≈15%–25% of patients with myelodysplastic

Significance

Mutations in genes involved in modification of chromatin have recently been identified in patients with leukemias and other malignancies. Here, we demonstrate a specific role for ASXL1, a putative epigenetic modifier frequently mutated in myeloid malignancies, in polycomb repressive complex 2 (PRC2)-mediated transcriptional repression in hematopoietic cells. *ASXL1* loss-of-function mutations in myeloid malignancies result in loss of PRC2-mediated gene repression of known leukemogenic target genes. Our data provide insight into how *ASXL1* mutations contribute to myeloid transformation through dysregulation of Polycomb-mediated gene silencing. This approach also demonstrates how epigenomic and functional studies can be used to elucidate the function of mutations in epigenetic modifiers in malignant transformation.

syndrome and ≈10%–15% of patients with myeloproliferative neoplasms and acute myeloid leukemia (Abdel-Wahab et al., 2011; Bejar et al., 2011; Gelsi-Boyer et al., 2009). Clinical studies have consistently indicated that mutations in *ASXL1* are associated with adverse survival in myelodysplastic syndrome and acute myeloid leukemia (Bejar et al., 2011; Metzeler et al., 2011; Pratcorona et al., 2012; Thol et al., 2011).

ASXL1 is the human homolog of *Drosophila Additional sex combs* (*Asx*). *Asx* deletion results in a homeotic phenotype characteristic of both Polycomb (PcG) and Trithorax group (TxG) gene deletions (Gaebler et al., 1999), which led to the hypothesis that Asx has dual functions in silencing and activation of homeotic gene expression. In addition, functional studies in *Drosophila* suggested that *Asx* encodes a chromatin-associated protein with similarities to PcG proteins (Sinclair et al., 1998). More recently, it was demonstrated that *Drosophila* Asx forms a complex with the chromatin deubiquitinase Calypso to form the Polycomb-repressive deubiquitinase (PR-DUB) complex, which removes monoubiquitin from histone H2A at lysine 119. The mammalian homolog of Calypso, BAP1, directly associates with ASXL1, and the mammalian BAP1-ASXL1 complex was shown to possess deubiquitinase activity in vitro (Scheuermann et al., 2010).

The mechanisms by which *ASXL1* mutations contribute to myeloid transformation have not been delineated. A series of in vitro studies in non-hematopoietic cells have suggested a variety of activities for ASXL1, including physical cooperativity with HP1a and LSD1 to repress retinoic acid-receptor activity and interaction with peroxisome proliferator-activated receptor gamma (PPARg) to suppress lipogenesis (Cho et al., 2006; Lee et al., 2010; Park et al., 2011). In addition, a recent study using a gene-trap model reported that constitutive disruption of *Asxl1* results in significant perinatal lethality; however, the authors did not note alterations in stem/progenitor numbers in surviving Asxl1 gene trap mice (Fisher et al., 2010a, 2010b). Importantly, the majority of mutations in *ASXL1* occur as nonsense mutations and insertions/deletions proximal or within the last exon prior to the highly conserved plant homeo domain. It is currently unknown whether mutations in *ASXL1* might confer a gain-of-function due to expression of a truncated protein, or whether somatic loss of ASXL1 in hematopoietic cells leads to specific changes in epigenetic state, gene expression, or hematopoietic functional output. The goals of this study were to determine the effects of *ASXL1* mutations on ASXL1 expression as well as the transcriptional and biological effects of perturbations in ASXL1 which might contribute toward myeloid transformation.

RESULTS

ASXL1 Mutations Result in Loss of ASXL1 Expression

ASXL1 mutations in patients with myeloproliferative neoplasms, myelodysplastic syndrome, and acute myeloid leukemia most commonly occur as somatic nonsense mutations and insertion/deletion mutations in a clustered region adjacent to the highly conserved PHD domain (Abdel-Wahab et al., 2011; Gelsi-Boyer et al., 2009). To assess whether these mutations result in loss of ASXL1 protein expression or in expression of a truncated isoform, we performed western blots using N- and C-terminal anti-ASXL1 antibodies in a panel of human myeloid leukemia cell lines and primary acute myeloid leukemia samples, which are wild-type or mutant for *ASXL1*. We found that myeloid leukemia cells with homozygous frameshift/nonsense mutations in *ASXL1* (NOMO1 and KBM5) have no detectable ASXL1 protein expression (Figure 1A). Similarly, leukemia cells with heterozygous *ASXL1* mutations have reduced or absent ASXL1 protein expression. Western blot analysis of ASXL1 using an N-terminal anti-ASXL1 antibody in primary acute myeloid leukemia samples wild-type and mutant for *ASXL1* revealed reduced/absent full-length ASXL1 expression in samples with *ASXL1* mutations compared to *ASXL1* wild-type samples (Figure S1A available online). Importantly, we did not identify truncated ASXL1 protein products in mutant samples using N- or C-terminal directed antibodies in primary acute myeloid leukemia samples or leukemia cell lines. Moreover, expression of wild-type ASXL1 cDNA or cDNA constructs bearing leukemia-associated mutant forms of ASXL1 revealed reduced stability of mutant forms of ASXL1 relative to wild-type ASXL1, with more rapid degradation of mutant ASXL1 isoforms following cycloheximide exposure (Figure S1B). These data are consistent with ASXL1 functioning as a tumor suppressor with loss of ASXL1 protein expression in leukemia cells with mutant *ASXL1* alleles.

ASXL1 Knockdown in Hematopoietic Cells Results in Upregulated *HOXA* Gene Expression

Given that *ASXL1* mutations result in loss of ASXL1 expression, we investigated the effects of ASXL1 knockdown in primary hematopoietic cells. We used a pool of small interfering RNAs (siRNA) to perform knockdown of ASXL1 in primary human CD34+ cells isolated from umbilical cord blood. ASXL1 knockdown was performed in triplicate and confirmed by qRT-PCR analysis (Figure 1B), followed by gene-expression microarray analysis. Gene-set enrichment analysis (GSEA) of this microarray data revealed a significant enrichment of genes found in a previously described gene expression signature of leukemic cells from bone marrow of *MLL-AF9* knock-in mice (Kumar et al., 2009), as well as highly significant enrichment of a gene signature found in primary human cord blood CD34+ cells expressing *NUP98-HOXA9* (Figure S1C and Table S1) (Takeda et al., 2006). Specifically, we found that ASXL1 knockdown in human primary CD34+ cells resulted in increased expression of 145 genes out of the 279 genes, which are overexpressed in the *MLL-AF9* gene expression signature ($p < 0.05$, FDR < 0.05). These gene expression signatures are characterized by increased expression of posterior *HOXA* cluster genes, including *HOXA5-9.*

In order to ascertain whether loss of ASXL1 was associated with similar transcriptional effects in leukemia cells, we performed short hairpin RNA (shRNA)-mediated stable knockdown of *ASXL1* in the *ASXL1*-wild-type human leukemia cell lines UKE1 (Figures 1C and 1D) and SET2 (Figure 1D) followed by microarray and qRT-PCR analysis. Gene expression analysis in UKE-1 cells expressing ASXL1 shRNA compared to control cells revealed significant enrichment of the same *HOXA* gene expression signatures as were seen with ASXL1 knockdown in CD34+ cells (Figure 1C and Table S2). Upregulation of 5′ *HOXA* genes was confirmed by qRT-PCR in UKE1 (Figure 1D) cells and by western blot analysis (Figure 1D) in SET2 cells expressing ASXL1 shRNA compared to control. Quantitative mRNA profiling (Nanostring nCounter) of the entire *HOXA* cluster revealed

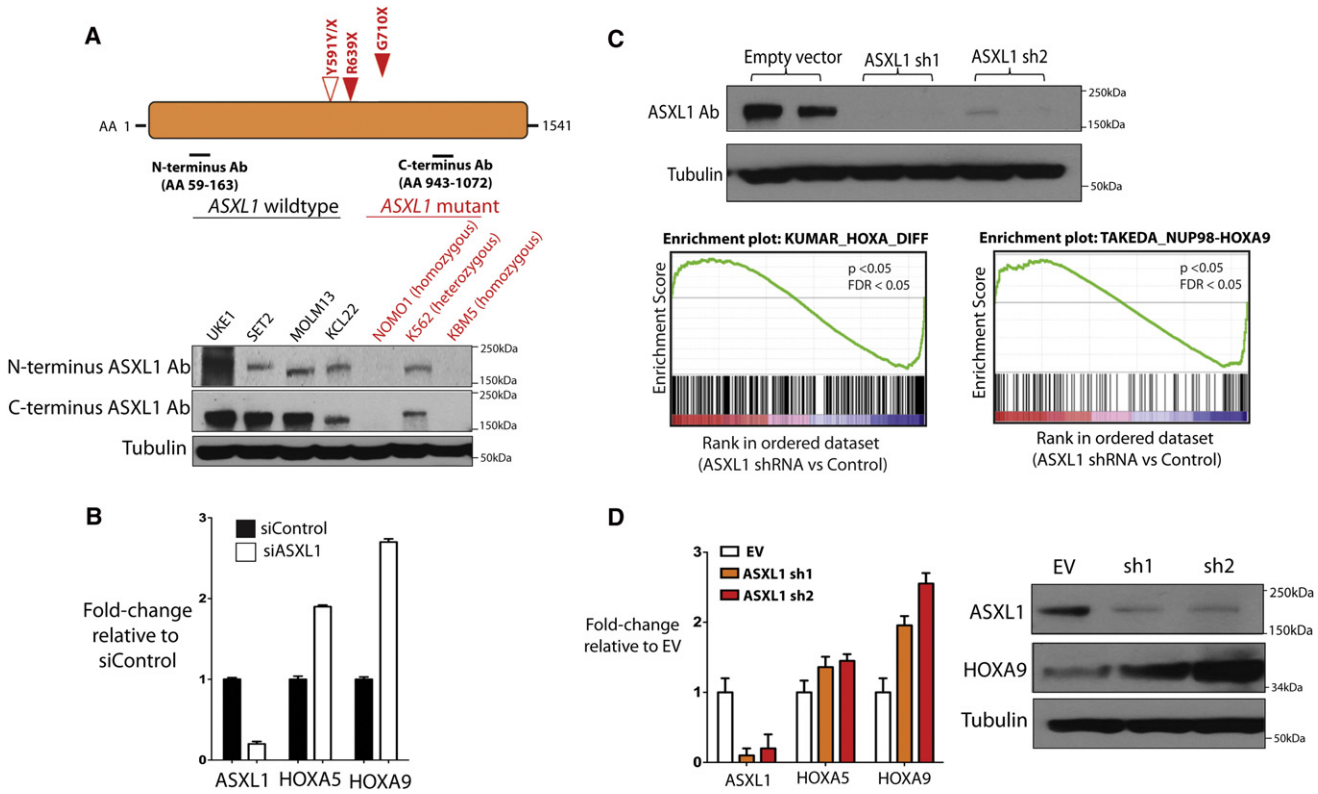

Figure 1. Leukemogenic *ASXL1* Mutations Are Loss-of-Function Mutations and ASXL1 Loss Is Associated with Upregulation of *HOXA* Gene Expression

(A) Characterization of ASXL1 expression in leukemia cells with nonsense mutations in *ASXL1* reveals loss of ASXL1 expression at the protein level in cells with homozygous *ASXL1* mutations as shown by western blotting using N- and C-terminal anti-ASXL1 antibodies.

(B) Displayed are the *ASXL1*-mutant cell line lines NOMO1 (homozygous *ASXL1* R639X), K562 (heterozygous *ASXL1* Y591Y/X), and KBM5 (homozygous *ASXL1 G710X*) and a panel of *ASXL1*-wild-type cell lines. *ASXL1* siRNA in human primary CD34+ cells form cord blood results in upregulation of *HOXA5* and *HOXA9* with ASXL1 knockdown (KD) as revealed by quantitative real-time PCR (qRT-PCR) analysis.

(C and D) Stable KD of ASXL1 in *ASXL1*-wild-type transformed human myeloid leukemia UKE1 cells (as shown by western blot) followed by GSEA reveals significant enrichment of gene sets characterized by upregulation of 5′ *HOXA* genes (C) as was confirmed by qRT-PCR (D). Statistical significance is indicated in (D) by the p value and false-discovery rate (FDR). Similar upregulation of *HOXA9* is seen by the western blot following stable ASXL1 KD in the *ASXL1*-wild-type human leukemia SET2 cells.

Error bars represent standard deviation of expression relative to control. See also Figure S1 and Tables S1 and S2.

upregulation of multiple *HOXA* members, including *HOXA5, 7, 9,* and *10*, in SET2 cells with ASXL1 knockdown compared to control cells (Figure S1D). These results indicate consistent upregulation of *HOXA* gene expression following ASXL1 loss in multiple hematopoietic contexts.

ASXL1 Forms a Complex with BAP1 in Leukemia Cells, but BAP1 Loss Does Not Upregulate *HoxA* Gene Expression in Hematopoietic Cells

Mammalian ASXL1 forms a protein complex in vitro with the chromatin deubiquitinase BAP1, which removes monoubiquitin from histone H2A at lysine 119 (H2AK119) (Scheuermann et al., 2010). In *Drosophila* loss of either Asx or Calypso resulted in similar effects on genome-wide H2AK119 ubiquitin levels and on target gene expression. Recent studies have revealed recurrent germline and somatic loss-of-function *BAP1* mutations in mesothelioma and uveal melanoma (Bott et al., 2011; Harbour et al., 2010; Testa et al., 2011). However, we have not identified *BAP1* mutations in patients with myeloproliferative neoplasms or acute myeloid leukemia (O.A.-W., J.P.P., and R.L.L., unpublished data). Co-immunopreciptation studies revealed an association between ASXL1 and BAP1 in human myeloid leukemia cells wild-type for *ASXL1* but not in those cells mutant for *ASXL1* due to reduced/absent ASXL1 expression (Figure 2A). Immunoprecipitation of FLAG-tagged wild-type ASXL1 and FLAG-tagged leukemia-associated mutant forms of ASXL1 revealed reduced interaction between mutant forms of ASXL1 and endogenous BAP1 (Figure S2A). Despite these findings, BAP1 knockdown did not result in upregulation of *HOXA5* and *HOXA9* in UKE1 cells, although a similar extent of ASXL1 knockdown in the same cells reproducibly increased *HOXA5* and *HOXA9* expression (Figure 2B). We obtained similar results with knockdown of Asxl1 or Bap1 in the Ba/F3 murine hematopoietic cell line (Figure 2C). In Ba/F3 cells, knockdown of *Asxl1* resulted in upregulated *Hoxa9* gene expression commensurate with the level of Asxl1 downregulation, whereas knockdown of Bap1 does not impact *Hoxa* expression (Figure 2C). ASXL1 knockdown in SET-2 cells failed to reveal an effect of ASXL1

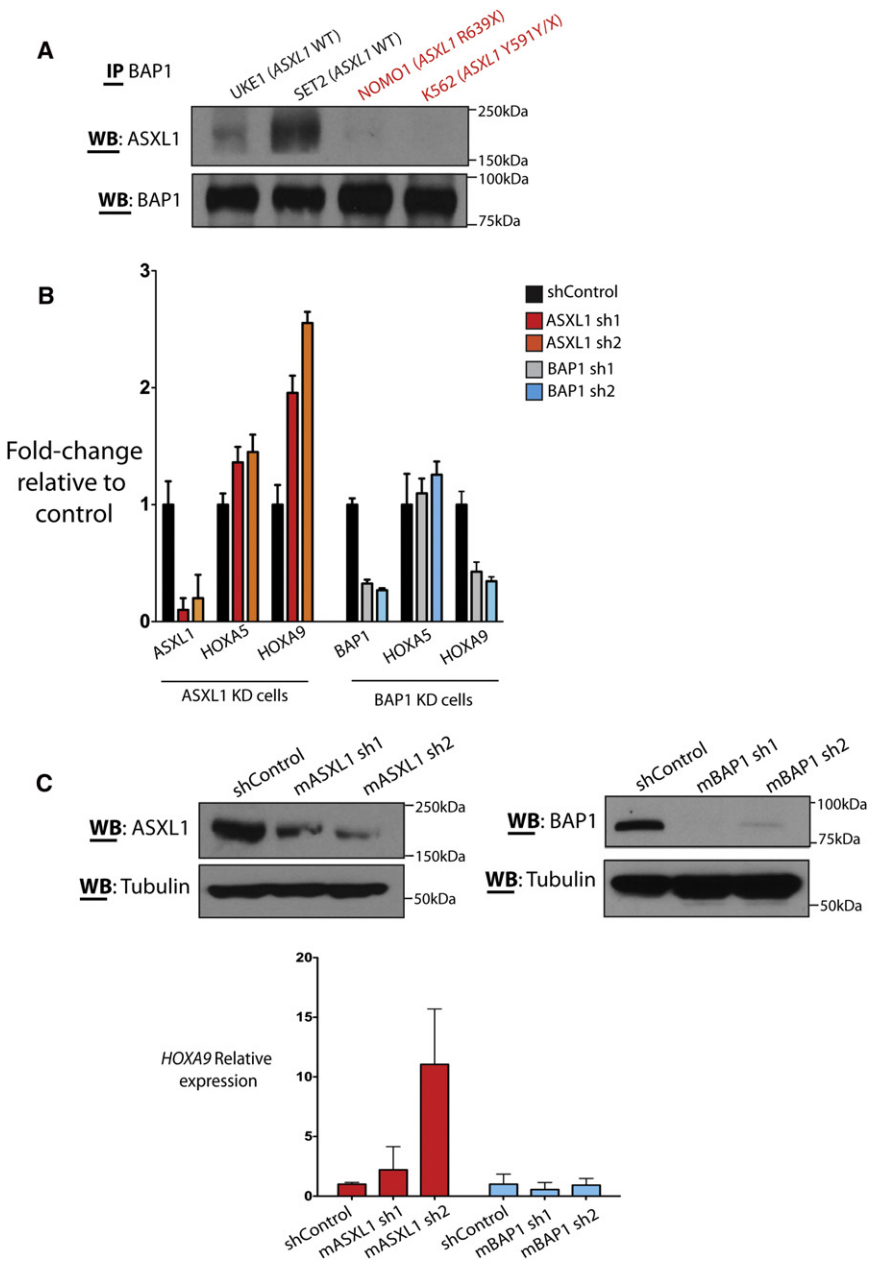

Figure 2. ASXL1 and BAP1 Physically Interact in Human Hematopoietic Cells but BAP1 Loss Does Not Result in Increased *HoxA* Gene Expression

(A) Immunoprecipitation of BAP1 in a panel of *ASXL1*-wild-type and mutant human myeloid leukemia cells reveals co-association of ASXL1 and BAP1.

(B) Cells with heterozygous or homozygous mutations in *ASXL1* with reduced or absent ASXL1 expression have minimal interaction with BAP1 in vitro. BAP1 knockdown in the *ASXL1*/*BAP1* wild-type human leukemia cell line UKE1 fails to alter *HOXA* gene expression. In contrast, stable knockdown of ASXL1 in the same cell type results in a significant upregulation of *HOXA9*.

(C) Similar results are seen with knockdown of Asxl1 or Bap1 in murine precursor-B lymphoid Ba/F3 cells.

Error bars represent standard deviation of expression relative to control. See also Figure S2.

loss on H2AK119Ub levels as assessed by western blot of purified histones from shRNA control and ASXL1 knockdown cells (Figure S2B). By contrast, SET2 cells treated with MG132 (25 μM) had a marked decrease in H2AK119Ub, as has been previously described (Dantuma et al., 2006). These data suggest that ASXL1 loss contributes to myeloid transformation through a BAP1-independent mechanism.

Loss of ASXL1 Is Associated with Global Loss of H3K27me3

The results described above led us to hypothesize that ASXL1 loss leads to BAP1-independent effects on chromatin state and on target gene expression. To assess the genome-wide effects of ASXL1 loss on chromatin state, we performed chromatin immunoprecipitation followed by next generation sequencing (ChIP-seq) for histone modifications known to be associated with PcG [histone H3 lysine 27 trimethylation (H3K27me3)] or TxG activity [histone H3 lysine 4 trimethylation (H3K4me3)] in UKE1 cells expressing empty vector or two independent validated shRNAs for ASXL1. ChIP-Seq data analysis revealed a significant reduction in genome-wide H3K27me3 transcriptional start site occupancy with ASXL1 knockdown compared to empty vector ($p = 2.2 \times 10^{-16}$; Figure 3A). Approximately 20% of genes (n = 4,686) were initially marked by H3K27me3 in their promoter regions (defined as 1.5 kb downstream and 0.5 kb upstream of the transcriptional start site). Among these genes, ~27% had a 2-fold reduction in H3K27me3 (n = 1,309) and ~66% had a 1.5-fold reduction in H3K27me3 (n = 3,092), respectively, upon ASXL1 knockdown. No significant effect was seen on H3K4me3 transcriptional start site occupancy with ASXL1 depletion (Figure 3A). We next evaluated whether loss of ASXL1 might be associated with loss of H3K27me3 globally by performing western blot analysis on purified histones from UKE1 cells transduced with empty vector or shRNAs for ASXL1 knockdown. This analysis revealed a significant decrease in global H3K27me3 with ASXL1 loss (Figure 3B), despite preserved expression of the core polycomb repressive complex 2 (PRC2) members EZH2, SUZ12, and EED. Similar effects on total H3K27me3 levels were seen following Asxl1 knockdown in Ba/F3 cells (Figure S3A). These results demonstrate that ASXL1 depletion leads to a marked reduction in genome-wide H3K27me3 in hematopoietic cells.

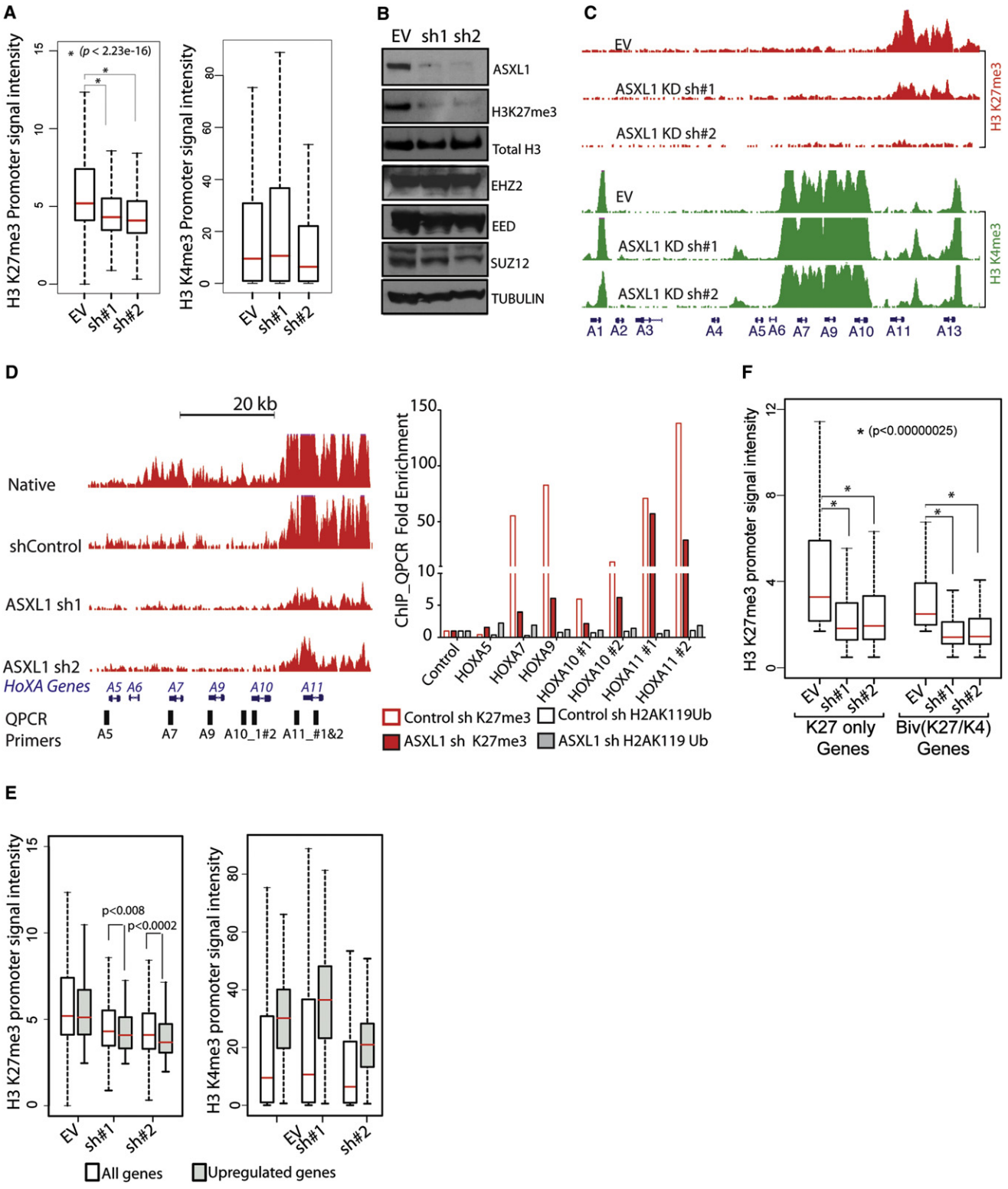

Figure 3. ASXL1 Loss Is Associated with Loss of H3K27me3 and with Increased Expression of Genes Poised for Transcription

(A) ASXL1 loss is associated with a significant genome-wide decrease in H3K27me3 as illustrated by box plot showing the 25th, 50th, and 75th percentiles for H3K27me3 and H3K4me3 enrichment at transcription start sites in UKE1 cells treated with an empty vector or shRNAs directed against ASXL1. The whiskers indicate the most extreme data point less than 1.5 interquartile range from box and the red bar represents the median.

(B) Loss of ASXL1 is associated with a global loss of H3K27me3 without affecting PRC2 component expression as shown by western blot of purified histones from cells with UKE1 knockdown and western blot for core PRC2 component in whole cell lysates from ASXL1 knockdown UKE1 cells.

Detailed analysis of ChIP-seq data revealed that genomic regions marked by large H3K27me3 domains in control cells displayed more profound loss of H3K27me3 upon loss of ASXL1. Genome-wide analysis of the ChIP-Seq data from control and ASXL1 shRNA treated cells revealed that the sites that lose H3K27me3 in the ASXL1 knockdown cells were on average ~6.6 kb in length, while the sites that maintained H3K27me3 were on average ~3.1 kb in length ($p < 10^{-16}$) (Figure S3B). This is visually illustrated by the reduction in H3K27me3 at the posterior *HOXA* cluster (Figure 3C) and at the *HOXB and HOXC* loci (Figure S3C). The association of ASXL1 loss with loss of H3K27me3 abundance at the *HOXA* locus was confirmed by ChIP for H3K27me3 in control and ASXL1 knockdown cells followed by qPCR (ChIP-qPCR) across the *HOXA* locus (Figure 3D). ChIP-qPCR in control and knockdown cells revealed a modest increase in H2AK119Ub with ASXL1 loss at the *HOXA* locus (Figure 3D), in contrast to the more significant reduction in H3K27me3. In contrast to the large decrease in H3K27me3 levels at the *HOXA* locus with ASXL1 knockdown, a subset of loci had much less significant reduction in H3K27me3, in particular at loci whose promoters were marked by sharp peaks of H3K27me3 (Figure S3D). Intersection of gene expression and ChIP-Seq data revealed that genes overexpressed in ASXL1 knockdown cells were simultaneously marked with both activating (H3K4me3) and repressive (H3K27me3) domains in control cells (Figures 3E and 3F). This finding suggests that the transcriptional repression mediated by ASXL1 in myeloid cells is most apparent at loci poised for transcription with bivalent chromatin domains. Indeed, the effects of ASXL1 loss on H3K27me3 occupancy were most apparent at genes whose promoters were marked by the dual presence of H3K27me3 and H3K4me3 (Figure 3F). We cannot exclude the possibility that H3K4me3 and H3K27me3 exist in different populations within the homogeneous cell lines being studied, but the chromatin and gene expression data are consistent with an effect of ASXL1 loss on loci with bivalent chromatin domains (Bernstein et al., 2006; Mikkelsen et al., 2007).

Enforced Expression of ASXL1 in Leukemic Cells Results in Suppression of *HOXA* Gene Expression, a Global Increase in H3K27me3, and Growth Suppression

We next investigated whether reintroduction of wild-type ASXL1 protein could restore H3K27me3 levels in *ASXL1* mutant leukemia cells. We stably expressed wild-type ASXL1 in NOMO1 and KBM5 cells, homozygous *ASXL1* mutant human leukemia cell lines, which do not express ASXL1 protein (Figure 4A and Figure S4A). ASXL1 expression resulted in a global increase in H3K27me3 as assessed by histone western blot analysis (Figure 4A). Liquid chromotography/mass spectrometry of purified histones in NOMO1 cells expressing ASXL1 confirmed a ~2.5-fold increase in trimethylated H3K27 peptide and significant increases in dimethylated H3K27 in NOMO1 cells expressing ASXL1 compared to empty vector control (Figure 4B). ASXL1 add-back resulted in growth suppression (Figure 4C) and in decreased *HOXA* gene expression in NOMO1 cells (Figure 4D). ASXL1 add-back similarly resulted in decreased expression of *HOXA* target genes in KBM5 cells (Figures S4A and S4B). ChIP-qPCR revealed a strong enrichment in ASXL1 binding at the *HOXA* locus in NOMO1 cells expressing ASXL1, demonstrating that the *HOXA* locus is a direct target of ASXL1 in hematopoietic cells (Figure 4E).

ASXL1 Loss Leads to Exclusion of H3K27me3 and EZH2 from the HoxA Cluster Consistent with a Direct Effect of ASXL1 on PRC2 Recruitment

We next investigated whether the effects of ASXL1 loss on H3K27me3 was due to inhibition of PRC2 recruitment to specific target loci. ChIP-qPCR for H3K27me3 in SET2 cells with ASXL1 knockdown or control revealed a loss of H3K27me3 enrichment at the posterior *HoxA* locus with ASXL1 knockdown (Figures 5A and 5B). We observed a modest, variable increase in H3K4me3 enrichment at the *HOXA* locus with *ASXL1* depletion in SET2 cells (Figure 5C). We similarly assessed H3K27me3 enrichment in primary bone marrow leukemic cells from acute myeloid leukemia patients, wild-type and mutant for *ASXL1,* which likewise revealed decreased H3K27me3 enrichment across the *HOXA* cluster in primary acute myeloid leukemia samples with *ASXL1* mutations compared to *ASXL1*-wild-type acute myeloid leukemia samples (Figure 5D).

Given the consistent effects of ASXL1 depletion on H3K27me3 abundance at the *HOXA* locus, we then evaluated the occupancy of EZH2, a core PRC2 member, at the *HoxA* locus. ChIP-Seq for H3K27me3 in native SET2 and UKE1 cells identified that H3K27me3 is present with a dome-like enrichment pattern at the 5′ end of the posterior *HOXA* cluster (Figure 5A); ChIP-qPCR revealed that EZH2 is prominently enriched in this same region in parental SET2 cells (Figure 5E). Importantly, ASXL1 depletion resulted in loss of EZH2 enrichment at the *HOXA* locus (Figure 5E), suggesting that ASXL1 is required for EZH2 occupancy and for PRC2-mediated repression of the posterior *HOXA* locus.

(C) Loss of H3K27me3 is evident at the *HOXA* locus as shown by ChIP-Seq promoter track signals across the *HOXA* locus in UKE1 cells treated with an EV or shRNA knockdown of ASXL1.

(D) H3K27me3 ChIP-Seq promoter track signals from *HOXA5* to *HOXA13* in UKE1 cells treated with shRNA control or one of 2 anti-*ASXL1* shRNAs with location of primers used in ChIP-quantitative PCR (ChIP-qPCR) validation. ChIP for H3K27me3 and H2AK119Ub followed by ChIP-qPCR in cells treated with control or ASXL1 knockdown confirms a significant decrease in H3K27me3 at the *HOXA* locus with ASXL1 knockdown but minimal effects of ASXL1 knockdown on H2AK119Ub levels at the same primer locations.

(E) Integrating gene-expression data with H3K27me3/H3K4me3 ChIP-Seq identifies a significant correlation between alterations in chromatin state and increases in gene expression following ASXL1 loss at loci normally marked by the simultaneous presence of H3K27me3 and H3K4me3 in control cells.

(F) Loss of H3K27me3 is seen at promoters normally marked by the presence of H3K27me3 alone or at promoters co-occupied by H3K27me3 and H3K4me3 in the control state.

See also Figure S3.

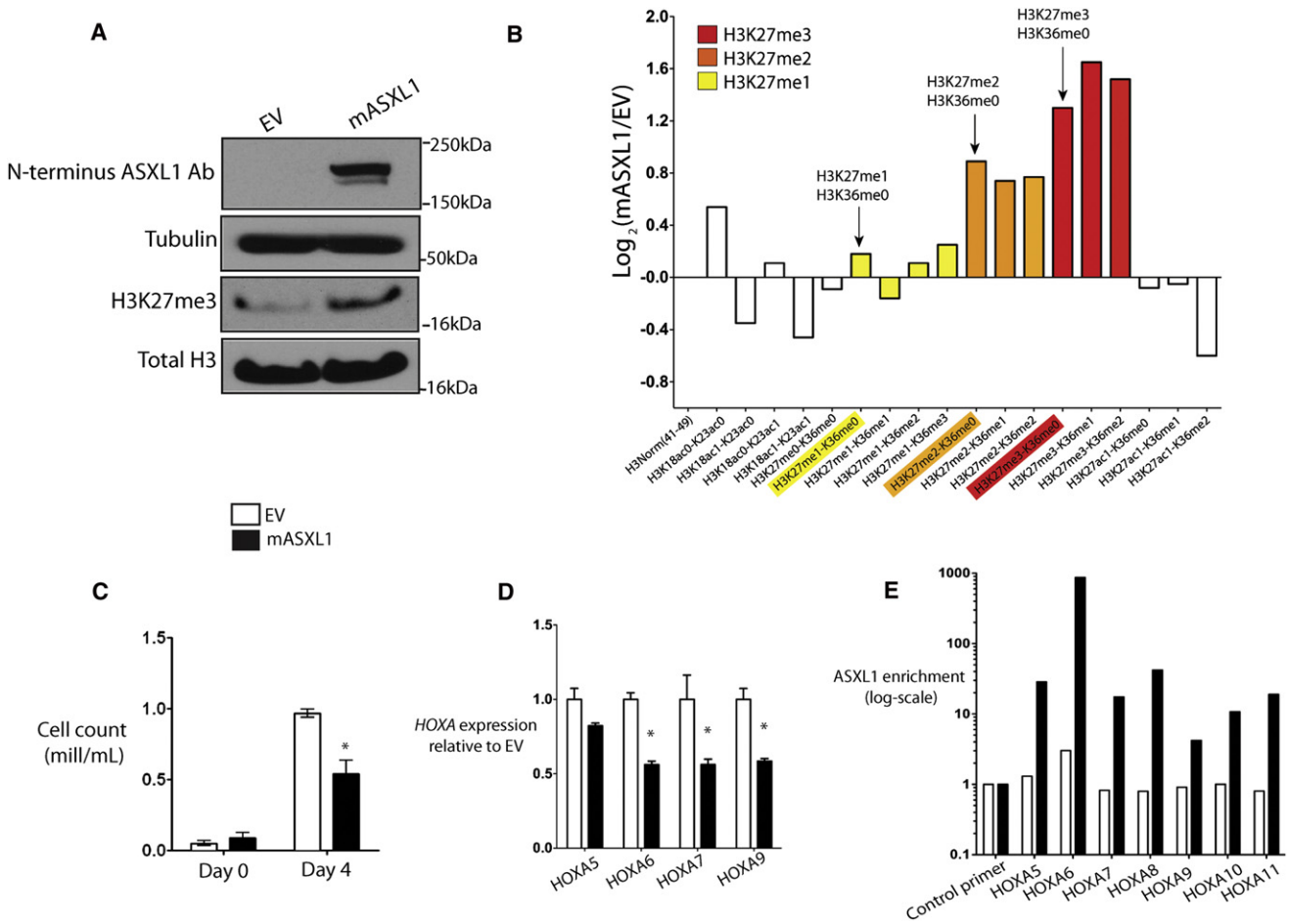

Figure 4. Expression of ASXL1 in ASXL1-Null Leukemic Cells Results in Global Increase in H3K27me2/3, Growth Suppression, and Suppression of *HoxA* Gene Expression

(A and B) ASXL1 expression in ASXL1 null NOMO1 cells is associated with a global increase in H3K27me3 as detected by western blot of purified histones (A) as well as by quantitative liquid-chromatography/mass spectrometry of H3 peptides from amino acids 18–40 (B) (arrows indicate quantification of H3K27me1/2/3).

(C) ASXL1 overexpression results in growth suppression in 7-day growth assay performed in triplicate.

(D) Overexpression of ASXL1 was associated with a decrement in posterior *HoxA* gene expression in NOMO1 cells as shown by qRT-PCR for *HOXA5, 6, 7, and 9*.

(E) This downregulation in *HOXA* gene expression was concomitant with a strong enrichment of ASXL1 at the loci of these genes as shown by chromatin immunoprecipitation of ASXL1 followed by quantitative PCR with BCRRP1 as a control locus.

Error bars represent standard deviation of target gene expression relative to control. See also Figure S4.

ASXL1 Physically Interacts with Members of the PRC2 in Human Myeloid Leukemic Cells

Given that ASXL1 localizes to PRC2 target loci and ASXL1 depletion leads to loss of PRC2 occupancy and H3K27me2, we investigated whether ASXL1 might physically interact with the PRC2 complex in hematopoietic cells. Co-immunoprecipitation studies using an anti-FLAG antibody in HEK293T cells expressing empty vector, hASXL1-FLAG alone, or hASXL1-FLAG plus hEZH2 cDNA revealed a clear co-immunoprecipitation of FLAG-ASXL1 with endogenous EZH2 and with ectopically expressed EZH2 (Figure 6A). Similarly, co-immuniprecipitation of FLAG-ASXL1 revealed physical association between ASXL1 and endogenous SUZ12 in 293T cells (Figure 6A). Immunoprecipitations were performed in the presence of benzonase to ensure that the protein-protein interactions observed were DNA-independent (Figure 6B) (Muntean et al., 2010). We then assessed whether endogenous ASXL1 formed a complex with PRC2 members in hematopoietic cells. We performed IP for EZH2 or ASXL1 followed by western blotting for partner proteins in SET2 and UKE1 cells, which are wild-type for *ASXL1*, *SUZ12, EZH2,* and *EED*. These co-immunoprecipitation assays all revealed a physical association between ASXL1 and EZH2 in SET2 (Figure 6B) and UKE1 cells (Figure S5). By contrast, immunoprecipitation of endogenous ASXL1 did not reveal evidence of protein-protein interactions between ASXL1 and BMI1 (Figure S5). Likewise, immunoprecipitation of BMI1 enriched for PRC1 member RING1A, but failed to enrich for ASXL1, suggesting a lack of interaction between ASXL1 and the PRC1 repressive complex (Figure 6C).

ASXL1 Loss Collaborates with NRasG12D In Vivo

We and others previously reported that *ASXL1* mutations are most common in chronic myelomonocytic leukemia and frequently co-occur with *N/K-Ras* mutations in chronic

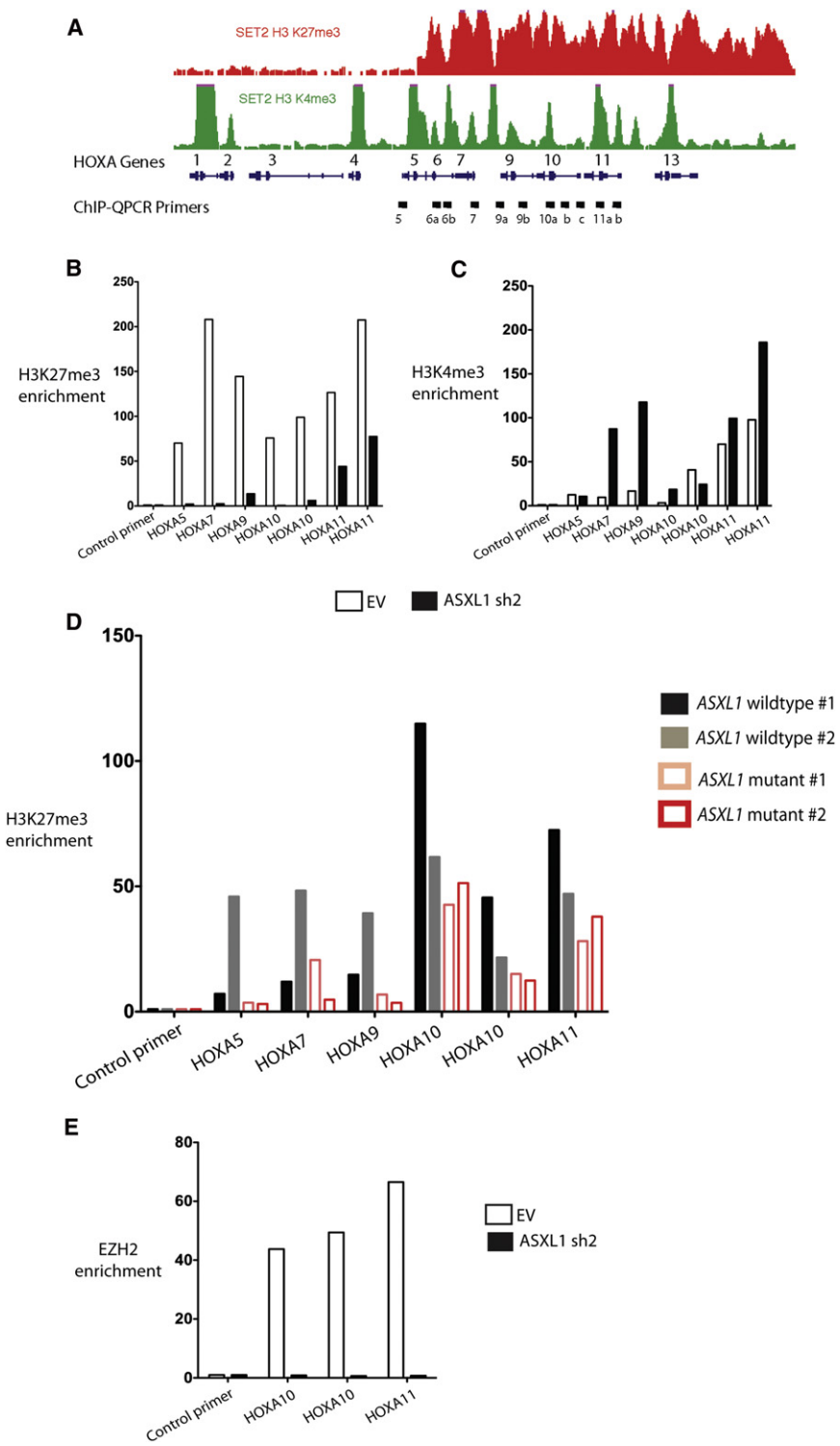

Figure 5. ASXL1 Loss Is Associated with Loss of PRC2 Recruitment at the *HOXA* Locus

(A) Chromatin-immunoprecipitation (ChIP) for H3K27me3 and H3K4me3 followed by next-generation sequencing reveals the abundance and localization of H3K27me3 and H3K4me3 at the *HoxA* locus in SET2 cells.

(B and C) ChIP for H3K27me3 (B) and H3K4me3 (C) followed by quantitative PCR (qPCR) across the 5′ *HOXA* locus in SET2 cells treated with an empty vector or stable knockdown of ASXL1 reveals a consistent downregulation of H3K27me3 across the 5′ *HOXA* locus following ASXL1 loss and a modest increase in H3K4me3 at the promoters of 5′ *HOXA* genes with ASXL1 loss [primer locations are shown in (A)].

(D) Similar ChIP for H3K27me3 followed by qPCR across the *HOXA* locus in primary leukemic blasts from two patients with *ASXL1* mutations versus two without *ASXL1* mutations reveals H3K27me3 loss across the *HOXA* locus in *ASXL1* mutant cells.

(E) ChIP for EZH2 followed by qPCR at the 5′ end of *HOXA* locus in SET2 cells reveals loss of EZH2 enrichment with ASXL1 loss in SET2 cells. CHIP-qPCR was performed in biologic duplicates and ChIP-qPCR data is displayed as enrichment relative to input. qPCR at the gene body of *RRP1,* a region devoid of H3K4me3 or H3K27me3, is utilized as a control locus.

The error bars represent standard deviation.

myelomonocytic leukemia (Abdel-Wahab et al., 2011; Patel et al., 2010). We therefore investigated the effects of combined *NRasG12D* expression and Asxl1 loss in vivo. To do this, we expressed *NRasG12D* in combination with an empty vector expressing GFP alone or one of two different Asxl1 shRNA constructs in whole bone marrow cells and transplanted these cells into lethally irradiated recipient mice. We validated our ability to effectively knock down ASXL1 in vivo by performing qRT-PCR in hematopoietic cells from recipient mice (Figure 7A and Figure S6A). Consistent with our in vitro data implicating the HoxA cluster as an ASXL1 target locus, we noted a marked increase in *HoxA9* and *HoxA10* expression in bone marrow nucleated cells from mice expressing *NRasG12D* in combination with Asxl1 shRNA compared to mice expressing *NRasG12D* alone (Figure 7B).

Expression of oncogenic *NRasG12D* and an empty shRNA vector control led to a progressive myeloproliferative disorder as previously described (MacKenzie et al., 1999). In contrast, expression of *NRasG12D* in combination with validated mASXL1 knockdown vectors resulted in accelerated myeloproliferation and impaired survival compared with mice transplanted with *NRasG12D*/EV (median survival 0.8 month for ASXL1 shRNA versus 3 months for control shRNA vector: $p < 0.005$; Figure 7C) We also noted impaired survival with an independent *mASXL1* shRNA construct ($p < 0.01$; Figure S6B) Mice transplanted with *NRasG12D/Asxl1*

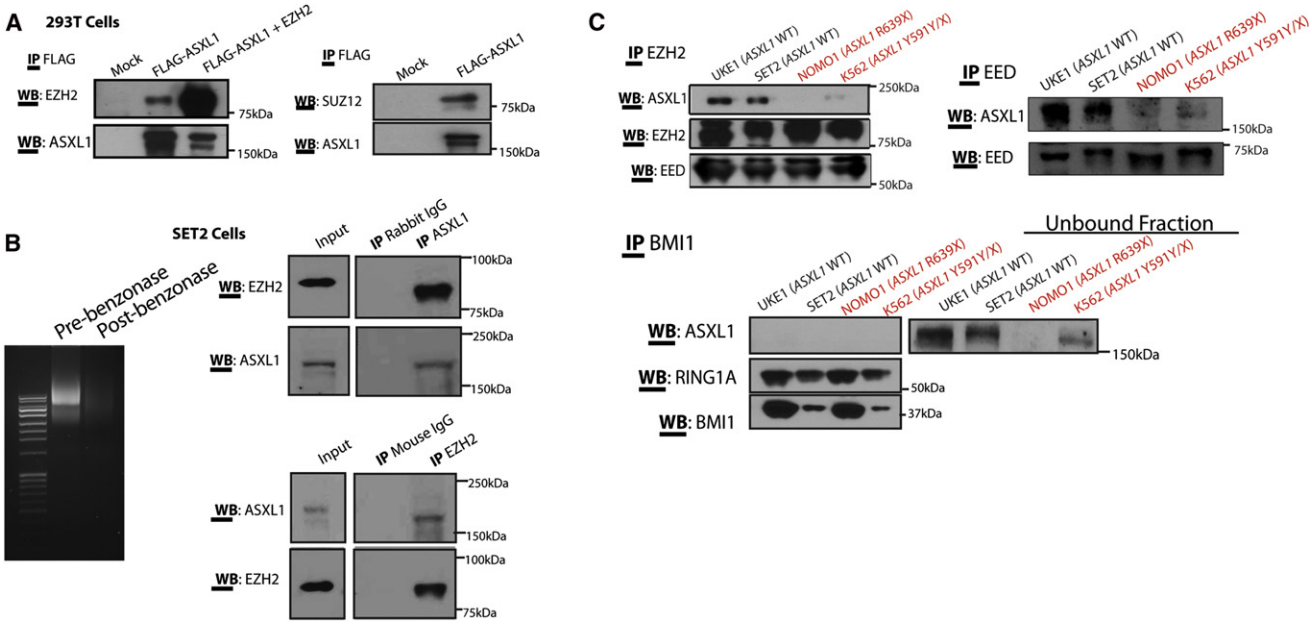

Figure 6. ASXL1 Interacts with the PRC2 in Hematopoietic Cells

(A) Physical interaction between ASXL1 and EZH2 is demonstrated by transient transfection of HEK293T cells with FLAG-hASXL1 cDNA with or without hEZH2 cDNA followed by immunoprecipitation (IP) of FLAG epitope and western blotting for EZH2 and ASXL1.

(B) HEK293T cells were transiently transfected with FLAG-hASXL1 cDNA followed by IP of FLAG epitope and western blotting for SUZ12 and ASXL1. Endogenous interaction of ASXL1 with PRC2 members was also demonstrated by IP of endogenous EZH2 and ASXL1 followed by western blotting of the other proteins in whole cell lysates from SET2 cells.

(C) Lysates from the experiment shown in (B) were treated with benzonase to ensure nucleic acid free conditions in the lysates prior to IP as shown by ethidium bromide staining of an agarose gel before and after benzonase treatment. IP of endogenous EZH2 and embryonic ectoderm development (EED) in a panel of ASXL1-wild-type and mutant human leukemia cells reveals a specific interaction between ASXL1 and PRC2 members in *ASXL1*-wildype human myeloid leukemia cells. In contrast, IP of the PRC1 member BMI1 failed to pull down ASXL1.

See also Figure S5.

shRNA had increased splenomegaly and hepatomegaly compared with *NRasG12D*/EV transplanted mice (Figures 7D and 7E; Figure S6C). Histological analysis revealed a significant increase in myeloid infiltration of the spleen and livers of mice transplanted with *NRasG12D/Asxl1* shRNA (Figure S6D).

Mice transplanted with *NRasG12D/Asxl1* shRNA, but not *NRasG12D/EV*, experienced progressive, severe anemia (Figure 7F). It has previously been identified that expression of oncogenic *K/N-Ras* in multiple models of human/murine hematopoietic systems results in alterations in the erythroid compartment (Braun et al., 2006; Darley et al., 1997; Zhang et al., 2003). We noted an expansion of $CD71^{high}/Ter119^{high}$ erythroblasts in the bone marrow of mice transplanted with *NRasG12D*/Asxl1 shRNA compared with *NRasG12D*/EV mice (Figure S6E). We also noted increased granulocytic expansion in mice engrafted with *NRasG12D/Asxl1* shRNA positive cells, as shown by the presence of increased neutrophils in the peripheral blood (Figure S6D) and the expansion of Gr1/Mac1 double-positive cells in the bone marrow by flow cytometry (Figure S6F).

Previous studies have shown that hematopoietic cells from mice expressing oncogenic *Ras* alleles or other mutations that activate kinase signaling pathways do not exhibit increased self-renewal in colony replating assays (Braun et al., 2004; MacKenzie et al., 1999). This is in contrast to the immortalization of hematopoietic cells in vitro seen with expression of *MLL-AF9* (Somervaille and Cleary, 2006) or deletion of *Tet2* (Moran-Crusio et al., 2011). Bone marrow cells from mice with combined overexpression of NRasG12D plus Asxl1 knockdown had increased serial replating (to five passages) compared to bone marrow cells from mice engrafted with *NRasG12D/EV* cells (Figure 7G). These studies demonstrate that Asxl1 loss cooperates with oncogenic *NRasG12D* in vivo.

DISCUSSION

The data presented here identify that ASXL1 loss in hematopoietic cells results in reduced H3K27me3 occupancy through inhibition of PRC2 recruitment to specific oncogenic target loci. Recent studies have demonstrated that genetic alterations in the PRC2 complex occur in a spectrum of human malignancies (Bracken and Helin, 2009; Margueron and Reinberg, 2011; Sauvageau and Sauvageau, 2010). Activating mutations and overexpression of *EZH2* occur most commonly in epithelial malignancies and in lymphoid malignancies (Morin et al., 2010; Varambally et al., 2002). However, there are increasing genetic data implicating mutations that impair PRC2 function in the pathogenesis of myeloid malignancies. These include the loss-of-function mutations in *EZH2* (Abdel-Wahab et al., 2011; Ernst et al., 2010; Nikoloski et al., 2010) and less common somatic loss-of-function mutations in *SUZ12*, *EED*, and *JARID2* (Score

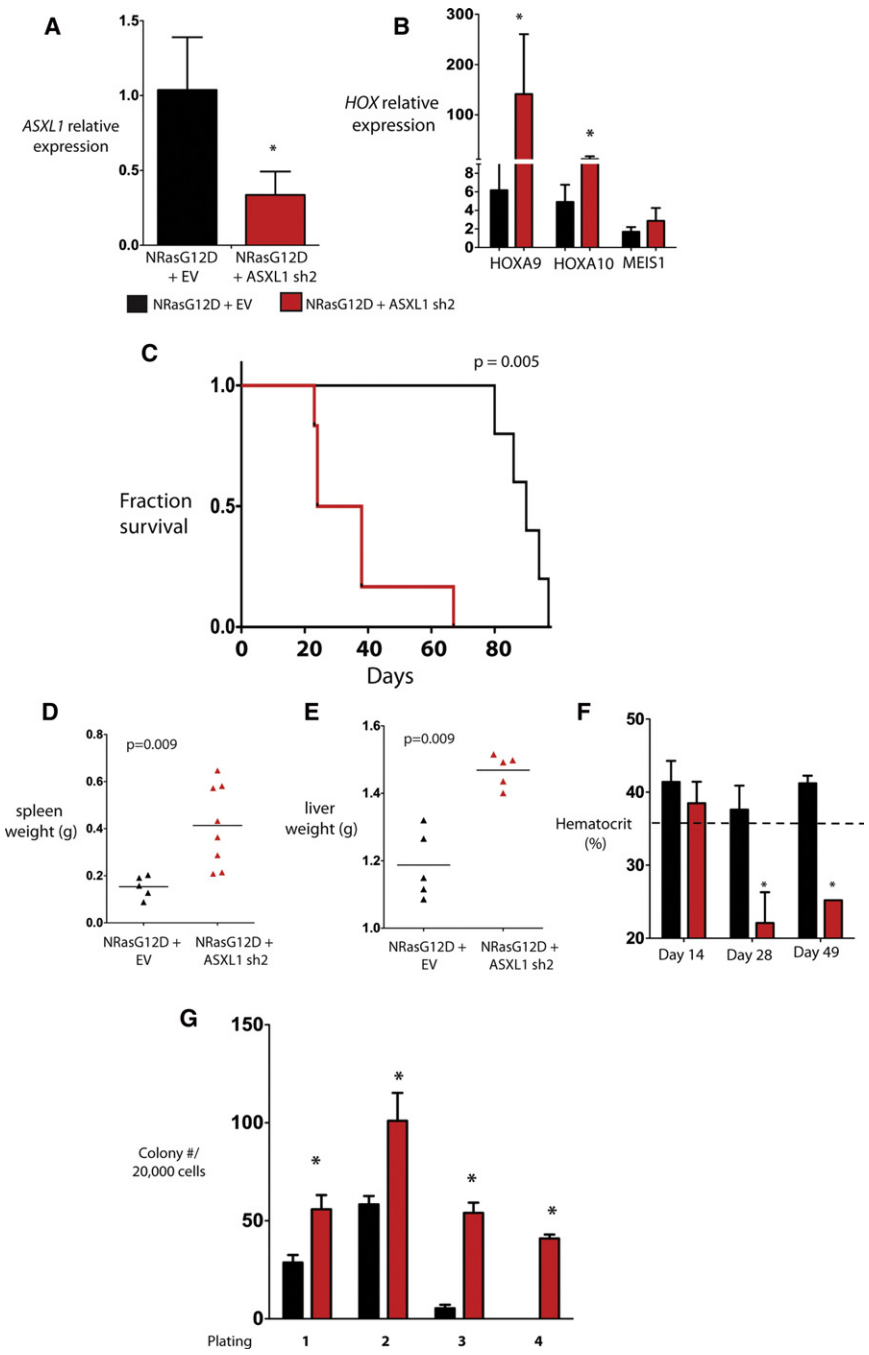

Figure 7. Asxl1 Silencing Cooperates with NRasG12D In Vivo

(A) Retroviral bone marrow transplantation of NRasG12D with or without an shRNA for Asxl1 resulted in decreased *Asxl1* mRNA expression as shown by qRT-PCR results in nucleated peripheral blood cells from transplanted mice at 14 days following transplant.

(B) qRT-PCR revealed an increased expression of *HOXA9* and *HOXA10* but not *MEIS1* in the bone marrow of mice sacrificed 19 days following transplantation.

(C) Transplantation of bone marrow cells bearing overexpression of NRasG12D in combination with downregulation of Asxl1 led to a significant hastening of death compared to mice transplanted with NRasG12D/EV.

(D–F) Mice transplanted with NRasG12D/ASXL1 shRNA experienced increased splenomegaly (D) and hepatomegaly (E), and progressive anemia (F) compared with mice transplanted with NRasG12D + an empty vector (EV).

(G) Bone marrow cells from mice with combined NRasG12D overexpression/Asxl1 knockdown revealed increased serial replating compared with cells from NRasG12D/EV mice. Error bars represent standard deviation relative to control. Asterisk indicates $p < 0.05$ (two-tailed, Mann Whitney U test).

See also Figure S6.

et al., 2012) in patients with myeloproliferative neoplasms, myelodysplastic syndrome, and chronic myelomonocytic leukemia. The data from genetically-engineered mice also support this concept with Ezh2 overexpression models, revealing evidence of promotion of malignant transformation (Herrera-Merchan et al., 2012), and recent studies demonstrate a role for Ezh2 loss in leukemogenesis (Simon et al., 2012). Thus, it appears that alterations in normal PRC2 activity and/or H3K27me3 abundance in either direction may promote malignant transformation. Our data implicate *ASXL1* mutations as an additional genetic alteration that leads to impaired PRC2 function in patients with myeloid malignancies. In many cases, patients present with concomitant heterozygous mutations in multiple PRC2 members or in *EZH2* and *ASXL1*; these data suggest that haploinsufficiency for multiple genes that regulate PRC2 function can cooperate in hematopoietic transformation through additive alterations in PRC2 function.

Many studies have investigated how mammalian PcG proteins are recruited to chromatin in order to repress gene transcription and specify cell fate in different tissue contexts. Recent in silico analysis suggested that ASXL proteins found in animals contain a number of domains that likely serve in the recruitment of chromatin modulators and transcriptional effectors to DNA (Aravind and Iyer, 2012). Data from ChIP and co-immunoprecipitation experiments presented here suggest a specific role for ASXL1 in epigenetic regulation of gene expression by facilitating PRC2-mediated transcriptional repression of known leukemic oncogenes. Thus, ASXL1 may serve as a scaffold for recruitment of the PRC2 complex to specific loci in hematopoietic cells, as has been demonstrated for JARID2 in embryonic stem cells (Landeira et al., 2010; Pasini et al., 2010; Peng et al., 2009; Shen et al., 2009).

Recent data suggested that ASXL1 might interact with BAP1 to form a H2AK119 deubiquitanase (Scheuermann et al., 2010).

However, our data suggest that ASXL1 loss leads to BAP1-independent alterations in chromatin state and gene expression in hematopoietic cells. These data are consonant with recent genetic studies, which have shown that germline loss of BAP1 increases susceptibility to uveal melanoma and mesothelioma (Testa et al., 2011; Wiesner et al., 2011). In contrast, germline loss of ASXL1 is seen in the developmental disorder Bohring-Opitz Syndrome (Hoischen et al., 2011), but has not, to date, been observed as a germline solid tumor susceptibility locus. Whether alterations in H2AK119 deubiquitanase function due to alterations in BAP1 and/or ASXL1 can contribute to leukemogenesis or to the pathogenesis of other malignancies remains to be determined.

Integration of gene expression and chromatin state data following ASXL1 loss identified specific loci with a known role in leukemogenesis that are altered in the setting of *ASXL1* mutations. These include the posterior *HOXA* cluster, including *HOXA9,* which has a known role in hematopoietic transformation. We demonstrate that ASXL1 normally serves to tightly regulate *HOXA* gene expression in hematopoietic cells, and that loss of ASXL1 leads to disordered *HOXA* gene expression in vitro and in vivo. Overexpression of 5′ *HOXA* genes is a well-described oncogenic event in hematopoietic malignancies (Lawrence et al., 1996), and previous studies have shown that *HOXA9* overexpression leads to transformation in vitro and in vivo when co-expressed with *MEIS1* (Kroon et al., 1998). Interestingly, *ASXL1* loss was not associated with an increase in *MEIS1* expression, suggesting that transformation by *ASXL1* mutations requires the co-occurrence of oncogenic disease alleles which dysregulate additional target loci. These data and our in vivo studies suggest that *ASXL1* loss, in combination with co-occurring oncogenes, can lead to hematopoietic transformation and increased self-renewal. Further studies in mice expressing ASXL1 shRNA or with conditional deletion of *Asxl1* alone and in concert with leukemogeneic disease alleles will provide additional insight into the role of ASXL1 loss in hematopoietic stem/progenitor function and in leukemogenesis.

Given that somatic mutations in chromatin modifying enzymes (Dalgliesh et al., 2010), DNA methyltransferases (Ley et al., 2010), and other genes implicated in epigenetic regulation occur commonly in human cancers, it will be important to use epigenomic platforms to elucidate how these disease alleles contribute to oncogenesis in different contexts. The data here demonstrate how integrated epigenetic and functional studies can be used to elucidate the function of somatic mutations in epigenetic modifiers. In addition, it is likely that many known oncogenes and tumor suppressors contribute, at least in part, to transformation through direct or indirect alterations in the epigenetic state (Dawson et al., 2009). Subsequent epigenomic studies of human malignancies will likely uncover novel routes to malignant transformation in different malignancies, and therapeutic strategies that reverse epigenetic alterations may be of specific benefit in patients with mutations in epigenetic modifiers.

EXPERIMENTAL PROCEDURES

Cell Culture

HEK293T cells were cultured in Dulbecco's modified Eagle's medium (DMEM) supplemented with 10% fetal bovine serum (FBS) and nonessential amino acids. Human leukemia cell lines were cultured in RPMI-1640 medium supplemented with 10% FBS+1 mM hydrocortisone+10% horse serum (UKE1 cells), RPMI-1640 supplemented with 10% FBS (K562, MOLM13, KCL22, KU812 cells), RPMI-1640 supplemented with 20% FBS (SET2, NOMO1, Monomac-6 cells), or IMDM + 20% FBS (KBM5 cells). For proliferation studies, 1×10^3 cells were seeded in 1 ml volume of media in triplicate and cell number was counted manually daily for 7 days by Trypan blue exclusion.

Plasmid Constructs, Mutagenesis Protocol, Short Hairpin RNA, and Small Interfering RNA

See Supplemental Information.

Primary Acute Myeloid Leukemia Patient Samples and *ASXL1*, *BAP1*, *EZH2*, *SUZ12*, and *EED* Genomic DNA Sequencing Analysis

Approval was obtained from the institutional review boards at Memorial Sloan-Kettering Cancer Center and at the Hospital of the University of Pennsylvania for these studies, and informed consent was provided according to the Declaration of Helsinki. Please see Supplemental Information for details on DNA sequence analysis.

Western Blot and Immunoprecipitation Analysis

Western blots were carried out using the following antibodies: ASXL1 (Clone N-13; Santa Cruz (sc-85283); N-terminus directed), ASXL1 (Clone 2049C2a; Santa Cruz (sc-81053); C terminus directed), BAP1 [clone 3C11; Santa Cruz (sc-13576)], BMI1 (Abcam ab14389), EED (Abcam ab4469), EZH2 (Active Motif 39933 or Millipore 07-689), FLAG (M2 FLAG; Sigma A2220), Histone H3 lysine 27 trimethyl (Abcam ab6002), Histone H2A Antibody II (Cell Signaling Technologies 2578), Ubiquityl-Histone H2AK119 (Clone D27C4; Cell Signaling Technologies 8240), RING1A (Abcam ab32807), SUZ12 (Abcam ab12073), and total histone H3 (Abcam ab1791), and tubulin (Sigma, T9026). Antibodies different from the above used for immunoprecipitation include: ASXL1 [clone H105X; Santa Cruz (sc-98302)], FLAG (Novus Biological Products; NBP1-06712), and EZH2 (Active Motif 39901). Immunoprecipitation and pull-down reactions were performed in an immunoprecipitation buffer (150 mM NaCl, 20 mM Tris (pH 7.4–7.5), 5 mM EDTA, 1% Triton, 100 mM sodium orthovanadate, protease arrest (Genotec), 1 mM PMSF, and phenylarsene oxide). To ensure nuclease-free immunoprecipitation conditions, immunoprecipitations were also performed using the following methodology (Muntean et al., 2010): cells were lysed in BC-300 buffer (20 mM Tris-HCl (pH 7.4), 10% glycerol, 300 mM KCl, 0.1% NP-40) and the cleared lysate was separated from the insoluble pellet and treated with MgCl2 to 2.5 mM and benzonase (Emanuel Merck, Darmstadt) at a concentration of 1,250 U/ml. The lysate was then incubated for 1–1.5 hr at 4°. The reaction was then stopped with addition of 5 mM EDTA. DNA digestion is confirmed on an ethidium bromide agarose gel. We then set up our immunoprecipitation by incubating our lysate overnight at 4°.

Histone Extraction and Histone LC/MS Analysis

See Supplemental Information.

Gene Expression Analysis

Total RNA was extracted from cells using QIAGEN's RNeasy Plus Mini kit (Valencia, CA, USA). cDNA synthesis, labeling, hybridization, and quality control were carried out as previously described (Figueroa et al., 2008). Ten micrograms of RNA was then used for generation of labeled cRNA according to the manufacturer's instructions (Affymetrix, Santa Clara, CA, USA). Hybridization of the labeled cRNA fragments and washing, staining, and scanning of the arrays were carried out as per instructions of the manufacturer. Labeled cRNA from CD34+ cells treated with either ASXL1 siRNA or controls were analyzed using the Affymetrix HG-U133-Plus2.0 platform and from UKE1 cells using the Illumina Href8 array. All expression profile experiments were carried out using biological duplicates. "Present" calls in ≥80% of samples were captured and quantile normalized across all samples on a per-chip basis. Raw expression values generated by Genome Studio (Illumina) were filtered to exclude probesets having expression values below negative background in ≥80% of samples. Probesets remaining after background filtering were log-2 transformed and quantile normalized on a per-chip basis. qRT-PCR was performed on cDNA using SYBR green quantification in an ABI 7500

sequence detection system. The sequences of all qRT-PCR primers are listed in the Supplemental Information.

Chromatin Immunoprecipitation and Antibodies

ChIP experiments for H3K4me3, H3K27me3, and H3K36me3 were carried out as described previously (Bernstein et al., 2006; Mikkelsen et al., 2007). Cells were cross-linked in 1% formaldehyde, lysed, and sonicated with a Branson 250 Sonifier to obtain chromatin fragments in a size range between 200 and 700 bp. Solubilized chromatin was diluted in ChIP dilution buffer (1:10) and incubated with antibody overnight at 4°C. Protein A sepharose beads (Sigma) were used to capture the antibody-chromatin complex and washed with low salt, LiCl, as well as TE (pH 8.0) wash buffers. Enriched chromatin fragments were eluted at 65°C for 10 min, subjected to cross-link reversal at 65°C for 5 hr, and treated with Proteinase K (1 mg/ml), before being extracted by phenol-chloroform-isoamyl alcohol, and ethanol precipitated. ChIP DNA was then quantified by QuantiT Picogreen dsDNA Assay kit (Invitrogen). ChIP experiments for ASXL1 were carried out on nuclear preps. Cross-linked cells were incubated in swelling buffer (0.1 M Tris pH 7.6, 10 mM KOAc, 15 mM MgOAc, 1% NP40), on ice for 20 minutes, passed through a 16G needle 20 times and centrifuged to collect nuclei. Isolated nuclei were then lysed, sonicated, and immunoprecipitated as described above. Antibodies used for ChIP include anti-H3K4me3 (Abcam ab8580), anti-H3K27me3 (Upstate 07-449), anti-H3K36me3 (Abcam ab9050), and anti-ASXL1 [clone H105X; Santa Cruz (sc-98302)], and Ubiquityl-Histone H2AK119 (Clone D27C4; Cell Signaling Technologies 8240).

Sequencing Library Preparation, Illumina/Solexa Sequencing, and Read Alignment and Generation of Density Maps

See Supplemental Information.

HOXA Nanostring nCounter Gene Expression CodeSet

Direct digital mRNA analysis of *HOXA* cluster gene expression was performed using a Custom CodeSet including each *HOXA gene* (NanoString Technologies). Synthesis of the oligonucleotides was done by NanoString Technologies, and hybridization and analysis were done using the Prep Station and Digital Analyzer purchased from the company.

Animal Use, Retroviral Bone Marrow Transplantation, Flow Cytometry, and Colony Assays

Animal care was in strict compliance with institutional guidelines established by the Memorial Sloan-Kettering Cancer Center, the National Academy of Sciences Guide for the Care and Use of Laboratory Animals, and the Association for Assessment and Accreditation of Laboratory Animal Care International. All animal procedures were approved by the Institutional Animal Care and Use Committee (IACUC) at Memorial Sloan-Kettering Cancer Center. See Supplemental Information for more details on animal experiments.

Statistical Analysis

Statistical significance was determined by the Mann-Whitney U test and Fisher's exact test using Prism GraphPad software. Significance of survival differences was calculated using Log-rank (Mantel-Cox) test. $p < 0.05$ was considered statistically significant. Normalized expression data from CD34+ cord blood was used as a Gene Set Enrichment Analysis query of the C2 database (MSig DB) where 1,000 permutations of the genes was used to generate a null distribution. A pre-ranked gene list, containing genes upregulated at least $\log_2$ 0.5-fold, in which the highest ranked genes corresponds to the genes, with the largest fold-difference between Asxl1 hairpin-treated UKE1 cells and those treated with empty vector, was used to query the C2 MSig DB as described above.

ACCESSION NUMBERS

All microarray data used in this manuscript are deposited in Gene Expression Omnibus (http://www.ncbi.nlm.nih.gov/geo/) under GEO accession number GSE38692. The ChIP-Seq data are deposited under GEO accession number GSE38861.

SUPPLEMENTAL INFORMATION

Supplemental Information includes six figures, two tables, and Supplemental Experimental Procedures and can be found with this article online at http://dx.doi.org/10.1016/j.ccr.2012.06.032.

ACKNOWLEDGMENTS

This work was supported by a grant from the Starr Cancer Consortium to R.L.L. and B.E.B., by grants from the Gabrielle's Angel Fund to R.L.L. and O.A.-W., by a grant from the Anna Fuller Fund to R.L.L., and by an NHLBI grant to B.E.B. (5U01HL100395). I.A. and B.E.B. are Howard Hughes Medical Institute Early Career Scientists. A.M. is a Burroughs Wellcome Clinical Translational Scholar and Scholar of the Leukemia and Lymphoma Society. X.Z. and S.D.N. are supported by a Leukemia and Lymphoma Society SCOR award, and F.P. is supported by an American Italian Cancer Foundation award. O.A.-W. is an American Society of Hematology Basic Research Fellow and is supported by a grant from the NIH K08 Clinical Investigator Award (1K08CA160647-01). J.P.P. is supported by an American Society of Hematology Trainee Research Award.

Received: January 7, 2012
Revised: May 21, 2012
Accepted: June 28, 2012
Published: August 13, 2012

REFERENCES

Abdel-Wahab, O., Pardanani, A., Patel, J., Wadleigh, M., Lasho, T., Heguy, A., Beran, M., Gilliland, D.G., Levine, R.L., and Tefferi, A. (2011). Concomitant analysis of EZH2 and ASXL1 mutations in myelofibrosis, chronic myelomonocytic leukemia and blast-phase myeloproliferative neoplasms. Leukemia *25*, 1200–1202.

Aravind, L., and Iyer, L.M. (2012). The HARE-HTH and associated domains: Novel modules in the coordination of epigenetic DNA and protein modifications. Cell Cycle *11*, 119–131.

Bejar, R., Stevenson, K., Abdel-Wahab, O., Galili, N., Nilsson, B., Garcia-Manero, G., Kantarjian, H., Raza, A., Levine, R.L., Neuberg, D., and Ebert, B.L. (2011). Clinical effect of point mutations in myelodysplastic syndromes. N. Engl. J. Med. *364*, 2496–2506.

Bernstein, B.E., Mikkelsen, T.S., Xie, X., Kamal, M., Huebert, D.J., Cuff, J., Fry, B., Meissner, A., Wernig, M., Plath, K., et al. (2006). A bivalent chromatin structure marks key developmental genes in embryonic stem cells. Cell *125*, 315–326.

Bott, M., Brevet, M., Taylor, B.S., Shimizu, S., Ito, T., Wang, L., Creaney, J., Lake, R.A., Zakowski, M.F., Reva, B., et al. (2011). The nuclear deubiquitinase BAP1 is commonly inactivated by somatic mutations and 3p21.1 losses in malignant pleural mesothelioma. Nat. Genet. *43*, 668–672.

Bracken, A.P., and Helin, K. (2009). Polycomb group proteins: navigators of lineage pathways led astray in cancer. Nat. Rev. Cancer *9*, 773–784.

Braun, B.S., Tuveson, D.A., Kong, N., Le, D.T., Kogan, S.C., Rozmus, J., Le Beau, M.M., Jacks, T.E., and Shannon, K.M. (2004). Somatic activation of oncogenic Kras in hematopoietic cells initiates a rapidly fatal myeloproliferative disorder. Proc. Natl. Acad. Sci. USA *101*, 597–602.

Braun, B.S., Archard, J.A., Van Ziffle, J.A., Tuveson, D.A., Jacks, T.E., and Shannon, K. (2006). Somatic activation of a conditional KrasG12D allele causes ineffective erythropoiesis in vivo. Blood *108*, 2041–2044.

Cho, Y.S., Kim, E.J., Park, U.H., Sin, H.S., and Um, S.J. (2006). Additional sex comb-like 1 (ASXL1), in cooperation with SRC-1, acts as a ligand-dependent coactivator for retinoic acid receptor. J. Biol. Chem. *281*, 17588–17598.

Dalgliesh, G.L., Furge, K., Greenman, C., Chen, L., Bignell, G., Butler, A., Davies, H., Edkins, S., Hardy, C., Latimer, C., et al. (2010). Systematic sequencing of renal carcinoma reveals inactivation of histone modifying genes. Nature *463*, 360–363.

Dantuma, N.P., Groothuis, T.A., Salomons, F.A., and Neefjes, J. (2006). A dynamic ubiquitin equilibrium couples proteasomal activity to chromatin remodeling. J. Cell Biol. *173*, 19–26.

Darley, R.L., Hoy, T.G., Baines, P., Padua, R.A., and Burnett, A.K. (1997). Mutant N-RAS induces erythroid lineage dysplasia in human CD34+ cells. J. Exp. Med. *185*, 1337–1347.

Dawson, M.A., Bannister, A.J., Göttgens, B., Foster, S.D., Bartke, T., Green, A.R., and Kouzarides, T. (2009). JAK2 phosphorylates histone H3Y41 and excludes HP1alpha from chromatin. Nature *461*, 819–822.

Ernst, T., Chase, A.J., Score, J., Hidalgo-Curtis, C.E., Bryant, C., Jones, A.V., Waghorn, K., Zoi, K., Ross, F.M., Reiter, A., et al. (2010). Inactivating mutations of the histone methyltransferase gene EZH2 in myeloid disorders. Nat. Genet. *42*, 722–726.

Figueroa, M.E., Reimers, M., Thompson, R.F., Ye, K., Li, Y., Selzer, R.R., Fridriksson, J., Paietta, E., Wiernik, P., Green, R.D., et al. (2008). An integrative genomic and epigenomic approach for the study of transcriptional regulation. PLoS One *3*, e1882.

Fisher, C.L., Lee, I., Bloyer, S., Bozza, S., Chevalier, J., Dahl, A., Bodner, C., Helgason, C.D., Hess, J.L., Humphries, R.K., and Brock, H.W. (2010a). Additional sex combs-like 1 belongs to the enhancer of trithorax and polycomb group and genetically interacts with Cbx2 in mice. Dev. Biol. *337*, 9–15.

Fisher, C.L., Pineault, N., Brookes, C., Helgason, C.D., Ohta, H., Bodner, C., Hess, J.L., Humphries, R.K., and Brock, H.W. (2010b). Loss-of-function Additional sex combs-like1 mutations disrupt hematopoiesis but do not cause severe myelodysplasia or leukemia. Blood *115*, 38–46.

Gaebler, C., Stanzl-Tschegg, S., Heinze, G., Holper, B., Milne, T., Berger, G., and Vécsei, V. (1999). Fatigue strength of locking screws and prototypes used in small-diameter tibial nails: a biomechanical study. J. Trauma *47*, 379–384.

Gelsi-Boyer, V., Trouplin, V., Adélaïde, J., Bonansea, J., Cervera, N., Carbuccia, N., Lagarde, A., Prebet, T., Nezri, M., Sainty, D., et al. (2009). Mutations of polycomb-associated gene ASXL1 in myelodysplastic syndromes and chronic myelomonocytic leukaemia. Br. J. Haematol. *145*, 788–800.

Harbour, J.W., Onken, M.D., Roberson, E.D., Duan, S., Cao, L., Worley, L.A., Council, M.L., Matatall, K.A., Helms, C., and Bowcock, A.M. (2010). Frequent mutation of BAP1 in metastasizing uveal melanomas. Science *330*, 1410–1413.

Herrera-Merchan, A., Arranz, L., Ligos, J.M., de Molina, A., Dominguez, O., and Gonzalez, S. (2012). Ectopic expression of the histone methyltransferase Ezh2 in haematopoietic stem cells causes myeloproliferative disease. Nat Commun *3*, 623.

Hoischen, A., van Bon, B.W., Rodríguez-Santiago, B., Gilissen, C., Vissers, L.E., de Vries, P., Janssen, I., van Lier, B., Hastings, R., Smithson, S.F., et al. (2011). De novo nonsense mutations in ASXL1 cause Bohring-Opitz syndrome. Nat. Genet. *43*, 729–731.

Kroon, E., Krosl, J., Thorsteinsdottir, U., Baban, S., Buchberg, A.M., and Sauvageau, G. (1998). Hoxa9 transforms primary bone marrow cells through specific collaboration with Meis1a but not Pbx1b. EMBO J. *17*, 3714–3725.

Kumar, A.R., Li, Q., Hudson, W.A., Chen, W., Sam, T., Yao, Q., Lund, E.A., Wu, B., Kowal, B.J., and Kersey, J.H. (2009). A role for MEIS1 in MLL-fusion gene leukemia. Blood *113*, 1756–1758.

Landeira, D., Sauer, S., Poot, R., Dvorkina, M., Mazzarella, L., Jørgensen, H.F., Pereira, C.F., Leleu, M., Piccolo, F.M., Spivakov, M., et al. (2010). Jarid2 is a PRC2 component in embryonic stem cells required for multi-lineage differentiation and recruitment of PRC1 and RNA Polymerase II to developmental regulators. Nat. Cell Biol. *12*, 618–624.

Lawrence, H.J., Sauvageau, G., Humphries, R.K., and Largman, C. (1996). The role of HOX homeobox genes in normal and leukemic hematopoiesis. Stem Cells *14*, 281–291.

Lee, S.W., Cho, Y.S., Na, J.M., Park, U.H., Kang, M., Kim, E.J., and Um, S.J. (2010). ASXL1 represses retinoic acid receptor-mediated transcription through associating with HP1 and LSD1. J. Biol. Chem. *285*, 18–29.

Ley, T.J., Ding, L., Walter, M.J., McLellan, M.D., Lamprecht, T., Larson, D.E., Kandoth, C., Payton, J.E., Baty, J., Welch, J., et al. (2010). DNMT3A mutations in acute myeloid leukemia. N. Engl. J. Med. *363*, 2424–2433.

MacKenzie, K.L., Dolnikov, A., Millington, M., Shounan, Y., and Symonds, G. (1999). Mutant N-ras induces myeloproliferative disorders and apoptosis in bone marrow repopulated mice. Blood *93*, 2043–2056.

Margueron, R., and Reinberg, D. (2011). The Polycomb complex PRC2 and its mark in life. Nature *469*, 343–349.

Metzeler, K.H., Becker, H., Maharry, K., Radmacher, M.D., Kohlschmidt, J., Mrózek, K., Nicolet, D., Whitman, S.P., Wu, Y.Z., Schwind, S., et al. (2011). ASXL1 mutations identify a high-risk subgroup of older patients with primary cytogenetically normal AML within the ELN Favorable genetic category. Blood *118*, 6920–6929.

Mikkelsen, T.S., Ku, M., Jaffe, D.B., Issac, B., Lieberman, E., Giannoukos, G., Alvarez, P., Brockman, W., Kim, T.K., Koche, R.P., et al. (2007). Genome-wide maps of chromatin state in pluripotent and lineage-committed cells. Nature *448*, 553–560.

Moran-Crusio, K., Reavie, L., Shih, A., Abdel-Wahab, O., Ndiaye-Lobry, D., Lobry, C., Figueroa, M.E., Vasanthakumar, A., Patel, J., Zhao, X., et al. (2011). Tet2 loss leads to increased hematopoietic stem cell self-renewal and myeloid transformation. Cancer Cell *20*, 11–24.

Morin, R.D., Johnson, N.A., Severson, T.M., Mungall, A.J., An, J., Goya, R., Paul, J.E., Boyle, M., Woolcock, B.W., Kuchenbauer, F., et al. (2010). Somatic mutations altering EZH2 (Tyr641) in follicular and diffuse large B-cell lymphomas of germinal-center origin. Nat. Genet. *42*, 181–185.

Muntean, A.G., Tan, J., Sitwala, K., Huang, Y., Bronstein, J., Connelly, J.A., Basrur, V., Elenitoba-Johnson, K.S., and Hess, J.L. (2010). The PAF complex synergizes with MLL fusion proteins at HOX loci to promote leukemogenesis. Cancer Cell *17*, 609–621.

Nikoloski, G., Langemeijer, S.M., Kuiper, R.P., Knops, R., Massop, M., Tönnissen, E.R., van der Heijden, A., Scheele, T.N., Vandenberghe, P., de Witte, T., et al. (2010). Somatic mutations of the histone methyltransferase gene EZH2 in myelodysplastic syndromes. Nat. Genet. *42*, 665–667.

Park, U.H., Yoon, S.K., Park, T., Kim, E.J., and Um, S.J. (2011). Additional sex comb-like (ASXL) proteins 1 and 2 play opposite roles in adipogenesis via reciprocal regulation of peroxisome proliferator-activated receptor gamma. J. Biol. Chem. *286*, 1354–1363.

Pasini, D., Cloos, P.A., Walfridsson, J., Olsson, L., Bukowski, J.P., Johansen, J.V., Bak, M., Tommerup, N., Rappsilber, J., and Helin, K. (2010). JARID2 regulates binding of the Polycomb repressive complex 2 to target genes in ES cells. Nature *464*, 306–310.

Peng, J.C., Valouev, A., Swigut, T., Zhang, J., Zhao, Y., Sidow, A., and Wysocka, J. (2009). Jarid2/Jumonji coordinates control of PRC2 enzymatic activity and target gene occupancy in pluripotent cells. Cell *139*, 1290–1302.

Pratcorona, M., Abbas, S., Sanders, M., Koenders, J., Kavelaars, F., Erpelinck-Verschueren, C., Zeilemaker, A., Lowenberg, B., and Valk, P. (2012). Acquired mutations in ASXL1 in acute myeloid leukemia: prevalence and prognostic value. Haematologica *97*, 388–392.

Sauvageau, M., and Sauvageau, G. (2010). Polycomb group proteins: multi-faceted regulators of somatic stem cells and cancer. Cell Stem Cell *7*, 299–313.

Scheuermann, J.C., de Ayala Alonso, A.G., Oktaba, K., Ly-Hartig, N., McGinty, R.K., Fraterman, S., Wilm, M., Muir, T.W., and Müller, J. (2010). Histone H2A deubiquitinase activity of the Polycomb repressive complex PR-DUB. Nature *465*, 243–247.

Score, J., Hidalgo-Curtis, C., Jones, A.V., Winkelmann, N., Skinner, A., Ward, D., Zoi, K., Ernst, T., Stegelmann, F., Dohner, K., et al. (2012). Inactivation of polycomb repressive complex 2 components in myeloproliferative and myelodysplastic/myeloproliferative neoplasms. Blood *119*, 1208–1213.

Shen, X., Kim, W., Fujiwara, Y., Simon, M.D., Liu, Y., Mysliwiec, M.R., Yuan, G.C., Lee, Y., and Orkin, S.H. (2009). Jumonji modulates polycomb activity and self-renewal versus differentiation of stem cells. Cell *139*, 1303–1314.

Simon, C., Chagraoui, J., Krosl, J., Gendron, P., Wilhelm, B., Lemieux, S., Boucher, G., Chagnon, P., Drouin, S., Lambert, R., et al. (2012). A key role

for EZH2 and associated genes in mouse and human adult T-cell acute leukemia. Genes Dev. *26*, 651–656.

Sinclair, D.A., Milne, T.A., Hodgson, J.W., Shellard, J., Salinas, C.A., Kyba, M., Randazzo, F., and Brock, H.W. (1998). The Additional sex combs gene of Drosophila encodes a chromatin protein that binds to shared and unique Polycomb group sites on polytene chromosomes. Development *125*, 1207–1216.

Somervaille, T.C., and Cleary, M.L. (2006). Identification and characterization of leukemia stem cells in murine MLL-AF9 acute myeloid leukemia. Cancer Cell *10*, 257–268.

Takeda, A., Goolsby, C., and Yaseen, N.R. (2006). NUP98-HOXA9 induces long-term proliferation and blocks differentiation of primary human CD34+ hematopoietic cells. Cancer Res. *66*, 6628–6637.

Testa, J.R., Cheung, M., Pei, J., Below, J.E., Tan, Y., Sementino, E., Cox, N.J., Dogan, A.U., Pass, H.I., Trusa, S., et al. (2011). Germline BAP1 mutations predispose to malignant mesothelioma. Nat. Genet. *43*, 1022–1025.

Thol, F., Friesen, I., Damm, F., Yun, H., Weissinger, E.M., Krauter, J., Wagner, K., Chaturvedi, A., Sharma, A., Wichmann, M., et al. (2011). Prognostic significance of ASXL1 mutations in patients with myelodysplastic syndromes. J. Clin. Oncol. *29*, 2499–2506.

Varambally, S., Dhanasekaran, S.M., Zhou, M., Barrette, T.R., Kumar-Sinha, C., Sanda, M.G., Ghosh, D., Pienta, K.J., Sewalt, R.G., Otte, A.P., et al. (2002). The polycomb group protein EZH2 is involved in progression of prostate cancer. Nature *419*, 624–629.

Wiesner, T., Obenauf, A.C., Murali, R., Fried, I., Griewank, K.G., Ulz, P., Windpassinger, C., Wackernagel, W., Loy, S., Wolf, I., et al. (2011). Germline mutations in BAP1 predispose to melanocytic tumors. Nat. Genet. *43*, 1018–1021.

Zhang, J., Socolovsky, M., Gross, A.W., and Lodish, H.F. (2003). Role of Ras signaling in erythroid differentiation of mouse fetal liver cells: functional analysis by a flow cytometry-based novel culture system. Blood *102*, 3938–3946.

Cancer Cell
Article

H2.0-like Homeobox Regulates Early Hematopoiesis and Promotes Acute Myeloid Leukemia

Masahiro Kawahara,[1,6] Ashley Pandolfi,[1,6] Boris Bartholdy,[1,6] Laura Barreyro,[1] Britta Will,[1] Michael Roth,[1] Ujunwa C. Okoye-Okafor,[1] Tihomira I. Todorova,[1] Maria E. Figueroa,[3] Ari Melnick,[3] Constantine S. Mitsiades,[4,5] and Ulrich Steidl[1,2,*]

[1]Department of Cell Biology and Albert Einstein Cancer Center
[2]Department of Medicine (Oncology)
Albert Einstein College of Medicine, Bronx, NY 10461, USA
[3]Hematology and Oncology Division, Department of Pharmacology, Weill Cornell Medical College, New York, NY 10065, USA
[4]Department of Medical Oncology, Dana Farber Cancer Institute, Boston, MA 02215, USA
[5]Department of Medicine, Harvard Medical School, Boston, MA 02215, USA
[6]These authors contributed equally to this work
*Correspondence: ulrich.steidl@einstein.yu.edu
http://dx.doi.org/10.1016/j.ccr.2012.06.027

SUMMARY

Homeobox domain-containing transcription factors are important regulators of hematopoiesis. Here, we report that increased levels of nonclustered H2.0-like homeobox (HLX) lead to loss of functional hematopoietic stem cells and formation of aberrant progenitors with unlimited serial clonogenicity and blocked differentiation. Inhibition of HLX reduces proliferation and clonogenicity of leukemia cells, overcomes the differentiation block, and leads to prolonged survival. HLX regulates a transcriptional program, including *PAK1* and *BTG1*, that controls cellular differentiation and proliferation. *HLX* is overexpressed in 87% of patients with acute myeloid leukemia (AML) and independently correlates with inferior overall survival ($n = 601$, $p = 2.3 \times 10^{-6}$). Our study identifies HLX as a key regulator in immature hematopoietic and leukemia cells and as a prognostic marker and therapeutic target in AML.

INTRODUCTION

Transcription factors are critical for the regulation of normal hematopoiesis as well as leukemogenesis (Friedman, 2007; Laiosa et al., 2006; Tenen, 2003). Several members of the *Hox* (class I homeobox genes) family of transcription factors, which contain a conserved homeobox domain and are organized into four major gene clusters in humans, have been implicated in the functioning of hematopoietic stem and progenitor cells (HSPC) as well as in leukemic transformation and the generation of leukemia-initiating cells (Argiropoulos and Humphries, 2007; Krumlauf, 1994; Sitwala et al., 2008). Less is known about the role of nonclustered (class II) homeobox genes in hematopoiesis and leukemia. Members of the *CDX* family, for instance, have been found to be overexpressed in acute leukemias and to regulate *Hox* gene expression (Bansal et al., 2006; Scholl et al., 2007). Transcriptional analysis of purified stem and progenitor populations has recently been utilized as a powerful tool to identify critical regulators of stem and progenitor cell function and transformation to leukemia-initiating cells (Krivtsov et al., 2006; Majeti et al., 2009; Passegué et al., 2004; Saito et al., 2010; Somervaille and Cleary, 2006; Steidl et al., 2006, 2007). Our analysis of preleukemic HSPC in a murine model of AML revealed the nonclustered H2.0-like homeobox (*Hlx*) gene to be 4-fold upregulated compared to wild-type (WT) HSPC (Steidl et al., 2006; data not shown), suggesting that *Hlx* may be involved in malignant transformation. *HLX* is the highly conserved human-murine homolog of the homeobox gene *H2.0*, which shows tissue-specific expression throughout development in *Drosophila melanogaster* (Allen et al., 1991; Hentsch et al., 1996). Additional

Significance

AML is a heterogeneous disease with poor clinical outcome. Less than one third of patients achieve durable remission with current treatment regimens, and prognostication and risk stratification of individual patients is challenging. New molecular targets are desired for more effective therapeutic intervention. We identify the nonclustered homeobox gene *Hlx* as a key regulator in immature hematopoietic and leukemia cells. *HLX* is overexpressed in the majority of patients with AML, and high levels of *HLX* correlate with inferior survival. Inhibition of HLX overcomes the differentiation block of AML and prolongs survival in an in vivo model. As a key factor controlling malignant cell growth and differentiation, *HLX* may be a prognostic and therapeutic target in AML and possibly other types of cancer.

studies two decades ago detected *HLX* expression in hematopoietic progenitors and in leukemic blasts of patients with AML, and a study of HLX-deficient fetal liver cells suggested a decrease of colony-formation capacity (Deguchi and Kehrl, 1991; Deguchi et al., 1992). However, the precise function of HLX in HSPC and its role in leukemia have not been studied, which was the objective of the present study. AML is a heterogeneous disease with overall poor clinical outcome (Marcucci et al., 2011). Less than one third of patients with AML achieve durable remission with current treatment regimens. Furthermore, prognostication and risk stratification of individual patients remains very challenging, in particular in favorable and standard risk groups. New targets need to be identified for effective and individualized therapeutic intervention.

RESULTS

HLX Overexpression Impairs Hematopoietic Reconstitution and Leads to a Decrease in Long-Term Hematopoietic Stem Cells and Persistence of a Small Progenitor Population

To examine the functional consequences of elevated HLX levels on hematopoiesis, we sorted lineage-negative (Lin^-), Kit^+ bone marrow (BM) cells from Ly5.2(CD45.2)$^+$ WT mice, transduced them with a lentivirus expressing HLX and GFP, or GFP alone as a control (Figures 1A and 1B), and transplanted them into lethally irradiated congenic Ly5.1(CD45.1)$^+$ recipient mice. Transduction efficiency of control lentivirus and Hlx lentivirus was comparable, with both at approximately 50% (see Figure S1A available online). Twenty-four hours after transplantation, both control and HLX-overexpressing GFP^+ $Ly5.2^+$ donor cells were detected in the BM at similar frequencies (42.8% and 41.6%, respectively) (Figure 1C), indicating equal homing of the transplanted cells. Twelve weeks after transplantation, we evaluated hematopoietic multilineage reconstitution in the peripheral blood. Both groups engrafted robustly with an average donor chimerism of Ly5.2 cells of 80% (SD: 10%) and 85% (SD: 9%) in the control and Hlx groups, respectively. However, although mice transplanted with control cells showed 35% (SD: 17%) GFP^+ cells in the peripheral blood 12 weeks after transplantation, mice transplanted with *Hlx*-transduced cells displayed drastically fewer GFP^+ cells, with only 0.07% (SD: 0.06%), demonstrating a severe defect of HLX-overexpressing cells in hematopoietic reconstitution (Figure 1D). To determine the cellular compartments in which HLX was effective, we analyzed stem and progenitor cells in recipient BM. No GFP^+ long-term hematopoietic stem cells (LT-HSC; $Thy1^{lo}Flk2^-LSK$ [$Lin^-Sca1^+Kit^+$]) in mice transplanted with HLX-expressing cells were detected, whereas control mice displayed, on average, 42% (SD: 20%) GFP^+ LT-HSC (Figure 1E). Furthermore, in contrast to control animals, we could not find any GFP^+ HLX-expressing short-term HSC (ST-HSCs; $Thy1^{lo}Flk2^+LSK$), multipotent progenitors (MPP; $Thy1^-$ $Flk2^+LSK$), common myeloid progenitors (CMP; $Lin^-Kit^+Sca\text{-}1^-Fc\gamma RII/III^{lo}CD34^{lo}$), granulocyte-monocyte progenitors (GMP; $Lin^-Kit^+Sca\text{-}1^-Fc\gamma RII/III^+CD34^+$). or megakaryocyte-erythrocyte progenitors (MEP; $Lin^-Kit^+Sca\text{-}1^-Fc\gamma RII/III^-CD34^-$), indicating that HLX acts at the level of the earliest hematopoietic stem cells (Figure S1B). When we analyzed *Hlx*-GFP-transduced Lin^-Kit^+ (KL) cells by AnnexinV/DAPI staining, both control and HLX-overexpressing cells displayed the same low percentage of apoptotic-necrotic cells (Figure S1C), indicating that HLX acts by a mechanism other than induction of apoptosis or necrosis. Further analysis for donor-derived cell populations persisting upon HLX overexpression revealed a small population of GFP^+, CD45.2(Ly.5.2)$^+$, Lin^-, $CD34^-$, and Kit^- cells, which were still present in the BM 12 weeks after transplantation (Figure 1F). Analysis for additional surface markers revealed that these cells were characterized by intermediate expression of CD11b, as well as high expression of CD49b and CD44 (Figure 1G, left panel), which is consistent with the surface phenotype of myeloid precursor cells slightly past the GMP stage (Novershtern et al., 2011). This $CD45^+CD11b^{mid}CD49b^+CD44^+$ cell population was 16-fold expanded upon HLX expression in comparison to control ($p = 1.1 \times 10^{-5}$) (Figure 1G, right panel).

HLX Confers Unlimited Serial Clonogenicity to $CD34^-Kit^-$ Hematopoietic Cells

Next, we performed in vitro colony formation assays of transduced LSK cells. *Hlx*-transduced LSK cells formed slightly fewer and smaller colonies than did control-transduced LSK cells in the initial plating (Figure 2A, left panel, and Figure S2A). To evaluate long-term clonogenic potential of HLX-overexpressing cells, we performed serial-replating assays. LSK cells overexpressing HLX showed greater clonogenic capacity in the second to fifth plating, in comparison to control-transduced cells, and maintained serial replating capacity through the sixth to ninth plating (Figure 2A, right panel), showing a de facto immortalization of this clonogenic progenitor population by HLX. In addition, colonies were noticeably larger in size after five platings compared to control (Figure 2B). Analysis of cells isolated from the initial plating revealed that HLX overexpression led to a decrease of Kit^+ cells, similar to the in vivo phenotype, and an increased proportion of phenotypically more mature $CD34^-Kit^-$ cells in comparison to control-transduced cells (Figure 2C). To further characterize this persisting population, we examined a panel of cell surface markers. Although the $CD34^-Kit^-$ cells were negative for CD11c, CD25, FcγRII/III, CD61, CD115, and CD150 (Figure S2B; and data not shown), they expressed CD49b and CD44, as well as intermediate levels of CD11b (Figure S2B), similar to our observations in vivo (Figure 1G). To determine which cellular subpopulation conferred the increased clonogenic capacity, we sorted equal numbers of $CD34^+Kit^+$ cells, $CD34^+Kit^-$ cells, $CD34^-Kit^+$ cells, and $CD34^-Kit^-$ cells from the first plating (populations I–IV, see Figure 2C), and subjected each individual population to colony formation assays. Only $CD34^-Kit^-$ cells derived from HLX-overexpressing cells formed a larger number of colonies in comparison to control cells, whereas all other populations did not display significant clonogenicity (Figure 2D). Furthermore, the HLX-overexpressing $GFP^+CD34^-Kit^-$ cells showed serial replating capacity through four rounds, whereas all other populations exhausted significantly earlier (Figure 2E). Finally, when we injected HLX-overexpressing $GFP^+CD34^-Kit^-$ cells from the fourth, sixth, or eighth plating into irradiated NOD-SCID-IL2Rgamma null (NSG) mice, GFP^+ cells were detectable after 7 weeks in the peripheral blood (Figure S2C; and data not shown). These data indicate that increased levels of HLX confer long-term clonogenicity to a population of $CD34^-Kit^-$ cells.

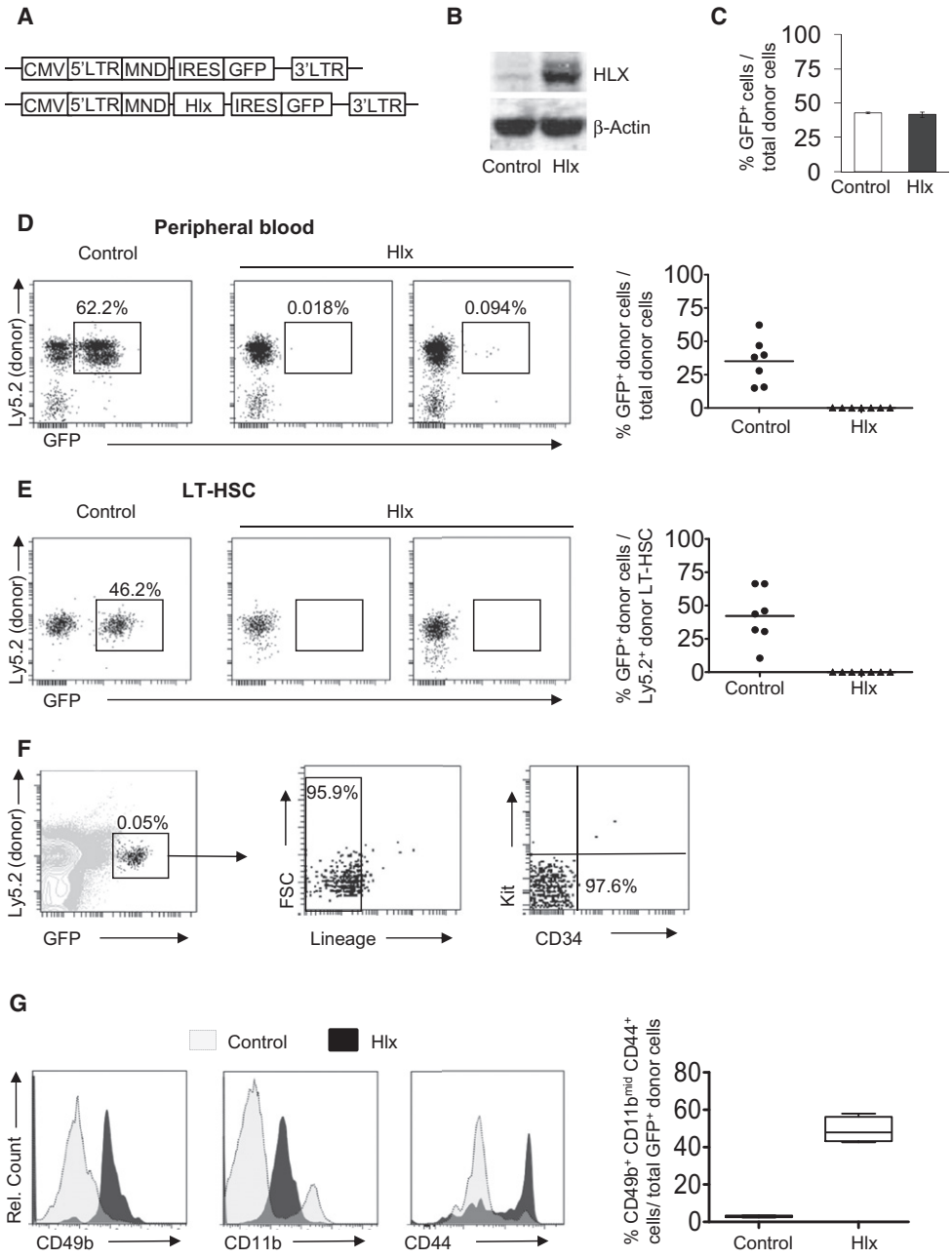

Figure 1. HLX Overexpression Impairs Hematopoietic Reconstitution and Leads to a Decrease in Long-Term Hematopoietic Stem Cells and Persistence of a Small Progenitor Population

(A) Schematics of lentiviral vectors.

(B) Increased protein expression of HLX in Lin$^-$Kit$^+$ cells after transduction with HLX-expressing lentivirus and sorting of GFP$^+$ cells.

(C) Homing is not affected by HLX overexpression. Lentivirus-transduced Lin$^-$Kit$^+$ cells (8×10^4) from WT C57BL/6 mice (Ly5.2) were transplanted into lethally irradiated congenic WT recipients (Ly5.1). Bone marrow mononuclear cells from recipients were analyzed 24 hr after transplantation. The frequency of GFP$^+$ cells in the donor population (Ly5.1$^-$Ly5.2$^+$) was assessed, and averages ± SD are shown (n = 3).

(D and E) Control- or Hlx-IRES-GFP-transduced Lin$^-$Kit$^+$ cells (Ly5.2) together with spleen cells from congenic WT mice (Ly5.1) were transplanted into lethally irradiated congenic WT recipients (Ly5.1) (n = 7) and analyzed 12 weeks after transplantation. Total GFP$^+$ cells in peripheral blood (D) and Lin$^-$Kit$^+$Sca$^+$ Thy1^{lo}Flk2$^-$ LT-HSC in bone marrow (E) are shown. Detailed gating scheme and additional analyses are shown in Figure S1. Means are indicated by horizontal lines in the panels on the right.

(F) Analysis of GFP$^+$ cells in total bone marrow cells from recipients transplanted with *Hlx*-transduced Lin$^-$Kit$^+$ cells after 12 weeks. Relative percentages of GFP$^+$, Lin$^-$, as well as CD34$^-$Kit$^-$ donor cells are indicated.

(G) CD49b, CD11b, and CD44 expression on donor Ly5.2$^+$GFP$^+$Lin$^-$Kit$^-$ cells from recipients transplanted with *Hlx*- or control-transduced Lin$^-$Kit$^+$ cells 6 weeks after transplantation. Representative histogram plots are shown on the left. Percentage of Ly5.2$^+$GFP$^+$Lin$^-$Kit$^-$ cells that coexpress CD49b$^+$, CD11b^{mid}, and CD44$^+$ are displayed for the control and Hlx groups in the right panel (n = 4/condition).

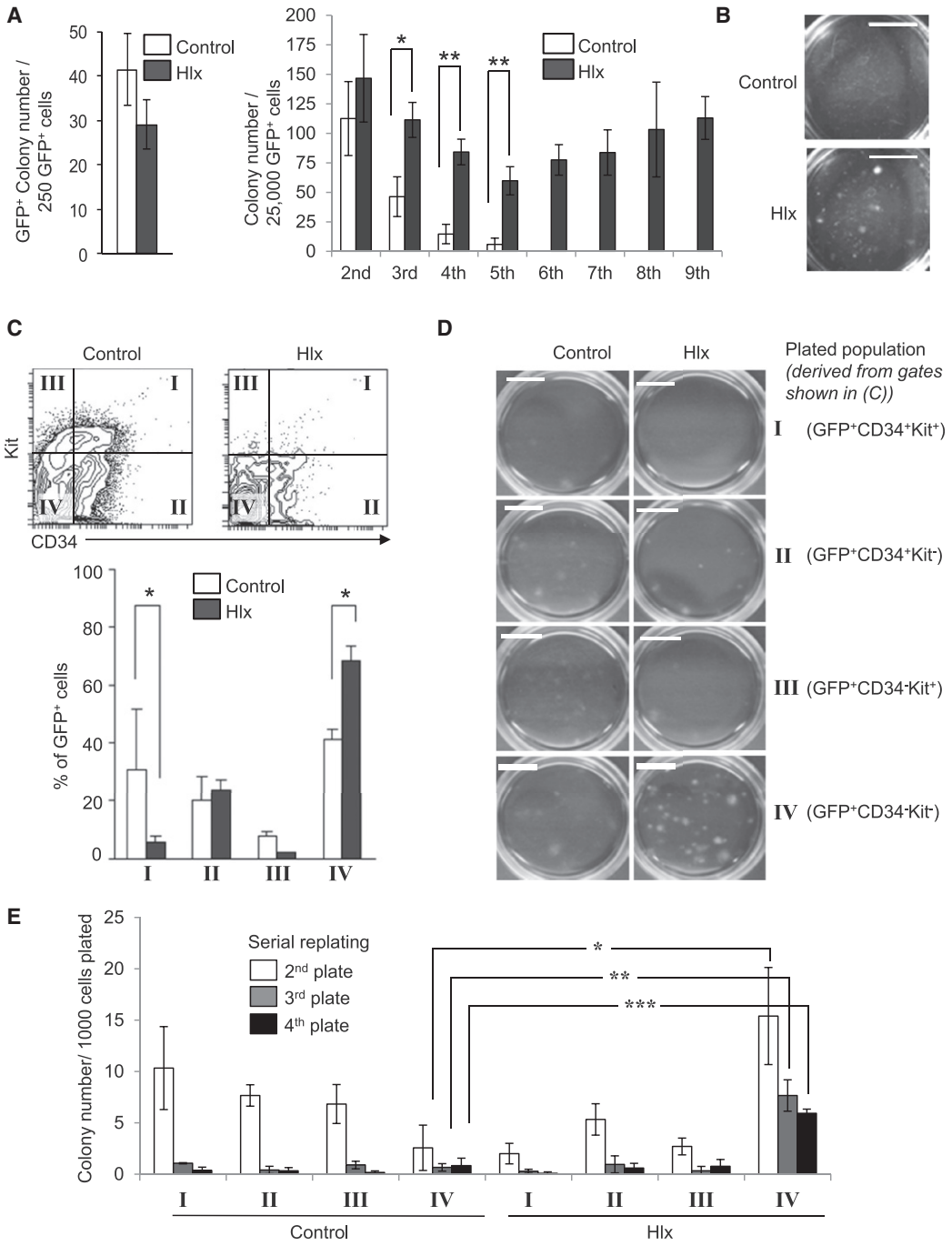

Figure 2. HLX Overexpression Confers Serial Replating Capacity to Lin$^-$CD34$^-$Kit$^-$ Cells

(A) Primary colony formation assay (left panel) and serial replating assay (right panel) of Lin$^-$Kit$^+$Sca1$^+$ cells after transduction with control lentivirus or *Hlx* lentivirus. GFP$^+$ colonies derived from control cells (white bars) and HLX-overexpressing cells (black bars) ± SD are shown. Statistical significance is indicated (*$p < 0.05$, and **$p < 0.005$, n = 3).

(B) Photograph of entire tissue culture dishes after fifth plating shows enlarged size of colonies derived from the *Hlx*-transduced cells. Scale bar indicates 1 cm.

(C) HLX overexpression leads to a decrease of CD34$^+$Kit$^+$ cells and increases the CD34$^-$Kit$^-$ population. Representative FACS plots are shown in the upper panel. The lower panel shows the frequency of each population within total GFP$^+$ cells (I = CD34$^+$Kit$^+$, II = CD34$^+$Kit$^-$, III = CD34$^-$Kit$^+$, and IV = CD34$^-$Kit$^-$). Means of control cells (white bars) and HLX-overexpressing cells (black bars) (± SD) are shown. Statistical significance is indicated (*$p < 0.05$, n = 3).

(D) Whole plate photographs of colonies derived from sorted cells from each population (I, II, III, and IV). Scale bars indicate 1 cm.

(E) Serial replating assay of each sorted population (I, II, III, and IV). Colony numbers (± SD) after second plating (white bars), third plating (gray bars), and fourth plating (black bars) are shown (n = 3). Statistical significance is indicated (*$p = 0.013$; **$p = 0.0015$; ***$p = 0.0004$). Additional data on the aberrant clonogenic population is shown in Figure S2.

HLX Induces a Myelomonocytic Differentiation Block

To investigate the effect of HLX overexpression on differentiation capacity, we analyzed the clonogenic $GFP^+CD34^-Kit^-$ cells from the first colony assay for the expression of additional cell surface markers. The proportions of $Gr1^+Mac1^+$-, $Gr1^-Mac1^+$-, and $F4/80^+Mac1^+$-expressing cells were significantly reduced ($Gr1^+Mac1^+$: from 29.7% [control] [SD: 6.6%] to 16.2% [Hlx] [SD: 1.9%], $p = 0.026$; $Gr1^-Mac1^+$: from 30.7% [SD: 4.5%] to 11.2% [SD: 2.6%], $p = 0.003$; $F4/80^+Mac1^+$: from 31.6% [SD: 4.9%] to 8.9% [SD: 2.8%], $p = 0.002$; $n = 3$), indicative of a defect in myelomonocytic differentiation (Figure 3A). Expression of erythroid, B-lymphoid, and T-lymphoid markers was unchanged. Furthermore, almost half of the HLX-overexpressing $GFP^+CD34^-Kit^-$ population (47.6% [SD: 2.8%]) was lineage-negative, in contrast to only 17% (SD: 1.2%) of $GFP^+CD34^-Kit^-$ control-transduced cells ($p = 0.005$) (Figure 3A). Sorted, HLX-overexpressing $GFP^+Lin^-CD34^-Kit^-$ cells also showed a significant increase in clonogenicity compared with control-transduced cells (Figure S3), indicating that HLX acts at the level of $Lin^-CD34^-Kit^-$ cells. To specifically test myelomonocytic differentiation, we carried out colony-formation assays with GM-CSF or M-CSF stimulation (Figures 3B–3E). *Hlx*-transduced cells gave rise to lower numbers of $Gr1^-Mac1^+$ and $F4/80^+Mac1^+$ cells, compared to control-transduced cells, upon either GM-CSF or M-CSF stimulation (Figures 3B and 3D). Cytomorphological evaluation of cells after stimulation showed an increased percentage of *Hlx*-transduced cells with immature progenitor morphology, in stark contrast to control-transduced cells which predominantly displayed mature monocytic morphology (Figures 3C and 3E). Taken together, our findings show that HLX not only enhances clonogenicity of an increased population of $Lin^-CD34^-Kit^-$ cells, but also confers a partial myelomonocytic differentiation block.

HLX Downregulation Inhibits AML

To test whether HLX overexpression is functionally important for AML, we targeted *Hlx* by RNA interference. We transduced leukemia cells derived from the PU.1 $URE^{\Delta/\Delta}$ AML model (URE cells) as well as human AML cells with lentiviral constructs expressing either *Hlx*-directed (sh Hlx) or control shRNA (sh control). Knockdown of HLX by 80% led to significantly reduced cell proliferation in suspension culture, as well as reduced formation of colonies of URE cells in methylcellulose assays in comparison to control cells ($p < 0.00001$) (Figures 4A–4C). Likewise, human KG1a, THP1, and MOLM13 AML cells showed 40%–60% reduced growth ($p = 0.003$, $p = 0.001$, and $p = 0.015$, respectively) in suspension culture, as well as significantly diminished clonogenicity ($p = 0.02$, $p = 0.038$, and $p = 0.004$, respectively) (Figure 4D). To test the antileukemic effect of HLX suppression in vivo, we performed murine transplantation assays. We found that reduction of HLX levels in transplanted URE cells significantly prolonged recipient survival in comparison to mice transplanted with control shRNA-transduced cells ($p = 0.0012$, and $p = 0.0041$) (Figure 4E). Taken together, our findings demonstrate that HLX is functionally important for AML cells and that targeting HLX can inhibit cellular growth, decrease clonogenicity, and lead to improved survival in a murine AML transplantation model. Of note, *Hlx* heterozygous mice, which show a 50% reduction of HLX protein levels in BM cells, did not show any noticeable effects on normal hematopoiesis, including hematopoietic stem cell functions, such as capacity for hematopoietic reconstitution and serial transplantability (Figure S4).

Inhibition of HLX Leads to Decreased Cell Cycling, Increased Cell Death, and Differentiation of AML Cells and Causes Significant Changes in Gene Expression

To obtain insight into the mechanism of action of HLX inhibition, we studied the cell biological and molecular consequences of knockdown of HLX in leukemia cells. We found that HLX downregulation in URE cells led to a decrease in viable cells and to an increase in necrotic cells (Figure 5A). This was accompanied by a lower number of cells in S phase ($p = 0.027$) and a higher number of cells in G0/G1 phase of cell cycle ($p = 0.002$) (Figure 5B). In addition, reduction of HLX led to an increased population of cells expressing lower levels of Kit and higher levels of Gr-1 and Mac1, indicative of myeloid differentiation (Figures 5C and 5D). Stimulation with GM-CSF further increased the number of Mac1- and Gr-1-expressing cells and led to increased differentiation of AML cells upon sh Hlx treatment in comparison to control-treated cells, which retained an immature, leukemic morphology (Figure 5E). This observation shows that inhibition of HLX can overcome the myeloid differentiation block of AML cells.

To gain insight into the molecular effects caused by HLX inhibition, we measured gene expression profiles of sh Hlx-transduced URE cells and control shRNA-transduced cells. Leukemia cells treated with *Hlx*-directed shRNAs displayed an altered gene expression pattern, with 392 genes being significantly differentially expressed (mean difference > 0.5 [log2], $p < 0.05$) (Figure 5F). Gene set enrichment analysis (GSEA) showed that "leukocyte differentiation," "cell activation," and "cell proliferation" were among the most significantly affected cellular functions (Figure 5G), which is consistent with the leukemia-inhibitory effect of HLX reduction in URE cells. We specifically found that several key genes involved in the regulation of cell cycle and proliferation, cell death, and myeloid differentiation, were significantly changed upon HLX downregulation (Figure 5H). We confirmed differential expression of several genes—namely, *Btg1*, *FoxO4*, *Fyn*, *Gadd45a*, *RhoB*, *Trp63*, *Zfp36l1*, *Hdac7*, and *Pak1*—by qRT-PCR (Figure 5I and Figure S5A). We also found enrichment of genes involved in pathways of other cellular functions (Figure S5B). Furthermore, we utilized GSEA to compare the *Hlx* knockdown data with the molecular signatures database (MSigDB) (Mootha et al., 2003; Subramanian et al., 2005) and found negative enrichment of several known leukemia- and stem cell-related gene signatures (Table S1). Taken together, these data are consistent with a model that HLX overexpression leads to activation of a specific transcriptional program in leukemia cells, which affects processes critical for leukemogenesis such as cell differentiation and proliferation, and which can at least partially be reversed by inhibition of HLX.

We focused on two downstream genes modulated upon HLX inhibition in AML cells, *Pak1* and *Btg1*, which have previously been implicated in the regulation of cell cycle and malignant proliferation (Ong et al., 2011; Kuo et al., 2003). Knockdown of *PAK1* in KG1a AML cells led to a significant inhibition of cell proliferation ($p < 0.05$) and clonogenicity ($p < 0.03$) (Figure 5J

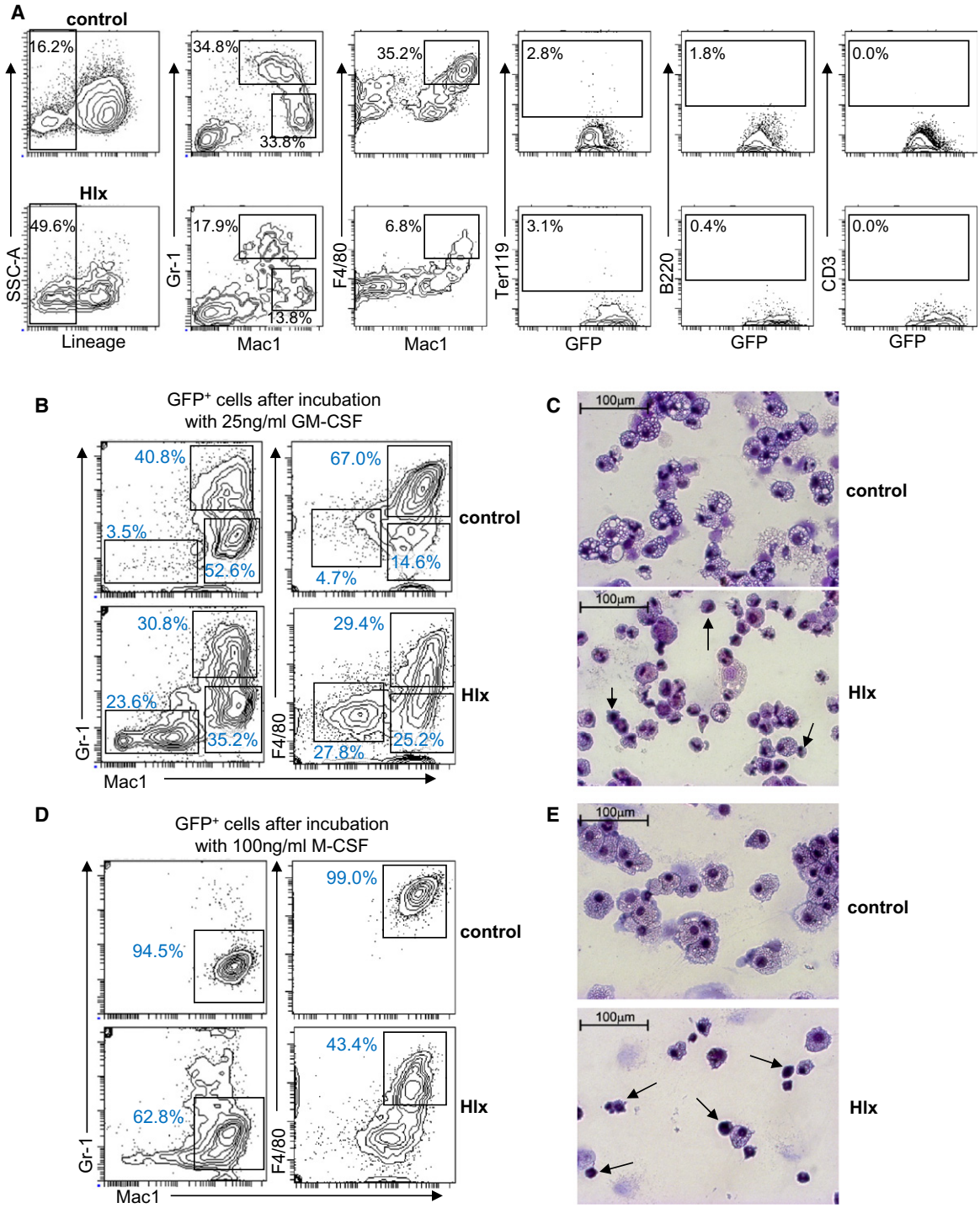

Figure 3. HLX Induces a Myelomonocytic Differentiation Block

(A) Representative FACS analysis of GFP$^+$CD34$^-$Kit$^-$ cells after the primary colony-forming assay. Relative percentages of cells in the indicated gates are given and show a reduction of mature myelomonocytic cells derived from the cells overexpressing HLX.

(B) FACS analysis of cells derived from control-transduced or *Hlx*-transduced LSK cells after culture in methylcellulose with 25 ng/ml GM-CSF. Relative percentages of cells are given for each gate and show a lower number of cells expressing mature myelomonocytic markers.

(C) Representative morphology of cells from (B). Cells with immature morphology can be found in the colonies derived from cells transduced with *Hlx* (indicated by arrows).

(D) FACS analysis of cells derived from control-transduced or *Hlx*-transduced LSK cells after culture in methylcellulose with 100 ng/ml M-CSF.

(E) Representative morphology of cells from (D), which confirms a monocytic differentiation block. Cells with immature morphology are indicated by arrows. See also Figure S3 for additional data.

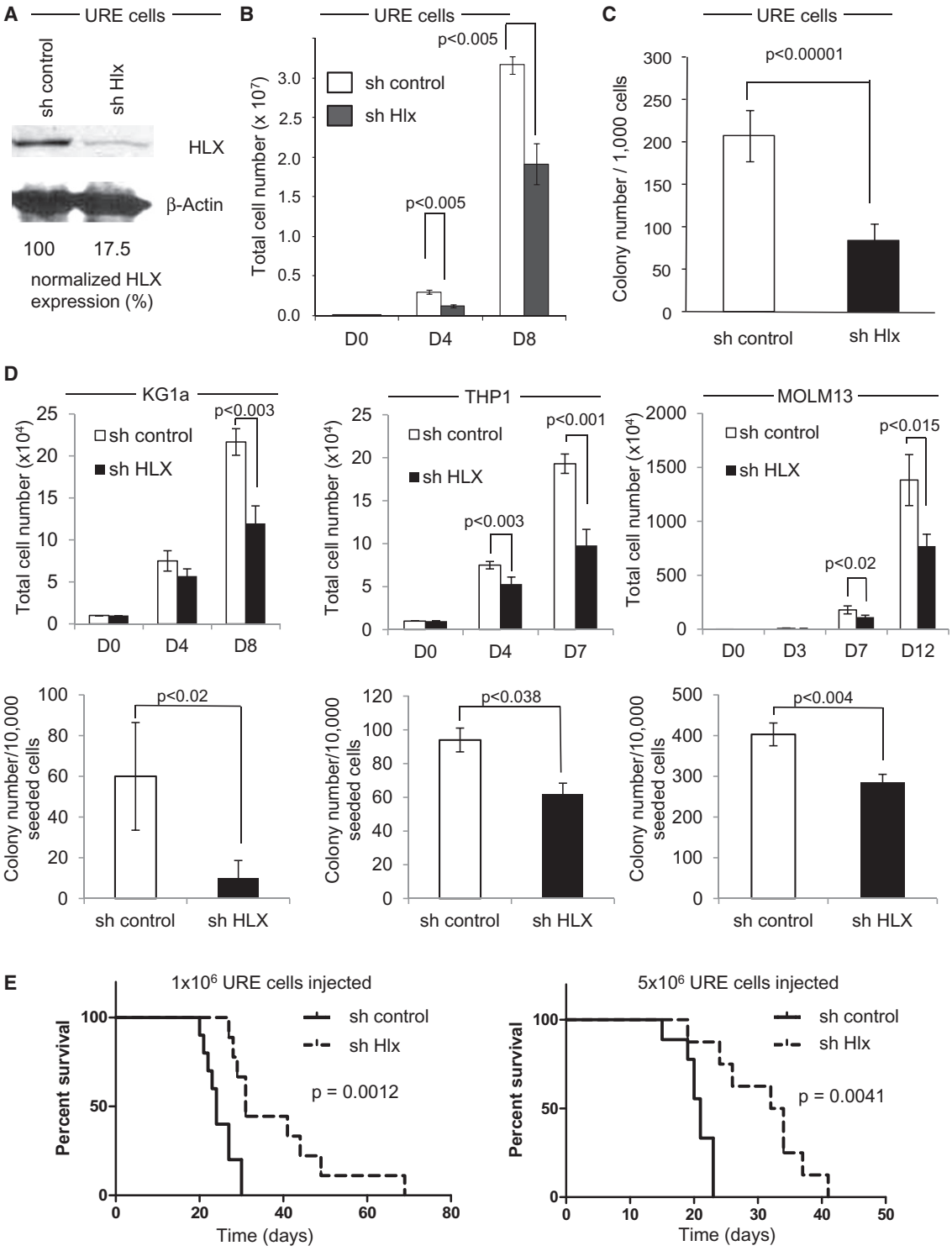

Figure 4. HLX Downregulation Inhibits AML

Lentiviruses expressing short hairpins directed against *Hlx* (sh Hlx) or a control (sh control) were used to downregulate HLX in mouse AML cells (panels A–C) and human AML cells (sh *HLX)* (panel D).

(A) Western blotting shows a >80% reduction of HLX protein by shRNA.

(B) Cell proliferation kinetics were determined by manual cell counts using trypan blue exclusion (n = 3) in sh control cells (white bars) and sh Hlx cells (black bars). Different time points (days) are indicated. Error bars indicate SD.

(C) Clonogenic assay of URE cells treated with sh control or sh Hlx; 1,000 cells each were cultured in methylcellulose, and GFP^+ colonies were counted. Error bars indicate SD (n = 3).

and Figure S5C), mimicking the effects we had observed by knockdown of HLX. Similarly, ectopic expression of *BTG1* led to a significant inhibition of cell growth ($p < 0.01$) and colony-forming capacity ($p < 0.008$) of KG1a cells (Figure 5K and Figure S5D). These findings suggest that downregulation of *PAK1* and upregulation of *BTG1* are functionally relevant for mediating the leukemia-inhibitory effects of HLX knockdown.

HLX Is Overexpressed in Patients with AML

To examine whether *HLX* overexpression plays a role in human leukemia, we analyzed gene expression data of 354 patients with AML (Figueroa et al., 2010; Wouters et al., 2009). *HLX* was overexpressed in 87% of patients with AML in comparison to $CD34^+$ cells of healthy donors (Figure 6A). On average, *HLX* expression was 2.03-fold higher in patients with AML ($p = 1.9 \times 10^{-9}$; Figure 6B). Fifty-four percent (190 of 354) of patients with AML overexpressed *HLX* more than 2-fold, with the range extending up to 6.8-fold overexpression. These results demonstrate that *HLX* overexpression is a common feature in patients with AML. *HLX* overexpression was found across different French-American-British (FAB) classification subsets of AML (Table S2). Of note, high *HLX* expression was significantly more frequent in AML with myelomonocytic (M4) and monoblastic (M5) morphology, which is consistent with the observed myelomonocytic differentiation block caused by HLX overexpression in vitro.

Increased *HLX* Expression Correlates with Inferior Survival

We further sought to examine whether *HLX* expression levels in patients were associated with known clinical or molecular parameters. We analyzed four published data sets of patients with AML, of whom gene expression and time-to-event data were available (NCBI GEO accession numbers GSE10358, GSE12417 [U133A], GSE12417 [U133plus2], and GSE14468) (Metzeler et al., 2008; Tomasson et al., 2008; Wouters et al., 2009). Because the lower 25% of patients had *HLX* expression levels very similar to $CD34^+$ cells of healthy donors (Figure 6B), we decided to use the 25^{th} percentile to dichotomize patients into "HLX high" and "HLX low" expressers. We compared the overall survival of patients with AML with low versus high *HLX*, and observed that in each of the four different data sets, high *HLX* expression was associated with inferior overall survival (Figures S6A–S6D). Overall survival (irrespective of *HLX* status) in data sets GSE12417 (U133plus2.0), GSE14468, and GSE10358 was very similar, with superimposable survival curves ($p = 0.4636$, log-rank test; Figure S6E), suggesting that these cohorts and their clinical outcomes could be combined for further analyses. The GSE12417 (U133A) data set showed a worse overall survival outcome compared with the other data sets (Figure S6F) and was therefore not included in the combined analysis. Consistent with the analyses of the individual data sets, the evaluation of the combined set of patients from the GSE10358, GSE12417 (U133plus2.0), and GSE14468 data sets ($n = 601$ total) confirmed that high *HLX* levels are associated with inferior overall survival ($p = 2.336 \times 10^{-6}$ [log-rank]; hazard ratio [HR] = 0.57 [95% CI: 0.046–0.71]; median survival: 17.05 months [HLX high], "not reached" [HLX low]; 5-year survival rate: 32.95% [HLX high], 55.85% [HLX low]) (Figure 6C). To assess whether the impact of *HLX* expression on overall survival is independent of known prognostic factors for AML, we performed multivariate analysis based on the data of the GSE14468 data set (Figueroa et al., 2010; Wouters et al., 2009), using a Cox regression model. In this analysis, high *HLX* status remained an independent prognostic factor ($p = 0.0416$; HR, 1.521) along with *FLT3* mutation status ($p = 0.0003$; HR, 1.925), *NPM1* mutation status ($p = 0.0006$; HR, 0.518), *CEBPA* mutation status ($p = 0.0371$; HR, 0.693), and cytogenetic risk group ($p = 0.0109$; HR, 1.382). Of note, the relative blast percentage in the bone marrow was not correlated with *HLX* expression or overall survival (Figures S6G–S6I). The independent prognostic role of *HLX* status led us to hypothesize that it may provide additional prognostic information for patients who belong to previously established, molecularly defined subtypes of AML. We indeed observed that, among patients with *FLT3* WT, *NPM1* mutations, or *CEBPA* mutations, high *HLX* expression was associated with inferior overall survival ($p = 0.0175$, $p = 0.0407$ and $p = 0.0306$, respectively) (Figures 6D–6F).

An *HLX*-Dependent Transcriptional Signature Is Functionally Relevant in Patients with AML

To obtain insight into the molecular consequences of elevated HLX levels, we overexpressed HLX in sorted murine LSK cells and performed genomewide transcriptional analysis. We found that 195 genes were significantly changed, resulting in a clearly distinguishable expression signature induced by HLX overexpression (Figure S6J). Using GSEA, we found enrichment of known leukemia- and stem cell-related gene signatures, consistent with our previous findings (Table S3).

Next, we tested whether this mouse LSK HLX overexpression gene set correlated with *HLX* expression in human patients with AML. Specifically, we compared the human orthologs of the mouse gene set to *HLX* expression levels of patients with AML in the different cohorts using *globaltest* (Goeman et al., 2004). We found a highly significant correlation between the mouse gene signature and *HLX* expression in human AML samples ($p = 7.43 \times 10^{-23}$ for GSE14468, $p = 2.13 \times 10^{-08}$ for GSE10358, $p = 2.31 \times 10^{-06}$ for GSE12417 [U133plus2.0], and $p = 5.01 \times 10^{-10}$ for GSE12417 [U133A]). Furthermore, we intersected differentially expressed genes from the HLX overexpression or inhibition studies with analogously differentially expressed genes in "HLX high" versus "HLX low" patients of the GSE14468 data set, and analyzed these genes for association with survival. Thereby, we were able to define an HLX-dependent

(D) Cell proliferation kinetics in suspension culture (top panel) and clonogenicity (bottom panel) of human AML cells (KG1a, left panel; THP1, middle panel; MOLM13, right panel). Time points (days) are indicated. Error bars (SD) and statistical significance is indicated (t test, n = 4).
(E) Transplantation of URE cells transduced with sh control or sh Hlx into NSG mice. One million (left panel) or 5 million cells (right panel) were retroorbitally injected into NSG mice after sublethal irradiation (250 cGy). Kaplan-Meier curves of overall survival of recipient mice are displayed. p values (log-rank) are indicated. See also Figure S4 for additional data.

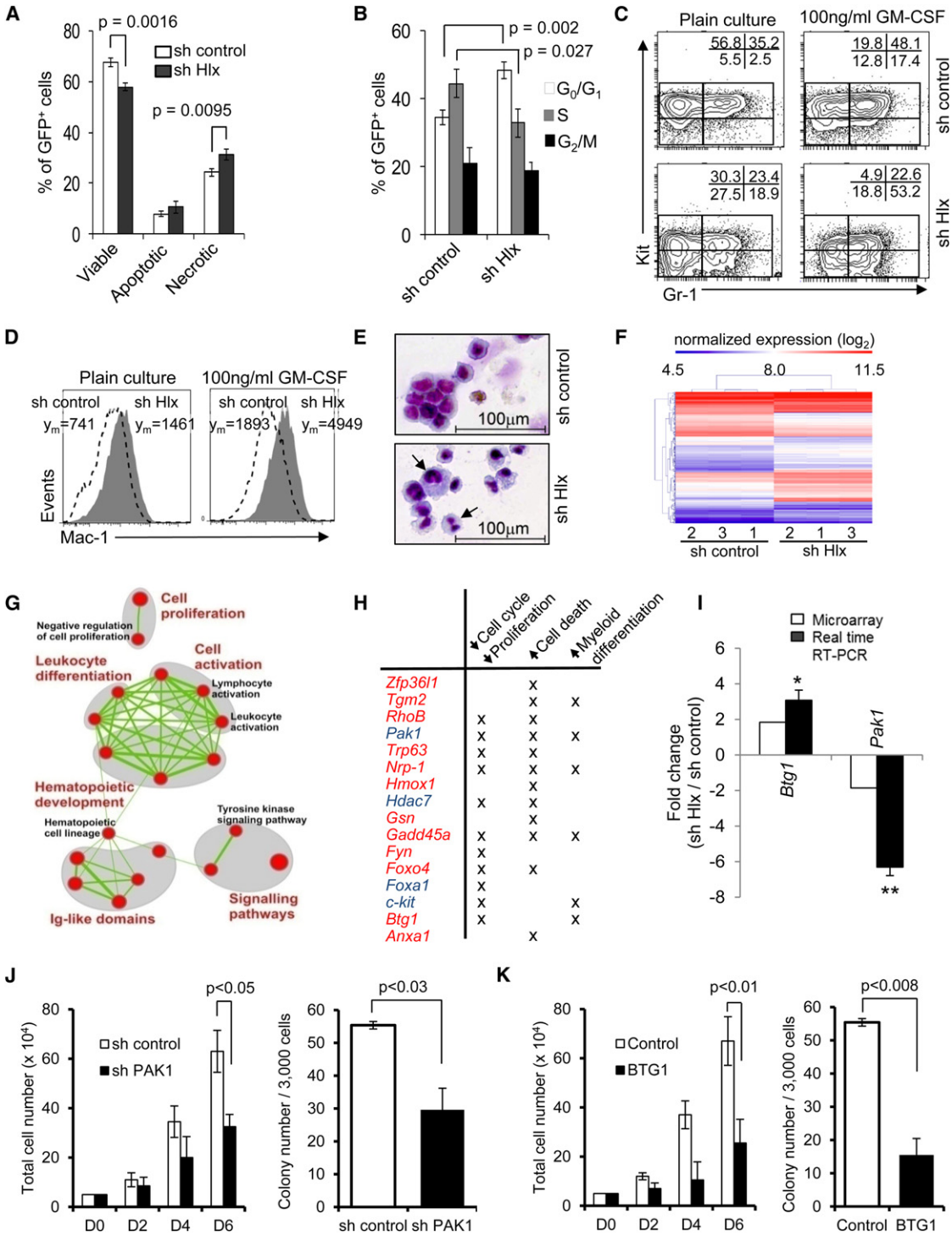

Figure 5. Inhibition of HLX Leads to Decreased Cell Cycling, Increased Cell Death, and Differentiation of AML Cells and Causes Significant Changes in Gene Expression

(A) Relative percentages (± SD) of viable cells (DAPI-negative/Annexin V-negative), apoptotic cells (DAPI-negative/AnnexinV-positive), and necrotic cells (entire DAPI-positive) in sh control cells (white bars) and sh Hlx cells (black bars). p values are indicated (n = 3).

(B) Cell cycle status of sh control and sh Hlx leukemia cells. Percentages of cells in G0/G1 (white bars), S (gray bars), and G2/M (black bars) phase of cell cycle are displayed. Statistical significance is indicated (n = 3).

(C and D) Cell surface marker analysis after suspension culture for 3 days. Relative percentages of cells in the indicated gates are given and show a decrease of immature Kit$^+$ cells and an increase of Kit$^-$Gr1$^+$ cells (C), and an increase of Mac1$^+$ cells (D).

(E) Morphology of cells after treatment with 100 ng/ml recombinant GM-CSF for 3 days. Cells with maturation signs are indicated by arrows.

core set of 17 genes (referred to as "HLX signature") correlating with *HLX* expression status in patients with AML (Figure 6G). When we dichotomized patients into "HLX signature high" versus "HLX signature low" patients (defined by the genes of the signature, excluding *HLX*), we found that "HLX signature high" patients had significantly inferior overall survival ($p = 0.0089$ [log-rank]; HR, 0.66 [95% CI: 0.48–0.90]; median survival: 17.22 months for HLX signature high, "not reached" for HLX signature low; 5-year survival rate: 34.5% for HLX signature high, 53.9% for HLX signature low) (Figure 6H).

We subsequently validated the *HLX* signature in an independent cohort of patients, the GSE10358 data set, and found that the signature correlated strongly ($p = 7.8 \times 10^{-11}$) with "HLX high" versus "HLX low" expression status in these patients with AML as well (Figure 6I). Furthermore, "HLX signature high" patients showed a strikingly inferior overall survival ($p = 1.89 \times 10^{-05}$ [log-rank]; HR, 0.42 [95% CI: 0.28–0.62]; median survival: 18.3 months [HLX signature high], "not reached" [HLX signature low]; 5-year survival rate: 29.0% [HLX signature high], 67.0% [HLX signature low]) (Figure 6J). Taken together, these data suggest that elevated *HLX* levels cause a specific, functionally critical gene expression signature in human AML.

Interestingly, *PAK1* was part of the HLX-induced prognostic signature. Given our finding that *PAK1* mediates the leukemia-inhibitory effects of HLX knockdown in AML cells (Figure 5J), we asked whether *PAK1* expression levels alone may be functionally relevant in patients with AML. We dichotomized patients with AML into "PAK1 high" and "PAK1 low" expressers and analyzed clinical outcome. "PAK1 high" patients showed significantly inferior overall survival ($p = 0.00014$ [log-rank]) than did "PAK1 low" patients (median: 17.7 months [PAK1 high] versus 109.1 months [PAK1 low]; 5-year survival rate: 34.0% [PAK1 high] versus 50.5% [PAK1 low]) (Figure S6K). Of note, high *PAK1* expression was associated with inferior overall survival only in patients of the "HLX high" group ($p = 0.0005$ [log-rank]; HR, 0.62 (95% CI: 0.48–0.81)); median survival: 15.8 months [PAK1 high], 42.0 months [PAK1 low]; 5-year survival rate: 29.7% [PAK1 high], 48.1% [PAK1 low]), but not in "HLX low" patients ($p = 0.77$ ([og-rank]; HR, 1.08 (95% CI: 0.65–1.78]); 5-year survival rate: 55.0% [PAK1 high], 55.0% [PAK1 low]) (Figures S6L and S6M). In addition, *PAK1* expression levels were on average 1.5-fold higher ($p = 2.2 \times 10^{-16}$) in "HLX high" patients compared to "HLX low" patients (Figure S6N), and *HLX* and *PAK1* expression levels in individual patients were also significantly correlated ($p = 8.8 \times 10^{-15}$, $R = 0.31$; Figure S6O). Furthermore, experimental overexpression of HLX in LSK cells led to a significant increase in *Pak1* mRNA expression (1.9-fold, $p = 0.017$; Figure S6P).

DISCUSSION

Utilizing both mouse and human model systems, we have shown that the class II homeobox protein HLX affects hematopoietic stem cell function, as well as clonogenicity and differentiation of immature hematopoietic progenitor cells. We found that *HLX* is significantly overexpressed in the majority of patients with AML and that high *HLX* expression levels are independently associated with inferior clinical outcome. Thereby, our study identifies *HLX* as a class II homeobox gene which is critically involved in the pathogenesis of AML. Our finding that increased *HLX* expression correlates with more aggressive disease, combined with the observation that HLX knockdown results in an inhibition of growth and clonogenicity of leukemia cells, further suggest that HLX may be a promising prognostic and therapeutic target. Future studies evaluating HLX in the context of different therapies will be required to determine whether HLX also has predictive relevance.

Many clustered (class I, or HOX) homeobox genes have been implicated in normal hematopoiesis as well as leukemia, but much less is known about the role of nonclustered (class II) homeobox transcription factors (for review, see Argiropoulos and Humphries, 2007). Several HOX genes are expressed at high levels in subtypes of AML (Alcalay et al., 2005; Ayton and Cleary, 2003; Bullinger et al., 2004; Horton et al., 2005). Important roles in leukemic transformation have been demonstrated specifically for several members of the HOX-A and the HOX-B cluster (Fischbach et al., 2005; Krivtsov et al., 2006; Kroon et al., 1998; Sauvageau et al., 1997; Somervaille and Cleary, 2006; Thorsteinsdottir et al., 1997). Also, the nonclustered homeobox gene *CDX2* was recently reported to be implicated in leukemogenesis (Scholl et al., 2007). However, the clinical significance of these known HOX genes is largely unclear. Here, we report that expression levels of a homeobox gene are strongly associated with inferior overall survival in several large, independent cohorts of patients with AML. Furthermore, the prognostic value of *HLX* is a broad phenomenon across several molecular subsets of patients, and *HLX* holds up as an independent prognostic factor in a multivariate model. Gene expression analyses upon experimental overexpression and inhibition of HLX demonstrated that HLX regulates the expression of

(F) Hierarchical clustering of genes differentially expressed in URE leukemia cells upon HLX knockdown. Expression levels are color-coded.

(G) Enrichment map representation of cellular processes perturbed in leukemia cells upon HLX knockdown. Enriched gene sets are represented as nodes (red circles) connected by edges (green links) denoting the degree of gene set overlap. The node size is proportional to the number of genes in the gene set and the edge thickness represents the number of genes that overlap between gene sets. The color intensity of the nodes indicates the statistical significance of enrichment of a particular gene set. Groups of functionally related gene sets are circled in gray and labeled. A more comprehensive enrichment map is shown in Figure S5. See Table S1 for additional information.

(H) Select genes altered by HLX inhibition in URE leukemia cells. Upregulated genes are shown in red, and downregulated genes are shown in blue. Their involvement in regulation of cell cycle-proliferation, cell death, and myeloid differentiation is indicated.

(I) Validation of differential mRNA expression of *Btg1* and *Pak1*. Fold changes (± SD) upon HLX knockdown are shown. (*$p < 0.05$; **$p < 0.01$, $n = 3$). Additional qRT-PCR validation is shown in Figure S5.

(J) Short hairpin (sh*PAK1*) or a control (sh control) were used to downregulate HLX downstream target *PAK1* in human AML cell line KG1a. Proliferation (left panel) and clonogenicity (right panel) are shown. Error bars indicate SD ($n = 4$).

(K) Effect of *BTG1* overexpression on KG1a proliferation (left panel) and colony formation capacity (right panel). Error bars indicate SD ($n = 4$). Quantification of *PAK1* knockdown and *BTG1* overexpression are shown in Figures S5C and S5D.

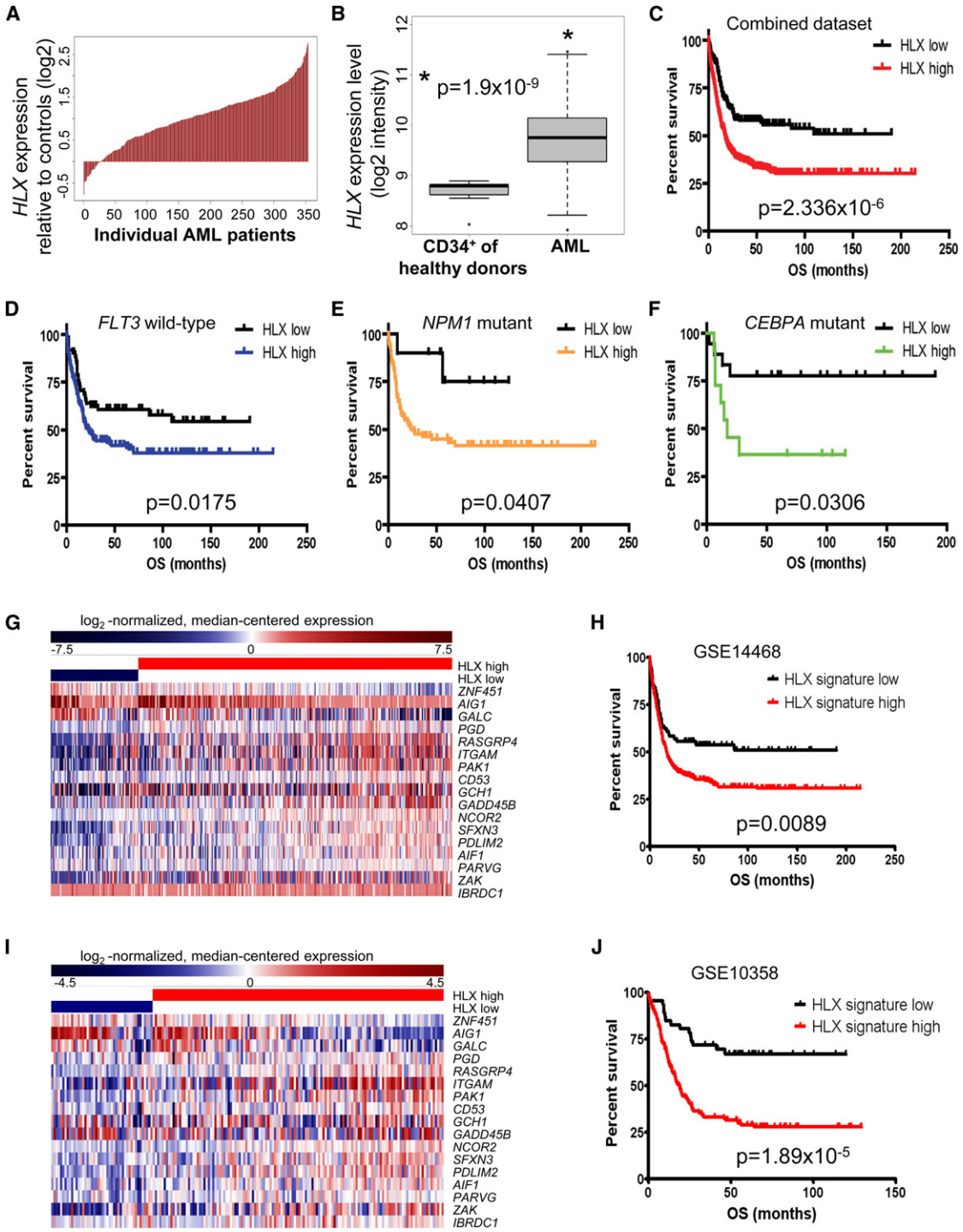

Figure 6. *HLX* Is Overexpressed in Patients with AML and Correlates with Poor Overall Survival

(A) Waterfall plot of relative expression (log2) of *HLX* of 354 patients with AML in comparison to CD34-enriched bone marrow cells from 11 healthy donors.

(B) Box plot summary of the *HLX* expression data shown in (A). *HLX* expression is significantly higher in patients with AML in comparison to $CD34^+$ cells from healthy donors ($p = 1.9 \times 10^{-9}$). The median expression values (bold lines), 25th and 75th percentile (bottom and top of box), and the minimum and maximum (lower and upper whiskers) of both groups are shown. See Table S2 for additional information.

(C) Kaplan-Meier survival plots of overall survival (OS) of patients with high versus low *HLX* expression in a combined data set of 601 patients with AML (GSE10358, GSE12417 (U133plus2.0) and GSE14468). Patients with high expression of *HLX* show drastically inferior clinical outcome. The p value (log-rank test) is indicated. Kaplan-Meier plots for all individual data sets are shown in Figures S6A–S6F.

(D–F) Kaplan-Meier survival plots comparing overall survival (OS) of patients with high versus low *HLX* expression in molecularly defined subsets of AML. High expression of *HLX* is associated with significantly inferior clinical outcome in all subsets. p values (log-rank test) are given.

a specific subset of genes, and that part of this "HLX signature" is also detectable in patients with AML and discriminates between patients with poor and favorable clinical outcome. Taken together, these observations suggest that HLX is a key regulator of a gene subset critical for AML pathogenesis and that it may define a previously unrecognized molecular subtype of AML with distinct biological features and clinical outcome.

We identified *PAK1* and *BTG1* as two genes downstream of HLX in myeloid cells and show that *PAK1* and *BTG1* are functionally relevant in AML cells. Notably, *PAK1* is upregulated in human patients with AML with high *HLX* expression, and it is also part of the *HLX*-induced core signature that independently predicts overall survival in patients with AML. Interestingly, high *PAK1* expression itself is associated with inferior overall survival, but only in patients with high *HLX* expression, indicating that there is an interaction of *HLX* and *PAK1* with respect to their impact on overall survival. The correlation of *HLX* and *PAK1* expression levels in the murine HLX knockdown model and in patients with AML, together with the observed induction of *Pak1* expression upon HLX overexpression in stem cells, strongly suggest that *Pak1* is a downstream target of HLX and critically mediates, at least in part, the leukemia-promoting effects of *HLX* in patients in vivo. Further studies will be required to determine the exact nature of this regulation, and whether it is direct or indirect.

Several HOX genes, such as *HOXB4*, have been reported to be stimulators of HSC function and expansion (Antonchuk et al., 2002; Sauvageau et al., 1995). Our data show that HLX suppresses the function of normal immature HSC and progenitors, but leads to an increase of clonogenicity, as well as a differentiation block at the level of phenotypically more mature progenitors. Because the loss of HSC does not seem to be mediated by induction of apoptosis or necrosis, one may speculate that HLX exerts this dual role by triggering initial differentiation of HSC and suppression of terminal differentiation at a more committed progenitor level. Further studies will be required to understand the molecular basis of this effect. Although overexpression of HLX led to the formation of myeloid progenitors with unlimited serial clonogenicity, we so far did not observe development of leukemia upon transplantation, suggesting that HLX elevation alone may not be sufficient for full transformation. Like other homeobox genes, *Hlx* may function in concert with cofactors (Moens and Selleri, 2006; Pineault et al., 2004). Such cofactors could confer cell type specificity to the effects of HLX overexpression and also contribute to leukemic transformation. It is also possible that increase of HLX plays a role in leukemia maintenance rather than leukemia induction.

Several transcription factors that govern normal hematopoietic differentiation have been implicated in leukemogenesis by blocking differentiation and promoting self-renewal and clonogenicity (for review, see Rosenbauer and Tenen, 2007). HLX may act similar to those factors by establishing a specific gene expression program in early HSPC, which results in increased long-term clonogenicity and a differentiation arrest, contributing to poor clinical outcome. Thus, *HLX* expression levels may be utilized to predict clinical outcome and improve risk stratification. Finally, inhibition of HLX may be a promising strategy for treatment of patients with AML.

EXPERIMENTAL PROCEDURES

Mice and Cells

FVB/nJ mice (Ly5.1), C57BL/6J (Ly5.2) mice, and B6.SJL-Ptprc^{a} Pepc^{b}/BoyJ (Pep boy, Ly5.1) and NOD.Cg-Prkdcscid Il2rgtm1Wjl/SzJ (NSG) mice were used for in vitro assays and in vivo transplantation assays. Mice with targeted disruption of the upstream regulatory element (URE) of the PU.1 gene have been previously described (Rosenbauer et al., 2004). All animal experiments were approved by the Institutional Animal Care and Use Committee of the Albert Einstein College of Medicine (protocol # 20080109). URE cells were established and maintained as described previously (Steidl et al., 2006). Human AML cell lines THP1, MOLM13, and KG1a were cultured under standard conditions.

Flow Cytometric Analysis and Sorting

Mononuclear cells were purified by lysis of erythrocytes. For analysis and sorting, we used antibodies directed against CD4[GK1.5], CD8a[53-6.7], CD19[eBio1D3], Gr-1[RB6-8C5], B220[RA3-6B2], F4/80[BM8], c-kit[ACK2], Sca-1[D7], CD34[RAM34], CD16/32[93], Flk-2[A2F10], Mac1[M1/70], Ter119 [TER-119], and Thy-1.2[53-2-1]. To distinguish donor from host cells in transplanted mice, cells were additionally stained with anti-CD45.1[A20] and CD45.2[104]. Analysis and sorting were performed using a FACSAria II Special Order System (BD Biosciences, San Jose, CA). See Supplemental Experimental Procedures for more details.

Lentiviral Vectors and Transduction

For overexpression studies, we introduced the mouse *Hlx* coding sequence into the EcoRI site of a pCAD-IRES-GFP lentiviral construct (Steidl et al., 2007). For *BTG1* overexpression, we introduced the human *BTG1* coding sequence into the EcoRI site of the pCAD-IRES-GFP construct. For murine knockdown studies, we inserted shRNA template oligonucleotides (target sense strand-loop-target antisense strand-TTTTT) into the pSIH1-H1-copGFP shRNA vector (System Biosciences, Mountain View, CA). For human knockdown studies, we utilized the pGIPZ system from Open Biosystems (Huntsville, AL). See Supplemental Experimental Procedures for sequence information. For knockdown of *PAK1*, we utilized the plko.1-puro vector system (Sigma) with nonsilencing control or human *PAK1* target. Lentiviral particles were produced utilizing 293T cells and were concentrated by ultracentrifugation. For overexpression studies, we treated sorted Lin^{-}Kit^{+} cells from WT C57BL/6J (Ly5.2) BM (for in vivo assays) or Lin^{-}Kit^{+}Sca-1^{+} cells from WT FVB/nJ BM (for in vitro assays) with control virus or *Hlx* virus. In brief,

(D) Patients with AML with no detectable mutations of the *FLT3* gene.
(E) Patients with AML with mutant *NPM1*.
(F) Patients with AML with mutant *CEBPA*.
(G) Heat map of log2-normalized, median-centered gene expression of a 17-gene "HLX signature" in patients with AML of the GSE14468 cohort. *HLX* expression status is indicated. Relative gene expression is color-coded (red: high, blue: low).
(H) Kaplan-Meier plot comparing overall survival (OS) of "HLX signature high" versus "HLX signature low" AML patients of the GSE14468 cohort. The p value (log-rank) is indicated.
(I) Heat map of log2-normalized, median-centered gene expression of the "HLX signature" in AML patients of the GSE10358 cohort.
(J) Kaplan-Meier survival plot comparing overall survival (OS) of "HLX signature high" versus "HLX signature low" patients with AML of the GSE10358 cohort. The p value (log-rank) is indicated. See also Figure S6 and Table S3 for additional information.

sorted cells were cultured with lentiviral supernatants in the presence of 8 μg/ml polybrene. Twenty-four hours after transduction, cells were washed with PBS and then used for experiments. After 40 hr, transduction efficiency was determined by flow cytometry. For knockdown studies, cells were incubated with short-hairpin-containing lentivirus for 24 hr. GFP^+ cells were sorted using a FACS Aria II sorter (BD Biosciences) and used for experiments.

Quantitative Real-Time PCR

We extracted total RNA from FACS-sorted cells or cultured cells using RNeasy Micro kit (QIAGEN, Valencia, CA) and synthesized cDNA by Superscript II reverse transcriptase (Invitrogen, Carlsbad, CA). We performed real-time PCR using an iQ5 real-time PCR detection system (BIO-RAD, Hercules, CA) with 1 cycle of 50°C (2 min) and 95°C (10 min) followed by 40 cycles of 95°C (15 sec) and 60°C (1 min) using Power SYBR Green PCR master mix (AB, Carlsbad, CA) (see Supplemental Experimental Procedures for primer sequences).

Western Blotting

See Supplemental Experimental Procedures.

Cell Proliferation, Cell Cycle, and Apoptosis Assays

See Supplemental Experimental Procedures.

Colony Formation Assays and Serial Replating Assays

Assays were performed in MethoCult M3434 (Stem Cell Technologies, Vancouver, BC) containing IL-3, IL-6, SCF, and EPO or in MethoCult M3234 supplemented with M-CSF or GM-CSF as previously described (Higuchi et al., 2002; Huntly et al., 2004; Will et al., 2009). GFP^+ colonies were scored 8–10 days after plating using an AXIOVERT 200M microscope (Zeiss, Maple Grove, MN). After scoring, we resorted GFP^+ cells after each round and then proceeded with serial replating assays. Cells were replated and colonies were again scored after 10–14 days.

Transplantation Assays

For HLX overexpression studies, 5×10^4 lentivirus-transduced Lin^-Kit^+ cells (Ly5.2) together with 2.5×10^5 spleen cells from congenic WT recipients (Ly5.1) were transplanted into lethally irradiated age-matched congenic WT recipients (Ly5.1) by retroorbital vein injection. Total body irradiation was delivered in a single dose of 950 cGy using a Shepherd 6810 sealed-source ^{137}Cs irradiator.

Micorarray Experiments and Analysis

RNA was extracted from sorted GFP^+ cells utilizing the RNeasy Micro Kit (QIAGEN). After evaluation of the quality of RNA with an Agilent2100 Bioanalyzer, total RNA was used for amplification utilizing the Nugen Ovation pico WTA system according to the manufacturer's instructions. After labeling with the GeneChip WT terminal labeling kit (Affymetrix), labeled cRNA of each individual sample was hybridized to Affymetrix Mouse Gene 1.0ST microarrays (Affymetrix), stained, and scanned by GeneChip Scanner 3000 7G system (Affymetrix) according to standard protocols. For data analysis, we utilized Multiple Experiment Viewer v.4 pilot2 (Saeed et al., 2006), DAVID bioinformatics tool (Huang et al., 2009a, 2009b), Enrichment Map Cytoscape plugin (Cline et al., 2007; Merico et al., 2010), and Gene Set Enrichment Analysis v2.0 (GSEA) (Mootha et al., 2003; Subramanian et al., 2005). See Supplemental Experimental Procedures for details.

Data Sets and Statistical Analysis

We analyzed the publicly available gene expression data sets with accession numbers GSE12417 (training set U133A and U133B; test set U133plus2.0), GSE14468, and GSE10358 (http://www.ncbi.nlm.nih.gov/geo/). Clinical outcome and mutational data for the GSE10358 data set were obtained from a recent study of the same group (Ley et al., 2010). Analyses of the gene expression profiles from GSE14468, GSE12417 training set, and GSE10358 were performed based on published (Gentles et al., 2010) and publicly available MAS5 files (GSE24006) with reanalyzed data. For analysis of the test set of the GSE12417 data set, CEL files were processed using GenePattern (Broad Institute, Cambridge MA) for normalization (ExpressionFileCreator algorithm). We utilized GraphPad Prism 5.0, R/Bioconductor sva package (R package version 3.2.0) (Leek et al., 2012), and SPSS 18.0 statistical package for further analyses. See Supplemental Experimental Procedures for details.

Signature Generation and Calculation of Signature Scores

We utilized dChip (http://biosun1.harvard.edu/complab/dchip/), SAM (significance analysis of microarrays), as well as R/Bioconductor globaltest (Goeman et al., 2004) for signature identification, followed by calculation of signature scores. See Supplemental Experimental Procedures for details.

ACCESSION NUMBER

Complete array data are available in the Gene Expression Omnibus (GEO) of NCBI (Edgar et al., 2002), accession number GSE27947.

SUPPLEMENTAL INFORMATION

Supplemental Information includes six figures, three tables, and Supplemental Experimental Procedures and can be found with this article online at http://dx.doi.org/10.1016/j.ccr.2012.06.027.

ACKNOWLEDGMENTS

We thank the Einstein Human Stem Cell FACS and Xenotransplantation Facility for expert technical assistance (supported by NYSTEM Grant no. C024172). This work was supported by a new investigator award of the Leukemia Research Foundation, an investigator-initiated research project of NYSTEM (Grant no. CO24350), a Howard Temin Award of the National Cancer Institute (Grant no. R00CA131503), and a Medical Research Award of the Gabrielle's Angel Foundation for Cancer Research (to U.S.). U.S. is the Diane and Arthur B. Belfer Faculty Scholar in Cancer Research of the Albert Einstein College of Medicine.

Received: August 8, 2011
Revised: February 29, 2012
Accepted: June 22, 2012
Published: August 13, 2012

REFERENCES

Alcalay, M., Tiacci, E., Bergomas, R., Bigerna, B., Venturini, E., Minardi, S.P., Meani, N., Diverio, D., Bernard, L., Tizzoni, L., et al. (2005). Acute myeloid leukemia bearing cytoplasmic nucleophosmin (NPMc+ AML) shows a distinct gene expression profile characterized by up-regulation of genes involved in stem-cell maintenance. Blood *106*, 899–902.

Allen, J.D., Lints, T., Jenkins, N.A., Copeland, N.G., Strasser, A., Harvey, R.P., and Adams, J.M. (1991). Novel murine homeo box gene on chromosome 1 expressed in specific hematopoietic lineages and during embryogenesis. Genes Dev. *5*, 509–520.

Antonchuk, J., Sauvageau, G., and Humphries, R.K. (2002). HOXB4-induced expansion of adult hematopoietic stem cells ex vivo. Cell *109*, 39–45.

Argiropoulos, B., and Humphries, R.K. (2007). Hox genes in hematopoiesis and leukemogenesis. Oncogene *26*, 6766–6776.

Ayton, P.M., and Cleary, M.L. (2003). Transformation of myeloid progenitors by MLL oncoproteins is dependent on Hoxa7 and Hoxa9. Genes Dev. *17*, 2298–2307.

Bansal, D., Scholl, C., Fröhling, S., McDowell, E., Lee, B.H., Döhner, K., Ernst, P., Davidson, A.J., Daley, G.Q., Zon, L.I., et al. (2006). Cdx4 dysregulates Hox gene expression and generates acute myeloid leukemia alone and in cooperation with Meis1a in a murine model. Proc. Natl. Acad. Sci. USA *103*, 16924–16929.

Bullinger, L., Döhner, K., Bair, E., Fröhling, S., Schlenk, R.F., Tibshirani, R., Döhner, H., and Pollack, J.R. (2004). Use of gene-expression profiling to identify prognostic subclasses in adult acute myeloid leukemia. N. Engl. J. Med. *350*, 1605–1616.

Cline, M.S., Smoot, M., Cerami, E., Kuchinsky, A., Landys, N., Workman, C., Christmas, R., Avila-Campilo, I., Creech, M., Gross, B., et al. (2007). Integration of biological networks and gene expression data using Cytoscape. Nat. Protoc. *2*, 2366–2382.

Deguchi, Y., and Kehrl, J.H. (1991). Selective expression of two homeobox genes in CD34-positive cells from human bone marrow. Blood *78*, 323–328.

Deguchi, Y., Kirschenbaum, A., and Kehrl, J.H. (1992). A diverged homeobox gene is involved in the proliferation and lineage commitment of human hematopoietic progenitors and highly expressed in acute myelogenous leukemia. Blood *79*, 2841–2848.

Edgar, R., Domrachev, M., and Lash, A.E. (2002). Gene Expression Omnibus: NCBI gene expression and hybridization array data repository. Nucleic Acids Res. *30*, 207–210.

Figueroa, M.E., Lugthart, S., Li, Y., Erpelinck-Verschueren, C., Deng, X., Christos, P.J., Schifano, E., Booth, J., van Putten, W., Skrabanek, L., et al. (2010). DNA methylation signatures identify biologically distinct subtypes in acute myeloid leukemia. Cancer Cell *17*, 13–27.

Fischbach, N.A., Rozenfeld, S., Shen, W., Fong, S., Chrobak, D., Ginzinger, D., Kogan, S.C., Radhakrishnan, A., Le Beau, M.M., Largman, C., and Lawrence, H.J. (2005). HOXB6 overexpression in murine bone marrow immortalizes a myelomonocytic precursor in vitro and causes hematopoietic stem cell expansion and acute myeloid leukemia in vivo. Blood *105*, 1456–1466.

Friedman, A.D. (2007). Transcriptional control of granulocyte and monocyte development. Oncogene *26*, 6816–6828.

Gentles, A.J., Plevritis, S.K., Majeti, R., and Alizadeh, A.A. (2010). Association of a leukemic stem cell gene expression signature with clinical outcomes in acute myeloid leukemia. JAMA *304*, 2706–2715.

Goeman, J.J., van de Geer, S.A., de Kort, F., and van Houwelingen, H.C. (2004). A global test for groups of genes: testing association with a clinical outcome. Bioinformatics *20*, 93–99.

Hentsch, B., Lyons, I., Li, R., Hartley, L., Lints, T.J., Adams, J.M., and Harvey, R.P. (1996). Hlx homeo box gene is essential for an inductive tissue interaction that drives expansion of embryonic liver and gut. Genes Dev. *10*, 70–79.

Higuchi, M., O'Brien, D., Kumaravelu, P., Lenny, N., Yeoh, E.J., and Downing, J.R. (2002). Expression of a conditional AML1-ETO oncogene bypasses embryonic lethality and establishes a murine model of human t(8;21) acute myeloid leukemia. Cancer Cell *1*, 63–74.

Horton, S.J., Grier, D.G., McGonigle, G.J., Thompson, A., Morrow, M., De Silva, I., Moulding, D.A., Kioussis, D., Lappin, T.R., Brady, H.J., and Williams, O. (2005). Continuous MLL-ENL expression is necessary to establish a "Hox Code" and maintain immortalization of hematopoietic progenitor cells. Cancer Res. *65*, 9245–9252.

Huang, W., Sherman, B.T., and Lempicki, R.A. (2009a). Bioinformatics enrichment tools: paths toward the comprehensive functional analysis of large gene lists. Nucleic Acids Res. *37*, 1–13.

Huang, W., Sherman, B.T., and Lempicki, R.A. (2009b). Systematic and integrative analysis of large gene lists using DAVID bioinformatics resources. Nat. Protoc. *4*, 44–57.

Huntly, B.J., Shigematsu, H., Deguchi, K., Lee, B.H., Mizuno, S., Duclos, N., Rowan, R., Amaral, S., Curley, D., Williams, I.R., et al. (2004). MOZ-TIF2, but not BCR-ABL, confers properties of leukemic stem cells to committed murine hematopoietic progenitors. Cancer Cell *6*, 587–596.

Krivtsov, A.V., Twomey, D., Feng, Z., Stubbs, M.C., Wang, Y., Faber, J., Levine, J.E., Wang, J., Hahn, W.C., Gilliland, D.G., et al. (2006). Transformation from committed progenitor to leukaemia stem cell initiated by MLL-AF9. Nature *442*, 818–822.

Kroon, E., Krosl, J., Thorsteinsdottir, U., Baban, S., Buchberg, A.M., and Sauvageau, G. (1998). Hoxa9 transforms primary bone marrow cells through specific collaboration with Meis1a but not Pbx1b. EMBO J. *17*, 3714–3725.

Krumlauf, R. (1994). Hox genes in vertebrate development. Cell *78*, 191–201.

Kuo, M.L., Duncavage, E.J., Mathew, R., den Besten, W., Pei, D., Naeve, D., Yamamoto, T., Cheng, C., Sherr, C.J., and Roussel, M.F. (2003). Arf induces p53-dependent and -independent antiproliferative genes. Cancer Res. *63*, 1046–1053.

Laiosa, C.V., Stadtfeld, M., and Graf, T. (2006). Determinants of lymphoid-myeloid lineage diversification. Annu. Rev. Immunol. *24*, 705–738.

Leek, J.T., Johnson, W.E., Parker, H.S., Jaffe, A.E., and Storey, J.D. (2012). The sva package for removing batch effects and other unwanted variation in high-throughput experiments. Bioinformatics *28*, 882–883.

Ley, T.J., Ding, L., Walter, M.J., McLellan, M.D., Lamprecht, T., Larson, D.E., Kandoth, C., Payton, J.E., Baty, J., Welch, J., et al. (2010). DNMT3A mutations in acute myeloid leukemia. N. Engl. J. Med. *363*, 2424–2433.

Majeti, R., Becker, M.W., Tian, Q., Lee, T.L., Yan, X., Liu, R., Chiang, J.H., Hood, L., Clarke, M.F., and Weissman, I.L. (2009). Dysregulated gene expression networks in human acute myelogenous leukemia stem cells. Proc. Natl. Acad. Sci. USA *106*, 3396–3401.

Marcucci, G., Haferlach, T., and Döhner, H. (2011). Molecular genetics of adult acute myeloid leukemia: prognostic and therapeutic implications. J. Clin. Oncol. *29*, 475–486.

Merico, D., Isserlin, R., Stueker, O., Emili, A., and Bader, G.D. (2010). Enrichment map: a network-based method for gene-set enrichment visualization and interpretation. PLoS ONE *5*, e13984.

Metzeler, K.H., Hummel, M., Bloomfield, C.D., Spiekermann, K., Braess, J., Sauerland, M.C., Heinecke, A., Radmacher, M., Marcucci, G., Whitman, S.P., et al.; Cancer and Leukemia Group B; German AML Cooperative Group. (2008). An 86-probe-set gene-expression signature predicts survival in cytogenetically normal acute myeloid leukemia. Blood *112*, 4193–4201.

Moens, C.B., and Selleri, L. (2006). Hox cofactors in vertebrate development. Dev. Biol. *291*, 193–206.

Mootha, V.K., Lindgren, C.M., Eriksson, K.F., Subramanian, A., Sihag, S., Lehar, J., Puigserver, P., Carlsson, E., Ridderstråle, M., Laurila, E., et al. (2003). PGC-1alpha-responsive genes involved in oxidative phosphorylation are coordinately downregulated in human diabetes. Nat. Genet. *34*, 267–273.

Novershtern, N., Subramanian, A., Lawton, L.N., Mak, R.H., Haining, W.N., McConkey, M.E., Habib, N., Yosef, N., Chang, C.Y., Shay, T., et al. (2011). Densely interconnected transcriptional circuits control cell states in human hematopoiesis. Cell *144*, 296–309.

Ong, C.C., Jubb, A.M., Zhou, W., Haverty, P.M., Harris, A.L., Belvin, M., Friedman, L.S., Koeppen, H., and Hoeflich, K.P. (2011). p21-activated kinase 1: PAK'ed with potential. Oncotarget *2*, 491–496.

Passegué, E., Wagner, E.F., and Weissman, I.L. (2004). JunB deficiency leads to a myeloproliferative disorder arising from hematopoietic stem cells. Cell *119*, 431–443.

Pineault, N., Abramovich, C., Ohta, H., and Humphries, R.K. (2004). Differential and common leukemogenic potentials of multiple NUP98-Hox fusion proteins alone or with Meis1. Mol. Cell. Biol. *24*, 1907–1917.

Rosenbauer, F., and Tenen, D.G. (2007). Transcription factors in myeloid development: balancing differentiation with transformation. Nat. Rev. Immunol. *7*, 105–117.

Rosenbauer, F., Wagner, K., Kutok, J.L., Iwasaki, H., Le Beau, M.M., Okuno, Y., Akashi, K., Fiering, S., and Tenen, D.G. (2004). Acute myeloid leukemia induced by graded reduction of a lineage-specific transcription factor, PU.1. Nat. Genet. *36*, 624–630.

Saeed, A.I., Bhagabati, N.K., Braisted, J.C., Liang, W., Sharov, V., Howe, E.A., Li, J., Thiagarajan, M., White, J.A., and Quackenbush, J. (2006). TM4 microarray software suite. Methods Enzymol. *411*, 134–193.

Saito, Y., Kitamura, H., Hijikata, A., Tomizawa-Murasawa, M., Tanaka, S., Takagi, S., Uchida, N., Suzuki, N., Sone, A., Najima, Y., et al. (2010). Identification of therapeutic targets for quiescent, chemotherapy-resistant human leukemia stem cells. Sci. Transl. Med. *2*, 17ra9.

Sauvageau, G., Thorsteinsdottir, U., Eaves, C.J., Lawrence, H.J., Largman, C., Lansdorp, P.M., and Humphries, R.K. (1995). Overexpression of HOXB4 in hematopoietic cells causes the selective expansion of more primitive populations in vitro and in vivo. Genes Dev. *9*, 1753–1765.

Sauvageau, G., Thorsteinsdottir, U., Hough, M.R., Hugo, P., Lawrence, H.J., Largman, C., and Humphries, R.K. (1997). Overexpression of HOXB3 in hematopoietic cells causes defective lymphoid development and progressive myeloproliferation. Immunity *6*, 13–22.

Scholl, C., Bansal, D., Döhner, K., Eiwen, K., Huntly, B.J., Lee, B.H., Rücker, F.G., Schlenk, R.F., Bullinger, L., Döhner, H., et al. (2007). The homeobox gene CDX2 is aberrantly expressed in most cases of acute myeloid leukemia and promotes leukemogenesis. J. Clin. Invest. *117*, 1037–1048.

Sitwala, K.V., Dandekar, M.N., and Hess, J.L. (2008). HOX proteins and leukemia. Int. J. Clin. Exp. Pathol. *1*, 461–474.

Somervaille, T.C., and Cleary, M.L. (2006). Identification and characterization of leukemia stem cells in murine MLL-AF9 acute myeloid leukemia. Cancer Cell *10*, 257–268.

Steidl, U., Rosenbauer, F., Verhaak, R.G., Gu, X., Ebralidze, A., Otu, H.H., Klippel, S., Steidl, C., Bruns, I., Costa, D.B., et al. (2006). Essential role of Jun family transcription factors in PU.1 knockdown-induced leukemic stem cells. Nat. Genet. *38*, 1269–1277.

Steidl, U., Steidl, C., Ebralidze, A., Chapuy, B., Han, H.J., Will, B., Rosenbauer, F., Becker, A., Wagner, K., Koschmieder, S., et al. (2007). A distal single nucleotide polymorphism alters long-range regulation of the PU.1 gene in acute myeloid leukemia. J. Clin. Invest. *117*, 2611–2620.

Subramanian, A., Tamayo, P., Mootha, V.K., Mukherjee, S., Ebert, B.L., Gillette, M.A., Paulovich, A., Pomeroy, S.L., Golub, T.R., Lander, E.S., and Mesirov, J.P. (2005). Gene set enrichment analysis: a knowledge-based approach for interpreting genome-wide expression profiles. Proc. Natl. Acad. Sci. USA *102*, 15545–15550.

Tenen, D.G. (2003). Disruption of differentiation in human cancer: AML shows the way. Nat. Rev. Cancer *3*, 89–101.

Thorsteinsdottir, U., Sauvageau, G., Hough, M.R., Dragowska, W., Lansdorp, P.M., Lawrence, H.J., Largman, C., and Humphries, R.K. (1997). Overexpression of HOXA10 in murine hematopoietic cells perturbs both myeloid and lymphoid differentiation and leads to acute myeloid leukemia. Mol. Cell. Biol. *17*, 495–505.

Tomasson, M.H., Xiang, Z., Walgren, R., Zhao, Y., Kasai, Y., Miner, T., Ries, R.E., Lubman, O., Fremont, D.H., McLellan, M.D., et al. (2008). Somatic mutations and germline sequence variants in the expressed tyrosine kinase genes of patients with de novo acute myeloid leukemia. Blood *111*, 4797–4808.

Will, B., Kawahara, M., Luciano, J.P., Bruns, I., Parekh, S., Erickson-Miller, C.L., Aivado, M.A., Verma, A., and Steidl, U. (2009). Effect of the nonpeptide thrombopoietin receptor agonist Eltrombopag on bone marrow cells from patients with acute myeloid leukemia and myelodysplastic syndrome. Blood *114*, 3899–3908.

Wouters, B.J., Löwenberg, B., Erpelinck-Verschueren, C.A., van Putten, W.L., Valk, P.J., and Delwel, R. (2009). Double CEBPA mutations, but not single CEBPA mutations, define a subgroup of acute myeloid leukemia with a distinctive gene expression profile that is uniquely associated with a favorable outcome. Blood *113*, 3088–3091.

Cancer Cell
Article

Core Transcriptional Regulatory Circuit Controlled by the TAL1 Complex in Human T Cell Acute Lymphoblastic Leukemia

Takaomi Sanda,[1,9] Lee N. Lawton,[2,9] M. Inmaculada Barrasa,[2] Zi Peng Fan,[2,3] Holger Kohlhammer,[5] Alejandro Gutierrez,[1,6] Wenxue Ma,[7] Jessica Tatarek,[8] Yebin Ahn,[1] Michelle A. Kelliher,[7] Catriona H.M. Jamieson,[7] Louis M. Staudt,[5] Richard A. Young,[2,4] and A. Thomas Look[1,6,*]

[1]Department of Pediatric Oncology, Dana-Farber Cancer Institute, Harvard Medical School, Boston, MA 02215, USA
[2]Whitehead Institute for Biomedical Research, Cambridge, MA 02142, USA
[3]Computational and Systems Biology Program
[4]Department of Biology
Massachusetts Institute of Technology, Cambridge, MA 02142, USA
[5]Metabolism Branch, National Cancer Institute, Bethesda, MD 20892, USA
[6]Division of Hematology/Oncology, Children's Hospital, Boston, MA 02115, USA
[7]Department of Medicine and Moores Cancer Center, University of California, San Diego, La Jolla, CA 92093, USA
[8]Department of Cancer Biology, University of Massachusetts Medical School, Worcester, MA 01605, USA
[9]These authors contributed equally to this work.
*Correspondence: thomas_look@dfci.harvard.edu
http://dx.doi.org/10.1016/j.ccr.2012.06.007

SUMMARY

The oncogenic transcription factor TAL1/SCL is aberrantly expressed in over 40% of cases of human T cell acute lymphoblastic leukemia (T-ALL), emphasizing its importance in the molecular pathogenesis of T-ALL. Here we identify the core transcriptional regulatory circuit controlled by TAL1 and its regulatory partners HEB, E2A, LMO1/2, GATA3, and RUNX1. We show that TAL1 forms a positive interconnected autoregulatory loop with GATA3 and RUNX1 and that the TAL1 complex directly activates the *MYB* oncogene, forming a positive feed-forward regulatory loop that reinforces and stabilizes the TAL1-regulated oncogenic program. One of the critical downstream targets in this circuitry is the *TRIB2* gene, which is oppositely regulated by TAL1 and E2A/HEB and is essential for the survival of T-ALL cells.

INTRODUCTION

In human T cell acute lymphoblastic leukemia (T-ALL), the normal molecular events contributing to thymocyte development are interrupted by genetic lesions that induce arrested differentiation, dysregulated proliferation, and aberrant survival, leading to clonal expansion of the fully transformed leukemic cells (Armstrong and Look, 2005; Look, 1997). TAL1/SCL, one of the most prevalent oncogenic transcription factors in T-ALL, is overexpressed in 40%–60% of T-ALL cases, owing to chromosomal translocations, an activating interstitial deletion (*SIL-TAL1* deletion), or undefined *trans*-acting mechanisms (Brown et al., 1990; Ferrando and Look, 2000; Ferrando et al., 2002). Results from gene expression analysis have demonstrated that TAL1 overexpression is associated with a differentiation block at the $CD4^+CD8^+$ double-positive (DP) stage of thymocytes in both human tumors and murine models (Ferrando et al., 2002; Larson et al., 1996; Tremblay et al., 2010).

TAL1 is a class II basic helix-loop-helix (bHLH) transcription factor that forms an obligate heterodimer with the class I bHLH E-proteins, which include TCF3/E2A and TCF12/HEB (Hsu et al., 1991, 1994). In hematopoietic cells, TAL1 regulates the

Significance

Studies in embryonic stem cells have revealed "core" transcriptional regulatory circuits that control pluripotency and self-renewal, raising the possibility that similar mechanisms might contribute to malignant transformation. Here we identify and dissect a core transcriptional regulatory circuit controlled by the aberrant expression of TAL1 in T-ALL cells. Our findings demonstrate that TAL1 and its binding partners GATA3 and RUNX1 form a positive autoregulatory loop, reinforced by a feed-forward mechanism involving the MYB oncoprotein, which likely contributes to the initiation and maintenance of the malignant state in thymocytes. Moreover, we implicate *TRIB2*, which is oppositely regulated by TAL1 and E2A/HEB and required for T-ALL cell survival.

transcription of its target genes by binding to E-box motifs and nucleating a large complex that includes the E-proteins, GATA family members, and several non-DNA-binding LMO proteins (Lécuyer et al., 2002; Wadman et al., 1997; Xu et al., 2003). TAL1 expression is normally silenced during early thymocyte development (Herblot et al., 2000); thus, its expression and the regulatory complex it recruits to its direct target genes are clearly aberrant in DP thymocytes. By contrast, E-proteins act as homo- or heterodimers to regulate gene expression (Kee, 2009) and are required for thymocyte development in a stage-specific manner (Bernard et al., 1998; Herblot et al., 2000). A number of genes have been implicated as direct targets of TAL1 and its regulatory partners in human T-ALL (Bernard et al., 1998; Herblot et al., 2000; Ono et al., 1998; Palii et al., 2011b; Palomero et al., 2006). Studies in murine models have shown that *E2a* and *Heb* are highly dosage dependent, in that haplo-insufficiency for either gene accelerates the onset of TAL1-induced T-ALL (O'Neil et al., 2004). Hence, although E2A and HEB are critical for the formation of the TAL1 transcriptional complex, a change in the relative dosage of each member can affect the onset and severity of leukemia, through mechanisms that remain to be elucidated.

Recently, several groups have identified high-level expression of genes encoding multiple transcription factors in the *TAL1*-overexpressing T-ALL subgroup, including *RUNX1*, *MYB*, *NKX3-1*, and *ETS* family members, such as *ERG* and *ETS1* (Clappier et al., 2007; Kusy et al., 2010; Lahortiga et al., 2007; O'Neil et al., 2007; Thoms et al., 2011). However, it has been difficult to integrate them into a unified network of altered gene regulation that promotes thymocyte transformation. The present study was designed to elucidate the role of TAL1 in this aberrant transcriptional circuitry.

RESULTS

TAL1 Binding Is Highly Overlapping in Multiple T-ALL Cell Lines and Primary T-ALL Cells

We generated high-resolution maps of the genomewide occupancy of TAL1 by chromatin immunoprecipitation coupled to massively parallel DNA sequencing (ChIP-seq; Table S1 available online). Multiple *TAL1*-expressing T-ALL samples were analyzed, which included two cell lines (Jurkat and CCRF-CEM; Figures S1A and 1B) and two "primagraft" samples ("Prima 2" and "Prima 5") derived from primary T-ALL cells expanded in immunocompromised mice without any exposure to in vitro culture. Aberrant expression of *TAL1* in both primagrafts and the CCRF-CEM cell line is due to an ~90-kb *SIL-TAL* deletion. The activity of the TAL1 antibody used was validated by ChIP followed by western blot analysis with a different specific antibody (Figure S1C). Of note, TAL1 was enriched in chromatin precipitated with anti-HEB and anti-E2A antibodies (Figure S1C) that do not cross-react (Figure S1D), consistent with its ability to heterodimerize with each of these E-proteins.

We first examined the results for known TAL1 target genes, including *CD69*, *TCRA* enhancer, and *NKX3-1* (Bernard et al., 1998; Kusy et al., 2010; Palii et al., 2011b), and detected TAL1 binding at sites in the regulatory regions of each gene (Figure 1A). Our results agree with previously reported TAL1 binding sites except for *NKX3-1* (Kusy et al., 2010), where we found that TAL1 occupied a region consistent with a candidate distal enhancer in each of the four T-ALL samples but not the previously identified promoter region (Figure 1A, right). We then investigated the relative overlap of high-confidence TAL1-bound regions across all four T-ALL samples. Pairwise comparisons of the top 200 TAL1-bound regions showed a high degree of agreement, compared with the results for NRSF-bound regions in Jurkat cells as a negative control (Figure 1B). Nearest neighbor analysis confirmed this result (Figure 1C). When we compared the relative distribution of TAL1-bound regions with the locations of protein-coding genes, the majority of the bound regions were within the gene body and intergenic regions of known protein-coding genes, consistent with the location of enhancer elements, as opposed to sites in the proximal or distal promoter (Figure 1D). Hence, the TAL1-binding sites identified in multiple T-ALL cell samples overlapped substantially at known and candidate regulatory elements.

We next sought to identify DNA motifs that were statistically overrepresented within 200 base pairs (bp) of the peak of TAL1 binding in each T-ALL sample. Four transcription factor binding motifs were enriched in TAL1-bound regions, including E-box (5′-CAG[CG]TG-3′), GATA (5′-AGATAA-3′), RUNX (5′-TGTGG TC-3′), and motifs recognized by the ETS family of transcription factors (5′-GGAA-3′) (Figure 1E). This complement of motifs is highly similar to the TAL1 motifs identified by ChIP-seq in normal murine hematopoietic progenitors and red cells (Kassouf et al., 2010; Wilson et al., 2010) and in human hematopoietic cells (Novershtern et al., 2011; Palii et al., 2011b; Tijssen et al., 2011). We expect that TAL1 is likely coregulating its target genes in T-ALL in a complex analogous to that identified in normal hematopoietic cells.

TAL1 Complex Controls Genes Involved in T Cell Homeostasis

To identify the regulatory network controlled by the TAL1 transcriptional complex in human T-ALL cells, we performed ChIP-seq analysis for TAL1 and its regulatory partners HEB, E2A, GATA3, RUNX1, and LMO1/2 in Jurkat and CCRF-CEM cells, which express high levels of LMO1 and LMO2, respectively (Figures S1A–S1C). The genomic sites occupied in T-ALL samples showed remarkable concordance for TAL1, its regulatory partners, and the transcriptional coactivator CBP, as illustrated for a known TAL1 complex target, the *TCRA* enhancer (Bernard et al., 1998; Hollenhorst et al., 2007) (Figure 2A). The E2A-bound regions we identified included a number of E2A target genes reported in murine thymocytes, including *PTCRA, NOTCH3, RAG1, RAG2*, and *GFI1* (Miyazaki et al., 2011).

Examination of the overlap among regions enriched for TAL1, HEB, E2A, LMO1/2, GATA3, or RUNX1 revealed that TAL1 binds to the majority of HEB- and E2A-enriched regions, which frequently overlap with the LMO1/2-, GATA3-, and RUNX1-enriched regions (Figures 2B and S2A). We next investigated the relative binding overlap of these factors within high-confidence enriched regions (Table S2), identifying three different classes of regulatory elements in both Jurkat (Figure 2C) and CCRF-CEM cells (Figure S2B). One showed concordant enrichment for multiple TAL1 complex members (Group 1), a second was predominantly occupied by GATA3 alone (Group 2), and a third was mainly occupied by RUNX1 alone (Group 3).

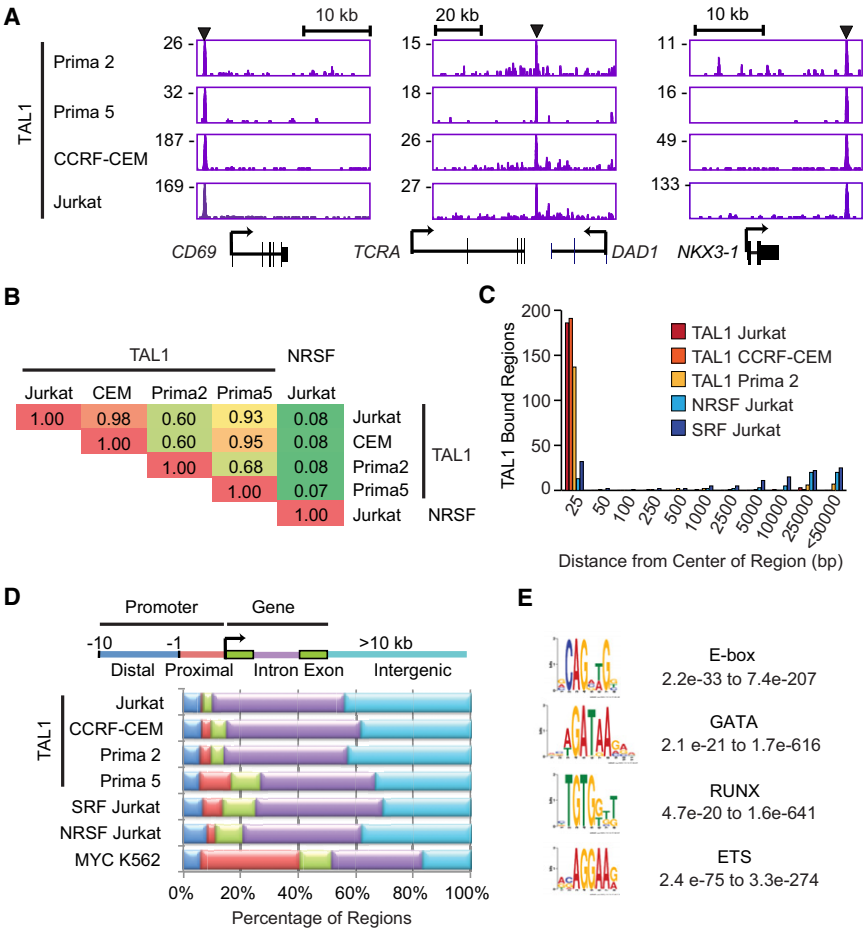

Figure 1. TAL1 Occupancy Is Highly Consistent across T-ALL Cell Lines and Primagraft Samples

(A) Gene tracks represent binding of TAL1 in T-ALL primagrafts (Prima 2 and Prima 5) and cell lines (CCRF-CEM and Jurkat) at the *CD69, TCRA*, and *NKX3-1* loci. The x axis indicates the linear sequence of genomic DNA, and the y axis the total number of mapped reads. The black horizontal bar above each gene example indicates the genomic scale in kilobases (kb). Black boxes in the gene map represent exons, and arrows indicate the location and direction of the transcriptional start site. Arrowheads denote regions bound by TAL1.

(B) Pairwise comparison of the TAL1-bound regions found in T-ALL primagrafts and cell lines. Fractions of the top 200 TAL1-bound regions in each cell type (rows) that were occupied by TAL1 in the other cell types (columns) are shown as a matrix. Regions occupied by the unrelated transcription factor NRSF in Jurkat served as a negative control.

(C) Distances from the center of the TAL1-bound region (top 200) in Prima 5 to the center of the nearest bound region of the indicated transcription factors were determined and grouped into bins (x axis); the heights of bars represent the sum of the bound regions in each bin (y axis).

(D) Each region bound by TAL1 was mapped to the closest Refseq gene: distal (blue) and proximal (red) promoters, exon (green), intron (violet), and intergenic regions (light blue) more than 10 kb from the gene.

(E) The representative position weight matrix for each motif enriched in TAL1 by ChIP-seq and the range of E-values found across different T-ALL cell types are shown.

See also Figure S1 and Table S1.

Several groups have reported that the TAL1 complex frequently contains ETS family members (e.g., *ETS1*) in multiple hematopoietic cell types (Palii et al., 2011b; Soler et al., 2010; Wilson et al., 2010). By comparing the ChIP-seq binding profiles for TAL1 complex members determined in our study with those described by three other groups (Hollenhorst et al., 2009; Palii et al., 2011b; Valouev et al., 2008), we determined that ETS1 occupancy correlates with the binding of other members of the TAL1 complex, as compared with two non-ETS transcription factors, SRF and NRSF (Figure S2C). *ERG*, an ETS family member, is also highly expressed and regulated by the TAL1 complex in human T-ALL cells (Thoms et al., 2011).

Analysis by the de novo motif discovery method, based on regions we have segregated into three groups, identified E-box, GATA, and RUNX motifs, as well as known motifs for the ETS family of transcription factors in Group 1, GATA and ETS motifs in Group 2, and RUNX, ETS, and SP1 motifs in Group 3 (Figure 2D). The distribution of consensus motifs for E-box, GATA, RUNX, and ETS motifs was centered under the peak of ChIP-seq enrichment within these three groups (Figure S2D). Moreover, the majority of enriched regions in Group 1 contained at least one E-box or one GATA motif within 200 bp of the center (n = 8,245/12,748 in Jurkat and n = 9,005/14,745 in CCRF-CEM). Many of the motifs enriched in E2A-bound regions had been identified in murine lymphocytes (Lin et al., 2010), where they also were frequently associated with ETS and RUNX binding sites.

To determine the dominant functions of the genes occupied by the TAL1 complex, we compared target genes (Table S3) to identify overrepresented functional groups (Figures S2E–S2G and Table S4). TAL1 complex targets were enriched in molecular pathways that regulate cell development, growth, and death, as well as those known to contribute to cancer and to hematological and immune diseases (Figures S2E and S2F). It is important to note that enriched genes include those regulating T cell development, differentiation, morphology, cell number, and activation (Figure S2G). These observations indicate that, in transformed thymocytes, the TAL1 complex sits at the apex of a network that drives aberrant proliferation, differentiation, and survival.

TAL1, GATA3, and RUNX1 Form a Positive Interconnected Autoregulatory Loop

It is important to note that we found that members of the TAL1 complex frequently occupy known and candidate regulatory regions of their own and each other's genes (Figure 3A). For example, members of the TAL1 complex co-occupy enhancers that have been identified by others in normal hematopoietic cells, including the *GATA3* 3′ T cell-specific enhancer (Hosoya-Ohmura et al., 2011), the *RUNX1* +23 enhancer (Nottingham et al., 2007) (Figure 3A), and the *LMO2* −24 enhancer (Landry

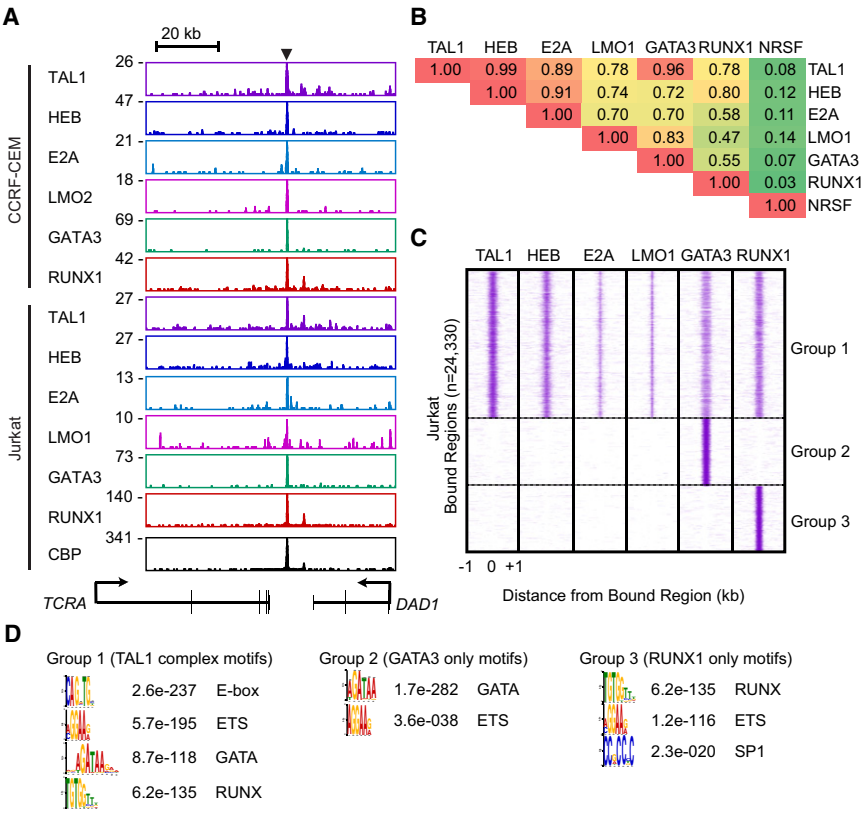

Figure 2. TAL1 Co-Occupies Genomic Sites with HEB, E2A, LMO1/2, GATA3, and RUNX1 in T-ALL Cells

(A) Gene tracks represent binding of TAL1, HEB, E2A, LMO1 or LMO2, GATA3, and RUNX1 at the *TCRA* locus in human T-ALL cell lines. See Figure 1A legend for details.

(B) Pairwise comparison of transcription factor-bound regions in Jurkat cells. Fraction of the top 200 bound regions for each transcription factor (rows) co-occupied by the all bound regions of the other transcription factors (columns) are shown as a matrix.

(C) Distributions of TAL1, HEB, E2A, LMO1, GATA3, and RUNX1 in regions bound by these transcription factors in Jurkat cells: Group 1 (bound by TAL1, HEB, E2A, LMO1, GATA3, or RUNX1), Group 2 (bound by GATA3 alone), or Group 3 (bound by RUNX1 alone). For each region (y axis), the sequence density centered at 0 indicates overlapping bound regions.

(D) DREME-based motif analysis of the regions shown in Figure 2C. The results are presented as position-weight matrices with the E-value significance and the name of the motif family within searched sequences.

See also Figure S2 and Tables S2, S3, and S4.

et al., 2009). A candidate enhancer 12 kb upstream of the *TAL1* gene, which is within the region between *SIL* and *TAL*1 that is frequently deleted in *TAL1*-positive T-ALL cases and is distinct from the regulatory elements previously described for normal hematopoietic cells (Göttgens et al., 2010), is co-occupied by TAL1 complex members and CBP in Jurkat cells (Figure 3A, left). Using ChIP-PCR, we found that these known and candidate regulatory elements for the *TAL1, RUNX1*, and *GATA3* loci are also frequently co-occupied by TAL1 complex members in primary T-ALL cases (Figure 3B).

To further dissect the function of the TAL1 complex, we used two independent short-hairpin RNAs (shRNAs) to knockdown the level of *TAL1* expression in T-ALL cell lines (Figure S3A). In this context, there was significant downregulation of a known target gene, *ALDH1A2* (Ono et al., 1998), which was rescued by re-expression of the *TAL1* cDNA (Figure S3B). Several cell surface markers related to T cell activation (CD69 and CD84) or cell survival in vivo (CD47) were also downregulated upon *TAL1* knockdown (Figure S3C and Table S5). Analysis of gene expression changes after *TAL1* knockdown in Jurkat cells showed that GATA3 and RUNX1 were significantly downregulated (Figure 3C). Similarly, knockdown of *GATA3* or *RUNX1* (Figure S3A) resulted in the coordinate downregulation of expression of each of these factors (Figure 3C). We observed the same relationships in CCRF-CEM cells (Figure S3D), except that knockdown of *GATA3* or *RUNX1* did not affect the levels of TAL1 expression, which was expected because in this cell line TAL1 expression is controlled by the *SIL* promoter. These alterations in expression after gene knockdown demonstrate the presence of a positive interconnected autoregulatory loop involving TAL1, GATA3, and RUNX1 and support the critical role of TAL1 overexpression in initiating the formation of the loop.

The knockdown of *TAL1* in Jurkat cells reduced the growth rate of these cells (Figures 3D and S3E), consistent with our previous study using *TAL1* shRNA #2 (Palomero et al., 2006) and published results of Palii and coworkers (Palii et al., 2011b). TAL1 shRNA #1 induced similar growth inhibition of multiple T-ALL cell lines expressing *TAL1* (Figure S3F and Table S5). We also detected increased fractions of apoptotic cells after transduction with shRNA #1, but not with shRNA #2 (Figure S3G), indicating that higher levels of *TAL1* knockdown are needed to detect cell death. Of note, knockdown of GATA3 and RUNX1 also inhibited cell growth and induced apoptosis (Figure 3D), indicating that each of these three components of the autoregulatory loop is required for cell growth and survival. Taken together, our results indicate that components of the TAL1 complex positively regulate each other in T-ALL and act to promote the growth and survival of T-ALL cells (Figure 3E), underscoring the importance of this positive interconnected autoregulatory loop in maintaining the malignant state.

Expression Levels of High-Confidence TAL1 Targets Classify T-ALL Subtypes

We next performed microarray gene expression analysis after knockdown of each transcription factor gene in Jurkat cells (Table S6). Gene set enrichment analysis (GSEA) revealed that genes enriched for TAL1 binding by ChIP-seq analysis were more likely to be downregulated upon *TAL1* knockdown than

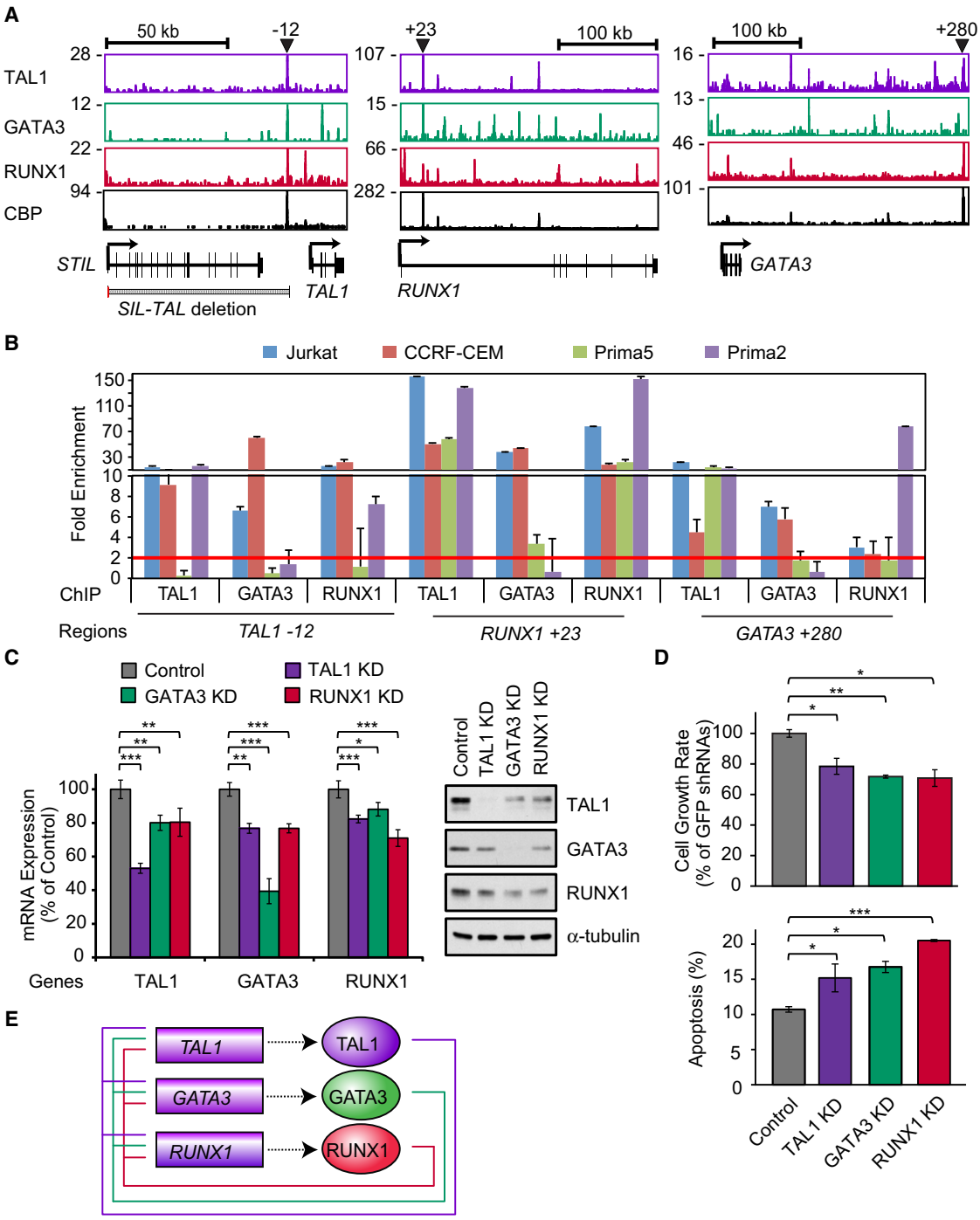

Figure 3. TAL1, GATA3, and RUNX1 Form a Positive Interconnected Autoregulatory Loop

(A) Gene tracks represent binding of TAL1, GATA3, RUNX1, and CBP at the *TAL1* (right), *RUNX1* (middle), and *GATA3* (left) loci in Jurkat cells. See Figure 1A legend for details.

(B) Co-occupancy by TAL1, GATA3, and RUNX1 at the *TAL1*, *RUNX1*, and *GATA3* gene loci in multiple T-ALL cells. Enrichment of regions indicated in panel A (*TAL1* enhancer, *RUNX1 +23*, and *GATA3 +280*) in four T-ALL cell samples (Jurkat, CCRF-CEM, Prima 2, and Prima 5) was analyzed by ChIP-PCR. The *NANOG* promoter was used as a negative control. The error bars represent the SD of the fold enrichment. The red line represents the 2-fold enrichment detection for the negative control.

(C) mRNA (left) and protein (right) levels of *TAL1, GATA3*, and *RUNX1* after knockdown (KD) of each of these factors in Jurkat cells. The data are means ± SD of duplicate experiments. *$p < 0.05$, **$p < 0.01$, and ***$p < 0.001$ by two-sample, two-tailed t test.

(D) Growth inhibition and apoptosis induction after knockdown of *TAL1, GATA3*, and *RUNX1* in Jurkat cells. Cell viability was measured after 3 and 7 days of lentivirus infection. The growth rate (Day 7/Day 3) is reported as means ± SD percentage of that for control shRNAs (*GFP* and *Luc*) in triplicate experiments.

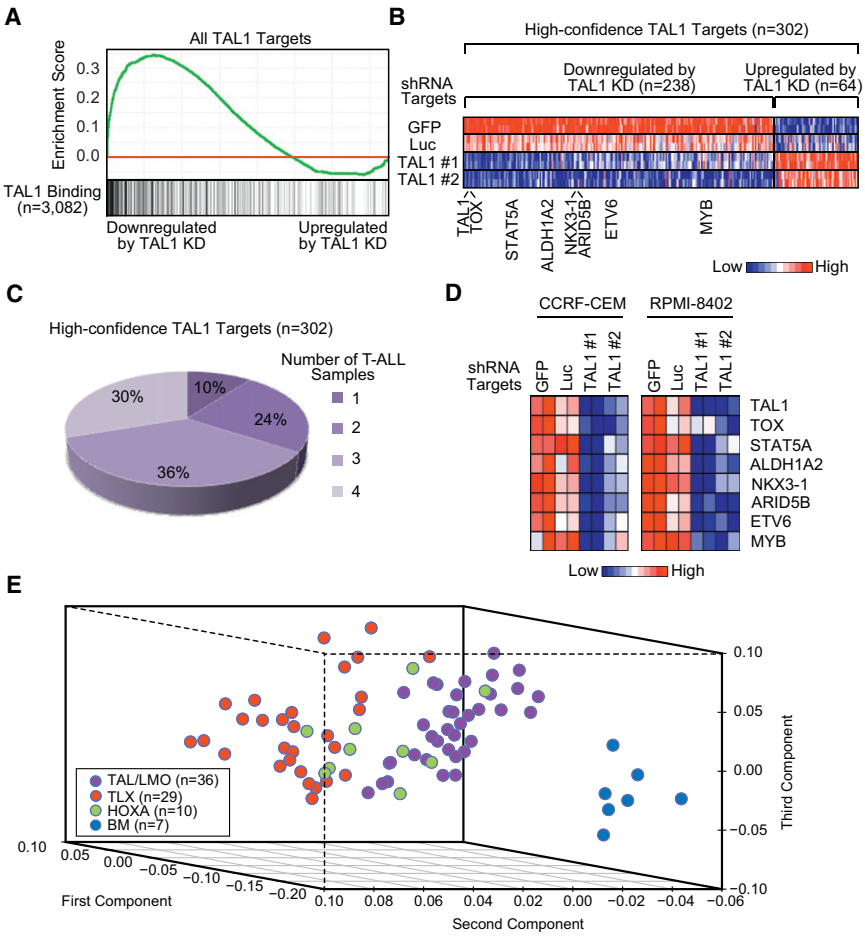

Figure 4. Expression of High-Confidence TAL1 Target Genes Classify T-ALL Subtypes

(A) GSEA to determine the correlation of DNA binding with gene expression change upon KD of *TAL1*. GSEA plot indicates the degree to which TAL1 targets are overrepresented at the extreme left (downregulated by KD) or right (upregulated by KD) of the entire ranked list. Solid bars represent bound genes.

(B) Heatmap images representing the relative expression levels of high-confidence TAL1 targets in Jurkat cells with or without KD of *TAL1*. Two independent shRNAs targeting *TAL1* as well as two control shRNAs (*GFP* and *Luc*) were transduced in Jurkat cells. Each row corresponds to a gene and is normalized across the row.

(C) TAL1 binding to high-confidence target genes (n = 302) in four T-ALL cell samples (Jurkat, CCRF-CEM, Prima 2, and Prima 5). The percentages of high-confidence TAL1 targets bound in Jurkat only (n = 1) or multiple T-ALL samples (n = 2–4) are indicated.

(D) Gene expression changes of TAL1 targets upon *TAL1* KD in CCRF-CEM and RPMI-8402 cells. Relative expression values (*TAL1*, *TOX*, *STAT5A*, *ALDH1A2*, *NKX3-1*, *ARID5B*, *ETV6*, and *MYB*) compared to *GAPDH* were calculated, normalized for each row, and shown as a heatmap. For all genes, the changes were significant at $p < 0.05$ by two-sample, two-tailed t test.

(E) Principal-component analysis of 75 primary T-ALL samples and seven BM samples based on the expression profile of high-confidence TAL1 target genes. Primary T-ALL samples were classified into three groups (*TAL/LMO*, *TLX*, and *HOXA*) based on the genetic alterations reported in the original article (Homminga et al., 2011). The analysis was performed with a set of 238 genes that are bound by TAL1 and significantly downregulated after *TAL1* knockdown (see Figure 4B, left).

See also Figure S4 and Tables S6 and S7.

genes lacking TAL1 occupancy (Figure 4A). This difference was statistically significant ($p < 2.2E-16$ by the Kolmogorov–Smirnov test), indicating that TAL1 acts predominantly as a positive regulator of the expression of its direct target genes in T-ALL.

Further analyses were based on high-confidence TAL1 target genes (n = 302) that showed TAL1 binding and significant alterations in expression ($p < 0.05$ with an absolute $\log_2$-fold change ≥ 0.24) upon *TAL1* knockdown (Figure 4B and Table S7). Since the *TAL1* gene was reduced by 1.89-fold, we were expecting modest but consistent expression changes in other target genes. The distribution of expression changes of genes selected was statistically different when compared to all genes ($p < 2.2E-16$; see also Figures S4A–S4C for details). The percentage of genes within the high-confidence targets occupied by TAL1 across the four T-ALL cells (Jurkat, CCRF-CEM, Prima 2, and Prima 5) showed that 90% of genes occupied in Jurkat cells were occupied by TAL1 in at least one of the other T-ALL samples (Figure 4C). To address whether the target genes that are directly regulated by TAL1 in Jurkat cells are similarly regulated in *TAL1*-positive T-ALL cells, we analyzed gene expression profiles in other *TAL1*-positive T-ALL cell lines and primary T-ALL samples. We observed consistent downregulation of selected TAL1 target genes upon *TAL1* knockdown in two additional T-ALL cell lines (CCRF-CEM and RPMI-8402; Figure 4D). Principal-component analysis of gene expression levels in 75 primary T-ALL samples with well-defined genetic alterations as well as seven normal bone marrow (BM) samples (Homminga et al., 2011), based on expression levels of the positively regulated high-confidence target genes (n = 238; Figure 4B, left), clearly distinguished the *TAL/LMO*-positive T-ALL subgroup from other subgroups (*TLX*- or *HOXA*-positive) and BM samples

Apoptosis was analyzed at Day 4 after lentiviral infection by flow cytometric analysis of cells stained with AnnexinV-fluorescein isothiocyanate (FITC). The values are means ± SD of duplicate experiments. Asterisks denote p values as described for (C).

(E) Positive interconnected autoregulatory loop formed by TAL1, GATA3, and RUNX1. Genes are represented by rectangles, and proteins are represented by ovals.

See also Figure S3 and Table S5.

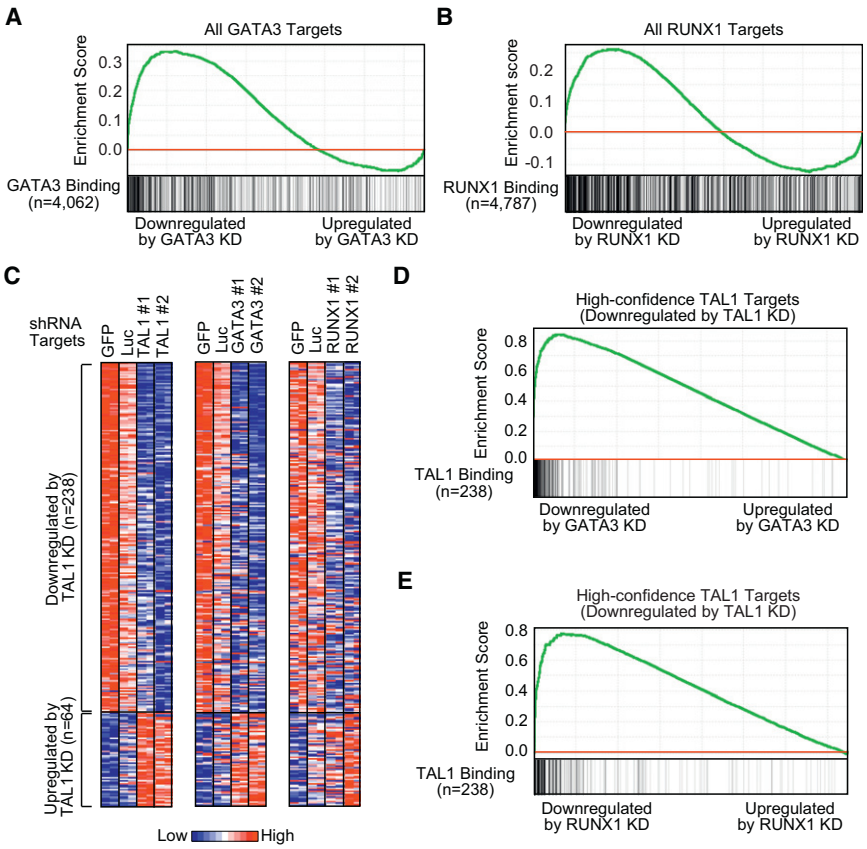

Figure 5. TAL1 Positively Regulates Target Genes with GATA3 and RUNX1 in Jurkat Cells

(A and B) GSEA to determine the correlation of DNA binding with gene expression changes upon knockdown (KD) of *GATA3* or *RUNX1*, respectively. See Figure 4A legend for details.

(C) Heatmap images representing the relative expression levels of high-confidence TAL1 targets in Jurkat cells with or without knockdown of *TAL1* (left), *GATA3* (middle), or *RUNX1* (right). See Figure 4B legend for details.

(D and E) GSEA of expression changes of high-confidence TAL1 targets upon KD of *GATA3* or *RUNX1*, respectively. TAL1 target genes (n = 238) that were significantly downregulated by TAL1 knockdown (Figure 4B, left) were used as a gene set.

(Figure 4E), confirming the importance of these TAL1 target genes in *TAL1*-positive T-ALL cases. High levels of expression of the TAL1 targets were observed in primary *TAL1*-positive T-ALL samples (Figure S4D).

TAL1 Positively Regulates Target Henes in Concert with GATA3 and RUNX1

An important question in this study was whether GATA3 and RUNX1 coordinately regulate gene expression with TAL1 in T-ALL cells. When genes enriched for GATA3 binding were analyzed by GSEA, most of them were downregulated after *GATA3* knockdown (Figure 5A), implicating GATA3 as a positive regulator of their expressions in T-ALL. By contrast, direct targets of RUNX1 were equally likely to be up- or downregulated when *RUNX1* was depleted (Figure 5B).

Interrogation of the effects of *GATA3* or *RUNX1* depletion on the expression of the 238 high-confidence TAL1 target genes revealed that the genes downregulated upon loss of *TAL1* expression were generally also downregulated by the loss of *GATA3* or *RUNX1* expression (Figures 5C–5E), indicating that TAL1 acts in concert with GATA3 and RUNX1 to positively regulate the majority of its direct target genes in T-ALL.

MYB Oncogene Coordinately Regulates TAL1 Target Henes

MYB overexpression, mediated in part through gene duplication, is commonly found in T-ALL (Clappier et al., 2007; Lahortiga et al., 2007; O'Neil et al., 2007) (Figure S5A). Interrogation of ChIP-seq data across the *MYB* locus indicated that *MYB* was a common target of the TAL1 complex in *TAL1*-positive T-ALL cell lines (Figure 6A), indicating that it is directly upregulated by the TAL1 complex due to the aberrant expression of *TAL1*. The TAL1-occupied regions included the known locus control region located 77 kb upstream of *Myb* in mice (Ramsay and Gonda, 2008) and a candidate regulatory element within intron 8 (+14) co-occupied by the TAL1 complex in T-ALL cells (Figure 6A). Co-occupancy of the TAL1 complex was observed at this candidate regulatory element in T-ALL primagrafts and cell lines by ChIP-PCR (Figure 6B). In all cases, *MYB* gene expression was sensitive to the reduction of multiple TAL1 complex members in Jurkat and CCRF-CEM cells (Figures 6C and S5B).

Since MYB is a known transcriptional regulator of normal and malignant hematopoiesis (Ramsay and Gonda, 2008), a reduction of its expression could indicate the transcriptional relationship between the TAL1 complex and this gene in T-ALL. We therefore performed knockdown analysis of *MYB* (Figure S5C), followed by microarray gene expression analysis. The result showed that many TAL1 targets were also significantly downregulated by *MYB* knockdown (Figures 6D and S5D), indicating that MYB not only is induced by TAL1 but also acts to coordinately upregulate overlapping sets of target genes controlled by TAL1. Thus, the *MYB* oncogene appears to reinforce the activities of the TAL1-regulated oncogenic network through a feed-forward circuit that maintains the gene expression program in T-ALL cells (Figure 6E).

HEB and E2A Oppose Positive Regulation by TAL1 at Critical Target Genes

Several groups have postulated that the ectopic expression of *TAL1* in normal thymocytes may antagonize the physiologic activities of E2A or HEB in thymocyte development by recruiting them into the TAL1 complex, where they could deregulate key target genes (Bain et al., 1997; Herblot et al., 2000; O'Neil

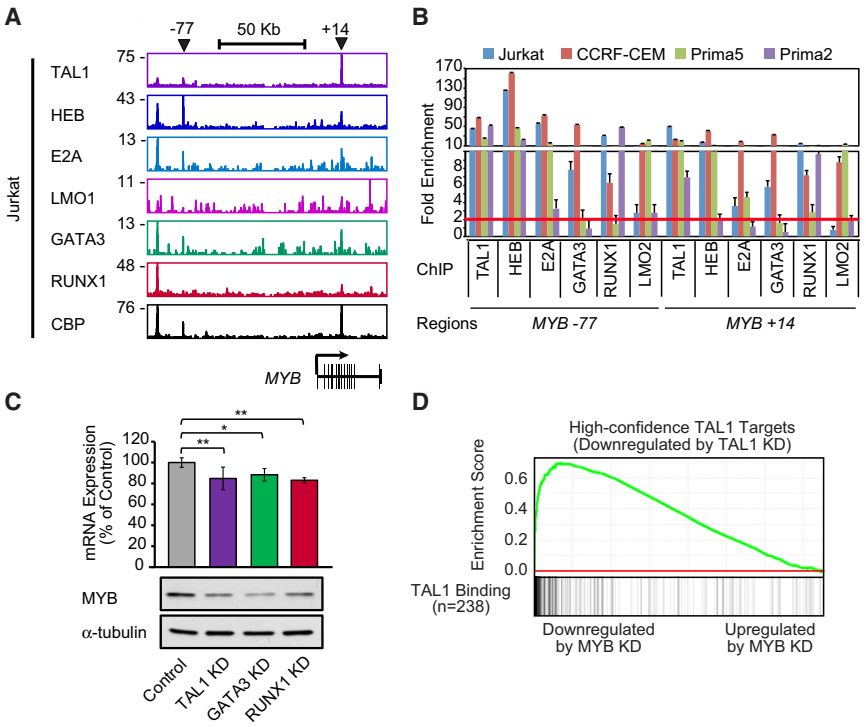

Figure 6. TAL1 Positively Regulates the *MYB* Oncogene, which Coordinately Regulates TAL1 Target Genes

(A) Gene tracks represent binding of TAL1, HEB, E2A, LMO1, GATA3, RUNX1, and CBP at the *MYB* gene locus in Jurkat cells. See Figure 1A legend for details.

(B) Co-occupancy by the TAL1 complex at the *MYB* gene in multiple T-ALL cell samples by ChIP-PCR. See Figure 3B legend for details.

(C) mRNA (top) and protein (bottom) levels of *MYB* after knockdown (KD) of *TAL1, GATA3*, and *RUNX1* in Jurkat cells. The data are means ± SD of duplicate experiments. *$p < 0.05$ and **$p < 0.01$ by two-sample, two-tailed t test.

(D) GSEA of expression changes of high-confidence TAL1 targets upon *MYB* knockdown. TAL1 target genes (n = 238) that were significantly downregulated by *TAL1* KD were used as a gene set. See Figure 4A legend for details.

(E) Positive feed-forward loop formed by the TAL1 complex and *MYB* that controls the gene expression program of T-ALL cells. *MYB* is bound and activated by the TAL1 complex and, in turn, regulates the same set of genes.

See also Figure S5.

et al., 2004). Hence, we next interrogated the effects of *HEB* and *E2A* knockdown (Figure S6) on the expression of their direct target genes. GSEA revealed that genes enriched for HEB or E2A binding by ChIP-seq analysis could be either down- or up-regulated after knockdown of each gene (Figures 7A and 7B). As expected, 40% of the TAL1 target genes that were downregulated after *TAL1* knockdown were also downregulated by the knockdown of either *E2A* or *HEB* (Figures 7C–7E, left). By contrast, 25% of the TAL1 target genes that were downregulated by TAL1 knockdown were upregulated by the loss of either *E2A* or *HEB* expression (Figures 7C–7E, right), indicating that they can act to repress gene expression in the absence of TAL1. Only 50 of the 238 genes that were downregulated after *TAL1* knockdown were significantly upregulated after knockdown of *HEB* and/or *E2A*, and an even smaller group of seven TAL1 target genes showed the inverse relationship (Table S8).

TRIB2 Is a Critical Target of TAL1 and Is Required for the Survival of T-ALL Cells

We also conducted an inducible RNA interference screen (Ngo et al., 2006) in two *TAL1*-positive T-ALL cell lines (Jurkat and CCRF-CEM) and identified four genes that were required for T-ALL growth among the high-confidence targets: *STAT5A*, *TNFSF4*, *PI3KC2B*, and *TRIB2* (Table S9). An especially attractive candidate target of the TAL1 complex is *TRIB2* (Figure 8A), whose expression was downregulated by *TAL1* knockdown and upregulated by *E2A* knockdown in multiple TAL1-positive T-ALL cell lines (Figure 8B). After 3 weeks of culture, Jurkat or CCRF-CEM cells expressing two different shRNAs targeting *TRIB2* were depleted (Figure 8C). This result was validated by knockdown of *TRIB2* using another shRNA (Figure 8D), which was partially rescued by the ectopic expression of the *TRIB2* cDNA (Figure 8E). *TRIB2* knockdown inhibited the growth of additional *TAL1*-positive T-ALL cell lines (Figure 8F) and induced apoptosis in each cell line (Figure 8G) but did not affect the cell cycle phase distribution (Figure S7), indicating that this factor is required for the survival of T-ALL cells. A reasonable hypothesis is that *TRIB2* is transcriptionally repressed by E-proteins and the aberrant expression of TAL1 by translocation or intrachromosomal rearrangement upregulates *TRIB2* expression by heterodimerizing with E2A and HEB, thus actively opposing their repressive effects on the *TRIB2* locus (Figure 8H).

DISCUSSION

We have identified a set of transcriptional regulators that collaborate with TAL1 to generate a ''core'' regulatory circuit that contributes to the initiation and maintenance of human T-ALL. Critically, we found that TAL1, GATA3, and RUNX1 co-occupy elements of their own and each other's genes, forming a positive interconnected autoregulatory loop. This network structure provides the means by which aberrant expression of a single oncogenic transcription factor can have sustained effects on an entire program of gene expression that contributes to

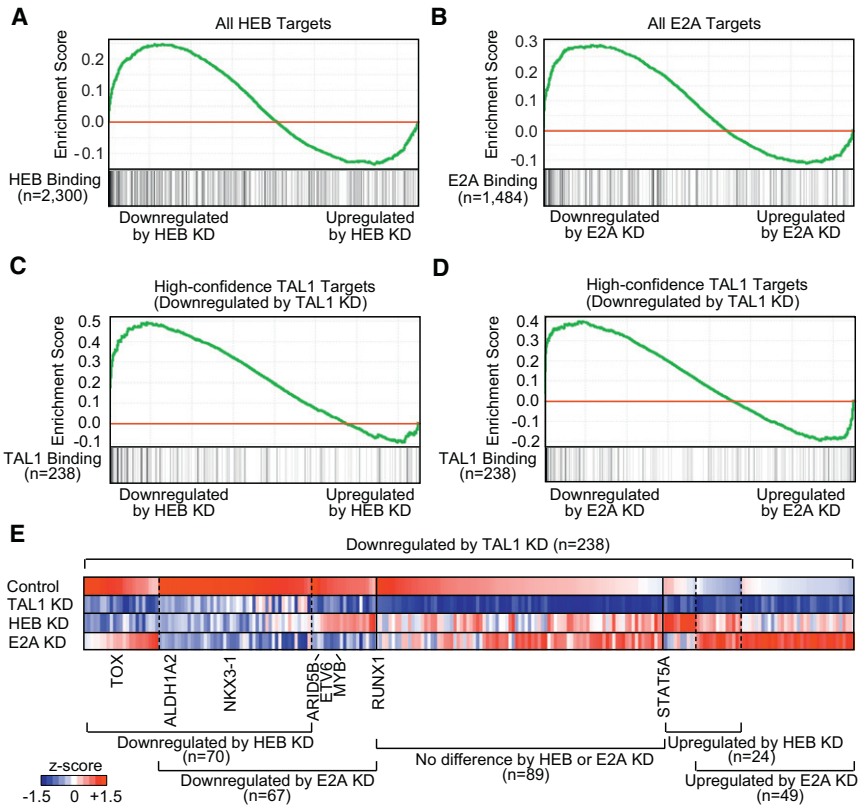

Figure 7. TAL1 Positively Regulates the Expression of a Specific Subset of Genes that Are Negatively Regulated by HEB and E2A

(A and B) GSEA to determine the correlation of DNA binding with gene expression changes upon knockdown (KD) of *HEB* or *E2A*, respectively. See Figure 4A legend for details.

(C and D) GSEA of expression changes of high-confidence TAL1 targets upon KD of *HEB* or E2A, respectively. TAL1 target genes (n = 238) that were significantly downregulated by *TAL1* KD (see Figure 4B, left) were used as a gene set.

(E) Heatmap image representing expression levels of the responsive TAL1 targets in Jurkat cells upon KD of *TAL1*, *HEB*, or *E2A*. Relative gene expression levels normalized for each gene are illustrated.

See also Figure S6 and Table S8.

malignant transformation. Indeed, such regulatory structures have been shown to reinforce and increase the stability of gene expression programs (Alon, 2007), which, in turn, act to establish and maintain critical cell states, such as pluripotency in embryonic stem cells (Young, 2011).

Expression of GATA3 and RUNX1 is required in normal T-lineage commitment to CD4 or CD8 single-positive cells, respectively (Collins et al., 2009; Ho et al., 2009). TAL1-sustained upregulation of GATA3 and RUNX1 may therefore contribute to the differentiation block at the DP stage. Thus, overexpression of RUNX1 appears to contribute to thymocyte transformation in *TAL1*-positive T-ALL, in marked contrast to its role as a tumor suppressor whose loss of function promotes the onset of acute myeloid leukemia (AML) and myelodysplastic syndromes. Two groups have also recently reported inactivating *RUNX1* mutations in the early thymocyte precursor (ETP) subgroup of T-ALL (Della Gatta et al., 2012; Grossmann et al., 2011). ETP leukemia is distinct from *TAL1*-positive T-ALL, which generally shows a block at the DP stage of thymocyte development and involves different aberrant molecular pathways leading to transformation (Coustan-Smith et al., 2009; Gutierrez et al., 2010; Zhang et al., 2012). Thus, despite the presence of inactivating *RUNX1* mutations in ETP T-ALL, our data show that, in T-ALLs blocked in a later DP stage of thymocyte development, RUNX1 serves as a key member of an interconnected autoregulatory loop involved in reinforcing and stabilizing the malignant cell state.

We also identified an oncogenic transcription factor gene, *MYB*, as a direct target of TAL1 that is expressed at high levels in *TAL1*-positive T-ALL cases. It integrates with the TAL1-controlled transcriptional network through a positive feed-forward loop that likely acts to stabilize the TAL1 oncogenic program, similar to mechanisms first identified in model organisms (Alon, 2007). The *Myb* gene was reported as a *Tal1* target in murine hematopoietic progenitor cells (Wilson et al., 2009), which may reflect an important regulatory module shared by leukemic and normal stem cells. MYB has recently been implicated in the control of aberrant self-renewal programs in AML (Zuber et al., 2011), reinforcing its potential importance as the target of a feed-forward regulatory motif mediated by the TAL1 complex in T-ALL. This transcriptional regulatory circuit is also implicated in normal hematopoiesis (Novershtern et al., 2011) and presumably contributes to the establishment and stability of the transformed state in TAL1-overexpressing thymocytes.

It will be important to confirm and extend our results with shRNA knockdown as we have done with ChIP-seq analysis in primary T-ALL cells. Several groups have reported success with shRNA gene knockdown in primary T-ALL cells (Gerby et al., 2010; Kusy et al., 2010; Palii et al., 2011a, 2011b). These procedures involve both improved lentivirus production using the new-generation plasmids (Palii et al., 2011a, 2011b) and the new pseudotyping vector, resulting in interleukin 7 (IL-7)-displaying lentiviral vectors that promote efficient gene transfer into primary T cells (Gerby et al., 2010; Kusy et al., 2010; Verhoeyen et al., 2003). We are now attempting to optimize these procedures for shRNA transduction into primary T-ALL cells explanted from our primagraft models. When established, this approach should be helpful in tracing the regulatory circuits in de novo T-ALL leukemias.

We also present a comprehensive analysis of the gene set that is differentially regulated by TAL1 and its partners, HEB and E2A. Many of the direct targets of these three interacting proteins are coordinately upregulated as a consequence of binding to key regulatory regions. Only a small subset of these

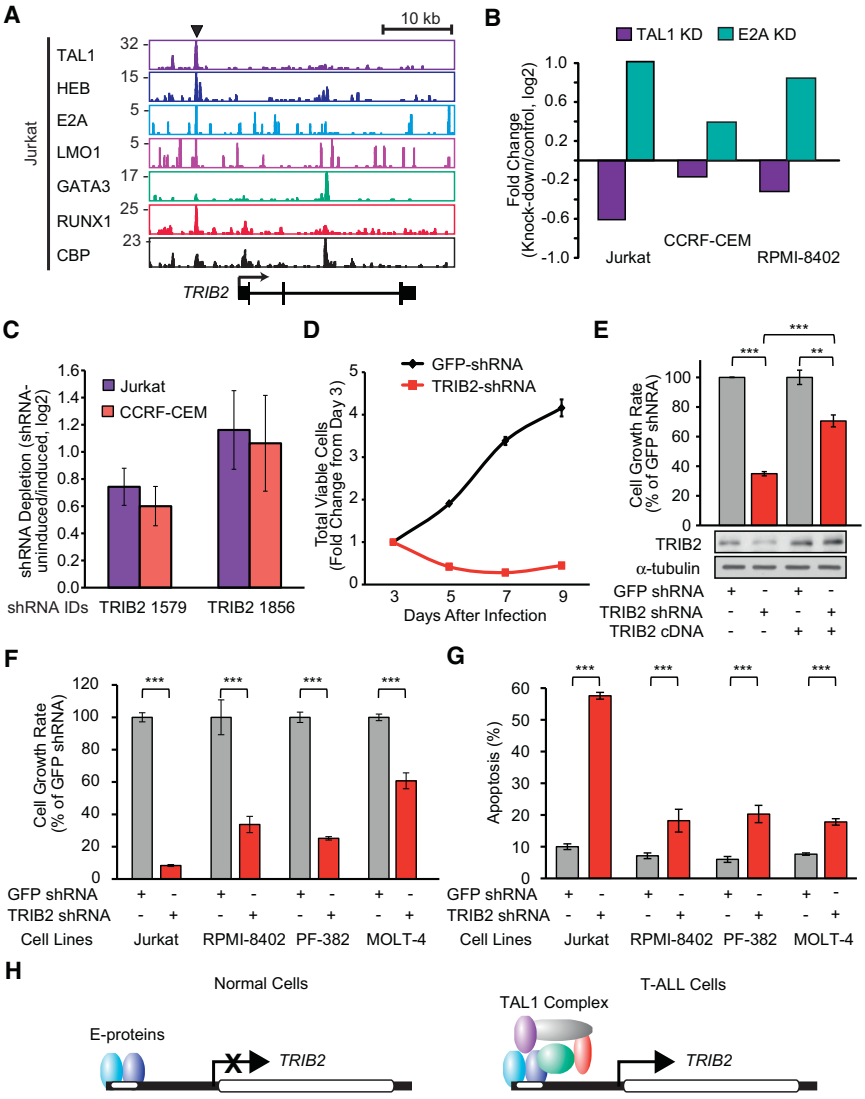

Figure 8. *TRIB2* Gene Is Required for the Survival of T-ALL Cells

(A) Gene tracks represent binding of TAL1, HEB, E2A, LMO1, GATA3, RUNX1, and CBP at the *TRIB2* gene locus in Jurkat cells. See Figure 1A legend for details.

(B) Comparison of mRNA expression of *TRIB2* gene in three TAL1-positive T-ALL cell lines transduced with shRNAs targeting *TAL1*, *E2A* or control shRNAs and analyzed by qRT-PCR. Mean fold-changes (knockdown/controls, $\log_2$) are shown.

(C) shRNA screen with 12,500 inducible shRNAs that target 1,050 genes, performed on two *TAL1*-positive T-ALL cell lines (Jurkat and CCRF-CEM). Depletion of *TRIB2* shRNAs from the cell population was calculated as uninduced/induced, $\log_2$, and shown as the mean ± SE of the mean of four independent experiments.

(D) Growth inhibition by *TRIB2* knockdown in Jurkat cells. Cell viability was measured after 3, 5, 7, and 9 days of lentivirus infection with control (GFP) and *TRIB2* shRNA. The growth rate (fold-change) compared to Day 3 is indicated. Values are given as mean ± SD of triplicate experiments.

(E) cDNA containing the wild-type *TRIB2* coding region was transduced by retroviral infection of Jurkat cells, followed by lentivirus-mediated transduction of infected cells with control *GFP* or *TRIB2* shRNA. The growth rate (Day 7/Day 3) after lentivirus infection was assessed for *TRIB2* shRNA relative to *GFP* shRNA and is shown as the mean ± SD of triplicate experiments. $^{**}p < 0.01$ and $^{***}p < 0.001$ by two-sample, two-tailed t test.

(F) Growth rate (Day 7/Day 3) was assessed for each *TRIB2* shRNA relative to control *GFP* shRNA in each cell line (Jurkat, RPMI-8402, PF-382, or MOLT-4) and is reported as the mean ± SD of triplicate experiments.

(G) Apoptosis was measured in four T–ALL cell lines after 4 days of lentiviral infection by flow cytometric analysis of cells stained with AnnexinV-FITC. The values are given as mean ± SD of triplicate experiments.

(H) Model of differential regulation of E-protein (HEB and E2A) targets in normal versus malignant T cells. *TRIB2* that is repressed by HEB and E2A in normal cells (left) is upregulated by the TAL1 complex in T-ALL (right).

See also Figure S7 and Table S9.

direct targets are differentially regulated physiologically when E2A and HEB are coexpressed compared to the cell state attained when TAL1 is aberrantly overexpressed. This aspect of our study is crucial to understanding T-ALL pathogenesis, because it directly addresses in vivo data indicating that haplo-insufficiency for either *E2a* or *Heb* markedly accelerates the onset of T-ALL in *Tal1*-transgenic mice (O'Neil et al., 2004). Among the relatively small set of genes directly targeted by TAL1 in T-ALL cells, only those activated by TAL1 but repressed by E2A and HEB would produce this phenotype. Some of these genes are likely inconsequential in terms of a contribution to the malignant phenotype, such as those normally expressed only in activated mature T cells (e.g., *CD28* and *GMZA*) as well as genes that are not associated at all with the T cell lineage (e.g., *KRT1* and *KRT2*).

Mammalian genes of the *Tribbles* family (*TRIB1, TRIB2*, and *TRIB3*) encode proteins that contain pseudokinase domains that are unable to directly phosphorylate target proteins but rather appear to act as adaptors that negatively regulate key cellular signaling pathways (Yokoyama and Nakamura, 2011). Overexpression of *TRIB2* by retroviral transduction in murine hematopoietic stem cells identified it as an oncogene that contributes to AML (Keeshan et al., 2006). Our data indicate that TRIB2 is required for the survival of T-ALL cells. Until our analysis, there had been no evidence implicating *TRIB2* in T-ALL pathogenesis, although this role was not entirely unexpected given the expression of *TRIB2* in a specific subset of AML cases that shared characteristics with T cells and the status of this gene as a target of NOTCH1 (Wouters et al., 2007). Since *TRIB2* is a direct target for upregulation by both the NOTCH1

and TAL1 transcription factors, our data suggest that a progressive increase in its expression levels contribute to the collaboration between aberrant *TAL1* expression and mutationally activated *NOTCH1* in the pathogenesis of T-ALL.

EXPERIMENTAL PROCEDURES

T-ALL Cell Samples

Human T-ALL cell lines were maintained in RPMI-1640 medium (Invitrogen, Carlsbad, CA, USA) supplemented with 10% fetal bovine serum (Sigma-Aldrich, St Louis, MO, USA), L-glutamine, and penicillin/streptomycin (Invitrogen). Diagnostic T-ALL samples were obtained with informed consent and institutional review board (IRB) approval from children treated in Dana-Farber Cancer Institute Study 05-01 and were used with existing IRB approval by the University of California, San Diego (UCSD), Human Research Protections Program, titled "Protocol 070678: Permission to Collect Blood and/or Bone Specimens and/or Tumor Samples and/or Saliva from Patients with Hematology Problems for Research (Adult)." Human $CD34^+$ T-ALL cells were transplanted into $Rag2^{-/-}\gamma c^{-/-}$ mice to propagate the cells as "primagrafts." This study was carried out in strict accordance with the recommendations of the Institutional Animal Care and Use Committee at the UCSD. The protocol was approved by the Committee Under Animal Use Protocol Number S06015. Human leukemia cells were isolated from these primagrafts and used in TAL1 ChIP-seq analysis.

ChIP

ChIP was performed according to previously described methods (Lee et al., 2006). The antibodies and detailed ChIP conditions can be found in the Supplemental Experimental Procedures. For ChIP-seq analysis, Solexa/Illumina sequencing and analysis were conducted according to the protocol described by Marson et al. (2008).

shRNA Knockdown Analysis

shRNA sequences were cloned into the lentiviral vector pLKO.1-puro. Each construct was cotransfected into 293T cells with delta 8.9 and VSV-G using FuGENE 6 reagent (Roche, Indianapolis, IN, USA). Supernatants containing the lentivirus were collected, filtered, and added to T-ALL cell lines in the presence of polybrene. The level of knockdown was verified by qRT-PCR for RNA or by western blot.

RNA Extraction, cDNA, and Expression Analysis

We extracted mRNA by Trizol (Invitrogen) followed by column purification using the RNeasy Mini Kit (QIAGEN, Valencia, CA, USA). Purified RNA was reverse-transcribed using QuantiTect (QIAGEN). Quantitative real-time qPCR was performed on the AB7300 Detection System (Applied Biosystems, Foster City, CA, USA) using gene-specific primers and Power SYBR Green PCR Master Mix (Applied Biosystems).

Microarray Expression Analysis

Total RNA samples from two biological replicates performed in Jurkat cells were used to assess gene expression change for two target shRNAs per transcription factor versus two control shRNA performed in duplicate on Affymetrix HG U133 2.0 plus microarrays. The detailed analysis can be found in the Supplemental Experimental Procedures. GSEA (Broad Institute, Cambridge, MA, USA) was performed for direct targets identified by ChIP-seq by comparing control samples with knockdown samples. The genes, which are direct TAL1 targets identified by ChIP-seq based on a significant gene expression change upon shRNA knockdown (absolute $\log_2$-fold change ≥ 0.24; $p < 0.05$), were defined as the high-confidence TAL1 targets and used as a gene set.

ACCESSION NUMBERS

Expression data and ChIP-seq can be found at http://www.ncbi.nlm.nih.gov/geo/ under superseries accession number GSE29181.

SUPPLEMENTAL INFORMATION

Supplemental Information includes seven figures, nine tables, and Supplemental Experimental Procedures and can be found with this article online at http://dx.doi.org/10.1016/j.ccr.2012.06.007.

ACKNOWLEDGMENTS

We thank the members of the Look and Young laboratories for discussions and critical review and Jennifer O'Neil for initial experimentation and TAL1 plasmids. We are grateful to Garrett Frampton and Dave Orlando for the development of ChIP-seq analysis tools and continued support with the analysis. We are also grateful to the Whitehead Genome Technology Core (V. Dhanapal, J.-A. Kwon, J. Love, S. Gupta, and T. Volkert) for assistance with ChIP-Seq and expression array hybridization and to Bingbing Yuan from BaRC for developing the phenotype ontology analysis. We acknowledge the RNAi Consortium for providing lentivirus shRNA constructs, and we thank John R. Gilbert for editing and critical review of the manuscript. This research was supported by grants (5P01CA109901, 5P01CA68484, and 1K99CA157951) from the National Cancer Institute and by the Intramural Research Program of the National Institutes of Health, National Cancer Institute, Center for Cancer Research. T.S. is supported by grants from the William Lawrence and Blanche Hughes Foundation, the Children's Leukemia Research Association, and the Japan Society for the Promotion of Science. W.M. and C.J. are supported by the California Institute for Regenerative Medicine Leukemia Team grant.

Received: April 15, 2011
Revised: March 9, 2012
Accepted: June 15, 2012
Published: August 13, 2012

REFERENCES

Alon, U. (2007). Network motifs: theory and experimental approaches. Nat. Rev. Genet. *8*, 450–461.

Armstrong, S.A., and Look, A.T. (2005). Molecular genetics of acute lymphoblastic leukemia. J. Clin. Oncol. *23*, 6306–6315.

Bain, G., Engel, I., Robanus Maandag, E.C., te Riele, H.P., Voland, J.R., Sharp, L.L., Chun, J., Huey, B., Pinkel, D., and Murre, C. (1997). E2A deficiency leads to abnormalities in alphabeta T-cell development and to rapid development of T-cell lymphomas. Mol. Cell. Biol. *17*, 4782–4791.

Bernard, M., Delabesse, E., Smit, L., Millien, C., Kirsch, I.R., Strominger, J.L., and Macintyre, E.A. (1998). Helix-loop-helix (E2-5, HEB, TAL1 and Id1) protein interaction with the TCRalphadelta enhancers. Int. Immunol. *10*, 1539–1549.

Brown, L., Cheng, J.T., Chen, Q., Siciliano, M.J., Crist, W., Buchanan, G., and Baer, R. (1990). Site-specific recombination of the tal-1 gene is a common occurrence in human T cell leukemia. EMBO J. *9*, 3343–3351.

Clappier, E., Cuccuini, W., Kalota, A., Crinquette, A., Cayuela, J.M., Dik, W.A., Langerak, A.W., Montpellier, B., Nadel, B., Walrafen, P., et al. (2007). The C-MYB locus is involved in chromosomal translocation and genomic duplications in human T-cell acute leukemia (T-ALL), the translocation defining a new T-ALL subtype in very young children. Blood *110*, 1251–1261.

Collins, A., Littman, D.R., and Taniuchi, I. (2009). RUNX proteins in transcription factor networks that regulate T-cell lineage choice. Nat. Rev. Immunol. *9*, 106–115.

Coustan-Smith, E., Mullighan, C.G., Onciu, M., Behm, F.G., Raimondi, S.C., Pei, D., Cheng, C., Su, X., Rubnitz, J.E., Basso, G., et al. (2009). Early T-cell precursor leukaemia: a subtype of very high-risk acute lymphoblastic leukaemia. Lancet Oncol. *10*, 147–156.

Della Gatta, G., Palomero, T., Perez-Garcia, A., Ambesi-Impiombato, A., Bansal, M., Carpenter, Z.W., De Keersmaecker, K., Sole, X., Xu, L., Paietta, E., et al. (2012). Reverse engineering of TLX oncogenic transcriptional networks identifies RUNX1 as tumor suppressor in T-ALL. Nat. Med. *18*, 436–440.

Ferrando, A.A., and Look, A.T. (2000). Clinical implications of recurring chromosomal and associated molecular abnormalities in acute lymphoblastic leukemia. Semin. Hematol. *37*, 381–395.

Ferrando, A.A., Neuberg, D.S., Staunton, J., Loh, M.L., Huard, C., Raimondi, S.C., Behm, F.G., Pui, C.H., Downing, J.R., Gilliland, D.G., et al. (2002). Gene expression signatures define novel oncogenic pathways in T cell acute lymphoblastic leukemia. Cancer Cell *1*, 75–87.

Gerby, B., Armstrong, F., de la Grange, P.B., Medyouf, H., Calvo, J., Verhoeyen, E., Cosset, F.L., Bernstein, I., Amselem, S., Boissel, N., et al. (2010). Optimized gene transfer into human primary leukemic T cell with NOD-SCID/leukemia-initiating cell activity. Leukemia *24*, 646–649.

Göttgens, B., Ferreira, R., Sanchez, M.J., Ishibashi, S., Li, J., Spensberger, D., Lefevre, P., Ottersbach, K., Chapman, M., Kinston, S., et al. (2010). cis-Regulatory remodeling of the SCL locus during vertebrate evolution. Mol. Cell. Biol. *30*, 5741–5751.

Grossmann, V., Kern, W., Harbich, S., Alpermann, T., Jeromin, S., Schnittger, S., Haferlach, C., Haferlach, T., and Kohlmann, A. (2011). Prognostic relevance of RUNX1 mutations in T-cell acute lymphoblastic leukemia. Haematologica *96*, 1874–1877.

Gutierrez, A., Dahlberg, S.E., Neuberg, D.S., Zhang, J., Grebliunaite, R., Sanda, T., Protopopov, A., Tosello, V., Kutok, J., Larson, R.S., et al. (2010). Absence of biallelic TCRgamma deletion predicts early treatment failure in pediatric T-cell acute lymphoblastic leukemia. J. Clin. Oncol. *28*, 3816–3823.

Herblot, S., Steff, A.M., Hugo, P., Aplan, P.D., and Hoang, T. (2000). SCL and LMO1 alter thymocyte differentiation: inhibition of E2A-HEB function and pre-T alpha chain expression. Nat. Immunol. *1*, 138–144.

Ho, I.C., Tai, T.S., and Pai, S.Y. (2009). GATA3 and the T-cell lineage: essential functions before and after T-helper-2-cell differentiation. Nat. Rev. Immunol. *9*, 125–135.

Hollenhorst, P.C., Shah, A.A., Hopkins, C., and Graves, B.J. (2007). Genome-wide analyses reveal properties of redundant and specific promoter occupancy within the ETS gene family. Genes Dev. *21*, 1882–1894.

Hollenhorst, P.C., Chandler, K.J., Poulsen, R.L., Johnson, W.E., Speck, N.A., and Graves, B.J. (2009). DNA specificity determinants associate with distinct transcription factor functions. PLoS Genet. *5*, e1000778.

Homminga, I., Pieters, R., Langerak, A.W., de Rooi, J.J., Stubbs, A., Verstegen, M., Vuerhard, M., Buijs-Gladdines, J., Kooi, C., Klous, P., et al. (2011). Integrated transcript and genome analyses reveal NKX2-1 and MEF2C as potential oncogenes in T cell acute lymphoblastic leukemia. Cancer Cell *19*, 484–497.

Hosoya-Ohmura, S., Lin, Y.H., Herrmann, M., Kuroha, T., Rao, A., Moriguchi, T., Lim, K.C., Hosoya, T., and Engel, J.D. (2011). An NK and T cell enhancer lies 280 kilobase pairs 3′ to the gata3 structural gene. Mol. Cell. Biol. *31*, 1894–1904.

Hsu, H.L., Cheng, J.T., Chen, Q., and Baer, R. (1991). Enhancer-binding activity of the tal-1 oncoprotein in association with the E47/E12 helix-loop-helix proteins. Mol. Cell. Biol. *11*, 3037–3042.

Hsu, H.L., Wadman, I., and Baer, R. (1994). Formation of in vivo complexes between the TAL1 and E2A polypeptides of leukemic T cells. Proc. Natl. Acad. Sci. USA *91*, 3181–3185.

Kassouf, M.T., Hughes, J.R., Taylor, S., McGowan, S.J., Soneji, S., Green, A.L., Vyas, P., and Porcher, C. (2010). Genome-wide identification of TAL1's functional targets: insights into its mechanisms of action in primary erythroid cells. Genome Res. *20*, 1064–1083.

Kee, B.L. (2009). E and ID proteins branch out. Nat. Rev. Immunol. *9*, 175–184.

Keeshan, K., He, Y., Wouters, B.J., Shestova, O., Xu, L., Sai, H., Rodriguez, C.G., Maillard, I., Tobias, J.W., Valk, P., et al. (2006). Tribbles homolog 2 inactivates C/EBPalpha and causes acute myelogenous leukemia. Cancer Cell *10*, 401–411.

Kusy, S., Gerby, B., Goardon, N., Gault, N., Ferri, F., Gérard, D., Armstrong, F., Ballerini, P., Cayuela, J.M., Baruchel, A., et al. (2010). NKX3.1 is a direct TAL1 target gene that mediates proliferation of TAL1-expressing human T cell acute lymphoblastic leukemia. J. Exp. Med. *207*, 2141–2156.

Lahortiga, I., De Keersmaecker, K., Van Vlierberghe, P., Graux, C., Cauwelier, B., Lambert, F., Mentens, N., Beverloo, H.B., Pieters, R., Speleman, F., et al. (2007). Duplication of the MYB oncogene in T cell acute lymphoblastic leukemia. Nat. Genet. *39*, 593–595.

Landry, J.R., Bonadies, N., Kinston, S., Knezevic, K., Wilson, N.K., Oram, S.H., Janes, M., Piltz, S., Hammett, M., Carter, J., et al. (2009). Expression of the leukemia oncogene Lmo2 is controlled by an array of tissue-specific elements dispersed over 100 kb and bound by Tal1/Lmo2, Ets, and Gata factors. Blood *113*, 5783–5792.

Larson, R.C., Lavenir, I., Larson, T.A., Baer, R., Warren, A.J., Wadman, I., Nottage, K., and Rabbitts, T.H. (1996). Protein dimerization between Lmo2 (Rbtn2) and Tal1 alters thymocyte development and potentiates T cell tumorigenesis in transgenic mice. EMBO J. *15*, 1021–1027.

Lécuyer, E., Herblot, S., Saint-Denis, M., Martin, R., Begley, C.G., Porcher, C., Orkin, S.H., and Hoang, T. (2002). The SCL complex regulates c-kit expression in hematopoietic cells through functional interaction with Sp1. Blood *100*, 2430–2440.

Lee, T.I., Johnstone, S.E., and Young, R.A. (2006). Chromatin immunoprecipitation and microarray-based analysis of protein location. Nat. Protoc. *1*, 729–748.

Lin, Y.C., Jhunjhunwala, S., Benner, C., Heinz, S., Welinder, E., Mansson, R., Sigvardsson, M., Hagman, J., Espinoza, C.A., Dutkowski, J., et al. (2010). A global network of transcription factors, involving E2A, EBF1 and Foxo1, that orchestrates B cell fate. Nat. Immunol. *11*, 635–643.

Look, A.T. (1997). Oncogenic transcription factors in the human acute leukemias. Science *278*, 1059–1064.

Marson, A., Levine, S.S., Cole, M.F., Frampton, G.M., Brambrink, T., Johnstone, S., Guenther, M.G., Johnston, W.K., Wernig, M., Newman, J., et al. (2008). Connecting microRNA genes to the core transcriptional regulatory circuitry of embryonic stem cells. Cell *134*, 521–533.

Miyazaki, M., Rivera, R.R., Miyazaki, K., Lin, Y.C., Agata, Y., and Murre, C. (2011). The opposing roles of the transcription factor E2A and its antagonist Id3 that orchestrate and enforce the naive fate of T cells. Nat. Immunol. *12*, 992–1001.

Ngo, V.N., Davis, R.E., Lamy, L., Yu, X., Zhao, H., Lenz, G., Lam, L.T., Dave, S., Yang, L., Powell, J., and Staudt, L.M. (2006). A loss-of-function RNA interference screen for molecular targets in cancer. Nature *441*, 106–110.

Nottingham, W.T., Jarratt, A., Burgess, M., Speck, C.L., Cheng, J.F., Prabhakar, S., Rubin, E.M., Li, P.S., Sloane-Stanley, J., Kong-A-San, J., and de Bruijn, M.F. (2007). Runx1-mediated hematopoietic stem-cell emergence is controlled by a Gata/Ets/SCL-regulated enhancer. Blood *110*, 4188–4197.

Novershtern, N., Subramanian, A., Lawton, L.N., Mak, R.H., Haining, W.N., McConkey, M.E., Habib, N., Yosef, N., Chang, C.Y., Shay, T., et al. (2011). Densely interconnected transcriptional circuits control cell states in human hematopoiesis. Cell *144*, 296–309.

O'Neil, J., Shank, J., Cusson, N., Murre, C., and Kelliher, M. (2004). TAL1/SCL induces leukemia by inhibiting the transcriptional activity of E47/HEB. Cancer Cell *5*, 587–596.

O'Neil, J., Tchinda, J., Gutierrez, A., Moreau, L., Maser, R.S., Wong, K.K., Li, W., McKenna, K., Liu, X.S., Feng, B., et al. (2007). Alu elements mediate MYB gene tandem duplication in human T-ALL. J. Exp. Med. *204*, 3059–3066.

Ono, Y., Fukuhara, N., and Yoshie, O. (1998). TAL1 and LIM-only proteins synergistically induce retinaldehyde dehydrogenase 2 expression in T-cell acute lymphoblastic leukemia by acting as cofactors for GATA3. Mol. Cell. Biol. *18*, 6939–6950.

Palii, C.G., Pasha, R., and Brand, M. (2011a). Lentiviral-mediated knockdown during ex vivo erythropoiesis of human hematopoietic stem cells. J. Vis. Exp. (53). http://www.jove.com/details.php?id=2813, http://dx.doi.org/10.3791/2813.

Palii, C.G., Perez-Iratxeta, C., Yao, Z., Cao, Y., Dai, F., Davison, J., Atkins, H., Allan, D., Dilworth, F.J., Gentleman, R., et al. (2011b). Differential genomic targeting of the transcription factor TAL1 in alternate haematopoietic lineages. EMBO J. *30*, 494–509.

Palomero, T., Odom, D.T., O'Neil, J., Ferrando, A.A., Margolin, A., Neuberg, D.S., Winter, S.S., Larson, R.S., Li, W., Liu, X.S., et al. (2006). Transcriptional regulatory networks downstream of TAL1/SCL in T-cell acute lymphoblastic leukemia. Blood *108*, 986–992.

Ramsay, R.G., and Gonda, T.J. (2008). MYB function in normal and cancer cells. Nat. Rev. Cancer *8*, 523–534.

Soler, E., Andrieu-Soler, C., de Boer, E., Bryne, J.C., Thongjuea, S., Stadhouders, R., Palstra, R.J., Stevens, M., Kockx, C., van Ijcken, W., et al. (2010). The genome-wide dynamics of the binding of Ldb1 complexes during erythroid differentiation. Genes Dev. *24*, 277–289.

Thoms, J.A., Birger, Y., Foster, S., Knezevic, K., Kirschenbaum, Y., Chandrakanthan, V., Jonquieres, G., Spensberger, D., Wong, J.W., Oram, S.H., et al. (2011). ERG promotes T-acute lymphoblastic leukemia and is transcriptionally regulated in leukemic cells by a stem cell enhancer. Blood *117*, 7079–7089.

Tijssen, M.R., Cvejic, A., Joshi, A., Hannah, R.L., Ferreira, R., Forrai, A., Bellissimo, D.C., Oram, S.H., Smethurst, P.A., Wilson, N.K., et al. (2011). Genome-wide analysis of simultaneous GATA1/2, RUNX1, FLI1, and SCL binding in megakaryocytes identifies hematopoietic regulators. Dev. Cell *20*, 597–609.

Tremblay, M., Tremblay, C.S., Herblot, S., Aplan, P.D., Hébert, J., Perreault, C., and Hoang, T. (2010). Modeling T-cell acute lymphoblastic leukemia induced by the SCL and LMO1 oncogenes. Genes Dev. *24*, 1093–1105.

Valouev, A., Johnson, D.S., Sundquist, A., Medina, C., Anton, E., Batzoglou, S., Myers, R.M., and Sidow, A. (2008). Genome-wide analysis of transcription factor binding sites based on ChIP-Seq data. Nat. Methods *5*, 829–834.

Verhoeyen, E., Dardalhon, V., Ducrey-Rundquist, O., Trono, D., Taylor, N., and Cosset, F.L. (2003). IL-7 surface-engineered lentiviral vectors promote survival and efficient gene transfer in resting primary T lymphocytes. Blood *101*, 2167–2174.

Wadman, I.A., Osada, H., Grütz, G.G., Agulnick, A.D., Westphal, H., Forster, A., and Rabbitts, T.H. (1997). The LIM-only protein Lmo2 is a bridging molecule assembling an erythroid, DNA-binding complex which includes the TAL1, E47, GATA-1 and Ldb1/NLI proteins. EMBO J. *16*, 3145–3157.

Wilson, N.K., Miranda-Saavedra, D., Kinston, S., Bonadies, N., Foster, S.D., Calero-Nieto, F., Dawson, M.A., Donaldson, I.J., Dumon, S., Frampton, J., et al. (2009). The transcriptional program controlled by the stem cell leukemia gene Scl/Tal1 during early embryonic hematopoietic development. Blood *113*, 5456–5465.

Wilson, N.K., Foster, S.D., Wang, X., Knezevic, K., Schütte, J., Kaimakis, P., Chilarska, P.M., Kinston, S., Ouwehand, W.H., Dzierzak, E., et al. (2010). Combinatorial transcriptional control in blood stem/progenitor cells: genome-wide analysis of ten major transcriptional regulators. Cell Stem Cell *7*, 532–544.

Wouters, B.J., Jordà, M.A., Keeshan, K., Louwers, I., Erpelinck-Verschueren, C.A., Tielemans, D., Langerak, A.W., He, Y., Yashiro-Ohtani, Y., Zhang, P., et al. (2007). Distinct gene expression profiles of acute myeloid/T-lymphoid leukemia with silenced CEBPA and mutations in NOTCH1. Blood *110*, 3706–3714.

Xu, Z., Huang, S., Chang, L.S., Agulnick, A.D., and Brandt, S.J. (2003). Identification of a TAL1 target gene reveals a positive role for the LIM domain-binding protein Ldb1 in erythroid gene expression and differentiation. Mol. Cell. Biol. *23*, 7585–7599.

Yokoyama, T., and Nakamura, T. (2011). Tribbles in disease: Signaling pathways important for cellular function and neoplastic transformation. Cancer Sci. *102*, 1115–1122.

Young, R.A. (2011). Control of the embryonic stem cell state. Cell *144*, 940–954.

Zhang, J., Ding, L., Holmfeldt, L., Wu, G., Heatley, S.L., Payne-Turner, D., Easton, J., Chen, X., Wang, J., Rusch, M., et al. (2012). The genetic basis of early T-cell precursor acute lymphoblastic leukaemia. Nature *481*, 157–163.

Zuber, J., Rappaport, A.R., Luo, W., Wang, E., Chen, C., Vaseva, A.V., Shi, J., Weissmueller, S., Fellmann, C., Taylor, M.J., et al. (2011). An integrated approach to dissecting oncogene addiction implicates a Myb-coordinated self-renewal program as essential for leukemia maintenance. Genes Dev. *25*, 1628–1640.

Cancer Cell
Article

Therapeutic Effect of γ-Secretase Inhibition in *Kras*^{G12V}-Driven Non-Small Cell Lung Carcinoma by Derepression of DUSP1 and Inhibition of ERK

Antonio Maraver,[1,*] Pablo J. Fernandez-Marcos,[1,12] Daniel Herranz,[1,9,12] Marta Cañamero,[2] Maribel Muñoz-Martin,[1] Gonzalo Gómez-López,[3] Francisca Mulero,[4] Diego Megías,[5] Marta Sanchez-Carbayo,[6] Jie Shen,[7] Montserrat Sanchez-Cespedes,[8] Teresa Palomero,[9,10] Adolfo Ferrando,[9,10,11] and Manuel Serrano[1,*]
[1]Tumor Suppression Group
[2]Comparative Pathology Unit
[3]Bioinformatics Unit
[4]Molecular Imaging Unit
[5]Confocal Microscopy Unit
[6]Tumor Markers Group
Spanish National Cancer Research Centre, E-28029 Madrid, Spain
[7]Center for Neurologic Diseases, Brigham and Women's Hospital and Harvard Medical School, Boston, MA 02115, USA
[8]Cancer Epigenetics and Biology Program, Bellvitge Biomedical Research Institute, 08007 Barcelona, Spain
[9]Institute for Cancer Genetics
[10]Department of Pathology
[11]Department of Pediatrics
Columbia University Medical Center, New York, NY 10032, USA
[12]These authors contributed equally to this work
*Correspondence: amaraver@cnio.es (A.M.), mserrano@cnio.es (M.S.)
http://dx.doi.org/10.1016/j.ccr.2012.06.014

SUMMARY

Here, we have investigated the role of the Notch pathway in the generation and maintenance of *Kras*^{G12V}-driven non-small cell lung carcinomas (NSCLCs). We demonstrate by genetic means that γ-secretase and RBPJ are essential for the formation of NSCLCs. Of importance, pharmacologic treatment of mice carrying autochthonous NSCLCs with a γ-secretase inhibitor (GSI) blocks cancer growth. Treated carcinomas present reduced HES1 levels and reduced phosphorylated ERK without changes in phosphorylated MEK. Mechanistically, we show that HES1 directly binds to and represses the promoter of *DUSP1*, encoding a dual phosphatase that is active against phospho-ERK. Accordingly, GSI treatment upregulates DUSP1 and decreases phospho-ERK. These data provide proof of the in vivo therapeutic potential of GSIs in primary NSCLCs.

INTRODUCTION

Lung cancer is the leading cause of cancer-related deaths in the world. A major challenge in treating lung cancer is to find novel therapeutic targets that can complement current chemotherapy.

The Notch pathway is highly complex and regulates various processes, such as embryonic development, cell fate decisions, and tissue homeostasis, and it has been implicated in a variety of human diseases, including cancer (Chiba, 2006; Demarest et al., 2008; Ferrando, 2009; Hass et al., 2009; Roy et al., 2007). Briefly, this pathway involves a total of five activatory ligands, four NOTCH receptors, sequential proteolytic processing of the ligand-bound receptors to generate active Notch intracellular domains (NICDs), and formation of DNA-binding complexes

Significance

NOTCH1 oncogenic mutations have been found in T cell leukemias and lung cancer. In T cell leukemias, the Notch pathway activates AKT and NFκB through HES1-mediated transcriptional repression of *PTEN* and *CYLD*, respectively. Little is known, however, about how the Notch pathway participates in lung cancer. Here, we show that Notch pathway inhibition, either genetically or pharmacologically, hampers primary *Kras*^{G12V}-driven non-small cell lung carcinomas (NSCLCs). We demonstrate that HES1 directly represses the promoter of *DUSP1*, which encodes a dual-specificity phosphatase with activity against phospho-ERK. Treatment with GSIs induces *DUSP1* expression, and this is associated with loss of ERK phosphorylation, a critical player in NSCLCs. These results validate the potential of GSIs for the treatment of primary NSCLCs.

with a number of DNA-binding partners, with RBPJ being the most important and the one that defines the so-called "canonical" Notch pathway (Chiba, 2006; Demarest et al., 2008; Ferrando, 2009; Heitzler, 2010; Roy et al., 2007). In turn, NICD-containing complexes activate the expression of a number of effectors, including the transcriptional repressor HES1 (Sang et al., 2010).

The γ-secretase complex is essential for the Notch pathway because it is responsible for the activation of NOTCH receptors by proteolytic cleavage (Hass et al., 2009). This complex is formed by the assembly of four protein subunits, namely, a presenilin subunit (PSEN1 or PSEN2), nicastrin (NCSTN), APH1, and PSNEN (Fraering, 2007). The proteolytic activity of the γ-secretase complex occurs within the PSEN subunit; however, each of the four subunits is essential for the formation of a functional γ-secretase complex (Fraering, 2007). In this regard, we have demonstrated that the combined deletion of the PSEN genes *Psen1* and *Psen2* results in ablation of NOTCH1 activation in T cells (Maraver et al., 2007). Additionally, small-molecule inhibitors that target the γ-secretase complex (known as γ-secretase inhibitors [GSIs]) (Wolfe, 2009) phenocopy Notch pathway inhibition in mouse models (van Es et al., 2005; Wong et al., 2004).

The oncogenic role of the Notch pathway is well established in T cell acute lymphoblastic leukemias (T-ALL), and *NOTCH1* is oncogenically mutated in ~60% of leukemias (Ferrando, 2009). Investigators have reported a number of alterations in the Notch pathway in human non-small cell lung carcinomas (NSCLCs), including NOTCH3 overexpression (Haruki et al., 2005); loss of expression of NUMB (Westhoff et al., 2009), a negative regulator of the Notch pathway; and activating mutations in *NOTCH1* (Westhoff et al., 2009). Previous reports have demonstrated that GSIs induce apoptosis in human lung cancer cells grown in vitro (Chen et al., 2007; Eliasz et al., 2010; Westhoff et al., 2009) and slow the growth of subcutaneous xenografts formed by human lung cancer cells (Konishi et al., 2007; Luistro et al., 2009; Paris et al., 2005). However, little is known about the activity of GSIs in primary autochthonous NSCLCs in their natural environment, or about the mechanisms by which GSIs could exert their antitumoral effect on NSCLCs.

In mice, inducible genetic activation of a latent *Kras* oncogenic allele in the lung initiates a stepwise tumorigenic process that culminates in NSCLCs very similar to those found in humans, sharing a common histology (Guerra et al., 2003; Jackson et al., 2001) and a common transcriptional profile (Sweet-Cordero et al., 2005). Therefore, we used this mouse model to analyze the effect of the Notch pathway on the development of NSCLCs.

RESULTS

The Notch Pathway Is Hyperactive in Murine *Kras*^{G12V}-Driven NSCLC

The Notch pathway is hyperactive in a subset of human NSCLCs (Westhoff et al., 2009). Therefore, we wanted to know whether this is also the case for murine *Kras*^{G12V}-driven adenocarcinoma, which is a common type of NSCLC (Guerra et al., 2003). All of the analyzed murine NSCLCs presented significantly higher levels of NICD and HES1 compared with normal lung (Figure 1A). To evaluate the levels of γ-secretase, we measured the abundance of

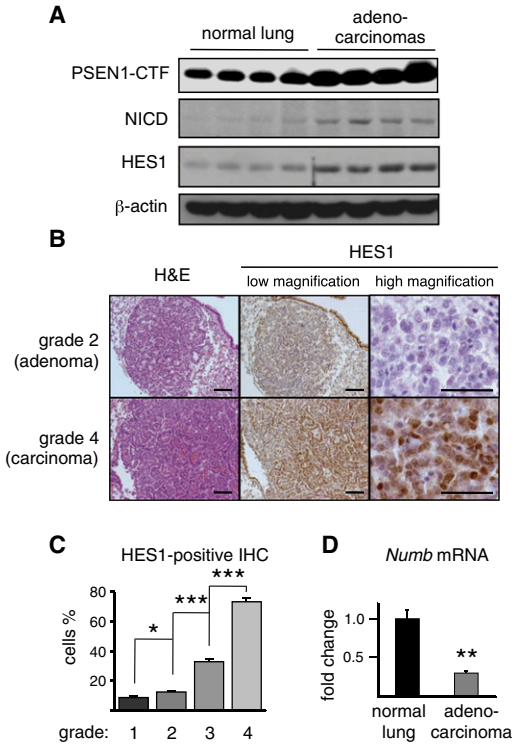

Figure 1. Activity of the Notch Pathway in Murine *Kras*^{G12V}-Driven NSCLC

(A) Analysis of γ-secretase activity by detection of PSEN1-CTF, and analysis of NOTCH1 activity by detection of NICD and HES1 by immunoblotting (normal lung: each lane corresponds to a different control WT mouse; adenocarcinomas: each lane corresponds to a grade 4 tumor from a different mouse).

(B) Detection of HES1 in murine *Kras*^{G12V} lung tumors. Representative examples of grade 2 (adenoma) and grade 4 (adenocarcinoma) tumors stained with hematoxylin and eosin (H&E, left) and HES1 (middle and right) at low magnification (middle) or high magnification (right). Bars in the four leftmost panels correspond to 100 μm. Bars in the two rightmost panels correspond to 50 μm.

(C) Quantification of HES1 during lung tumorigenesis. The graph depicts the percentage of HES1-positive nuclei (detected by IHC as in B) within tumors of different grades (n = 5 for each tumor grade).

(D) Levels of *Numb* mRNA measured by qRT-PCR in WT mouse lungs (n = 4) and grade 4 tumors (n = 4).

Values correspond to the average ± SEM. Statistical significance was determined by a two-tailed Student's t test: *p < 0.05; **p < 0.01; ***p < 0.001.

See also Figure S1.

the active forms of PSEN1 and NCSTN. In the case of PSEN1, assembly into the γ-secretase complex is associated with proteolytic cleavage (Fraering, 2007). We observed higher levels of the carboxy-terminal fragment of PSEN1 (PSEN1-CTF) in murine NSCLCs compared with normal lung (Figure 1A), whereas the levels of *Psen1* mRNA were unchanged (Figure S1A available online). These results agree with a previous study using human fibroblasts cultured in vitro, in which ectopic overexpression of oncogenic *HRAS* was found to increase PSEN1 protein levels without affecting its mRNA levels (Weijzen et al., 2002). In the case of NCSTN, its assembly into the γ-secretase complex is associated with glycosylation and slower electrophoretic mobility (Edbauer et al., 2002). As in the case of PSEN1, we also observed higher levels of mature NCSTN in murine NSCLCs

(Figure S1B). These observations indicate higher levels of functional γ-secretase complex in murine *Kras*^{G12V}-driven NSCLCs.

To define the kinetics of Notch pathway activation during lung tumorigenesis, we tested the expression of HES1 by immunohistochemistry (IHC) in murine lesions at different stages, from grade 1 to grade 4 (with grades 1–3 corresponding to adenomas, and grade 4 to adenocarcinomas) (Jackson et al., 2005). We observed a direct association between tumor grade and HES1 nuclear signal, which reached its maximum in grade 4 lesions (adenocarcinomas; Figures 1B and 1C, and Figure S1C). As an internal control, we also observed strong nuclear expression of HES1 in murine bronchioles (Collins et al., 2004; Ito et al., 2000; Morimoto et al., 2010; Tsao et al., 2009) (Figure S1C). Finally, we found lower levels of expression of *Numb* mRNA (Figure 1D), a negative regulator of the Notch pathway whose expression is also diminished in human NSCLCs (Westhoff et al., 2009). Together, these data indicate that murine *Kras*^{G12V}-driven NSCLCs faithfully recapitulate the activation of the Notch pathway reported in human NSCLCs, validating that this mouse lung cancer model is appropriate for analyzing therapeutic strategies and mechanisms related to the Notch pathway.

The γ-Secretase Complex Is Needed for *Kras*^{G12V}-Driven NSCLCs

To evaluate the relevance of the Notch pathway in lung tumorigenesis, we combined a Cre-inducible *Kras*^{G12V} oncogenic allele (*Kras*^{LSLG12Vgeo}) (Guerra et al., 2003) and *Psen1*$^{f/f}$;*Psen2*$^{-/-}$ alleles (i.e., *Psen1* flanked by *loxP* sites excisable by Cre recombinase, and *Psen2* null) (Saura et al., 2004), thus generating compound *Kras*$^{+/LSLG12Vgeo}$;*Psen1*$^{f/f}$;*Psen2*$^{-/-}$ animals. Mice were treated with intratracheal delivery of adeno-Cre (for brevity, we refer to the resulting lungs as *KrasV12/PSKO*). Control mice (*Kras*$^{+/LSLG12Vgeo}$;*Psen1*$^{+/+}$;*Psen2*$^{+/+}$) were derived from the same set of crosses as the *Kras*$^{+/LSLG12Vgeo}$;*Psen1*$^{f/f}$;*Psen2*$^{-/-}$ mice [for brevity, we refer to the adeno-Cre treated lungs as *KrasV12*/wild-type (WT) lungs]. Mice were killed between 5.5 and 7.5 months post-adeno-Cre delivery, and lung tumors were graded and quantified (Figure 2A). Most tumors in control *KrasV12*/WT lungs had progressed to grades 3 and 4; however, in the case of *KrasV12/PSKO* lungs, there was no progression beyond grade 1 (Figure 2A). We also measured the percentage of animals with at least one grade 4 tumor (i.e., adenocarcinoma). Of importance, whereas 44% of *KrasV12*/WT lungs presented adenocarcinomas, none of the *KrasV12/PSKO* lungs developed NSCLCs (Figure 2B).

The Canonical Notch Pathway Is Needed for *Kras*^{G12V}-Driven NSCLCs

Having established the requirement of the γ-secretase complex for generating *Kras*^{G12V}-driven NSCLCs, we wanted to test directly the role of the canonical Notch pathway in this process. To that end, we generated compound mice carrying the Cre-inducible *Kras*^{G12V} oncogenic allele in combination with a floxed allele of *Rbpj*, *Rbpj*$^{f/f}$ (Tanigaki et al., 2002). These mice and their corresponding controls (for brevity, termed *KrasV12/RbpjKO* and *KrasV12*/WT, respectively) were treated by intratracheal delivery of adeno-Cre. It should be noted that in this experiment, the batch of adeno-Cre was more active than in the previous experiment (see Experimental Procedures), and thus yielded

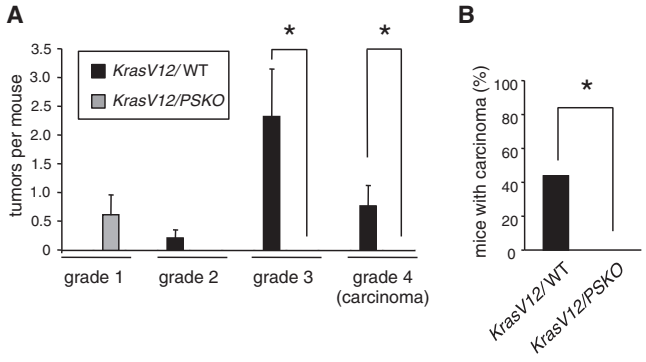

Figure 2. PSEN1 and PSEN2 Are Needed for the Generation of *Kras*^{G12V}-Driven NSCLC

(A) Graph depicting the number and grade of tumors per animal. Lungs from *KrasV12*/WT and *KrasV12/PSKO* mice were pathologically analyzed 5.5–7.5 months after adeno-Cre delivery. For each genotype, n = 9 mice.

(B) Percentage of mice carrying grade 4 (adenocarcinoma) tumors. For each genotype, n = 9 mice.

Values correspond to the average ± SEM. Statistical significance was determined by a two-tailed Student's t test (A) or by Fisher's exact test (B): *$p < 0.05$.

a higher number of tumors per mouse. As was the case for the *KrasV12/PSKO* mice, in the *KrasV12/RbpjKO* mice, grade 4 tumors (adenocarcinomas) were absent 5.5–7.5 months post-adeno-Cre delivery (Figures 3A and 3B). We wondered whether the grade 3 tumors present in *KrasV12/RbpjKO* mice had actually deleted the *Rbpj* gene or, alternatively, were nondeleted *Rbpj*-floxed tumors ("escapers"). To address this issue, we microdissected grade 3 tumors (n = 3), and we observed that all of them were escapers (Figure S2). Taken together, the results of our genetic analyses indicate that the Notch pathway is essential for NSCLC formation driven by *Kras*^{G12V}.

Pharmacological Inhibition of γ-Secretase Arrests *Kras*^{G12V}-Driven NSCLCs

Having demonstrated that γ-secretase is highly relevant for lung tumorigenesis, and that the Notch pathway is strongly active in lung cancer, we conducted a preclinical assay to test the impact of γ-secretase inhibition on primary NSCLCs. Previous reports demonstrated that small-molecule inhibitors of the γ-secretase pathway (generally known as GSIs) induce apoptosis in lung cancer cells grown in vitro (Chen et al., 2007; Eliasz et al., 2010; Westhoff et al., 2009) and slow the growth of subcutaneous xenografts formed by lung cancer cells (Konishi et al., 2007; Luistro et al., 2009; Paris et al., 2005). However, nothing is known about the impact of GSIs on autochthonous primary NSCLCs, i.e., in their natural microenvironment. For this assay, we used compound LSN-411575 (Wong et al., 2004). This compound has been well validated in rodents (Best et al., 2005; Wong et al., 2004) and is one of the most potent GSIs (Wolfe, 2009). To test the therapeutic potential of LSN-411575 in NSCLCs, we used mice carrying the above-mentioned Cre-inducible *Kras*^{G12V} oncogenic allele (*Kras*^{LSLG12Vgeo}) together with a tamoxifen-inducible Cre systemically expressed under the RNA polymerase II promoter (Guerra et al., 2003). These mice develop a mixture of lung adenomas (grades 1–3) and adenocarcinomas (grade 4) upon induction with tamoxifen. After

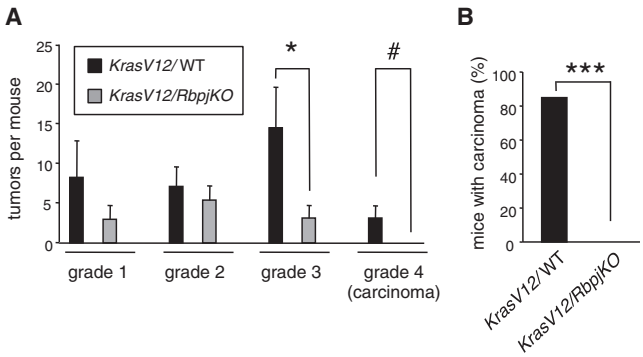

Figure 3. The Canonical Notch Pathway Is Needed for the Generation of *Kras*^{G12V}-Driven NSCLC

(A) Graph depicting the number and grade of tumors per animal. Lungs from *KrasV12*/WT and *KrasV12/RbpjKO* mice were pathologically analyzed 5.5–7.5 months after adeno-Cre delivery. For each genotype, n = 7 mice.

(B) Percentage of mice carrying grade 4 (adenocarcinoma) tumors. For each genotype, n = 7 mice.

Values correspond to the average ± SEM. Statistical significance was determined by a two-tailed Student's t test (A) or Fisher's exact test (B): #$p < 0.1$; *$p < 0.05$; ***$p < 0.001$.

See also Figure S2.

6–8 months of the tamoxifen induction, we analyzed changes in tumor size and tumor metabolism by X-ray computed tomography (CT) and positron emission tomography (PET), respectively. Tumors greater than 0.5 mm in diameter were detectable by CT, but only those of grade 4 (i.e. adenocarcinomas) were PET positive (Figures S3A–S3C). Again, this recapitulates the human pathology, in which only malignant tumors are PET positive (Fischer et al., 2001; Gould et al., 2001). Mice carrying *Kras*^{G12V}-driven tumors periodically underwent PET/CT scans, and those carrying at least one PET-positive tumor were randomly allocated into two groups that were treated daily by gavage with vehicle for 15 days or with 3 mg/kg of LSN-411575 for 15 or 22 days.

Previous investigators reported deleterious side effects associated with the use of GSIs, especially in the gut (van Es et al., 2005; Wong et al., 2004). In the case of LSN-411575, it was reported that a dose of 10 mg/kg administered for 15 days in mice produced toxicity in the intestine and weight loss, whereas a dose of 1 mg/kg had no detectable effects and the animals did not lose weight (Wong et al., 2004). In our current study, mice maintained their normal weight after 15 days of treatment with 3 mg/kg, suggesting the absence of deleterious side effects (Figure S3D).

We obtained PET/CT scans of the same mice before and after 15 or 22 days of treatment (Figure 4A). Quantification of the size of the tumors by CT (regardless of whether they were PET positive or negative) revealed that the vehicle-treated tumors increased in size (3.7-fold) after 15 days, whereas the LSN-411575-treated ones grew significantly less than the vehicle-treated controls (1.7-fold after 15 days and 1.2-fold after 22 days; Figure 4B). It is important to note that some of the animals presented atelectasis, which prevents detection by CT. Given the fact that CT cannot discriminate between nonmalignant and malignant tumors, we selectively focused on the response of PET-positive tumors (i.e. adenocarcinomas) and quantified their total ^{18}F-fluor-deoxyglucose (FDG) uptake pre- and post-treatment. In the case of vehicle-treated mice, PET-positive tumors increased their total FDG uptake an average of 2.2-fold during the 15 days of treatment (Figure 4C). In the case of LSN-411575-treated mice, the average change was 0.7-fold after 15 days and 1.0-fold after 22 days (Figure 4C). These results indicate that LSN-411575 has a significant inhibitory effect on the growth of autochthonous murine *Kras*^{G12V}-driven NSCLCs.

Pharmacological Inhibition of γ-Secretase Interferes with ERK Phosphorylation in *Kras*^{G12V}-Driven NSCLCs

Treated *Kras*^{G12V}-driven NSCLCs (see Figure 4C) were analyzed by IHC (samples were obtained 4–8 hr after the last treatment). Our first goal was to evaluate whether the GSI treatment had reached its target, and to that end we used the levels of HES1 as a surrogate marker of γ-secretase activity. In accordance with our previous observations (see Figure 1), the vehicle-treated NSCLCs were strongly positive for HES1 (Figure 5A). In contrast, NSCLCs treated with LSN-411575 for 15 days showed a clear reduction in HES1 levels, confirming that the drug was actually reaching its target within the tumors and at their natural localization (Figure 5A). Also, in agreement with the robust increase in FDG uptake observed during the 15-day interval (Figure 4C), these tumors were highly proliferative (Ki67 staining) and had a low level of apoptosis (activated caspase-3 staining; Figure 5A). NSCLCs treated with LSN-411575 for 15 days presented decreased levels of Ki67-positive cells and a higher frequency of apoptotic cells compared with vehicle-treated tumors (Figure 5A). Of note, these tumors, except for their loss of mitotic cells, retained all other histological features of grade 4 tumors (characteristically defined by the presence of enlarged pleomorphic nuclei exhibiting a high degree of nuclear atypia and multinucleated giant cells) (Jackson et al., 2005). These observations strongly suggest that LSN-411575 arrests cancer growth by inhibiting proliferation and increasing apoptosis.

In an effort to understand the antitumoral effect of LSN-411575, we explored a number of key players in lung cancer, such as ERK (Engelman et al., 2008), AKT (Yang et al., 2008), S6K (Liang et al., 2010), and NFκB (Meylan et al., 2009). In the case of AKT (phospho-Ser473-AKT1), S6K (phospho-Thr389-S6K1), and NFκB (nuclear p65), we could not find any differences between NSCLCs treated for 15 days with vehicle or with LSN-411575 (Figure S4A). However, we did find a remarkable effect on the activity of ERK. In particular, vehicle-treated NSCLCs were strongly positive for pERK1/pERK2 (phospho-Thr202/Tyr204-ERK1 and phospho-Thr185/Tyr187-ERK2), whereas LSN-411575-treated NSCLCs were significantly less positive for pERK (Figure 5A). The results obtained by IHC were confirmed by immunoblotting of tumor extracts. Specifically, we observed lower levels of HES1 and pERK1/pERK2 in LSN-411575-treated (15 days) NSCLCs compared with the corresponding vehicle-treated tumors (Figures 5B and S4B). We wondered whether the lower levels of pERK1/pERK2 were associated with lower levels of its activating kinase, MEK; however, the levels of pMEK1/2 (phospho-Ser217/Ser221-MEK1/2) remained similar in vehicle- and LSN-411575-treated NSCLCs (Figures 5B and S4B), suggesting that the inhibition of pERK

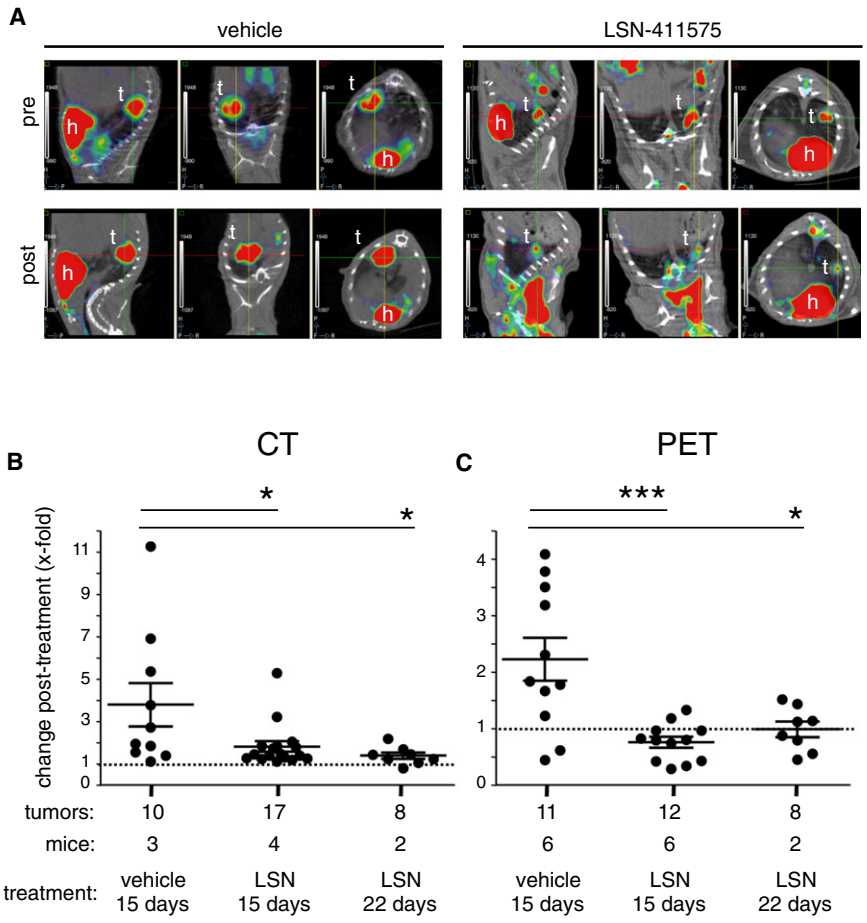

Figure 4. Pharmacological Inhibition of γ-Secretase Arrests *Kras*^{G12V}-Driven NSCLCs

(A) Representative examples of PET/CT analyses of a single *Kras*^{G12V} mouse at the beginning (pre) and end (post) of 15 days of treatment with vehicle (left) or LSN-411575 (right). Images correspond to sagittal (left), coronal (middle), and transverse (right) views. The positions of the PET-positive tumor (t) and the heart (h) are labeled.

(B) Change in total tumor size detected by CT after 15 days of treatment with vehicle, and after 15 or 22 days of treatment with LSN-411575.

(C) Change in total ^{18}F-FDG uptake of PET-positive tumors after 15 days of treatment with vehicle, and after 15 or 22 days of treatment with LSN-411575.

Values correspond to the relative change of each individual tumor from the day before initiation of treatment to the last day of treatment. Bars correspond to the average ± SEM. Top of graph: A two-tailed Student's t test (*$p < 0.05$; ***$p < 0.001$) was used for statistical analysis.

See also Figure S3.

exerted by LSN-411575 is independent of MEK activity. Finally, we wanted to test whether the key observed changes in HES1 and pERK were early events upon initiation of LSN-411575 treatment. We treated mice for 4 days with LSN-411575, and found that the levels of HES1 and pERK in NSCLCs were already lower than in vehicle-treated tumors and similar to those observed in tumors treated with the drug for 15 days (Figure 5C). Collectively, these observations indicate that treatment with LSN-411575 arrests *Kras*^{G12V}-driven NSCLCs in association with inhibition of HES1 expression and ERK phosphorylation.

Inhibition of γ-Secretase Increases DUSP1 in Human and Murine Oncogenic-*Kras* NSCLCs

Previous investigators reported that the Notch pathway upregulates pERK levels in cultured cells in vitro (Kim et al., 2005; Konishi et al., 2007; Michie et al., 2007). However, the mechanisms involved remained unexplored. In an effort to understand the link between the Notch pathway and pERK in the context of lung cancer cells, we focused on the human NSCLC cell line H358, which carries an oncogenic *KRAS* allele (*KRAS*^{G12C}) and requires the activity of the oncogene for its viability (Singh et al., 2009). H358 cells were treated with the GSI DAPT, which is a widely used GSI for assays with in vitro cultured cells (Wolfe, 2009). Recapitulating the results obtained in our lung mouse model, DAPT-treated H358 cells also showed lower levels of pERK (Figure 6A). We also explored two other human *KRAS*-mutated NSCLC cell lines, namely, A549 and H23, which carry *KRAS*^{G12S} and *KRAS*^{G12C} alleles, respectively (Blanco et al., 2009), but whose growth is independent of KRAS activity (Singh et al., 2009). These cell lines also showed decreased levels of pERK upon DAPT treatment (Figure S5A), but the magnitude of the effect was not as pronounced as in KRAS-dependent H358 cells.

To gain insight into the mechanism by which inhibition of the Notch pathway interferes with ERK phosphorylation, we performed RNA microarray analyses to compare GSI-treated and nontreated H358 cells (Table S1). As expected, among the genes that were significantly downregulated by DAPT [false discovery rate (FDR) $p < 0.05$; magnitude $\log_2$ fold change $\leq$ 0.5-fold], we identified *HES1*. Among the genes that showed significant upregulation by DAPT (FDR $p < 0.05$; magnitude $\log_2$ fold change $\geq$ 0.5-fold), we noticed the dual-specificity phosphatases *DUSP1* and *DUSP6*, which are well-known negative regulators of MAP kinases, including ERK (Patterson et al., 2009). Of interest, *DUSP1* is repressed by the Notch pathway in a NSCLC cell line (Haruki et al., 2005); however, we are not aware of a similar link for *DUSP6*. Validation by quantitative RT-PCR (qRT-PCR) confirmed that both the *DUSP1* and *DUSP6* mRNAs were upregulated after treatment of H358 cells with DAPT, whereas *HES1* mRNA levels were downregulated (Figure 6B and Figure S5B). We confirmed that these changes in *HES1* and *DUSP1* mRNA levels correlated with similar changes in the corresponding proteins (Figure 6C). In the case of A549 and H23 cells, both showed a decrease in *HES1* and an upregulation of *DUSP1* upon DAPT treatment; however, only A549 cells presented an upregulation of *DUSP6* (Figures S5B and S5C). In an effort to extrapolate these findings to a different type of Notch-dependent cancer, we performed γ-secretase inhibition of a panel of human T-ALL cell lines. We observed *DUSP1* mRNA

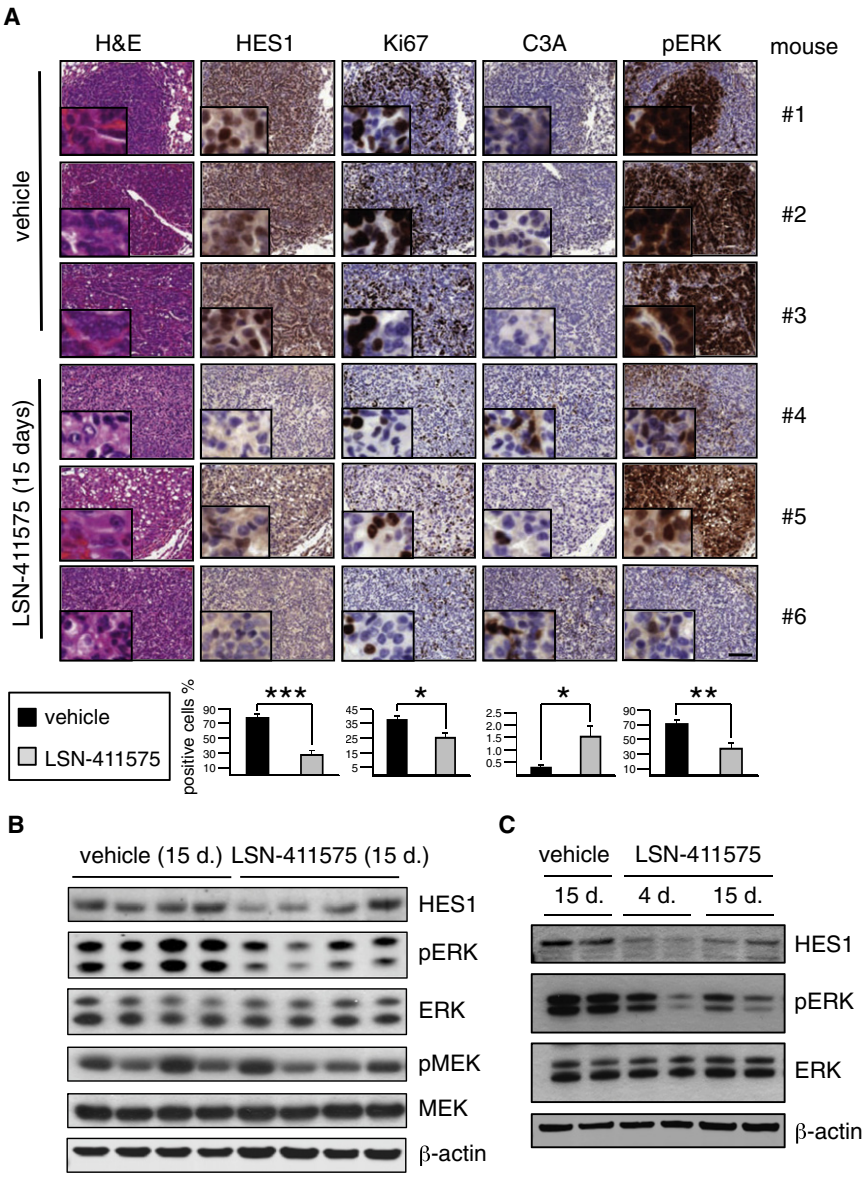

Figure 5. Pharmacological Inhibition of γ-Secretase Diminishes HES1 and pERK in *Kras*^{G12V}-Driven NSCLCs

(A) IHC analyses of NSCLCs after 15 days of treatment with vehicle or LSN-411575. Rows correspond to serial sections of the same tumor. Three examples of vehicle-treated tumors and LSN-411575-treated tumors, each from a different mouse, are shown. All pictures are at the same magnification. The bar in the lower-right panel corresponds to 100 μm. The quantifications shown at the bottom correspond to all of the analyzed NSCLCs: vehicle, 11 tumors (n = 11) present in 6 mice; LSN-411575, 12 tumors (n = 12) present in 6 mice. For each staining, two separate fields at 20× magnification were counted and an average of 1,500 cells were scored per tumor. Values correspond to the average ± SEM. Statistical significance was determined by a two-tailed Student's t test: *p < 0.05; **p < 0.01; ***p < 0.001.

(B) Immunoblotting of the indicated proteins in PET-positive NSCLCs treated for 15 days with vehicle or LSN-411575. Each lane corresponds to a different tumor from a different mouse.

(C) Immunoblotting of the indicated proteins in PET-positive NSCLCs treated with vehicle or LSN-411575 for the indicated periods of time (4 days or 15 days). Each lane corresponds to a different tumor from a different mouse.

See also Figure S4.

upregulation in all of the cell lines, albeit of variable magnitude (Figure S5D), whereas *DUSP6* had an erratic behavior (Figure S5D). These results suggest that the upregulation of *DUSP1* is a general feature of γ-secretase inhibition in cancer.

DUSP1 has been implicated in the dephosphorylation of ERK, JNK, and p38 (Patterson et al., 2009). However, treatment with DAPT resulted in reduced levels of pERK (see Figure 6A) but did not affect the levels of phospho-JNK or phospho-p38 (Figure S5E). We wanted to confirm that DUSP1 was dephosphorylating pERK in our experimental system, and to that end, we ectopically overexpressed a GFP-DUSP1 fusion (Wu et al., 2005) and measured the levels of pERK by immunofluorescence in the GFP-positive cells. Of interest, we observed that H358 cells expressing GFP-DUSP1 had very low levels of pERK upon serum stimulation (10 min), whereas GFP control cells had high levels of pERK under the same conditions (Figures 6D and 6E). Again, we obtained similar results in A549 and H23 cells (Figure S5F). We then performed loss-of-function studies. After testing a total of 12 different interfering RNAs (four siRNAs and eight shRNAs) against *DUSP1*, we observed only a rather modest effect from combining two shRNAs (sh2+sh3; Figure S5G). Despite the partial decrease in DUSP1 levels, expression of the two shRNAs (sh2+sh3) increased the levels of pERK in transfected H358 compared with a scrambled shRNA (shSC; Figure 6F). Moreover, expression of sh2+sh3 abolished the inhibitory effect of DAPT on pERK (Figure 6G), suggesting that the effects of DAPT on pERK are mediated by DUSP1. We also wondered whether DAPT treatment affected the levels of pMEK in H358 cells. We did not observe any changes in pMEK induced by DAPT (Figure S5H), in agreement with our previous observations in GSI-treated tumors (Figures 5B and S4B). These results support the concept that GSI treatment inhibits KRAS signaling through DUSP1 by decreasing the levels of pERK, and without affecting the activity of MEK.

To validate the above data in vivo, we compared the levels of *Dusp1* and *Dusp6* mRNAs in primary murine *Kras*^{G12V}-driven NSCLCs treated for 15 days with LSN-411575 or with vehicle. Of importance, adenocarcinomas from mice treated with LSN-411575 presented increased levels of *Dusp1*/DUSP1 (Figures 6H and 6I) and decreased levels of *Hes1*/HES1 (Figures 5B and 6H) mRNA and protein compared with vehicle-treated adenocarcinomas. In contrast, we did not observe any changes

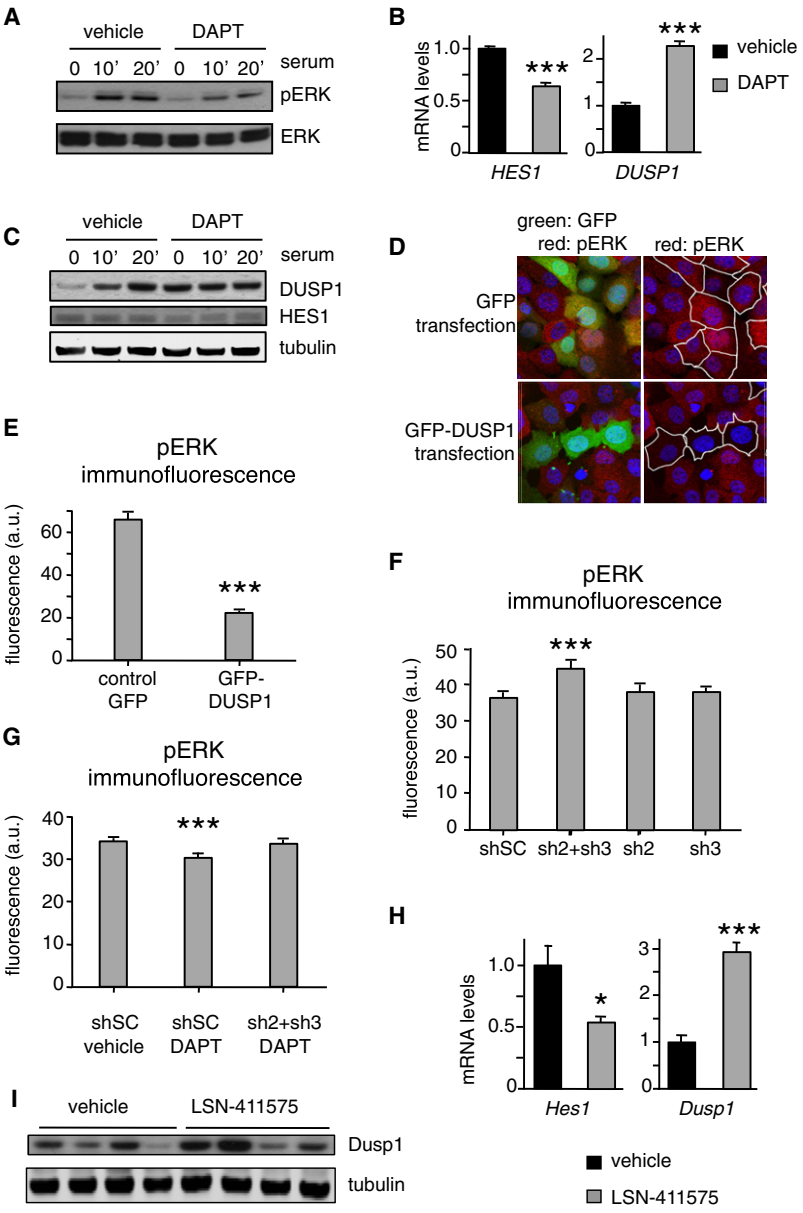

Figure 6. Inhibition of γ-Secretase Increases DUSP1 in Human and Mouse NSCLCs

(A) Analysis of pERK in H358 cells treated with 5 μM DAPT or with vehicle. Cells were treated for 48 hr (36 hr in the presence of serum and then 12 hr in the absence of serum) and then stimulated with serum for the indicated times (in minutes).

(B) Analysis of *DUSP1* and *HES1* expression by qRT-PCR in nontreated (vehicle, n = 3) or DAPT-treated (5 μM DAPT, n = 3) H358 cells. Cells were treated for 48 hr (36 hr in the presence of serum and then 12 hr in the absence of serum).

(C) Analysis of HES1 and DUSP1 in H358 cells treated with 5 μM DAPT or with vehicle. Cells were treated for 48 hr (36 hr in the presence of serum and then 12 hr in the absence of serum) and then stimulated with serum for the indicated times (in minutes).

(D) Fluorescence detection of GFP and phospho-ERK in H358 cells transfected with GFP alone or with a GFP-DUSP1 fusion. Cells were starved and serum stimulated for 10 min. GFP-positive cells are marked with a white line. All images are at the same magnification. The bar in the lower right panel corresponds to 20 μm.

(E) Quantification of the experiment shown in (D). GFP-positive cells (n = 75) were quantified with an automatic software for each transfection (GFP alone, or GFP-DUSP1).

(F) Fluorescence detection of GFP and quantification of phospho-ERK in H358 cells transfected with pGIPZ scramble (shSC), with pGIPZ anti-DUSP1 shRNAs (sh2, sh3, and sh2+sh3). Thirty-six hours after transfection, cells were starved for 12 hr and then serum stimulated for 10 min. GFP-positive cells (n = 120) were quantified with automatic software for each transfection.

(G) Cells were transfected as in (F), and 6 hr after transfection the cells were treated with vehicle or with DAPT (5 μM) for 48 hr (36 hr in the presence of serum and then 12 hr in the absence of serum) and then stimulated with serum for 10 min. GFP-positive cells (n = 120) were quantified with automatic software for each transfection.

(H) Analysis of *Hes1* and *Dusp1* expression by qRT-PCR in PET-positive $Kras^{G12V}$-driven NSCLCs treated with LSN-411575 (n = 4) or vehicle (n = 4) for 15 days.

(I) Immunoblotting of the indicated proteins in PET-positive $Kras^{G12V}$-driven NSCLCs treated for 15 days with vehicle or LSN-411575. Each lane corresponds to a different adenocarcinoma from a different mouse. These adenocarcinomas are the same ones analyzed in Figure 5B and were loaded in the same order.

Values correspond to the average ± SEM. Statistical significance was determined by a two-tailed Student's t test: *$p < 0.05$; ***$p < 0.001$.

See also Figure S5 and Table S1.

in *Dusp6* (Figure S5I). Taken together, these data establish a tight association between HES1 downregulation and DUSP1 induction upon GSI treatment in cancer.

HES1 Directly Binds and Represses the *DUSP1* Promoter

The transcriptional repressor HES1 is a critical mediator of NOTCH1-driven cancer (Wendorff et al., 2010). On the basis of this finding and our above data, we hypothesized that HES1 can repress *DUSP1*. To explore this possibility, we began by performing *DUSP1* promoter assays using a luciferase reporter. Of note, treatment of H358 cells with DAPT induced the *DUSP1* promoter, and this was canceled when HES1 was cotransfected (Figure 7A). These results further reinforce our previous observations that γ-secretase inhibition upregulates the expression of *DUSP1* by downregulating HES1. Additionally, the basal activity of the *DUSP1* promoter was decreased by HES1 expression (Figures 7A and 7B). Also, as a marginal note, treatment of cells with a pharmacological MEK inhibitor (PD0325901) decreased the activity of the *DUSP1* promoter (Figure 7B), in accordance with the known role of MEK as a positive regulator of *DUSP1* expression (Brondello et al., 1997), again suggesting that γ-secretase inhibition exerts its actions in a MEK-independent manner.

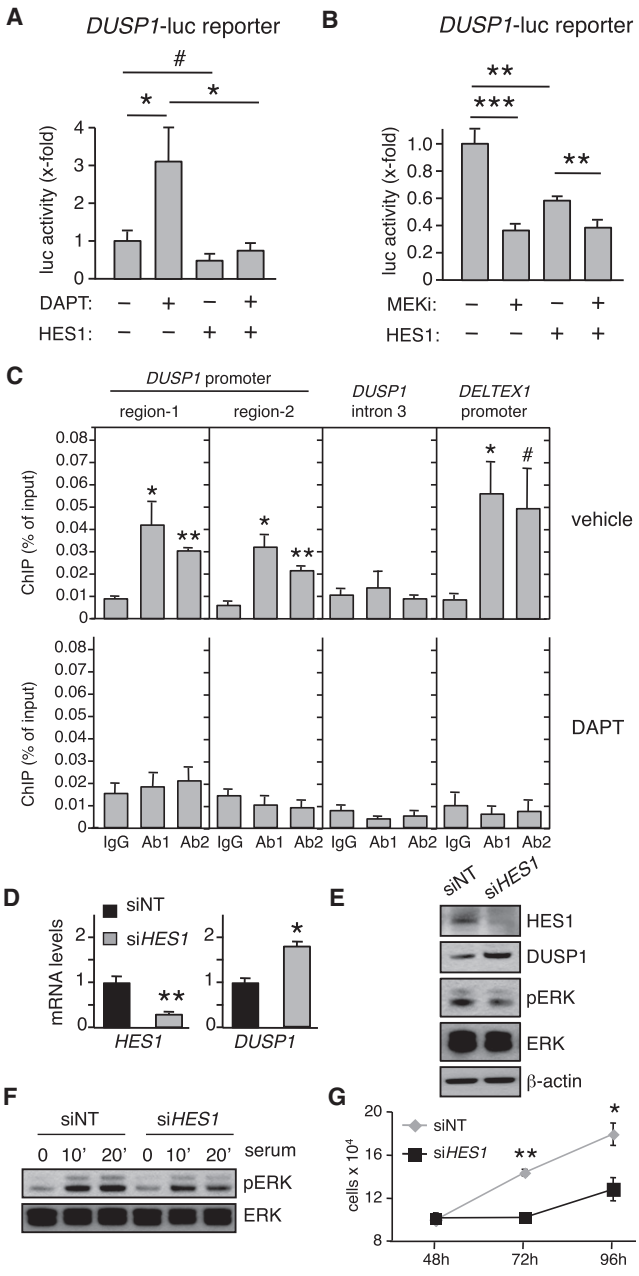

Figure 7. HES1 Directly Binds and Represses the *DUSP1* Promoter

(A) Luciferase activity of H358 cells transfected with a *DUSP1*-luc reporter together with a plasmid expressing HES1 or its corresponding empty control. Cells were treated for 48 hr with 5 μM DAPT or its vehicle in the presence of complete medium.

(B) Luciferase activity of H358 cells transfected with a *DUSP1*-luc reporter together with a plasmid expressing HES1 or its corresponding empty control. Cells were treated for 48 hr with a MEK inhibitor (PD0325901) or its vehicle in the presence of complete medium.

(C) ChIP analysis of the *DUSP1* promoter using two different HES1 antibodies [Ab1, 4H1 (Novus Biologicals) and Ab2, H140 (Santa Cruz Biotechnology)] in H358 cells. Four different DNA regions were analyzed by qPCR: two from the *DUSP1* promoter (see Figure S5), an intronic region from *DUSP1* (intron 3), and the promoter of *DELTEX1*. Cells were treated with 5 μM DAPT or vehicle (ETOH) for 48 hr. Data correspond to three independent biological replicates.

(D) Levels of *HES1* and *DUSP1* expression measured by qRT-PCR in H358 cells treated with si*HES1* (*HES1* siRNA, n = 3) or nontargeting siRNA (siNT, n = 3) for 48 hr (36 hr in the presence of serum and then 12 hr in the absence of serum).

(E) Protein levels of DUSP1, HES1, pERK, and total ERK in H358 cells treated as in (D).

(F) Phosphorylation of ERK in H358 cells treated with si*HES1* (*HES1* siRNA) or siNT for 48 hr (36 hr in the presence of serum and then 12 hr in the absence of serum) and then stimulated with serum for the indicated times (in minutes).

(G) H358 cells were treated with si*HES1* (*HES1* siRNA, n = 3) or siNT (n = 3), and cell numbers were counted at the indicated time points after siRNA transfection.

Values correspond to the average ± SEM. Statistical significance was determined by a two-tailed Student's t test: #$p < 0.1$; *$p < 0.05$; **$p < 0.01$.

See also Figure S6.

Having observed that HES1 has the ability to repress the *DUSP1* promoter, we sought to determine whether HES1 directly binds to the *DUSP1* promoter. HES1 binds two similar sequence motifs, known as class C sites and N-boxes (Iso et al., 2003), and an examination of the human and murine *DUSP1*/*Dusp1* promoters revealed the presence of several putative HES1 binding sites (Figure S6). We tested whether HES1 directly binds to the human *DUSP1* promoter by chromatin immunoprecipitation (ChIP) using two different antibodies against HES1 in H358 cells. Of interest, HES1 immunoprecipitation with two different antibodies resulted in significant enrichment of two regions of the *DUSP1* promoter compared with a control IgG immunoprecipitation (Figure 7C). In contrast, no enrichment was observed when a *DUSP1* intronic region was amplified or when cells were treated with DAPT (Figure 7C). As a positive control, we used the *DELTEX1* promoter, which is directly repressed by HES1 (Zhang et al., 2010). As expected, binding of HES1 to the *DELTEX1* promoter was observed in the absence of DAPT, but not in its presence (Figure 7C).

We wanted to test the effect of *HES1* inhibition on *DUSP1* levels and ERK phosphorylation. Treatment of H358 cells with a pool of siRNAs targeting *HES1* mRNA (si*HES1*) effectively reduced HES1 mRNA and protein levels (Figures 7D and 7E), and, of importance, this resulted in significant upregulation of DUSP1 mRNA and protein levels (Figures 7D and 7E). We previously demonstrated that DUSP1 dephosphorylates pERK (Figures 6D and 6E), and in agreement with this, si*HES1* reduced the levels of phosphorylated ERK (Figures 7E and 7F). Finally, previous reports showed that GSIs can prevent the growth of human cancer cell lines (Chen et al., 2007; Eliasz et al., 2010; Westhoff et al., 2009), and we wondered whether this could also be the case for si*HES1*. Indeed, cells treated with si*HES1* had an impaired proliferative capacity (Figure 7G). All together, these findings show that inhibition of *HES1* in NSCLCs cells recapitulates the effect of DAPT treatment on *DUSP1* expression, ERK phosphorylation, and cell proliferation.

High HES1 and Low DUSP1 Levels Are Associated with Poor Clinical Outcome in Patients with NSCLC

Previous investigators reported that subsets of patients with NSCLC have a hyperactivated Notch pathway (Haruki et al., 2005; Westhoff et al., 2009), which correlates with a poor clinical outcome (Westhoff et al., 2009). In the light of our above results, we wanted to extend this observation to HES1 and examine its relation to DUSP1. We examined the levels of HES1 in a series

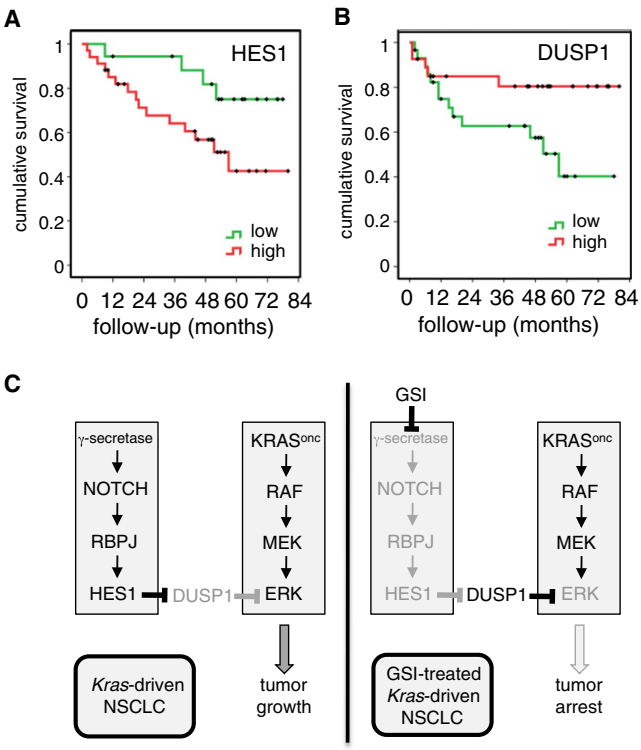

Figure 8. High HES1 and Low DUSP1 Levels Are Associated with Poor Clinical Outcome in Primary Human NSCLCs

(A) Kaplan-Meier curve indicating that patients with NSCLCs with high expression of nuclear HES1 present shorter overall survival ($p = 0.045$). High nuclear HES1 expression corresponds to tumors in which at least 40% of their neoplastic cells are positive for HES1.

(B) Kaplan-Meier curve indicating that patients with NSCLCs with low expression of cytoplasmic DUSP1 present poorer overall survival ($p = 0.048$). Low cytoplasmic DUSP1 expression corresponds to tumors in which <70% of their neoplastic cells are positive for DUSP1.

(C) Summary of the data presented in this work. See Discussion for a detailed explanation.

A logrank test was used to determine statistical significance.

See also Figure S7.

of NSCLCs (n = 82), and observed that tumors with high levels of nuclear HES1 were associated with a shorter overall survival (logrank, $p = 0.045$; Figure 8A and Figure S7A). Previous investigators found a positive correlation between DUSP1 levels and survival in human NSCLCs (Vicent et al., 2004). We confirmed this result in our NSCLC series, in which we obtained a positive correlation between DUSP1 cytoplasmic expression and better overall survival (logrank, $p = 0.048$; Figure 8B and Figure S7A). Moreover, when patients were stratified according to HES1 and DUSP1, those who showed a combination of high HES1 intensity and low DUSP1 expression had the poorest outcome compared with the other three possible combinations (logrank test, $p = 0.09$; Figure S7B). Finally, there was a negative correlation between HES1 intensity and DUSP1 expression (correlation coefficient −0.219; Kendall Tau-b test, $p = 0.07$). Collectively, these observations support the relevance of HES1 in human NSCLCs and reinforce the concept that HES1 represses DUSP1.

DISCUSSION

In this work, we investigated the role of the Notch pathway in the generation and maintenance of primary *Kras*^{G12V}-driven NSCLCs.

Previous studies showed that a significant proportion of patients with NSCLC have a hyperactive Notch pathway (Haruki et al., 2005; Westhoff et al., 2009), but did not examine the role of the Notch pathway in the development of NSCLCs. To address this question, we used a mouse model with a latent *Kras* oncogene that faithfully recapitulates the development of human NSCLCs (Guerra et al., 2003; Jackson et al., 2001; Sweet-Cordero et al., 2005). First, we validated our mouse model by observing that, as in humans, the Notch pathway is hyperactive in murine *Kras*^{G12V}-driven NSCLCs compared with normal lung. This is evidenced by higher levels of active γ-secretase complex, increased levels of NICD (the activated form of NOTCH1), decreased *Numb* mRNA (a negative regulator of the Notch pathway), and increased HES1 protein (a downstream target of the Notch pathway). HES1 protein levels increased in parallel with the degree of malignization, suggesting a requirement of Notch pathway activity during this process. Of note, genetic elimination of either the γ-secretase complex (upstream of the Notch pathway) or *Rbpj* (encoding the canonical DNA-binding partner of NICDs) abolished the formation of *Kras*^{G12V}-driven NSCLCs. These results indicate that the generation of NSCLCs by oncogenic *Kras* requires the activation of the Notch pathway.

On the basis of the above findings, we hypothesized that Notch activity may also be required for the maintenance of primary *Kras*^{G12V}-driven NSCLCs. Previous reports in this direction showed that γ-secretase inhibition slows the growth of subcutaneous xenografts formed by lung cancer cells (Konishi et al., 2007; Luistro et al., 2009; Paris et al., 2005). Xenografts, despite their utility, do not recapitulate the microenvironment of the natural primary tumors, and this may have a critical impact on therapeutic activity, as was elegantly illustrated in the case of pancreatic cancer (Olive et al., 2009). Only a handful of studies have evaluated the efficacy of chemotherapy for primary murine lung tumors (Engelman et al., 2008; Ji et al., 2007; Yang et al., 2008). These studies were largely based on MRI or CT, which cannot discriminate nonmalignant tumors from malignant ones. Here, in an effort to recapitulate a human clinical setting, we also evaluated therapeutic responses by using PET, thus focusing exclusively on malignant tumors. Of importance, mice treated with the pharmacologically active GSI LSN-411575 showed a complete blockade of cancer growth. These results demonstrate that GSIs are therapeutically effective for primary autochthonous *Kras*^{G12V}-driven NSCLCs in mice.

Analyses of LSN-411575-treated, *Kras*^{G12V}-driven NSCLCs indicated a significant reduction in the levels of HES1 as soon as 4 days after treatment, thus confirming that the GSI reached its target. In addition, treated NSCLCs presented decreased proliferation and increased apoptosis. Among a number of key candidate proteins that could be affected by GSI treatment, we selectively detected an effect on the phosphorylation of ERK, which was dramatically reduced after treatment. This observation is in accordance with previous data obtained in in vitro cultured cells, which showed that the Notch pathway upregulates the levels of ERK phosphorylation (Kim et al., 2005; Konishi

et al., 2007; Michie et al., 2007). The role of ERK phosphorylation in *Kras*-driven NSCLCs was recently highlighted by the demonstration that ERK activity is essential for *Kras*-driven lung tumorigenesis (Blasco et al., 2011; Feldser et al., 2010; Junttila et al., 2010). Because MEK is the critical kinase responsible for ERK phosphorylation, we also examined the levels of phosphorylated MEK in GSI-treated NSCLCs; however, in contrast to phospho-ERK, the levels of phospho-MEK were not affected by the GSI. In summary, we found that GSI treatment of primary autochthonous $Kras^{G12V}$-driven NSCLCs impinges on the phosphorylation of ERK without affecting MEK activity.

To dissect the mechanism that links γ-secretase inhibition with dephosphorylation of ERK, we analyzed the transcriptional changes induced by GSI. In particular, we used a human NSCLC cell line, H358, which is addicted to oncogenic *KRAS* (Singh et al., 2009). These cells, as we have shown here, dephosphorylate ERK in response to GSI treatment without affecting phospho-MEK, thus recapitulating the behavior of primary $Kras^{G12V}$-driven NSCLCs. Among the set of genes whose expression was induced by GSI treatment, we focused our attention on the dual-specificity phosphatase DUSP1 because previous data obtained in human NSCLC cells indicate that this phosphatase is regulated by the Notch pathway (Haruki et al., 2005) and dephosphorylates ERK (Lin et al., 2003; Patterson et al., 2009). Indeed, using both gain- and loss-of-function experiments, we confirmed the concept that DUSP1 affects ERK phosphorylation in human H358 cells. Moreover, the induction of *DUSP1* after GSI treatment was confirmed in another two human NSCLC cell lines and in six human T-ALL cell lines, thus giving more general validity to our findings. Finally, we observed *Dusp1* upregulation in GSI-treated murine primary $Kras^{G12V}$-driven NSCLCs. Therefore, the observed association between GSI treatment and *DUSP1* upregulation occurs in the context of primary NSCLCs, and could explain the reduction in ERK phosphorylation upon GSI treatment.

HES1 is a well known transcriptional repressor of multiple genes (Iso et al., 2003; Sang et al., 2010), including genes that are relevant for T-ALL, such as *PTEN* (Palomero et al., 2007) and *CYLD* (Espinosa et al., 2010), which activate AKT and NFκB, respectively. Furthermore, it was recently demonstrated that HES1 plays a critical role in the maintenance of NOTCH1-driven murine T-ALL (Wendorff et al., 2010). Based on our observation that HES1 levels increase in association with malignization and decrease upon GSI treatment of $Kras^{G12V}$-driven NSCLCs, we hypothesized that GSI-induced dephosphorylation of ERK could be mediated by HES1-mediated repression of *DUSP1*. Indeed, luciferase reporter assays supported the concept that HES1 is a negative regulator of *DUSP1*. Furthermore, ChIP showed that HES1 directly binds to and represses *DUSP1*, and that this process can be reverted by GSI treatment. In addition, treatment of H358 cells with si*HES1* promoted a phenotype very similar to that obtained by GSI treatment in terms of ERK phosphorylation, *DUSP1* upregulation, and cell growth arrest.

Finally, we checked the status of HES1 and DUSP1 in primary human NSCLCs. We found that low DUSP1 is associated with poor survival, which is in agreement with previous data (Vicent et al., 2004). In support of our proposed mechanism, we found that high HES1 levels are also associated with poor survival. Moreover, we also observed a suggestive negative correlation between HES1 intensity and DUSP1 expression. These observations support the relevance of HES1 in human NSCLCs and reinforce the concept that HES1 represses DUSP1.

Collectively, our observations establish a direct causal link among γ-secretase inhibition, HES1 downregulation, *DUSP1* derepression, and ERK dephosphorylation (Figure 8C). As mentioned above, high ERK activity is crucial for the development of *Kras*-driven NSCLCs (Blasco et al., 2011; Feldser et al., 2010; Junttila et al., 2010), and, in this regard, we propose that our observation that the Notch pathway is required for NSCLC formation is related to the capacity of HES1 to increase ERK activity through repression of *Dusp1*. Although our current data point to HES1 and DUSP1 as relevant mediators of the effects of GSI treatment on the KRAS signaling pathway, we cannot exclude the possibility that other members of the HES1 family or DUSP1 family, or other unrelated mechanisms, may also participate in mediating the effects of GSI treatment.

The results presented in this work support the therapeutic potential of targeting γ-secretase in NSCLC. We show that GSI treatment inhibits ERK without affecting MEK, and hence we envision a synergistic effect of MEK inhibitors and GSIs on *KRAS*-driven NSCLCs. Of importance, GSIs have been shown to be pharmacologically active in humans (Bateman et al., 2009) and have been tested in clinical trials for Alzheimer disease (Fleisher et al., 2008; Panza et al., 2009; Wolfe, 2009), which could facilitate the evaluation of these compounds for the treatment of human lung cancer, the leading cause of cancer-related deaths in the world.

EXPERIMENTAL PROCEDURES

Mice

Mice were generated by crossing $Kras^{+/LSLG12Vgeo}$ mice (Guerra et al., 2003) with $Psen1^{f/f}$;$Psen2^{-/-}$ (Saura et al., 2004) or $Rbpj^{f/f}$ (Tanigaki et al., 2002) mice. All animal procedures were performed according to protocols approved by the National Cancer Research Center-Instituto de Salud Carlos III (CNIO-ISCIII) Ethics Committee for Research and Animal Welfare.

DNA, RNA, and Protein Analyses

Details regarding the PCR primers, antibodies, and other standard molecular biology methods used in this work are provided in Supplemental Experimental Procedures.

Micro-PET/CT

Imaging was done essentially as described previously (Mulero et al., 2011). See the summary in Supplemental Experimental Procedures.

Treatment with LSN-411575

The LSN-411575 compound was kindly provided by Eli Lilly and Company and formulated in 1% carboxymethyl cellulose, 0.25% Tween 80. The compound was given orally by gavage early in the morning, at a dose of 3 mg/kg/day for the indicated number of days. Control mice were treated with the vehicle following an identical procedure. On the last day of treatment, PET was performed within 2–6 hr after gavage (vehicle- and compound-treated mice were in alternate order for the analysis). Mice were killed within 4–8 hr after gavage, and samples were obtained for pathological and IHC analyses.

Cellular Treatments

H358 human NSCLC cells were purchased from ATCC. Cells were treated with 5 μM DAPT (Calbiochem) for 36 hr in the presence of serum. The cells were then serum starved for 12 hr in the presence of DAPT or vehicle, as indicated in the corresponding figures. When noted, cells were serum stimulated for the

indicated time. For additional details, see Supplemental Experimental Procedures.

Human Samples

Primary lung tumors were collected and handled anonymously at collaborating institutions (Instituto Angel H. Roffo and Hospital Britanico) with the approval of their institutional review boards and following standard ethical and legal protection guidelines regarding human subjects, including informed consent.

Statistical Analysis

Unless otherwise specified, data are presented as mean ± SEM. Student's t test was used to assess the significance of expression levels by both qRT-PCR and IHC. Student's t test was also used to determine the differences among groups for changes in tumor size or animal weight. Associations of protein expression patterns in human TMA of HES1 and DUSP1 were evaluated using the Kendall tau test. Survival curves were tested by logrank test.

ACCESSION NUMBERS

Microarray data were deposited in the National Center for Biotechnology Information's Gene Expression Omnibus (accession number GSE38054).

SUPPLEMENTAL INFORMATION

Supplemental Information includes seven figures, one table, and Supplemental Experimental Procedures and can be found with this article online at http://dx.doi.org/10.1016/j.ccr.2012.06.014.

ACKNOWLEDGMENTS

We thank Mariano Barbacid (CNIO, Madrid, Spain) for kindly providing us with inducible KrasG12V mice and Eli Lilly and Company (Indianapolis, IN) for providing us with LSN-411575. We also thank Andrew Clark (Imperial College London), Anton Bennett (Yale University), Jose F. Rodríguez (National Center of Biotechnology, Madrid, Spain), Ramon Diaz-Uriarte (CNIO), Jose L. de la Pompa (CNIC), and Daniel Muñoz (CNIO) for sharing reagents, giving advice, and critical readings of the manuscript. We also thank all of our clinical collaborators at the Angel H. Roffo and Hospital Britanico (Buenos Aires, Argentina) for their help in obtaining the tumor specimens and for corresponding clinical follow-up. A.M. received a postdoctoral grant from the Miguel Servet Program of the Spanish Ministry of Science. Work in the laboratory of M.S. is funded by the CNIO and by grants from the Spanish Ministry of Science (SAF and CONSOLIDER), the European Research Council (ERC Advanced Grant), and the Marcelino Botin Foundation. A.M. designed and performed most of the experiments and contributed to data analysis, discussion, and writing the manuscript. P.J.F.-M. and D.H. performed some experiments and contributed to data analysis. M.C. performed the murine IHC and pathological analyses. M.M.-M. performed all of the animal manipulations. F.M. performed all analyses of the microPET/CT imaging. D.M. quantified the confocal microscopy. J.S. provided supervision and the mouse model with inducible deletion of γ-secretase. M.S.-Cespedes and M.S.-Carbayo provided the human samples and performed IHC and pathological analyses. T.P. and A.F. gave advice and participated in the design of the study. M.S. designed and supervised the study, secured funding, analyzed the data, and wrote the manuscript. All authors discussed the results and commented on the manuscript.

Received: September 2, 2011
Revised: February 2, 2012
Accepted: June 19, 2012
Published: August 13, 2012

REFERENCES

Bateman, R.J., Siemers, E.R., Mawuenyega, K.G., Wen, G., Browning, K.R., Sigurdson, W.C., Yarasheski, K.E., Friedrich, S.W., Demattos, R.B., May, P.C., et al. (2009). A gamma-secretase inhibitor decreases amyloid-beta production in the central nervous system. Ann. Neurol. *66*, 48–54.

Best, J.D., Jay, M.T., Otu, F., Ma, J., Nadin, A., Ellis, S., Lewis, H.D., Pattison, C., Reilly, M., Harrison, T., et al. (2005). Quantitative measurement of changes in amyloid-beta(40) in the rat brain and cerebrospinal fluid following treatment with the gamma-secretase inhibitor LY-411575 [N2-[(2S)-2-(3,5-difluorophenyl)-2-hydroxyethanoyl]-N1-[(7S)-5-methyl-6-oxo-6,7-dihydro-5H-dibenzo[b,d]azepin-7-yl]-L-alaninamide]. J. Pharmacol. Exp. Ther. *313*, 902–908.

Blanco, R., Iwakawa, R., Tang, M., Kohno, T., Angulo, B., Pio, R., Montuenga, L.M., Minna, J.D., Yokota, J., and Sanchez-Cespedes, M. (2009). A gene-alteration profile of human lung cancer cell lines. Hum. Mutat. *30*, 1199–1206.

Blasco, R.B., Francoz, S., Santamaría, D., Cañamero, M., Dubus, P., Charron, J., Baccarini, M., and Barbacid, M. (2011). c-Raf, but not B-Raf, is essential for development of K-Ras oncogene-driven non-small cell lung carcinoma. Cancer Cell *19*, 652–663.

Brondello, J.M., Brunet, A., Pouysségur, J., and McKenzie, F.R. (1997). The dual specificity mitogen-activated protein kinase phosphatase-1 and -2 are induced by the p42/p44MAPK cascade. J. Biol. Chem. *272*, 1368–1376.

Chen, Y., De Marco, M.A., Graziani, I., Gazdar, A.F., Strack, P.R., Miele, L., and Bocchetta, M. (2007). Oxygen concentration determines the biological effects of NOTCH-1 signaling in adenocarcinoma of the lung. Cancer Res. *67*, 7954–7959.

Chiba, S. (2006). Notch signaling in stem cell systems. Stem Cells *24*, 2437–2447.

Collins, B.J., Kleeberger, W., and Ball, D.W. (2004). Notch in lung development and lung cancer. Semin. Cancer Biol. *14*, 357–364.

Demarest, R.M., Ratti, F., and Capobianco, A.J. (2008). It's T-ALL about Notch. Oncogene *27*, 5082–5091.

Edbauer, D., Winkler, E., Haass, C., and Steiner, H. (2002). Presenilin and nicastrin regulate each other and determine amyloid beta-peptide production via complex formation. Proc. Natl. Acad. Sci. USA *99*, 8666–8671.

Eliasz, S., Liang, S., Chen, Y., De Marco, M.A., Machek, O., Skucha, S., Miele, L., and Bocchetta, M. (2010). Notch-1 stimulates survival of lung adenocarcinoma cells during hypoxia by activating the IGF-1R pathway. Oncogene *29*, 2488–2498.

Engelman, J.A., Chen, L., Tan, X., Crosby, K., Guimaraes, A.R., Upadhyay, R., Maira, M., McNamara, K., Perera, S.A., Song, Y., et al. (2008). Effective use of PI3K and MEK inhibitors to treat mutant Kras G12D and PIK3CA H1047R murine lung cancers. Nat. Med. *14*, 1351–1356.

Espinosa, L., Cathelin, S., D'Altri, T., Trimarchi, T., Statnikov, A., Guiu, J., Rodilla, V., Inglés-Esteve, J., Nomdedeu, J., Bellosillo, B., et al. (2010). The Notch/Hes1 pathway sustains NF-κB activation through CYLD repression in T cell leukemia. Cancer Cell *18*, 268–281.

Feldser, D.M., Kostova, K.K., Winslow, M.M., Taylor, S.E., Cashman, C., Whittaker, C.A., Sanchez-Rivera, F.J., Resnick, R., Bronson, R., Hemann, M.T., and Jacks, T. (2010). Stage-specific sensitivity to p53 restoration during lung cancer progression. Nature *468*, 572–575.

Ferrando, A.A. (2009). The role of NOTCH1 signaling in T-ALL. Hematology (Am Soc Hematol Educ Program) *2009*, 353–361.

Fischer, B.M., Mortensen, J., and Højgaard, L. (2001). Positron emission tomography in the diagnosis and staging of lung cancer: a systematic, quantitative review. Lancet Oncol. *2*, 659–666.

Fleisher, A.S., Raman, R., Siemers, E.R., Becerra, L., Clark, C.M., Dean, R.A., Farlow, M.R., Galvin, J.E., Peskind, E.R., Quinn, J.F., et al. (2008). Phase 2 safety trial targeting amyloid beta production with a gamma-secretase inhibitor in Alzheimer disease. Arch. Neurol. *65*, 1031–1038.

Fraering, P.C. (2007). Structural and functional determinants of gamma-secretase, an intramembrane protease implicated in Alzheimer's disease. Curr. Genomics *8*, 531–549.

Gould, M.K., Maclean, C.C., Kuschner, W.G., Rydzak, C.E., and Owens, D.K. (2001). Accuracy of positron emission tomography for diagnosis of pulmonary nodules and mass lesions: a meta-analysis. JAMA *285*, 914–924.

Guerra, C., Mijimolle, N., Dhawahir, A., Dubus, P., Barradas, M., Serrano, M., Campuzano, V., and Barbacid, M. (2003). Tumor induction by an endogenous

K-ras oncogene is highly dependent on cellular context. Cancer Cell *4*, 111–120.

Haruki, N., Kawaguchi, K.S., Eichenberger, S., Massion, P.P., Olson, S., Gonzalez, A., Carbone, D.P., and Dang, T.P. (2005). Dominant-negative Notch3 receptor inhibits mitogen-activated protein kinase pathway and the growth of human lung cancers. Cancer Res. *65*, 3555–3561.

Hass, M.R., Sato, C., Kopan, R., and Zhao, G. (2009). Presenilin: RIP and beyond. Semin. Cell Dev. Biol. *20*, 201–210.

Heitzler, P. (2010). Biodiversity and noncanonical Notch signaling. Curr. Top. Dev. Biol. *92*, 457–481.

Iso, T., Kedes, L., and Hamamori, Y. (2003). HES and HERP families: multiple effectors of the Notch signaling pathway. J. Cell. Physiol. *194*, 237–255.

Ito, T., Udaka, N., Yazawa, T., Okudela, K., Hayashi, H., Sudo, T., Guillemot, F., Kageyama, R., and Kitamura, H. (2000). Basic helix-loop-helix transcription factors regulate the neuroendocrine differentiation of fetal mouse pulmonary epithelium. Development *127*, 3913–3921.

Jackson, E.L., Willis, N., Mercer, K., Bronson, R.T., Crowley, D., Montoya, R., Jacks, T., and Tuveson, D.A. (2001). Analysis of lung tumor initiation and progression using conditional expression of oncogenic K-ras. Genes Dev. *15*, 3243–3248.

Jackson, E.L., Olive, K.P., Tuveson, D.A., Bronson, R., Crowley, D., Brown, M., and Jacks, T. (2005). The differential effects of mutant p53 alleles on advanced murine lung cancer. Cancer Res. *65*, 10280–10288.

Ji, H., Wang, Z., Perera, S.A., Li, D., Liang, M.C., Zaghlul, S., McNamara, K., Chen, L., Albert, M., Sun, Y., et al. (2007). Mutations in BRAF and KRAS converge on activation of the mitogen-activated protein kinase pathway in lung cancer mouse models. Cancer Res. *67*, 4933–4939.

Junttila, M.R., Karnezis, A.N., Garcia, D., Madriles, F., Kortlever, R.M., Rostker, F., Brown Swigart, L., Pham, D.M., Seo, Y., Evan, G.I., and Martins, C.P. (2010). Selective activation of p53-mediated tumour suppression in high-grade tumours. Nature *468*, 567–571.

Kim, M.Y., Park, J.H., Choi, E.J., and Park, H.S. (2005). Presenilin acts as a positive regulator of basal level activity of ERK through the Raf-MEK1 signaling pathway. Biochem. Biophys. Res. Commun. *332*, 609–613.

Konishi, J., Kawaguchi, K.S., Vo, H., Haruki, N., Gonzalez, A., Carbone, D.P., and Dang, T.P. (2007). Gamma-secretase inhibitor prevents Notch3 activation and reduces proliferation in human lung cancers. Cancer Res. *67*, 8051–8057.

Liang, M.C., Ma, J., Chen, L., Kozlowski, P., Qin, W., Li, D., Goto, J., Shimamura, T., Hayes, D.N., Meyerson, M., et al. (2010). TSC1 loss synergizes with KRAS activation in lung cancer development in the mouse and confers rapamycin sensitivity. Oncogene *29*, 1588–1597.

Lin, Y.W., Chuang, S.M., and Yang, J.L. (2003). ERK1/2 achieves sustained activation by stimulating MAPK phosphatase-1 degradation via the ubiquitin-proteasome pathway. J. Biol. Chem. *278*, 21534–21541.

Luistro, L., He, W., Smith, M., Packman, K., Vilenchik, M., Carvajal, D., Roberts, J., Cai, J., Berkofsky-Fessler, W., Hilton, H., et al. (2009). Preclinical profile of a potent gamma-secretase inhibitor targeting notch signaling with in vivo efficacy and pharmacodynamic properties. Cancer Res. *69*, 7672–7680.

Maraver, A., Tadokoro, C.E., Badura, M.L., Shen, J., Serrano, M., and Lafaille, J.J. (2007). Effect of presenilins in the apoptosis of thymocytes and homeostasis of CD8+ T cells. Blood *110*, 3218–3225.

Meylan, E., Dooley, A.L., Feldser, D.M., Shen, L., Turk, E., Ouyang, C., and Jacks, T. (2009). Requirement for NF-kappaB signalling in a mouse model of lung adenocarcinoma. Nature *462*, 104–107.

Michie, A.M., Chan, A.C., Ciofani, M., Carleton, M., Lefebvre, J.M., He, Y., Allman, D.M., Wiest, D.L., Zúñiga-Pflücker, J.C., and Izon, D.J. (2007). Constitutive Notch signalling promotes CD4 CD8 thymocyte differentiation in the absence of the pre-TCR complex, by mimicking pre-TCR signals. Int. Immunol. *19*, 1421–1430.

Morimoto, M., Liu, Z., Cheng, H.T., Winters, N., Bader, D., and Kopan, R. (2010). Canonical Notch signaling in the developing lung is required for determination of arterial smooth muscle cells and selection of Clara versus ciliated cell fate. J. Cell Sci. *123*, 213–224.

Mulero, F., Donate, L.E., and Serrano, M. (2011). Imaging cancer in mice by PET, CT, and combined PET-CT. Curr Protoc Mouse Biol *1*, 85–103.

Olive, K.P., Jacobetz, M.A., Davidson, C.J., Gopinathan, A., McIntyre, D., Honess, D., Madhu, B., Goldgraben, M.A., Caldwell, M.E., Allard, D., et al. (2009). Inhibition of Hedgehog signaling enhances delivery of chemotherapy in a mouse model of pancreatic cancer. Science *324*, 1457–1461.

Palomero, T., Sulis, M.L., Cortina, M., Real, P.J., Barnes, K., Ciofani, M., Caparros, E., Buteau, J., Brown, K., Perkins, S.L., et al. (2007). Mutational loss of PTEN induces resistance to NOTCH1 inhibition in T-cell leukemia. Nat. Med. *13*, 1203–1210.

Panza, F., Solfrizzi, V., Frisardi, V., Imbimbo, B.P., Capurso, C., D'Introno, A., Colacicco, A.M., Seripa, D., Vendemiale, G., Capurso, A., and Pilotto, A. (2009). Beyond the neurotransmitter-focused approach in treating Alzheimer's disease: drugs targeting beta-amyloid and tau protein. Aging Clin. Exp. Res. *21*, 386–406.

Paris, D., Quadros, A., Patel, N., DelleDonne, A., Humphrey, J., and Mullan, M. (2005). Inhibition of angiogenesis and tumor growth by beta and gamma-secretase inhibitors. Eur. J. Pharmacol. *514*, 1–15.

Patterson, K.I., Brummer, T., O'Brien, P.M., and Daly, R.J. (2009). Dual-specificity phosphatases: critical regulators with diverse cellular targets. Biochem. J. *418*, 475–489.

Roy, M., Pear, W.S., and Aster, J.C. (2007). The multifaceted role of Notch in cancer. Curr. Opin. Genet. Dev. *17*, 52–59.

Sang, L., Roberts, J.M., and Coller, H.A. (2010). Hijacking HES1: how tumors co-opt the anti-differentiation strategies of quiescent cells. Trends Mol. Med. *16*, 17–26.

Saura, C.A., Choi, S.Y., Beglopoulos, V., Malkani, S., Zhang, D., Shankaranarayana Rao, B.S., Chattarji, S., Kelleher, R.J., 3rd, Kandel, E.R., Duff, K., et al. (2004). Loss of presenilin function causes impairments of memory and synaptic plasticity followed by age-dependent neurodegeneration. Neuron *42*, 23–36.

Singh, A., Greninger, P., Rhodes, D., Koopman, L., Violette, S., Bardeesy, N., and Settleman, J. (2009). A gene expression signature associated with "K-Ras addiction" reveals regulators of EMT and tumor cell survival. Cancer Cell *15*, 489–500.

Sweet-Cordero, A., Mukherjee, S., Subramanian, A., You, H., Roix, J.J., Ladd-Acosta, C., Mesirov, J., Golub, T.R., and Jacks, T. (2005). An oncogenic KRAS2 expression signature identified by cross-species gene-expression analysis. Nat. Genet. *37*, 48–55.

Tanigaki, K., Han, H., Yamamoto, N., Tashiro, K., Ikegawa, M., Kuroda, K., Suzuki, A., Nakano, T., and Honjo, T. (2002). Notch-RBP-J signaling is involved in cell fate determination of marginal zone B cells. Nat. Immunol. *3*, 443–450.

Tsao, P.N., Vasconcelos, M., Izvolsky, K.I., Qian, J., Lu, J., and Cardoso, W.V. (2009). Notch signaling controls the balance of ciliated and secretory cell fates in developing airways. Development *136*, 2297–2307.

van Es, J.H., van Gijn, M.E., Riccio, O., van den Born, M., Vooijs, M., Begthel, H., Cozijnsen, M., Robine, S., Winton, D.J., Radtke, F., and Clevers, H. (2005). Notch/gamma-secretase inhibition turns proliferative cells in intestinal crypts and adenomas into goblet cells. Nature *435*, 959–963.

Vicent, S., Garayoa, M., López-Picazo, J.M., Lozano, M.D., Toledo, G., Thunnissen, F.B., Manzano, R.G., and Montuenga, L.M. (2004). Mitogen-activated protein kinase phosphatase-1 is overexpressed in non-small cell lung cancer and is an independent predictor of outcome in patients. Clin. Cancer Res. *10*, 3639–3649.

Weijzen, S., Rizzo, P., Braid, M., Vaishnav, R., Jonkheer, S.M., Zlobin, A., Osborne, B.A., Gottipati, S., Aster, J.C., Hahn, W.C., et al. (2002). Activation of Notch-1 signaling maintains the neoplastic phenotype in human Ras-transformed cells. Nat. Med. *8*, 979–986.

Wendorff, A.A., Koch, U., Wunderlich, F.T., Wirth, S., Dubey, C., Brüning, J.C., MacDonald, H.R., and Radtke, F. (2010). Hes1 is a critical but context-dependent mediator of canonical Notch signaling in lymphocyte development and transformation. Immunity *33*, 671–684.

Westhoff, B., Colaluca, I.N., D'Ario, G., Donzelli, M., Tosoni, D., Volorio, S., Pelosi, G., Spaggiari, L., Mazzarol, G., Viale, G., et al. (2009). Alterations of

the Notch pathway in lung cancer. Proc. Natl. Acad. Sci. USA *106*, 22293–22298.

Wolfe, M.S. (2009). gamma-Secretase in biology and medicine. Semin. Cell Dev. Biol. *20*, 219–224.

Wong, G.T., Manfra, D., Poulet, F.M., Zhang, Q., Josien, H., Bara, T., Engstrom, L., Pinzon-Ortiz, M., Fine, J.S., Lee, H.J., et al. (2004). Chronic treatment with the gamma-secretase inhibitor LY-411,575 inhibits beta-amyloid peptide production and alters lymphopoiesis and intestinal cell differentiation. J. Biol. Chem. *279*, 12876–12882.

Wu, J.J., Zhang, L., and Bennett, A.M. (2005). The noncatalytic amino terminus of mitogen-activated protein kinase phosphatase 1 directs nuclear targeting and serum response element transcriptional regulation. Mol. Cell. Biol. *25*, 4792–4803.

Yang, Y., Iwanaga, K., Raso, M.G., Wislez, M., Hanna, A.E., Wieder, E.D., Molldrem, J.J., Wistuba, I.I., Powis, G., Demayo, F.J., et al. (2008). Phosphatidylinositol 3-kinase mediates bronchioalveolar stem cell expansion in mouse models of oncogenic K-ras-induced lung cancer. PLoS ONE *3*, e2220.

Zhang, P., Yang, Y., Nolo, R., Zweidler-McKay, P.A., and Hughes, D.P. (2010). Regulation of NOTCH signaling by reciprocal inhibition of HES1 and Deltex 1 and its role in osteosarcoma invasiveness. Oncogene *29*, 2916–2926.

Cancer Cell
Article

Small GTPase R-Ras Regulates Integrity and Functionality of Tumor Blood Vessels

Junko Sawada,[1] Takeo Urakami,[1] Fangfei Li,[1] Akane Urakami,[1] Weiquan Zhu,[2] Minoru Fukuda,[3] Dean Y. Li,[2] Erkki Ruoslahti,[3,4] and Masanobu Komatsu[1,3,*]
[1]Sanford-Burnham Medical Research Institute at Lake Nona, Orlando, FL 32827, USA
[2]Department of Medicine and Cardiology, University of Utah, Molecular Medicine (U2M2) Program and Cardiology, Salt Lake City, UT 84112, USA
[3]Tumor Microenvironment Program, Cancer Center, Sanford-Burnham Medical Research Institute, La Jolla, CA 92037, USA
[4]Center for Nanomedicine and Department of Molecular Cell and Developmental Biology, University of California, Santa Barbara, CA 93106, USA
*Correspondence: mkomatsu@sanfordburnham.org
http://dx.doi.org/10.1016/j.ccr.2012.06.013

SUMMARY

We show that R-Ras, a small GTPase of the Ras family, is essential for the establishment of mature, functional blood vessels in tumors. The genetic disruption of R-Ras severely impaired the maturation processes of tumor vessels in mice. Conversely, the gain of function of R-Ras improved vessel structure and blood perfusion and blocked plasma leakage by enhanced endothelial barrier function and pericyte association with nascent blood vessels. Thus, R-Ras promotes normalization of the tumor vasculature. These findings identify R-Ras as a critical regulator of vessel integrity and function during tumor vascularization.

INTRODUCTION

Tumor vasculature is structurally and functionally abnormal (Jain, 2005). These vessels are highly permeable, tortuous, dilated, and saccular, and are poorly covered by mural cells (pericytes). These properties, which are mainly attributed to the impaired maturation process of the tumor vessels, cause inadequate blood circulation and poor oxygenation of the tumors. Although this could slow down tumor growth, it also reduces the sensitivity of the tumors to ionizing radiation and impedes the delivery of chemotherapeutic agents, allowing the tumors to become resistant to cytotoxic therapies (Jain, 2005). The plasma leakage from tumor vessels elevates the interstitial fluid pressure within the tumor and significantly reduces the diffusion of therapeutic agents (Jain, 2005). Cerebral edema caused by leaky vessels is a serious complication in brain cancer. The vessel leakiness also allows invasive tumor cells to penetrate into circulation and facilitates distant metastasis (Weis et al., 2004). Therefore, the functionality of tumor blood vessels critically impacts tumor progression and tumors responses to therapeutic regimens (Bergers and Hanahan, 2008; Carmeliet and Jain, 2011b).

Previous studies suggested that vascular endothelial growth factor (VEGF)-targeted cancer therapies lead not only to inhibition of tumor angiogenesis but also to transient maturation and normalization of tumor vasculature, thereby improving the delivery of chemotherapeutic compounds, enhancing the efficacy of chemotherapy (Carmeliet and Jain, 2011b). However, recent reports have demonstrated that VEGF-targeted therapies also result in increased tumor invasiveness and distant metastasis in mice, potentially explaining the lack of lasting clinical responses to the current antiangiogenic treatments (Ebos et al., 2009; Pàez-Ribes et al., 2009). These studies highlight the importance of a better understanding of the biology of tumor angiogenesis and its implications in tumor malignancy and therapies. The molecular and cellular mechanisms that govern vessel maturation, especially in tumor vasculature, remain elusive at present. The currently held view is that the

Significance

Newly formed blood vessels in tumors fail to mature into fully functional vessels due to the chronically angiogenic microenvironment. The functional impairment of these vessels hampers drug delivery, thereby diminishing the efficacy of antitumor therapies. Excessive vessel permeability associated with tumors also causes clinical complications such as cerebral edema in brain cancer patients. Therefore, the ability to control vessel maturity in tumors provides a potential therapeutic opportunity. This study revealed a key role for R-Ras in promoting tumor vessel maturation and normalization. Consistent with this role, R-Ras expressed in endothelial cells and in pericytes both contribute individually to the vessel regulation. This study suggests R-Ras as a potential target for controlling blood circulation and vascular permeability in solid tumors.

processes of vessel formation and maturation are regulated by the balance between pro-angiogenic and antiangiogenic signals (Carmeliet and Jain, 2011a; Darland and D'Amore, 1999).

Previously, we identified an antiangiogenic activity of a small GTPase, R-Ras (Komatsu and Ruoslahti, 2005). R-Ras is strongly expressed in fully differentiated, quiescent vascular smooth muscle cells and endothelial cells of normal adult vasculature. Unlike the prototypic Ras oncoproteins such as K-Ras and H-Ras, R-Ras inhibits vascular cell proliferation and invasion, and promotes vascular quiescence via yet unidentified pathways. Challenging R-Ras knockout mice with arterial injury or tumor implantation induced exaggerated neointimal thickening and increased angiogenesis in the tumors. Thus, R-Ras signaling primarily affects vessel remodeling and regeneration by counterbalancing the vessel activation. However, the effect of R-Ras is distinct from the effect of classic antiangiogenic agents: R-Ras does not induce endothelial cell death. Instead, it induces quiescence of endothelial cells while supporting their survival—activities that promote vessel maturation. R-Ras expression level correlates with the maturation status of the vessels, suggesting a role of R-Ras in the cellular processes essential for the vessel maturation. Little expression of R-Ras was detected in the developmentally growing or pathologically regenerating vessels such as angiogenic vessels in the tumor and hyperplastic neointimal lesion in acute arterial injury in mice. In comparison, abundant expression was found in mature functional vessels of normal adult tissues and in dormant arterial lesions (Komatsu and Ruoslahti, 2005). Based on these observations, we hypothesized that R-Ras promotes maturation of regenerating adult vasculature and that chronically reduced R-Ras expression in tumor vessels causes the immaturity and poor functionality of these vessels. In the present study, we tested this hypothesis by analyzing the effect of R-Ras deficiency or upregulation on the structural and functional integrity of tumor vessels.

RESULTS

R-Ras Deficiency Severely Impairs Maturation Process of Tumor Blood Vessels

Close interaction between nascent endothelium and pericytes is crucial for vessel maturation, and tumor vasculature is characterized by insufficient pericyte association (Jain, 2003). Using a computer-assisted three-dimensional (3D) image reconstruction (Movies S1A and S1B available online), we found a significant reduction of the direct physical contact between pericytes and the endothelium of blood vessels developed in subcutaneous tumor implants in R-Ras knockout mice (Figures 1A and 1B). A similar 3D analysis of these vessels revealed severely impaired coverage by collagen IV, a major constituent of normal endothelial basement membrane (Figures 1C and 1D). Reflecting a weakened pericyte and basement membrane support, these vessels were often found to be more dilated or saccular, and their endothelium exhibited more severe deformations compared with that of the wild-type tumor vessels (Figures 1E–1H). Our analysis suggests that the vessel deformity caused by the R-Ras deficiency is also linked to the abnormality in the VE-cadherin-mediated vessel stabilization. VE-cadherin is essential for the structural integrity of blood vessels, and its genetic disruption leads to leaky vessels, hemorrhaging, and prenatal lethality (Crosby et al., 2005; Gory-Fauré et al., 1999). The intensity of VE-cadherin immunostaining was diminished in the R-Ras-deficient vessels (Figure 1E), suggesting that the endothelial adherens junctions of the tumor vessels are disrupted or unstable in the absence of R-Ras. Taken together, these results indicate an important role of R-Ras in establishing close endothelial cell-pericyte interaction, basement membrane formation, and endothelial integrity, which are essential for the maturation of blood vessels. Consequently, the R-Ras deficiency greatly exacerbates the tumor-associated immature and abnormal characteristics of blood vessels.

R-Ras Dictates Blood Vessel Phenotype in Tumors

To further evaluate the ability of R-Ras to regulate blood vessel maturation in the tumor microenvironment, we determined the expression status of VEGF receptor 2 (VEGFR2), a molecular marker highly expressed by the endothelium of growing, immature vessels (Heidenreich et al., 2000; Kappel et al., 1999). VEGFR2 and R-Ras show opposite temporal expression patterns during mouse development: developing prenatal vessels are VEGFR2^{high}, R-Ras^{undetected}, whereas quiescent adult vessels are VEGFR2^{low}, R-Ras^{high} (Heidenreich et al., 2000; Kappel et al., 1999; Komatsu and Ruoslahti, 2005). In the present study, using B16F10 melanoma implants, tumor vasculature in wild-type control mice contained a mixed population of vessels expressing high to low levels of VEGFR2, with the majority of the vessel population being VEGFR2^{high} (Figures 2A and 2B). This result reflects the fact that tumor vessels are generally immature, while containing a small subpopulation of relatively mature vessels formed by VEGFR2^{low} endothelium (Heidenreich et al., 2000; Mancuso et al., 2006) (Figure 2B). These relatively established vessels are a minority, but functionally important, because they can deliver blood and drugs more efficiently to the tumor than immature vessels and are resistant to antiangiogenic treatment by VEGF blockade (Helfrich et al., 2010; Jain, 2005; Mancuso et al., 2006). In R-Ras knockout mice, this VEGFR2^{low} subpopulation was absent from the tumor vasculature. Instead, the vessel population has largely shifted to VEGFR2^{high}, immature phenotype (Figure 2B) demonstrating that R-Ras is required for maturation of tumor blood vessels. Analysis of the angiogenic EC marker, α_v integrin subunit expression (Stupack and Cheresh, 2002), also demonstrated a major shift of vessel populations to a highly angiogenic α_v integrin^{high} phenotype in the R-Ras-deficient vasculature (Figure 2C), again indicating a state of unattenuated vessel activation, consistent with their failure to mature. Similar results were obtained in subcutaneous implants of Lewis lung carcinoma (LLC) tumors (Figure S1).

Malfunctions of Tumor Vessels Are Augmented by the R-Ras Deficiency

The defects in pericyte support, aberrant basement membrane, and structural deformity of blood vessels are associated with poor functionality of the vasculature (Jain, 2005). Consistent with this notion, tumors in the R-Ras knockout mice showed increased vessel permeability and plasma leakage, as indicated by elevated levels of provisional matrix (fibrinogen/fibrin) deposition around the tumor vessels (Figures 3A and 3B). Further

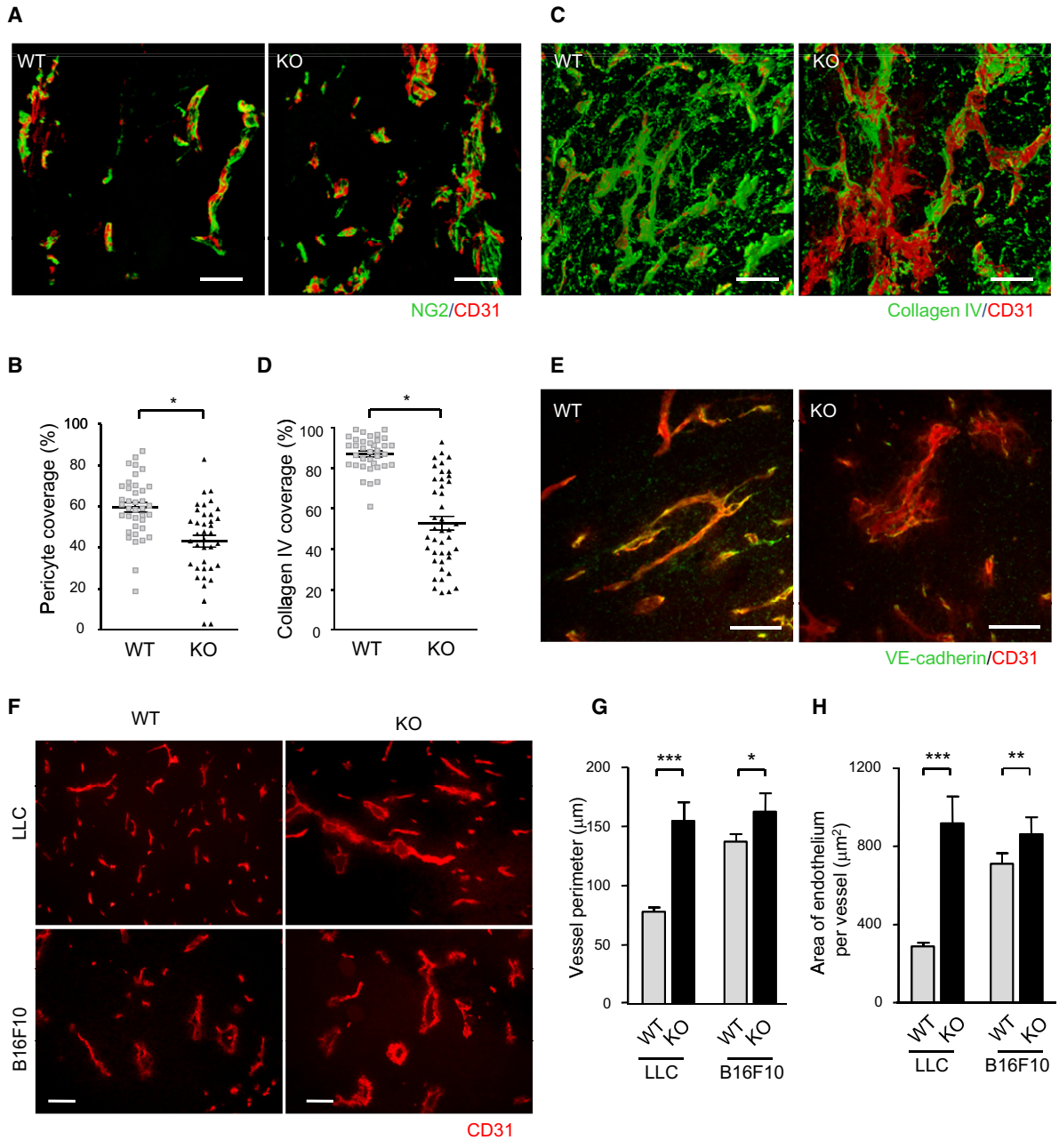

Figure 1. Pronounced Structural Abnormalities of Tumor Vessels Caused by the R-Ras Deficiency

(A) Endothelium and associated pericytes were visualized by CD31 (red) and NG2 (green) immunofluorescence staining of B16F10 tumor implants. Representative images of wild-type (WT) and R-Ras knockout (KO) tumor vessels are shown. See also Movies S1A and S1B.

(B) Pericyte coverage was quantified by calculating the percent fraction of vessel surface (CD31) area that overlapped with NG2 staining in the 3D image of the vessels to determine direct contact between the two cell types. *p = 0.001, ± SEM.

(C and D) A 3D analysis of collagen IV coverage. CD31, red; collagen IV, green. *$p = 4 \times 10^{-13}$.

(E) Double staining of Lewis lung carcinoma cells (LLC) tumors for CD31 (red) and VE-cadherin (green).

(F) CD31-staining of LLC and B16F10 tumor sections.

Scale bars, 100 μm (A, C, F), 50 μm (E).

(G and H) The perimeter and thickness of the endothelium (assessed by average $CD31^+$ area per vessel) of tumor vessels were increased in R-Ras KO mice, reflecting the augmented vessel deformations. *p = 0.01, **p < 0.001, ***$p < 1 \times 10^{-4}$.

indicating abnormal permeability, extensive leakage of intravenously administered fluorescein isothiocyanate (FITC)-dextran was found in these tumors (Figures 3C and 3D). The increased permeability of the R-Ras-deficient tumor vessels is consistent with the reduced immunoreactivity to VE-cadherin of these vessels (Figure 1E), suggesting that the disruption of R-Ras

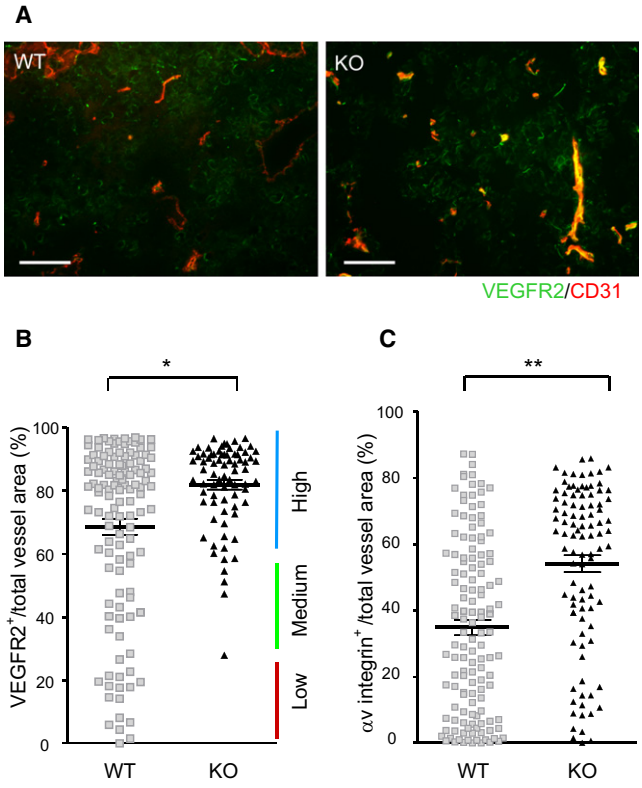

Figure 2. R-Ras Regulates Tumor Vessel Phenotype

(A) Immunostaining of B16F10 tumor implants for CD31 (red) and VEGFR2 (green). Yellow, double-stained area.

(B) The VEGFR2 expression status of the tumor vasculature was assessed by the fraction of VEGFR2-expressing vessel area ($VEGFR2^+CD31^+$ double-positive) as a percentage of the total vessel area (total CD31). Each dot represents the average of several vessels found in a micrograph. Fifteen micrographs were obtained randomly from multiple tumor sections. Eight wild-type and five R-Ras KO mice were examined. *$p = 1 \times 10^{-5}$, ± SEM.

(C) A similar analysis with α_v integrin staining as a marker for angiogenic vessels. Scale bar, 100 μm. **$p = 2 \times 10^{-11}$.

See also Figure S1.

destabilizes endothelial adherent junctions of tumor vessels increasing their permeability. Supporting the role of R-Ras in endothelial integrity, ultrastructural analysis of the tumor vessels revealed significantly increased presence of disrupted endothelial cell-cell junctions in the R-Ras knockout mice, causing spatial gaps between adjacent endothelial cells (Figure 3E).

Disruption of endothelial adherens junctions allows increased penetration of tumor cells into the circulation (Weis et al., 2004). Pericyte coverage of tumor vessels is also critical for limiting blood-borne metastasis (Gerhardt and Semb, 2008). In our study, tumor cells were rarely detected by PCR in the peripheral blood of control mice bearing subcutaneous tumors. In contrast, circulating tumor cells were readily detectable in the R-Ras knockout mice bearing primary tumors of similar sizes, suggesting that significantly increased number of tumor cells escaped into the blood circulation in the knockout mice (Table S1). This finding is consistent with the impaired endothelial barrier function and poor pericyte support of the R-Ras-deficient tumor vasculature. Interestingly, we found a 4-fold increase in metastatic foci counts in the lungs of knockout mice after tail vein injection of tumor cells, suggesting that R-Ras may also regulate the penetration of circulating tumor cells or tumor establishment at secondary target tissues (Figure S2A).

We next determined the efficiency of blood perfusion through the tumor vasculature by intravenously injecting biotin-labeled tomato lectin, which highlights vessel lumens. Vessel perfusion was markedly reduced in tumors growing in R-Ras knockout mice compared to tumors in wild-type mice (Figures 3F, 3G, and S2B). Furthermore, a contrast-enhanced ultrasonography study showed delayed time to peak intensity of the contrast perfusion in tumors in the knockout mice (Figures 3H and 3I), an observation consistent with more irregular and deformed vascular structure (Kersting et al., 2009). The reduced tumor vessel perfusion coincided with elevated levels of tumor hypoxia in R-Ras knockout mice (Figure 3J) despite a significant increase in the vessel density in these tumors (Figure 3K). In addition, the tumor size was not increased in R-Ras knockout mice despite the increased vascularization (Figure 3L). These observations indicate that the new vessels are immature to an extent that renders them functionally defective. Importantly, in wild-type mice, R-Ras was expressed at a 10-fold higher level by the blood-perfused tumor vessel population than the nonperfused, nonfunctional vessels (Figures 3M and 3N). A correlation between increased R-Ras expression and vessel perfusion was also found in human prostate tumor xenografts grown in nude mice (Figure S2C). Thus, R-Ras expression is associated with better blood flow in tumors, further reinforcing the link between R-Ras expression and tumor vessel functions.

Since poor vascular function in tumors could lessen the effectiveness of radiation treatments, we tested how R-Ras deficiency affects the efficacy of local irradiation to the subcutaneous Lewis lung carcinoma tumor implants. In the wild-type control group, a single dose of irradiation (12 Gy) resulted in 59% tumor volume reduction compared with the volume of untreated group at 7 days post irradiation. In comparison, only 41% reduction was observed in the R-Ras knockout mice (Figure 3O). A similar decrease in the treatment effect was demonstrated by in vivo bioluminescence intensity measurement, which quantifies the amount of live tumor cell mass (Figures 3P and 3R). Accordingly, the tumor growth delay by irradiation was reduced in R-Ras knockout mice compared with wild-type mice (Figure 3Q). These results indicate that R-Ras deficiency negatively affects the effectiveness of radiotherapy. This finding was consistent with the poor vessel function and elevated hypoxia level in tumors of the R-Ras knockout mice (Figures 3A–3J).

Next, we examined the effect of VEGF blockade on R-Ras-deficient tumor vessels. A single dose DC101 (anti-VEGFR2) antibody treatment resulted in 50% reduction in the tumor vessel density in the knockout mice while the same treatment had minimal effect in wild-type mice at 3 days post treatment (Figure S2D). Because R-Ras deficiency exacerbates immaturity of tumor vessels (Figures 1, 2, and S1), our result is consistent with the previous findings indicating that immature vessels are vulnerable to VEGF blockade (Benjamin et al., 1999). At the dosage and treatment schedule we used, DC101 had little effect on the growth of Lewis lung carcinoma tumors in wild-type or R-Ras knockout mice (Figure S2E).

R-Ras Is Downregulated in Human Tumor Vasculature

In mice, R-Ras is highly expressed in mature functional vessels of normal tissues while it is downregulated to a level undetectable by immunofluorescence in the majority of tumor vessels (Komatsu and Ruoslahti, 2005), except for the blood-perfused functional vessels (Figures 3M and 3N). Notably, significant downregulation of R-Ras was also observed in tumor vessels in the majority of human breast cancers we examined, compared with blood vessels in normal breast tissue (Figures 4A and 4B; Table S2). This result corroborates the previous finding in gene expression profiling study, which revealed significantly reduced R-Ras mRNA level in the endothelium of human breast carcinoma compared with the normal counterpart (Allinen et al., 2004). Thus, R-Ras downregulation in tumor vasculature is found in both mice and humans supporting the hypothesis that R-Ras expression is chronically reduced in tumor vasculature contributing to immaturity and poor functionality of these vessels.

Upregulation of R-Ras Signaling Leads to Normalization of Pathologically Regenerating Blood Vessels

The above observations prompted us to examine whether restoring R-Ras signaling to pathologically regenerating blood vessels will promote vessel maturation and improve structure and functions of the defective vessels. For this purpose, lentivirus carrying activated R-Ras (R-Ras38V) or mock control virus was injected into pre-implanted, VEGF-containing Matrigel plugs that have developed angiogenic vessels in this tumor-like environment in R-Ras knockout mice (Figure S3A). Following forced expression of R-Ras38V (Figure S3B), the pericyte-endothelial cell association of the newly formed microvessels in the R-Ras knockout mice increased to a level comparable to that in wild-type animals (Figures 4C and 4D). This effect was accompanied by reduced vessel dilation and thickness of the endothelium, minimizing the deformation of the VEGF-induced vessels in Matrigel (Figures 4E and 4F). Concomitantly, the efficiency of blood perfusion improved by 74% in the R-Ras knockout vessels that were successfully transduced with R-Ras38V compared with non-transduced vessels within the same Matrigel plugs (Figures 4G and 4H). Thus, the in vivo upregulation of R-Ras signaling reverses the vessel phenotype and restores vessel function in the pathologically developing vasculature.

Role of Endothelial R-Ras in Controlling Vessel Sprouting and Maturation

R-Ras is expressed in both the endothelium and mural cells (smooth muscle cells and pericytes). To determine the endothelial cell-specific contribution of R-Ras, we used a technique that combines lentivirus-mediated in vivo gene transduction and Tie-2 promoter-driven gene expression. In this model, VEGF-containing Matrigel was implanted into Tie2-rtTA mice, which express reverse transactivator in an endothelial cell-specific manner (Bao et al., 2010). Lentivirus carrying a vector for reverse transactivator-dependent expression of activated R-Ras (pLVX-Tight-Puro/R-Ras38V) was then injected into the pre-implanted Matrigel plugs that were developing new vessels in response to VEGF (Figure 5A). The mice received doxycycline daily to induce the expression of R-Ras38V in a Tie2-rtTA-dependent manner (Figures S4A and S4B). In this study, Dox-treated (Dox^+) mice showed significantly reduced vessel density in the Matrigel plugs compared with the plugs of Dox^- animals demonstrating a strong inhibitory activity of endothelial R-Ras against vessel sprouting induced by VEGF (Figure 5B). Doxycycline itself did not have any noticeable effect on the neovascularization in the control mice without R-Ras38V virus infection (data not shown). Importantly, the vessels developed in Matrigel were significantly better perfused in Dox^+ mice than in Dox^- mice, indicating improved circulation in these vessels following R-Ras38V induction (Figure 5C). Furthermore, pericyte coverage of these vessels was also improved upon R-Ras38V induction in the endothelium (Figures 5D and 5E). Because Matrigel itself contains large amount of matrix components, it was not possible to do specific immunostaining to assess basement membrane coverage of these vessels; however, we observed enhanced extracellular matrix depositions by cultured endothelial cells upon R-Ras38V expression supporting a role of R-Ras in basement membrane formation (Figure S4C). These observations demonstrate an important activity of endothelial R-Ras, promoting the formation of functional vessels after VEGF induction while inhibiting further vessel sprouting.

Role of R-Ras in Pericytes for Enhancing Vessel Integrity

We next used an ex vivo gene manipulation/cell transplantation approach to determine the role of R-Ras signaling in pericytes in vivo. Microvascular pericytes were isolated from wild-type neonatal mouse brain (Wu et al., 2003) (Figures S4D–S4F) and transduced ex vivo with cDNA for activated R-Ras (R-Ras38V) or dominant negative R-Ras (R-Ras43N). R-Ras knockout mice typically exhibit extensive hemorrhage in Matrigel plugs during VEGF-induced angiogenesis (Figure 5F). However, implantation of pericytes, which were ex vivo-transduced with activated R-Ras, significantly prevented blood leakage in the plugs implanted into R-Ras knockout mice (Figure 5G). Histological analysis of the plugs revealed association of the implanted pericytes (green) with the tips of newly formed R-Ras-deficient vessels (red) (Figure 5H). Pericytes transduced with the dominant negative R-Ras43N failed to show this effect, and the implanted pericytes were mostly unassociated with the vessels (Figure 5H). These findings are consistent with the fact that pericyte association with endothelium is crucial for vessel integrity (Lindahl et al., 1997; McDonald and Choyke, 2003). Thus, R-Ras activity in pericytes alone can significantly contribute to the vessel maturation process independently from endothelial R-Ras signaling. However, R-Ras38V expression in the transplanted pericytes was not very effective at improving blood circulation in the plugs as measured by lectin perfusion (Figure S4G). This result suggests that R-Ras signaling in pericytes contributes to vessel maturation by promoting pericyte-endothelial cell interaction thereby improving vessel integrity (reducing permeability), whereas endothelial R-Ras is necessary to significantly improve blood perfusion in VEGF-induced vessels (Figure 5C). Collectively, our results demonstrate that R-Ras activity in endothelial cells and in pericytes individually contribute to maturation and normalization of pathologically regenerating blood vessels.

R-Ras Does Not Affect PHD2 or HIF-2 Levels during Hypoxia

A recent study by Mazzone et al. showed that haplodeficiency of the oxygen-sensing prolyl hydroxylase domain protein 2 (PHD2)

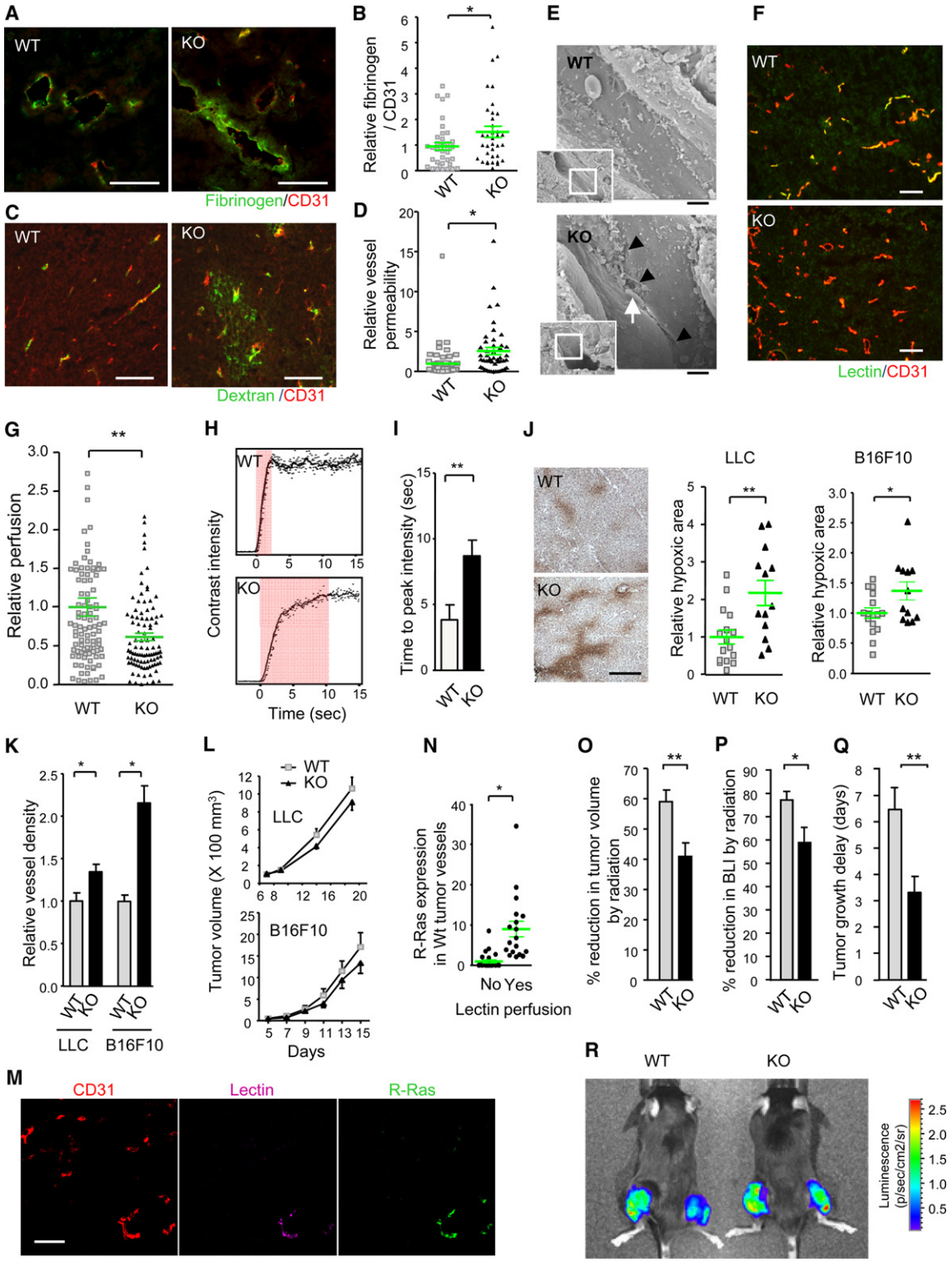

Figure 3. R-Ras Deficiency Diminishes Tumor Vessel Function

(A–D) Analyses of vessel leakiness. Fibrinogen and CD31 staining for plasma leakage in B16F10 tumors (A). To quantify the level of plasma leakage and standardize it for tumor vessel area, the ratio of fibrinogen (fibrin)-stained area to CD31 area was determined and is presented as relative values (B). *p = 0.035, ± SEM. Dextran-FITC was injected i.v. into mice bearing Lewis lung carcinoma (LLC) tumors (C). The fluorescence intensity of extravasated FITC in the tumors was standardized for the perfused vessel counts to assess vessel permeability (D). *p = 0.002.

(E) Ultrastructure of tumor vessels by scanning electron microscopy. The R-Ras knockout (KO) tumor endothelium shows significant special gaps at the cell-cell junctions (arrowheads). Arrow, a red blood cell extravasating between the cellular gap. Scale bar, 2 μm.

leads to normalization of tumor vasculature through stabilization of endothelial HIF-2α and a consequent upregulation of soluble VEGFR1 and VE-cadherin expression in endothelial cells (Mazzone et al., 2009). The effect of PHD2 haplodeficiency and HIF-2α stabilization exemplifies the significance of oxygen sensing by endothelial cells for vessel integrity (Coulon et al., 2010). We examined a potential role of R-Ras in regulating the levels of these oxygen sensors. The expression of R-Ras38V did not affect the levels of PHD2 or HIF-2α in cultured endothelial cells in hypoxia or normoxia (Figure S5A). Likewise, downregulation of endogenous R-Ras by shRNA knockdown had no effect on the levels of these proteins (Figure S5B). These data do not support the idea that R-Ras modulates PHD2/HIF-2 pathway or that the vessel normalization effect of R-Ras is mediated via HIF-2α stabilization. In addition, the expression of endogenous R-Ras was not affected by hypoxia either in endothelial cells or in pericytes (Figure S5C).

In vivo, we did not find any evidence to suggest that HIF-2α level is decreased in the tumor vessels in R-Ras knockout mice compared with wild-type control (Figure S5D). Furthermore, unlike the PHD2/HIF-2 model (Mazzone et al., 2009), the expression levels of HIF-2 target genes, *Cdh5* (VE-cadherin) and *Flt1* (VEGFR1), were not increased (Figure S5E) concurrently with the vascular normalization promoted by endothelial R-Ras in the doxycycline-inducible model (Figures 5A–5E). These observations strongly suggest that R-Ras is not involved in oxygen-sensing mechanisms of vessel regulations mediated by the PHD2/HIF-2 pathway.

R-Ras Enhances Endothelial Barrier Function via Suppression of VE-Cadherin Internalization

One possible mechanism of R-Ras-induced vessel normalization is stabilization of endothelial adherens junctions via stabilization of VE-cadherin. VE-cadherin is essential for the integrity of blood vessel wall and for the regulation of vessel permeability (Fukuhara et al., 2005). We observed disruption of endothelial cell-cell junction (Figure 3E), elevated plasma leakage (Figures 3A–3D), and reduced VE-cadherin immunostaining of the tumor vessels in R-Ras knockout mice (Figure 1E). Therefore, we next examined the effect of R-Ras signaling on VE-cadherin.

In confluent endothelial cell cultures, R-Ras38V expression induced marked accumulation of VE-cadherin and β-catenin at the cell-to-cell interface producing prominent and continuous barrier walls of the adherens junctions (Figures 6A and 6B). Despite this effect, the total expression level of neither VE-cadherin nor β-catenin protein in the cell was altered by activated or dominant negative R-Ras (Figure 6C). In vivo, the VE-cadherin immunofluorescence intensity was diminished in R-Ras-deficient tumor vasculature (Figure 1E) although the VE-cadherin protein level was unaltered (Figure S5F). This may be because the detectable fluorescence signal declines with the loss of VE-cadherin clustering at the cell-cell junctions. Therefore, we hypothesized that R-Ras signaling may affect the localization of VE-cadherin rather than regulating its gene expression. VEGF stimulation of endothelial cells induces internalization of VE-cadherin (Gavard and Gutkind, 2006). VE-cadherin localization upon VEGF stimulation was analyzed using a monoclonal antibody that recognizes the extracellular domain of VE-cadherin (Figure 6D). The antibody displayed cell surface staining of VE-cadherin that is sensitive to a mild acid wash. The acid-resistant vesicular staining pattern represented the intracellular vesicles containing VE-cadherin molecules that are internalized (endocytosed) upon VEGF stimulation (Gavard and Gutkind, 2006). This analysis showed that R-Ras38V expression significantly reduces the internalization of VE-cadherin (Figures 6D–6F and S5G), causing an accumulation of VE-cadherin at the cell-cell junctions despite the VEGF stimulation. The R-Ras43N expression (Figures 6E and 6F) or knockdown of endogenous R-Ras (Figure S5H) showed an opposite effect, increasing VE-cadherin internalization during VEGF stimulation.

It has been shown that the phosphorylation of VE-cadherin at Ser 665 in the cytoplasmic domain promotes VE-cadherin internalization upon VEGF stimulation (Gavard and Gutkind, 2006). Interestingly, we found that this serine phosphorylation was reduced by R-Ras38V expression almost to the level of the non-stimulated control during VEGF stimulation (Figure 6G). Thus, the reduction of Ser 665 phosphorylation observed here was consistent with the reduction of VE-cadherin internalization by R-Ras (Figures 6D–6F). The other VE-cadherin phosphorylation sites important for adherens junction disruption and endothelial permeability, Tyr 658 (Dejana et al., 2008) and Tyr 731 (Allingham et al., 2007) were unaffected by R-Ras (Figure 6H) or R-Ras knockdown (data not shown) during VEGF-stimulation. Consistent with the role of R-Ras in VE-cadherin regulation and

(F and G) Blood perfusion efficiency. Lectin perfusion and CD31 staining of B16F10 tumor sections (F). Yellow color indicates double-stained vessel area. Percent lectin$^+$CD31$^+$ double-positive area/total CD31$^+$ area was determined to assess perfusion efficiency of tumor vasculature (G). $^{**}p = 2 \times 10^{-4}$.
(H and I) Study of tumor vessel perfusion by contrast-enhanced ultrasound imaging. Examples of raw contrast kinetics acquired after bolus i.v. injection of microbubble contrast agent (H). Delayed time-to-peak-intensity in KO mice indicating poor perfusion efficiency (I). $^{**}p = 0.02$.
(J) Analysis of tumor hypoxia. The ratio of the hypoxic area/total area of the tumor section was determined and presented as relative values. Representative anti-Hypoxyprobe staining of LLC tumors is shown. $^{*}p = 0.03$, $^{**}p = 0.003$.
(K) Number of tumor vessels per unit area (vessel density) is presented relative to the control group. $^{*}p < 0.05$.
(L) Growth of LLC and B16F10 tumors.
(M and N) Analysis of R-Ras expression in wild-type vessels. Sections of lectin-perfused tumors were stained for CD31, lectin, and R-Ras (M). The tumor vessels were classified as lectin-perfused and non-perfused vessels, and the level of R-Ras expression was determined for individual vessels in each group (N). $^{*}p = 7 \times 10^{-4}$.
(O–R) Effect of radiotherapy. (O) The percent reduction in the tumor volume (as compared with untreated tumors) was determined at 7 days after a local 12 Gy irradiation of LLC tumors (O). $^{**}p < 0.01$ (P) Percent inhibition of tumor growth was also assessed by bioluminescence tumor imaging at day 7. BLI, bioluminescence intensity. $^{*}p = 0.02$. (Q) Tumor growth delay as defined by delay in tumor volume quadrupling time as a result of irradiation treatment. The average delay time (in days) is presented. $^{**}p < 0.01$. (R) Bioluminescence imaging of Luc2-transfected LLC tumors. Tumors on the right thigh received 12Gy irradiation, whereas tumors on the left thigh did not. WT, wild-type; KO, R-Ras KO mice.
Scale bars, 100 μm (A, C, F, and M), 200 μm (J). See also Figure S2 and Table S1.

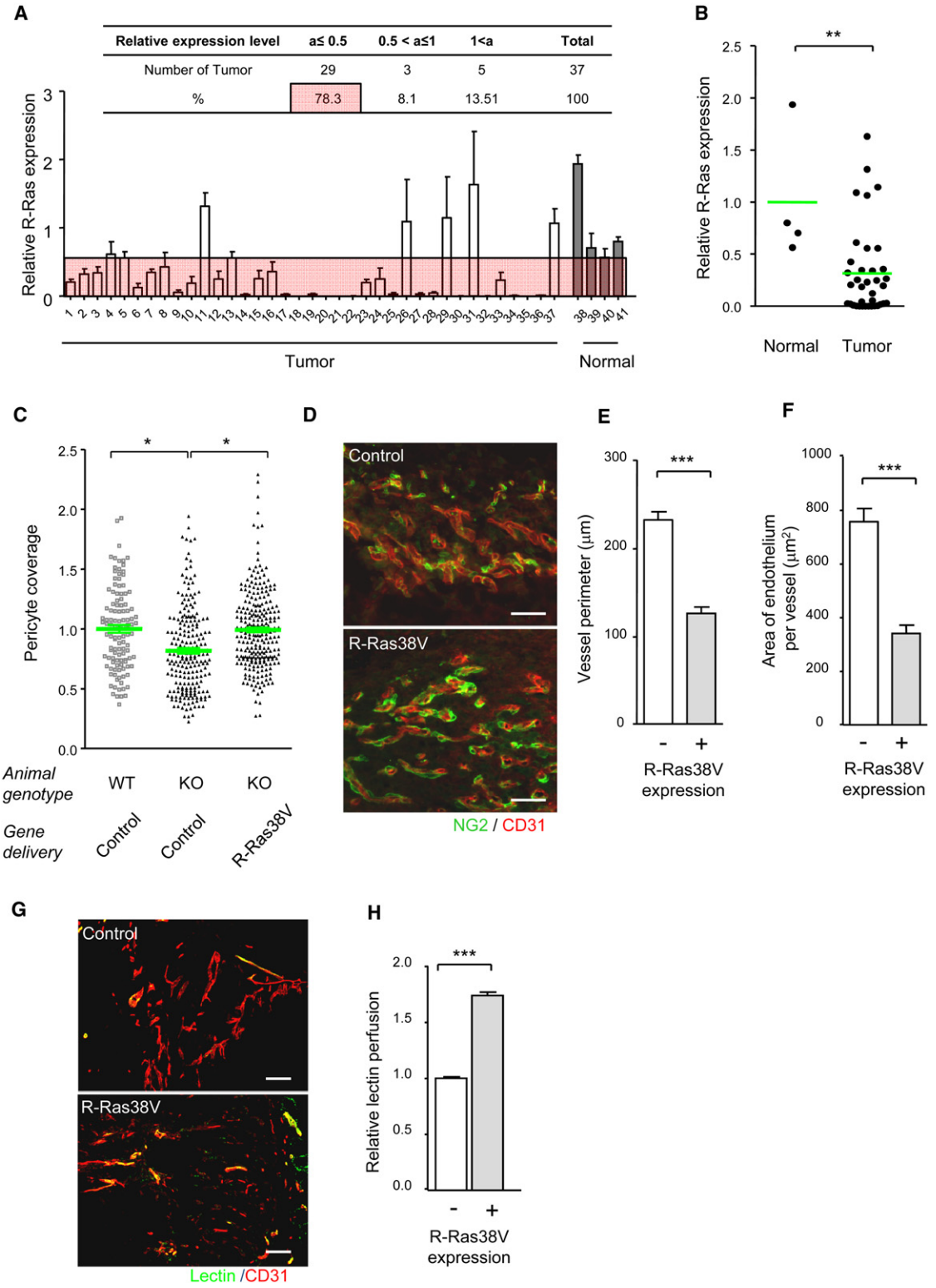

Figure 4. R-Ras Promotes Normalization of VEGF-Induced Pathologically Regenerating Vasculature

(A and B) R-Ras is downregulated in human tumor vasculature. The level of R-Ras expression in tumor vessels was analyzed in a human breast cancer tissue array by immunostaining for R-Ras and CD31 (A). Dot plot representation of A (B). **p = 0.004. See also Table S2.

(C–H) R-Ras signaling improves structure and function of VEGF-induced vessels. VEGF-induced angiogenic vessels developed in Matrigel plugs were transduced in vivo with R-Ras38V or control lentivirus. Six days later, pericyte association with the endothelium was determined (C) by NG2 and CD31 immunofluorescence (D). The data are presented as relative values. (E–H) The vessels in the R-Ras38V virus-infected plugs were classified as R-Ras-positive (successfully

adherens junction stabilization, the expression of R-Ras38V strongly suppressed the permeability of endothelial monolayer (Figure 6I). R-Ras knockdown had an opposite effect (Figure S5I). These results substantiated the in vivo observations of increased tumor vessel permeability in R-Ras knockout mice (Figures 3A–3D). Furthermore, the in vivo transduction of R-Ras38V enhanced VE-cadherin immunostaining at the endothelial cell-cell junctions of angiogenic sprouts induced by VEGF in R-Ras knockout mice (Figures 6J and 6K), supporting the importance of R-Ras in the integrity of tumor vessels. Taken together, R-Ras plays a crucial role in reinforcing the VE-cadherin-dependent endothelial adherens junctions while counterbalancing the effect of VEGF stimulation in the tumor microenvironment.

R-Ras Activation in Pericytes Induces Normal Capillary-like Vessel Morphogenesis

The physical interaction of pericytes with endothelial cells is essential to vessel maturation and functions. Our in vivo studies showed that R-Ras activity in pericytes promotes the pericyte-endothelial cell interaction in regenerating vessels (Figure 5H). To recapitulate this phenomenon in vitro and to further analyze the relative contribution of the pericyte-expressed R-Ras to vessel formation, we used an endothelial cell/pericyte 3D coculture that reconstitutes microvessels in Matrigel (Figures 7A–7E).

In this model, the coculture produced networks of vessel-like, elongated endothelial structures with associated pericytes (Figures 7A–7C). In the control coculture with mock-transduced pericytes, the pericytes were found loosely or incompletely associated with endothelial cells and appeared to be activated, invasive, and irregularly extended out from the main stalk of the vessels with long cytoplasmic processes (Figure 7A). These features are strikingly similar to the abnormalities in pericytes associated with tumor blood vessels (McDonald and Choyke, 2003). In contrast, such tumor-associated characteristics of pericytes were significantly diminished by the expression of activated R-Ras in pericytes (Figure 7B). Instead, most pericytes were flattened, widely spread, or extended with long thin processes over the surface of the vessel-like structures, and were intimately associated with endothelial cells, as seen for the pericytes of normal capillary or microvessels. The dominant negative R-Ras did not show this effect (Figure 7C). The number of pericyte projections was also decreased by the activated R-Ras but increased by the dominant negative R-Ras signifying pericyte stabilization by R-Ras activity (Figures 7D and 7E). The ability of R-Ras to suppress invasive nature of pericytes was substantiated by the observation that R-Ras38V expression but not R-Ras43N or R-Ras knockdown strongly suppressed dynamic membrane projection/retraction activities (Figures 7F–7H and Figure S6A), motility on the Matrigel-coated surface (Figure 7I and Figure S6B), and invasion through Matrigel (Figure 7J) of the pericytes. These effects were also observed in cultured endothelial cells (Figures S6C–S6E) but not in C2C12 myoblasts or NIH 3T3 fibroblasts demonstrating cell type-dependent effect of R-Ras (Figures S6F and S6G).

Pericytes interact closely with endothelial cells by adhering to the endothelial basement membrane that is shared by both cell types (Armulik et al., 2005). The ability of R-Ras to promote intimate association of pericytes with endothelial cells observed in vivo (Figure 5H) and in vitro (Figure 7B) may be attributable to enhancement of integrin-mediated cell adhesion to the extracellular matrix (ECM) (Kinbara et al., 2003; Zhang et al., 1996). R-Ras38V expression in pericytes resulted in enhanced pericyte adhesion to endothelial basement membrane components, collagen IV and laminin (Figure S6H). In the control pericytes with mock-transduction or shRNA knockdown of endogenous R-Ras, the presence of focal adhesion complexes was limited to the leading edge of migrating cells or protruding membranes (Figure 7K). In contrast, R-Ras38V expression resulted in assembly of numerous focal adhesion complexes throughout the cell perimeter, facilitating the flattening and wide spreading of cell membrane over the ECM-coated surface (Figure 7K). These results demonstrated the profound effect of R-Ras on pericyte-ECM interaction and support the importance of pericyte-expressed R-Ras for pericyte association with nascent microvessels and the stabilization of these vessels as observed in vivo (Figure 5H).

DISCUSSION

Studies by others have elucidated the importance of early-acting signaling pathways for vessel maturation, such as angiopoietin-1/Tie-2 and platelet-derived growth factor (Andrae et al., 2008; Thomas and Augustin, 2009). However, it has been unclear what directs the maturation process further to establish functional vessels during tumor angiogenesis. This is an important question because tumor progression and the efficacy of therapeutic regimens both depend on blood circulation in the tumors. In this study, we showed that R-Ras promotes the maturation of blood vessels in the tumor microenvironment and that, through this activity, R-Ras governs integrity and functionality of tumor vasculature (Figure 8).

Malformation and malfunction of tumor vessels are exacerbated by genetic disruption of R-Ras. Increased tumor cell penetration into the circulation in R-Ras knockout mice also supports the role of R-Ras in controlling the permeability of tumor vessels. The reduced perfusion of tumor vessels was consistent with elevated tumor hypoxia, which, in turn, led to reduced efficacy of radiotherapy in R-Ras knockout mice. In addition, R-Ras knockout tumor vessels were sensitized to VEGF blockade, as expected from exacerbated immaturity of these vessels (Benjamin et al., 1999). However, the antitumor effect of DC101 was not enhanced in the knockout mice. A possible

transduced) or negative (non-transduced) vessels. The in vivo R-Ras transduction reduced the vessel perimeter (reduced vessel dilation) in R-Ras knockout (KO) mice (E). The thickness of the endothelium (assessed by average $CD31^+$ area per vessel) was also reduced in the KO mice by R-Ras transduction (F). The histological sections of Matrigel implants in R-Ras KO mice, which received control or R-Ras38V virus, were stained for perfused lectin, and CD31 to determine the blood perfusion of the vessels (G). Blood perfusion efficiency was compared between the R-Ras-transduced and non-transduced vessels (H). $^*p < 0.05$, $^{***}p < 1 \times 10^{-3}$, ± SEM. Scale bars, 100 μm.
See also Figure S3.

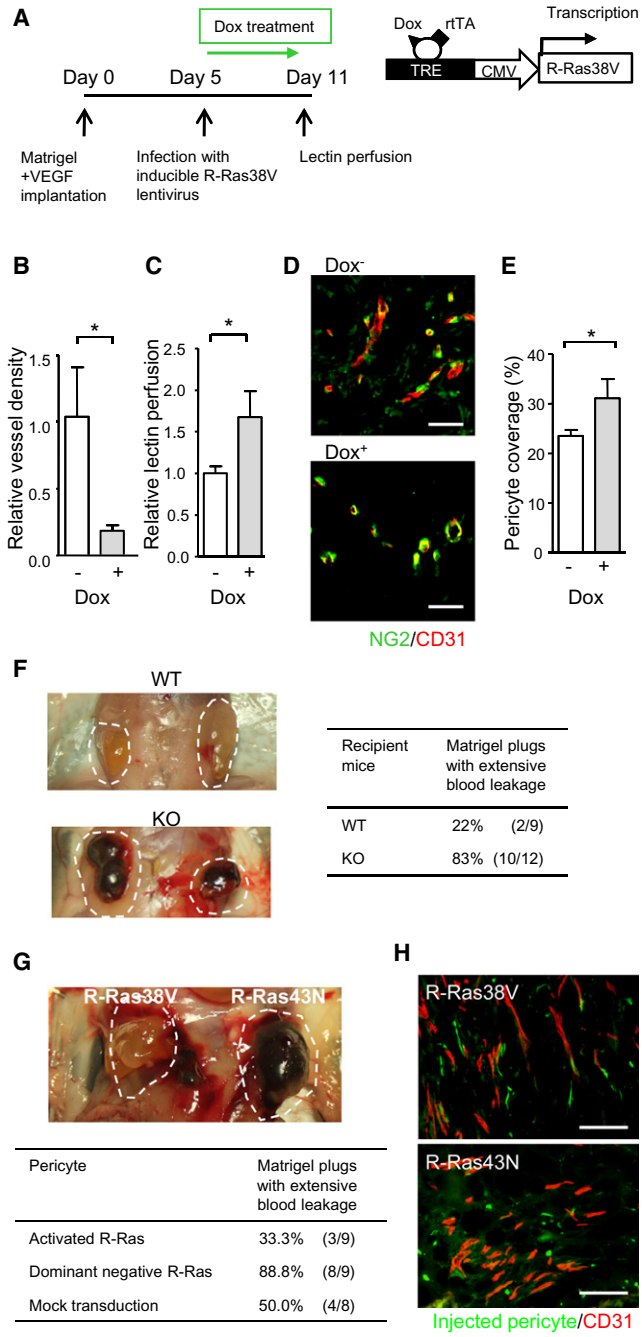

Recipient mice	Matrigel plugs with extensive blood leakage	
WT	22%	(2/9)
KO	83%	(10/12)

Pericyte	Matrigel plugs with extensive blood leakage	
Activated R-Ras	33.3%	(3/9)
Dominant negative R-Ras	88.8%	(8/9)
Mock transduction	50.0%	(4/8)

Figure 5. The Effect of Cell-Type Specific Upregulation of R-Ras on Vessel Maturation and Functions

(A–E) The effect of endothelial specific R-Ras. A timetable of Matrigel implantation in Tie2-rtTA transgenic mice, lentivirus infection, R-Ras38V induction by doxycycline (Dox), and lectin i.v. perfusion is shown (A). Vessel density in the Matrigel plugs at Day 11 (B). Relative perfusion efficiency of i.v. injected lectin at Day 11 (C). (D and E) Matrigel sections were stained for NG2 and CD31 (D), and pericyte coverage of the vessels was determined by image analysis (E).

(F) VEGF-induced Matrigel angiogenesis produces extensively "bloody" plugs in R-Ras knockout (KO) mice demonstrating enhanced leakiness of pathologically regenerating vessels in the absence of R-Ras.

(G and H) The effect of pericyte specific R-Ras. Fluorescently labeled, ex vivo-transduced pericytes were implanted with VEGF-containing Matrigel into the flank of R-Ras KO mice. Matrigel plugs were examined 7 days later (indicated by dashed lines) (G). Histological analysis of the plugs (H). The ex vivo-transduced, implanted pericytes were visualized by green fluorescence. Microvessels were stained with CD31 (red). Scale bars, 100 μm (H), 50 μm (D).

*$p < 0.05$, ± SEM.

See also Figure S4.

explanation for this may be that DC101 at the dosage we used mainly destroyed highly immature nonfunctional vessels, which did not significantly contribute to tumor growth.

In contrast to the R-Ras gene disruption, the gain of function of R-Ras improved the structure and perfusion of blood vessels induced by VEGF in tumor ECM extract (Matrigel) implants. Other cell types such as infiltrating macrophages and fibroblasts may have also contributed to the observed effects. However, the studies using endothelial cell-specific or pericyte-specific expression of R-Ras gave insights into how R-Ras in each vascular cell type contributes to the overall vessel formation process. For instance, R-Ras activity in endothelial cells was sufficient to inhibit VEGF-induced vessel outgrowth. This effect coincided with improved pericyte coverage and enhanced blood perfusion of newly formed vessels. These observations suggest that endothelial R-Ras activity redirects nascent vessel formation from angiogenic process to maturation process. In contrast, R-Ras activity in pericytes prevented severe leakiness of the R-Ras knockout endothelium through facilitating pericyte association with the sprouting vessels. This result indicates that R-Ras activity in pericytes alone can significantly contribute to the vessel maturation process independently from endothelial R-Ras. However, enhanced R-Ras signaling in pericytes was not very effective at improving perfusion of the vessels to which the pericytes are attached. Therefore, the role of pericyte R-Ras in vessel maturation may be primarily to promote pericyte association with endothelial cells, thereby providing integrity to the vessel structure and reducing permeability. The endothelial R-Ras activity appears to be more effective in improving blood perfusion of newly formed vessels. However, we cannot rule out the possibility that the ex vivo R-Ras transduction and pericyte transplantation model we used in this study may have not been fully recapitulating the in vivo functions of R-Ras in pericytes. A transgenic mouse model for pericyte-specific R-Ras expression will be needed to clarify this point in future studies.

A recent study by Mazzone et al. demonstrated vascular normalization phenomenon caused by PHD2 haplodeficiency and consequential HIF-2 upregulation (Mazzone et al., 2009). Our data did not support the PHD2/HIF-2-dependent endothelial cell regulation as a mechanism by which R-Ras promotes vascular normalization. In the study by Mazzone et al., haplodeficiency of PHD2 resulted in an elevated HIF-2α level in endothelial cells during hypoxia, which led to HIF-2-driven upregulation of VE-cadherin and soluble-VEGFR1 expressions in endothelial cells. This cascade, in turn, led to vascular normalization (Mazzone et al., 2009). In our study, constitutively activated R-Ras did not affect VE-cadherin expression in endothelial cells. Instead, it inhibited VE-cadherin internalization induced by VEGF stimulation of endothelial cells. This resulted in VE-cadherin accumulation at adherens junctions and stabilization of the endothelial barrier. In our previous study of transcriptional regulation of human *RRAS* gene, we did not find

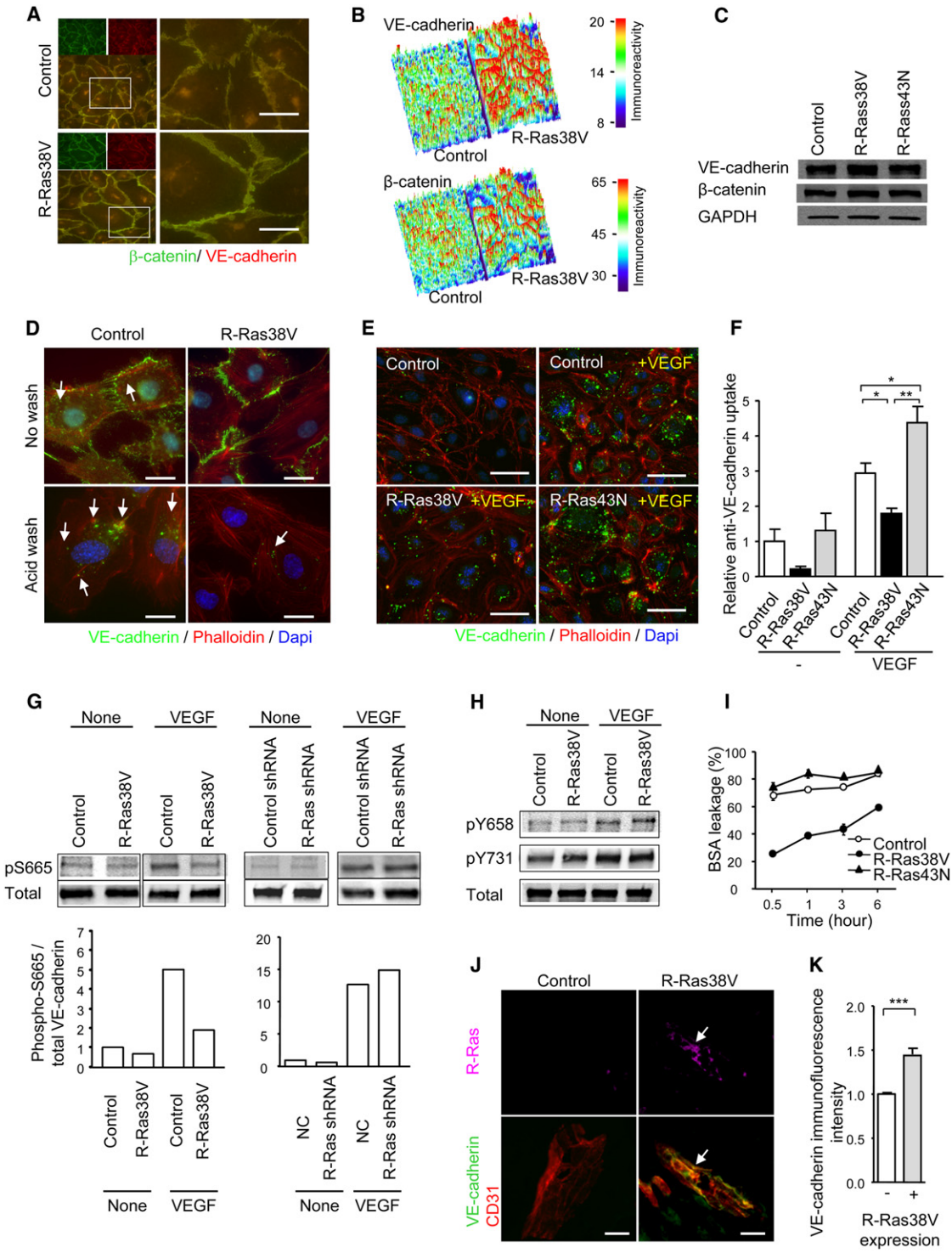

Figure 6. R-Ras Stabilizes Endothelial Adherens Junctions and Improves Endothelial Barrier Function via Suppression of VE-Cadherin Internalization

(A) R-Ras enhances adherens junction formation in EC monolayer. VE-cadherin (green) and β-catenin (red) staining of human umbilical vein endothelial cell (HUVEC) monolayers transduced with R-Ras38V or control vector. Lower left panels and right panels are merged images of the double staining. Right panels show higher magnification at cell-cell junctions.

(B) Surface plot of VE-cadherin and β-catenin immunofluorescence intensity shows marked accumulation of both proteins at the cell-cell interface upon R-Ras38V expression. The immunoreactivity is shown with arbitrary unit.

(C) VE-cadherin and β-catenin immunoblotting of whole cell lysate. Glyceraldehyde 3-phosphate dehydrogenase (GAPDH) is shown as a loading control.

hypoxia-inducible factor (HIF) response elements in the promoter region or the 5′ upstream *cis*-regulatory sequences (Xu and Komatsu, 2009). This suggests that, unlike many hypoxia induced angiogenesis regulators, R-Ras expression is not controlled by oxygen sensing mechanism involving HIFs. Indeed, R-Ras expression level did not increase in endothelial cells or pericytes under hypoxia. There is an additional important difference between the vessel regulations by PHD2/HIF-2 and by R-Ras. PHD2 haplodeficiency does not affect vessel density, area, or vessel dilation while it normalizes the endothelial barrier and stability (Mazzone et al., 2009). In comparison, R-Ras does normalize all of these vessel parameters while halting angiogenic sprouting. Based on these observations, we propose that the R-Ras-dependent mechanism is distinct from the oxygen sensing mechanism of vascular normalization. The chronic low-oxygen environment is a hallmark of solid tumors, and the levels of HIF proteins are elevated in the cells in the tumor microenvironment. Yet tumor vessels are chronically abnormal instead of being normalized. The observations reported in this study suggest an alternative, oxygen sensing-independent vascular normalization phenomenon.

This study also identified a cellular function of R-Ras: enhancement of endothelial cell-cell adhesion via regulation of VE-cadherin internalization induced by VEGF. R-Ras inhibits VE-cadherin phosphorylation at Ser 665 residue that is critical for the VE-cadherin internalization process upon VEGF stimulation, suggesting the modulation of this site by R-Ras. Additional mechanism(s) independent of Ser 665 may also be involved in the R-Ras-mediated VE-cadherin regulation. Identification of the signaling pathways for these regulations is an important goal of future work that could further advance our understanding in the vascular normalization process.

The upregulation of R-Ras activity in pericytes resulted in enhanced pericyte adhesion to ECM and formation of focal adhesion complexes around cell perimeter facilitating the flattening and wide spreading of pericyte cell membrane over the adhering surface. Consistent with this effect, the activated R-Ras facilitated close association of pericytes with nascent microvessel sprouts in vivo, and this phenomenon was recapitulated in a 3D coculture system. These studies show that R-Ras plays important roles in both pericytes and endothelial cells. Thus, R-Ras in each cell type is vital to tumor vessel maturation process.

Our results suggest that means to upregulate R-Ras would be useful for normalizing tumor vasculature. In contrast to the VEGF blockade, which only induces transient vascular normalization with the narrow window of therapeutic opportunity (Carmeliet and Jain, 2011b), the R-Ras effect is sustained. Also, unlike the VEGF blockade, R-Ras does not cause subsequent destruction of the newly formed vessels. Instead, R-Ras stabilizes these vessels. This may be a significant advantage in improving drug delivery to the tumors and in other situations in which stable, functional vascularization is beneficial, for example, angiogenesis in ischemic heart. R-Ras may also be useful as a biomarker for the vessel maturity and functionality, for instance, to assess vessel normalization, and for drug screens/validation. As maturation of blood vessels is essential for the establishment of functional vasculature in regenerating adult tissues, our findings suggest the significance of R-Ras to a broad range of clinical challenges, from cancer to therapeutic angiogenesis and tissue engineering.

EXPERIMENTAL PROCEDURES

Analyses of Tumor Blood Vessels

All animal experiments were performed in accordance with protocols approved by the institutional animal care and use committees of the Sanford-Burnham Medical Research Institute (SBMRI) and the University of Alabama at Birmingham. The R-Ras knockout mouse line has been described previously (Komatsu and Ruoslahti, 2005). The mice received subcutaneous implantations of 1×10^6 B16F10 mouse melanoma cells or Lewis lung carcinoma cells at the flank, and the tumors were excised at days 10 and 14, respectively. The 3×10^6 PPC-1 human prostate tumor cells in 50%-diluted Matrigel were inoculated subcutaneously at the flank of athymic nude mice. The tumors were excised 2 weeks later. Tumors were cryosectioned and tumor vessels were analyzed by immunofluorescence (see Supplemental Information). Six to seven mice per group were used, and vessels in several micrographs from each tumor section were analyzed unless indicated otherwise.

In Vivo Gene Transfer

Matrigel (BD Bioscience; 0.5 ml) containing 60 ng/ml VEGF (R&D systems) and 60 U/ml heparin (Sigma) was injected into the flanks of wild-type or R-Ras knockout mice. Five days later, lentivirus carrying activated R-Ras (R-Ras38V) or control vector was injected into the Matrigel plugs at 1×10^6 transduction unit. At 6 days post lentivirus inoculation, mice received intravenous injection of biotinylated lycopersicon esculentum (tomato) lectin to analyze vessel perfusion. Five to six mice per group were used. Matrigel plugs were collected and the sections stained for CD31, NG2, R-Ras, and streptavidin to analyze the vessel structure, pericyte association, and perfusion efficiency.

(D) Analysis of VEGF-induced VE-cadherin internalization. The monoclonal antibody (BV6) recognizes the extracellular domain of VE-cadherin (green). Following antibody incubation of the EC culture and stimulation with VEGF, the cell surface membrane-bound BV6 antibodies (upper panels) were removed by a mild acid wash (lower panels). The presence of internal acid-resistant vesicles stained with the BV6 antibody indicates the internalization of VE-cadherin. Phalloidin (actin), red; nucleus, blue; arrows, BV6-stained vesicles containing internalized VE-cadherin.

(E) Dominant negative R-Ras43N enhances VE-cadherin internalization.

(F) VE-cadherin internalization was quantified by the percentage of the cells showing internal acid-resistant vesicles. $^*p < 0.05$, $^{**}p < 0.001$, ± SEM. In the no-VEGF stimulation condition (−), statistical significance was not found between the control, R-Ras38V, and R-Ras43N.

(G) Phosphorylation of VE-cadherin S665 was analyzed in the lysate of VEGF-stimulated endothelial cells (ECs) (100 ng/ml) using phospho-specific antibody.

(H) Phosphorylation of VE-cadherin Y658 and Y731 residues.

(I) The effect of R-Ras on the endothelial permeability was determined in HUVEC monolayer cultures. BSA leakage through the culture insert membrane without cells was set as 100%.

(J) The in vivo transduction of R-Ras38V increased VE-cadherin immunoreactivity of angiogenic sprouts in Matrigel plugs implanted in R-Ras KO mice. Immunofluorescence showed accumulation of VE-cadherin at the endothelial cell-cell junctions upon R-Ras transgene expression (arrows).

(K) Quantification of VE-cadherin immunoreactivity standardized with CD31 area was compared between R-Ras38V and mock transduced control plugs. $^{***}p < 0.001$.

Scale bars, 20 μm (J), 25 μm (D), 50 μm (A, E). See also Figure S5.

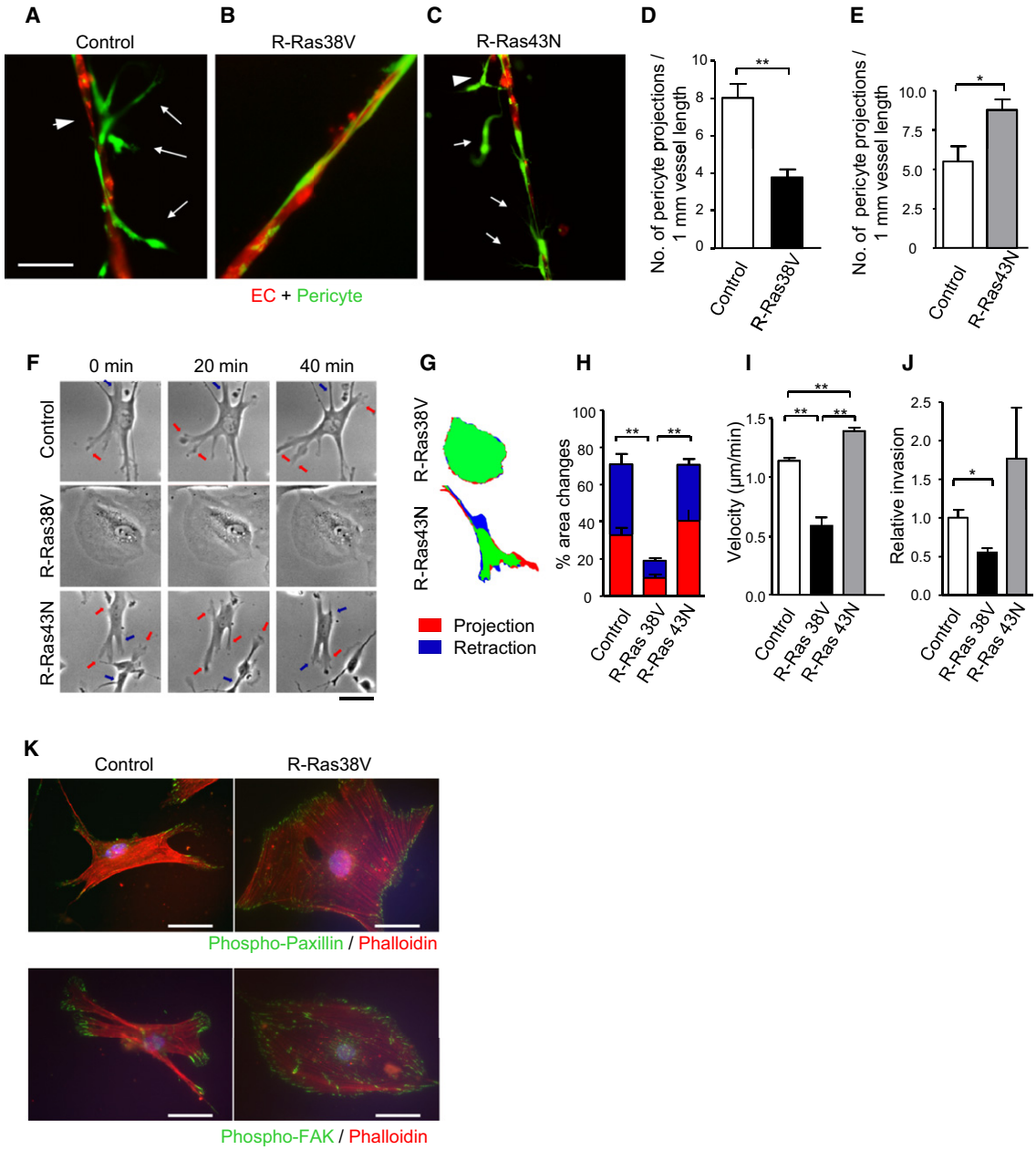

Figure 7. R-Ras Regulates Pericytes in the In Vitro-Reconstituted Microvessels

(A and B) Fluorescently labeled pericytes (green) were transduced with R-Ras38V or control vector and, at 3 hr post transduction, they were plated together with red-labeled endothelial cells (ECs) onto Matrigel at a 4:1 (EC: pericyte) ratio, cultured for 24 hr, and the resulting vessel-like structures were analyzed by fluorescent microscopy. In the control cocultures (A), pericytes were loosely attached to the vessel-like EC structures (arrowhead) with cytoplasmic processes (arrows). Upon R-Ras38V expression in pericytes, these abnormal characteristics were significantly diminished, and ECs and pericytes became tightly associated (B).

(C) R-Ras43N expression in pericytes did not have this effect.

(D and E) The number of pericyte projections from the reconstituted microvessels was significantly decreased by R-Ras38V (D) but increased by R-Ras43N expression (E).

(F) Time-laps video microscopy of pericytes on the Matrigel-coated two-dimensional (2D) surface shows membrane projection/retraction activities of the pericytes. Arrows indicate dynamic membrane activities (orange, projections; blue, retractions).

(G and H) The fractions of projecting (red) and retracting (blue) membrane area versus total cell area (% area change) were determined between the time points 0 and 5 min. See also Figure S6.

(I) The mean velocity of pericyte motility was calculated from 20 hr-long time-lap observations in 2D culture.

(J) Pericyte invasion through Matrigel-coated filter membrane.

(K) Immunofluorescence of phospho-paxillin Y118 and phospho-FAK Y397 to highlight focal adhesions complexes (green) assembled throughout the cell perimeter upon R-Ras38V expression. Scale bars, 50 μm. *$p < 0.05$, **$p < 0.001$, ± SEM.

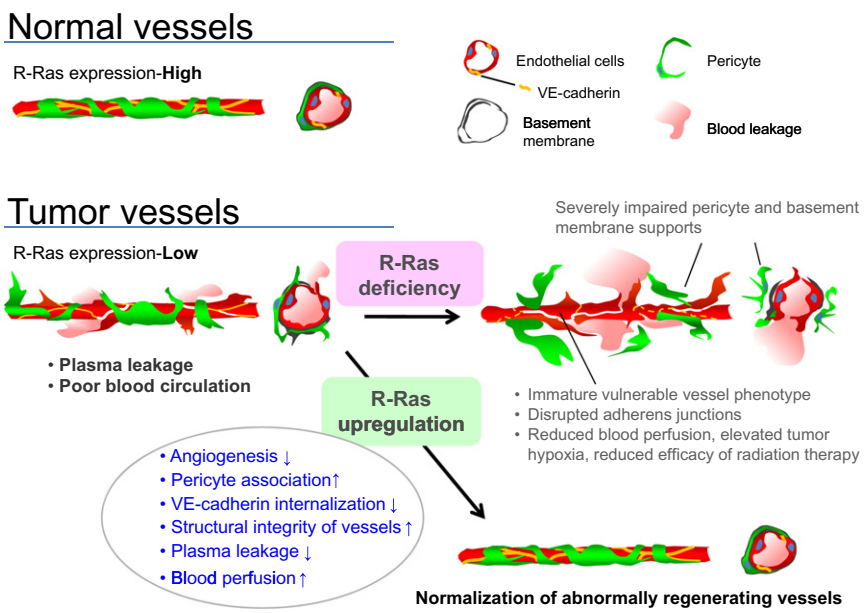

Figure 8. Regulation of Tumor Vessel Maturation by R-Ras

Schematic summary of the consequences of R-Ras disruption and upregulation in tumor blood vessels. The disruption of R-Ras severely impairs structural and functional maturation of tumor vessels. These vessels exhibit the poorly pericyte-supported "vulnerable" immature phenotype, which highly expresses VEGFR2 and α_v integrins. The structural abnormalities are associated with extensive blood leakage, reduced blood perfusion, and elevated hypoxia within tumors. In contrast, upregulation of R-Ras signaling enhances pericyte association and stabilizes VE-cadherin at the endothelial adherens junctions, leading to improved vessel structure and endothelial barrier function with improved blood perfusion. Thus, R-Ras signaling promotes normalization of pathologically regenerating blood vessels.

Endothelial Cell-Specific Tetracycline-Inducible Expression of R-Ras

The Tie2-rtTA transgenic mouse line has been described previously (Bao et al., 2010). Matrigel containing 60 ng/ml VEGF and 60 U/ml heparin was injected into the flanks of Tie2-rtTA transgenic mice. Five days later, lentivirus harboring pLVX-Tight-Puro/R-Ras38V expression vector was injected into the Matrigel plugs at 10^6 transduction units. Doxycycline was administrated i.p. daily at 5 mg/kg from Day 5 to Day 10. At Day 11, mice were perfused with biotinylated tomato lectin. Four mice per group were examined. To confirm the induction of R-Ras38V, mRNA was isolated from the plugs, and RT-PCR was conducted using a primer set for human R-Ras: 5′-GACCCCACTATTGAGGACTCC-3′ and 5′-CTACAGGAGGACGCAGGG-3′. RT-PCR for cyclophilin A was used as control.

Pericyte Implantation into R-Ras Knockout Mice

Microvascular pericytes were isolated from wild-type neonatal mouse brain (Wu et al., 2003) and transduced ex vivo with R-Ras38V, R-Ras43N, or control lentivirus. These pericytes were fluorescently labeled with 8 μM CellTracker green for 30 min, and 3×10^5 cells were implanted into the flank of R-Ras knockout mice after mixed with 0.5 ml Matrigel containing VEGF and Heparin. Seven days later, the Matrigel plugs were grossly examined for the extent of blood leakage in the plugs. The association of the implanted pericytes (green-labeled) with vessels was analyzed in histological sections by fluorescence microscopy.

Statistics

Statics were performed using the two-tailed Student's t test to compare wild-type with R-Ras knockout mice and the one-way ANOVA with Tukey's multiple comparison test for in vitro experiment. Error bars represent SEM.

Additional Supplemental Experimental Procedures are available online in the Supplemental Information.

SUPPLEMENTAL INFORMATION

Supplemental Information includes two movies, six figures, two tables, and Supplemental Experimental Procedures and can be found with this article online at http://dx.doi.org/10.1016/j.ccr.2012.06.013.

ACKNOWLEDGMENTS

Anti-NG2 antibody was a gift from Dr. William Stallcup of SBMRI. The antibody for phospho-specific VE-cadherin Ser 665 was a gift from Drs. Silvio Gutkind and Julie Garvard of NIH. We thank Drs. Sara Courtneidge and Sunyoung Lee for their advices on the manuscript. Scanning electron microscopy was done at Advanced Materials Processing and Analysis Center, University of Central Florida. Histological preparations and fluorescence microscopy were done at the Histology and Imaging core facilities of SBMRI and University of Alabama at Birmingham. RT-qPCR was done at the Analytical Genomics Core of SBMRI. This work was supported by National Cancer Institute Grants CA125255, CA030199, and CA104898, American Cancer Society Grant IRG6000147, Bankhead-Coley Cancer Research Program 1BD11-34213, the Florida Breast Cancer Foundation Fellowship Award, and departmental funds provided by the Department of Pathology, University of Alabama at Birmingham, and by SBMRI.

Received: March 15, 2010
Revised: August 29, 2011
Accepted: June 18, 2012
Published: August 13, 2012

REFERENCES

Allinen, M., Beroukhim, R., Cai, L., Brennan, C., Lahti-Domenici, J., Huang, H., Porter, D., Hu, M., Chin, L., Richardson, A., et al. (2004). Molecular characterization of the tumor microenvironment in breast cancer. Cancer Cell *6*, 17–32.

Allingham, M.J., van Buul, J.D., and Burridge, K. (2007). ICAM-1-mediated, Src- and Pyk2-dependent vascular endothelial cadherin tyrosine phosphorylation is required for leukocyte transendothelial migration. J. Immunol. *179*, 4053–4064.

Andrae, J., Gallini, R., and Betsholtz, C. (2008). Role of platelet-derived growth factors in physiology and medicine. Genes Dev. *22*, 1276–1312.

Armulik, A., Abramsson, A., and Betsholtz, C. (2005). Endothelial/pericyte interactions. Circ. Res. *97*, 512–523.

Bao, X., Moseman, E.A., Saito, H., Petryniak, B., Thiriot, A., Hatakeyama, S., Ito, Y., Kawashima, H., Yamaguchi, Y., Lowe, J.B., et al. (2010). Endothelial heparan sulfate controls chemokine presentation in recruitment of lymphocytes and dendritic cells to lymph nodes. Immunity *33*, 817–829.

Benjamin, L.E., Golijanin, D., Itin, A., Pode, D., and Keshet, E. (1999). Selective ablation of immature blood vessels in established human tumors follows vascular endothelial growth factor withdrawal. J. Clin. Invest. *103*, 159–165.

Bergers, G., and Hanahan, D. (2008). Modes of resistance to anti-angiogenic therapy. Nat. Rev. Cancer *8*, 592–603.

Carmeliet, P., and Jain, R.K. (2011a). Molecular mechanisms and clinical applications of angiogenesis. Nature *473*, 298–307.

Carmeliet, P., and Jain, R.K. (2011b). Principles and mechanisms of vessel normalization for cancer and other angiogenic diseases. Nat. Rev. Drug Discov. *10*, 417–427.

Coulon, C., Georgiadou, M., Roncal, C., De Bock, K., Langenberg, T., and Carmeliet, P. (2010). From vessel sprouting to normalization: role of the prolyl hydroxylase domain protein/hypoxia-inducible factor oxygen-sensing machinery. Arterioscler. Thromb. Vasc. Biol. *30*, 2331–2336.

Crosby, C.V., Fleming, P.A., Argraves, W.S., Corada, M., Zanetta, L., Dejana, E., and Drake, C.J. (2005). VE-cadherin is not required for the formation of nascent blood vessels but acts to prevent their disassembly. Blood *105*, 2771–2776.

Darland, D.C., and D'Amore, P.A. (1999). Blood vessel maturation: vascular development comes of age. J. Clin. Invest. *103*, 157–158.

Dejana, E., Orsenigo, F., and Lampugnani, M.G. (2008). The role of adherens junctions and VE-cadherin in the control of vascular permeability. J. Cell Sci. *121*, 2115–2122.

Ebos, J.M., Lee, C.R., Cruz-Munoz, W., Bjarnason, G.A., Christensen, J.G., and Kerbel, R.S. (2009). Accelerated metastasis after short-term treatment with a potent inhibitor of tumor angiogenesis. Cancer Cell *15*, 232–239.

Fukuhara, S., Sakurai, A., Sano, H., Yamagishi, A., Somekawa, S., Takakura, N., Saito, Y., Kangawa, K., and Mochizuki, N. (2005). Cyclic AMP potentiates vascular endothelial cadherin-mediated cell-cell contact to enhance endothelial barrier function through an Epac-Rap1 signaling pathway. Mol. Cell. Biol. *25*, 136–146.

Gavard, J., and Gutkind, J.S. (2006). VEGF controls endothelial-cell permeability by promoting the beta-arrestin-dependent endocytosis of VE-cadherin. Nat. Cell Biol. *8*, 1223–1234.

Gerhardt, H., and Semb, H. (2008). Pericytes: gatekeepers in tumour cell metastasis? J. Mol. Med. *86*, 135–144.

Gory-Fauré, S., Prandini, M.H., Pointu, H., Roullot, V., Pignot-Paintrand, I., Vernet, M., and Huber, P. (1999). Role of vascular endothelial-cadherin in vascular morphogenesis. Development *126*, 2093–2102.

Heidenreich, R., Kappel, A., and Breier, G. (2000). Tumor endothelium-specific transgene expression directed by vascular endothelial growth factor receptor-2 (Flk-1) promoter/enhancer sequences. Cancer Res. *60*, 6142–6147.

Helfrich, I., Scheffrahn, I., Bartling, S., Weis, J., von Felbert, V., Middleton, M., Kato, M., Ergün, S., and Schadendorf, D. (2010). Resistance to antiangiogenic therapy is directed by vascular phenotype, vessel stabilization, and maturation in malignant melanoma. J. Exp. Med. *207*, 491–503.

Jain, R.K. (2003). Molecular regulation of vessel maturation. Nat. Med. *9*, 685–693.

Jain, R.K. (2005). Normalization of tumor vasculature: an emerging concept in antiangiogenic therapy. Science *307*, 58–62.

Kappel, A., Rönicke, V., Damert, A., Flamme, I., Risau, W., and Breier, G. (1999). Identification of vascular endothelial growth factor (VEGF) receptor-2 (Flk-1) promoter/enhancer sequences sufficient for angioblast and endothelial cell-specific transcription in transgenic mice. Blood *93*, 4284–4292.

Kersting, S., Konopke, R., Kersting, F., Volk, A., Distler, M., Bergert, H., Saeger, H.D., Grützmann, R., and Bunk, A. (2009). Quantitative perfusion analysis of transabdominal contrast-enhanced ultrasonography of pancreatic masses and carcinomas. Gastroenterology *137*, 1903–1911.

Kinbara, K., Goldfinger, L.E., Hansen, M., Chou, F.L., and Ginsberg, M.H. (2003). Ras GTPases: integrins' friends or foes? Nat. Rev. Mol. Cell Biol. *4*, 767–776.

Komatsu, M., and Ruoslahti, E. (2005). R-Ras is a global regulator of vascular regeneration that suppresses intimal hyperplasia and tumor angiogenesis. Nat. Med. *11*, 1346–1350.

Lindahl, P., Johansson, B.R., Levéen, P., and Betsholtz, C. (1997). Pericyte loss and microaneurysm formation in PDGF-B-deficient mice. Science *277*, 242–245.

Mancuso, M.R., Davis, R., Norberg, S.M., O'Brien, S., Sennino, B., Nakahara, T., Yao, V.J., Inai, T., Brooks, P., Freimark, B., et al. (2006). Rapid vascular regrowth in tumors after reversal of VEGF inhibition. J. Clin. Invest. *116*, 2610–2621.

Mazzone, M., Dettori, D., Leite de Oliveira, R., Loges, S., Schmidt, T., Jonckx, B., Tian, Y.M., Lanahan, A.A., Pollard, P., Ruiz de Almodovar, C., et al. (2009). Heterozygous deficiency of PHD2 restores tumor oxygenation and inhibits metastasis via endothelial normalization. Cell *136*, 839–851.

McDonald, D.M., and Choyke, P.L. (2003). Imaging of angiogenesis: from microscope to clinic. Nat. Med. *9*, 713–725.

Pàez-Ribes, M., Allen, E., Hudock, J., Takeda, T., Okuyama, H., Viñals, F., Inoue, M., Bergers, G., Hanahan, D., and Casanovas, O. (2009). Antiangiogenic therapy elicits malignant progression of tumors to increased local invasion and distant metastasis. Cancer Cell *15*, 220–231.

Stupack, D.G., and Cheresh, D.A. (2002). ECM remodeling regulates angiogenesis: endothelial integrins look for new ligands. Sci. STKE *2002*, pe7.

Thomas, M., and Augustin, H.G. (2009). The role of the Angiopoietins in vascular morphogenesis. Angiogenesis *12*, 125–137.

Weis, S., Cui, J., Barnes, L., and Cheresh, D. (2004). Endothelial barrier disruption by VEGF-mediated Src activity potentiates tumor cell extravasation and metastasis. J. Cell Biol. *167*, 223–229.

Wu, Z., Hofman, F.M., and Zlokovic, B.V. (2003). A simple method for isolation and characterization of mouse brain microvascular endothelial cells. J. Neurosci. Methods *130*, 53–63.

Xu, L., and Komatsu, M. (2009). Promoter cloning and characterization of the anti-vascular proliferation gene, R-ras: role of Ets- and Sp-binding motifs. J. Biol. Chem. *284*, 2706–2718.

Zhang, Z., Vuori, K., Wang, H., Reed, J.C., and Ruoslahti, E. (1996). Integrin activation by R-ras. Cell *85*, 61–69.

Cancer Cell
Article

Targeted Disruption of Heparan Sulfate Interaction with Hepatocyte and Vascular Endothelial Growth Factors Blocks Normal and Oncogenic Signaling

Fabiola Cecchi,[1] Deborah Pajalunga,[2,3,6] C. Andrew Fowler,[2,7] Aykut Üren,[4] Daniel C. Rabe,[1] Benedetta Peruzzi,[1,8] Nicholas J. MacDonald,[3,9] Davida K. Blackman,[3,10] Stephen J. Stahl,[5] R. Andrew Byrd,[2] and Donald P. Bottaro[1,*]
[1]Urologic Oncology Branch, National Cancer Institute, Bethesda, MD 20892-1501, USA
[2]Macromolecular NMR Section, Structural Biophysics Laboratory, Frederick National Laboratory for Cancer Research, Frederick, MD 21702-1201, USA
[3]EntreMed, Inc., Rockville, MD 20850, USA
[4]Lombardi Comprehensive Cancer Center, Georgetown University Medical Center, Washington, DC 20057-1469, USA
[5]Protein Expression Laboratory, National Institute of Arthritis and Musculoskeletal and Skin Diseases, National Institutes of Health, Bethesda, MD 20892-2775, USA
[6]Present address: Department of Cell Biology and Neuroscience, Higher Institute of Health, Viale Regina Elena, 299, 00161 Rome, Italy
[7]Present address: Medical NMR Facility, Carver College of Medicine, University of Iowa, B291 CBRB, Iowa City, IA 52242, USA
[8]Present address: DAI Laboratory, SODc General Laboratory, AOU-Careggi, University of Florence, Largo Brambilla 3-50134 Florence, Italy
[9]Present address: Laboratory of Malaria Immunology and Vaccinology, NIAID, National Institutes of Health, Rockville, MD 20892-8252, USA
[10]Present address: ProMetic BioTherapeutics, Inc., Rockville, MD 20850, USA
*Correspondence: dbottaro@helix.nih.gov
http://dx.doi.org/10.1016/j.ccr.2012.06.029

SUMMARY

Hepatocyte growth factor (HGF) and vascular endothelial cell growth factor (VEGF) regulate normal development and homeostasis and drive disease progression in many forms of cancer. Both proteins signal by binding to receptor tyrosine kinases and heparan sulfate (HS) proteoglycans on target cell surfaces. Basic residues comprising the primary HS binding sites on HGF and VEGF provide similar surface charge distributions without underlying structural similarity. Combining three acidic amino acid substitutions in these sites in the HGF isoform NK1 or the VEGF isoform VEGF165 transformed each into potent, selective competitive antagonists of their respective normal and oncogenic signaling pathways. Our findings illustrate the importance of HS in growth factor driven cancer progression and reveal an efficient strategy for therapeutic antagonist development.

INTRODUCTION

Heparan sulfate (HS) glycosaminoglycans (GAGs) are complex polysaccharides present on cell surfaces and in extracellular matrices that modulate cell growth and differentiation, and in turn, embryogenesis, angiogenesis, and homeostasis (reviewed in Sarrazin et al., 2011). Their extended conformation and high negative charge enhance tissue integrity, and their inherent complexity provides selective yet substantial protein binding capacity (Sarrazin et al., 2011). Protein binding enables the formation of growth factor gradients during development and reservoirs for factors needed rapidly for tissue repair and regeneration in adults (Sarrazin et al., 2011). Cell surface HS proteoglycans form ternary complexes with growth factors and their receptors, enhancing complex stability and signaling (Sarrazin et al., 2011; Mohammadi et al., 2005).

Significance

Heparan sulfate (HS) proteoglycans are widely expressed, structurally diverse biopolymers that modulate many important protein-protein interactions. Hepatocyte growth factor (HGF) and vascular endothelial cell growth factor (VEGF) regulate development and homeostasis and drive tumorigenesis, tumor angiogenesis, and metastasis in many forms of cancer. We show that targeted disruption of specific HS binding residues in HGF and VEGF yields selective competitive inhibitors of these pathways. The similar roles of HS in enabling receptor activation, in the absence of underlying structural similarity, suggest that this occurs through convergent evolutionary adaptation to the common binding partner, HS. Our results reveal an efficient strategy for the development of antagonists of these and potentially other HS binding growth factors with widespread involvement in cancer.

Hepatocyte growth factor (HGF) and vascular endothelial cell growth factor (VEGF) bind HS and regulate development and homeostasis (Ferrara, 2004; Matsumoto and Nakamura, 1996; Michalopoulos, 2007) and drive tumor growth, angiogenesis, and metastasis in many cancers (Boccaccio and Comoglio, 2006; Ferrara, 2004; Peschard and Park, 2007). HGF induces growth, motility, and morphogenesis in a variety of cell types via the Met receptor kinase (Peschard and Park, 2007). VEGF-A is an essential regulator of angiogenesis (Ferrara, 2004) that stimulates growth, motility, and tubulogenesis in vascular endothelial cells through the receptor kinases VEGFR1 (Flt-1) and VEGFR2 (Flk-1, kinase insert domain receptor [KDR]) and the coreceptors neuropilin-1 (NRP1) and NRP2 (Ferrara, 2004; Favier et al., 2006; Gluzman-Poltorak et al., 2000).

The *HGF* and *VEGF* genes encode multiple isoforms. Mature HGF is a plasminogen-like protein that comprises an amino-terminal heavy chain with four kringle motifs and a carboxyl-terminal light chain with a serine protease-like domain (Matsumoto and Nakamura, 1996). Two truncated HGF isoforms also exist: the shorter of these retains HGF activities at modestly reduced potency and consists of the amino-terminal (N) domain linked to kringle 1 (NK1) (Stahl et al., 1997). Within NK1, N contains the HS binding site (Hartmann et al., 1998; Kinosaki et al., 1998; Lietha et al., 2001; Mizuno et al., 1994; Okigaki et al., 1992; Sakata et al., 1997; Zhou et al., 1998, 1999), and K1 contains the primary Met binding site (Lokker et al., 1994; Rubin et al., 2001).

VEGF-A pre-mRNA splicing yields multiple VEGF-A isoforms, primarily VEGF121, VEGF165, and VEGF189 (Ferrara, 2004). These contain the same binding sites for VEGFR1 and R2, but differ in HS binding capacity by the presence or absence of domains encoded by exon 6 and exon 7 (Robinson and Stringer, 2001). Exon 7- and exon 8-encoded domains enable VEGF-A to bind NRP1 (Appleton et al., 2007; Ferrara, 2004). Unlike VEGF165 and VEGF189, VEGF121 lacks HS binding and is freely diffusible (Carmeliet et al., 1999). HS binding has significant impact on VEGF-A biology: mice engineered to express only VEGF121 display defective microvessel branching and lethality shortly after birth (Carmeliet et al., 1999). Yet, even VEGF121 signaling is HS dependent: similar to fibroblast growth factors (FGFs) and HGF, HS facilitates VEGF signaling through interactions with both ligand and receptor (Lyon et al., 2002; Mohammadi et al., 2005; Rubin et al., 2001; Sarrazin et al., 2011). Thus, complete disruption of HS function in VEGF signaling is likely to mimic the embryonic lethality associated with homozygous deletions of VEGF, VEGFR, or the HS proteoglycan perlecan (Ferrara, 2004; Sarrazin et al., 2011).

Basic residues critical for HS binding have been identified in HGF and VEGF165 (Chirgadze et al., 1999; Krilleke et al., 2007; Lietha et al., 2001; Ultsch et al., 1998; Zhou et al., 1998, 1999). Combined alanine substitutions in the VEGF165 HS binding site resulted in reduced binding to NRP1 and VEGFR1 (Krilleke et al., 2007). Alanine substitutions in the HS binding site of HGF (Kinosaki et al., 1998) or NK1 (Lokker et al., 1994; Sakata et al., 1997) resulted in modest functional change. Negative charge substitutions that more effectively disrupt HS binding distinguished functionally relevant sites in HGF over earlier studies (Hartmann et al., 1998), so this strategy was used to further define the importance of HS binding for Met and VEGFR signaling.

RESULTS

Substituted NK1 Forms Have Normal Folding and Met Binding but Diminished HS Binding and Signaling

The highly conserved N domain residues K60, K62, and R73 form the primary HS binding site in HGF and R76, K78, R35, and R36 contribute secondarily (Chirgadze et al., 1999; Lietha et al., 2001; Ultsch et al., 1998; Zhou et al., 1998, 1999; Table S1 available online). Within the HS binding domain of VEGF165, residues R123, R124, and R159 are also highly conserved and critical for heparin binding (Krilleke et al., 2007; Table S1). Although HGF and VEGF have neither significant sequence identity nor similarity in peptide backbone fold, the tripartite HS binding sites in both show a similar distribution of positive surface charge (Figure S1).

Expression plasmids were constructed that substituted acidic for basic residues to disrupt the surface charge distribution on NK1: R73E (designated 1S), K60E/K62E (2S), and K60E/K62E/R73E (3S). Substituted and wild-type (WT) NK1 proteins were expressed and purified to >99% homogeneity (Figure S2). To confirm proper folding of the substituted proteins, their structures were compared with WT by nuclear magnetic resonance (NMR) spectrometry (Figure 1). Minor shifts in the pattern of two-dimensional ^{1}H-^{15}N correlation spectra for substituted proteins overlaid on NK1 WT spectra clustered near the substitution sites, indicating minimal perturbation of the three-dimensional structure in the substituted proteins.

Competitive binding experiments using ruthenium (Ru) tagged NK1 WT protein bound to immobilized heparin with displacement by untagged WT or 3S proteins showed that binding by the 3S form was 10-fold lower than WT ($p < 0.001$; Figure 2A). The IC_{50} for WT was consistent with prior estimates of NK1- and NK2-heparin binding (Hartmann et al., 1998; Rubin et al., 2001). Elution of the substituted proteins from a heparin affinity column by a NaCl gradient also showed reduced binding relative to WT, most severely in NK1 3S, reinforcing prior evidence that residues 60, 62, and 73 are sites of HS interaction (Table S2).

Saturation binding of tagged NK1 WT and 3S proteins to a Met ectodomain-Ig fusion protein in the presence of HS oligomer (4.2 kDa) or HS tetramer (1.2 kDa) produced similar results (Figures 2B and 2C), indicating that Met binding was unchanged, as anticipated. Competitive displacement of HGF by NK1 WT or 3S also yielded IC_{50} values of ~1 nM (data not shown). Saturation binding of tagged NK1 3S to the Met-Ig protein was unaffected by the absence of HS (Figure 2B, triangles); in contrast, NK1 WT binding to Met-Ig in the absence of HS was significantly compromised (Figure 2C, triangles). Heparin (18 kDa) substituted effectively for either HS form in enhancing NK1 WT-Met binding (data not shown). Together, these results suggest that masking the positive surface charge of residues 60, 62, and 73 with bound HS in NK1 WT improves its Met binding affinity and that this was achieved artificially in NK1 3S by the negative charge substitutions.

Disruption of the primary HS binding site in NK1 diminished its biological activity in cultured cells. Ligand-induced Met autophosphorylation in human epithelial (184B5) cells was lower in cells treated with NK1 1S or 2S proteins relative to NK1 WT or HGF (data not shown) and undetectable in cells treated with NK1 3S protein (Figure 2D). Ligand-stimulated cell migration (Figure 2E) and mitogenesis (Figure 2F) revealed similar patterns

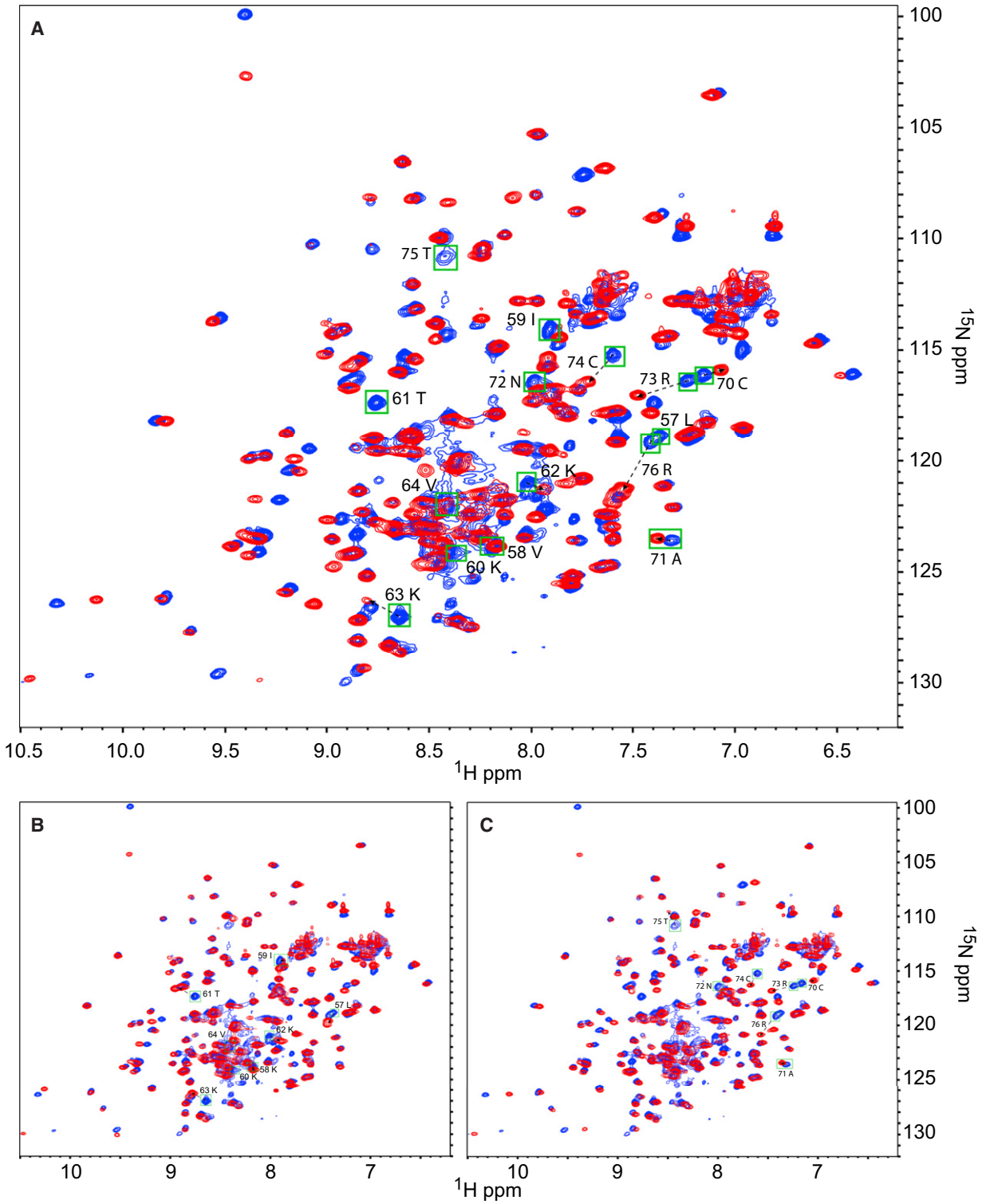

Figure 1. NMR Analysis of NK1 Proteins

^{1}H-^{15}N correlation spectra for substituted NK1 proteins (red) superimposed on NK1 WT spectra (blue).

(A) NK1 3S.

(B) NK1 2S.

(C) NK1 1S.

Spectra that are shifted in the substituted proteins are labeled in (A), (B), and (C).

See also Figure S1 and Table S1.

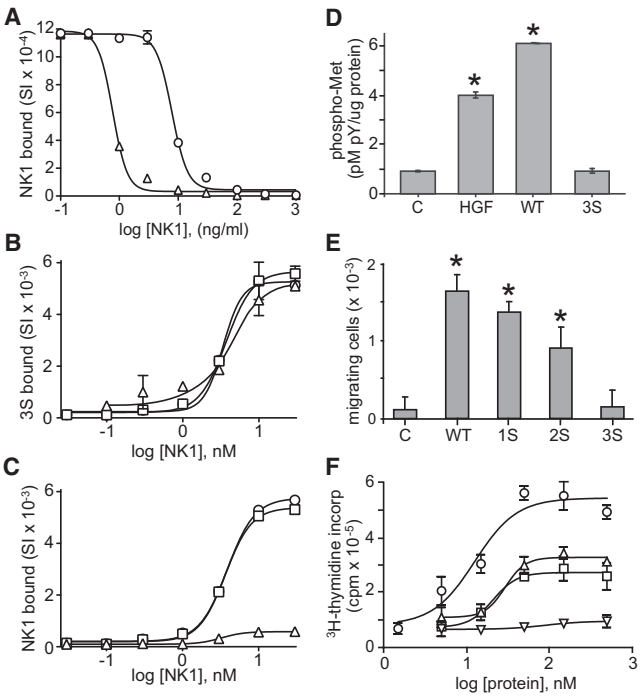

Figure 2. NK1 3S Has Reduced HS Binding and Normal Met Binding and Fails to Activate Met Signaling

(A–C) Competitive displacement of Ru tagged NK1 WT from immobilized heparin by untagged NK1 WT (triangles) or 3S (circles) (A). Saturation binding of Ru tagged NK1 3S (B) or NK1 WT (C) to Met ectodomain-Ig in the absence (triangles) or presence of HS oligomer (circles) or HS tetramer (squares). For (A), (B), and (C) values are mean signal intensity (SI) ± SD (n = 3).

(D) Mean Met activation (phospho-Met [pM] per total protein [ug] ± SD; n = 3) in 184B5 cells left untreated ("C") or treated with HGF (1 nM), NK1 WT (5 nM), or NK1 3S (5 nM) for 20 min. Met content was equivalent in all samples. Asterisks indicate significant differences from control ($p < 0.01$).

(E) Mean number of 184B5 cells (± SD; n = 3) migrating in response to treatment with NK1 WT or substituted NK1 proteins (7 nM each) in 24 hr. Asterisks indicate significant differences from control ($p < 0.01$).

(F) Mean DNA synthesis values ([^{3}H]thymidine incorporation cpm ± SD; n = 3) in 184B5 cells after 16 hr treatment with NK1 WT or substituted proteins at the indicated concentrations: WT (circles); 1S (triangles); 2S (squares); and 3S (inverted triangles).

See also Figure S2 and Table S2.

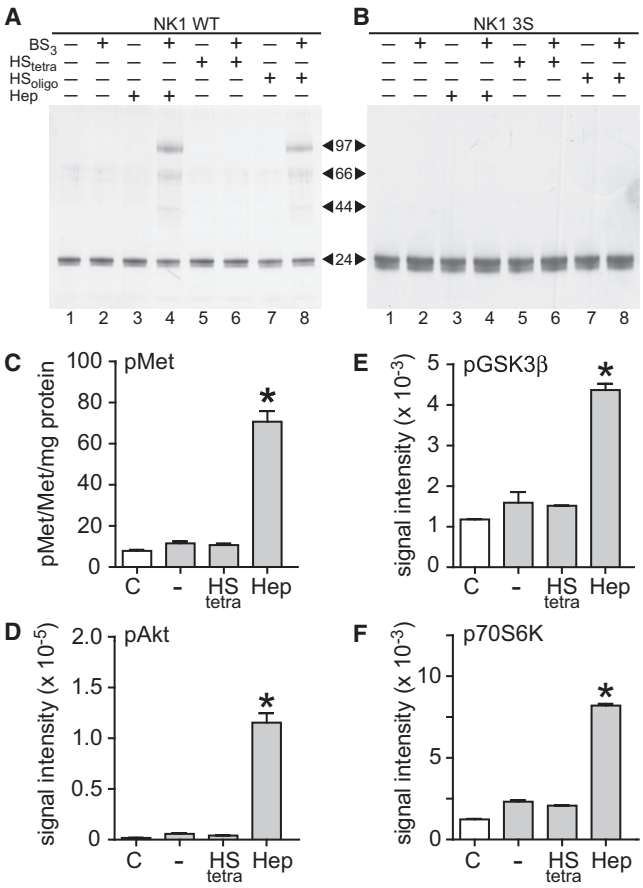

Figure 3. Long HS Polymers Promote NK1 Clustering, Met Activation, and Signaling

(A and B) Purified NK1 WT (A), or NK1 3S proteins were incubated alone or with BS_3 crosslinker in the absence or presence of heparin (Hep), HS oligomers (HS_{oligo}), or HS tetramers (HS_{tetra}) before analysis by SDS-PAGE and immunoblotting (B). Arrows between (A) and (B) indicate the masses of NK1 monomer (24 kDa) and NK1 multimers.

(C–F) The activation states of Met (mean phospho-Met/Met/total protein ± SD; n = 3; C), Akt (D), GSK3β (E), or p70S6K (F) in serum-deprived CHO 745 cells that were untreated (unfilled bars, "C") or treated with NK1 WT (200 pM; gray bars) in the absence (–) or presence of HS tetramer (HS_{tetra}) or heparin (Hep). Values for (D–F) are mean signal intensity units (± SD; n = 3). Asterisks indicate significant differences from control ($p < 0.01$).

of functional compromise among the substituted NK1 forms: the 1S and 2S proteins showed reduced activity ($p < 0.01$), and the 3S protein was inactive.

NK1-HS Binding Enables NK1 Clustering, Met Activation, and Signaling

Loss of signaling by NK1 3S despite native Met binding implied that HS binding enabled a critical step in Met activation. HGF and NK1 are monomers in solution, and it is thought that long HS chains capable of binding several HGF molecules promote and stabilize ligand clustering, and in turn, the clustering of ligand-receptor complexes (Chirgadze et al., 1999; Gherardi et al., 2006; Lietha et al., 2001; Hartmann et al., 1998; Rubin et al., 2001; Schwall et al., 1996; Tolbert et al., 2007; Zhou et al., 1999). Consistent with this concept, 18 kDa heparin or 4.2 kDa HS oligomer supported NK1 WT multimer formation detected after covalent affinity crosslinking, SDS-PAGE, and immunoblotting (Figure 3A, lanes 4 and 8). HS tetramers (1.2 kDa) unable to bind more than one NK1 molecule (Lyon et al., 2002) did not support NK1 WT multimer formation (Figure 3A, lane 6). The masses of the observed NK1 WT oligomers corresponded to dimers, trimers, and tetramers of NK1 (Figure 3A). As anticipated, HS-NK1 3S complexes were not detected (Figure 3B).

The impact of HS chain length on NK1-driven Met signaling was investigated using Chinese hamster ovary (CHO) 745 cells, which lack HS (Sarrazin et al., 2011). NK1-Met binding and NK1 clustering on cell surfaces were found to be HS dependent in CHO 745 (Sakata et al., 1997). Consistent with this, and other studies (Lyon et al., 2002, 2004), Met TK activation (Figure 3C) and consequent activation of Akt (Figure 3D), glycogen synthase kinase 3β

(GSK3β) (Figure 3E), and p70S6K (Figure 3F) by NK1 WT in this cell line was enhanced by added 18 kDa heparin. In contrast, added 1.2 kDa HS tetramer did not enhance NK1 WT signaling (Figures 3C–3F), despite enabling high affinity NK1-Met binding (Figure 2C). These observations suggest that the clustering of NK1 afforded by longer HS chains stabilized NK1-Met complex oligomerization, and, in turn, Met signaling. The relative order in which ligand-HS, ligand-Met, and Met-HS binding events occur is unknown and may be dictated by the relative abundance of HS and Met on target cells. We note that HS tetramer enabled modest mitogen-activated protein kinase (MAPK) activation by HGF (Lyon et al., 2002); as suggested by Stamos et al. (2004), the HGF light chain may contribute to HGF/Met/HS complex dimerization through homotypic interactions between light-chain protomers.

NK1 3S Is a Potent, Selective Competitive Antagonist of NK1 and HGF Signaling

The properties of the NK1 3S protein suggested that it might competitively antagonize HGF activity. Indeed, addition of 3S protein to HGF- and NK1-treated cells resulted in dose-dependent inhibition Met kinase activation in normal cells (Figure 4A, circles and squares). The IC_{50} values for 3S inhibition of Met activation by HGF and NK1 WT were 6 nM, 10-fold more potent than the Met antagonist PHA665752 (IC_{50} = 60 nM; Figure 4A, triangles). NK1 WT-induced DNA synthesis was also inhibited by 3S protein, with >90% inhibition at 10-fold molar excess 3S over WT NK1 (Figure 4B, circles).

CD44 variants containing exon 6 (v6) are implicated in oncogenic Met signaling (Orian-Rousseau et al., 2002), and those containing exon 3 are often modified with HS and promote HGF-Met interaction (van der Voort et al., 1999; Wielenga et al., 2000). CD44 variants containing both exons occur frequently in colon and prostate cancer-derived cell lines, such as HT29 and PC3M, respectively, and in colon and prostate carcinomas where their expression correlates with poor prognosis (van der Voort et al., 1999; Wielenga et al., 2000). We analyzed Met-CD44 association to determine if NK1 3S-Met binding affected this process. Met-CD44 association was induced by HGF or NK1 WT in HT29 cells (Figure 4C, lanes 2 and 3) and by HGF in PC3M cells (Figure 4D, lane 2), but not by NK1 3S in either cell line (Figure 4C, lane 4; Figure 4D, lane 6). In PC3M, NK1 3S antagonized HGF-induced Met-CD44 association in a dose-dependent manner, while PHA665752 was less effective (Figure 4D, lanes 2–5 versus lanes 7–9).

Oncogenic autocrine HGF/Met signaling occurs frequently in glioblastoma (Boccaccio and Comoglio, 2006) and drives tumorigenicity in the glioblastoma-derived cell line U87 MG. Stable expression of NK1 3S in U87 MG cells significantly reduced proliferation relative to cells expressing NK1 WT or empty vector (Figure 4E). HGF and Met protein levels were comparable in the three cell lines, as were the levels of NK1 WT and 3S proteins (Figures S3A–S3E). U87 MG cells do not express NK1 mRNA, thus reduced growth resulted from NK1 3S inhibition of endogenous HGF signaling.

We extended our initial analysis of NK1 3S inhibition of cell motility (Figure 2E) using the Madin-Darby Canine Kidney (MDCK) cell scatter assay (Figure 4F). NK1 3S had no intrinsic scatter activity (Figure 4F, third panel from left); inhibition of HGF-induced scatter was dose-dependent and complete at 50-fold molar excess (Figure 4F, right three panels).

NK1 3S also blocked anchorage independent growth by U87 MG cells (Figure 4G). U87 MG cells grow robustly in soft agar, (Figure 4G, left panel), but cells expressing NK1 3S failed to form colonies under identical conditions (Figure 4G, second panel from left). Colony formation was also suppressed by adding purified NK1 3S protein to the medium, with ~50% inhibition by 70 nM 3S and complete blockade by 300 nM relative to controls (Figure 4G, third and fourth panels from left); similar levels of inhibition were observed for PHA665752 (Figure 4G, right two panels).

The Met selectivity of NK1 3S antagonism was confirmed using the endothelial hybrid cell line EA.hy 926, which expresses both Met and KDR. Cells were stimulated with either NK1 WT or VEGF165 in the presence or absence of 10-fold molar excess NK1 3S, and the activation levels of Met, Akt, GSK3β, and p70S6K were measured by 2-site immunoassays (Figures S3F–S3I). NK1 3S did not activate Met or downstream effectors (Figures S3F–S3I, left versus right white bars). NK1 WT activated Met, Akt, and its targets relative to control cells (Figures S3F–S3I, left white versus left gray bars), and this signaling cascade was completely suppressed by added excess NK1 3S (Figures S3F–S3I, right gray bars). In contrast, although VEGF165 fully activated the Akt pathway, excess NK1 3S had no effect (Figures S3F–S3I, left versus right black bars). Similar results were observed for VEGF165 activation of the MAPK pathway kinases pERK-1/2, pJNK, and pp38 MAPK in the presence or absence of NK1 3S (data not shown).

NK1 3S Inhibits HGF Signaling, Tumor Growth, and Metastasis In Vivo

NK1 3S antitumor activity was first assessed by xenograft studies of transfected U87 MG cell lines in severe combined immunodeficiency (SCID)/beige mice (Figure 5A). Animals receiving the U87 MG/NK1 WT cell line started to develop tumors in 5 days (Figure 5A, squares), and tumor growth rate was twice that of the control cell line (Figure 5A, circles), consistent with the additive effects of ectopic NK1 WT and endogenous HGF. In contrast, tumor growth in animals receiving U87 MG/NK1 3S cells was not measurable before 50 days (Figure 5A, triangles). Like U87 MG, the human leiomyosarcoma-derived cell line SK-LMS-1 has autocrine HGF/Met activation. SK-LMS-1 cells were transfected with plasmids for NK1 WT, NK1 3S, or with empty vector, and cell clones were selected for equivalent expression of endogenous HGF and Met and ectopic NK1 WT and NK1 3S proteins (Figures S3A–S3E). Again, NK1 WT expression accelerated tumor growth (Figure 5B, squares), whereas NK1 3S expression reduced mean tumor volume by 75% after 68 days relative to controls (Figure 5B, triangles versus circles; $p < 0.001$). Tumors resected from these mice displayed equivalent Met content among the three groups (not shown); Met activation was highest in NK1 WT transfectant tumors (Figure 5C, black bar), significantly lower in tumors from controls (Figure 5C, gray bar), and lowest in tumors from the NK1 3S implanted group (Figure 5C, white bar; $p < 0.001$).

HGF/Met signaling is a critical contributor to tumor metastasis (Boccaccio and Comoglio, 2006). NK1 3S was tested in the B16 murine melanoma model of induced metastasis, where

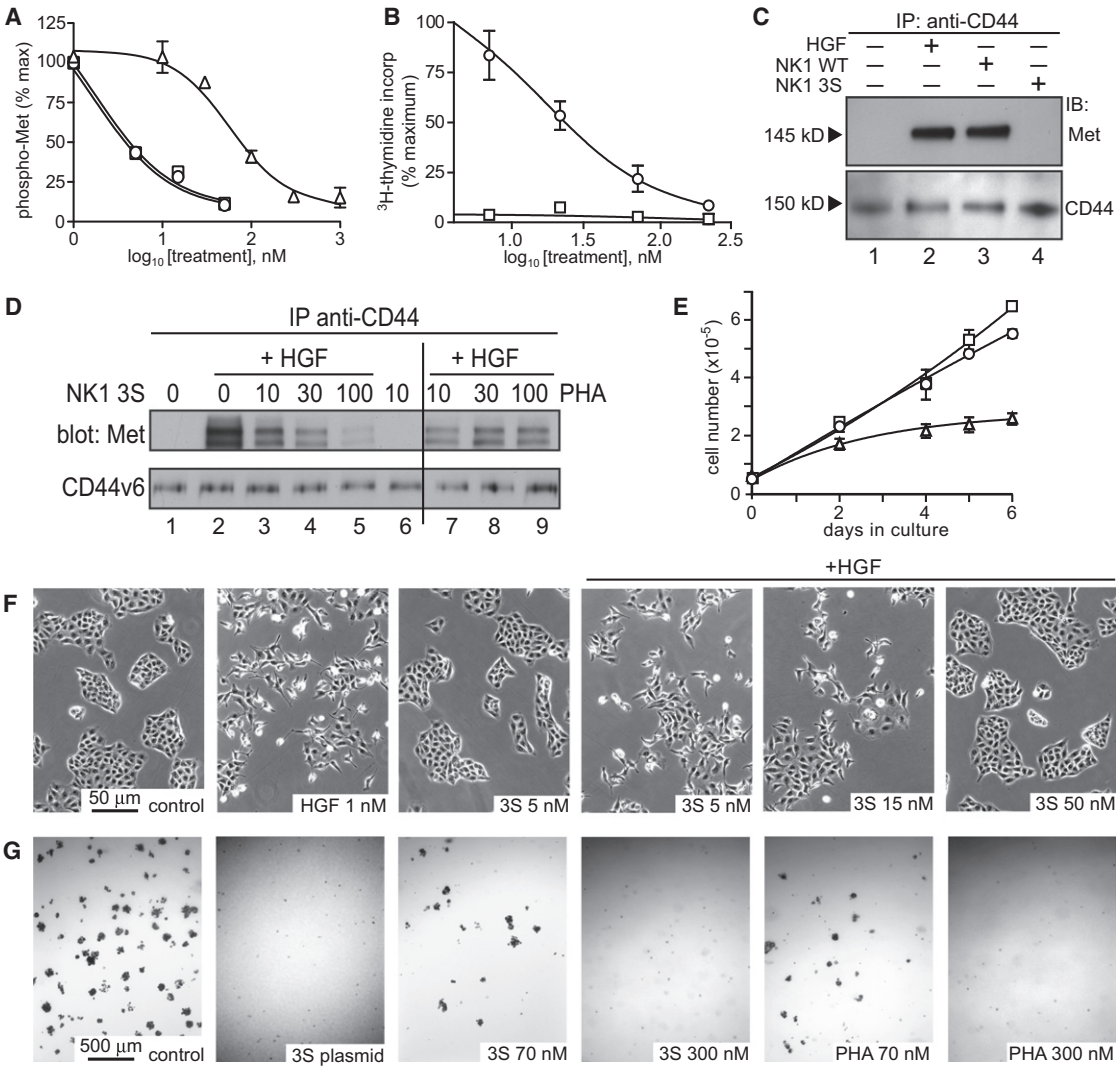

Figure 4. NK1 3S Is a Potent Antagonist of NK1 and HGF Signaling

(A) Mean Met activation level (% maximum ± SD; n = 3) in 184B5 cells treated with HGF (1 nM; circles) or NK1 WT (5 nM; squares) and with increasing concentrations of NK1 3S. HGF-stimulated cells were treated with PHA665752 (triangles) over the same dose range in parallel.

(B) Mean DNA synthesis level (% maximum [^{3}H]thymidine incorporation ± SD; n = 3) in 184B5 cells treated with NK1 WT and NK1 3S (circles), or in cells treated with NK1 3S alone (squares) at the indicated doses.

(C) Met-CD44 association in HT29 cells incubated with NK1 3S (5 nM), NK1 WT (5 nM), or HGF (1 nM) as indicated, in the presence of DTSSP prior to immunoprecipitation with anti-CD44, SDS-PAGE, and immunoblotting with anti-Met (upper panel) or anti-CD44 (lower panel).

(D) Met-CD44 association in PC3M cells treated with HGF (1 nM) and DTSSP in the absence or presence of NK1 3S or PHA665752 (PHA) at the indicated concentrations (nM) prior to immunoprecipitation with anti-CD44, SDS-PAGE, and immunoblotting with anti-Met (upper panel) or anti-CD44 (lower panel).

(E) Proliferation of U87 MG cells (mean cell number ± SD; n = 3) expressing NK1 WT (squares), NK1 3S (triangles), or empty vector (circles).

(F) NK1 3S antagonism of HGF-stimulated MDCK cell scatter. Unstimulated control cells or cells treated with HGF or NK1 3S at the indicated concentrations (left three panels). HGF-stimulated cells treated with NK1 3S at the indicated concentrations (right three panels).

(G) Soft agar colony formation by U87 MG cells transfected with vector (control) or NK1 3S cDNA (3S plasmid) or control cells treated with NK1 3S protein or PHA665752 (PHA) at the indicated concentrations.

See also Figure S3.

endogenous HGF drives metastatic colonization. B16 cells expressing luciferase (B16-luc) were used to enable tumor burden assessment by optical imaging. Metastasis in animals injected with B16-luc cells expressing NK1 3S was compared with metastasis in animals injected with empty vector cells and with metastasis in animals injected with the empty vector cells and then treated by daily intraperitoneal (i.p.) injection of purified NK1 3S protein at 50 mg/kg (Figure 5D). Metastatic burden rose rapidly in the mice receiving empty vector cells (Figure 5D, circles), whereas mice receiving 3S plasmid bearing cells (Figure 5D, squares) or control cells and i.p. treatment with 3S protein (Figure 5D, triangles) showed few, if any, metastases by study

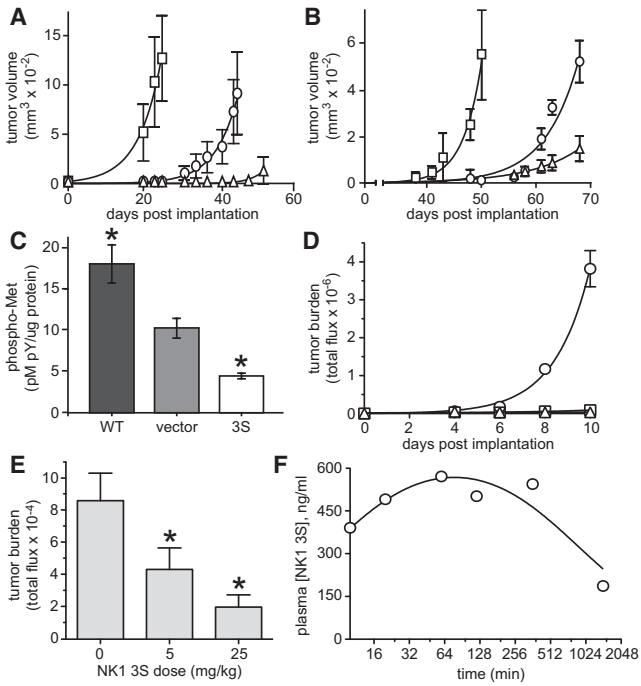

Figure 5. NK1 3S Inhibits HGF-Driven Tumor Growth, Metastasis, and Met Kinase Activation In Vivo

(A) Mean tumor volume (± SD) in mice (n = 6/group) implanted with U87 MG transfectants expressing NK1 WT (squares), NK1 3S (triangles), or empty vector (circles) at the indicated days postimplantation.

(B) Mean tumor volume (± SD) in mice (n = 6/group) implanted with clonal SK-LMS-1-derived cell lines expressing NK1 WT (squares), NK1 3S (triangles), or empty vector (circles) at the indicated days postimplantation.

(C) Mean Met activation level (phospho-Met/Met/total protein ± SD; n = 3) in SK-LMS-1 tumors derived from SK-LMS-1 cells expressing NK1 WT (black), empty vector (gray), and NK1 3S (unfilled). Asterisks indicate significant differences from vector control ($p < 0.01$).

(D) Mean metastatic burden (total photon flux ± SD) over time in mice (n = 10/group) injected via tail vein with B16-luc cells transfected with empty vector (circles) or NK1 3S (squares) or injected with empty vector cells and then treated on day 2 and thereafter with NK1 3S (50 mg/kg) by daily i.p. injection (triangles).

(E) Mean metastatic burden (total photon flux ± SD on day 27 postimplantation) in mice (n = 10/group) implanted subcutaneously with PC3M-luc cells and treated on day 5 and daily thereafter with NK1 3S protein by i.p. injection at 5 or 25 mg/kg or treated with vehicle alone.

(F) Mean plasma NK1 3S protein concentration (ng/ml, n = 2) in mice (n = 6) measured at the indicated times following a single i.p. injection of NK1 3S at 50 mg/kg.

See also Figure S4.

termination ($p < 0.001$). Lung specimens from each group examined ex vivo at study termination for melanin-producing colonies were consistent with the imaging results (data not shown). The B16-luc melanoma model was also used for a preliminary dose-ranging study where mice received i.p. injections of NK1 3S protein at day 2 post-tail vein injection and daily thereafter for 15 days at 5, 25, and 50 mg/kg (Figure S4). Significant metastatic suppression was observed at every NK1 3S dose ($p < 0.001$).

The antimetastatic efficacy of NK1 3S was also evaluated in the PC3M spontaneous metastasis model (Figure 5E). The PC3M cells used in these studies also expressed luciferase for metastatic burden assessment. Palpable subcutaneous primary tumors developed within 5 days after cell implantation; mice then received daily i.p. injections of purified NK1 3S protein at 5 or 25 mg/kg, or vehicle alone. Primary tumor growth was measured at regular intervals using calipers, and metastatic burden was measured by imaging at study termination. Interestingly, NK1 3S treatment had no significant effect on primary tumor growth in this model (data not shown); however, a significant and dose-dependent inhibition of metastasis was observed, with 80% reduction at 25 mg/kg ($p < 0.01$; Figure 5E).

Analysis of NK1 3S pharmacokinetics in mice (n = 6) showed that plasma NK1 level peaked between 1 and 3 hr after a single i.p. injection (50 mg/kg) and declined thereafter (Figure 5F). Plasma NK1 3S concentration 24 hr postinjection was ~150 ng/ml or ~300-fold over typical murine plasma HGF levels. Mice treated daily with this dose for 10 days showed no weight loss, lethargy, or other signs of toxicity. Mice (n = 5) treated on this dose and schedule, but not implanted with tumor cells, displayed normal clinical blood chemistry, differential blood cell count, and hematocrit values; full necropsy analysis of all tissues and organs showed no signs of toxicity or abnormality (data not shown).

VEGF165 3S Is a Potent Competitive VEGF Antagonist

To determine whether the strategy used to transform NK1 from agonist to antagonist could be generalized, we generated a cDNA encoding opposite charge substitution at the critical HS binding residues identified by Krilleke et al. (2007) in VEGF165 (R123E/R124E/R159E or VEGF165 3S). Plasmids encoding vector alone, VEGF165 WT or VEGF165 3S, were stably transfected into HEK293 cells that were engineered previously to express 2.5×10^6 VEGFR2 per cell (293/KDR; Backer et al., 2005). VEGF165 WT expression in these cells was expected to result in autocrine KDR activation and transformation, whereas VEGF165 3S was expected to lack KDR activating ability and have no effect on phenotype. Ectopic VEGF protein production by transfectants was measured using a 2-site immunoassay with a 1.5 pM detection limit. Marker selected cultures of WT transfectants produced ~1.0 ng/ml/24 hr VEGF165 protein in conditioned media, 3S transfectants produced ~2.5 ng/ml/24 hr, and VEGF protein was undetectable in vector control media (Figure 6A). Like VEGF165 WT, VEGF 3S dimers and monomers of expected mass were detected under nonreducing and reducing conditions, respectively (Figure 6B). Saturation binding of VEGF165 3S to KDR in vitro (Figure 6C, squares; K_D ~19 pM) was equivalent to VEGF165 WT binding (Figure 6C, circles; K_D ~23 pM) and consistent with published values (Ferrara, 2004).

KDR autophosphorylation in each cell line was measured after 24 hr of serum deprivation (Figure 6D). The basal KDR phosphorylation level in empty vector transfectants (Figure 6D, white bar) was similar to that of the parental cell line (not shown) and 3S transfectants (Figure 6D, dark gray bar). In contrast, WT transfectant basal KDR phosphorylation level was 4-fold higher than control or 3S (Figure 6D, light gray bar; $p < 0.001$). The KDR autophosphorylation level of the vector transfectant after 20 min exposure to added VEGF165 protein (2.5 nM) is shown for reference (Figure 6D, black bar).

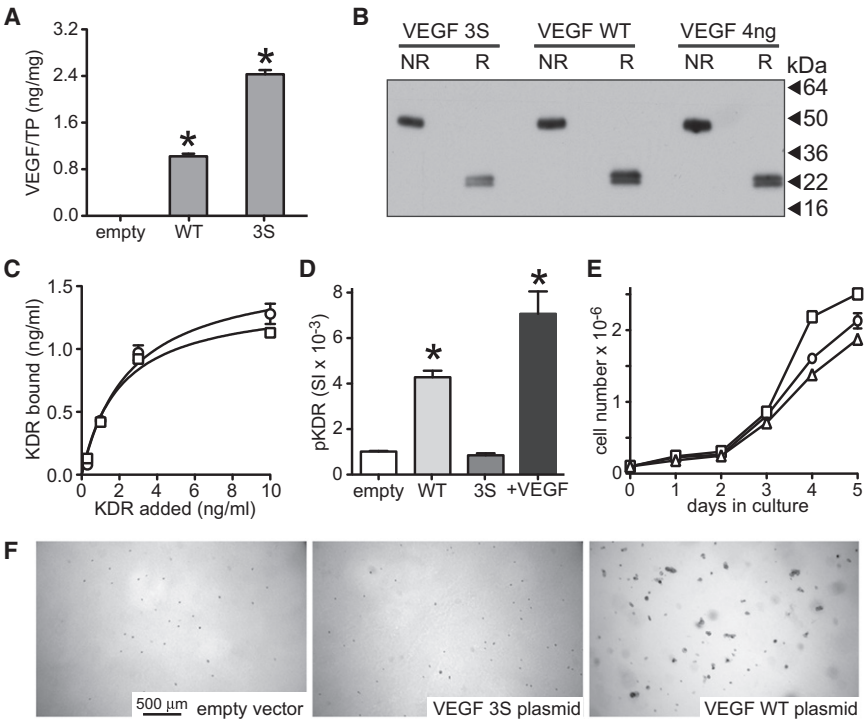

Figure 6. VEGF165 3S Dimer Binds KDR Normally but Does Not Signal

(A) Mean VEGF165 content (ng/mg total cell protein ± SD; n = 3) in 24 hr conditioned media prepared from 293/KDR cells transfected with empty vector (empty), VEGF165 WT (WT), or VEGF165 3S (3S). Asterisks indicate significant differences from vector control ($p < 0.01$).

(B) VEGF165 3S (VEGF 3S; left) and VEGF165 WT (VEGF WT; middle) proteins in 24 hr conditioned media prepared from 293/KDR transfectants and purified recombinant VEGF165 protein (VEGF 4 ng; right) after SDS-PAGE under nonreducing (NR) and reducing (R) conditions and immunoblotting with anti-VEGF. Migration of molecular mass standards (kDa) is indicated by arrows.

(C) Saturation binding of KDR ectodomain-IgG fusion protein to VEGF165 WT (squares) or VEGF165 3S proteins (circles) in vitro. Values are mean KDR bound (ng/ml ± SD; n = 3).

(D) Mean phospho-KDR level (signal intensity ± SD; n = 3) in 293/KDR cells transfected with empty vector (empty; unfilled bar), VEGF165 WT (WT; light gray bar), VEGF165 3S (3S; dark gray bar), or empty vector cells treated with purified VEGF165 WT protein (2.5 nM) for 20 min (+VEGF; black bar). Asterisks indicate significant differences from empty vector control ($p < 0.01$).

(E) Growth rate (mean cell number ± SD; n = 3) of cultured 293/KDR cells transfected with empty vector (circles), VEGF165 WT (squares), or VEGF165 3S (triangles).

(F) Soft agar colony formation by 239/KDR cells transfected with empty vector, (left), VEGF 3S (middle), or VEGF WT (right).

Consistent with the levels of KDR activation among the transfectants, significant differences in cell proliferation rate were observed from day 3 onward: WT transfectants (Figure 6E, squares) grew significantly faster than the vector control (Figure 6E, circles) or 3S transfectants (Figure 6E, triangles; $p < 0.001$ between WT and control or WT and 3S for days 3–5). These results indicated that WT transfectants, but not 3S transfectants, had acquired autocrine VEGF signaling, even though 3S protein production was twice that of WT. In soft agar colony formation assays, empty vector and 3S transfectants grew modestly, if at all (Figure 6F, left and middle panels), whereas WT transfectants grew robustly (Figure 6F, right panel). All of these results indicated loss of signaling by VEGF165 3S despite native KDR binding.

VEGF165 3S also antagonized VEGF165 WT signaling in intact cells. Concentrated conditioned media harvested from 3S transfectants was added to 293/KDR cells in the presence of purified VEGF165 WT protein and phospho-KDR levels were measured (Figures 7A and 7B). Since the conditioned media could contain other inhibitors of KDR activation, VEGF165 3S was selectively removed from the media by immunodepletion with anti-VEGF antibody. A mock immunodepletion was performed in parallel using a nonspecific antibody and the VEGF165 3S content of the anti-VEGF, and mock-immunodepleted media was measured (Figure 7A). VEGF 3S levels in nonimmunodepleted and mock-immunodepleted media were similar (1.93 and 1.89 ng/mg total cell protein, respectively; Figure 7A, white bars), while immunodepletion with anti-VEGF removed 95% of the 3S protein (0.096 ng/mg total cell protein; Figure 7A, gray bar). VEGF was not detected in media from empty vector transfectants before or after immunodepletion (Figure 7A, right). KDR autophosphorylation stimulated by purified VEGF165 protein (10 ng/ml) in serum-deprived 293/KDR cells (Figure 7B) was inhibited modestly by VEGF-immunodepleted media (Figure 7B, circles), but mock-immunodepleted media showed significant, dose-dependent inhibition, with >80% inhibition by media containing 2.5-fold molar excess VEGF 3S protein (Figure 7B, triangles). In soft agar colony formation assays, robust growth of 293/KDR cells transfected with VEGF165 WT (Figure 7C, upper left panel) was inhibited in a dose-dependent manner by the VEGFR inhibitor pazopanib (Figure 7C, middle and right upper panels), providing additional evidence that colony formation was driven by autocrine VEGF/KDR signaling. VEGF165 3S protein added at 0.06, 0.15, and 0.6 nM also resulted in significant, dose-dependent inhibition (Figure 7C, lower panels).

Analysis of the spectrum of VEGF 3S antagonism showed that VEGF165 3S inhibited placenta growth factor (PlGF)-induced Akt activation (phospho-Akt/total Akt) in EA.hy 926 cells, which express VEGFR1 and R2, with potency similar to pazopanib (Figure 7D). In contrast, VEGF 3S did not block Akt activation induced by VEGF-D in SCC-25 cells, which express VEGFR1, R2, and R3 (Figures S5A and S5B). Thus, the pattern of VEGF 3S inhibition followed the pattern of VEGF-A binding to VEGFR1 and R2 but not homodimers of VEGFR3, as anticipated (Ferrara, 2004).

VEGF165 3S antagonism was independent of NRP1-VEGF-A protein-protein interaction. NRP1 binds to the VEGF-A HS

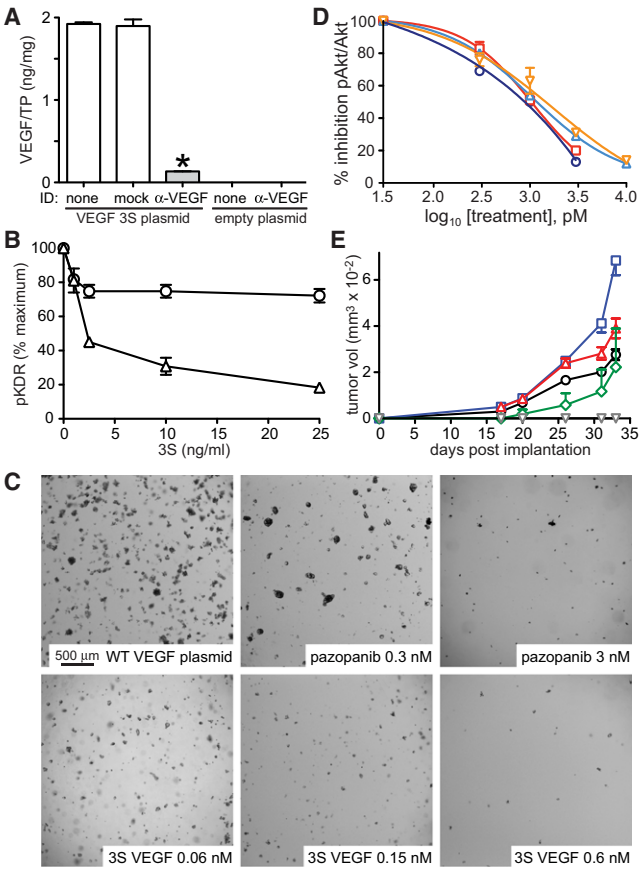

Figure 7. VEGF165 3S Antagonizes VEGFR Activation, Colony Formation, and Tumorigenesis

(A) VEGF165 content in media conditioned by 293/KDR cells transfected with VEGF165 3S (left) or empty plasmid (right), before ("none") or after immunodepletion by anti-VEGF-A ("α-VEGF") or an unrelated control antibody ("mock"), expressed as mean ng/mg total protein ± SD (n = 3). Asterisk indicates significant difference from media prior to immunodepletion ($p < 0.01$).

(B) Phospho-KDR levels (% maximum, ± SD; n = 3) in serum-deprived 293/KDR cells treated with VEGF165 WT (10 ng/ml) in the presence of concentrated conditioned media from 293/KDR VEGF 3S transfectants that were immunodepleted using a nonspecific control antibody (triangles) or anti-VEGF (circles). The x axis indicates VEGF165 3S concentration (ng/ml) in conditioned media before immunodepletion.

(C) Soft agar colony formation by 239/KDR cells expressing VEGF165 WT (upper left panel), cells treated with the indicated concentrations of pazopanib (upper middle and right panels), or cells treated with media containing the indicated concentrations of VEGF165 3S (lower panels).

(D) Dose-dependent inhibition of VEGF- or PlGF-induced Akt activation (mean % inhibition phospho-Akt/total Akt ± SD) in EA.hy 926 cells. VEGF 3S blocked Akt activation by VEGF-A (dark blue circles) or PlGF (red squares) with potency similar to pazopanib (light blue triangles and yellow inverted triangles, respectively).

(E) Mean tumor volume (mm^3 ± SD) in mice (n = 5/group) implanted with 293/KDR cells (3×10^6 cells per animal) expressing VEGF165 3S (gray inverted triangles), VEGF165 WT (blue squares), or empty vector (black circles) at the indicated times postimplantation. Other groups were implanted with a mixture of empty vector cells and VEGF165 WT transfectants at 1.5×10^6 cells each (red triangles) or a mixture of VEGF165 WT and VEGF165 3S transfectants at 1.5×10^6 cells each (green diamonds).

See also Figure S5.

binding domain primarily at R165 and secondarily at K147, E152, and E155 (Parker et al., 2012), i.e., to a surface opposite that of HS (Figure S5C). Crosslinking studies further showed that VEGF165 WT and VEGF165 3S bound similarly to NRP1 in vitro (Figure S5D). Functionally, VEGF165 3S antagonized VEGF signaling similarly in 293/KDR derived cells (Figures 7B, 7C, and 7E), which lack NRP1 (Figure S5E, lanes 4–6), and in EA.hy 926 cells (Figure 7D), which are NRP1 positive (Figure S5E, lane 2). The NRP1 present in our experiments was not HS modified, which is thought to promote NRP1 multimerization and, in turn, NRP1-VEGFR2 binding and signaling (Shintani et al., 2006). Like NK1, we found that heparin promoted clustering of VEGF165 WT, but not of VEGF165 3S (Figure S5F). Thus, if HS-modified NRP1 enhances VEGF signaling in part by promoting VEGF clustering, VEGF165 3S would be expected to antagonize that process.

VEGF 3S Inhibits VEGF-Driven Tumor Growth and Angiogenesis In Vivo

To test whether VEGF165 3S protein could antagonize KDR-driven tumorigenicity in mice, animals were implanted subcutaneously with VEGF165 WT transfected 293/KDR cells (3×10^6 per animal), with the same number of VEGF165 3S transfected cells or with a suspension containing 1.5×10^6 cells of each line. Additional control groups received the empty vector 293/KDR cells (3×10^6 per animal) or the empty vector cells combined with VEGF WT transfectants at 1.5×10^6 cells each. The latter group indicated the growth rate of tumors arising from 1.5×10^6 VEGF WT transfectants in the presence of "neutral" cells providing the same initial mass; a growth rate below this threshold in the group implanted with VEGF WT + VEGF 3S transfectants could be attributed to inhibition of VEGF WT-driven tumor growth by VEGF165 3S. Indeed, VEGF WT transfected 293/KDR cells formed tumors fastest (Figure 7D, blue squares), whereas VEGF 3S transfectants did not form tumors prior to study termination (Figure 7D, gray inverted triangles), and animals implanted with the WT + 3S cell mix (Figure 7D, green diamonds) formed tumors at a significantly lower rate than the control WT + empty vector group (Figure 7D, red triangles) throughout the study ($p < 0.05$).

Tumorigenesis by the parental cell line, despite its inability to grow in soft agar, indicated that it was driven by host VEGF. This conclusion is supported by prior work where the generation of knockin mice expressing a humanized form of VEGF-A was needed to overcome incomplete suppression of human tumor xenograft growth by antihuman VEGF-A antibodies that did not block murine VEGF activity (Gerber et al., 2007). Therefore, the failure of the 3S transfectants to form tumors indicates VEGF 3S antagonism of tumorigenesis driven by murine VEGF. Moreover, significant inhibition of tumor growth by VEGF165 3S in animals receiving the WT + 3S transfectant cell mix indicates antagonism of the combined impact of paracrine murine VEGF and autocrine human VEGF.

Tumor angiogenesis was also significantly blocked in mice receiving VEGF 3S transfected cells (Figure 8). Immunohistochemisty using anti-CD34 showed that the extent of tumor vascularization, from highest to lowest, was 293/KDR/WT VEGF transfectants alone (Figure 8A), 293/KDR/WT VEGF cells + vector transfected 293/KDR cells mixed 1:1 (Figure 8B), vector

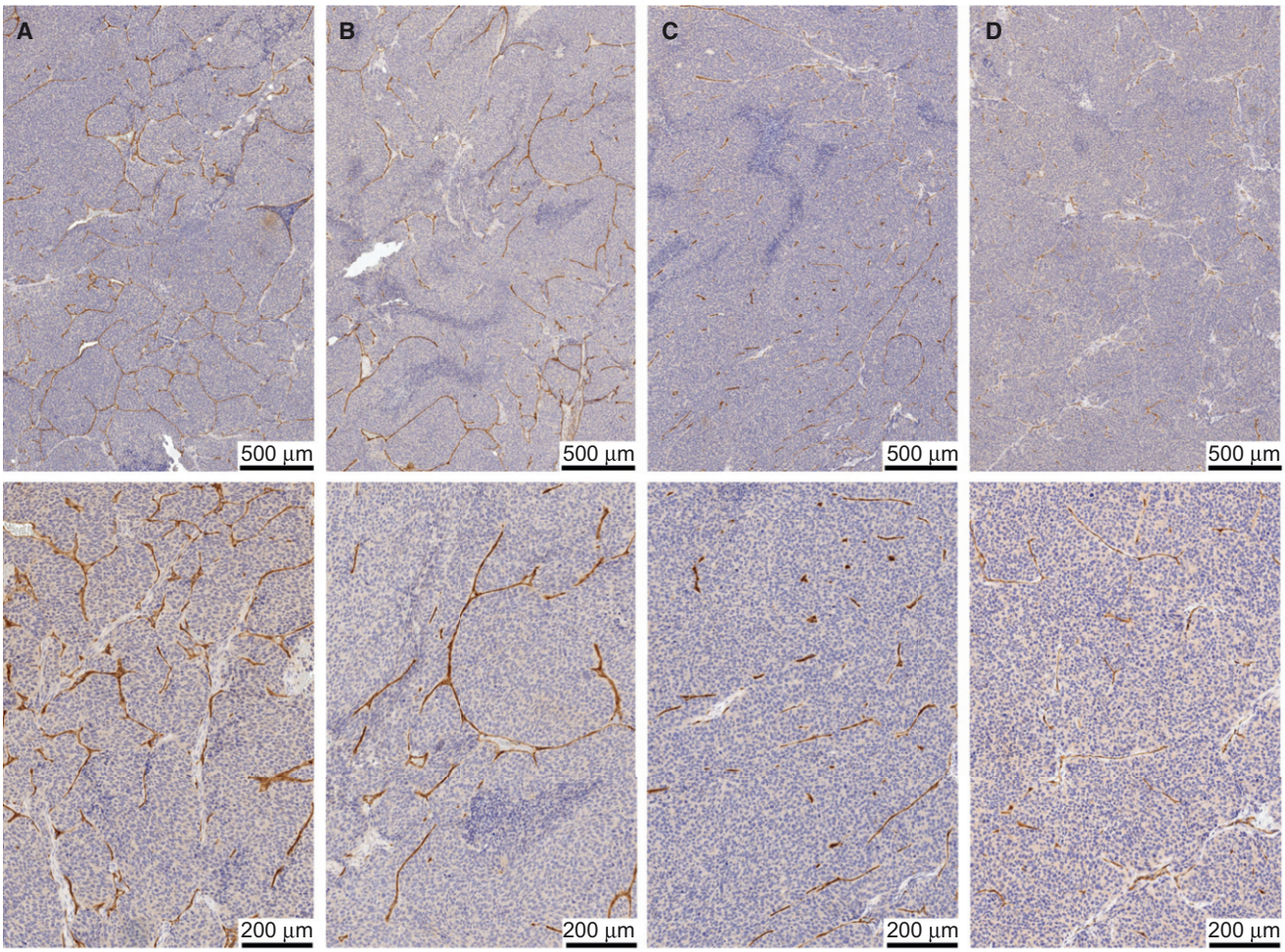

Figure 8. VEGF165 3S Antagonizes VEGF-Driven Tumor Angiogenesis

Murine CD34 immunohistochemical analysis (low magnification above, higher magnification below) of tumors from animal groups as described in Figure 7. (A) 293/KDR/VEGF WT cell tumors; (B) 293/KDR/VEGF WT + control 293/KDR cell (1:1) tumors; (C) control 293/KDR cell tumors; (D) 293/KDR/VEGF WT + 293/KDR/VEGF 3S cell (1:1) tumors.

transfectants alone (Figure 8C), and 293/KDR/WT VEGF + 293/KDR/3S VEGF transfectants mixed 1:1 (Figure 8D). This pattern is consistent with tumor angiogenesis driven by both autocrine human and paracrine murine VEGF (Figures 8A and 8B) relative to tumor angiogenesis driven by murine VEGF alone (Figure 8C) and with substantial inhibition of tumor angiogenesis by VEGF 3S (Figure 8D).

Histopathology analysis indicated that the tumors formed by 293/KDR cell transfectants (vector, VEGF WT, VEGF WT + vector, VEGF WT + VEGF 3S) were uniformly carcinoma. Full necropsy analysis of all tissue and organs showed no signs of toxicity or damage in any tissue from mice implanted with 293/KDR transfectants.

DISCUSSION

Our work builds on several prior studies showing that HS-HGF interaction is critical for HGF signaling (Hartmann et al., 1998; Lietha et al., 2001; Sakata et al., 1997; Schwall et al., 1996; Zioncheck et al., 1995). The loss of biological activity by combined substitution of K60, K62, and R73 with acidic residues identifies this surface region as essential for NK1 biological signaling and implies that HS binding at secondary sites is insufficient for NK1 signaling. The partial loss of activity associated with substitutions at 73 and 60/62 suggests that each contribute to HS interactions at this site. Our results further indicate that HS-NK1 interactions promote receptor activation and signaling by enhancing NK1-Met interaction and by stabilizing NK1 multimers, which may in turn facilitate receptor clustering, kinase activation, and effector recruitment (Gherardi et al., 2006; Hartmann et al., 1998; Lietha et al., 2001; Sakata et al., 1997; Schwall et al., 1996; Tolbert et al., 2010).

We believe that three critical features define the mechanism of HGF inhibition by NK1 3S: (1) retention of optimal N domain-Met binding through negative charge substitutions in NK1 3S that mimic occupancy of the primary HS binding site; a prior report provides structural evidence to this effect (Tolbert et al., 2010), (2) repulsion of HS from the ligand-receptor complex by the negative charge substitutions, and (3) competitive displacement of HGF from Met by the native K1 domain of NK1 3S. We propose

that occupancy of the primary ligand binding site in Met without HS support of ligand-Met complex clustering and associated conformational changes results in a signaling blockade.

In addition to its value as a research tool, NK1 3S may have therapeutic potential. The critical role of HGF-Met signaling in a variety of human cancers has made Met an important anticancer drug target. Met blockade has been achieved using ATP binding site antagonists, neutralizing antibodies, decoy receptors, single-chain HGF derivatives (Cecchi et al., 2010), synthetic HS mimetics (Fuster and Esko, 2005), and engineered NK1 forms affecting the dimerization interface in K1 (Tolbert et al., 2010; Youles et al., 2008). Like the latter, NK1 3S blocks signaling by disrupting ligand dimer/multimer formation, but unlike those mutants it does so by blocking HS facilitation of that process. Each of these approaches has advantages as well as limitations. Our choice to develop NK1 instead of full-length HGF is based on the complexity of HGF protein and the technical obstacles this imposes on its manufacture. The challenges of administering large HGF-derived antagonists, such as NK4 and uncleavable pro-HGF, have been met by using viral vectors or naked DNA plasmids (Cecchi et al., 2010). These methods can provide sustained delivery but do not allow the level of control inherent in administering the encoded proteins. NK1 can be expressed in *P. pastoris* at yields high enough (>1 g/l) to be commercially tractable. Our results support the efficacy of systemically delivered NK1 3S protein as an antitumor and antimetastatic agent as well as its practicality as an alternative to larger HGF-derived antagonists.

We find that VEGF165 3S binds KDR-like VEGF165 WT protein, fails to induce KDR kinase activity, and antagonizes VEGF165 WT binding and signaling in vitro and in vivo. A critical distinction between VEGF165 3S and alanine substitutions made at these positions (Krilleke et al., 2007), or the VEGF isoform VEGF121, is that the opposite charge substitutions in VEGF 3S are designed to repel HS and thereby disrupt both ligand-HS and weaker receptor-HS interactions. The striking parallels in antagonism by 3S forms of NK1 and VEGF165 strengthen our assertion of a common role for HS in receptor activation and show that targeted disruption of critical HS binding sites is an antagonist development strategy that can be extended to other HS-binding growth factors. Consistent with findings for NK1, VEGF-HS interaction occurs through sulfated HS side-chains and three key VEGF residues, with secondary contributions from one or two others (Krilleke et al., 2007). The analogous roles of HS in NK1/Met and VEGF165/KDR signaling, in the absence of underlying structural similarity, suggests that this occurs through convergent evolution. Thus, any similarity in the spatial arrangement of the primary HS binding site surfaces themselves would be driven by adaptation to the common binding partner, HS, as opposed to a common ancestral protein sequence or structure.

The present understanding of KDR activation by VEGF165 and HS suggests a mechanistic basis for signaling antagonism by the targeted disruption of HS-ligand binding. The VEGF binding site in KDR encompasses IgG-like domains (D) 1–3: D2 contains primary contacts, and D1 and D3 contribute to overall binding affinity and specificity (Christinger et al., 2004; Fuh et al., 1998). Consistent with findings presented here for NK1, HS was found to be required for high-affinity binding of VEGF165 to KDR ectopically expressed in HS-negative CHO 745 cells (Dougher et al., 1997). Similar to Met (Rubin et al., 2001) and FGF receptors (Mohammadi et al., 2005), KDR also interacts directly with HS through at least one site located between D6 and D7 (Dougher et al., 1997). Recent structural studies of KIT, PDGFR, and VEGFR highlight the importance of homotypic receptor-receptor interaction domains in stabilizing receptor dimerization and kinase transactivation: direct contacts between D4 domains for KIT and D7 domains for KDR are enabled by ligand-induced conformational changes in the receptor ectodomain (Lemmon and Schlessinger, 2010; Tao et al., 2001; Yang et al., 2010). In these models, sequential binding events promote and incrementally stabilize HS-ligand-receptor aggregates capable of signaling. We hypothesize that VEGF165 first binds KDR D2; the weaker VEGF165 D1 and VEGF165 D3 interactions may be stabilized by HS-VEGF interaction and by HS-VEGF-KDR bridging at D6/D7. For VEGF165 3S, receptor binding at D2 should occur, but subsequent weaker interactions normally stabilized by HS and induced changes in receptor conformation could fail. VEGF-HS interactions may also induce conformational changes that enable the apposition of KDR D7 domains (Wijelath et al., 2010) and, in turn, homotypic interaction and kinase transactivation; VEGF165 3S is likely to disrupt such events. The role of NRP1 in VEGF signaling is complex, involving protein-protein interactions and protein-HS interactions when NRP1 is HS modified (Shintani et al., 2006). VEGF165 3S engages NRP1 via the former, but would be expected to disrupt the latter. Collectively, our observations underscore the importance of specific HS interactions in facilitating events after ligand binding, which are required for KDR activation, and expose their susceptibility to targeted disruption.

HS binding growth factors promote tumor growth, angiogenesis, and metastasis in a variety of human cancers. In addition to the strategy described here, oligosaccharide HS mimetics and modified heparin fragments can act as HS binding antagonists (Fuster and Esko, 2005). However, the complexity of HS GAGs challenges the development of potent and selective agents, and frequent alterations in HS GAG composition in tumors (Fuster and Esko, 2005) may render such agents less competitive for ligand binding. In contrast, opposite substitutions to critical HS binding residues in an otherwise wild-type protein ligand are simple to introduce, unaffected by tumor HS GAG composition, and inherently pathway selective. These features suggest that it may be an expedient and practical route for the development of antagonists of HS binding growth factors.

EXPERIMENTAL PROCEDURES

Reagents and Cell Culture

See Supplemental Information.

Plasmids for NK1 and VEGF165, Protein Expression, and Purification

NK1 proteins were produced in *E. coli* as described (Stahl et al., 1997). Plasmids for expression of NK1 3S, NK1 WT, VEGF165 WT, and VEGF165 3S under cytomegalovirus promoters possess their native signal peptide sequences and G418 resistance. Plasmids for *P. pastoris* expression of NK1 proteins were generated and protein purified as described in Supplemental Information.

NMR Structural Analysis

Isotope-labeled proteins were expressed *E. coli* in minimal media containing either $^{15}NH_4Cl$ or both $^{15}NH_4Cl$ and ^{13}C-labeled glucose. Triple-labeled

proteins ($^{15}N/^{13}C/^{2}H$) were prepared similarly, except the media contained 98% D_2O. ^{1}H-^{15}N correlation spectra for substituted and WT NK1 proteins were collected as described (Zhou et al., 1999). NK1 backbone resonance assignments were made using $^{15}N/^{13}C/^{2}H$-NK1 and standard triple resonance experiments.

Immunoassays and Binding Assays

Met, KDR, HGF, and VEGF content in cell lysates, tissue extracts, and conditioned media was determined using 2-site immunoassays developed for use with the Meso Scale Discovery (MSD) SectorImager 2400 plate reader; HGF and Met assays are described in Supplemental Information; other assays were from MSD. Met and KDR activation in cell lysates or tumor tissue extracts included parallel detection with antireceptor antibodies and specific antiphospho-receptor antibodies or 4G10 (Millipore).

Binding assays were also performed on the MSD platform. NK1 saturation binding to immobilized Met ectodomain-IgG fusion protein was measured using Ru tagged WT or 3S ligand. Displacement experiments included multiple untagged ligand concentrations in the presence of Ru tagged ligand. NK1-HS saturation binding to immobilized heparin-biotin was measured using Ru tagged NK1 WT or 3S proteins. KDR-Ig ectodomain saturation binding to immobilized VEGF165 WT or 3S was measured using Ru tagged anti-KDR. All measurements were made on triplicate samples. GraphPad Prism v5.0 was used for all statistical analyses. Additional details are included in Supplemental Information.

Cell Motility, Mitogenesis, and Colony Formation Assays

Cell motility in modified Boyden chambers and DNA synthesis by [^{3}H]thymidine incorporation were measured as described (Rubin et al., 2001). MDCK cell scatter was assessed as described (Stahl et al., 1997). U87 MG or 293/KDR derived cell line proliferation in quadruplicate wells of 6-well plates was measured by counting in a Cellometer (Nexcelom Bioscience). Assays for colony formation in soft agar were performed as described (Castagnino et al., 2000). Differences between mean values were determined by t test using GraphPad Prism v5.0.

Tumorigenesis, Metastasis, and Pharmacokinetic Assays

Experiments with SCID/beige mice were performed in accordance with National Institutes of Health (NIH) Guidelines for Care and Use of Laboratory Animals using protocols approved by the Institutional Animal Care and Use Committee of the Center for Cancer Research, National Cancer Institute. Details for all animal studies are included in Supplemental Information. Briefly, U87 MG, SK-LMS-1, or 293/KDR derived cell lines were injected subcutaneously into mice, and tumor volumes were calculated from caliper measurements. 293/KDR cell derived tumors were harvested at study termination for histopathology and immunohistochemical analysis of murine CD34 protein localization. B16-luc derived cells for induced metastasis studies were injected through the tail vein; in some studies, mice also received daily i.p. injections of purified NK1 3S (or vehicle) at doses indicated in the text. For spontaneous metastasis studies, PC3M-luc cells were implanted subcutaneously, and mice were treated by i.p. injection of vehicle or NK1 3S starting on day 5. Metastatic burden was determined by luciferase imaging. Plasma NK1 3S levels were measured in mice after a single i.p. injection of NK1 3S at the indicated times postinjection. NK1 protein was analyzed by SDS-PAGE and immunoblotting. Statistical analysis, curve fitting, and IC_{50} determinations were performed using GraphPad Prism v5.0.

SUPPLEMENTAL INFORMATION

Supplemental Information includes two tables, five figures, and Supplemental Experimental Procedures and can be found with this article online at http://dx.doi.org/10.1016/j.ccr.2012.06.029.

ACKNOWLEDGMENTS

This research was supported by the Intramural Research Program of the NIH, National Cancer Institute, Center for Cancer Research. We thank the late Dr. Ralph Schwall for recombinant Met-Ig fusion protein; Dr. Jeffrey Esko for CHO 745 cells; Drs. Dominic Esposito, Troy Taylor, and William Gillette for plasmid and protein production and purification; and Drs. Miriam Anver, Lawrence Sternberg, and Roberta Smith for pathology, immunohistochemistry analysis, and clinical chemistry analyses.

Received: October 18, 2011
Revised: April 4, 2012
Accepted: June 26, 2012
Published: August 13, 2012

REFERENCES

Appleton, B.A., Wu, P., Maloney, J., Yin, J., Liang, W.C., Stawicki, S., Mortara, K., Bowman, K.K., Elliott, J.M., Desmarais, W., et al. (2007). Structural studies of neuropilin/antibody complexes provide insights into semaphorin and VEGF binding. EMBO J. *26*, 4902–4912.

Backer, M.V., Gaynutdinov, T.I., Patel, V., Bandyopadhyaya, A.K., Thirumamagal, B.T., Tjarks, W., Barth, R.F., Claffey, K., and Backer, J.M. (2005). Vascular endothelial growth factor selectively targets boronated dendrimers to tumor vasculature. Mol. Cancer Ther. *4*, 1423–1429.

Boccaccio, C., and Comoglio, P.M. (2006). Invasive growth: a MET-driven genetic programme for cancer and stem cells. Nat. Rev. Cancer *6*, 637–645.

Carmeliet, P., Ng, Y.S., Nuyens, D., Theilmeier, G., Brusselmans, K., Cornelissen, I., Ehler, E., Kakkar, V.V., Stalmans, I., Mattot, V., et al. (1999). Impaired myocardial angiogenesis and ischemic cardiomyopathy in mice lacking the vascular endothelial growth factor isoforms VEGF164 and VEGF188. Nat. Med. *5*, 495–502.

Castagnino, P., Lorenzi, M.V., Yeh, J., Breckenridge, D., Sakata, H., Munz, B., Werner, S., and Bottaro, D.P. (2000). Neu differentiation factor/heregulin induction by hepatocyte and keratinocyte growth factors. Oncogene *19*, 640–648.

Cecchi, F., Rabe, D.C., and Bottaro, D.P. (2010). Targeting the HGF/Met signalling pathway in cancer. Eur. J. Cancer *46*, 1260–1270.

Chirgadze, D.Y., Hepple, J.P., Zhou, H., Byrd, R.A., Blundell, T.L., and Gherardi, E. (1999). Crystal structure of the NK1 fragment of HGF/SF suggests a novel mode for growth factor dimerization and receptor binding. Nat. Struct. Biol. *6*, 72–79.

Christinger, H.W., Fuh, G., de Vos, A.M., and Wiesmann, C. (2004). The crystal structure of placental growth factor in complex with domain 2 of vascular endothelial growth factor receptor-1. J. Biol. Chem. *279*, 10382–10388.

Dougher, A.M., Wasserstrom, H., Torley, L., Shridaran, L., Westdock, P., Hileman, R.E., Fromm, J.R., Anderberg, R., Lyman, S., Linhardt, R.J., et al. (1997). Identification of a heparin binding peptide on the extracellular domain of the KDR VEGF receptor. Growth Factors *14*, 257–268.

Favier, B., Alam, A., Barron, P., Bonnin, J., Laboudie, P., Fons, P., Mandron, M., Herault, J.P., Neufeld, G., Savi, P., et al. (2006). Neuropilin-2 interacts with VEGFR-2 and VEGFR-3 and promotes human endothelial cell survival and migration. Blood *108*, 1243–1250.

Ferrara, N. (2004). Vascular endothelial growth factor: basic science and clinical progress. Endocr. Rev. *25*, 581–611.

Fuh, G., Li, B., Crowley, C., Cunningham, B., and Wells, J.A. (1998). Requirements for binding and signaling of the kinase domain receptor for vascular endothelial growth factor. J. Biol. Chem. *273*, 11197–11204.

Fuster, M.M., and Esko, J.D. (2005). The sweet and sour of cancer: glycans as novel therapeutic targets. Nat. Rev. Cancer *5*, 526–542.

Gerber, H.P., Wu, X., Yu, L., Wiesmann, C., Liang, X.H., Lee, C.V., Fuh, G., Olsson, C., Damico, L., Xie, D., et al. (2007). Mice expressing a humanized form of VEGF-A may provide insights into the safety and efficacy of anti-VEGF antibodies. Proc. Natl. Acad. Sci. USA *104*, 3478–3483.

Gherardi, E., Sandin, S., Petoukhov, M.V., Finch, J., Youles, M.E., Ofverstedt, L.G., Miguel, R.N., Blundell, T.L., Vande Woude, G.F., Skoglund, U., and Svergun, D.I. (2006). Structural basis of hepatocyte growth factor/scatter factor and MET signalling. Proc. Natl. Acad. Sci. USA *103*, 4046–4051.

Gluzman-Poltorak, Z., Cohen, T., Herzog, Y., and Neufeld, G. (2000). Neuropilin-2 is a receptor for the vascular endothelial growth factor (VEGF) forms VEGF-145 and VEGF-165 [corrected]. J. Biol. Chem. *275*, 18040–18045.

Hartmann, G., Prospero, T., Brinkmann, V., Ozcelik, C., Winter, G., Hepple, J., Batley, S., Bladt, F., Sachs, M., Birchmeier, C., et al. (1998). Engineered mutants of HGF/SF with reduced binding to heparan sulphate proteoglycans, decreased clearance and enhanced activity in vivo. Curr. Biol. *8*, 125–134.

Kinosaki, M., Yamaguchi, K., Murakami, A., Ueda, M., Morinaga, T., and Higashio, K. (1998). Identification of heparin-binding stretches of a naturally occurring deleted variant of hepatocyte growth factor (dHGF). Biochim. Biophys. Acta *1384*, 93–102.

Krilleke, D., DeErkenez, A., Schubert, W., Giri, I., Robinson, G.S., Ng, Y.S., and Shima, D.T. (2007). Molecular mapping and functional characterization of the VEGF164 heparin-binding domain. J. Biol. Chem. *282*, 28045–28056.

Lemmon, M.A., and Schlessinger, J. (2010). Cell signaling by receptor tyrosine kinases. Cell *141*, 1117–1134.

Lietha, D., Chirgadze, D.Y., Mulloy, B., Blundell, T.L., and Gherardi, E. (2001). Crystal structures of NK1-heparin complexes reveal the basis for NK1 activity and enable engineering of potent agonists of the MET receptor. EMBO J. *20*, 5543–5555.

Lokker, N.A., Presta, L.G., and Godowski, P.J. (1994). Mutational analysis and molecular modeling of the N-terminal kringle-containing domain of hepatocyte growth factor identifies amino acid side chains important for interaction with the c-Met receptor. Protein Eng. *7*, 895–903.

Lyon, M., Deakin, J.A., and Gallagher, J.T. (2002). The mode of action of heparan and dermatan sulfates in the regulation of hepatocyte growth factor/scatter factor. J. Biol. Chem. *277*, 1040–1046.

Lyon, M., Deakin, J.A., Lietha, D., Gherardi, E., and Gallagher, J.T. (2004). The interactions of hepatocyte growth factor/scatter factor and its NK1 and NK2 variants with glycosaminoglycans using a modified gel mobility shift assay. Elucidation of the minimal size of binding and activatory oligosaccharides. J. Biol. Chem. *279*, 43560–43567.

Matsumoto, K., and Nakamura, T. (1996). Emerging multipotent aspects of hepatocyte growth factor. J. Biochem. *119*, 591–600.

Michalopoulos, G.K. (2007). Liver regeneration. J. Cell. Physiol. *213*, 286–300.

Mizuno, K., Inoue, H., Hagiya, M., Shimizu, S., Nose, T., Shimohigashi, Y., and Nakamura, T. (1994). Hairpin loop and second kringle domain are essential sites for heparin binding and biological activity of hepatocyte growth factor. J. Biol. Chem. *269*, 1131–1136.

Mohammadi, M., Olsen, S.K., and Ibrahimi, O.A. (2005). Structural basis for fibroblast growth factor receptor activation. Cytokine Growth Factor Rev. *16*, 107–137.

Okigaki, M., Komada, M., Uehara, Y., Miyazawa, K., and Kitamura, N. (1992). Functional characterization of human hepatocyte growth factor mutants obtained by deletion of structural domains. Biochemistry *31*, 9555–9561.

Orian-Rousseau, V., Chen, L., Sleeman, J.P., Herrlich, P., and Ponta, H. (2002). CD44 is required for two consecutive steps in HGF/c-Met signaling. Genes Dev. *16*, 3074–3086.

Parker, M.W., Xu, P., Li, X., and Vander Kooi, C.W. (2012). Structural basis for the selective vascular endothelial growth factor-A (VEGF-A) binding to neuropilin-1. J. Biol. Chem. *2012*, 7.

Peschard, P., and Park, M. (2007). From Tpr-Met to Met, tumorigenesis and tubes. Oncogene *26*, 1276–1285.

Robinson, C.J., and Stringer, S.E. (2001). The splice variants of vascular endothelial growth factor (VEGF) and their receptors. J. Cell Sci. *114*, 853–865.

Rubin, J.S., Day, R.M., Breckenridge, D., Atabey, N., Taylor, W.G., Stahl, S.J., Wingfield, P.T., Kaufman, J.D., Schwall, R., and Bottaro, D.P. (2001). Dissociation of heparan sulfate and receptor binding domains of hepatocyte growth factor reveals that heparan sulfate-c-met interaction facilitates signaling. J. Biol. Chem. *276*, 32977–32983.

Sakata, H., Stahl, S.J., Taylor, W.G., Rosenberg, J.M., Sakaguchi, K., Wingfield, P.T., and Rubin, J.S. (1997). Heparin binding and oligomerization of hepatocyte growth factor/scatter factor isoforms. Heparan sulfate glycosaminoglycan requirement for Met binding and signaling. J. Biol. Chem. *272*, 9457–9463.

Sarrazin, S., Lamanna, W.C., and Esko, J.D. (2011). Heparan sulfate proteoglycans. Cold Spring Harb. Perspect. Biol. *3*, 1–33.

Schwall, R.H., Chang, L.Y., Godowski, P.J., Kahn, D.W., Hillan, K.J., Bauer, K.D., and Zioncheck, T.F. (1996). Heparin induces dimerization and confers proliferative activity onto the hepatocyte growth factor antagonists NK1 and NK2. J. Cell Biol. *133*, 709–718.

Shintani, Y., Takashima, S., Asano, Y., Kato, H., Liao, Y., Yamazaki, S., Tsukamoto, O., Seguchi, O., Yamamoto, H., Fukushima, T., et al. (2006). Glycosaminoglycan modification of neuropilin-1 modulates VEGFR2 signaling. EMBO J. *25*, 3045–3055.

Stahl, S.J., Wingfield, P.T., Kaufman, J.D., Pannell, L.K., Cioce, V., Sakata, H., Taylor, W.G., Rubin, J.S., and Bottaro, D.P. (1997). Functional and biophysical characterization of recombinant human hepatocyte growth factor isoforms produced in Escherichia coli. Biochem. J. *326*, 763–772.

Stamos, J., Lazarus, R.A., Yao, X., Kirchhofer, D., and Wiesmann, C. (2004). Crystal structure of the HGF β-chain in complex with the Sema domain of the Met receptor. EMBO J. *23*, 2325–2335.

Tao, Q., Backer, M.V., Backer, J.M., and Terman, B.I. (2001). Kinase insert domain receptor (KDR) extracellular immunoglobulin-like domains 4-7 contain structural features that block receptor dimerization and vascular endothelial growth factor-induced signaling. J. Biol. Chem. *276*, 21916–21923.

Tolbert, W.D., Daugherty, J., Gao, C., Xie, Q., Miranti, C., Gherardi, E., Woude, G.V., and Xu, H.E. (2007). A mechanistic basis for converting a receptor tyrosine kinase agonist to an antagonist. Proc. Natl. Acad. Sci. USA *104*, 14592–14597.

Ultsch, M., Lokker, N.A., Godowski, P.J., and de Vos, A.M. (1998). Crystal structure of the NK1 fragment of human hepatocyte growth factor at 2.0 A resolution. Structure *6*, 1383–1393.

van der Voort, R., Taher, T.E., Wielenga, V.J., Spaargaren, M., Prevo, R., Smit, L., David, G., Hartmann, G., Gherardi, E., and Pals, S.T. (1999). Heparan sulfate-modified CD44 promotes hepatocyte growth factor/scatter factor-induced signal transduction through the receptor tyrosine kinase c-Met. J. Biol. Chem. *274*, 6499–6506.

Wielenga, V.J., van der Voort, R., Taher, T.E., Smit, L., Beuling, E.A., van Krimpen, C., Spaargaren, M., and Pals, S.T. (2000). Expression of c-Met and heparan-sulfate proteoglycan forms of CD44 in colorectal cancer. Am. J. Pathol. *157*, 1563–1573.

Wijelath, E., Namekata, M., Murray, J., Furuyashiki, M., Zhang, S., Coan, D., Wakao, M., Harris, R.B., Suda, Y., Wang, L., and Sobel, M. (2010). Multiple mechanisms for exogenous heparin modulation of vascular endothelial growth factor activity. J. Cell. Biochem. *111*, 461–468.

Yang, Y., Xie, P., Opatowsky, Y., and Schlessinger, J. (2010). Direct contacts between extracellular membrane-proximal domains are required for VEGF receptor activation and cell signaling. Proc. Natl. Acad. Sci. USA *107*, 1906–1911.

Youles, M., Holmes, O., Petoukhov, M.V., Nessen, M.A., Stivala, S., Svergun, D.I., and Gherardi, E. (2008). Engineering the NK1 fragment of hepatocyte growth factor/scatter factor as a MET receptor antagonist. J. Mol. Biol. *377*, 616–622.

Zhou, H., Mazzulla, M.J., Kaufman, J.D., Stahl, S.J., Wingfield, P.T., Rubin, J.S., Bottaro, D.P., and Byrd, R.A. (1998). The solution structure of the N-terminal domain of hepatocyte growth factor reveals a potential heparin-binding site. Structure *6*, 109–116.

Zhou, H., Casas-Finet, J.R., Heath Coats, R., Kaufman, J.D., Stahl, S.J., Wingfield, P.T., Rubin, J.S., Bottaro, D.P., and Byrd, R.A. (1999). Identification and dynamics of a heparin-binding site in hepatocyte growth factor. Biochemistry *38*, 14793–14802.

Zioncheck, T.F., Richardson, L., Liu, J., Chang, L., King, K.L., Bennett, G.L., Fügedi, P., Chamow, S.M., Schwall, R.H., and Stack, R.J. (1995). Sulfated oligosaccharides promote hepatocyte growth factor association and govern its mitogenic activity. J. Biol. Chem. *270*, 16871–16878.

Cancer Cell
Article

Gene-Targeting of *Phd2* Improves Tumor Response to Chemotherapy and Prevents Side-Toxicity

Rodrigo Leite de Oliveira,[1,2,3,4,10] Sofie Deschoemaeker,[1,3,10] Anne-Theres Henze,[1,3] Koen Debackere,[1,3] Veronica Finisguerra,[1,3] Yukiji Takeda,[1,2,3,4] Carmen Roncal,[1,2,3,4,5] Daniela Dettori,[1,2,3,4] Evelyne Tack,[1,3] Yannick Jönsson,[1,3] Lorenzo Veschini,[1,3] Annelies Peeters,[6] Andrey Anisimov,[8] Matthias Hofmann,[9] Kari Alitalo,[8] Myriam Baes,[6] Jan D'hooge,[7] Peter Carmeliet,[2,4] and Massimiliano Mazzone[1,3,*]
[1]Lab of Molecular Oncology and Angiogenesis
[2]Lab of Angiogenesis and Neurovascular Link
Vesalius Research Center, VIB, 3000 Leuven, Belgium
[3]Lab of Molecular Oncology and Angiogenesis
[4]Lab of Angiogenesis and Neurovascular Link, Department of Oncology
Vesalius Research Center, KU Leuven, 3000 Leuven, Belgium
[5]Atherosclerosis Research Laboratory, CIMA-University of Navarra, 31008 Pamplona, Spain
[6]Laboratory of Cell Metabolism
[7]Division of Cardiovascular Imaging and Dynamics
KU Leuven, 3000 Leuven, Belgium
[8]Molecular/Cancer Biology Laboratory, Research Programs Unit, Institute for Molecular Medicine, 00014 Helsinki, Finland
[9]Department of Dermatology, Johann Wolfgang Goethe-University, 60590 Frankfurt am Main, Germany
[10]These authors contributed equally to this work
*Correspondence: massimiliano.mazzone@vib-kuleuven.be
http://dx.doi.org/10.1016/j.ccr.2012.06.028

SUMMARY

The success of chemotherapy in cancer treatment is limited by scarce drug delivery to the tumor and severe side-toxicity. Prolyl hydroxylase domain protein 2 (PHD2) is an oxygen/redox-sensitive enzyme that induces cellular adaptations to stress conditions. Reduced activity of PHD2 in endothelial cells normalizes tumor vessels and enhances perfusion. Here, we show that tumor vessel normalization by genetic inactivation of *Phd2* increases the delivery of chemotherapeutics to the tumor and, hence, their antitumor and antimetastatic effect, regardless of combined inhibition of *Phd2* in cancer cells. In response to chemotherapy-induced oxidative stress, pharmacological inhibition or genetic inactivation of *Phd2* enhances a hypoxia-inducible transcription factor (HIF)-mediated detoxification program in healthy organs, which prevents oxidative damage, organ failure, and tissue demise. Altogether, our study discloses alternative strategies for chemotherapy optimization.

INTRODUCTION

Part of the failure that still escorts cancer treatment is due to the abnormal tumor vasculature, characterized by leaky, tortuous, and fragile vessels; loss of hierarchical architecture; and an abnormal endothelial layer. The resultant hypoxia promotes invasion and metastasis (Carmeliet and Jain, 2011). In addition, hypoperfused vessels and increased interstitial tumor pressure impede the delivery of anticancer drugs to the tumors and thus limit their efficacy (Carmeliet and Jain, 2011).

To date, anti-vascular endothelial growth factor and anti-vascular endothelial growth factor receptor [VEGF(R)] approaches have therefore gained interest as a therapeutic option to improve drug delivery and the overall response to anticancer treatment,

Significance

Chemotherapy remains the most common treatment option for cancer patients. However, dysfunctional blood vessels and severe side effects impede delivery of chemotherapeutic drugs to the tumor, thus limiting their use in the clinic. Traditional antiangiogenic strategies can worsen this situation by hindering tumor perfusion and exacerbating adverse reactions. Here, we identify PHD2 as a molecular target to enhance chemotherapeutic drug delivery to the tumor via vessel normalization and to counter chemotherapy-induced side effects via a HIF-mediated detoxification response. These data unveil an essential role of PHD2 as gatekeeper for oxidative stress, and they warrant caution for considerate use of HIF blockers in cancer in association with chemotherapy. Taken together, our study offers the rationale for developing PHD2 specific inhibitors for cancer therapy.

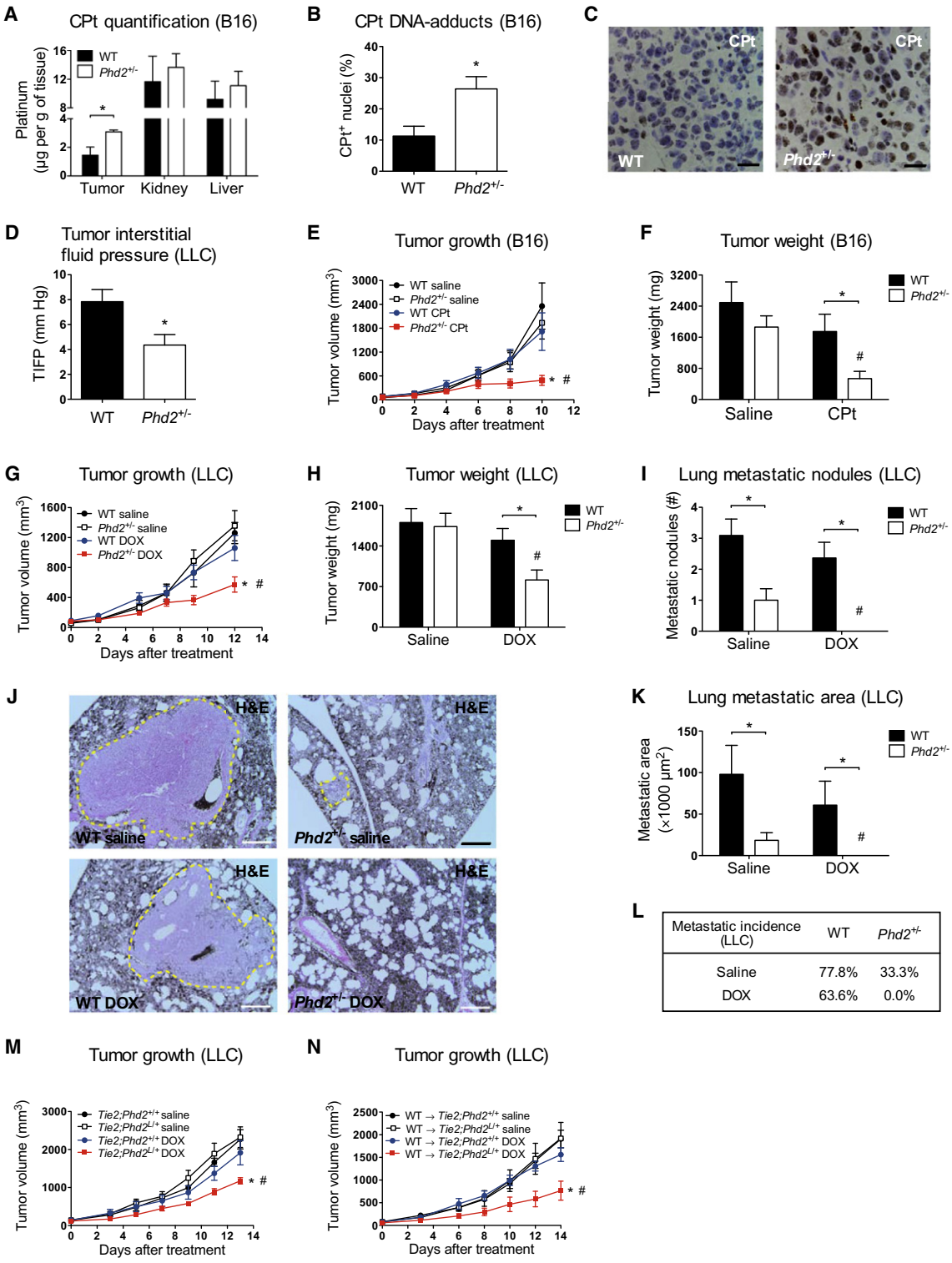

Metastatic incidence (LLC)	WT	*Phd2*$^{+/-}$
Saline	77.8%	33.3%
DOX	63.6%	0.0%

Figure 1. Stromal *Phd2* Haplodeficiency Enhances Tumor Response to Chemotherapy

(A) Platinum levels (as readout of cisplatin, CPt) in tumors and healthy organs (kidney and liver) of WT and *Phd2*$^{+/-}$ mice (n = 4–5).

(B and C) Quantification (B) and representative images (C) showing increased intratumoral CPt DNA-adducts in *Phd2*$^{+/-}$ mice (n = 3).

(D) Interstitial fluid pressure of LLC tumors is decreased in *Phd2*$^{+/-}$ mice (n = 6–7).

(E–H) Reduced growth and weight of B16 melanoma tumors (E and F) or LLC tumors (G and H) in *Phd2*$^{+/-}$ mice upon suboptimal doses (2.5 mg/kg; 3× per week) of CPt or doxorubicin (DOX), respectively (n = 5–9).

(I) Number of lung metastatic nodules in LLC tumor-bearing mice (n = 5–6).

given their ability to promote tumor vessel normalization in preclinical and clinical studies (Carmeliet and Jain, 2011; Goel et al., 2011). Nonetheless, this concept has been recently challenged by the observation that bevacizumab, a humanized monoclonal antibody that blocks VEGF, reduces both perfusion and tumor drug uptake in non-small cell lung cancer patients (Van der Veldt et al., 2012). Importantly, current antiangiogenic therapies are more toxic than anticipated, particularly when used in combination with chemotherapeutic drugs (D'Adamo et al., 2005). Alternative approaches have been evaluated in preclinical tumor models in order to increase the local concentration of chemotherapeutics, either by normalizing tumor blood flow (Fischer et al., 2007; Rolny et al., 2011; Stockmann et al., 2008) or by using tumor specific deliveries (Dhar et al., 2011; Jain, 2010). However, so far, none of the strategies tested show efficient drug delivery to the tumor and simultaneous protection of vital organs, thus optimizing the cytostatic efficiency of the drug and preventing undesired, life-threatening toxic effects.

Prolyl hydroxylase domain proteins (PHD1-3) are enzymes that utilize oxygen to hydroxylate and target the alpha subunit of the hypoxia-inducible transcription factors HIF-1 and HIF-2 for proteasomal degradation (Epstein et al., 2001). When oxygen tension drops, PHDs become less active, leading to hypoxia-inducible transcription factor (HIF) stabilization and, consequently, to the initiation of an adaptive response, including angiogenesis, metabolic reprogramming, erythropoiesis, and scavenging of reactive oxygen species (ROS) (Aragonés et al., 2008; Lee et al., 1997; Mukhopadhyay et al., 2000; Scortegagna et al., 2003). By using cancer as a model of abnormal angiogenesis, we recently showed that heterozygous deficiency of *Phd2* (also known as *Egln1*) in endothelial cells (EC) does not affect vessel density or lumen size, but normalizes their endothelial lining, barrier, stability, and pericyte coverage, at least in part, via HIF-2-mediated upregulation of the adherens junction vascular endothelial-cadherin and the soluble VEGF trap sFlt1. This change in vessel structure and endothelial shape improves tumor perfusion and oxygenation and, hence, inhibits cancer cell intravasation and metastasis (Mazzone et al., 2009). Moreover, gene deletion or knockdown of *Phd1* confers tissue protection against ischemia/reperfusion-induced oxidative damage (Aragonés et al., 2008; Schneider et al., 2010); conversely, reduced activity of HIF-1 or HIF-2 has been associated to increased ROS production and, thereby, tissue dysfunction in both normal and stress conditions (Lee et al., 1997; Mukhopadhyay et al., 2000; Scortegagna et al., 2003). This has critical implications in cancer therapy, since both chemotherapeutic- and irradiation-based treatments generate ROS that impair normal organ function and cause tissue demise (Anscher et al., 2005; Berthiaume and Wallace, 2007; Pabla and Dong, 2008).

In the present study, we investigate the biological and therapeutic relevance of gene-targeting the oxygen/redox-sensitive enzyme PHD2 in different cell compartments on the tumor response to chemotherapy. At the same time, we pursue a mechanistic understanding on how pharmacological and genetic inhibition of PHD2 affects chemotherapy-associated ROS production in healthy organs and, subsequently, tissue damage and function.

RESULTS

Stromal Loss of *Phd2* Sensitizes the Tumor to Chemotherapy

We recently showed that endothelial haplodeficiency of *Phd2* ($Phd2^{+/-}$) streamlines the tumor vasculature (Mazzone et al., 2009). Prompted by these results, we examined whether partial loss of *Phd2* also enhances the delivery of chemotherapeutic drugs. We therefore subjected wild-type (WT) and $Phd2^{+/-}$ mice carrying equal-size B16 melanomas to a single dose of cisplatin (20 mg/kg) and measured platinum accumulation in tumor, kidney, and liver 1 hr after drug injection. While normal organs showed similar cisplatin concentrations in both WT and $Phd2^{+/-}$ mice (Figure 1A), intratumoral platinum and drug diffusion out of the tumor vessels was higher in $Phd2^{+/-}$ than in WT mice (Figures 1A–1C), the latter being consistent with a reduction of tumor interstitial fluid pressure (Figure 1D), a physical parameter hindering efficient transit of drugs within the tumor (Heldin et al., 2004).

To assess whether the improved drug delivery translated into enhanced antitumor effects, we treated B16 tumor-bearing mice with a suboptimal dose of cisplatin (2.5 mg/kg; 3× per week), which did not have any therapeutic effect in WT mice (Figures 1E and 1F). In contrast, end-stage tumor volume and tumor weight were reduced in $Phd2^{+/-}$ mice by more than 70% (Figures 1E and 1F). We then extended our study to a different tumor histotype, i.e., Lewis lung adenocarcinoma (LLC), which was treated with doxorubicin. A suboptimal dose of doxorubicin (2.5 mg/kg; 3× per week) did not affect the growth of subcutaneously implanted LLC tumors in WT mice, whereas it reduced end-stage volume and weight by about 60% in $Phd2^{+/-}$ mice (Figures 1G and 1H). As previously shown (Mazzone et al., 2009), number, area, and incidence of pulmonary metastasis were reduced in $Phd2^{+/-}$ versus WT untreated mice (Figures 1I–1L). Doxorubicin treatment did not affect metastatic burden in WT mice, while it completely prevented metastasis formation in $Phd2^{+/-}$ mice, likely due to the strong inhibition of primary tumor growth (Figures 1G–1L). Deletion of one *Phd2* allele in EC, but not in myeloid cells or in fibroblasts, induced chemosensitization of LLC tumors to a suboptimal dose of doxorubicin (Figures 1M and 1N; Figures S1A and S1B available online).

In B16 tumors, suboptimal doses of cisplatin promoted tumor cell apoptosis and reduced proliferation in $Phd2^{+/-}$ mice (Figures

(J and K) Representative micrographs (J) and morphometric quantification (K) of hematoxylin and eosin (H&E)-stained lung sections revealing reduced metastatic area (yellow dashed line) in $Phd2^{+/-}$ LLC tumor-bearing mice and no metastases in $Phd2^{+/-}$ mice treated with DOX (n = 5–6).

(L) Metastatic incidence in LLC tumor-bearing mice (n = 5–6).

(M and N) LLC tumor growth in response to suboptimal doses of DOX (2.5 mg/kg; 3× per week) in $Tie2;Phd2^{L/+}$ mice (M; n = 6–9) or in $Tie2;Phd2^{L/+}$ and $Tie2;Phd2^{+/+}$ mice transplanted with WT bone marrow, WT → $Tie2;Phd2^{L/+}$ and WT → $Tie2;Phd2^{+/+}$, respectively (N; n = 5–9). The bone marrow transplantation is to ensure that *Phd2* is not deleted in the hematopoietic compartment, where the $Tie2^{Cre}$ deleter is also active.

*$p < 0.05$ versus WT, #$p < 0.05$ versus saline. Scale bars denote 20 μm in (C) and 200 μm in (J). All graphs show mean ± SEM. See also Figure S1.

2A–2F and Table S1). In doxorubicin-treated LLC tumors, apoptosis, but not proliferation, was higher in $Phd2^{+/-}$ versus WT mice (Figures 2G and 2H and Table S1). Tumor apoptosis and proliferation did not change in WT and $Phd2^{+/-}$ untreated mice (Figures 2B, 2C, and 2E–2H and Table S1).

Cytostatic drugs can display some antiangiogenic effects (Kerbel and Kamen, 2004). However, baseline and posttreatment tumor vessel perfusion and oxygenation were comparably higher in $Phd2^{+/-}$ versus WT mice, despite similar vessel density and area (Figures 2I–2N). Similarly, endothelial *Phd2* haplodeficiency increased tumor perfusion in both doxorubicin-treated and untreated mice (Figure S2).

Altogether, these data show that reduction of *Phd2* in EC enhances the response of the tumor to chemotherapy by increasing vessel perfusion and drug delivery.

Acute Loss of One or Two *Phd2* Alleles Enhances Chemotherapy

The above findings show that constitutive deletion of *Phd2* in EC induces tumor vessel normalization and thus increases tumor response to chemotherapeutics. To assess the effect of inducible deletion of *Phd2* on chemoresponse, we intercrossed *Phd2*-floxed mice with the tamoxifen-inducible $Rosa26^{CreERT2}$ mouse strain, where the *Rosa26* (*R26*) promoter directs the ubiquitous expression of the fusion protein Cre-ERT2. We also exploited this system to compare the effect of heterozygous ($R26;Phd2^{L/+}$) versus homozygous ($R26;Phd2^{L/L}$) deletion, leading, respectively, to about 50% and 2%–5% of the PHD2 protein levels in different tissues of WT ($R26;Phd2^{+/+}$) mice (Figures 3A and S3A and Table S2). In vitro, primary EC isolated from $R26;Phd2^{L/+}$ and $R26;Phd2^{L/L}$ mice displayed increasing accumulation of HIF-1α (Figure 3A and Table S2). Conversely, HIF-2α was higher, but elevated to the same level in both $R26;Phd2^{L/+}$ and $R26;Phd2^{L/L}$ primary EC, likely due to compensatory mechanisms promoted by induction of *Phd3* (Figures 3A and S3B and Table S2).

In vivo, deletion of one or two *Phd2* alleles in stromal cells (achieved by tamoxifen administration for 5 consecutive days following LLC cell injection) did not alter tumor growth in untreated mice, but was equally potent in sensitizing the tumor to the effect of doxorubicin (Figures 3B and 3C). Metastatic dissemination was almost completely prevented in both $R26;Phd2^{L/+}$ and $R26;Phd2^{L/L}$ mice after doxorubicin (Figure 3D). Features of tumor vessel normalization, as vessel coverage (Figures 3E and 3F), vessel perfusion (Figures 3G and S3C), and tumor oxygenation (Figure 3H), were promoted in both doxorubicin-treated and untreated $R26;Phd2^{L/+}$ and $R26;Phd2^{L/L}$ mice.

Vegf is an oxygen-sensitive gene that is strongly expressed by the tumor in response to hypoxia as well as oncogenic activation (Semenza, 2003). Previous reports have shown that systemic levels of VEGF following postnatal deletion of *Phd2* increase or can remain unchanged, depending on the experimental settings (Minamishima et al., 2008; Takeda et al., 2007). Thirty days after genetic deletion of *Phd2* (i.e., about the duration of our tumor experiments), plasma levels of VEGF were slightly increased by 12% and 29%, respectively, in $R26;Phd2^{L/+}$ and $R26;Phd2^{L/L}$ tumor-free mice (Figure 3I). In tumor-bearing mice, as expected, VEGF levels were generally higher, but in both $R26;Phd2^{L/+}$ and $R26;Phd2^{L/L}$ tumor-bearing mice, these levels were lower than in $R26;Phd2^{+/+}$ tumor-bearing mice, because vessel normalization and improved oxygenation partly prevented VEGF production by the tumor itself (Figures 3I and 3J).

The effect of *Phd2* knockdown in cancer cells depends on the tumor histotype (Ameln et al., 2011; Andersen et al., 2011; Bordoli et al., 2011; Chan et al., 2009; Kamphues et al., 2012; Lee et al., 2008; Peurala et al., 2012; Su et al., 2012), while our data show a better disease outcome when the tumor stroma is insufficient for *Phd2*. To assess the effect of combined *Phd2* inactivation in cancer cells and stromal cells, we subcutaneously injected scramble and *Phd2*-silenced LLC cells in $R26;Phd2^{+/+}$ and $R26;Phd2^{L/+}$ mice. The efficiency of PHD2 silencing was 65% on both RNA and protein levels (Figure S3D). In vitro, hypoxia, but not *Phd2* silencing, enhanced the expression of VEGF (Figure S3E). In vivo, due to vessel normalization and the subsequent decrease in tumor hypoxia, intratumoral VEGF in $R26;Phd2^{L/+}$ mice was lower than in $R26;Phd2^{+/+}$ mice, regardless of *Phd2* silencing in cancer cells (Figures 3K and S3F). Following doxorubicin treatment, the chemoresponse of both scramble and *Phd2*-silenced LLC tumors was equally improved in $R26;Phd2^{L/+}$ mice (Figure 3L).

These data suggest that systemic inhibition of PHD2 might offer a therapeutic benefit.

Loss of *Phd2* Protects Normal Organs against Side-Toxicity of Chemotherapy

Side-toxicity limits the clinical use of chemotherapeutic drugs. Thus, we wanted to assess the effect of cisplatin and doxorubicin on WT and $Phd2^{+/-}$ kidneys and hearts, respective target organs for drug toxicity. Three days after acute cisplatin administration (20 mg/kg), blood urea and creatinine were 7.9- and 21.9-fold increased in WT mice, but only 4.7 and 4.3 times higher in $Phd2^{+/-}$ mice (Figure 4A). Histological inspection of periodic acid-Schiff (PAS)-stained kidney sections from WT mice revealed severe proximal tubular necrosis and dilatation with formation of protein casts into the lumen, overt destruction of the brush border, and consequent deformations/atrophy of the glomerular structures (Figure 4B). In contrast, the histological morphology of $Phd2^{+/-}$ kidneys was preserved and more comparable to the one of untreated kidneys (Figures 4B and S4A). Transcript levels of kidney injury molecule 1 (*Kim1*) and protein levels of the apoptotic marker-cleaved caspase-3 were strongly induced by cisplatin in WT, but barely in $Phd2^{+/-}$ kidneys (Figures 4C and 4D and Table S3). Consistently, the mean survival after cisplatin was 7 days in $Phd2^{+/-}$ mice, while only 3 days in WT mice (Figure 4E). Upon chronic administration of cisplatin (2.5 mg/kg; 3× per week), only urea, but not creatinine, rose to indicative levels of nephrotoxicity in WT mice, while $Phd2^{+/-}$ mice showed great protection (Figure S4B).

Similarly, WT and $Phd2^{+/-}$ mice were treated with an acute dose of doxorubicin (20 mg/kg). Five days after drug administration, doxorubicin reduced cardiac output by 22.3% in WT mice, while it did not display any effect in $Phd2^{+/-}$ mice (Figure 5A). In doxorubicin-treated WT mice, histological analysis of heart sections revealed disarray and vacuolization of myofibers with excessive collagen deposition, all histopathological signs of cardiomyopathy (Figures 5B and 5C). In $Phd2^{+/-}$ hearts, these features were milder and rarely observed, overall resembling the structure of untreated hearts (Figures 5B and S5A). Creatine

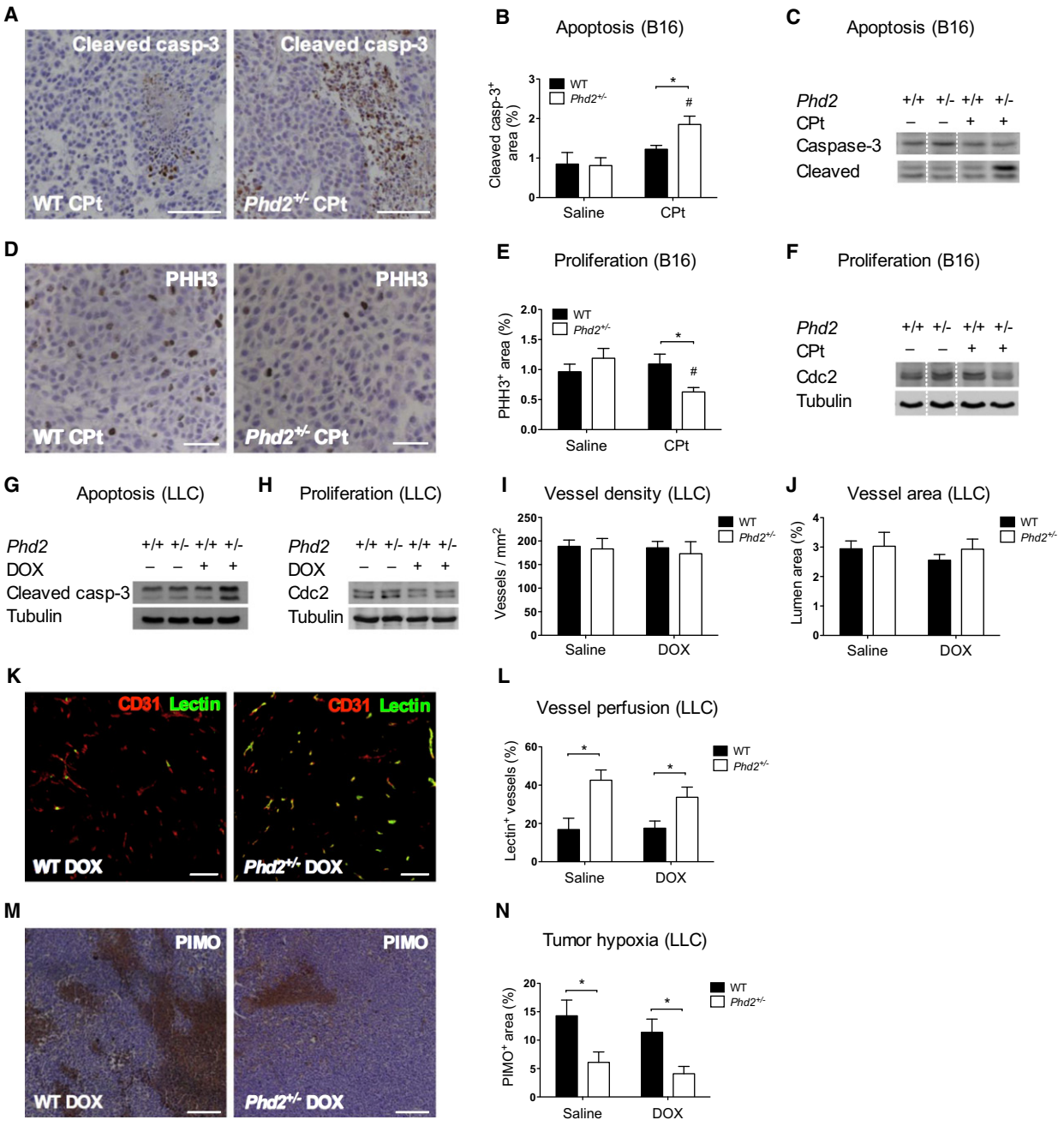

Figure 2. Histological Analysis of Tumors in *Phd2*$^{+/-}$ Mice after Chemotherapy

(A and B) Cleaved caspase-3 staining (A) and morphometric quantification (B) on B16 tumor sections, showing increased tumor apoptosis in *Phd2*$^{+/-}$ mice after CPt (n = 5–6).

(C) Immunoblot for cleaved and total caspase-3, revealing increased tumor apoptosis in *Phd2*$^{+/-}$ mice after CPt (n = 3).

(D and E) Phosphohistone H3 staining (D) and morphometric quantification (E) on B16 tumor sections, showing reduced tumor cell proliferation in *Phd2*$^{+/-}$ mice after CPt (n = 5–6).

(F) Immunoblot for the proliferation marker Cdc2 on untreated and Cpt-treated B16 tumors; tubulin is used as loading control (n = 3).

(G and H) Immunoblot for cleaved caspase-3 (G) and Cdc2 (H) on untreated and DOX-treated LLC tumors (n = 3).

(I and J) Vessel density (I) and vessel area (J) of LLC tumors (n = 6–10).

(K and L) Representative micrographs (K) and morphometric quantification (L) of LLC tumor sections stained for the endothelial marker CD31 (red) and for intravenously injected lectin (green), showing higher vessel perfusion in both untreated and DOX-treated *Phd2*$^{+/-}$ mice (n = 7–9).

(M and N) Pimonidazole (PIMO) staining (M) and morphometric quantification (N) on LLC tumor sections, showing reduced tumor hypoxia in both untreated and DOX-treated *Phd2*$^{+/-}$ mice (n = 7–9).

$^{*}p < 0.05$ versus WT; $^{\#}p < 0.05$ versus saline. Scale bars denote 100 μm in (A), (K), and (M) and 20 μm in (D). All graphs show mean ± SEM. See also Figure S2 and Table S1.

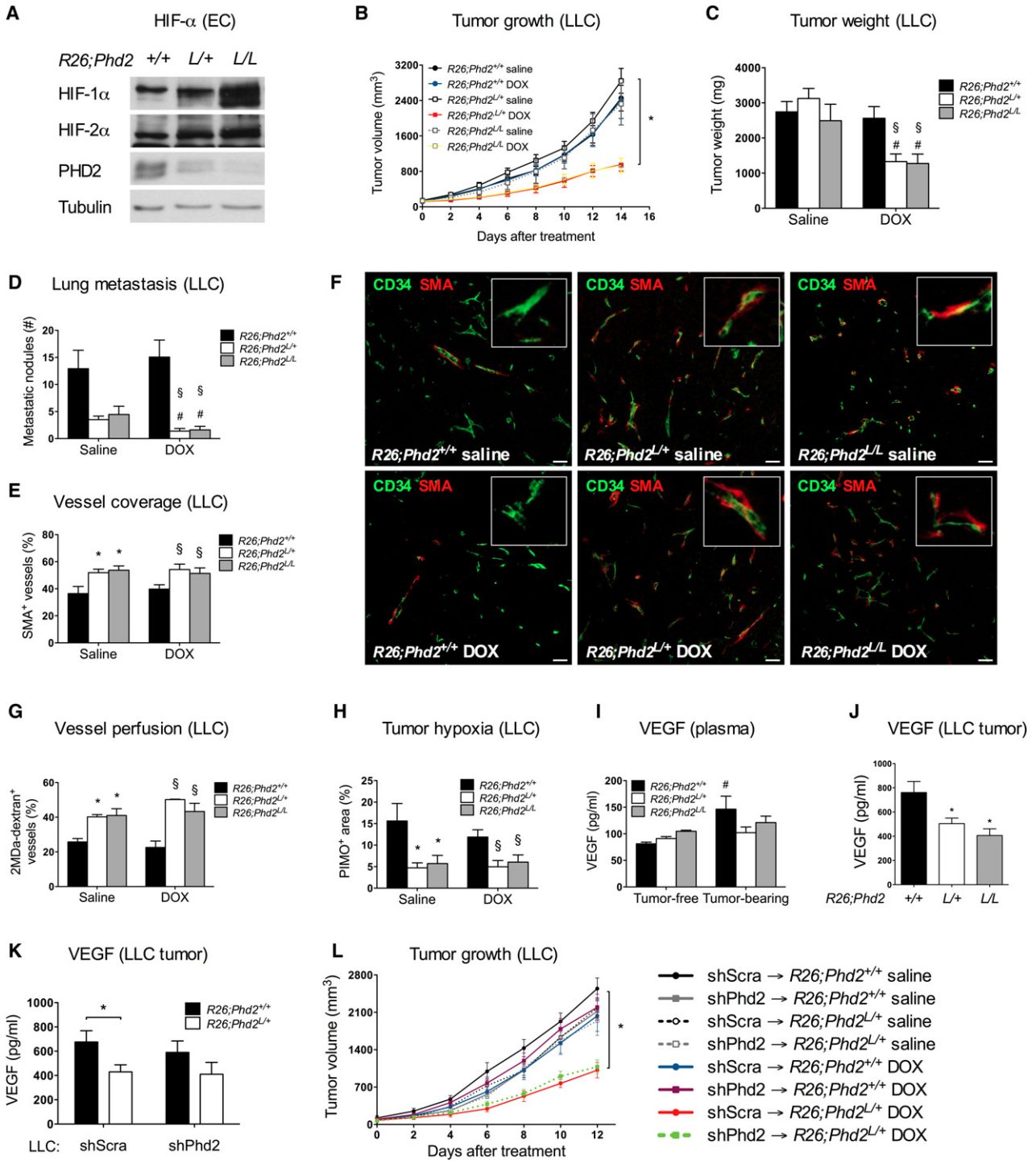

Figure 3. Acute Loss of *Phd2* Enhances Tumor Response to Chemotherapy

(A) Immunoblot for HIF-1α and HIF-2α in WT (*R26;Phd2*$^{+/+}$), *Phd2* haplodeficient (*R26;Phd2*$^{L/+}$), and *Phd2* null (*R26;Phd2*$^{L/L}$) endothelial cells (EC).

(B and C) Reduced LLC tumor growth (B) and weight (C) following DOX (2.5 mg/kg, 3× per week) upon tamoxifen-induced deletion of one (*R26;Phd2*$^{L/+}$) or two (*R26;Phd2*$^{L/L}$) *Phd2* alleles (n = 10–12; *p < 0.05).

(D) Metastasis inhibition in *R26;Phd2*$^{L/+}$ and *R26;Phd2*$^{L/L}$ LLC tumor-bearing mice; lung metastatic nodules were further reduced upon DOX (n = 10–12).

(E and F) Quantification (E) and staining (F) for CD34 (green) and alpha-smooth muscle actin (SMA) (red), revealing increased pericyte coverage of tumor vessels in untreated and DOX-treated *R26;Phd2*$^{L/+}$ and *R26;Phd2*$^{L/L}$ mice. Higher magnification images are shown as insets (n = 6–8).

(G and H) Morphometric quantification of LLC tumor sections stained for the endothelial marker CD31 and intravenously injected 2 MDa dextran-FITC (G) or PIMO (H), showing, respectively, increased tumor vessel perfusion or reduced tumor hypoxia in both untreated and DOX-treated *R26;Phd2*$^{L/+}$ and *R26;Phd2*$^{L/L}$ mice (n = 10–12 or n = 4–6, respectively).

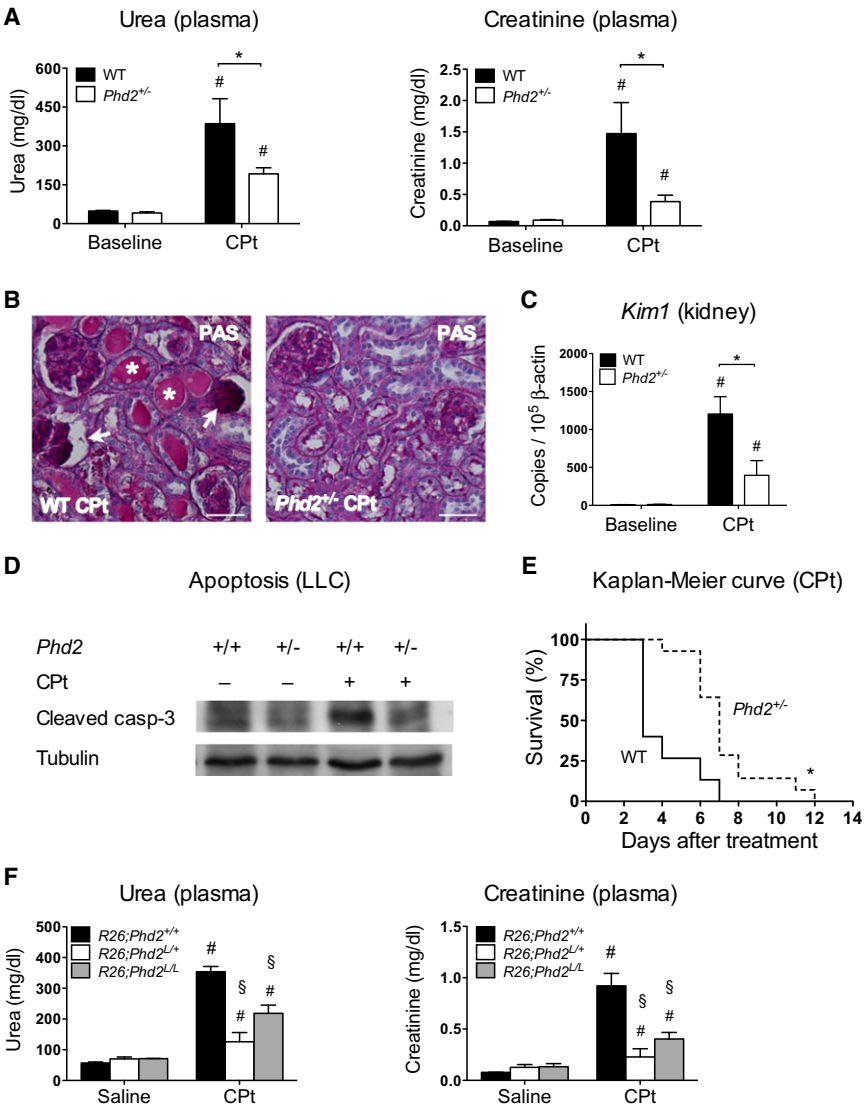

Figure 4. *Phd2* Loss Protects against Cisplatin-Induced Nephrotoxicity

(A) Reduced plasma urea and creatinine in $Phd2^{+/-}$ mice 72 hr post-CPt injection (20 mg/kg; n = 6–10).

(B) PAS staining on kidney sections from CPt-treated mice, revealing severe tubular dilation, protein cast (white asterisks), and detachment of atrophic glomeruli (white arrow) in WT, but not in $Phd2^{+/-}$ mice.

(C) RNA levels of kidney injury molecule 1 (*Kim1*) after CPt (n = 6–10).

(D) Immunoblot for cleaved caspase-3 on kidneys showing protection in $Phd2^{+/-}$ mice against CPt-induced apoptosis.

(E) Kaplan-Meier survival curve, illustrating increased survival of $Phd2^{+/-}$ mice upon acute administration of CPt.

(F) Reduced plasma urea and creatinine levels in CPt-treated $R26;Phd2^{L/+}$ and $R26;Phd2^{L/L}$ mice (n = 5–7; $^{\#}p < 0.05$ versus baseline $R26;Phd2^{+/+}$; $^{\S}p < 0.05$ versus $R26;Phd2^{+/+}$ CPt).

Unless otherwise denoted: $^{*}p < 0.05$ versus WT, $^{\#}p < 0.05$ versus baseline. Scale bars denote 40 μm in (B). All graphs show mean ± SEM. See also Figure S4 and Table S3.

kinase (CK), released in the plasma upon acute cardiac injury, was strongly elevated in WT mice, but 2-fold lower in $Phd2^{+/-}$ mice (Figure 5D). Myocardial death following doxorubicin administration was completely prevented in $Phd2^{+/-}$ mice (Figure 5E and Table S4). Consistently, the mean survival after doxorubicin was 20 days in $Phd2^{+/-}$ mice, while only 5 days in WT mice (Figure 5F). A chronic regimen of doxorubicin as well (2.5 mg/kg; 3× per week) preserved cardiac ejection fraction in $Phd2^{+/-}$ mice (Figure 5G). Gene expression of brain natriuretic peptide (*Bnp*), a marker of chronic heart toxicity, was 35.2% lower in $Phd2^{+/-}$ than WT mice after doxorubicin (Figure 5H).

The protection of healthy organs against chemotherapy can be mainly ascribed to reduced activity of PHD2 in tissue cells, since heterozygous deletion of *Phd2* in EC (and infiltrating leukocytes) did not prevent side-toxicity of cisplatin and doxorubicin (Figures S4C and S5B).

We then assessed the effect of acute deletion of one versus two *Phd2* alleles. To this end, $R26;Phd2^{L/+}$, $R26;Phd2^{L/L}$, and $R26;Phd2^{+/+}$ control mice, pretreated with tamoxifen for 5 days, were injected with an acute dose of cisplatin (20 mg/kg) or doxorubicin (20 mg/kg). Both heterozygous and homozygous deletion of *Phd2* were equally able to prevent renal and cardiac damage, as assessed by lower concentrations of plasma urea, creatinine, and CK in $R26;Phd2^{L/+}$ and $R26;Phd2^{+/+}$ mice after drug administration (Figures 4F and 5I).

Altogether, these results indicate that genetic inactivation of *Phd2* confers protection against chemotherapy-associated nephropathy and cardiomyopathy.

(I) Plasma VEGF levels quantified by ELISA in $R26;Phd2^{+/+}$, $R26;Phd2^{L/+}$, and $R26;Phd2^{L/L}$ LLC tumor-free as well as tumor-bearing mice (n = 5–10; $^{\#}p < 0.05$ versus $R26;Phd2^{+/+}$ tumor-free).

(J) Intratumoral VEGF levels are decreased in $R26;Phd2^{L/+}$ and $R26;Phd2^{L/L}$ mice (n = 6–8).

(K) Intratumoral VEGF levels are decreased in $R26;Phd2^{L/+}$ mice, regardless of *Phd2* silencing in cancer cells (n = 8–10; $^{*}p < 0.05$).

(L) Combined inactivation of *Phd2* in both stroma ($R26;Phd2^{+/+}$ and $R26;Phd2^{L/+}$ mice) and cancer cells (shPhd2) equally enhances LLC tumor response to DOX (2.5 mg/kg, 3× per week) (n = 8–10; $^{*}p < 0.05$).

Unless otherwise denoted: $^{*}p < 0.05$ versus $R26;Phd2^{+/+}$ saline, $^{\#}p < 0.05$ versus saline, $^{\S}p < 0.05$ versus $R26;Phd2^{+/+}$ DOX. Scale bars denote 50 μm in (F). All graphs show mean ± SEM. See also Figure S3 and Table S2.

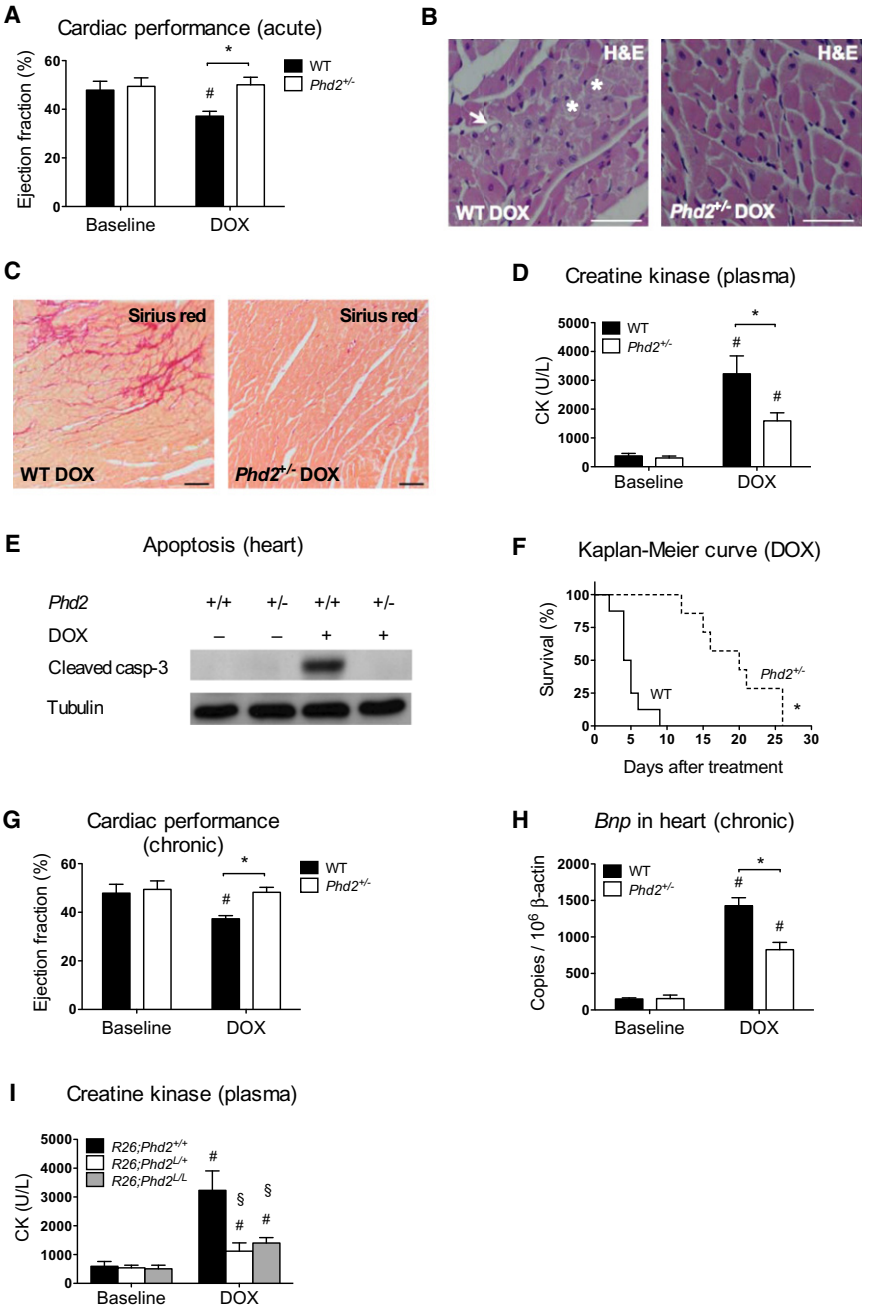

Figure 5. *Phd2* Loss Protects against Doxorubicin-Induced Cardiotoxicity

(A) B-mode measurement of left ventricular function, revealing unaltered ejection fraction in $Phd2^{+/-}$ mice 5 days after acute administration of DOX (20 mg/kg; n = 7–11).

(B) H&E-staining on DOX-treated heart sections reveals extensive cytoplasmic vacuolization (white arrow), myofibrillar loss, and cell death (white asterisks) in WT, but not in $Phd2^{+/-}$ mice.

(C) Sirius red staining on DOX-treated heart sections identifies extensive fibrotic areas in WT, but not in $Phd2^{+/-}$ mice.

(D) Increased plasma creatine kinase (CK) by DOX is prevented in $Phd2^{+/-}$ mice (n = 5–7).

(E) Immunoblot for cleaved caspase-3 on hearts showing prevention of DOX-induced apoptotis in $Phd2^{+/-}$ mice.

(F) Kaplan-Meier curve, illustrating increased survival of $Phd2^{+/-}$ mice upon acute administration of DOX (n = 7–8; *p < 0.001 versus WT).

(G) B-mode measurement of left ventricular function in $Phd2^{+/-}$ and WT mice 1 month after chronic treatment (2.5 mg/kg; 3× per week) with DOX (n = 30; *p < 0.001; #p < 0.001 versus baseline).

(H) RNA levels of brain natriuretic peptide (*Bnp*) in heart after chronic administration of DOX (n = 9–11).

(I) Plasma CK values upon acute DOX treatment in tamoxifen-treated in $R26;Phd2^{+/+}$, $R26;Phd2^{L/+}$, and $R26;Phd2^{L/L}$ mice (n = 5–7; #p < 0.05 versus baseline $R26;Phd2^{+/+}$; §p < 0.05 versus $R26;Phd2^{+/+}$ DOX).

Unless otherwise denoted: *p < 0.05 versus WT, #p < 0.05 versus baseline. Scale bars denote 20 μm in (B) and (C). All graphs show mean ± SEM. See also Figure S5 and Table S4.

Loss of *Phd2* Mounts an Antioxidative Response in Normal Organs

The toxicity of cisplatin and doxorubicin on quiescent and healthy organs has been, in part, ascribed to oxidative stress formation (Berthiaume and Wallace, 2007; Pabla and Dong, 2008). We therefore assessed the burst of ROS after chemotherapy by staining kidney and heart sections for 8-hydroxy deoxyguanosine (8-OHdG), a marker of oxidative DNA damage. Acute cisplatin administration raised the number of 8-OHdG^+ nuclei in WT kidneys to 52.3%, while only to 35% in $Phd2^{+/-}$ kidneys (Figures 6A and 6B). 8-OHdG^+ nuclei were undetectable at baseline in both genotypes (Figure S6A). Similarly, both acute and chronic administration of doxorubicin resulted in reduced oxidative damage in $Phd2^{+/-}$ versus WT hearts (Figures 6C–6E). 8-OHdG^+ nuclei in baseline hearts were similar in both genotypes (Figures S6B and S6C). When treated with acute regimens of doxorubicin or cisplatin, RNA, protein levels, and activity of primary antioxidative enzymes (AOE), such as superoxide dismutase 1 (*Sod1*), superoxide dismutase 2 (*Sod2*), catalase (*Cat*), and glutathione peroxidase 1 (*Gpx1*), were significantly higher in $Phd2^{+/-}$ than in WT organs (Figures 6F–6H and Tables S5 and S6). Baseline levels and activity of these enzymes were similar in both genotypes (not shown). Administration of the ROS scavenger Mn(III)tetrakis(4-benzoic acid)porphyrin (MnTBAP) greatly prevented the induction of AOE in $Phd2^{+/-}$ hearts after doxorubicin, indicating that ROS production by chemotherapy is necessary to trigger this detoxification response (Figure 6I). Pharmacological inhibition of these AOE in combination with doxorubicin completely abrogated the cardiac protection conferred by loss of *Phd2* (Figure 6J).

We then assessed whether the nonspecific prolyl hydroxylase inhibitor dimethyloxaloylglycine (DMOG) could offer a similar cardiac protection as genetic inactivation of *Phd2*. When measuring plasma CK as readout of toxicity, DMOG-treated WT mice displayed a 53% reduction of CK release after doxorubicin (Figure 6K). From a molecular point of view, DMOG alone did not induce AOE upregulation, in line with our observations in $Phd2^{+/-}$ mice at baseline. However, the combination of DMOG and doxorubicin enhanced the expression of *Cat*, *Sod1*, *Sod2*, and *Gpx1*, consistent with the fact that an oxidative challenge is required to initiate the detoxification response (Figure 6L).

We also evaluated the biological consequences of reduced PHD2 activity on ROS homeostasis in LLC cancer cells, where the cytostatic effect of these drugs is primarily linked to cell proliferation (not shown). Silencing of *Phd2* did not affect the expression of AOE either in vitro or in vivo: neither did it affect ROS induction (Figures S6D–S6G). Consistently, in vitro cell death in response to doxorubicin was comparable in both scramble and *Phd2*-silenced LLC (Figure S6H).

Thus, a reduction of PHD2 triggers effective antioxidative responses in normal organs, but not in tumors, in response to chemotherapy.

The Antioxidative Response by Loss of *Phd2* Is HIF-1 and HIF-2 Dependent

The AOE upregulated in $Phd2^{+/-}$ organs are HIF downstream targets (Scortegagna et al., 2003). To assess HIF transcriptional activity in WT and $Phd2^{+/-}$ hearts at baseline and after doxorubicin, we used an adenoassociated virus serotype-9 (AAV9) carrying a HIF-responsive firefly luciferase reporter (Figure 7A). HIF activity was comparable in both genotypes at baseline. However, 24 hr after doxorubicin administration, HIF activity was 5.4 times higher in WT hearts, but 9.8 times higher in $Phd2^{+/-}$ hearts (Figure 7A). This effect was specific and not secondary to hypoxia, since the constitutive cytomegalovirus (CMV) promoter was not differentially regulated and we were not able to detect any hypoxic regions in response to doxorubicin (Figure S7A and not shown). Similar results were obtained in kidneys, where HIF activity 24 hr after a bolus of cisplatin was 8.1-fold increased in WT mice, but 13.5-fold increased in $Phd2^{+/-}$ mice (Figure 7B).

To assess the contribution of HIF-1α versus HIF-2α, we intercrossed $Phd2^{+/-}$ mice with $Hif1a^{+/-}$ or $Hif2a^{+/-}$ mice, displaying about 50% reduction in *Hif1a* or *Hif2a*, respectively (Figures S7B and S7C). Heterozygous deficiency of either *Hif1a* or *Hif2a* in $Phd2^{+/-}$ mice abrogated the upregulation of *Sod1*, *Sod2*, *Cat*, and *Gpx1* after doxorubicin (Figures 7C and 7D). In vitro, both HIF-1α and HIF-2α were more abundant in $Phd2^{+/-}$ cardiomyocytes compared to WT and accumulated to even higher levels in $Phd2^{-/-}$ cardiomyocytes (Figure 7E and Table S7). In response to doxorubicin, both HIFs were slightly higher in WT cardiomyocytes, but they were more potently induced in $Phd2^{+/-}$ and in $Phd2^{-/-}$ cells up to comparable levels (Figure 7E and Table S7).

In order to block simultaneously HIF-1 and HIF-2, we treated WT and $Phd2^{+/-}$ mice with chetomin, which disrupts the interaction of the transcriptional coactivator p300 with the alpha subunit of HIF (Kung et al., 2004). Administration of chetomin prevented the induction of *Sod1*, *Sod2*, *Cat*, and *Gpx1* and completely abrogated the protection against oxidative stress and tissue damage conferred by *Phd2* haplodeficiency in response to doxorubicin (Figures 8A–8C), supporting that both HIFs are responsible for the chemoprotection in $Phd2^{+/-}$ mice.

DISCUSSION

During the last decade, much progress has been made in increasing the arsenal and selectivity of anticancer drugs. However, side effects and resistance to therapy still remain major issues (Berthiaume and Wallace, 2007; Pabla and Dong, 2008). Based on previous research (Mazzone et al., 2009), we now describe PHD2 as a potential and promising target, not only to improve delivery of cytotoxic drugs selectively to the tumor, but also to protect normal organ functions from side-toxicity of chemotherapy. From a biological point of view, two distinct mechanisms underlie these different phenomena. In tumors, on one hand, we show that acute deletion of one or two *Phd2* alleles in stromal cells increases tumor vessel perfusion and thus allows doxorubicin and cisplatin to better reach the tumor, regardless of *Phd2* targeting in cancer cells. Together with the inhibition of metastasis, PHD2 inactivation provides a potent antitumor effect when combined with conventional chemotherapeutic regimens (Figure 8D, left panel). In healthy organs, on the other hand, reduced activity of PHD2 in hearts and kidneys amplifies the antioxidative response and thus counters the oxidative burst and subsequent tissue damage caused by doxorubicin and cisplatin (Figure 8D, right panel).

Previous studies have shown that VEGF(R) blockade promotes a transient window of tumor vessel normalization in which the chemo- and radio-response of the tumor is enhanced (Goel et al., 2011; Winkler et al., 2004). Beyond this "normalization window," VEGF blockade leads to vessel pruning, which might increase hypoxia and fuel a shift to malignancy, together with an overall reduction of drug delivery and tumor uptake (Loges et al., 2009). In addition, resistance mechanisms are evoked by the antiangiogenic treatment itself (Loges et al., 2009). By using different genetic tools, we show that reduced activity of PHD2 in EC normalizes the tumor vasculature, not vessel numbers, and increases drug efficiency. This effect is similar and preserved until the end stage of the disease if *Phd2* is inactivated either before or after tumor onset or following systemic inactivation of one or two *Phd2* alleles. Moreover, chemotherapeutic drugs in $Phd2^{+/-}$ mice have a synergic effect on metastasis inhibition. Finally, $Phd2^{+/-}$ vessels have improved functionality prior to and postchemotherapy, altogether suggesting the absence of resistance modes. Nevertheless, we cannot formally exclude that PHD2 might affect tumor-stromal interactions that confer protection on cancer cells from the cytotoxic effect of anticancer agents (Provenzano et al., 2012; Nakasone et al., 2012). A deletion of *Phd2* in the host stroma may alter its interactions with cancer cells, resulting in an unfavorable microenvironment that could render tumor cells more sensitive to drug treatment.

Phd2 silencing in cancer cells can display both a pro- and antitumoral effect, depending on the cellular context (Ameln et al., 2011; Andersen et al., 2011; Bordoli et al., 2011; Chan et al., 2009; Kamphues et al., 2012; Lee et al., 2008; Peurala et al., 2012; Su et al., 2012). However, there are more tumor

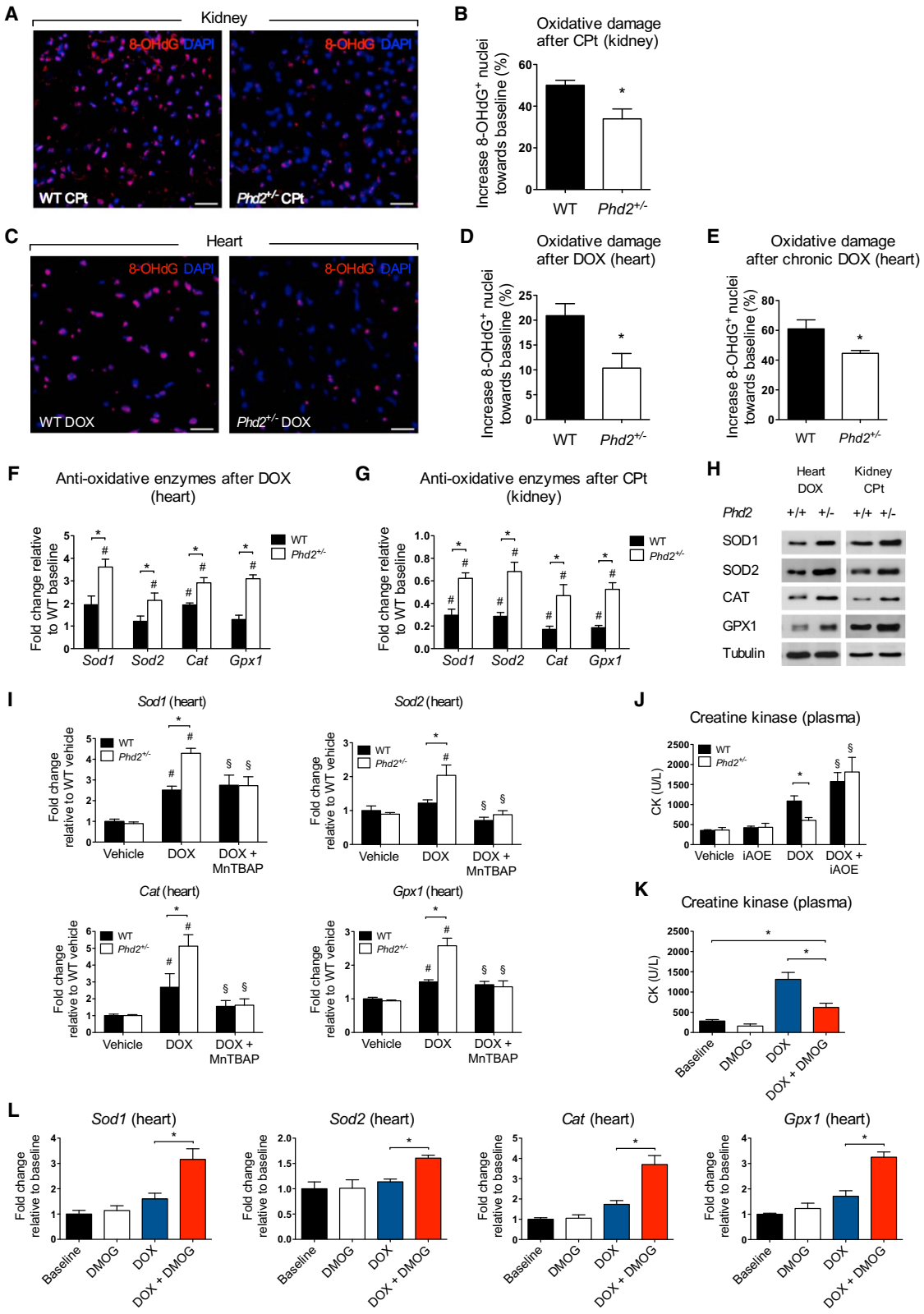

Figure 6. *Phd2* Loss Favors an Antioxidative Response in Normal Organs

(A–D) Representative micrographs (A,C) and morphometric quantification (B,D) of 8-hydroxy deoxyguanosine (8-OHdG; red) positive nuclei in kidney sections 72 hr after acute administration of CPt (20 mg/kg) or in heart sections 5 days after acute administration of DOX (20 mg/kg), respectively; DAPI (blue) was used for nuclear localization (n = 5).

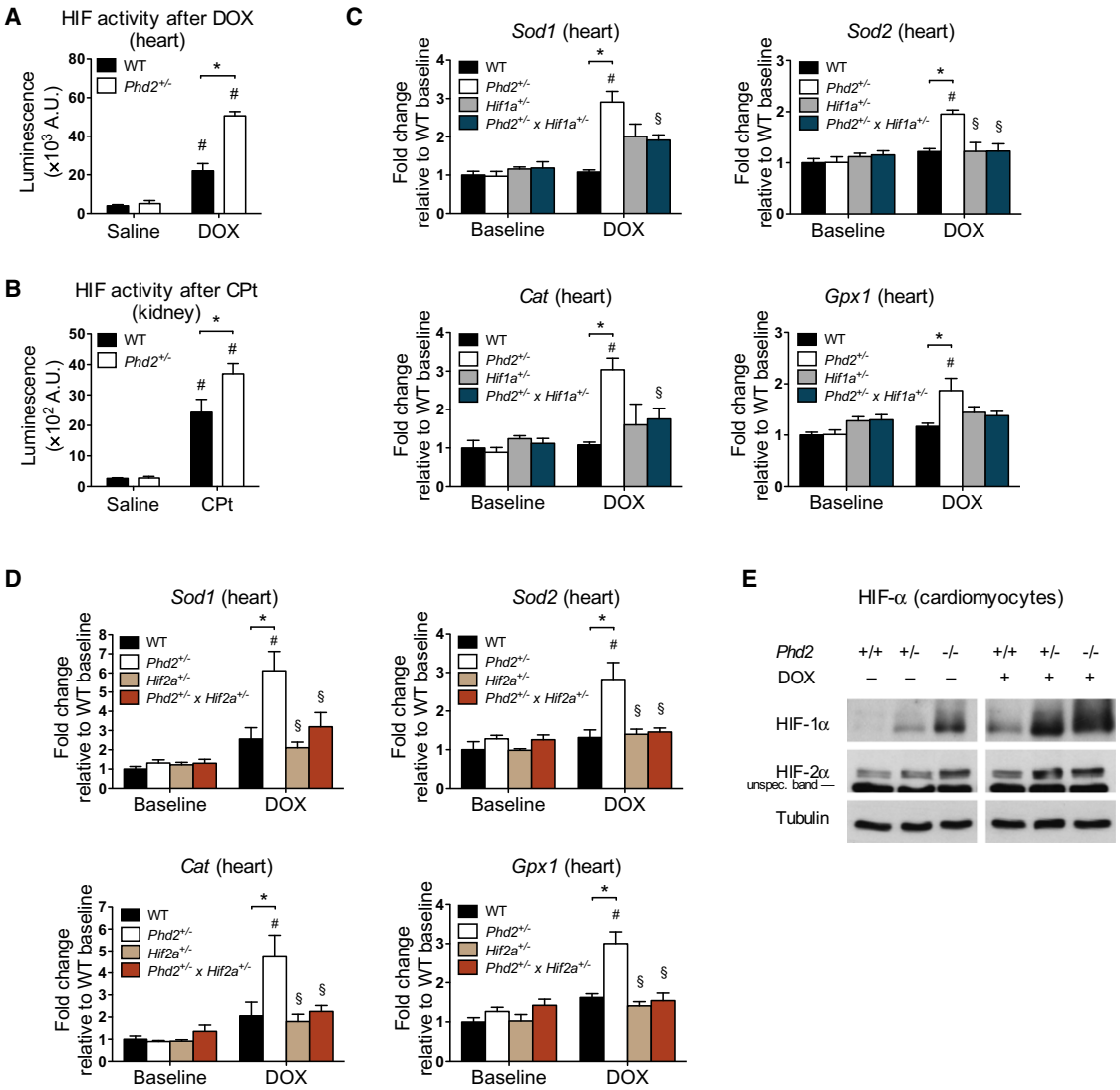

Figure 7. Chemoprotection of Normal Organs by *Phd2* Loss Requires HIF-1 and HIF-2

(A and B) HIF-reporter luciferase assay, showing enhanced HIF activity upon chemotherapy in $Phd2^{+/-}$ hearts (A) and kidneys (B) (n = 4).

(C and D) Either *Hif1a* (C) or *Hif2a* (D) heterozygosity prevents the transcriptional induction of AOE in $Phd2^{+/-}$ mice upon DOX treatment (n = 5–10).

(E) Immunoblot for HIF-1α and HIF-2α in untreated and DOX-treated WT, $Phd2^{+/-}$, and $Phd2^{-/-}$ cardiomyocytes.

*p < 0.05 versus WT, #p < 0.05 versus baseline, §p < 0.05 versus $Phd2^{+/-}$ DOX. All graphs show mean ± SEM. See also Figure S7 and Table S7.

types that overexpress *Phd2* compared to their normal histological counterpart than tumor types that underexpress this gene, thus indicating *Phd2* as an oncogene more than an oncosuppressor (Ameln et al., 2011). For this reason, simultaneous inactivation of *Phd2* in both tumor stroma and cancer cells remained enigmatic. Our data show that tumors generated by *Phd2* hypomorphic LLC cells still display an advantageous response to chemotherapy when the tumor is embedded in

(E) 8-OHdG positive nuclei are significantly reduced in $Phd2^{+/-}$ hearts under a chronic regimen of DOX (2.5 mg/kg; 3× per week; n = 4–8; *p < 0.05).

(F–H) Enhanced expression of antioxidative enzymes (AOE) in $Phd2^{+/-}$ hearts (F) and kidneys (G) after chemotherapy, both at the RNA (F and G; n = 6) and protein (H; n = 3) levels.

(I) RNA levels of AOE in DOX-treated $Phd2^{+/-}$ mice upon administration of the ROS scavenger MnTBAP (n = 3–5; #p < 0.05 versus WT vehicle).

(J) Plasma CK upon combined treatment with DOX and AOE inhibitors (n = 3–6).

(K) Treatment of WT mice with the nonspecific PHD2 inhibitor DMOG prevents the increase of plasma CK after DOX (n = 5–6).

(L) Combined administration of DMOG and DOX strongly upregulates AOE transcript levels in WT hearts (n = 5–6).

Unless otherwise denoted: *p < 0.05 versus WT, #p < 0.05 versus WT baseline (not shown) or vehicle, §p < 0.05 versus $Phd2^{+/-}$ DOX. Scale bars denote 20 μm in (A) and (C). All graphs show mean ± SEM. See also Figure S6 and Tables S5 and S6.

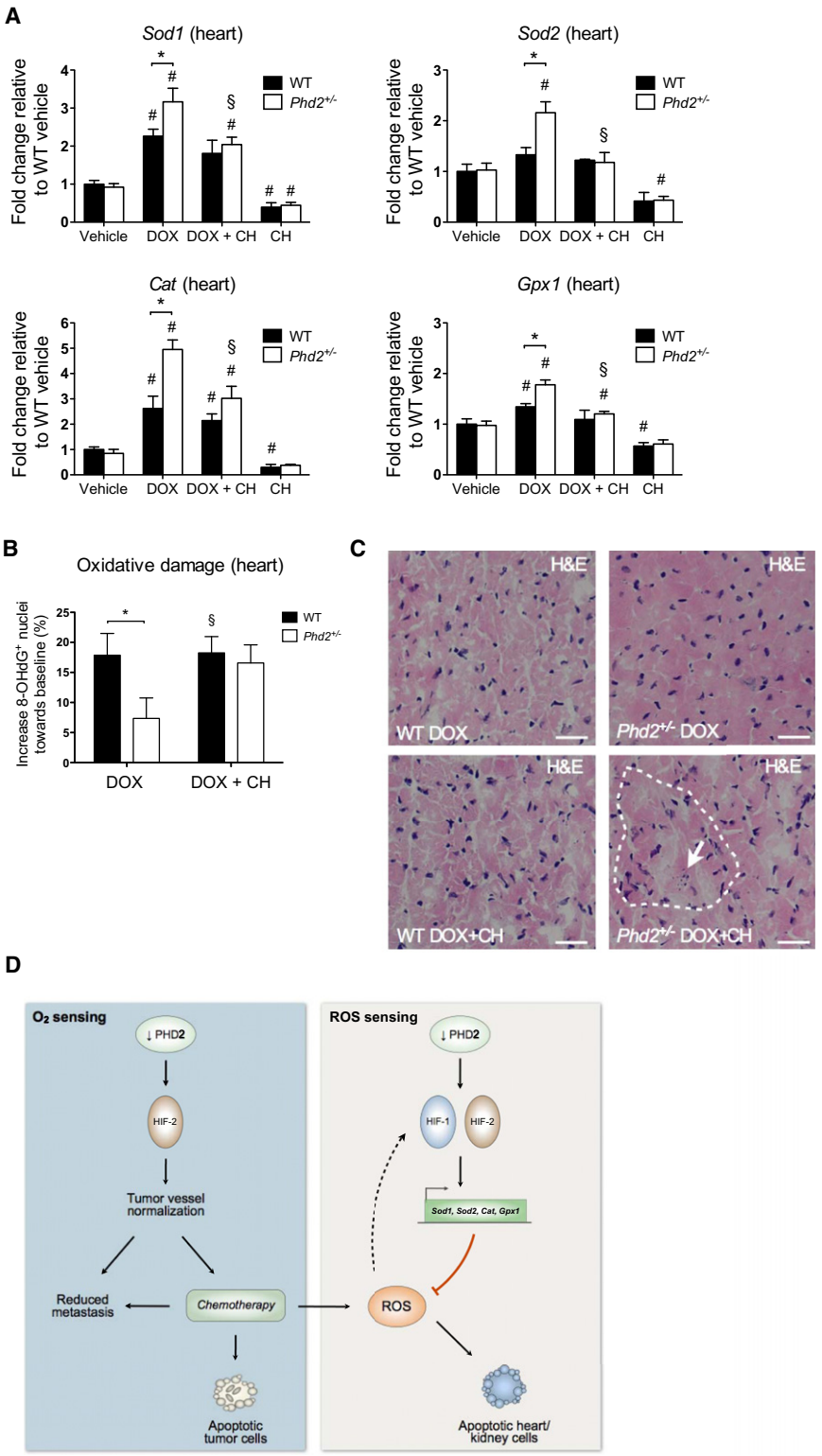

Figure 8. HIF-Inhibition Abrogates Chemoprotection in *Phd2*$^{+/-}$ Mice

(A) RNA levels of AOE in WT and *Phd2*$^{+/-}$ hearts upon combined treatment with DOX and the HIF-inhibitor chetomin (CH; n = 6).

(B) Morphometric quantification of 8-OHdG^{+} nuclei, showing increased oxidative stress in *Phd2*$^{+/-}$ mice upon combined DOX and CH treatment (n = 5).

(C) H&E-stained heart sections show increased myofiber disarray (dotted line) and apoptotic features (arrow) in *Phd2*$^{+/-}$ mice after combined treatment of DOX and CH.

(D) Acting as an oxygen-sensitive enzyme, reduced activity of PHD2 in EC promotes tumor vessel normalization in a HIF-2α-dependent manner, thus optimizing the delivery of chemotherapeutic drugs to the tumor, increasing their antitumor and antimetastatic effects (left panel). In healthy organs, the overall prolyl hydroxylase activity is hampered by chemotherapy-induced reactive oxygen species (ROS), resulting in HIF-1α and HIF-2α stabilization and subsequent transcription of antioxidative defenses (*Sod1, Sod2, Cat*, and *Gpx1*). Genetic deletion of *Phd2* reduces the threshold of HIFs activation and thus favors this feedback loop, which promptly counters oxidative damage and prevents organ failure and tissue demise (right panel). Targeting PHD2 might therefore offer a double advantage in the treatment of oncological diseases.

*p < 0.05 versus WT, #p < 0.05 versus baseline, §p < 0.05 versus *Phd2*$^{+/-}$ DOX. Scale bars denote 100 μm in (C). All graphs show mean ± SEM.

a *Phd2*-deficient environment, suggesting that systemic inhibition of PHD2 might offer beneficial effects in cancer treatment. Further studies are needed to extend these findings to different tumor cell types.

PHD2 inactivation also prevented cardiac and renal toxicity derived by chemotherapy-induced ROS. Inactivation of PHDs predisposes responses to hypoxia and preconditioning stimuli (Aragonés et al., 2009; Eckle et al., 2008; Huang et al., 2008; Hyvärinen et al., 2010; Mazzone et al., 2009; Takeda et al., 2011). Indeed, oxygen consumption in hypoxia is associated with generation of ROS that peaks after tissue reoxygenation; stabilization of HIF-1α and/or HIF-2α have been associated with transcription of antioxidative defenses that protect the cell from oxidative damage (Date et al., 2005; Lee et al., 1997; Martin et al., 2005; Mukhopadhyay et al., 2000; Scortegagna et al., 2003). However, when the production of ROS overwhelms the detoxification capacity of the cell, excessive oxidative damage leads to cell death (Aragonés et al., 2008; Minotti et al., 2004; Shokolenko et al., 2009; Unnikrishnan et al., 2009). The same phenomenon occurs during treatment with doxorubicin and cisplatin (Berthiaume and Wallace, 2007; Pabla and Dong, 2008).

The current study suggests that an initial burst of ROS production by chemotherapeutic drugs is required to stabilize both HIF-1α and HIF-2α and to promote their activity in normoxic conditions. Indeed, when ROS are increased, iron oxidation results in the inactivation of prolyl hydroxylase activity, since this metal is an essential cofactor for these enzymes (Gerald et al., 2004). This feedback loop provides a built-in safety mechanism to diminish tissue damage. *Phd2* (haplo)deficiency decreases the threshold of HIF activation and favors the transcription of antioxidative defenses that further limit the abundance of ROS. A reduction of prolyl hydroxylase activity by chemotherapy-associated ROS production will also trigger the same detoxification program in WT organs, but less efficiently than in *Phd2* (haplo)deficient organs. In other words, by rendering the organs better preadapted to oxidative stress, (haplo)deficiency of *Phd2* promptly counteracts ROS-induced tissue damage. These findings unravel a mechanism for ROS homeostasis by PHD2, which is independent of hypoxia, and implies a relevance of PHD2 in other oxidative stress-related pathophysiological conditions, such as neurodegenerative disorders, diabetes, and aging (Fraisl et al., 2009).

Our data indicate that the involvement of PHD2 in response to chemotherapeutic drugs is highly context and cell-type dependent, since *Phd2* silencing in proliferating cancer cells did not affect AOE in response to doxorubicin: neither did it modify ROS production. However, the factors conferring cell specificity to this response need to be defined. From a therapeutic point of view, our findings support the idea that systemic inhibition of PHD2 might offer chemoprotection of normal organs without promoting chemoresistance in cancer cells.

In our previous study, we show that HIF-2α is mainly responsible for $Phd2^{+/-}$ EC quiescence/normalization (Mazzone et al., 2009); in this study, we show that both HIF-1α and HIF-2α are involved in the detoxification program in $Phd2^{+/-}$ organs. Both HIFs have been previously reported as upstream regulators of an antioxidative response in different cell types (Bertout et al., 2009; Mukhopadhyay et al., 2000; Scortegagna et al., 2003). Genetic inactivation of *Hif2a* reduced the levels of *Sod1*, *Sod2*, *Cat*, and *Gpx1* and resulted in multiple organ failure in developing embryos and neonates (Scortegagna et al., 2003). However, *Phd2* inactivation will lead to simultaneous accumulation of both HIF isoforms, representing a different scenario from the one described in previous studies, showing genetic deletion (or silencing) of *Hif1a* or *Hif2a* (Bertout et al., 2009; Scortegagna et al., 2003; Vengellur et al., 2003, 2011). Overall, the involvement of HIF in favoring tumor vessel normalization and limiting the undesired effects of chemotherapy warrants some caution for considerate use of HIF inhibitors for cancer therapy (Semenza, 2003).

Finally, heterozygous and homozygous deletion of *Phd2* comparably sensitizes the tumor to chemotherapeutic drugs and minimizes their adverse effects. From a molecular point of view, HIF-2α (the main driver of vessel normalization) was higher, but equally elevated in both $Phd2^{+/-}$ and $Phd2^{-/-}$ EC. This is likely due to compensatory mechanisms in *Phd2* null cells, where *Phd3* upregulation might tune down to the heterozygous levels the genetic response triggered by complete loss of *Phd2*, as reported during embryo development (Minamishima et al., 2009). In cardiomyocytes, despite a dose-dependent effect of heterozygous versus homozygous *Phd2* deletion on HIF-1α and HIF-2α stabilization at baseline, in response to doxorubicin, both HIFs reached their plateau in $Phd2^{+/-}$ and $Phd2^{-/-}$ cells, thus displaying a comparable antioxidative response.

To date, PHD2-specific inhibitors are not commercially available, although several screening platforms have been established (Fraisl et al., 2009). It will be clinically relevant to validate these drugs in mouse models of cancer in combination with chemotherapy. At this stage, our study provides insight on how PHD2 can regulate drug delivery to the tumor by sensing oxygen availability and readapting vessel perfusion and can counter the onset of chemotherapy-associated side-toxicity by working as a gatekeeper for ROS production.

EXPERIMENTAL PROCEDURES

More detailed methods can be found in the Supplemental Information.

Syngeneic Tumor Models

10^6 B16F10.9 melanoma (B16) cells or 10^6 Lewis lung carcinoma (LLC) cells were injected subcutaneously. Tumor volumes were measured 3× per week with a caliper and calculated using the formula: $V = \pi \times [\text{width}^2 \times \text{length}] / 6$. At an average of 100 mm^3, mice were randomized for intraperitoneal (i.p.) administration (2.5 mg/kg; 3× per week) of cisplatin (CPt) or doxorubicin (DOX) in B16 or LLC tumor-bearing mice, respectively. In tumor experiments using the $Rosa26^{CreERT2}$ deleter, tamoxifen treatment (1 mg/mouse/day i.p. for 5 consecutive days) was started on the day of cancer cell injection. Housing and all experimental animal procedures were approved by the Institutional Animal Care and Research Advisory Committee of the KU Leuven.

Cisplatin Quantification

The CPt in B16 tumors was quantified by inductively coupled plasma mass spectrometry (ICP820-MS, Varian, USA) or by immunohistochemical staining against CPt DNA-adducts (NKI-159; a gift of Dr. B. Floot, Netherlands Cancer Institute).

Tumor Interstitial Fluid Pressure

Tumor interstitial fluid pressure was evaluated in the central cystic tumor area of subcutaneous LLC tumors using the "wick-in-needle" technique (Hofmann et al., 2006).

Acute or Chronic Doxorubicin Cardiotoxicity

Tumor-free mice were injected with a single dose of 20 mg/kg DOX (i.p.) and assessed for cardiotoxicity after 5 days or with 2.5 mg/kg DOX (i.p.) three times a week for a total of 4 weeks, respectively.

Acute or Chronic Cisplatin Nephrotoxicity

Tumor-free mice were injected with a single dose of 20 mg/kg CPt (i.p.) and assessed for renal toxicity after 3 days or with 2.5 mg/kg CPt (i.p.) three times a week for a total of 4 weeks, respectively.

HIF Activity In Vivo

The adenovirus-associated virus 9 (AAV9) HIF reporter plasmid (AAV9-HRE-LUC) contains a minimal promoter fused to 9 copies of hypoxia-responsive elements (HRE) followed by the firefly luciferase (LUC)(Aragonés et al., 2001) in pSubCMV-WPRE (Paterna et al., 2000). AAV9 particles were generated as previously described (Anisimov et al., 2009). A dose of 0.25×10^{11} viral genomic copies of AAV9-HRE-LUC or the control AAV9-CMV-LUC were injected in the tail vein 3 days before administration of 20 mg/kg DOX or CPt.

Immunoblot and Immunochemistry

Protein extraction was performed using RIPA (50 mM Tris HCl pH 8, 150 mM NaCl, 1% Triton X-100, 0.1% SDS, 0.5% sodium deoxycolate). All methods for histology and immunostainings have been described before (Mazzone et al., 2009).

QRT-PCR

Quantitative RT-PCR (QRT-PCR) was performed as described (Fischer et al., 2007). The Assay ID (Applied Biosystems) or the sequence of primers and probes (when homemade) are listed in the Supplement Experimental Procedures.

Hypoxia and Tumor Perfusion

Tumor hypoxia was detected as before (Mazzone et al., 2009). Tumor perfusion was assessed by injecting intravenously 0.05 mg lectin-FITC (*Lycopersicon esculentum*; Vector Laboratories) or 5 mg high molecular weight (2 MDa) dextran-FITC (Sigma).

Statistics

Data represent mean ± SEM of representative experiments. Statistical significance was calculated by a two-tailed unpaired t test for two data sets and ANOVA followed by a Bonferroni post hoc test for multiple data sets using Prism (GraphPad, Inc.), with $p < 0.05$ considered statistically significant.

SUPPLEMENTAL INFORMATION

Supplemental Information includes seven figures, seven tables, and Supplemental Experimental Procedures and can be found with this article online at http://dx.doi.org/10.1016/j.ccr.2012.06.028.

ACKNOWLEDGMENTS

The authors thank J. Serneels and B. Das for technical assistance. This work was supported by grants from FWO (G.0718.10N) and Stichting tegen Kanker (2010-169). R.L.O., A.-T.H., and V.F. are granted by FWO.

Received: October 12, 2011
Revised: May 8, 2012
Accepted: June 26, 2012
Published: August 13, 2012

REFERENCES

Ameln, A.K., Muschter, A., Mamlouk, S., Kalucka, J., Prade, I., Franke, K., Rezaei, M., Poitz, D.M., Breier, G., and Wielockx, B. (2011). Inhibition of HIF prolyl hydroxylase-2 blocks tumor growth in mice through the antiproliferative activity of TGFβ. Cancer Res. *71*, 3306–3316.

Andersen, S., Donnem, T., Stenvold, H., Al-Saad, S., Al-Shibli, K., Busund, L.T., and Bremnes, R.M. (2011). Overexpression of the HIF hydroxylases PHD1, PHD2, PHD3 and FIH are individually and collectively unfavorable prognosticators for NSCLC survival. PLoS ONE *6*, e23847.

Anisimov, A., Alitalo, A., Korpisalo, P., Soronen, J., Kaijalainen, S., Leppänen, V.M., Jeltsch, M., Ylä-Herttuala, S., and Alitalo, K. (2009). Activated forms of VEGF-C and VEGF-D provide improved vascular function in skeletal muscle. Circ. Res. *104*, 1302–1312.

Anscher, M.S., Chen, L., Rabbani, Z., Kang, S., Larrier, N., Huang, H., Samulski, T.V., Dewhirst, M.W., Brizel, D.M., Folz, R.J., and Vujaskovic, Z. (2005). Recent progress in defining mechanisms and potential targets for prevention of normal tissue injury after radiation therapy. Int. J. Radiat. Oncol. Biol. Phys. *62*, 255–259.

Aragonés, J., Jones, D.R., Martin, S., San Juan, M.A., Alfranca, A., Vidal, F., Vara, A., Mérida, I., and Landázuri, M.O. (2001). Evidence for the involvement of diacylglycerol kinase in the activation of hypoxia-inducible transcription factor 1 by low oxygen tension. J. Biol. Chem. *276*, 10548–10555.

Aragonés, J., Schneider, M., Van Geyte, K., Fraisl, P., Dresselaers, T., Mazzone, M., Dirkx, R., Zacchigna, S., Lemieux, H., Jeoung, N.H., et al. (2008). Deficiency or inhibition of oxygen sensor Phd1 induces hypoxia tolerance by reprogramming basal metabolism. Nat. Genet. *40*, 170–180.

Aragonés, J., Fraisl, P., Baes, M., and Carmeliet, P. (2009). Oxygen sensors at the crossroad of metabolism. Cell Metab. *9*, 11–22.

Berthiaume, J.M., and Wallace, K.B. (2007). Adriamycin-induced oxidative mitochondrial cardiotoxicity. Cell Biol. Toxicol. *23*, 15–25.

Bertout, J.A., Majmundar, A.J., Gordan, J.D., Lam, J.C., Ditsworth, D., Keith, B., Brown, E.J., Nathanson, K.L., and Simon, M.C. (2009). HIF2alpha inhibition promotes p53 pathway activity, tumor cell death, and radiation responses. Proc. Natl. Acad. Sci. USA *106*, 14391–14396.

Bordoli, M.R., Stiehl, D.P., Borsig, L., Kristiansen, G., Hausladen, S., Schraml, P., Wenger, R.H., and Camenisch, G. (2011). Prolyl-4-hydroxylase PHD2- and hypoxia-inducible factor 2-dependent regulation of amphiregulin contributes to breast tumorigenesis. Oncogene *30*, 548–560.

Carmeliet, P., and Jain, R.K. (2011). Principles and mechanisms of vessel normalization for cancer and other angiogenic diseases. Nat. Rev. Drug Discov. *10*, 417–427.

Chan, D.A., Kawahara, T.L., Sutphin, P.D., Chang, H.Y., Chi, J.T., and Giaccia, A.J. (2009). Tumor vasculature is regulated by PHD2-mediated angiogenesis and bone marrow-derived cell recruitment. Cancer Cell *15*, 527–538.

D'Adamo, D.R., Anderson, S.E., Albritton, K., Yamada, J., Riedel, E., Scheu, K., Schwartz, G.K., Chen, H., and Maki, R.G. (2005). Phase II study of doxorubicin and bevacizumab for patients with metastatic soft-tissue sarcomas. J. Clin. Oncol. *23*, 7135–7142.

Date, T., Mochizuki, S., Belanger, A.J., Yamakawa, M., Luo, Z., Vincent, K.A., Cheng, S.H., Gregory, R.J., and Jiang, C. (2005). Expression of constitutively stable hybrid hypoxia-inducible factor-1alpha protects cultured rat cardiomyocytes against simulated ischemia-reperfusion injury. Am. J. Physiol. Cell Physiol. *288*, C314–C320.

Dhar, S., Kolishetti, N., Lippard, S.J., and Farokhzad, O.C. (2011). Targeted delivery of a cisplatin prodrug for safer and more effective prostate cancer therapy in vivo. Proc. Natl. Acad. Sci. USA *108*, 1850–1855.

Eckle, T., Köhler, D., Lehmann, R., El Kasmi, K., and Eltzschig, H.K. (2008). Hypoxia-inducible factor-1 is central to cardioprotection: a new paradigm for ischemic preconditioning. Circulation *118*, 166–175.

Epstein, A.C., Gleadle, J.M., McNeill, L.A., Hewitson, K.S., O'Rourke, J., Mole, D.R., Mukherji, M., Metzen, E., Wilson, M.I., Dhanda, A., et al. (2001). C. elegans EGL-9 and mammalian homologs define a family of dioxygenases that regulate HIF by prolyl hydroxylation. Cell *107*, 43–54.

Fischer, C., Jonckx, B., Mazzone, M., Zacchigna, S., Loges, S., Pattarini, L., Chorianopoulos, E., Liesenborghs, L., Koch, M., De Mol, M., et al. (2007). Anti-PlGF inhibits growth of VEGF(R)-inhibitor-resistant tumors without affecting healthy vessels. Cell *131*, 463–475.

Fraisl, P., Aragonés, J., and Carmeliet, P. (2009). Inhibition of oxygen sensors as a therapeutic strategy for ischaemic and inflammatory disease. Nat. Rev. Drug Discov. *8*, 139–152.

Gerald, D., Berra, E., Frapart, Y.M., Chan, D.A., Giaccia, A.J., Mansuy, D., Pouyssegur, J., Yaniv, M., and Mechta-Grigoriou, F. (2004). JunD reduces tumor angiogenesis by protecting cells from oxidative stress. Cell *118*, 781–794.

Goel, S., Duda, D.G., Xu, L., Munn, L.L., Boucher, Y., Fukumura, D., and Jain, R.K. (2011). Normalization of the vasculature for treatment of cancer and other diseases. Physiol. Rev. *91*, 1071–1121.

Heldin, C.H., Rubin, K., Pietras, K., and Ostman, A. (2004). High interstitial fluid pressure - an obstacle in cancer therapy. Nat. Rev. Cancer *4*, 806–813.

Hofmann, M., Guschel, M., Bernd, A., Bereiter-Hahn, J., Kaufmann, R., Tandi, C., Wiig, H., and Kippenberger, S. (2006). Lowering of tumor interstitial fluid pressure reduces tumor cell proliferation in a xenograft tumor model. Neoplasia *8*, 89–95.

Huang, M., Chan, D.A., Jia, F., Xie, X., Li, Z., Hoyt, G., Robbins, R.C., Chen, X., Giaccia, A.J., and Wu, J.C. (2008). Short hairpin RNA interference therapy for ischemic heart disease. Circulation *118* (14, Suppl), S226–S233.

Hyvärinen, J., Hassinen, I.E., Sormunen, R., Mäki, J.M., Kivirikko, K.I., Koivunen, P., and Myllyharju, J. (2010). Hearts of hypoxia-inducible factor prolyl 4-hydroxylase-2 hypomorphic mice show protection against acute ischemia-reperfusion injury. J. Biol. Chem. *285*, 13646–13657.

Jain, K.K. (2010). Advances in the field of nanooncology. BMC Med. *8*, 83.

Kamphues, C., Wittschieber, D., Klauschen, F., Kasajima, A., Dietel, M., Schmidt, S.C., Glanemann, M., Bahra, M., Neuhaus, P., Weichert, W., and

Stenzinger, A. (2012). Prolyl hydroxylase domain 2 protein is a strong prognostic marker in human gastric cancer. Pathobiology *79*, 11–17.

Kerbel, R.S., and Kamen, B.A. (2004). The anti-angiogenic basis of metronomic chemotherapy. Nat. Rev. Cancer *4*, 423–436.

Kung, A.L., Zabludoff, S.D., France, D.S., Freedman, S.J., Tanner, E.A., Vieira, A., Cornell-Kennon, S., Lee, J., Wang, B., Wang, J., et al. (2004). Small molecule blockade of transcriptional coactivation of the hypoxia-inducible factor pathway. Cancer Cell *6*, 33–43.

Lee, K.A., Lynd, J.D., O'Reilly, S., Kiupel, M., McCormick, J.J., and LaPres, J.J. (2008). The biphasic role of the hypoxia-inducible factor prolyl-4-hydroxylase, PHD2, in modulating tumor-forming potential. Mol. Cancer Res. *6*, 829–842.

Lee, P.J., Jiang, B.H., Chin, B.Y., Iyer, N.V., Alam, J., Semenza, G.L., and Choi, A.M. (1997). Hypoxia-inducible factor-1 mediates transcriptional activation of the heme oxygenase-1 gene in response to hypoxia. J. Biol. Chem. *272*, 5375–5381.

Loges, S., Mazzone, M., Hohensinner, P., and Carmeliet, P. (2009). Silencing or fueling metastasis with VEGF inhibitors: antiangiogenesis revisited. Cancer Cell *15*, 167–170.

Martin, F., Linden, T., Katschinski, D.M., Oehme, F., Flamme, I., Mukhopadhyay, C.K., Eckhardt, K., Tröger, J., Barth, S., Camenisch, G., and Wenger, R.H. (2005). Copper-dependent activation of hypoxia-inducible factor (HIF)-1: implications for ceruloplasmin regulation. Blood *105*, 4613–4619.

Mazzone, M., Dettori, D., Leite de Oliveira, R., Loges, S., Schmidt, T., Jonckx, B., Tian, Y.M., Lanahan, A.A., Pollard, P., Ruiz de Almodovar, C., et al. (2009). Heterozygous deficiency of PHD2 restores tumor oxygenation and inhibits metastasis via endothelial normalization. Cell *136*, 839–851.

Minamishima, Y.A., Moslehi, J., Bardeesy, N., Cullen, D., Bronson, R.T., and Kaelin, W.G., Jr. (2008). Somatic inactivation of the PHD2 prolyl hydroxylase causes polycythemia and congestive heart failure. Blood *111*, 3236–3244.

Minamishima, Y.A., Moslehi, J., Padera, R.F., Bronson, R.T., Liao, R., and Kaelin, W.G., Jr. (2009). A feedback loop involving the Phd3 prolyl hydroxylase tunes the mammalian hypoxic response in vivo. Mol. Cell. Biol. *29*, 5729–5741.

Minotti, G., Menna, P., Salvatorelli, E., Cairo, G., and Gianni, L. (2004). Anthracyclines: molecular advances and pharmacologic developments in antitumor activity and cardiotoxicity. Pharmacol. Rev. *56*, 185–229.

Mukhopadhyay, C.K., Mazumder, B., and Fox, P.L. (2000). Role of hypoxia-inducible factor-1 in transcriptional activation of ceruloplasmin by iron deficiency. J. Biol. Chem. *275*, 21048–21054.

Nakasone, E.S., Askautrud, H.A., Kees, T., Park, J.H., Plaks, V., Ewald, A.J., Fein, M., Rasch, M.G., Tan, Y.X., Qiu, J., et al. (2012). Imaging tumor-stroma interactions during chemotherapy reveals contributions of the microenvironment to resistance. Cancer Cell *21*, 488–503.

Pabla, N., and Dong, Z. (2008). Cisplatin nephrotoxicity: mechanisms and renoprotective strategies. Kidney Int. *73*, 994–1007.

Paterna, J.C., Moccetti, T., Mura, A., Feldon, J., and Büeler, H. (2000). Influence of promoter and WHV post-transcriptional regulatory element on AAV-mediated transgene expression in the rat brain. Gene Ther. *7*, 1304–1311.

Peurala, E., Koivunen, P., Bloigu, R., Haapasaari, K.M., and Jukkola-Vuorinen, A. (2012). Expressions of individual PHDs associate with good prognostic factors and increased proliferation in breast cancer patients. Breast Cancer Res. Treat. *133*, 179–188.

Provenzano, P.P., Cuevas, C., Chang, A.E., Goel, V.K., Von Hoff, D.D., and Hingorani, S.R. (2012). Enzymatic targeting of the stroma ablates physical barriers to treatment of pancreatic ductal adenocarcinoma. Cancer Cell *21*, 418–429.

Rolny, C., Mazzone, M., Tugues, S., Laoui, D., Johansson, I., Coulon, C., Squadrito, M.L., Segura, I., Li, X., Knevels, E., et al. (2011). HRG inhibits tumor growth and metastasis by inducing macrophage polarization and vessel normalization through downregulation of PlGF. Cancer Cell *19*, 31–44.

Schneider, M., Van Geyte, K., Fraisl, P., Kiss, J., Aragonés, J., Mazzone, M., Mairbäurl, H., De Bock, K., Jeoung, N.H., Mollenhauer, M., et al. (2010). Loss or silencing of the PHD1 prolyl hydroxylase protects livers of mice against ischemia/reperfusion injury. Gastroenterology *138*, 1143–1154.

Scortegagna, M., Ding, K., Oktay, Y., Gaur, A., Thurmond, F., Yan, L.J., Marck, B.T., Matsumoto, A.M., Shelton, J.M., Richardson, J.A., et al. (2003). Multiple organ pathology, metabolic abnormalities and impaired homeostasis of reactive oxygen species in Epas1-/- mice. Nat. Genet. *35*, 331–340.

Semenza, G.L. (2003). Targeting HIF-1 for cancer therapy. Nat. Rev. Cancer *3*, 721–732.

Shokolenko, I., Venediktova, N., Bochkareva, A., Wilson, G.L., and Alexeyev, M.F. (2009). Oxidative stress induces degradation of mitochondrial DNA. Nucleic Acids Res. *37*, 2539–2548.

Stockmann, C., Doedens, A., Weidemann, A., Zhang, N., Takeda, N., Greenberg, J.I., Cheresh, D.A., and Johnson, R.S. (2008). Deletion of vascular endothelial growth factor in myeloid cells accelerates tumorigenesis. Nature *456*, 814–818.

Su, Y., Loos, M., Giese, N., Metzen, E., Büchler, M.W., Friess, H., Kornberg, A., and Büchler, P. (2012). Prolyl hydroxylase-2 (PHD2) exerts tumor-suppressive activity in pancreatic cancer. Cancer *118*, 960–972.

Takeda, K., Cowan, A., and Fong, G.H. (2007). Essential role for prolyl hydroxylase domain protein 2 in oxygen homeostasis of the adult vascular system. Circulation *116*, 774–781.

Takeda, Y., Costa, S., Delamarre, E., Roncal, C., Leite de Oliveira, R., Squadrito, M.L., Finisguerra, V., Deschoemaeker, S., Bruyère, F., Wenes, M., et al. (2011). Macrophage skewing by Phd2 haplodeficiency prevents ischaemia by inducing arteriogenesis. Nature *479*, 122–126.

Unnikrishnan, A., Raffoul, J.J., Patel, H.V., Prychitko, T.M., Anyangwe, N., Meira, L.B., Friedberg, E.C., Cabelof, D.C., and Heydari, A.R. (2009). Oxidative stress alters base excision repair pathway and increases apoptotic response in apurinic/apyrimidinic endonuclease 1/redox factor-1 haploinsufficient mice. Free Radic. Biol. Med. *46*, 1488–1499.

Van der Veldt, A.A., Lubberink, M., Bahce, I., Walraven, M., de Boer, M.P., Greuter, H.N., Hendrikse, N.H., Eriksson, J., Windhorst, A.D., Postmus, P.E., et al. (2012). Rapid decrease in delivery of chemotherapy to tumors after anti-VEGF therapy: implications for scheduling of anti-angiogenic drugs. Cancer Cell *21*, 82–91.

Vengellur, A., Woods, B.G., Ryan, H.E., Johnson, R.S., and LaPres, J.J. (2003). Gene expression profiling of the hypoxia signaling pathway in hypoxia-inducible factor 1alpha null mouse embryonic fibroblasts. Gene Expr. *11*, 181–197.

Vengellur, A., Grier, E., and Lapres, J.J. (2011). The Loss of HIF1α Leads to Increased Susceptibility to Cadmium-Chloride-Induced Toxicity in Mouse Embryonic Fibroblasts. J. Toxicol. *2011*, 391074.

Winkler, F., Kozin, S.V., Tong, R.T., Chae, S.S., Booth, M.F., Garkavtsev, I., Xu, L., Hicklin, D.J., Fukumura, D., di Tomaso, E., et al. (2004). Kinetics of vascular normalization by VEGFR2 blockade governs brain tumor response to radiation: role of oxygenation, angiopoietin-1, and matrix metalloproteinases. Cancer Cell *6*, 553–563.